Universidade de Aveiro
Universidade Estadual Paulista “Júlio de Mesquita Filho”
2024

Fernando Eduardo Maturi

Estudo da anomalia estrutural da água líquida usando termometria por conversão ascendente de energia de nanopartículas Brownianas

Study of the structural anomaly of liquid water using upconverting thermometry of Brownian nanocrystals

Universidade de Aveiro
Universidade Estadual Paulista "Júlio de Mesquita Filho"
2024

Fernando Eduardo Maturi

Estudo da anomalia estrutural da água líquida usando termometria por conversão ascendente de energia de nanopartículas Brownianas

Study of the structural anomaly of liquid water using upconverting thermometry of Brownian nanoparticles

Tese apresentada à Universidade de Aveiro para cumprimento dos requisitos necessários à obtenção do grau de Doutor em Física, realizada sob a orientação científica do Doutor Luís António Ferreira Martins Dias Carlos, Professor Catedrático do Departamento de Física da Universidade de Aveiro, do Doutor Carlos António Delgado de Sousa Brites, Professor Auxiliar do Departamento de Física da Universidade de Aveiro e do Doutor Sidney José Lima Ribeiro, Professor Titular do Instituto de Química da Universidade Estadual Paulista "Júlio de Mesquita Filho".

Modalidade alternativa à apresentação de Tese, nos termos dos Artigos 63.º e 64.º do Regulamento de Estudos da Universidade de Aveiro

Trabalho desenvolvido no âmbito do projeto CICECO-Instituto de Materiais de Aveiro, UIDB/50011/2020, UIDP/50011/2020 & LA/P/0006/2020 e Forma da Água (PTDC/NAN-PRO/3881/2020) através da FCT/MEC (PIDDAC).

Trabalho financiado pela FCT através da bolsa de doutoramento UI/BD/151445/2021 e pela União Europeia Horizon 2020 através dos projetos FET Open No. 801305 (NanoTBTech) e Marie Skłodowska-Curie No. 823941 (FUNGLASS). Trabalho parcialmente financiado pelo CNPq (Processo 142566/2018-7).

Dedico esta tese ao povo Brasileiro e Europeu que, através de suas obrigações fiscais, financiaram o desenvolvimento deste trabalho.

o júri

Presidente
President

Prof. Doutor Óscar Emanuel Chaves Mealha
Professor Catedrático, Universidade de Aveiro

Vogais
Members

Prof. Doutor José Luís Campos de Oliveira Santos
Professor Catedrático, Universidade do Porto

Prof. Doutor Ricardo Luiz Longo
Professor Titular, Universidade Federal de Pernambuco

Profa. Doutora Andréa Simone Stucchi de Camargo
Full Professor, Friedrich-Schiller-Universität Jena

Profa. Doutora Lucía Labrador Páez
Profesora Ayudante Doctor, Universidad Complutense de Madrid

Profa. Doutora Maria Rute de Amorim e Sá Ferreira André
Professora Associada com Agregação, Universidade de Aveiro

Prof. Doutor Luís António Ferreira Martins Dias Carlos (Orientador)
Professor Catedrático, Universidade de Aveiro

Prof. Doutor Sidney José Lima Ribeiro (Orientador)
Professor Titular, Universidade Estadual Paulista “Júlio de Mesquita Filho”

Agradecimentos

Agradeço aos meus orientadores Prof. Luís Carlos, Prof. Carlos Brites e Prof. Sidney Ribeiro pela mentoria e orientação científica, para além da oportunidade de crescimento profissional, intelectual e pessoal que me concederam.

Agradeço aos meus colegas dos grupos PhantomG (Departamento Física, Universidade de Aveiro, Aveiro, Portugal) e Laboratório de Materiais Fotônicos (Instituto de Química, Unesp, Araraquara–SP, Brasil) pelos ensinamentos e momentos de diversão e discussão científica/filosófica, que tornaram a jornada do doutoramento mais leve e agradável.

Dou graças aos meu familiares e amigos que, mesmo distantes, me oferecem todo o incentivo e apoio necessário.

Deixo um agradecimento especial aos meus pais e irmã, pelo apoio incondicional ao longo da minha vida, que foi fundamental para a realização dos meus estudos e realização dos meus sonhos.

Por último, mas não menos importante, sou extremamente grato à minha esposa, cujos incentivo, companheirismo e paciência tornaram possível a finalização de mais esta etapa importante da minha vida.

palavras-chave

Água, anomalias, ligações de hidrogénio, termometria de luminescência, lantanídeos, converversão ascendente de energia

Resumo

Embora seja o líquido mais utilizado, a água é uma das substâncias mais intrigantes do planeta Terra. Isso ocorre porque, apesar de apresentar composição química e estrutura molecular simples, a água líquida revela um comportamento extraordinariamente complexo quando sujeita a variações de temperatura e pressão, o que a distingue de outros líquidos comumente utilizados. Essas anomalias no comportamento da água são facilmente observadas em condições de superarrefecimento, quando a água é arrefecida a temperaturas abaixo do seu ponto de congelamento, mantendo-se na fase líquida, e, revelando assim a existência de dois estados líquidos distintos.

Apesar de considerada uma explicação notável para a ocorrência de suas propriedades anómalas, a coexistência desses dois estados líquidos da água é difícil de comprovar em condições normais de temperatura e pressão. Isso exige o desenvolvimento de novas abordagens experimentais para investigar as características peculiares da água que tornam a vida como conhecermos possível em nosso planeta. Dado que a transição entre as estruturas dos dois estados líquidos da água ocorre em nível local, é necessária então a utilização de técnicas capazes de observar as flutuações de eventos microscópicos.

Portanto, este trabalho de doutoramento emprega a técnica de termometria de luminescência como uma ferramenta poderosa para identificar flutuações entre dois tipos de organização de ligações de hidrogénio em moléculas de água dispostas ao redor da superfície de nanopartículas Brownianas. Os resultados obtidos revelam que, além de ser possível identificar domínios líquidos de baixa e alta densidade, o equilíbrio delicado entre a coexistência desses diferentes domínios de água é fortemente influenciado pelo tamanho das nanopartículas e pelo pH do meio aquoso, correspondendo, respetivamente, às variações de temperatura e pressão em um novo diagrama hipotético de fases da água proposto recentemente.

keywords

Water, anomalies, hydrogen bonds, luminescence thermometry, lanthanides, upconversion

abstract

Although water is the most commonly used liquid, it is one of the most intriguing substances on planet Earth. This is because, despite having a simple chemical composition and molecular structure, liquid water exhibits an extraordinarily complex behavior when subjected to variations in temperature and pressure, setting it apart from other commonly used liquids. These anomalies in the behavior of water are easily observed under supercooling conditions, where water is cooled to temperatures below its freezing point, remaining in the liquid phase, thus revealing the existence of two distinct liquid states.

While considered a remarkable explanation for the occurrence of its anomalous properties, the coexistence of these two liquid states of water is difficult to prove under normal conditions of temperature and pressure. This requires the development of new experimental approaches to investigate the peculiar characteristics of water that make life as we know it possible on our planet. Since the transition between the structures of the two liquid states of water occurs at a local level, the use of techniques capable of observing fluctuations in microscopic events is required.

Therefore, this doctoral research work employs the technique of luminescence thermometry as a powerful tool to identify fluctuations between two types of hydrogen bond organizations in water molecules arranged around the surface of Brownian nanoparticles. The obtained results reveal that, in addition to identifying low and high-density liquid domains, the delicate balance between the coexistence of these different water domains is strongly influenced by the size of the nanoparticles and the pH of the aqueous medium, respectively corresponding to variations in temperature and pressure in a newly proposed hypothetical phase diagram of water.

Index

Manuscripts and supporting information compilation

Manuscript 1

Deciphering density fluctuations in the hydration water of Brownian nanoparticles via upconversion thermometry

F. E. Maturi, R. S. R. Filho, C. D. S. Brites, J. Fan, R. He, B. Zhuang, X. Liu, L. D. Carlos

Submitted.

Deciphering density fluctuations in the hydration water of Brownian nanoparticles via upconversion thermometry

Fernando E. Maturi[1,2], Ramon S. Raposo Filho[1], Carlos D. S. Brites[1], Jingyue Fan[3], Ruihua He[3], Bilin Zhuang[4], Xiaogang Liu[3], and Luís D. Carlos[1]**

[1] Phantom-g, CICECO - Aveiro Institute of Materials, Department of Physics, University of Aveiro, 3810-193 Aveiro, Portugal

[2] Institute of Chemistry, São Paulo State University (UNESP), 14800-060 Araraquara-SP, Brazil

[3] Department of Chemistry, National University of Singapore, 117543 Singapore, Singapore

[4] Harvey Mudd College, 301 Platt Boulevard, California 91711, USA

*E-mail: chmlx@nus.edu.sg; lcarlos@ua.pt

Abstract: We investigate the intricate relationship between temperature, pH, and Brownian velocity in a spectrum of differently sized upconversion nanoparticles (UCNPs) dispersed in water. These UCNPs, acting as nano-rulers, offer insights into assessing the relative proportion of high-density and low-density liquid in the surrounding hydration water. The study reveals a size-dependent reduction in the onset temperature of liquid-water fluctuations, indicating an augmented presence of high-density liquid domains at nanoparticle surfaces. The observed upper-temperature threshold is consistent with a hypothetical phase diagram of water, validating the two-state model. Moreover, increasing pH disrupts water molecule organization, similar to external pressure effects, allowing simulation of the effects of temperature and pressure on hydrogen bonding networks. The study highlights the versatility of UCNPs as tools to quantify high-density/low-density liquid ratios and sheds light on the intricate interplay between water and diverse interfaces. The findings underscore the significance of the surface-to-volume ratio in suspended nanoparticles or biomolecules for understanding liquid fluctuations and water behavior at charged interfaces.

1. Introduction

Liquid water is the main constituent of the human body and covers the majority of Earth's surface. It plays a vital role in a myriad of biological, chemical, physical, geological, industrial, and environmental processes.[1-7] In addition to its chemical properties as a solvent, proton transfer medium, and active component of reactions, the physical properties of water are also of fundamental relevance.[8] Although water is the most commonly used liquid, its complex behavior under varying pressure and temperature conditions leads to numerous anomalies in its properties that differ significantly from those of other commonly used liquids. To date, over sixty anomalous properties have been reported for water,[9-12] including a minimum specific heat at 308 K, a negative thermal expansion coefficient below 277 K, and a minimum isothermal compressibility at 319 K.

The underlying reason for these anomalous characteristics is related to water's remarkable ability to form strong and directional hydrogen bonds. As these hydrogen bonds are constantly breaking and reforming on a picosecond timescale, fluctuations occur in the local structure of water, leading to the emergence of water motifs with different densities.[11,12] Nowadays, two contrasting schools of thought seek to explain the anomalous properties of water by investigating its structural fluctuations. One proposes that density fluctuations follow a unimodal distribution as predicted by continuous distribution models for water.[13-15] The other argues that these anomalies stem from the coexistence of two distinct arrangements of water molecules that have different physical properties (*e.g.*, the density differs by about 20%[16]) and which become increasingly well-defined upon supercooling: a low-density liquid (LDL) and a high-density liquid (HDL).[4,8,11] While LDL is an open tetrahedral configuration with predominantly low-energy H-bonds, HDL is a network with shorter and highly disordered H-bonds.[17-23]

This two-state scenario appears nowadays very likely, as both theoretical[24-29] and experimental results[30-41] support the existence of a liquid-liquid critical point located in the supercooled liquid region of the water phase diagram, separating a one-phase region from a two-phase region where the LDL and HDL patches coexist, separated by a first-order transition line.[4,11,42-44] The coexistence of these two structural motifs of water has been observed both *in silico*[42,45-47] and experimental[22,48-54] works, especially upon supercooling. Although further experimental evidence for inhomogeneous structures of liquid water and fluctuations between HDL and LDL patches were provided by the isosbestic point in the temperature-dependent OH stretching Raman signal,[55,56] temperature-dependent infrared spectra of liquid water,[57] optical Kerr effect measurements,[58] and X-ray absorption and emission spectroscopy,[43,48-50,59] the

coexistence of these fluctuations at ambient conditions and their implications remain elusive and controversial.[13,18,22,60-67] Nonetheless, showcasing two distinct arrangements of water molecules and their fluctuations is crucial, as it has the potential to revolutionize our understanding of biochemistry and reveal that life-supporting conditions may hinge on the presence of two kinds of H-bond organization in liquid water.[1,3,68]

Little is known about the topology of liquid water, specifically regarding the existence of motifs forming the H-bond networks such as rings, clathrates, and clusters, which, although numerically proposed through molecular dynamics,[16,46,69,70] have not been experimentally observed. This knowledge gap arises because techniques commonly employed to investigate density fluctuations in liquid water and H-bond network structures are limited to a length scale of approximately 1 nm (Fig. 1). Therefore, there is a strong demand for experimental techniques to microscopically decipher H-bond structures in liquid water, as well as in aqueous solutions of electrolytes, suspensions of biomolecules, and inorganic materials. These systems have garnered growing attention due to their potential to unveil the intricate relationship between charged interfaces, high-to-low density liquid fluctuations, and their role in the formation of large-scale H-bond supramolecular structures, as suggested by molecular dynamics simulations of the hydration shell of lysozyme protein.[71] Supramolecular structures of orientationally ordered water as large as 1 μm have been reported in light scattering measurements of aqueous solutions of low molar mass compounds,[72-74] and in wide-field second harmonic microscopy of divalent cations interacting with water and negatively charged freestanding lipid bilayers,[75,76] although not explicitly connected to HDL and LDL domains.

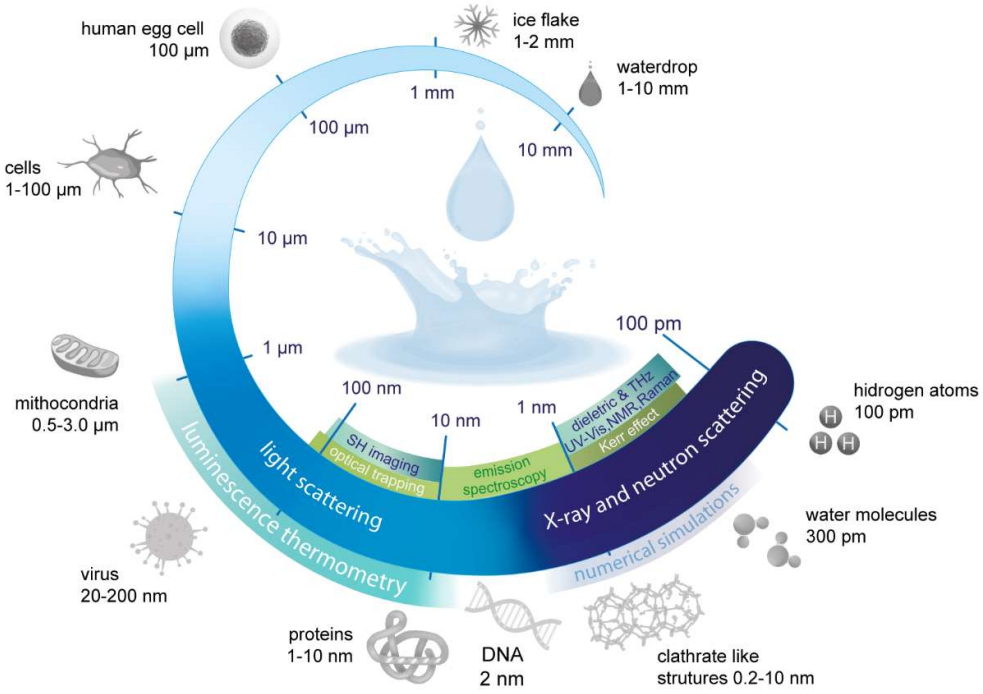

Fig. 1 Infographic of the various techniques used to investigate anomalies in liquid water across different length scales. The temperature dependence of the H-bond networks has been explored at different length scales. While X-ray and neutron scattering, numerical simulations, Kerr effect, dielectric, THz, UV-Vis, NMR, and Raman spectroscopies operate at the length scale of hydrogen atoms and water molecules, second harmonic (SH) imaging works at longer scales. Light scattering and luminescence nanothermometry, as shown in this work, can also be used up to a submicrometric length scale.

In recent years, there has been extensive research into the temperature dependence of the optical properties of a wide range of water-suspended materials such as quantum dots,[53] plasmonic[77] and luminescent[78] nanoparticles, organic molecules,[79-81] and trivalent lanthanide-based materials,[82-84] including upconverting nanoparticles (UCNPs).[85-87] The temperature at which these materials exhibit a notable change in their optical properties, is often referred to as the crossover temperature (T_c).[53] It predominantly falls within the 320–340 K range and coincides with the minimum of the isothermal compressibility of water.[51] Surprisingly, although some of these measurements have been interpreted in the light of the two-state model of water,[53,80] the observed bilinear trend has not been explicitly attributed to the presence of HDL and LDL motifs or the fluctuations between them. To the best of our knowledge, there exists only one paper that explores the intriguing relationship between the bilinear temperature dependence of the instantaneous Brownian velocity of $NaYF_4$:Yb/Er UCNPs suspended in water and the high-to-low density liquid fluctuations.[87] These experimental data, corroborated

by molecular dynamics simulations, elucidated a geometric phase transition where the LDL phase percolates below 330 K. T_c, in this context, was interpreted as the onset of fluctuations between high- and low-density water.[87]

In the present work, we delve into the unique ability of upconversion nanothermometry[88] to measure the temperature and pH dependence of the Brownian velocity[89] of UCNPs of varying sizes (15-106 nm diameter) dispersed in water (so-called nanofluids, Supplementary Section I). We estimate an upper-temperature threshold for the liquid water density fluctuations in the region dominated by HDL domains at ambient conditions, which agrees with the value suggested in the hypothetical phase diagram of liquid water under ambient conditions (Supplementary Fig. S1).[4,8,11,24,32,90] We also show that raising the pH of the nanofluids fragments the LDL domains, similar to increasing pressure in this phase diagram. Furthermore, our results provide new insights into the relative proportion of HDL and LDL motifs that coexist around the nanoparticle surface at ambient conditions in the hydration water. We find that the high-to-low-density liquid fluctuations depend on the size of the suspended nanoparticle and the pH of the nanofluid. As the size increases, the relative proportion of HDL domains increases, while as the surface charge increases (controlled by pH), the relative proportion of LDL patches increases.

2. Results and discussion

2.1. Uniqueness of H-bond networks in water

We measured the instantaneous Brownian velocity of $NaGdF_4$:Yb/Er(18%/2%)@$NaGdF_4$ core-shell UCNPs of 15 nm (in diameter, d) dispersed in water (pH = 5.10), heavy water (D_2O), and ethanol (EtOH) at a volume fraction of 0.085% (Fig. 2a). The colloidal stability of the nanofluids and the size distribution of the UCNPs are presented in Supplementary Figs. S2-S6. The experimental setup, similar to that in Reference 89, is described in Supplementary Sections II and III (Supplementary Figs. S7-S10). As the solvent density (ρ) increases, the Brownian velocity decreases because denser liquids have a higher effective mass (defined as the combined mass of the UCNPs and half of the liquid mass moving cooperatively with them[91]). This is well illustrated by the difference in density between EtOH and D_2O (781 and 1105 $kg \cdot m^{-3}$, respectively, at 303 K[92]). The lower density of EtOH facilitates the faster motion of the UCNPs within the nanofluid, whereas the higher density of D_2O results in a considerably slower motion (Fig. 2a). An analogous density dependence was observed in the Brownian velocity of UCNPs containing an oleic acid coating and dispersed in toluene and cyclohexane, with an increase in solvent density decelerates the motion of particles.[87]

Notably, the Brownian velocity of the UCNPs in the aqueous nanofluids exhibits a bilinear trend, regardless of the size of the particles (Fig. 2b). This behavior is attributed to the presence of two distinct motion regimes for UCNPs. At $T<T_c$ (300–330 K), there are HDL fluctuations into more voluminous LDL regions within the HDL dominant phase. Consequently, this gives rise to a greater effective mass of the nanoparticles, resulting in lower Brownian velocity values. Conversely, when the temperature exceeds the critical temperature (T) threshold ($T>T_c$), density fluctuations cease because all LDL motifs were already converted into HDL ones. This leads to a liquid state characterized by localized fluctuations within the HDL phase, leading to higher Brownian velocity values.

It is worth stressing that the obtained T_c value is in close correspondence with the minimum value of the isothermal compressibility of liquid water, which is related to the change from a more to a less organized tetrahedral organization due to the density increase.[51] Since isothermal compressibility depends on fluctuations in density indicating a relative change of the volume, the similarity between the T_c values of the Brownian velocity of UCNPs and the minimum isothermal compressibility of liquid water is explained by the change in volume of the HDL and LDL motifs with increasing temperature.[93]

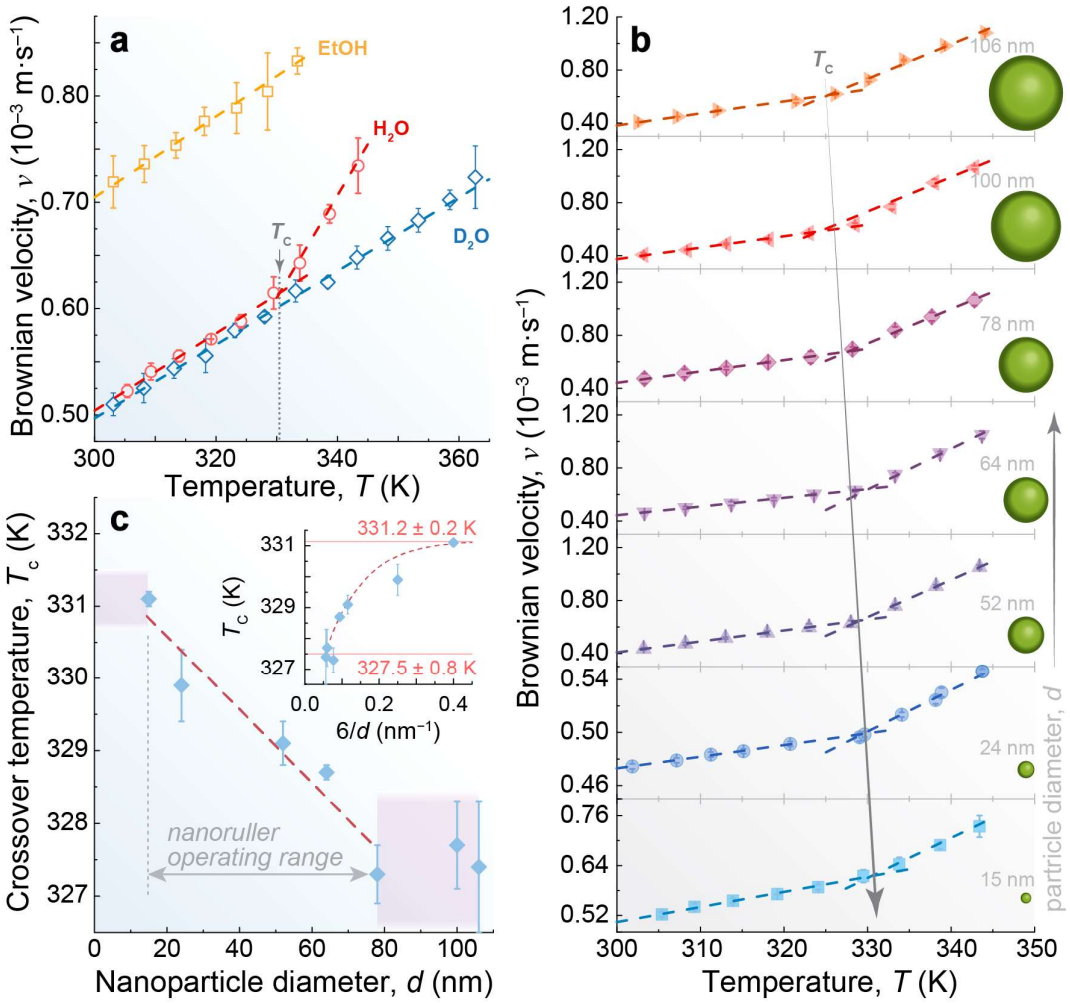

Fig. 2 Solvent effect and size dependence in the Brownian velocity of UCNPs. (a) Temperature-dependent Brownian velocity of the 15 nm UCNPs suspended in EtOH, H_2O, and D_2O. The grey arrow highlights the existence of a crossover temperature in the water-suspended UCNPs around 330 K, indicating the anomalous behavior of water. **(b)** Temperature-dependent Brownian velocity of different-sized UCNPs (15–106 nm) at pH = 5.10. **(c)** Size-dependent crossover temperature of the nanofluids from panel **b**, where the red dashed line is a guide for the eyes, highlighting the operating range of sizes that can be used to probe the different motifs of liquid water. The inset presents the T_c dependence on the surface-to-volume ratio ($\boldsymbol{S/V = 6/d}$). The lines are guides for the eyes.

Compared to liquid water, the weaker hydrogen bonds in ethanol[94] result in a continuous linear increase in the Brownian velocity of UCNPs upon heating. Although the low boiling point of EtOH limits its study at temperatures above 333 K, the lack of tetrahedral arrangements means that T_c is not expected to occur.[95] Regarding liquid D_2O, while the HDL and LDL motifs have also been identified,[96,97] the presence of isotopic quantum effects generates a more ordered structure that enhances thermodynamic stability,[98,99] displacing the Widom line toward

higher temperatures.[32] Then, T_c might be shifted to higher temperatures, as suggested by the displacement of the maximum density and minimum isothermal compressibility,[100,101] potentially residing beyond the confines of the liquid phase. However, recent findings on the 3D confinement of light and heavy water within zwitterionic liposomes of different sizes, as determined through second harmonic imaging and scattering experiments, have yielded a noteworthy conclusion: the H-bond networks in D_2O differ not only at sub-nanometric length scales but also at length scales up to ~100 nm.[76] The reason why the Brownian velocity of UCNPs dispersed in heavy water displays an uninterrupted linear increase from room temperature to the boiling point, similar to the behavior observed for water at temperatures below T_c (Fig. 2a), can be simply explained by the much larger spatial extent over which H_2O molecules interact (corresponding to a much larger spatial extent for low-to-high-density liquid water fluctuations).

2.2. The particle size dependence of the HDL/LDL proportion

We observed a pronounced reduction in the T_c values of the nanofluids as the diameter d of the UCNPs increases (Fig. 2c). To understand this intriguing size-dependent trend and due to the quasi-spherical morphology of UCNPs (Supplementary Fig. S5), we investigated this dependence using their surface-to-volume (S/V) ratio. As this ratio progressively increases (as $d \rightarrow 0$), T_c asymptotically converges towards a limit of 331.2 ± 0.2 K. This temperature should therefore correspond to the onset temperature of the fluctuations between high and low-density liquid states in pure water ($d = 0$ in Fig. 2c). Interestingly, this upper-temperature threshold for fluctuations in the HDL domain-dominated region at ambient conditions agrees with the value (325.0 ± 1.0 K) estimated from the hypothetical phase diagram of water under ambient conditions published in References 4,8 (Fig. 3 and Supplementary Fig. S1).

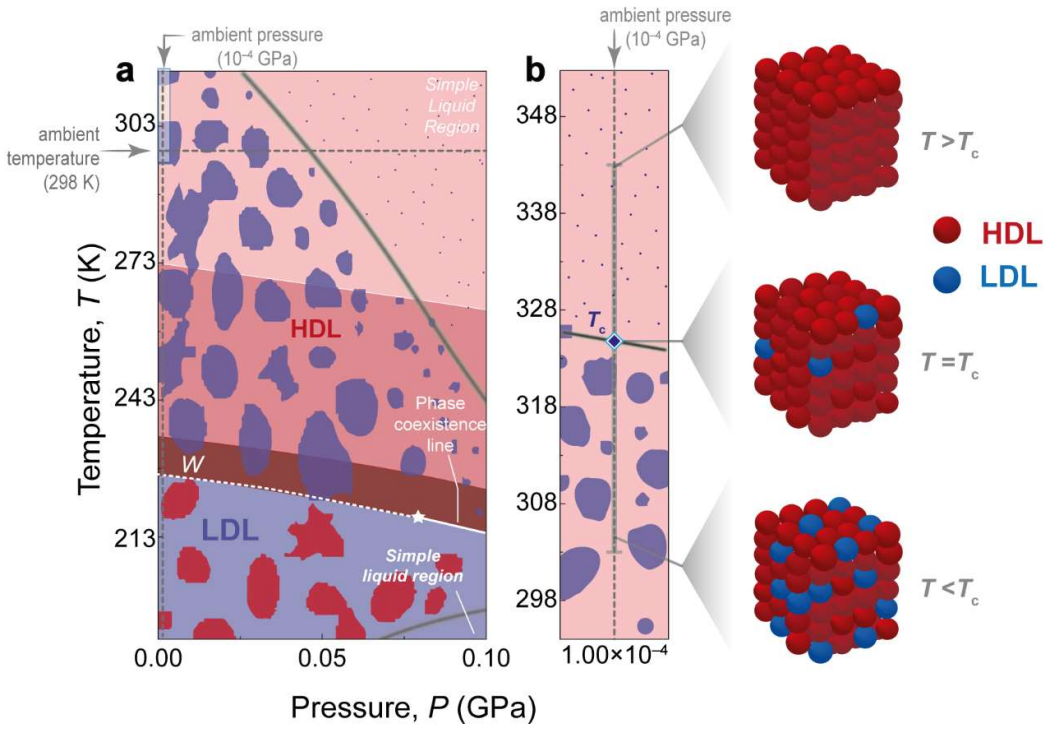

Fig. 3 Hypothetical phase diagram of liquid water. (a) Coexistence of HDL (red) and LDL (blue) domains near the Widom line (W). Below W, LDL dominates with fluctuations in HDL domains whereas above W, HDL dominates with LDL fluctuations. The white star represents the liquid-liquid critical point. Moving away from the critical point, fluctuations decrease in size, as indicated by the blobs. The grey line outlines the "funnel of life," where water exhibits unusual properties crucial for life maintenance. Outside the funnel, at higher temperatures, only local fluctuations occur in the HDL liquid (indicated by small red dots on the blue background). Adapted and modified from Reference 8. **(b)** Zooming into the shadowed area in panel (a) shows the upper-temperature limit of the "funnel of life" at ambient pressure, corresponding to the crossover temperature T_c (diamond), and illustrative schemes of the temperature dependence of high-to-low density liquid fluctuations.

Furthermore, we hypothesize that the decrease in the T_c of the aqueous nanofluids derived from Fig. 2c compared to pure water stems from a decrease in high-to-low-density liquid water fluctuations as a consequence of the prevalence of a higher concentration of HDL patches relative to LDL regions in the volume of nanofluid moving cooperatively with UCNPs. Notably, this hypothesis corroborates previous findings, both experimental[102] and *in silico*,[71] about the hydration water of the lysozyme protein. This hydration water (defined as the water molecules encompassing the protein within a 0.6 nm shell[71]), exhibits local distortions when compared to bulk water. For instance, its density is much higher than that of the bulk[103] and the dielectric constant of interfacial water in the double layer is much lower than that of bulk water.[104] These distortions induce a different ordering of water molecules at the interface,

characterized by a higher concentration of HDL domains than LDL domains, compared to bulk water.[71,102] Like the impact of the lysozyme protein in liquid water, the presence of UCNPs also influences the local structure of water within the aqueous nanofluids. Consequently, nanofluids with lower S/V ratios (larger UCNPs) contain a relatively smaller proportion of HDL domains in the hydration shell of the nanoparticles, leading to lower T_c values (Fig. 2c). When $d > 78$ nm, T_c reaches a plateau at approximately 327.5 K. This occurs because the S/V ratio experiences negligible changes beyond this size threshold (S/V increases by a factor of ~5.2, as d decreases from 78 to 15 nm, but only by ~1.4 times, as d decreases from 106 nm to 78 nm). Remarkably, the T_c of ligand-free and silica-coated UCNPs of comparable size is similar (Fig. 2c), suggesting an analogous relative HDL/LDL proportion at the particle surface, in agreement with an identical charge density of the water-silica and water $NaYF_4$ interfaces ($|\zeta| \sim 35$ mV, Supplementary Figs. S3, S4).

2.3. The dependence of Brownian velocity and crossover temperature on the pH

The vicinity of the UCNPs can be sensitively influenced by local ions and ligands, with effects already occurring at extremely low concentrations.[105] Fine-tuning the pH of suspensions at the water-silica interface was found to induce changes in charge density, impacting the orientation of water molecules.[103,106] Recent surface-enhanced infrared absorption spectroscopy results have also shed light on the influence of pH on hydrogen and water binding energies on platinum surfaces.[107] Also, a pH dependence of the onset temperature of the anomaly related to the minimum isothermal compressibility of liquid water was reported for aqueous suspensions, including 1-methyl-5-nitroindoline,[80] Eu^{3+} complexes,[82,83] and $NaYF_4$:Yb/Er UCNPs.[86] These findings suggest a potential role of pH in influencing high-to-low-density fluctuations within aqueous nanofluids.

To explore this possibility, we evaluated the temperature-dependent Brownian velocity of the UCNPs dispersed in aqueous nanofluids with systematically varied pH values from 2.70 to 8.50 (Fig. 4a for d = 15, 64, and 78 nm and Supplementary Fig. S11 for d = 24, 52, and 106 nm). Except for pH values between 7.0 and 8.0, the measured absolute zeta potential values, $|\zeta| > 20$ mV, indicate stability with no UCNP aggregation (Supplementary Figs. S3, S4).

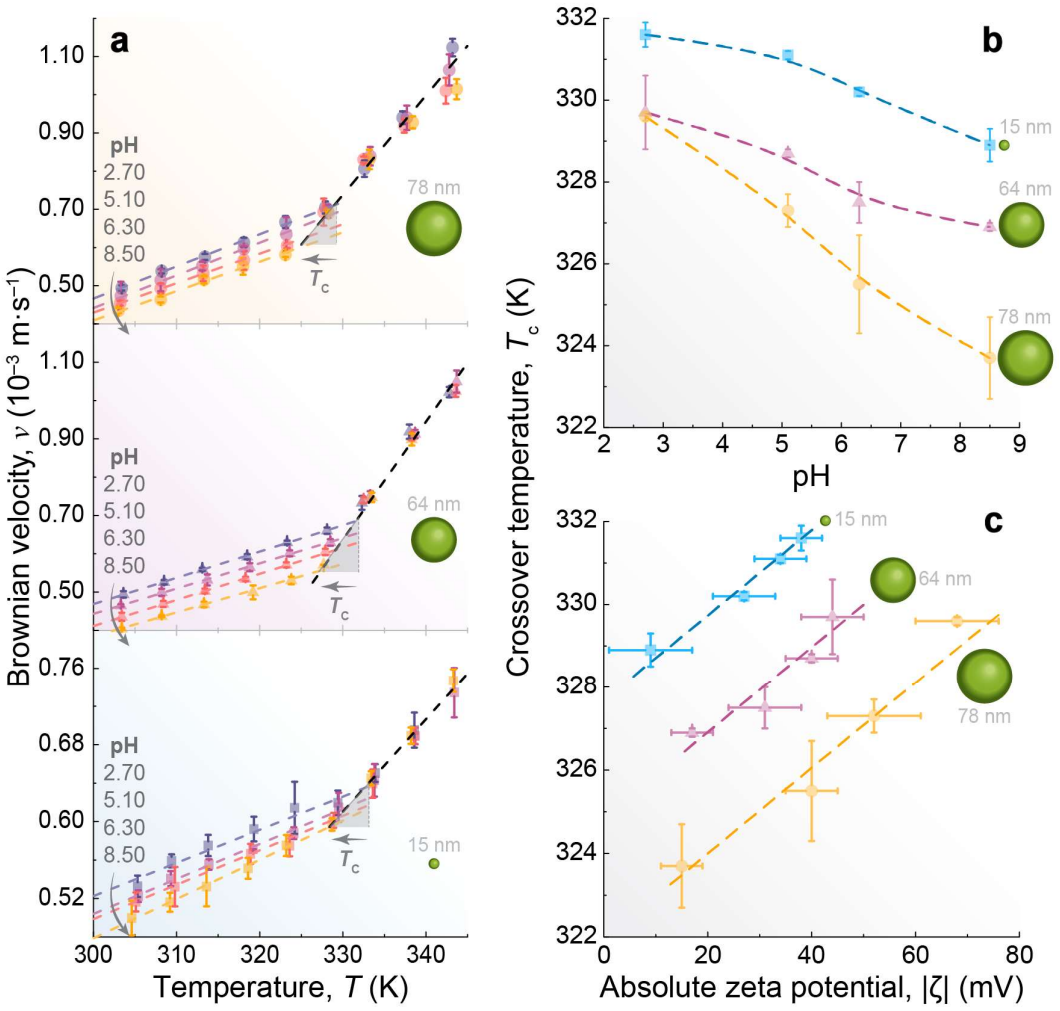

Fig. 4 Correlation between crossover temperature, pH, and zeta potential. (a) Effect of the pH on the Brownian velocity of UCNPs with diameters within the nano-rullers' operating range, as defined in Fig. 2c. The lines are the best linear fits at each pH for $T<T_c$ and the same linear fit for all the pH values for $T>T_c$ ($r^2>0.98$ for all samples). T_c as a function of **(b)** pH and **(c)** |ζ|. The lines are guides to the eyes.

The pH exerts a notable influence on Brownian velocity, with an increase in pH leading to a reduction in Brownian velocity for $T<T_c$, while the pH dependence becomes negligible for $T>T_c$. This primarily impacts LDL domains, present only for $T<T_c$. Increasing pH weakens the H-bond network due to an increased concentration of OH^- ions, disrupting the tetrahedral organization of LDL domains due to their voluminous planar structure.[108] Increasing pH triggers the fragmentation of LDL domains into smaller ones, while keeping the HDL/LDL ratio, leading to a deceleration in the motion of the UCNPs. This effect mirrors the application of high pressures, as suggested by previous neutron diffraction measurements[108,109] and Monte

Carlo simulations.[110] As pressure increases, at a constant temperature, there is a fragmentation of LDL domains (Fig. 3 and Supplementary Fig. S1). However, recent machine learning-based molecular dynamics simulations of ions in salt water have shown that the ions do not homogeneously distort the structure of water, but instead have localized structural effects in the first solvation shell.[111] Our results agree with this scenario, as raising the pH of the nanofluids is an ingenious strategy for simulating a pressure-like effect and evaluating microscopic changes in H-bond networks.

The decrease in Brownian velocity upon increasing pH results in the concomitant decrease in T_c values (Fig. 4b), indicating that low-to-high-density liquid fluctuations at nanoparticle surfaces cease at lower temperatures in basic media compared to an acidic one. To explain this dependence, we consider the influence of pH on the surface charge of UCNPs, with experiments demonstrating how surface charge controls water structure near the interface. The fine-tuning of pH affects the orientation extent of water molecules near the interface, as reported for water-silica interfaces.[103,104] Therefore, to study the effect of pH on the electric double layer of UCNPs, the zeta potential of the distinct aqueous nanofluids was measured. Our results show a decrease in $|\zeta|$ as pH increases (Supplementary Fig. S4) in good accordance with previous reports on upconverting[112] and plasmonic[105] nanoparticles. This mirrors the trend observed for T_c (Fig. 4b and Supplementary Fig. S12), highlighting how the presence of ions in the medium can affect the surface charge of the UCNPs. The increase in electrostatic repulsion of the UCNPs causes a higher T_c (Fig. 4c). A hypothesis is proposed that a greater surface charge (or the potential at the slipping plane) requires more thermal energy to activate HDL-to-LDL fluctuations at the nanoparticle interface. Consequently, more LDL domains exist in the hydration water of the particles. This hypothesis agrees with simulations conducted by Gallo's group, indicating a slower rate decrease in LDL domains at the biomolecule interface with rising temperature.[71] Moreover, for a constant $|\zeta|$ value, nanofluids with smaller UCNPs exhibit a higher T_c, consistent with the findings in Fig. 2c. It is noteworthy that the same conclusion can be drawn exclusively from upconversion thermometry and by combining upconversion thermometry with zeta potential measurements. Similar results were reported by Kim *et al.*,[104] demonstrating how temperature changes the interfacial structure of water by mitigating the effect of surface charge at water-oil interfaces.

Interestingly, Barisik *et al.*[111] showed that, at a constant pH, the surface charge density of Si-NPs decreases with increasing particle size until it stabilizes after reaching a critical diameter of 100 nm. A similar trend was observed for metal oxide nanoparticles.[112] These

findings align with our T_c size-dependence results (Fig. 2c), revealing a decrease in T_c with increasing particle size up to a critical value (> 78 nm), beyond which it remains constant.

Conclusions

In summary, our study systematically investigated the impact of temperature and pH on Brownian velocity in a range of UCNPs (15-106 nm diameter) dispersed in water. We consistently observed a decrease in the onset temperature of high-to-low-density liquid water fluctuations with increasing nanoparticle size, indicative of an increased presence of HDL domains at nanoparticle surfaces. UCNPs, therefore, behave as nano-rulers for assessing HDL/LDL proportion in surrounding hydration water.

Moreover, the upper-temperature threshold for these fluctuations, as predicted by our experiments, agrees with values proposed in the hypothetical phase diagram of water under ambient conditions based on the two-state model. Additionally, we have shown that increasing pH disrupts the tetrahedral organization of water molecules, akin to external pressure on pure water. By precisely controlling both UCNP size and pH levels, we have simulated the effects of temperature and pressure on HDL and LDL hydrogen bonding networks, mirroring predictions in the hypothesized phase diagram. Within nanofluids, the local environment around nanoparticles exerts a significant influence on their physical-chemical properties, being different from bulk due to interaction with the particle surface.[105] This work elegantly underscores the substantial impact of these interactions, serving as compelling evidence of this effect for the specific example of luminescent nanoparticles. It demonstrates that the versatility of UCNPs, with modifiable size and surface properties, makes them invaluable for experimentally quantifying HDL/LDL proportions in the hydration water surrounding particles.

These findings resonate with the intricate interplay between water and various nonpolar media, metals, oxides, and biomembranes, emphasizing the importance of water charge-asymmetrical molecular configuration at interfaces.[75,103,104] In conclusion, our results provide compelling experimental evidence regarding the significance of the S/V ratio of suspended nanoparticles or biomolecules in understanding the dynamics of high-to-low-density liquid fluctuations and water behavior at charged interfaces.

Experimental section

Synthesis of upconverting nanoparticles. $NaGdF_4$:Yb/Er(18/2%)@$NaGdF_4$ (average diameter 15 nm, core-shell), $NaYF_4$:Yb/Er(18/2%)@$NaYF_4$ (average diameter 24 nm, core-

shell), $NaYF_4$:Lu/Yb/Er(40/18/2%) (average diameter 52 nm, core-only), $NaYF_4$:Lu/Yb/Er(47/18/2%) (average diameter 64 nm, core-only), $NaYF_4$:Lu/Yb/Er(47/18/2%) (average diameter 78 nm, core-only), $NaYF_4$:Lu/Yb/Er(47/18/2%)@SiO_2 (average diameter 100 nm, core-shell), and $NaYF_4$:Lu/Yb/Er(50/18/2%) (average diameter 106 nm, core-only) ligand-free UCNPs were synthesized through a coprecipitation method based on a previous report.[113] The detailed synthesis procedure and the characterization of the UCNPs are described in Supplementary Section I.

Preparation of the nanofluids. Aqueous nanofluids containing ligand-free UCNPs were obtained by adjusting the pH of water between 2.70 and 5.10 by adding aqueous solutions of sodium hydroxide or hydrochloric acid (0.1 $mol \cdot L^{-1}$) at a volume fraction (ϕ) of 0.085%. The aqueous nanofluids of 15 nm UCNPs were freeze-dried and the resulting powder was dispersed in heavy water and ethanol under sonication to obtain the corresponding nanofluids at ϕ = 0.085%. A detailed description of pH measurements and the preparation of nanofluids is presented in Supplementary Section I.

Upconversion spectroscopy. The upconverting emission spectra of the nanofluids were recorded using the experimental setup shown in Supplementary Fig. S7. A quartz cuvette (9F-Q-10, Starna Cells) filled with 0.50 mL of the nanofluids was irradiated with a near-infrared 980 nm continuous-wave laser diode (DL980-3W0-T, CrystaLaser) operating with a power density P_D = 62 $W \cdot cm^{-2}$. The excitation radiation was collimated with a plano-convex lens (LA1145-AB, Thorlabs). The upconversion emission spectra were registered with a USB portable spectrometer (Maya 2000 Pro, Ocean Insight) coupled to an optical fiber (P600-1-UV-VIS, Ocean Insight). A short pass filter (FESH0750, Thorlabs) was used to cut off the 980 nm laser signal from the emission spectra. The temperature of the nanofluids was increased through the Joule effect by attaching a Kapton thermofoil heater (HK6906, Minco) in thermal contact with one side of the cuvette containing the nanofluids. This setup allows us to control both the initial temperature and the temperature rise. Further information is provided in Supplementary Section II.

Measurement of temperature through upconversion nanothermometry. The luminescence intensity ratio between the emission bands corresponding to the Er^{3+} $^2H_{11/2} \rightarrow {}^4I_{15/2}$ (I_H, 510–534 nm) and $^4S_{3/2} \rightarrow {}^4I_{15/2}$ (I_S, 534–554 nm) transitions was used to define a thermometric

parameter ($\Delta = I_H/I_S$) and predict the absolute temperature T of the nanofluids as detailed in Supplementary Section III.

Determination of the Brownian velocity of the UCNPs in the nanofluids. The emission spectra were measured at different distances x_i from the Kapton thermofoil heater to construct time-dependent temperature profiles through upconversion nanothermometry. An excellent linear correlation between x_i and the onset time (the time at which the temperature rises above its uncertainty) was systematically obtained. The slope of the linear fit to each dataset represents the Brownian velocity of the UCNPs in the nanofluids. Further details are provided in Supplementary Sections IV and V.

Acknowledgments

This work was partially developed under the project CICECO-Aveiro Institute of Materials UIDB/50011/2020, UIDP/50011/2020 & LA/P/0006/2020, financed by funds through the FCT/MEC (PIDDAC). This work was also financially supported by the project Shape of Water (PTDC/NAN-PRO/3881/2020) through Portuguese funds. F.E.M. acknowledges funding from the European Union's Horizon 2020 research and innovation program under the Marie Sklodowska-Curie grant agreement No. 823941 (FUNGLASS) and financial support from the Foundation for Science and Technology (FCT) through the Portuguese research grant UI/BD/151445/2021. The authors thank Ricardo Longo (Federal University of Pernambuco), Christoph Rose-Petruck (Brown University), and Artemov Vasily (EPFL) for fruitful discussions.

References

1 Chaplin, M. Do we underestimate the importance of water in cell biology? *Nat. Rev. Mol. Cell Bio.* **7**, 861-866 (2006).

2 Ball, P. Water — an enduring mystery. *Nature* **452**, 291-292 (2008).

3 Pohorille, A. & Pratt, L. R. Is water the universal solvent for life? *Orig. Life Evol. Biosph.* **42**, 405-409 (2012).

4 Gallo, P. *et al.* Water: A tale of two liquids. *Chem. Rev.* **116**, 7463-7500 (2016).

5 Bellissent-Funel, M. C. *et al.* Water determines the structure and dynamics of proteins. *Chem. Rev.* **116**, 7673-7697 (2016).

6 Brini, E. *et al.* How water's properties are encoded in its molecular structure and energies. *Chem. Rev.* **117**, 12385-12414 (2017).

7 Ball, P. Water is an active matrix of life for cell and molecular biology. *Proc. Natl. Acad. Sci. USA* **114**, 13327-13335 (2017).

8 Pettersson, L. G. M. in *Modern Problems of the Physics of Liquid Systems.* (eds Bulavin L.A. & Xu L.) 3-39 (Springer Proceedings in Physics).

9 Errington, J. R. & Debenedetti, P. G. Relationship between structural order and the anomalies of liquid water. *Nature* **409**, 318-321 (2001).

10 Chaplin, M. *Water structure and science*, <https://water.lsbu.ac.uk/water/water_structure_science.html> (2017).

11 Nilsson, A. & Pettersson, L. G. M. The structural origin of anomalous properties of liquid water. *Nat. Commun.* **6**, 8998 (2015).

12 Russo, J., Akahane, K. & Tanaka, H. Water-like anomalies as a function of tetrahedrality. *Proc. Natl. Acad. Sci. USA* **115**, 3333-3341 (2018).

13 Soper, A. K. Is water one liquid or two? *J. Chem. Phys.* **150**, 234503 (2019).

14 Niskanen, J. *et al.* Compatibility of quantitative X-ray spectroscopy with continuous distribution models of water at ambient conditions. *Proc. Natl. Acad. Sci. USA* **116**, 4058-4063 (2019).

15 Pietzsch, A. *et al.* Cuts through the manifold of molecular H_2O potential energy surfaces in liquid water at ambient conditions. *Proc. Natl. Acad. Sci. USA* **119**, e2118101119 (2022).

16 Camisasca, G., Schlesinger, D., Zhovtobriukh, I., Pitsevich, G. & Pettersson, L. G. M. A proposal for the structure of high- and low-density fluctuations in liquid water. *J. Chem. Phys.* **151**, 034508 (2019).

17 Soper, A. K. & Ricci, M. A. Structures of high-density and low-density water. *Phys. Rev. Lett.* **84**, 2881-2884 (2000).

18 Huang, C. *et al.* The inhomogeneous structure of water at ambient conditions. *Proc. Natl. Acad. Sci. USA* **106**, 15214-15218 (2009).

19 Mallamace, F., Corsaro, C. & Stanley, H. E. Possible relation of water structural relaxation to water anomalies. *Proc. Natl Acad. Sci. USA* **110**, 4899-4904 (2013).

20 Shi, R., Russo, J. & Tanaka, H. Common microscopic structural origin for water's thermodynamic and dynamic anomalies. *J. Chem. Phys.* **149**, 224502 (2018).

21 Lin, C., Smith, J. S., Sinogeikin, S. V. & Shen, G. Experimental evidence of low-density liquid water upon rapid decompression. *Proc. Natl. Acad. Sci. USA* **115**, 2010-2015 (2018).

22 Shi, R. & Tanaka, H. Direct evidence in the scattering function for the coexistence of two types of local structures in liquid water. *J. Am. Chem. Soc.* **142**, 2868-2875 (2020).

23 Oka, K. *et al.* Two states of water converge to one state below 215 K. *J. Phys. Chem. Lett.* **12**, 5802-5806 (2021).

24 Poole, P. H., Sciortino, F., Essmann, U. & Stanley, H. E. Phase-behavior of metastable water. *Nature* **360**, 324-328 (1992).

25 Palmer, J. C. *et al.* Metastable liquid–liquid transition in a molecular model of water. *Nature* **510**, 385-388 (2014).
26 Palmer, J. C., Poole, P. H., Sciortino, F. & Debenedetti, P. G. Advances in computational studies of the liquid-liquid transition in water and water-like models. *Chem. Rev.* **118**, 9129-9151 (2018).
27 Debenedetti, P. G., Sciortino, F. & Zerze, G. H. Second critical point in two realistic models of water. *Science* **369**, 289-292 (2020).
28 Weis, J., Sciortino, F., Panagiotopoulos, A. Z. & Debenedetti, P. G. Liquid-liquid criticality in the WAIL water model. *J. Chem. Phys.* **157**, 024502 (2022).
29 Yu, Z. H., Shi, R. & Tanaka, H. A unified description of the liquid structure, static and dynamic anomalies, and criticality of TIP4P/2005 water by a hierarchical two-state model. *J. Phys. Chem. B* **127**, 3452-3462 (2023).
30 Angell, C. A. Insights into phases of liquid water from study of its unusual glass-forming properties. *Science* **319**, 582-587 (2008).
31 Angell, C. A. Supercooled water two phases? *Nat. Mater.* **13**, 673-675 (2014).
32 Kim, K. H. *et al.* Maxima in the thermodynamic response and correlation functions of deeply supercooled water. *Science* **358**, 1589-1593 (2017).
33 Gallo, P. & Stanley, H. E. Experiments provide evidence for two liquid phases in supercooled water droplets. *Science* **358**, 1543-1544 (2017).
34 Handle, P. H., Loerting, T. & Sciortino, F. Supercooled and glassy water: Metastable liquid(s), amorphous solid(s), and a no-man's land. *Proc. Natl. Acad. Sci. USA* **114**, 13336-13344 (2017).
35 Woutersen, S., Ensing, B., Hilbers, M., Zhao, Z. & Angell, C. A. A liquid-liquid transition in supercooled aqueous solution related to the HDA-LDA transition. *Science* **359**, 1127-1131 (2018).
36 Kringle, L., Thornley, W. A., Kay, B. D. & Kimmel, G. A. Reversible structural transformations in supercooled liquid water from 135 to 245 K. *Science* **369**, 1490-1492 (2020).
37 Kim, K. H. *et al.* Experimental observation of the liquid-liquid transition in bulk supercooled water under pressure. *Science* **370**, 978-982 (2020).
38 Gallo, P. *et al.* Advances in the study of supercooled water. *Eur. Phys. J. E* **44**, 143 (2021).
39 Suzuki, Y. Direct observation of reversible liquid-liquid transition in a trehalose aqueous solution. *Proc. Natl. Acad. Sci. USA* **119**, e2113411119 (2022).
40 Amann-Winkel, K. *et al.* Liquid-liquid phase separation in supercooled water from ultrafast heating of low-density amorphous ice. *Nat. Commun.* **14**, 442 (2023).
41 Kruger, C. R., Mowry, N. J., Bongiovanni, G., Drabbels, M. & Lorenz, U. J. Electron diffraction of deeply supercooled water in no man's land. *Nat. Commun.* **14**, 2812 (2023).
42 Russo, J. & Tanaka, H. Understanding water's anomalies with locally favoured structures. *Nat. Commun.* **5**, 3556 (2014).
43 Amann-Winkel, K. *et al.* X-ray and neutron scattering of water. *Chem. Rev.* **116**, 7570-7589 (2016).
44 Hamm, P. Markov state model of the two-state behaviour of water. *J. Chem. Phys.* **145**, 134501 (2016).
45 Martelli, F. Unravelling the contribution of local structures to the anomalies of water: The synergistic action of several factors. *J. Chem. Phys.* **150**, 094506 (2019).
46 Gao, Y. T., Fang, H. W., Ni, K. & Feng, Y. X. Water clusters and density fluctuations in liquid water based on extended hierarchical clustering methods. *Sci. Rep.* **12**, 8036 (2022).

47 de Oliveira, P. M. C., de Souza, J. I. R., da Silva, J. A. B. & Longo, R. L. Temperature dependence of hydrogen bond networks of liquid water: Thermodynamic properties and structural heterogeneity from topological descriptors. *J. Phys. Chem. B* **127**, 2250-2257 (2023).
48 Wernet, P. *et al.* The structure of the first coordination shell in liquid water. *Science* **304**, 995-999 (2004).
49 Tokushima, T. *et al.* High resolution X-ray emission spectroscopy of liquid water: The observation of two structural motifs. *Chem. Phys. Lett.* **460**, 387-400 (2008).
50 Harada, Y. *et al.* Selective probing of the OH or OD stretch vibration in liquid water using resonant inelastic soft-x-ray scattering. *Phys. Rev. Lett.* **111**, 193001 (2013).
51 Skinner, L. B., Benmore, C. J., Neuefeind, J. C. & Parise, J. B. The structure of water around the compressibility minimum. *J. Chem. Phys.* **141**, 214507 (2014).
52 Sellberg, J. A. *et al.* Ultrafast X-ray probing of water structure below the homogeneous ice nucleation temperature. *Nature* **510**, 381-384 (2014).
53 Maestro, L. M. *et al.* On the existence of two states in liquid water: Impact on biological and nanoscopic systems. *Int. J. Nanotechnol.* **13**, 667-677 (2016).
54 Stern, J. N., Seidl-Nigsch, M. & Loerting, T. Evidence for high-density liquid water between 0.1 and 0.3 GPa near 150 K. *Proc. Natl. Acad. Sci. USA* **116**, 9191-9196 (2019).
55 Sun, Q. Local statistical interpretation for water structure. *Chem. Phys. Lett.* **568-569**, 90-94 (2013).
56 Morawietz, T. *et al.* The interplay of structure and dynamics in the Raman spectrum of liquid water over the full frequency and temperature range. *J. Phys. Chem. Lett.* **9**, 851-857 (2018).
57 Maréchal, Y. The molecular structure of liquid water delivered by absorption spectroscopy in the whole IR region completed with thermodynamics data. *J. Mol. Struct.* **1004**, 146-155 (2011).
58 Taschin, A., Bartolini, P., Eramo, R., Righini, R. & Torre, R. Evidence of two distinct local structures of water from ambient to supercooled conditions. *Nat. Commun.* **4**, 2401 (2013).
59 Zhovtobriukh, I., Besley, N. A., Fransson, T., Nilsson, A. & Pettersson, L. G. M. Relationship between X-ray emission and absorption spectroscopy and the local H-bond environment in water. *J. Chem. Phys.* **148**, 144507 (2018).
60 Pettersson, L. G. M., Harada, Y. & Nilsson, A. Do X-ray spectroscopies provide evidence for continuous distribution models of water at ambient conditions? *Proc. Natl. Acad. Sci. USA* **116**, 17156-17157 (2019).
61 Niskanen, J. *et al.* Reply to Pettersson *et al.*: Why X-ray spectral features are compatible to continuous distribution models in ambient water. *Proc. Natl. Acad. Sci. USA* **116**, 17158-17159 (2019).
62 Caupin, F. *et al.* Comment on "Maxima in the thermodynamic response and correlation functions of deeply supercooled water". *Science* **360**, eaat1634 (2018).
63 Kim, K. H. *et al.* Response to comment on "Maxima in the thermodynamic response and correlation functions of deeply supercooled water". *Science* **360**, eaat1729 (2018).
64 Limmer, D. T. & Chandler, D. The putative liquid-liquid transition is a liquid-solid transition in atomistic models of water. *J. Chem. Phys.* **135**, 134503 (2011).
65 Limmer, D. T. & Chandler, D. The putative liquid-liquid transition is a liquid-solid transition in atomistic models of water. II. *J. Chem. Phys.* **138**, 214504 (2013).
66 Palmer, J. C. *et al.* Comment on "The putative liquid-liquid transition is a liquid-solid transition in atomistic models of water" [I and II: J. Chem. Phys. 135, 134503 (2011); J. Chem. Phys. 138, 214504 (2013)]. *J. Chem. Phys.* **148**, 137101 (2018).

67 Naserifar, S. & Goddard, W. A. Liquid water is a dynamic polydisperse branched polymer. *Proc. Natl. Acad. Sci. USA* **116**, 1998-2003 (2019).
68 Wiggins, P. Life depends upon two kinds of water. *Plos One* **3**, e1406 (2008).
69 Ansari, N., Dandekar, R., Caravati, S., Sosso, G. C. & Hassanali, A. High and low density patches in simulated liquid water. *J. Chem. Phys.* **149**, 204507 (2018).
70 Neophytou, A., Chakrabarti, D. & Sciortino, F. Topological nature of the liquid–liquid phase transition in tetrahedral liquids. *Nat. Phys.* **18**, 1248-1253 (2022).
71 Camisasca, G., Tenuzzo, L. & Gallo, P. Protein hydration water: Focus on low density and high density local structures upon cooling. *J. Mol. Liq.* **370**, 120962 (2023).
72 Sedlák, M. Large-scale supramolecular structure in solutions of low molar mass compounds and mixtures of liquids: I. Light scattering characterization. *J. Phys. Chem. B* **110**, 4329-4338 (2006).
73 Sedlák, M. & Rak, D. Large-scale inhomogeneities in solutions of low molar mass compounds and mixtures of liquids: Supramolecular structures or nanobubbles? *J. Phys. Chem. B* **117**, 2495-2504 (2013).
74 Sedlák, M. Large-scale supramolecular structure in solutions of low molar mass compounds and mixtures of liquids. III. Correlation with molecular properties and interactions. *J. Phys. Chem. B* **110**, 13976-13984 (2006).
75 Tarun, O. B., Okur, H. I., Rangamani, P. & Roke, S. Transient domains of ordered water induced by divalent ions lead to lipid membrane curvature fluctuations. *Commun. Chem.* **3**, 17 (2020).
76 Dupertuis, N., Tarun, O. B., Lutgebaucks, C. & Roke, S. Three-dimensional confinement of water: H_2O exhibits long-range (>50 nm) structure while D_2O does not. *Nano Lett.* **22**, 7394-7400 (2022).
77 del Valle, J. C. *et al.* Dielectric anomalous response of water at 60 °C. *Philos. Mag.* **95**, 683-690 (2015).
78 Munoz-Ortiz, T. *et al.* Temperature dependence of water absorption in the biological windows and its impact on the performance of Ag_2S luminescent nanothermometers. *Part. Part. Syst. Charact.* **39**, 2200100 (2022).
79 Catalan, J. & Gonzalo, J. A. Liquid water changes its structure at 43 °C. *Chem. Phys. Lett.* **679**, 86-89 (2017).
80 Catalan, J. & del Valle, J. C. Molecule 1-methyl-5-nitroindoline probes the structural change of liquid water with temperature. *ACS Omega* **3**, 18930-18934 (2018).
81 Cheng, Y.-H., Yang, H.-C. & Chou, P.-T. Could chemical reaction at the molecular level show distinction between two liquid-water states? Study of the excited-state water-catalyzed proton transfer reaction provides a clue. *J. Phys. Chem. Lett.* **11**, 9468-9475 (2020).
82 Labrador-Páez, L. *et al.* Effect of H_2O and D_2O thermal anomalies on the luminescence of Eu^{3+} aqueous complexes. *J. Phys. Chem. C* **122**, 14838-14845 (2018).
83 Labrador-Páez, L. *et al.* pH dependence of water anomaly temperature investigated by Eu(III) cryptate luminescence. *Anal. Bioanal. Chem.* **412**, 73-80 (2020).
84 Labrador-Páez, L., Kostiv, U., Widengren, J. & Liu, H. C. Water: An influential agent for lanthanide-doped luminescent nanoparticles in nanomedicine. *Adv. Opt. Mater.* **11**, 2200513 (2022).
85 Labrador-Páez, L. *et al.* Unveiling molecular changes in water by small luminescent nanoparticles. *Small* **13**, 1700968 (2017).
86 Lu, D. S. *et al.* Exploring single-nanoparticle dynamics at high temperature by optical tweezers. *Nano Lett.* **20**, 8024-8031 (2020).
87 Brites, C. D. S. *et al.* Decoding a percolation phase transition of water at ~330 K with a nanoparticle ruler. *J. Phys. Chem. Lett.* **11**, 6704-6711 (2020).

88 Brites, C. D. S. *et al.* Spotlight on luminescence thermometry: Basics, challenges, and cutting-edge applications. *Adv. Mater.* **35** (2023).
89 Brites, C. D. *et al.* Instantaneous ballistic velocity of suspended brownian nanocrystals measured by upconversion nanothermometry. *Nat. Nanotechnol.* **11**, 851-856 (2016).
90 Stanley, H. E. in *Hydration processes in biology: Theoretical and experimental approaches, Proceedings of the NATO Advanced Study Institute* Vol. 305 (ed. Marie-Claire Bellissent-Funel) (IOS Press, 1999).
91 Huang, R. X. *et al.* Direct observation of the full transition from ballistic to diffusive Brownian motion in a liquid. *Nat. Phys.* **7**, 576-580 (2011).
92 Haynes, W. M. & Lide, D. R. *CRC Handbook of Chemistry and Physics*. 92nd ed., (CRC Press, 2011).
93 Nilsson, A., Huang, C. & Pettersson, L. G. M. Fluctuations in ambient water. *J. Mol. Liq.* **176**, 2-16 (2012).
94 Finneran, I. A., Carroll, P. B., Allodi, M. A. & Blake, G. A. Hydrogen bonding in the ethanol-water dimer. *Phys. Chem. Chem. Phys.* **17**, 24210-24214 (2015).
95 Ghanghas, R., Jindal, A. & Vasudevan, S. Geometry of hydrogen bonds in liquid ethanol probed by proton NMR experiments. *J. Phys. Chem. B* **124**, 662-667 (2020).
96 Wang, Z., Liu, K. H., Harriger, L., Leao, J. B. & Chen, S. H. Evidence of the existence of the high-density and low-density phases in deeply-cooled confined heavy water under high pressures. *J. Chem. Phys.* **141**, 014501 (2014).
97 Wang, Z. *et al.* Liquid–liquid phase transition and its phase diagram in deeply-cooled heavy water confined in a nanoporous silica matrix. *J. Phys. Chem. Lett.* **6**, 2009-2014 (2015).
98 Hart, R. T. *et al.* Isotope quantum effects in water around the freezing point. *J. Chem. Phys.* **124**, 134505 (2006).
99 Soper, A. K. & Benmore, C. J. Quantum differences between heavy and light water. *Phys. Rev. Lett.* **101**, 065502 (2008).
100 Millero, F. J. & Lepple, F. K. Isothermal compressibility of deuterium oxide at various temperatures. *J. Chem. Phys.* **54**, 946-949 (1971).
101 Badyal, Y. S., Price, D. L., Saboungi, M.-L., Haeffner, D. R. & Shastri, S. D. Quantum effects on the structure of water at constant temperature and constant atomic density. *J. Chem. Phys.* **116**, 10833-10837 (2002).
102 Svergun, D. I. *et al.* Protein hydration in solution: Experimental observation by X-ray and neutron scattering. *Proc. Natl. Acad. Sci. USA* **95**, 267–2272 (1998).
103 Gonella, G. *et al.* Water at charged interfaces. *Nat. Rev. Chem.* **5**, 466-485 (2021).
104 Kim, Y., Ding, H. R. & Zheng, Y. B. Investigating water/oil interfaces with opto-thermophoresis. *Nat. Commun.* **13**, 3742 (2022).
105 Pfeiffer, C. *et al.* Interaction of colloidal nanoparticles with their local environment: The (ionic) nanoenvironment around nanoparticles is different from bulk and determines the physico-chemical properties of the nanoparticles. *J. R. Soc. Interface* **11** (2014).
106 Darlington, A. M. & Gibbs-Davis, J. M. Bimodal or trimodal? The influence of starting pH on site identity and distribution at the low salt aqueous/silica interface. *J. Phys. Chem. C* **119**, 16560-16567 (2015).
107 Zhu, S., Qin, X., Yao, Y. & Shao, M. pH-dependent hydrogen and water binding energies on platinum surfaces as directly probed through surface-enhanced infrared absorption spectroscopy. *J. Am. Chem. Soc.* **142**, 8748-8754 (2020).
108 Bruni, F., Ricci, M. A. & Soper, A. K. Structural characterization of NaOH aqueous solution in the glass and liquid states. *J. Chem. Phys.* **114**, 8056-8063 (2001).

109 Botti, A., Bruni, F., Imberti, S., Ricci, M. A. & Soper, A. K. Ions in water: The microscopic structure of concentrated NaOH solutions. *J. Chem. Phys.* **120**, 10154-10162 (2004).
110 Mancinelli, R., Botti, A., Bruni, F., Ricci, M. A. & Soper, A. K. Perturbation of water structure due to monovalent ions in solution. *Phys. Chem. Chem. Phys.* **9**, 2959-2967 (2007).
111 Barisik, M., Atalay, S., Beskok, A. & Qian, S. Size dependent surface charge properties of silica nanoparticles. *J. Phys. Chem. C* **118**, 1836-1842 (2014).
112 Abbas, Z., Labbez, C., Nordholm, S. & Ahlberg, E. Size-dependent surface charging of nanoparticles. *J. Phys. Chem. C* **112**, 5715-5723 (2008).
113 Wang, F. *et al.* Simultaneous phase and size control of upconversion nanocrystals through lanthanide doping. *Nature* **463**, 1061-1065 (2010).

SUPPLEMENTARY INFORMATION

Deciphering density fluctuations in the hydration water of Brownian nanoparticles via upconversion thermometry

Fernando E. Maturi[1,2], Ramon S. Raposo Filho[1], Carlos D. S. Brites[1], Jingyue Fan[3], Ruihua He[3], Bilin Zhuang[4], Xiaogang Liu[3], and Luís D. Carlos[1]**

[1] Phantom-g, CICECO - Aveiro Institute of Materials, Department of Physics, University of Aveiro, 3810-193 Aveiro, Portugal

[2] Institute of Chemistry, São Paulo State University (UNESP), 14800-060 Araraquara-SP, Brazil

[3] Department of Chemistry, National University of Singapore, 117543 Singapore, Singapore

[4] Harvey Mudd College, 301 Platt Boulevard, California 91711, USA

*E-mail: chmlx@nus.edu.sg; lcarlos@ua.pt

This PDF file includes:

Table of Contents

I. Synthesis and characterization

Materials. Yttrium(III) acetate hydrate (99.9%), ytterbium(III) acetate hydrate (99.9%), erbium(III) acetate hydrate (99.9%), lutetium(III) acetate hydrate (99.9%), ammonium fluoride (>98%), 1-octadecene (90%), oleic acid (90%), cyclohexane (99.5%), absolute ethanol (>98%), methanol (99.9%), hydrochloric acid (37%), sodium hydroxide (>98%), deuterium oxide (99.9 atom % D), polyvinylpyrrolidone, and tetraethyl orthosilicate were purchased from Sigma-Aldrich and used as received.

Synthesis of $NaGdF_4$:Yb/Er(18/2%)@$NaGdF_4$ core-shell nanoparticles (15 nm). The synthesis of upconverting nanoparticles (UCNPs) was carried out according to a previously reported procedure.[1] In a 50 mL flask, an aqueous solution (2 mL) containing $Gd(CH_3CO_2)_3$ (0.097 g, 0.320 mmol), $Yb(CH_3CO_2)_3$ (0.030 g, 0.072 mmol), and $Er(CH_3CO_2)_3$ (0.003 g, 0.008 mmol) was mixed with oleic acid (4 mL) and 1-octadecene (6 mL) to obtain the core of UCNPs. The resulting mixture was heated at 423 K for 1.3 h, forming lanthanide oleate complexes, before cooling to room temperature. Subsequently, ammonium fluoride (1.2 mmol) and sodium hydroxide (1.0 mmol) dissolved in 5 mL of methanol were added and stirred at 318 K for 3.5 h. To remove the methanol, the reaction temperature was increased to 378 K. The solution was then heated to 553 K under an argon flow for 1.5 h, followed by cooling to room temperature. The resulting nanoparticles were precipitated by adding ethanol, collected by centrifugation, washed with ethanol, and finally redispersed in 4 mL of cyclohexane.

For the optically inert shell of the 15 nm UCNPs, an aqueous solution (2 mL) containing $Gd(CH_3CO_2)_3$ (0.121 g, 0.400 mmol) was combined with oleic acid (3 mL) and 1-octadecene (7 mL) in a 50 mL flask. The resulting mixture was heated at 423 K for 1 h under stirring and then cooled to 323 K. The as-synthesized $NaGdF_4$:Yb/Er(18/2%) 15 nm core nanoparticles, dispersed in 4 mL of cyclohexane, were then added to the flask, followed by the addition of a 6 mL methanol solution of ammonium fluoride (1.6 mmol) and sodium hydroxide (1.0 mmol). The mixture was stirred at 323 K for 30 min and then the reaction temperature was increased to 373 K. After removing the methanol, the solution was heated at 563 K under an argon atmosphere for 1.5 h and then cooled to room temperature. The resulting core-shell nanoparticles were precipitated by the addition of ethanol, collected via centrifugation, washed with ethanol, and redispersed in cyclohexane.

Synthesis of $NaYF_4$:Yb/Er(18/2%)@$NaYF_4$ core-shell nanoparticles (24 nm). The synthesis of 24 nm core-shell UCNPs followed the same procedure as described in the

synthesis of the 15 nm core-shell UCNPs, except for replacing $Gd(CH_3CO_2)_3$ with $Y(CH_3CO_2)_3$.

Synthesis of $NaYF_4$:Lu/Yb/Er core-only nanoparticles (52, 64, 78, and 106 nm). In a typical experimental procedure, a 2 mL aqueous solution of $Ln(CH_3CO_2)_3$ (0.2 $mol \cdot L^{-1}$, Ln = Lu, Y, Yb, and Er) was added to a 50 mL flask containing oleic acid (3 mL) and 1-octadecene (7 mL). The mixture was heated to 423 K for 1 h. After cooling to 323 K, a methanol solution (6 mL) containing ammonium fluoride (1.6 mmol) and sodium hydroxide (1.0 mmol) was added under stirring for 30 min. After removing the methanol through evaporation, the solution was heated at 563 K under argon for 3 h and then cooled down to room temperature. The resulting nanoparticles were washed several times with ethanol and redispersed in 4 mL of cyclohexane. The same procedure was used to obtain UCNPs of varying sizes. The heating duration, temperature, and concentration composition were tuned to achieve different doping ratios of Lu/Yb/Er: 40/18/2% (52 nm), 47/18/2% (64 and 78 nm), and 50/18/2% (106 nm).

Preparation of ligand-free nanoparticles. The as-synthesized oleate-capped UCNPs were dispersed in a solution containing 1 mL of ethanol and 1 mL of hydrochloric acid (2 $mol \cdot L^{-1}$), followed by ultrasonication for 10 min to remove the oleate capping. The resulting ligand-free UCNPs were collected by centrifugation at 16,500 rpm for 20 min, washed with ethanol and deionized water several times, and then redispersed in deionized water. The same procedure was used for all the different-sized UCNPs, resulting in aqueous dispersions of ~100 $mg \cdot mL^{-1}$.

Synthesis of $NaYF_4$:Lu/Yb/Er(47/18/2%)@SiO_2 core-shell nanoparticles (100 nm). In a standard method, an amorphous silica (SiO_2) shell was grown onto the surface of the 78 nm ligand-free UCNPs using polyvinylpyrrolidone (PVP) as a mediator.[2] PVP (250 mg) was dissolved under stirring in a 50 mL round-bottom flask containing 5 mL of deionized water and 15 mL of ethanol until its total dissolution. The ligand-free 78 nm $NaYF_4$:Lu/Yb/Er(47/18/2%) UCNPs (0.2f PVP mmol) were added to the flask and kept under stirring for 30 min. Then, a solution of tetraethyl orthosilicate (50 μL) dissolved in ethanol (300 μL) was added to the flask. The mixture was reacted overnight under stirring. Core-shell $NaYF_4$:Lu/Yb/Er(47/18/2%)@SiO_2 UCNPs were collected via centrifugation at 16,500 rpm for 30 min and washed twice with ethanol. The silica-coated UCNPs were obtained with an average outer diameter of 100 nm (the thickness of the silica shell is 11 nm).

Preparation of the nanofluids. The pH of the solutions and suspensions was measured with a compact pH meter (SC S210-K, Mettler Toledo) at 293 K. The pH meter was calibrated by using a two-point calibration method with technical buffer calibration solutions at pH values of 4.01 and 10.01 (Mettler Toledo). Stock solutions with pH values of 2.70 ± 0.01, 5.10 ± 0.01, 6.30 ± 0.01, and 8.50 ± 0.01 were obtained by adding aqueous solutions of hydrochloric acid (0.1 $mol \cdot L^{-1}$) or sodium hydroxide (0.1 $mol \cdot L^{-1}$) to deionized water. Then, aqueous nanofluids were obtained at different pH values by dispersing the different-sized ligand-free UCNPs in the corresponding pH stock solutions under sonication. All nanofluids were prepared with a volume fraction (ϕ) of UCNPs of 0.085%. This choice ensures a sufficient signal-to-noise ratio in the photoluminescence studies while keeping the concentration of the UCNPs as low as possible, thus decreasing particle-particle interactions, known to increase Brownian velocity.[3] For the nanofluids obtained in heavy water (D_2O) and ethanol (EtOH), aqueous dispersions of 15 nm ligand-free UCNPs were freeze-dried to remove water by sublimation. The mass of dried UCNPs required to obtain ϕ = 0.085% was then dispersed in the proper volume of D_2O or EtOH under sonication. Table S1 summarizes the mass concentration (ρ_c) and density ($\rho_\mathbf{n}$) according to the chemical composition of UCNPs used to obtain the different nanofluids at $\phi = \rho_c/\rho_n$ = 0.085%.

Colloidal characterization. The hydrodynamic diameter (d_H) of UCNPs was measured by dynamic light scattering (DLS) in a Malvern Zetasizer Nano ZS instrument (red badge ZEN3600, Malvern Instruments) operating with a 632.8 nm laser. To analyze the colloidal stability of UCNPs, zeta potential (ζ) measurements were carried out with the same instrument applying the Smoluchowski model. The d_H and ζ measurements were performed at 298 K in a folded capillary cell (DTS1070, Malvern Instruments). Three measurements with ten scans each were performed and the average values were used for data analysis. The resulting distribution of sizes and zeta potentials was adjusted to lognormal and Gaussian functions, respectively, using the mean and standard deviations to determine the average d_H and ζ and their uncertainties (Fig. S2, Fig. S3, Fig. S4, and Table S2).

Electron microscopy. Transmission electron microscopy (TEM) images of the UCNPs (Figs. S5) were obtained using a field-emission transmission electron microscope (JEM-2100F, JEOL) operated at an acceleration voltage of 200 kV. The values of the diameters (d) and their

corresponding uncertainties were retrieved from the mean and standard deviations of the lognormal function adjusted to the size distribution of the UCNPs (Fig. S6 and Table S2).

II. Experimental setup for temperature-dependent photoluminescence measurements

The emission spectra of UCNPs were recorded in the experimental setup presented in Fig. S7 (adapted from Reference [4]). The nanofluids were excited with a continuous-wave (CW) near-infrared laser diode (DL980-3W0-T, CrystaLaser) at 980 nm. The laser beam was collimated by a plano-convex lens (LA1145-AB, Thorlabs), resulting in a power density of 62 $W \cdot cm^{-2}$. The laser beam irradiates a semi-micro rectangular quartz cuvette (9F-Q-10, Starna Cells) filled with 0.50 mL of the nanofluids. The scanning position of the cuvette along the *x*-axis was controlled by a moving stage with a minimum step of 0.1 mm. Detection of the upconverting emission was performed by a USB portable spectrometer (Maya 2000 Pro, Ocean Insight) coupled to an optical fiber (P600-1-UV-VIS, Ocean Insight) using a short-pass filter (FESH0750, Thorlabs) to cut off the peak of the laser during spectral acquisition. Spectral acquisition was performed with a constant boxcar width (one pixel, 0.5 nm) and integration time of 250 ms. The temperature of the nanofluids was increased at one side of the cuvette through thermal contact by attaching it to a Kapton thermofoil heater (HK6906, Minco) mounted in a copper plate (4.6 × 2.5 cm^2) and coupled to a temperature controller (E5CN, Omron). The temperature controller is equipped with a K-type thermocouple (KA01-3, TME Thermometers) with a thermal resolution of 0.1 K.

III. Temperature mapping through upconversion nanothermometry

In the experimental setup depicted in Fig. S7, the nanofluids were irradiated with a CW 980 nm laser diode until the stabilization of the temperature. After reaching different initial equilibrium temperatures (ranging from 303 to 343 K), one side of the cuvette (containing the nanofluids) was heated (temperature increment of 15 K for 300 s) and time-dependent upconversion emission spectra were recorded at different fixed positions along the *xx*-direction perpendicular to the laser beam (x_i = 0.0–6.0 mm, i = 1–4). For each time instant, the luminescence intensity ratio between the emission bands corresponding to $^2H_{11/2} \rightarrow {}^4I_{15/2}$ (I_H, 510–534 nm) and $^4S_{3/2} \rightarrow {}^4I_{15/2}$ (I_S, 534–554 nm) transitions was used to define the thermometric parameter ($\Delta = I_H/I_S$) and calculated the absolute temperature (T) as:[5]

$$\frac{1}{T} = \frac{1}{T_0} - \frac{k_B}{\Delta E} \ln\left(\frac{\Delta}{\Delta_0}\right) \quad \textbf{(S1)}$$

where ΔE is the energy separation between the Er^{3+} $^2H_{11/2}$ and $^4S_{3/2}$ thermally coupled levels, k_B is the Boltzmann constant, and Δ_0 is the thermometric parameter at room temperature (T_0). The value of ΔE was calculated as the difference between the barycenters of the $^2H_{11/2}$ (~525 nm) and $^4S_{3/2}$ (~545 nm) emitting levels (Fig. S8a). Since Δ_0 corresponds to the value of Δ without laser-induced heating, its value can be obtained from the intercept of the curve of Δ measured as a function of the laser power density (Fig. S8b). The thermometric parameter Δ increases as the temperature rises because the relative population between the $^2H_{11/2}$ and $^4S_{3/2}$ levels is in thermal equilibrium, following Boltzmann's distribution.[5] Therefore, this approach provides a reliable parameter to record time-dependent temperature profiles based on the emission spectra of the nanofluids containing UCNPs while heating them (Fig. S8c).

The thermal sensing ability of the nanofluids can be assessed by the relative thermal sensitivity (S_r) and uncertainty in temperature (δT), which are the two Fig.s of merit commonly used to compare the thermometric performance of luminescent thermometers. The value of S_r represents the Δ change per degree of temperature (in $\%\cdot K^{-1}$):

$$S_r = \left|\frac{1}{\Delta}\frac{d\Delta}{dT}\right| = \frac{\Delta E}{k_B T^2} \quad (\mathbf{S2})$$

where $d\Delta/dT$ is the rate of change of Δ in response to the variation of temperature, k_B is Boltzmann's constant, and T is the absolute temperature. The value of δT corresponds to the smallest temperature resolvable by the thermometer (in K):

$$\delta T = \frac{1}{S_r}\frac{\delta\Delta}{\Delta} \quad (\mathbf{S3})$$

where $\delta\Delta/\Delta$ is the relative uncertainty of Δ. The maximum relative thermal sensitivity and minimum uncertainty at the temperature obtained for each nanofluid are summarized in Table S3.

IV. Data denoising and determination of the instantaneous ballistic Brownian velocity

The absolute temperature values measured by upconversion nanothermometry were computed as the reduced temperature $\theta(t)$:

$$\theta(t) = \frac{T(t) - T_i}{T_f - T_i} \quad (\mathbf{S4})$$

where $T(t)$, T_i, and T_f are the instantaneous, initial, and final values of the temperature, respectively. The values of $T(t)$ were obtained by applying Equation S1 to the time-dependent upconverting emission spectra of the samples. Once the temperature profiles were recorded at

distinct T_i, this procedure was performed to obtain thermal transients with the same range of temperature for comparison purposes.

A nonlinear noise reduction method based on the discrete wavelet transform (DWT) was used to reduce the noise arising from the $\theta(t)$ curves.[6] The denoising procedure was implemented through a custom MATLAB R2022a script in five steps, following a previously reported procedure.[4] The used script i) imports the thermometric parameter $\Delta = I_H/I_S$ from the as-measured temperature-dependent emission spectra; ii) computes the temperature by applying Equation S1 to the resulting time-dependent Δ; iii) converts the temperature into reduced temperature through Equation S4; iv) applies the DWT denoising method to obtain a denoised reduced temperature (threshold parameter: 15, 5 stages); and v) calculate the noise from the difference between the denoised and measured reduced temperature. The histograms of the noise obtained for all the denoised $\theta(t)$ curves result in a Gaussian distribution ($r^2 > 0.98$) centered at zero, following an additive white Gaussian noise that validates the denoising method herein applied.[7,8]

The denoised $\theta(t)$ curves were used to compute the critical onset time (t_i), which corresponds to the instant time at which the initial temperature starts to increase. After analyzing the data, the script marks t_i as the instant time at which the change in the denoised signal is higher than the standard deviation of the noise (extracted from the corresponding histogram). For the same initial temperature, the $\theta(t)$ curves were registered by irradiating the laser at distinct positions along the *xx*-direction (x_i = 0.0–6.0 mm, i = 1–4). The instantaneous ballistic Brownian velocity was then estimated as the slope of the x_i *versus* t_i plot, as demonstrated in Fig. S9.

V. Calculation of crossover temperature

The value of the crossover temperature (T_c) was calculated from the intersection between the two straight lines adjusted to the bilinear trend of the temperature-dependent Brownian velocity of the UCNPs in the aqueous nanofluids. All possible combinations of two straight lines giving the best fit to the bilinear trend observed in the 300–350 K temperature range were computed by using a custom script written in MATLAB R2022a. The T_c values were then determined from the intersection between the two linear fits that give the maximum product of the coefficient of the determination (r^2) from each line. The uncertainty in T_c (δT_c) was estimated as:

$$\delta T_c = \frac{T_{cmax} - T_{cmin}}{2} = -\frac{(\sigma_{E2} + \sigma_{E1})}{m_1 - m_2} \quad \textbf{(S5)}$$

where T_{cmax} and T_{cmin} are the maximum and minimum predicted values of T_c, respectively, σ_{E1} and $\sigma_{E2,}$ and m_1 and m_2 are the standard error of the estimate (σ_E) and the slope (m) of the linear dependency below and above T_c, respectively. σ_E is defined as:

$$\sigma_E = \sqrt{\frac{\sum(v - v')^2}{n - 2}} \quad \textbf{(S6)}$$

with v and v' corresponding to the measured and fitted values of the Brownian velocity, respectively, and n is the number of data points from each fitted line. The estimation of δT_c is illustrated in the schematic representation in Fig. S10. The same procedure was employed regardless of the UCNPs' size or pH of the aqueous media.

VI. The two-state model and a hypothetical phase diagram of liquid water

The strongest evidence supporting the two-state model of water comes from the liquid-liquid phase transition (LLPT) hypothesis proposed by Poole, Sciortino, Essmann, and Stanley based on molecular dynamics simulations.[9] According to this hypothesis, a second critical point for water in the supercooled regime separates the LDL from the HDL in a discontinuous phase transition.[10,11] At the molecular level, the spacious LDL is formed when water molecules in the first hydration shell assemble in a more organized tetrahedral hydrogen-bonding network, while the more tightly connected HDL forms when an additional water molecule from the second hydration shell enters the first hydration shell, disrupting the LDL organization and creating a smaller and distorted hydrogen-bonding motif.[12] Direct observations of the LLPT are difficult due to the quick crystallization of supercooled liquid water, which only exists in one state below 215 K.[13,14] Nevertheless, recent studies of isothermal volume changes in diluted

polyol and trehalose aqueous solutions under varying pressures have confirmed the existence of two states of water experiencing an LLPT between the metastable LDL and HDL,[15,16] corroborating the hypothesis that pure water undergoes an LLPT as well.

The LLPT hypothesis offers a fresh perspective for understanding the singular behavior of liquid water in terms of LDL and HDL motifs at varying pressures and temperatures, as demonstrated by the hypothetical phase diagram depicted in Fig. S1. The phase diagram portrays the liquid-liquid coexistence line between LDL and HDL in terms of simple liquid regions. Additionally, the diagram includes the liquid-liquid critical point (LLCP), which may be either real or virtual, the Widom line (W) marking the crossover between the metastable and stable regions in the one-phase region, and fluctuations on various length scales emerging from LLCP, resulting in local spatially separated regions in the anomalous region. The amorphous solid states of LDL and HDL can exist at extremely low temperatures as low-density (LDA, low pressure) and high-density (HDA, high pressure) amorphous ice, respectively. In fact, recent findings have also demonstrated the possibility of obtaining medium-density amorphous ice under specific conditions of pressure and temperature.[17] This discovery indicates that the proposed phase diagram still has room for optimization and potential for further improvements.

VII. Equipartition theorem

Equipartition theorem. The equipartition theorem describes the Brownian velocity as $\nu = \sqrt{k_B T/m^*}$, where k_B is the Boltzmann constant, T is the temperature, and m^* is the effective mass of the nanoparticles, representing the combined mass of UCNPs and half of the liquid mass moving cooperatively with them.[18] In this sense, dispersing UCNPs within denser solvents results in a lower ν, as shown in Fig. 2a of the main text.

VIII. Supplementary Figures

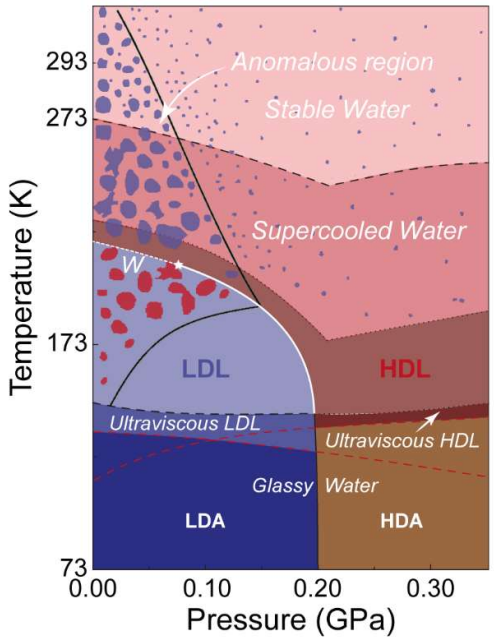

Fig. S1 Hypothetical phase diagram of water. Adapted from Reference 19.

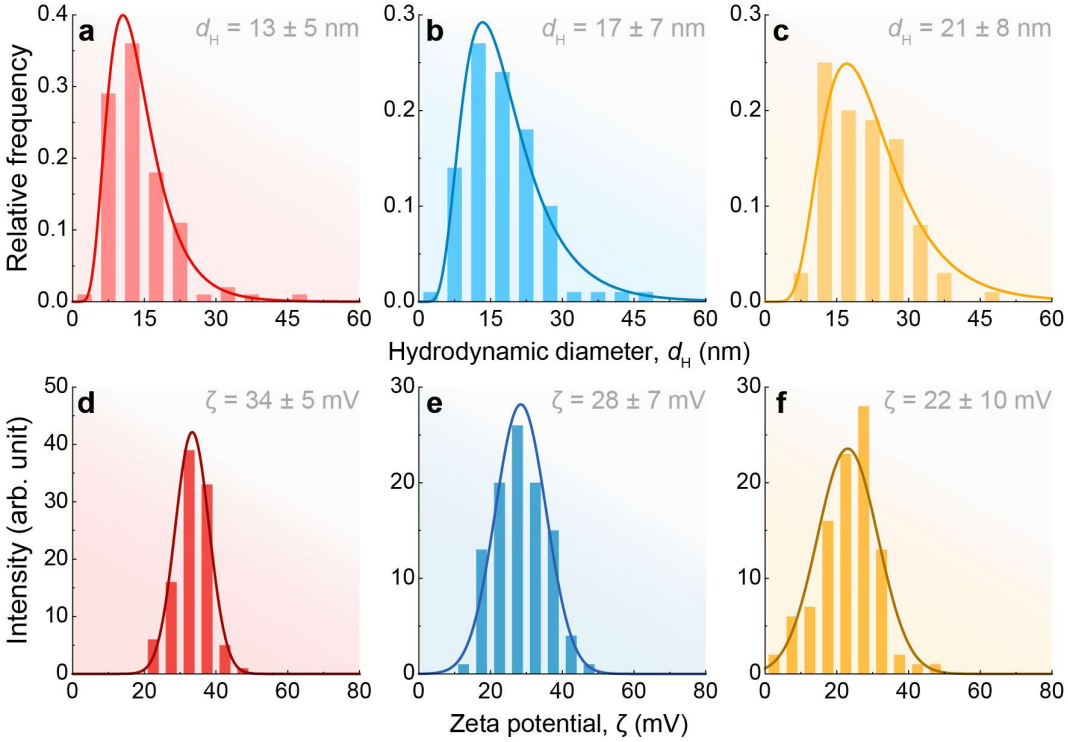

Fig. S2 Particle size and zeta potential of the 15 nm UCNPs. Hydrodynamic diameter (d_H, top) and ζ (bottom) of the 15 nm nanofluids prepared in **(a, d)** water (pH = 5.10), **(b, e)** heavy water, and **(c, f)** ethanol. The lines are the best fits to the data using lognormal (d_H) and Gaussian (ζ) functions ($r^2 > 0.97$). The values of d_H obtained for the other nanofluids prepared in water are summarized in Table S2.

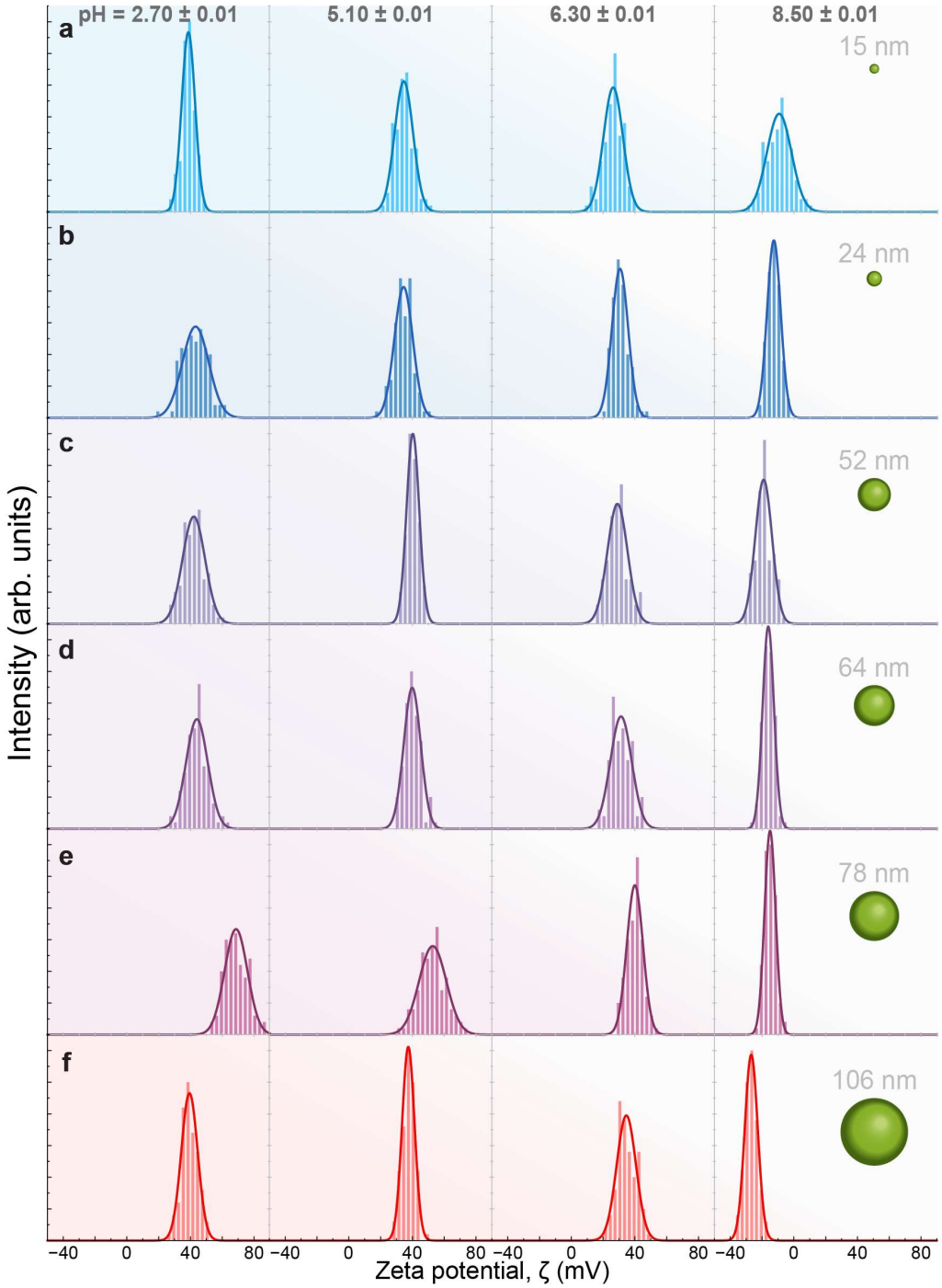

Fig. S3 pH dependence of the zeta potential of the aqueous nanofluids. Zeta potential of UCNPs with diameters of **(a)** 15, **(b)** 24, **(c)** 52, **(d)** 64, **(e)** 78, and **(f)** 106 nm measured in water at four pH values. The lines are the best fits for ζ (Gaussian distribution, $r^2 > 0.98$). The fitting results (ζ values and corresponding uncertainties) are shown in Fig. S4. For the studied volume fraction, the 100 nm UCNP with a silica shell is only stable at pH = 5.10, at which ζ = −33 ± 11 mV.

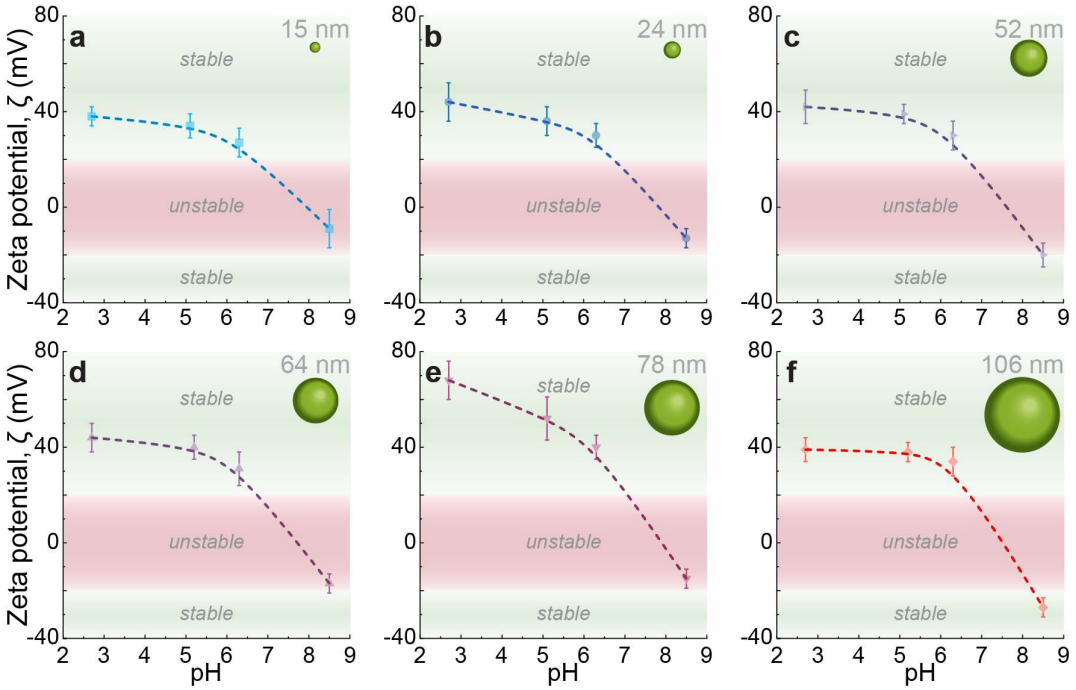

Fig. S4 pH dependence of the Zeta potential. pH dependence of ζ for the **(a)** 15 nm, **(b)** 24 nm, **(c)** 52 nm, **(d)** 64 nm, **(e)** 78 nm, and **(f)** 106 nm UCNPs dispersed in water, obtained from the data in Fig. S3. The lines are guides for the eyes. The decrease in ζ with the increase in pH is in good accordance with previous reports,[20] highlighting how the presence of ions in the medium can affect the surface charge of UCNPs. The stability of a colloid is the result of van der Waals attraction and repulsion (steric and electrostatic). The zeta potential provides information about the repulsive forces due to the electric double layer and, thus, the absolute values, $|\zeta|$, measure the magnitude of the electrostatic repulsion. The nanofluids are considered stable if $|\zeta| \geq 20$ mV (green-shaded regions).[21]

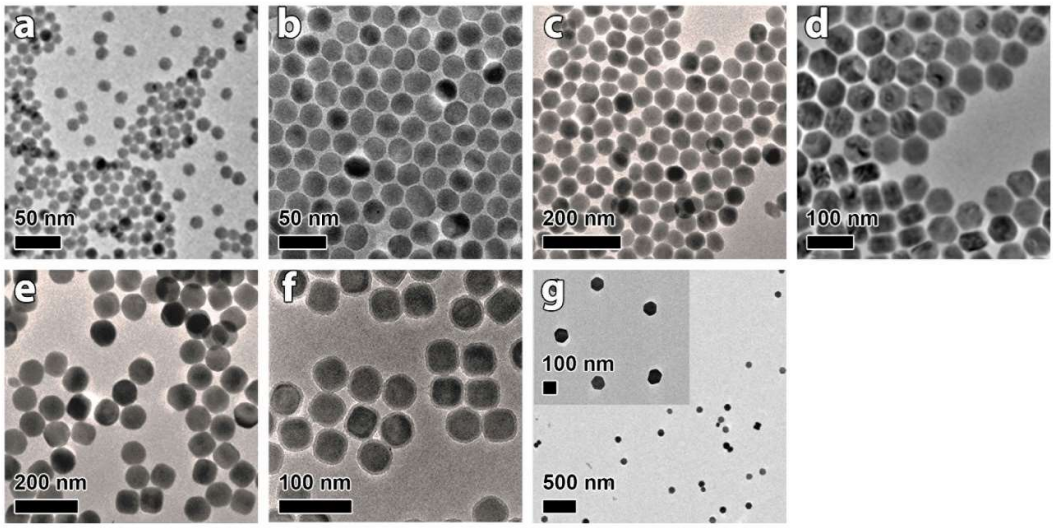

Fig. S5 Transmission electronic microscopy. TEM micrographs of **(a)** 15 nm, **(b)** 24 nm, **(c)** 52 nm, **(d)** 64 nm, **(e)** 78 nm, **(f)** 100 nm (core = 78 nm and a SiO_2 shell of 11 nm thick), and **(g)** 106 nm ligand-free UCNPs.

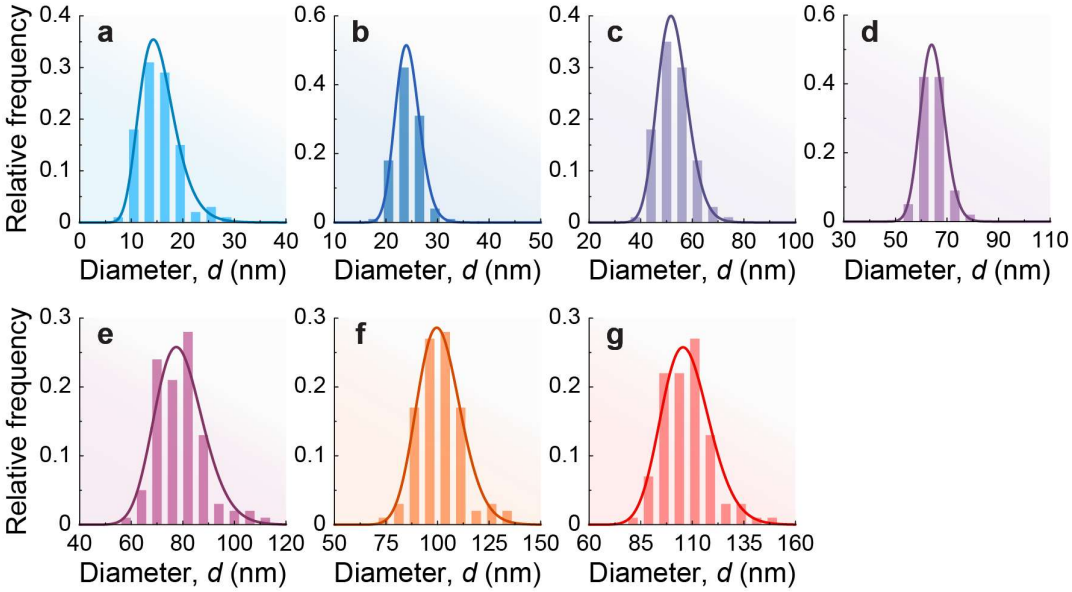

Fig. S6 Particle size of the nanocrystals. TEM size distribution of the **(a)** 15, **(b)** 24, **(c)** 52, **(d)** 64, **(e)** 78, **(f)** 100 nm (SiO_2 shell), and **(g)** 106 nm ligand-free UCNPs. The lines are the best fits for TEM size data (Fig. S5) using a lognormal distribution ($r^2 > 0.97$). Fitting results (diameter *d* and corresponding uncertainty) are presented in Table S2.

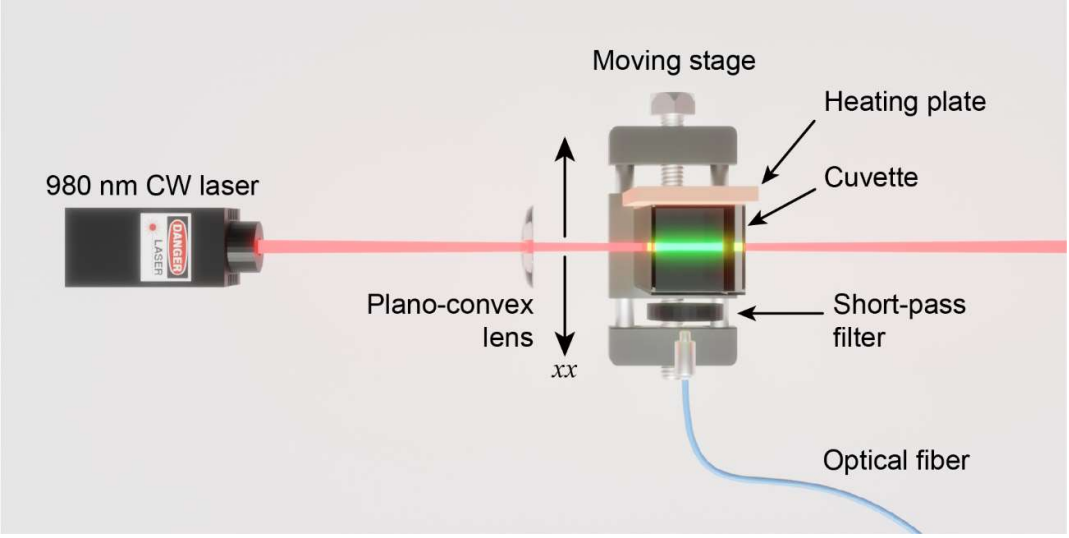

Fig. S7 Schematic of the experimental setup used to record the thermal transients of the nanofluids. The cuvette is placed on a controlled moving stage that allows the nanofluid to be irradiated at different positions along the *xx* direction. The 980 nm laser beam is collimated by a plano-convex lens and the light emission from the nanofluid is collected by an optical fiber coupled to a portable spectrometer.

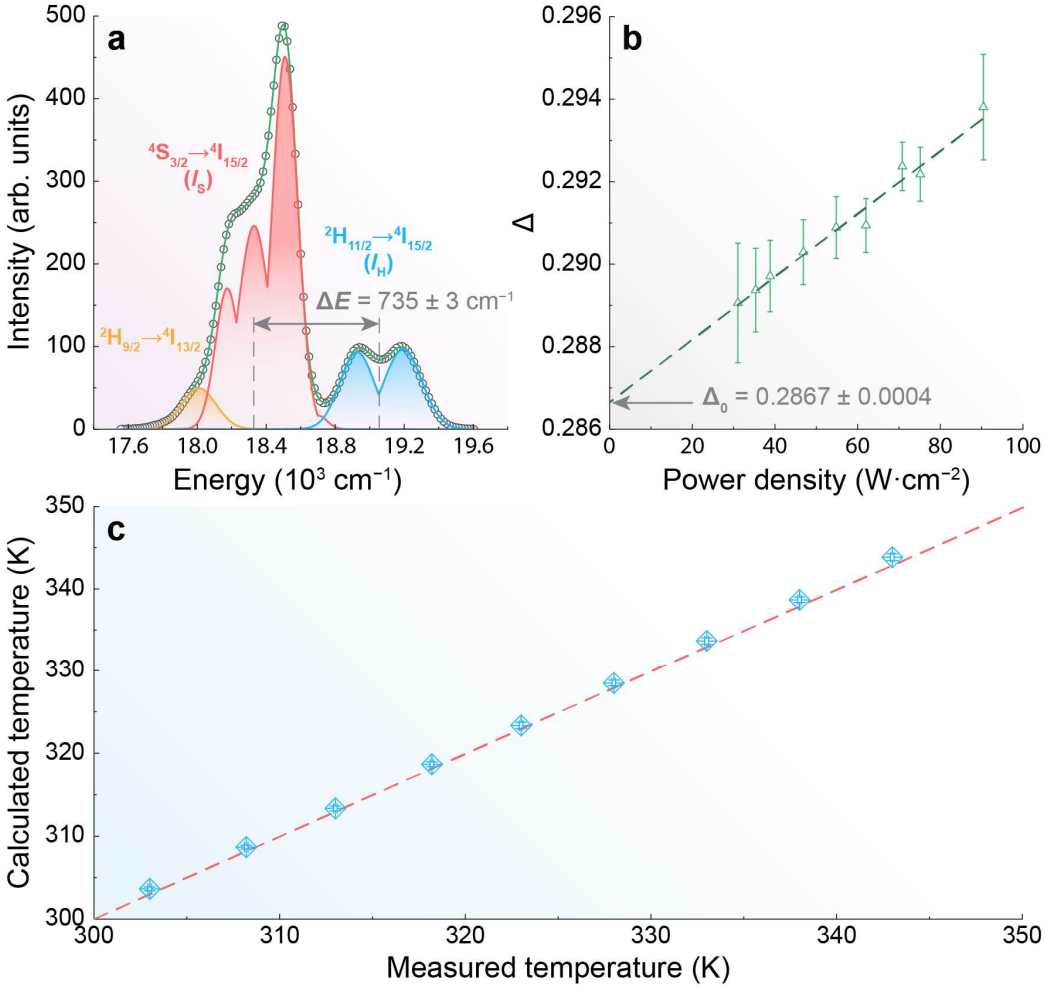

Fig. S8 Calibration curve of the 15 nm aqueous nanofluid (pH = 5.10). (a) Determination of the energy separation ΔE at 303.0 K. The areas shaded in yellow, red, and blue are the integrated intensities of the $^2H_{9/2}\rightarrow{}^4I_{13/2}$, $^4S_{3/2}\rightarrow{}^4I_{15/2}$ (I_S), and $^2H_{11/2}\rightarrow{}^4I_{15/2}$ (I_H) transitions of Er^{3+}. The green solid line is the fit envelope while the grey circles are the data from the emission spectrum measured at 303 K under excitation at 980 nm (62·W cm^{-2}). **(b)** Power dependence on the thermometric parameter Δ. The dashed green line is the best fit of the experimental data to a straight line ($r^2 > 0.99$), allowing to determine the value of Δ_0 at $T_0 = 300.0 \pm 0.1$ K. **(c)** Temperature calculated from Equation S1 (x-axis) *versus* the temperature measured with a K-type thermocouple (y-axis). The dashed red line is a guide for the eyes corresponding to $x = y$.

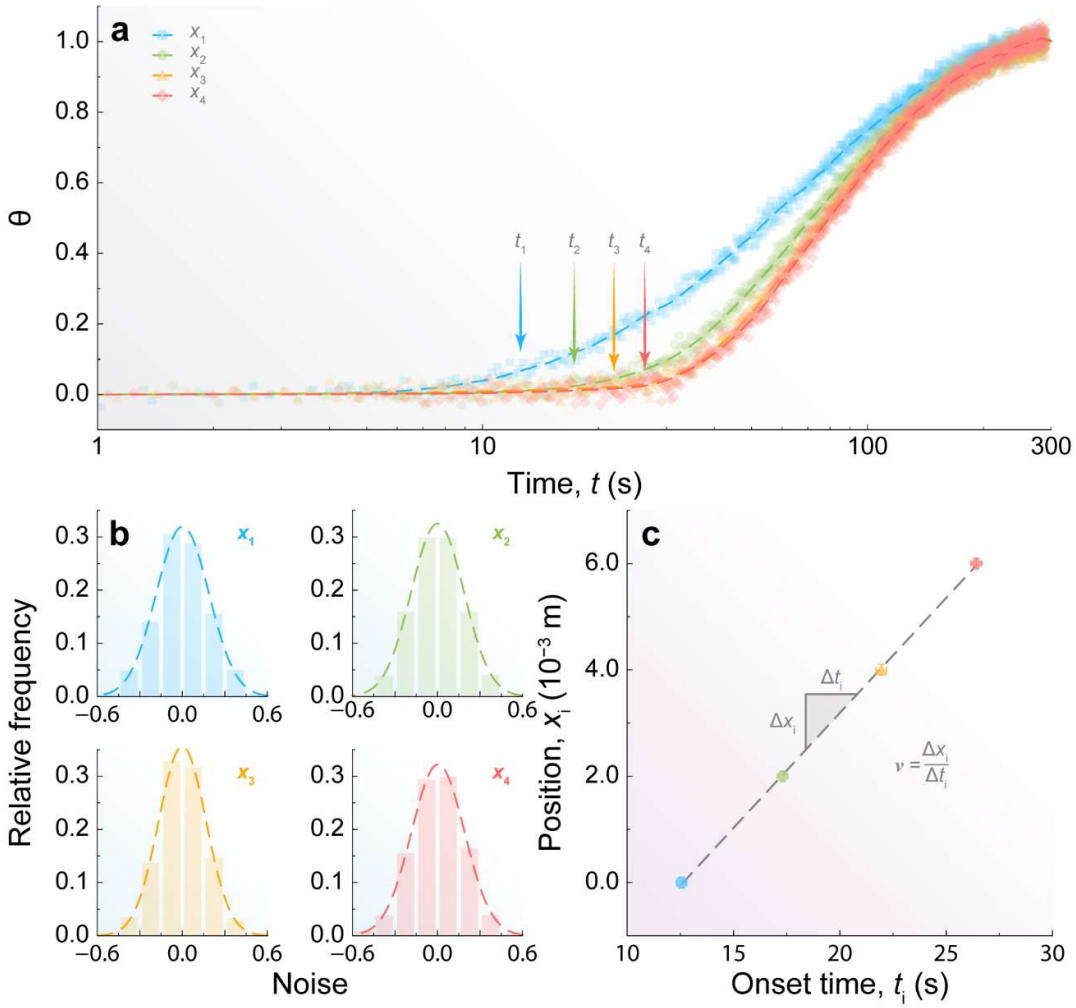

Fig. S9 Determination of the instantaneous Brownian velocity of 15 nm UCNPs dispersed in water (pH = 5.10 ± 0.01). (a) Illustrative denoising procedure applied to four reduced temperatures (symbols) recorded at positions x_1 = 0.0 mm, x_2 = 2.0 mm, x_3 = 4.0 mm, and x_4 = 6.0 mm. The dashed lines are the denoised signal obtained through the DWT procedure, where the onset t_i values are indicated. **(b)** Noise histograms (8 classes) from the curves in panel **a**. The dashed lines are the best fits to experimental data using Gaussian functions. It is possible to observe that the noise is nearly centered at zero, presenting a high coefficient of determination ($r^2 > 0.98$) for all samples, indicating that it corresponds to an additive Gaussian noise. **(c)** Determination of the instantaneous Brownian velocity v, corresponding to the slope ($\Delta x_i/\Delta t_i$) of the straight line adjusted to the experimental data from panel **a**. The error bars in x_i and t_i are the uncertainty in the position of the moving stage from Fig. S7 (0.1 mm) and the integration time used for spectral acquisition (250 ms), respectively.

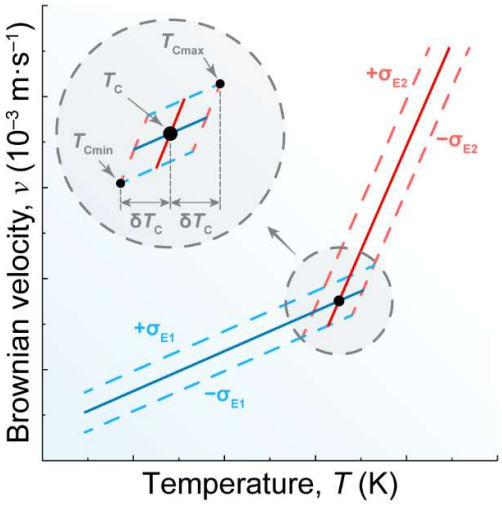

Fig. S10 Schematic representation of the calculation of the crossover temperature and its uncertainty ($T_c \pm \delta T_c$). The solid blue and red lines represent linear fits to the experimental data before and after T_c, respectively. The corresponding dashed lines depict the average deviation in the prediction of the Brownian velocity.

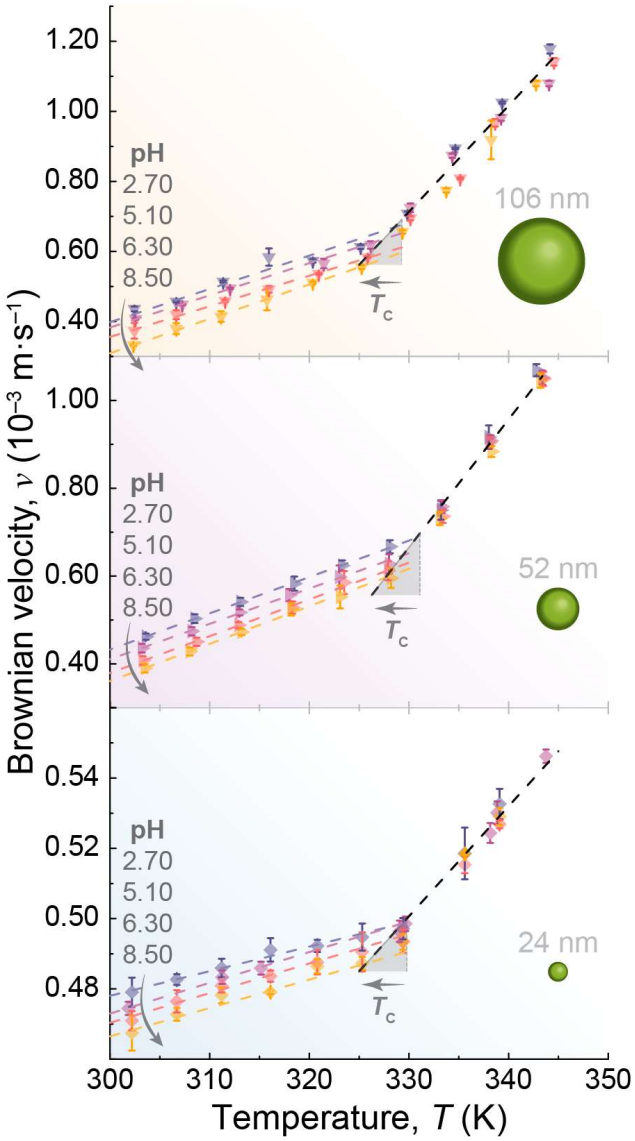

Fig. S11 Effect of pH on Brownian velocity of nanocrystals. pH dependence of the Brownian velocity of 24 nm, 52 nm, and 106 nm UCNPs. The lines are the best linear fits at each pH for $T<T_c$ and the same linear fit for all the pH values for $T>T_c$ ($r^2>0.98$ for all samples). The pH-dependent variation in the Brownian velocity of the 100 nm UCNPs with a silica shell was not assessed due to their lower colloidal stability for pH values different than 5.10.

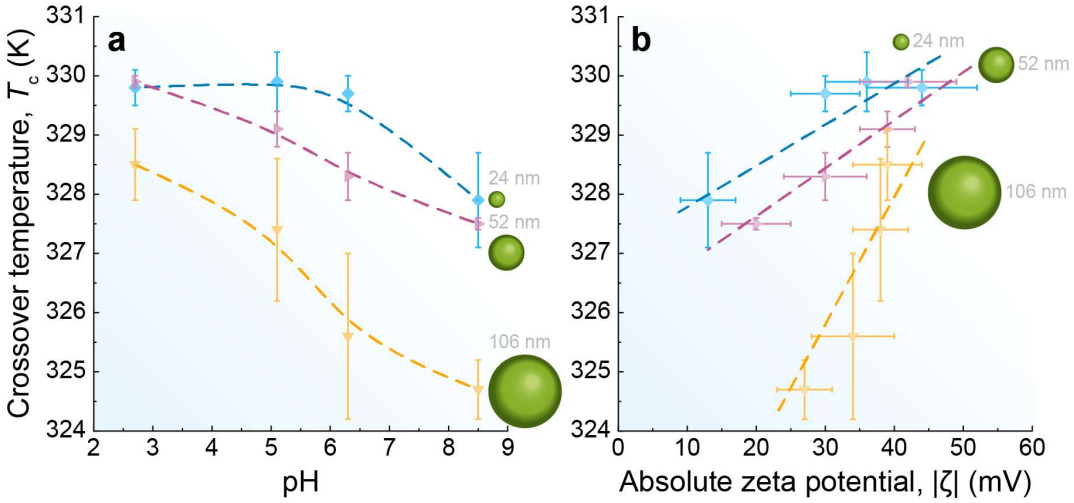

Fig. S12 pH and zeta dependence of the crossover temperature. Crossover temperature as a function of the **(a)** pH and **(b)** |ζ| for the 24, 52, and 106 nm diameter UCNPs. The lines are guides for the eyes.

IX. Supplementary Tables

Table S1. Size, chemical compositions of the core and shell, density (ρ_n), mass concentration (ρ_c), and volume fraction ($\phi = \rho_c/\rho_n$) of UCNPs dispersed in EtOH, D_2O, and H_2O.

Solvent	Size (nm)	Core	Shell	ρ_n (kg·m^{-3})	ρ_c (kg·m^{-3})	ϕ (%)
EtOH D_2O H_2O	15	$NaGdF_4$:Yb/Er(18/2%)	$NaGdF_4$	5,653	4.81	0.085
H_2O	24	$NaYF_4$:Yb/Er(18/2%)	$NaYF_4$	4,384	3.73	
	52	$NaYF_4$:Lu/Yb/Er(40/18/2%)	-	5,456	4.64	
	64	$NaYF_4$:Lu/Yb/Er(47/18/2%)	-	5,616	4.77	
	78	$NaYF_4$:Lu/Yb/Er(47/18/2%)	-	5,616	4.77	
	100	$NaYF_4$:Lu/Yb/Er(47/18/2%)	SiO_2	3,821	3.25	
	106	$NaYF_4$:Lu/Yb/Er(50/18/2%)	-	5,685	4.83	

Table S2. TEM (d) and hydrodynamic (d_H) diameters of the obtained UCNPs. The values of hydrodynamic diameters from DLS measurements correspond to the water-based nanofluids at pH = 5.10 ± 0.01. An excellent agreement was observed for the mean diameters reported by TEM and DLS.

UCNP	TEM diameter, d (nm)	Hydrodynamic diameter, d_H (nm)
$NaGdF_4$:Yb/Er(18/2%)@$NaGdF_4$	15 ± 3	13 ± 5
$NaYF_4$:Yb/Er(18/2%)@$NaYF_4$	24 ± 2	36 ± 8
$NaYF_4$:Lu/Yb/Er(40/18/2%)	52 ± 5	50 ± 7
$NaYF_4$:Lu/Yb/Er(47/18/2%)	64 ± 4	60 ± 8
$NaYF_4$:Lu/Yb/Er(47/18/2%)	78 ± 8	80 ± 12
$NaYF_4$:Lu/Yb/Er(47/18/2%)@SiO_2	100 ± 9	90 ± 22
$NaYF_4$:Lu/Yb/Er(50/18/2%)	106 ± 10	93 ± 26

Table S3. Energy separation (ΔE), maximum S_r (S_m), minimum temperature uncertainty (δT), and corresponding temperature at which they occur for each nanofluid.

Solvent	**Size (nm)**	**ΔE (cm^{-1})**	**S_m ($\%\cdot K^{-1}$)**	**δT (K)**	**T (K)**
EtOH				0.6	
D_2O	15	735 ± 3	1.15	0.3	
H_2O				0.4	
H_2O	24	680 ± 11	1.07	0.5	303.0 ± 0.1
	52	722 ± 9	1.13	0.4	
	64	740 ± 12	1.16	0.4	
	78	688 ± 8	1.08	0.5	
	100	688 ± 8	1.08	0.5	
	106	699 ± 10	1.10	0.5	

X. References

1 Wang, F. *et al.* Simultaneous phase and size control of upconversion nanocrystals through lanthanide doping. *Nature* **463**, 1061-1065 (2010).

2 Wu, Y., Xu, J., Qin, X., Xu, J. & Liu, X. Dynamic upconversion multicolour editing enabled by molecule-assisted opto-electrochemical modulation. *Nat. Commun.* **12**, 2022 (2021).

3 Brites, C. D. *et al.* Instantaneous ballistic velocity of suspended Brownian nanocrystals measured by upconversion nanothermometry. *Nat. Nanotechnol.* **11**, 851-856 (2016).

4 Brites, C. D. S. *et al.* Decoding a Percolation Phase Transition of Water at ~330 K with a Nanoparticle Ruler. *J. Phys. Chem. Lett.* **11**, 6704-6711 (2020).

5 Balabhadra, S., Debasu, M. L., Brites, C. D. S., Ferreira, R. A. S. & Carlos, L. D. Upconverting nanoparticles working as primary thermometers in different media. *J. Phys. Chem. C* **121**, 13962-13968 (2017).

6 Lang, M., Guo, H., Odegard, J. E., Burrus, C. S. & Wells, R. O. in *Wavelet Applications II,* Vol. 2491 (ed. Harold H. Szu) 640-651 (Proceedings SPIE, 1995).

7 Donoho, D. L. & Johnstone, I. M. Ideal spatial adaptation by wavelet shrinkage. *Biometrika* **81**, 425-455 (1994).

8 Donoho, D. L. De-noising by soft-thresholding. *IEEE Trans. Inf. Theory* **41**, 613-627 (1995).

9 Poole, P. H., Sciortino, F., Essmann, U. & Stanley, H. E. Phase-behavior of metastable water. *Nature* **360**, 324-328 (1992).

10 Neophytou, A., Chakrabarti, D. & Sciortino, F. Topological nature of the liquid–liquid phase transition in tetrahedral liquids. *Nat. Phys.* **18**, 1248-1253 (2022).

11 Debenedetti, P. G., Sciortino, F. & Zerze, G. H. Second critical point in two realistic models of water. *Science* **369**, 289-292 (2020).

12 Fanetti, S. *et al.* Structure and dynamics of low-density and high-density liquid water at high pressure. *J. Phys. Chem. Lett.* **5**, 235-240 (2014).

13 Oka, K. *et al.* Two states of water converge to one state below 215 K. *J. Phys. Chem. Lett.* **12**, 5802-5806 (2021).

14 Kringle, L., Thornley, W. A., Kay, B. D. & Kimmel, G. A. Reversible structural transformations in supercooled liquid water from 135 to 245 K. *Science* **369**, 1490-149 (2020).

15 Suzuki, Y. Experimental estimation of the location of liquid-liquid critical point for polyol aqueous solutions. *J. Chem. Phys.* **149**, 204501 (2018).

16 Suzuki, Y. Direct observation of reversible liquid-liquid transition in a trehalose aqueous solution. *Proc. Natl. Acad. Sci. USA* **119**, e2113411119 (2022).

17 Rosu-Finsen, A. *et al.* Medium-density amorphous ice. *Science* **379**, 474-478 (2023).

18 Huang, R. X. *et al.* Direct observation of the full transition from ballistic to diffusive Brownian motion in a liquid. *Nat. Phys.* **7**, 576-580 (2011).

19 Pettersson, L. G. M. in *Modern Problems of the Physics of Liquid Systems.* (eds. Bulavin L.A. & Xu L.) 3-39 (Springer Proceedings in Physics).

20 Bogdan, N., Vetrone, F., Ozin, G. A. & Capobianco, J. A. Synthesis of ligand-free colloidally stable water dispersible brightly luminescent lanthanide-doped upconverting nanoparticles. *Nano Lett.* **11**, 835-840 (2011).

21 Bhattacharjee, S. DLS and zeta potential – What they are and what they are not? *J. Control. Release* **235**, 337-351 (2016).

Manuscript 2

Decoding a Percolation Phase Transition of Water at ~330 K with a Nanoparticle Ruler

C. D. S. Brites, B. Zhuang, M. L. Debasu, D. Ding, X. Qin, F. E. Maturi, W. W. Y. Lim, D. W. Soh, J. Rocha, Z. Yi, X. Liu, L. D. Carlos.

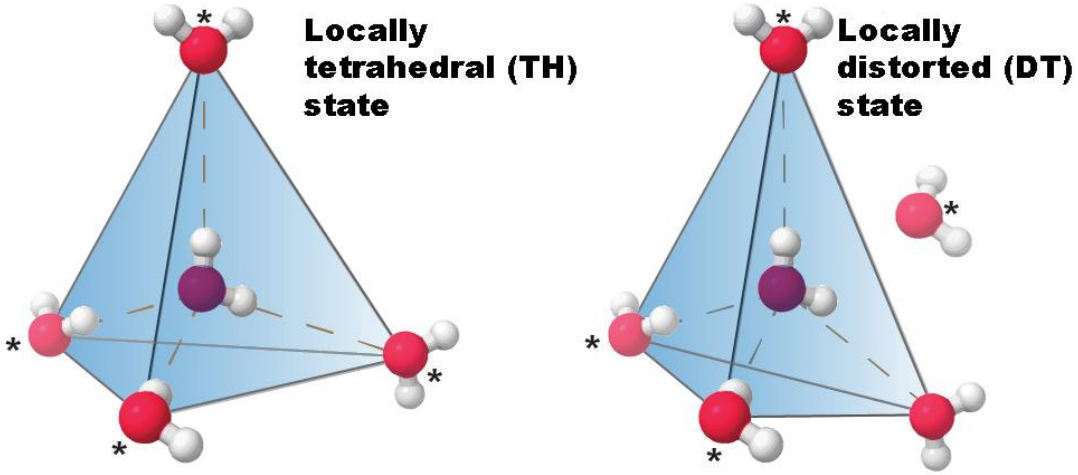

The Journal of Physical Chemistry Letters, 11 (16), 6704-6711, 2020.

DOI: https://doi.org/10.1021/acs.jpclett.0c02147

THE JOURNAL OF PHYSICAL CHEMISTRY Letters

pubs.acs.org/JPCL

Letter

Decoding a Percolation Phase Transition of Water at ~330 K with a Nanoparticle Ruler

Carlos D. S. Brites,[▽] Bilin Zhuang,*[,▽] Mengistie L. Debasu, Ding Ding, Xian Qin, Fernando E. Maturi, Winnie W. Y. Lim, De Wen Soh, J. Rocha, Zhigao Yi, Xiaogang Liu,* and Luís D. Carlos*

Cite This: *J. Phys. Chem. Lett.* 2020, 11, 6704–6711

Read Online

ACCESS | Metrics & More | Article Recommendations | Supporting Information

ABSTRACT: Liquid water, despite its simple molecular structure, remains one of the most fascinating and complex substances. Most notably, many questions continue to exist regarding the phase transitions and anomalous properties of water, which are subtle to observe experimentally. Here, we report a sharp transition in water at 330 K unveiled through experimental measurements of the instantaneous Brownian velocity of $NaYF_4$:Yb/Er upconversion nanoparticles in water. Our experimental investigations, corroborated by molecular dynamics simulations, elucidate a geometrical phase transition where a low-density liquid (LDL) clusters become percolated below 330 K. Around this critical temperature, we find the sizes of the LDL clusters to be similar to those of the nanoparticles, confirming the role of the upconversion nanoparticle as a powerful ruler for measuring the extensiveness of the LDL hydrogen-bond network and nanometer-scale spatial changes (20−100 nm) in liquids. Additionally, a new order parameter that unequivocally classifies water molecules into two local geometric states is introduced, providing a new tool for understanding and modeling water's many anomalous properties and phase transitions.

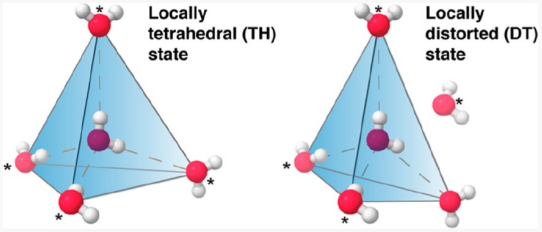

Water is the most important liquid for the existence of all life on Earth. Though it is the most common liquid, it is also the most uncommon in its behaviors, exhibiting a range of anomalous properties such as increased density upon melting, density maximum at 277 K (4 °C), reduced viscosity under pressure at below 306 K (33 °C), high surface tension, and decreased isothermal compressibility and heat capacity with temperature at ambient conditions (minimum values at 319 K (46 °C) and 308 K (35 °C), respectively).[1−3] In fact, it is quite questionable if life could have developed on the planet without these anomalous behaviors of water.[4,5] To explain these anomalous behaviors, the hypothesis of two organizations of hydrogen bonds competing at thermal equilibrium has been proposed.[3,6−11] These two hydrogen-bond organizations manifest as two phases, namely, the low-density liquid (LDL) and the high-density liquid (HDL), in the supercooled regime.[12−15] However, at ambient conditions, the existence of two distinct structural organizations and their implications remain elusive and controversial.

In the supercooled regime, the LDL is a predominantly low-energy hydrogen-bonded open tetrahedral configuration, while the HDL is a collection of interpenetrating shorter-ranged hydrogen-bond networks.[3,16−19] Despite the observation of the coexistence of these two structural motifs of water through spectroscopy[20,21] and scattering measurements,[22−25] the liquid structure inferred from these experiments is strongly debated. In this context, there is an intense demand for experimental techniques to microscopically decipher water's hydrogen-bonding structure.

Recently, upconversion nanothermometry was utilized to measure the instantaneous Brownian velocity of luminescent nanocrystals suspended in liquids.[26] Because the instantaneous Brownian velocity is sensitive to the local liquid environment, we use this method to measure the LDL motif that is known as a large tetrahedral network featuring strong cooperativity.[27] As a proof-of-concept experiment, we prepared and measured the instantaneous Brownian velocity of luminescent nanofluids containing $NaYF_4$:Yb/Er@$NaYF_4$ and $NaYF_4$:Lu/Yb/Er upconversion nanocrystals of 24 and 106 nm in diameter, respectively, dispersed in water, cyclohexene, and toluene with volume fractions (ϕ) of 0.085% and 0.066%, for the smaller and bigger nanocrystals, respectively (Supplementary Figures S1 and S2 and Tables S1 and S2). The experimental setup is similar to that in ref 26 and is detailed in Supporting Information. Whereas for cyclohexene and toluene the Brownian velocities increase linearly with increasing temperature, for water a bilinear behavior with a crossover temperature T_c = 329.9 ± 0.5 K (57 °C) for the 24 nm nanoparticles (pH 5.10 ± 0.01) and T_c = 327.4 ± 1.2 K (54 °C) for the 106 nm nanoparticles (pH 5.20 ± 0.01) is clearly

Received: July 14, 2020
Accepted: July 16, 2020
Published: July 16, 2020

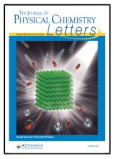

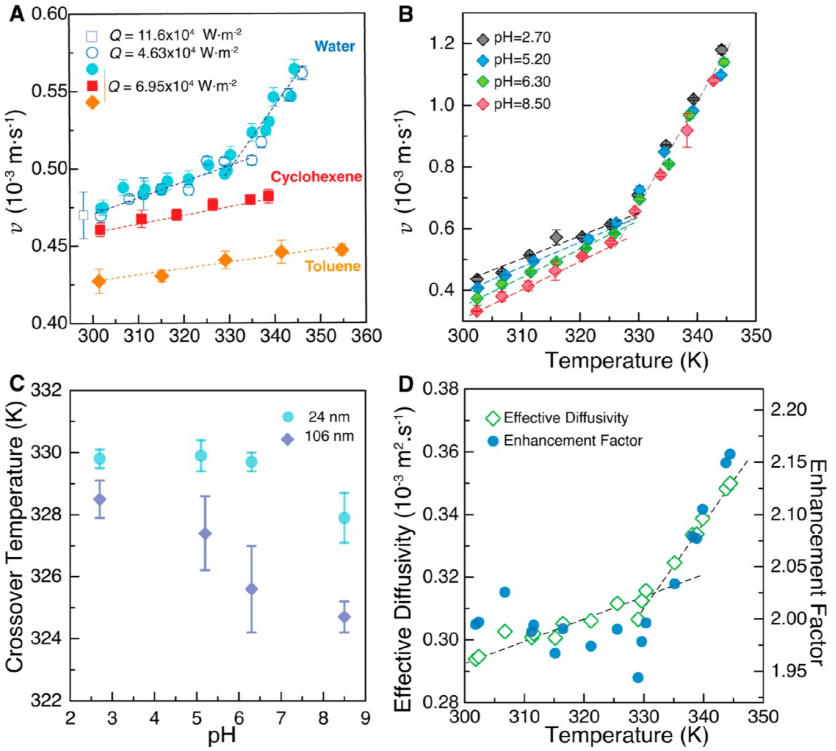

Figure 1. Dependence of the instantaneous Brownian velocity of the upconverting nanocrystals on the initial temperature and pH of the suspensions. (a) Temperature-dependent instantaneous Brownian velocities of the 24 nm nanoparticles suspended in water (pH 5.10 ± 0.01), cyclohexene and toluene at initial (equilibrium) temperatures between 300 and 355 K. Vertical error bars represent mean ± SD, whereas the uncertainty in the temperature values (thermocouple accuracy, 0.1 K) is too small to be discernible in the plots. The Brownian velocities are independent of the heat flux transferred to the nanofluid (Q). The open square depicts data previously reported in similar upconverting nanoparticles.[26] The crossing of the two straight lines in the water suspensions corresponds to the crossover temperature T_c. (b) Temperature dependence of the Brownian velocity of the 106 nm nanoparticles in water suspensions with distinct pH values. (c) The dependence on pH of the crossover temperatures. (d) Effective diffusivity and enhancement factor of the nanofluid with 24 nm nanoparticles (pH 5.10 ± 0.01) with respect to pure water. All lines are the best fits to straight lines (slopes and correlation coefficients r^2 are shown in Supplementary Table S3).

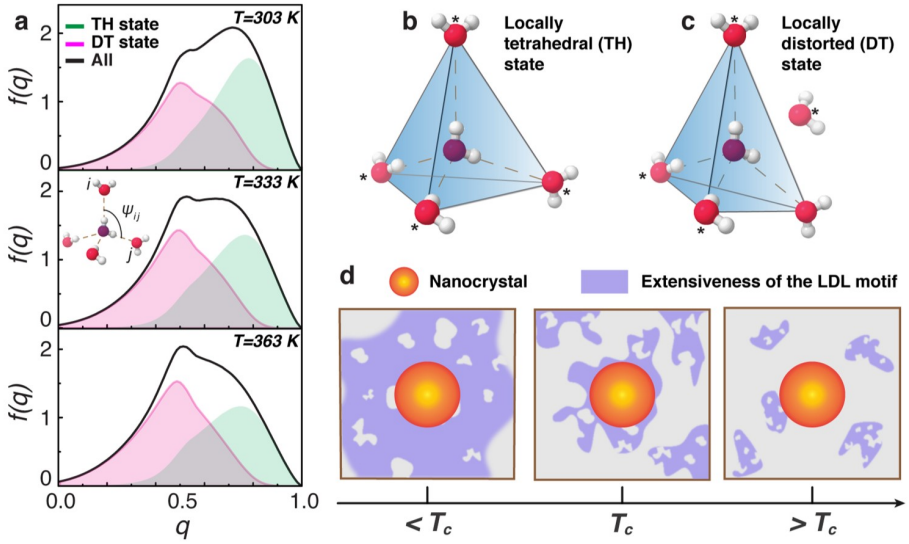

Figure 2. Structural investigations of liquid water. (a) Probability density function $f(q)$ of the orientational order parameter q (eq 1) for water at 303, 333, and 363 K, calculated based on the molecular dynamics simulation of a cubic box of 1024 water molecules with the polarizable SWM4-NDP water model. The contributions toward $f(q)$ of the locally tetrahedral (TH) state and the locally disturbed (DT) state are shown as shaded areas. (b and c) Schematics of the molecular arrangements around a water molecule (denoted with oxygen atoms in purple) in the TH state and the DT state. The asterisk next to the oxygen atoms denotes the four nearest neighbors. (d) Schematic of the length scale of the LDL motif (in purple) made up of connected TH-state molecules in comparison to the nanoparticle size (in orange).

https://dx.doi.org/10.1021/acs.jpclett.0c02147
J. Phys. Chem. Lett. 2020, 11, 6704−6711

discerned (Figure 1a,b and Supplementary Figures S9−S14). Moreover, for $T > T_c$, there is a noticeable increase in the slope of the linear correlation between v and T (Supplementary Table 3). These values of T_c are within the range of those reported for different physical properties of liquid water: thermal conductivity (337 ± 5 K), proton spin−lattice relaxation time (323 ± 5 K), refractive index (323 ± 5 K), conductivity (326 ± 5 K), surface tension (330 ± 5 K), and kinetic viscosity (323 ± 6 K),[11] as described in Supplementary Figure 12. Moreover, this bilinear trend was also observed in studies involving metallic nanoparticles,[28] colloidal Ln^{3+}-based nanocrystals,[29] Eu^{3+} aqueous complexes,[30,31] and organic molecules.[32,33]

The bilinear behavior observed in the instantaneous velocity of nanoparticles in water indicates two regimes of nanoparticle motion, where the nanoparticles exhibit a different effective mass m^*, signaling a change in the water−nanoparticle interaction. For a nanoparticle 24 nm in diameter, m^* changes drastically at T_c, because the slope of v^2 versus T for $T > T_c$ increases 4- to 5-fold relative to that for $T < T_c$ (Figure 2a and Supplementary Table S4), based on the equipartition theorem $v^2 = k_B T/m^*$. Because the effective mass is influenced by both the nanoparticle's mass m_N and the mass of the fluid m_C moving cooperatively with the nanocrystal, the drastic alteration of effective mass at T_c indicates a discontinuous change in the amount of fluid that moves cooperatively with the nanoparticle. By estimating the size of the LDL motif (Supporting Information Section 2.1), we find a plausible mechanistic explanation that, at T_c, the sizes of LDL motifs and nanoparticles are comparable, so that below T_c the nanocrystal has to move collectively with the surrounding LDL motif (Figure 2d). In this respect, by measuring the T_c, one may use the nanoparticle as a ruler to measure the size of the LDL motif.

To rationalize the transition observed in the nanoparticles' effective mass, we investigate the underlying local order of the liquid water through molecular dynamics (MD) simulation based on the polarizable SWM4-NDP water model.[34] Because the tetrahedral geometry is key to distinguish the two different structures as the low-density water is thought to be more "ice-like",[35] we first examine a tetrahedral orientational order parameter q for each water molecule,[36,37] given by

$$q = 1 - \frac{3}{8}\sum_{j=1}^{3}\sum_{k=j+1}^{4}\left(\cos\psi_{jk} + \frac{1}{3}\right)^2 \quad (1)$$

This q-value considers the relative angular positions in the four nearest neighbors around each water molecule. The summations run over all six jk pairs among the four nearest neighbors. ψ_{jk} denotes the angle extended from the oxygen atom of the molecule to the oxygen atoms of neighbors j and k (inset of Figure 2a). The q-value grows with the tetrahedral order around a molecule, with its average value equal to one for ordinary ice and zero for an ideal gas. At ambient conditions, the probability density function $f(q)$ exhibits two overlapping peaks (Figure 2a): one at higher q that decreases with temperature and the other at lower q that increases with temperature.[37] These two peaks suggest the existence of two local structural states of water with different tetrahedral orders, but to date, their origin has not been elucidated.

Here, we introduce a new method to classify water molecules into two local structural states that give rise to the two peaks in $f(q)$. Because the peak at higher q indicates a state with a higher tetrahedral order, the positions of the four nearest neighbors are close to the vertices of a regular tetrahedron (Figure 2b). We denote this state as the locally tetrahedral (TH) state. The peak at lower q, on the other hand, indicates a state with less tetrahedral order. Owing to the open configuration in the TH-state, the second state involves an additional water molecule at an interstitial site that makes the liquid structure more tightly packed. We denote this state as the locally distorted (DT) state (Figure 2c). For a molecule in the DT-state, as the newly added molecule may become one of the four nearest neighbors, greater tetrahedral order may be found when the fifth nearest neighbor is taken into account. Therefore, we consider a generalized tetrahedral orientational order parameter q_5 to be given by the maximum value of q for any 4 out of the 5 nearest neighbors (see the Supporting Information for a detailed description):

$$q_5 = \max_{\substack{\text{any 4 out of}\\ \text{5 nearest}\\ \text{neighbors}}}\left[1 - \frac{3}{8}\sum_{jk}\left(\cos\psi_{jk} + \frac{1}{3}\right)^2\right] \quad (2)$$

where the summation runs over all pairs jk among the 4 chosen neighbors. A comparison between q and q_5 allows us to distinguish the two local structural states. In the TH state, the 4 nearest neighbors give the maximal tetrahedral order, and thus $q_5 = q$. In contrast, in the DT state, the maximal tetrahedral order arises when the fifth nearest neighbor is considered, and thus $q_5 > q$. With this rule distinguishing the two underlying states, the two closely spaced peaks in $f(q)$ (Figure 2a) are decoupled. In view of the simplicity of this classifying rule, the decoupling of the two states is considered effective, despite a slight shoulder peak that can still be discerned in the distribution of the DT state. Additional simulations based on the TIP4P-FB water model[38] support the two-state behavior observed in the SWM4-NDP model (see the Supporting Information). While there have been attempts to elucidate the two-state nature of water,[7,11,39−41] to the best of our knowledge, this is the first rule that allows one to classify water molecules into two states without introducing *ad hoc* cutoff values or fitting parameters.

Connected TH-state molecules can form a long-ranged hydrogen-bond network, consistent with the LDL liquid structure as a large tetrahedral network featuring strong cooperativity.[27] In contrast, such cooperativity is much weaker in the HDL motif formed by the DT-state molecules, in which the hydrogen bond network is less structured and shorter-ranged. Because of the two-state nature of the hydrogen-bond network, there is necessarily a geometric percolation transition that is not thermodynamic in origin. Although the two motifs interpenetrate with each other, the network formed by TH-state molecules is long-ranged and is consequential for transport properties on a larger length scale. It should be noted that the TH-state defined here is not equivalent to the low-density state that is defined elsewhere,[7,42,43] and the connection between different two-state classifications is a subject of future work.

With nanoparticles of different sizes, the difference between T_c values of smaller and bigger nanocrystals is, in all the pH range tested, around 3 K (Figure 1c), suggesting a drastic change in the length scale of the LDL motif around T_c (Supplementary Figure S11). This suggests that the fluctuations of LDL motifs become correlated and grow in spatial

https://dx.doi.org/10.1021/acs.jpclett.0c02147
J. Phys. Chem. Lett. 2020, 11, 6704−6711

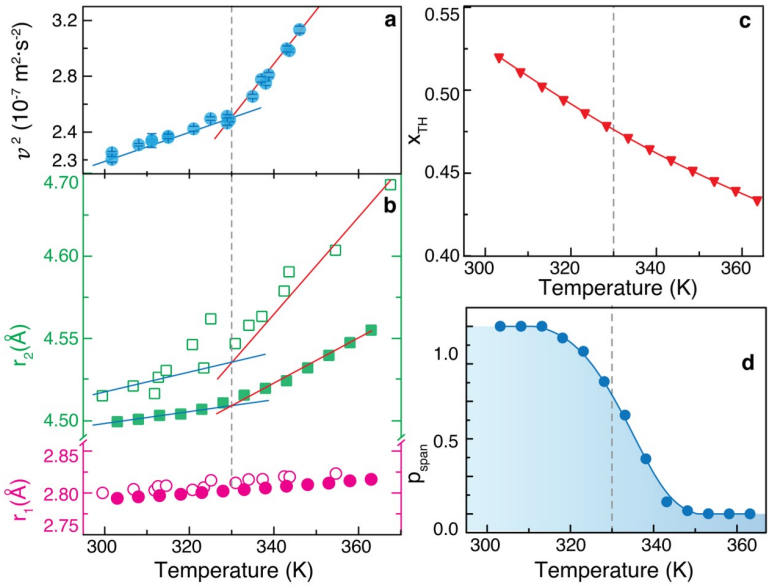

Figure 3. Brownian velocity of the upconverting nanocrystals versus liquid water structural data. (a) Temperature dependence of the square of the instantaneous Brownian velocity of the 24 nm nanocrystals in water suspension. The straight lines are the best fit to the experimental data (r^2 > 0.989 and correlation coefficients in Supplementary Table S7). (b) Simulated and experimental data on the positions of the first maximum (r_1) and second maximum (r_2) in the O−O pair distribution function. The open circles and squares depict high-energy X-ray diffraction data and the solid circles and squares result from the MD simulations of the SWM4-NDP water model, adapted (without error bars) from ref 23 (points below 300 K are not displayed). Copyright 2014. AIP Publishing. The straight lines are the best fit to the diffraction and simulation data (correlation coefficients in Supplementary Table S6). (c) Fraction of molecules in the TH-state, x_{TH}, computed from MD simulations of SWM4-NDP water model. (d) Estimated probability for finding an LDL motif spanning the size of a 24 nm nanocrystal, where a strong crossover from 1 to 0 is observed at around 330 K. The dashed lines indicate the crossover temperature observed in the instantaneous Brownian velocity of 24 nm nanocrystals.

extent below T_c,[3,44] and this could be due to the underlying percolation transition such that the LDL motif formed by TH-state molecules becomes percolated below T_c. While liquid water has been known to be a large cluster of connected hydrogen-bonded network,[45−47] here, we are concerned with the more tetrahedrally structured network formed by TH-state molecules. Although individual hydrogen bonds in the network have short lifetime, they are likely to reform because of the favorable tetrahedral geometry. Therefore, the network formed by TH-state molecules would be more cooperative over a longer range and more persistent. Moreover, it should be noted that the LDL motifs cannot be thought of as density heterogeneities measured by small-angle X-ray scattering (SAXS) measurements (dimensions of the order of 1 nm at ambient conditions).[16,48,49] The LDL motifs are formed by a tetrahedral (ice-like) network of TH-state molecules with many empty pockets between for the less-ordered, shorter-ranged HDL water network (dominant in ambient conditions) and thus are larger than the density heterogeneities measured by SAXS measurements (regions occupied by TH-state molecules exclusively). Upon computing the fraction of TH-state molecules (Figure 3c), x_{TH}, we notice that the fraction at $T_c \approx 330$ K is close to the site percolation threshold for a diamond lattice, $x_{c,diamond} \approx 0.43$.[50] On the basis of molecular configurations sampled in MD simulations, we estimate the probability of finding an LDL motif spanning the size of the 24 nm nanoparticle and observe that this probability changes rapidly from 1 to 0 around T_c (Figure 3d, calculation details in the Supporting Information), consistent with the behavior of a percolation transition.[50]

Because of this transition, there is a swift crossover in many water properties. Below T_c, LDL motifs span the liquid, increasing the structural fluctuation between the two classes of H-bond networks. Above T_c, LDL structures are short-ranged such that water behaves like a simple liquid. An example of the swift crossover has been observed in the position of the second maximum of O−O pair distribution function as a function of temperature obtained through high-energy X-ray-scattering measurements[23] and our MD simulations. While the position of the first maximum (r_1) increases linearly with temperature, the second maximum (r_2) exhibits a bilinear behavior with a crossover at T_c at around 330 K (Figure 3b). The agreement between X-ray diffraction and the simulation is remarkably close given that no simulation model exactly reproduces real water. The agreement between the T_c values of our experiment and of the $v^2(T)$ and $r_2(T)$ is also remarkable.

In a further set of experiments, we measured the temperature dependence of the Brownian velocity of colloidal nanocrystals in the water at pH values in the range of 2.70−8.50, as illustrated in Figure 1b. Notably, for both $NaYF_4$:Yb/Er@$NaYF_4$ and $NaYF_4$:Lu/Yb/Er nanocrystals, whereas for $T > T_c$ the rate of increase of the Brownian velocity with temperature is independent of the nanofluid's pH, for $T < T_c$ that rate changes with the pH in such a way that the Brownian velocity increases with decreasing pH (Figure 1b). Furthermore, T_c increases with decreasing pH (Figure 1c), suggesting H_3O^+ increases the size of the LDL motif because its oxygen atom is sp^3-hybridized and, thus, geometrically similar to TH-state water molecules. However, the observed increase of the Brownian velocity with decreasing pH for $T < T_c$ suggests that H_3O^+ destabilizes the hydrogen-bond network in the LDL motif, making the network motion less cooperative.

Using a two-plate thermal diffusion model, we can accurately describe our measured instantaneous Brownian velocity with

https://dx.doi.org/10.1021/acs.jpclett.0c02147
J. Phys. Chem. Lett. 2020, 11, 6704−6711

thermal diffusion (see Supporting Information). The two-plate model predicts a linear trend of t_0 versus x_i in Figure S3 and shows a linear relationship between thermal diffusivity and the predicted velocity (Supplementary Figures S15−S18). Extrapolating this relation using the thermal diffusivity for pure water,[51−53] we predict the thermal diffusivity for the 24 nm nanoparticles suspended in water to be enhanced more than two times, as compared to that of pure water in the same temperature range (Figure 1d). Though this large enhancement is a prediction based on thermal modeling, it is within the range of enhancements observed experimentally in some nanofluids.[54,55] It is worth noting that our numerical model highlights the fact that the temperature detected by luminescence nanocrystals obeys macroscopic thermal transport. However, to understand the exact nature of the Brownian motion at nonequilibrium conditions, comprehensive models accounting for nanoconvection and other nanoscale effects are required. Additionally, effects of ions and the surface water structure on nanoparticles may be considered in a more comprehensive model of the system.

Using suspended nanocrystals as rulers, we have been able to detect a crossover temperature in the nanoparticle's instantaneous Brownian velocity in water, at which temperature the size of the nanoparticle and the LDL motif are comparable. This rapid change of the size of the LDL motif at around 330 K is a result of an underlying percolation transition. Because the long-range hydrogen-bond network in LDL motif is the key to decipher the behavior of water,[56] understanding the temperature dependence of its length scale will provide insight into the properties as well as the mechanisms, functions, and roles of water, for instance, in influencing the stability of proteins[57,58] and how they are denatured at temperatures close to the T_c value reported. Beyond the properties of water, the experimental technique of upconversion thermometry of suspended Brownian nanocrystals also has broader significance for probing interactions in fluids, for example, in the physics of the glass transition, where the cooperatively rearranging region in the glassy liquid is the central concept.[59]

METHODS

General Description. We prepared luminescent nanofluids containing $NaYF_4$:Yb/Er@$NaYF_4$ and $NaYF_4$:Lu/Yb/Er upconversion nanocrystals of different sizes (24 and 106 nm in diameter, respectively) dispersed in water, cyclohexene, and toluene with volume fractions (ϕ) of 0.085% and 0.066%, for the smaller and bigger nanocrystals, respectively (Supplementary Figures S1 and S2 and Tables S1 and S2). For distinct initial equilibrium temperatures (ranging between 300 and 355 K), we heated the nanofluids and recorded their time-dependent emission spectra upon 980 nm excitation in different fixed positions along the *xx* direction (x_i = 0.2−0.9 cm, i = 1−6, Supplementary Figures S3 and S4). For each time instance, the absolute temperature (T) is calculated through the intensity ratio (the thermometric parameter Δ) between the $^2H_{11/2} \rightarrow {}^4I_{15/2}$ (I_H, 510−535 nm) and $^4S_{3/2} \rightarrow {}^4I_{15/2}$ (I_S, 535−565 nm) Er^{3+} emission bands, as[26]

$$\frac{1}{T} = \frac{1}{T_0} - \frac{k_B}{\Delta E}\ln\left(\frac{\Delta}{\Delta_0}\right) \quad (3)$$

where Δ_0 is the thermometric parameter at a reference temperature T_0, k_B the Boltzmann constant, and ΔE the energy gap between the $^2H_{11/2}$ and $^4S_{3/2}$ levels. The ΔE and Δ_0 values are determined independently by taking into account the barycenter of the $^2H_{11/2}$ (~525 nm), $^4S_{3/2}$ (~545 nm), and $^4I_{15/2}$ energy levels and from the dependence with the laser excitation power of the thermometric parameter, respectively (Supplementary Figures S5 and S6). The thermometric parameter $\Delta = I_H/I_S$ increases with rising temperature,[26] because the relative population of the $^2H_{11/2}$ and $^4S_{3/2}$ levels are in thermal equilibrium, following the Boltzmann's distribution.[26] In Supplementary Figures S3a,b and S4 (where T is expressed as a reduced temperature, Supporting Information), a critical time t_{0i} is determined from the onset of change in the Er^{3+} upconversion induced by the temperature variation, and the slope of the line plot between x_i and t_{0i} gives the instantaneous Brownian velocity v of the suspended upconverting nanocrystals[26] (Supplementary Figure 3c,d). The critical time t_{0i} is determined from the onset of the temperature variation (Supplementary Figures 3 and 4) and the slope of the line plot between x_i and t_{0i} gives the instantaneous Brownian velocity v of the suspended $NaYF_4$:Yb/Er@$NaYF_4$ and $NaYF_4$:Lu/Yb/Er upconversion nanocrystals (see ref 26 for details). For each fixed position x_i, we observe a marked decrease of t_{0i} with rising initial equilibrium temperature of the nanofluid (Supplementary Figure 3c,d for the illustrative example $x_i = 0.8 \times 10^{-2}$ m).

Preparation of Upconversion Nanocrystals. $NaYF_4$:Yb/Er(18/2%)@$NaYF_4$ (average diameter 24 nm) and $NaYF_4$:Lu/Yb/Er (50/18/2%) (average diameter 106 nm) nanocrystals were synthesized by a standard coprecipitation or modified hydrothermal method according to ref 60. Further experimental details are available in the Supporting Information.

Operating Procedure for Temperature Mapping. In a typical experiment, a Thorlabs quartz cuvette (CV10Q1400) was used as the container and filled with 0.50 mL of nanofluid at an initial temperature between 300 and 355 K. For water suspensions, the pH ranges from 2.70 to 8.50 (±0.01). The nanofluid's temperature is further increased through the Joule effect using a Kapton thermofoil heater (Minco) in thermal contact with one side of the cuvette. The initial temperature of the nanofluids was measured by an immersed thermocouple (I620-20147, VWR) with an accuracy of 0.1 K, according to the manufacturer. Temperature increments of 10 and 15 K were generated corresponding to a heat flux transferred to the nanofluid (Q) of 4.64×10^4 and 6.96×10^4 W·m^{-2}, respectively. A continuous-wave (CW) laser diode (980 nm, 0.5 W), positioned next to the container, is focused through an optical lens (7.5 cm focal distance) and is controlled by a moving stage with a minimum step of 0.001 mm. Under 980 nm excitation, the nanocrystals' upconversion emission is collected by a collimating lens (74-UV, Ocean Optics), and the signals are subsequently guided to the detector (Maya 2000 Pro, Ocean Optics) through a QP450-1-XSR optical fiber (Ocean Optics). The signals were denoised through the DWT procedure. Further experimental details and experimental data treatments are available in the Supporting Information.

Molecular Dynamics Simulation of Water. Molecular dynamics simulation for the polarizable SWM4-NDP water model[34] was carried out using an extended Lagrangian dynamics with a dual-Langevin thermostat[61] with the OpenMM package.[62] At each temperature, the size of the cubic simulation box was set such that the density of water molecules in the simulation box matched the density of water at atmospheric pressure (Supplementary Table S6). Periodic boundary conditions are applied. For the dual-Langevin thermostat, the friction

https://dx.doi.org/10.1021/acs.jpclett.0c02147
J. Phys. Chem. Lett. 2020, 11, 6704−6711

coefficients for the center-of-mass and for the internal Drude-pair degrees of freedom were 20 ps^{-1} and 1 ps^{-1}, respectively, and the temperature set for the internal Drude-pair was 1 K. The time step for the integration was 1 fs. For each randomly generated initial configuration, the system was first annealed from 373.15 K to the desired temperature in 100 equal-interval temperature steps and 1 ps per step, followed by equilibration at the desired temperature for 1 ns. Then, the configuration state of the water was sampled every 10 ps for 70 ns. The sampling was repeated independently for 8 times for each system size and temperature.

■ ASSOCIATED CONTENT

Supporting Information

The Supporting Information is available free of charge at https://pubs.acs.org/doi/10.1021/acs.jpclett.0c02147.

Nanoparticle synthesis, materials characterizations, computational methods, study of the effective mass of the nanoparticles, and investigation of instantaneous Brownian velocity and thermal diffusivity (PDF)

■ AUTHOR INFORMATION

Corresponding Authors

Bilin Zhuang − *Institute of High Performance Computing, Singapore 138632 Singapore; Yale-NUS College, Singapore 138527 Singapore*; Email: zhuangbl@ihpc.a-star.edu.sg

Xiaogang Liu − *Department of Chemistry, National University of Singapore, Singapore 117543 Singapore; Joint School of National University of Singapore and Tianjin University, International Campus of Tianjin University, Fuzhou 350207, P.R. China*; orcid.org/0000-0003-2517-5790; Email: chmlx@nus.edu.sg

Luís D. Carlos − *Phantom-g, CICECO − Aveiro Institute of Materials, Department of Physics, Universidade de Aveiro, 3810−193 Aveiro, Portugal*; orcid.org/0000-0003-4747-6535; Email: lcarlos@ua.pt

Authors

Carlos D. S. Brites − *Phantom-g, CICECO − Aveiro Institute of Materials, Department of Physics, Universidade de Aveiro, 3810−193 Aveiro, Portugal*; orcid.org/0000-0001-9636-2628

Mengistie L. Debasu − *Phantom-g, CICECO − Aveiro Institute of Materials, Department of Physics and Department of Chemistry and CICECO − Aveiro Institute of Materials, Universidade de Aveiro, 3810−193 Aveiro, Portugal*; orcid.org/0000-0003-2516-9665

Ding Ding − *Institute of Materials Research and Engineering, Singapore 138634 Singapore*

Xian Qin − *Department of Chemistry, National University of Singapore, Singapore 117543 Singapore*

Fernando E. Maturi − *Phantom-g, CICECO − Aveiro Institute of Materials, Department of Physics, Universidade de Aveiro, 3810−193 Aveiro, Portugal*

Winnie W. Y. Lim − *Institute of High Performance Computing, Singapore 138632 Singapore*

De Wen Soh − *Institute of High Performance Computing, Singapore 138632 Singapore*

J. Rocha − *Department of Chemistry and CICECO − Aveiro Institute of Materials, Universidade de Aveiro, 3810−193 Aveiro, Portugal*; orcid.org/0000-0002-0417-9402

Zhigao Yi − *Department of Chemistry, National University of Singapore, Singapore 117543 Singapore*; orcid.org/0000-0003-0853-2055

Complete contact information is available at: https://pubs.acs.org/10.1021/acs.jpclett.0c02147

Author Contributions

[V]C.D.S.B. and B.Z. contributed equally to this work. C.D.S.B., B.Z., and L.D.C. conceived the project. B.Z., D.D., W.W.Y.L., and D.W.S. performed the simulations and theoretical calculations, whereas C.D.S.B., M.L.D., F.E.M., and Z.Y. performed the experiments. X.Q., J.R., B.Z., X.L., and L.D.C. provided input into the design of the experiments (the two last authors supervised the whole project). B.Z., D.D., X.L., and L.D.C. cowrote the manuscript with input from other authors.

Notes

The authors declare no competing financial interest.

■ ACKNOWLEDGMENTS

This work was partially developed within the scope of the project CICECO-Aveiro Institute of Materials, UIDB/50011/2020 & UIDP/50011/2020, financed by national funds through the FCT/MEC and when appropriate cofinanced by FEDER under the PT2020 Partnership Agreement. Financial support from the European Union's Horizon 2020 FET Open programme under Grant Agreement No. 801305 and FCT (PTDC/CTM-NAN/4647/2014 and NANOHEATCONTROL - POCI-01-0145-FEDER-031469 funded by FEDER, through POCI and by national funds, OE, through FCT/MCTES) is also acknowledged. The authors acknowledge JFCBR (University of Aveiro) for his help with the signal denoising procedure. C.D.S.B. thanks SusPhotoSolutions project, CENTRO-01-0145-FEDER-000005, Portugal. X.L. is grateful for the support by the Singapore Ministry of Education (MOE2017-T2-2-110), Agency for Science, Technology and Research (A*STAR) (Grant No. A1883c0011 and A1983c0038), National Research Foundation, Prime Minister's Office, Singapore under the NRF Investigator ship programme (Award No. NRF-NRFI05-2019-0003). D.D. acknowledges support by A*STAR under an AME Young Individual Research Grant (Grant No. A1884c0020). B.Z. acknowledges support by A*STAR under the SERC Career Development Award (Grant No. A1820g0085).

■ REFERENCES

(1) Ball, P. Water - an enduring mystery. *Nature* **2008**, *452*, 291−292.

(2) Pettersson, L. G. M.; Henchman, R. H.; Nilsson, A. Water - the most anomalous liquid. *Chem. Rev.* **2016**, *116*, 7459−7462.

(3) Nilsson, A.; Pettersson, L. G. M. The structural origin of anomalous properties of liquid water. *Nat. Commun.* **2015**, *6*, 8998.

(4) Chaplin, M. Opinion - do we underestimate the importance of water in cell biology? *Nat. Rev. Mol. Cell Biol.* **2006**, *7*, 861−866.

(5) Pohorille, A.; Pratt, L. R. Is water the universal solvent for life? *Origins Life Evol. Biospheres* **2012**, *42*, 405−409.

(6) Poole, P. H.; Sciortino, F.; Essmann, U.; Stanley, H. E. Phase-behavior of metastable water. *Nature* **1992**, *360*, 324−328.

(7) Russo, J.; Tanaka, H. Understanding water's anomalies with locally favoured structures. *Nat. Commun.* **2014**, *5*, 3556.

(8) Amann-Winkel, K.; et al. X-ray and neutron scattering of water. *Chem. Rev.* **2016**, *116*, 7570−7589.

(9) Gallo, P.; et al. Water: A tale of two liquids. *Chem. Rev.* **2016**, *116*, 7463−7500.

(10) Hamm, P. Markov state model of the two-state behaviour of water. *J. Chem. Phys.* **2016**, *145*, 134501.
(11) Maestro, L. M.; et al. On the existence of two states in liquid water: Impact on biological and nanoscopic systems. *Int. J. Nanotechnol.* **2016**, *13*, 667−677.
(12) Palmer, J. C.; et al. Metastable liquid-liquid transition in a molecular model of water. *Nature* **2014**, *510*, 385−388.
(13) Perakis, F.; et al. Diffusive dynamics during the high-to-low density transition in amorphous ice. *Proc. Natl. Acad. Sci. U. S. A.* **2017**, *114*, 8193−8198.
(14) Lin, C.; Smith, J. S.; Sinogeikin, S. V.; Shen, G. Experimental evidence of low-density liquid water upon rapid decompression. *Proc. Natl. Acad. Sci. U. S. A.* **2018**, *115*, 2010−2015.
(15) Woutersen, S.; Ensing, B.; Hilbers, M.; Zhao, Z.; Angell, C. A. A liquid-liquid transition in supercooled aqueous solution related to the hda-lda transition. *Science* **2018**, *359*, 1127−1131.
(16) Huang, C.; et al. The inhomogeneous structure of water at ambient conditions. *Proc. Natl. Acad. Sci. U. S. A.* **2009**, *106*, 15214−15218.
(17) Mallamace, F.; Corsaro, C.; Stanley, H. E. Possible relation of water structural relaxation to water anomalies. *Proc. Natl. Acad. Sci. U. S. A.* **2013**, *110*, 4899−4904.
(18) Mishima, O.; Stanley, H. E. The relationship between liquid, supercooled and glassy water. *Nature* **1998**, *396*, 329−335.
(19) Soper, A. K.; Ricci, M. A. Structures of high-density and low-density water. *Phys. Rev. Lett.* **2000**, *84*, 2881−2884.
(20) Tokushima, T.; et al. High resolution X-ray emission spectroscopy of liquid water: The observation of two structural motifs. *Chem. Phys. Lett.* **2008**, *460*, 387−400.
(21) Wernet, P.; et al. The structure of the first coordination shell in liquid water. *Science* **2004**, *304*, 995−999.
(22) Davis, J. G.; Gierszal, K. P.; Wang, P.; Ben-Amotz, D. Water structural transformation at molecular hydrophobic interfaces. *Nature* **2012**, *491*, 582−585.
(23) Skinner, L. B.; Benmore, C. J.; Neuefeind, J. C.; Parise, J. B. The structure of water around the compressibility minimum. *J. Chem. Phys.* **2014**, *141*, 214507.
(24) Harada, Y.; et al. Selective probing of the OH or OD stretch vibration in liquid water using resonant inelastic soft-X-ray scattering. *Phys. Rev. Lett.* **2013**, *111*, 193001.
(25) Sellberg, J. A.; et al. Ultrafast X-ray probing of water structure below the homogeneous ice nucleation temperature. *Nature* **2014**, *510*, 381−384.
(26) Brites, C. D.; et al. Instantaneous ballistic velocity of suspended brownian nanocrystals measured by upconversion nanothermometry. *Nat. Nanotechnol.* **2016**, *11*, 851−856.
(27) Errington, J. R.; Debenedetti, P. G.; Torquato, S. Cooperative origin of low-density domains in liquid water. *Phys. Rev. Lett.* **2002**, *89*, 215503.
(28) del Valle, J. C.; et al. Dielectric anomalous response of water at 60 °C. *Philos. Mag.* **2015**, *95*, 683−690.
(29) Labrador-Páez, L.; et al. Unveiling molecular changes in water by small luminescent nanoparticles. *Small* **2017**, *13*, 1700968.
(30) Labrador-Paez, L.; et al. Effect of H^2O and D^2O thermal anomalies on the luminescence of Eu^{3+} aqueous complexes. *J. Phys. Chem. C* **2018**, *122*, 14838−14845.
(31) Labrador-Paez, L.; et al. Ph dependence of water anomaly temperature investigated by Eu(III) cryptate luminescence. *Anal. Bioanal. Chem.* **2020**, *412*, 73−80.
(32) Catalan, J.; Gonzalo, J. A. Liquid water changes its structure at 43 °C. *Chem. Phys. Lett.* **2017**, *679*, 86−89.
(33) Catalan, J.; del Valle, J. C. Molecule 1-methyl-5-nitroindoline probes the structural change of liquid water with temperature. *ACS Omega* **2018**, *3*, 18930−18934.
(34) Lamoureux, G.; Harder, E.; Vorobyov, I. V.; Roux, B.; MacKerell, A. D., Jr. A polarizable model of water for molecular dynamics simulations of biomolecules. *Chem. Phys. Lett.* **2006**, *418*, 245−249.
(35) Kumar, P.; Wikfeldt, K. T.; Schlesinger, D.; Pettersson, L. G. M.; Stanley, H. E. The boson peak in supercooled water. *Sci. Rep.* **2013**, *3*, 1980.
(36) Chau, P.-L.; Hardwick, A. J. A new order parameter for tetrahedral configurations. *Mol. Phys.* **1998**, *93*, 511−518.
(37) Errington, J. R.; Debenedetti, P. G. Relationship between structural order and the anomalies of liquid water. *Nature* **2001**, *409*, 318−321.
(38) Wang, L.-P.; Martinez, T. J.; Pande, V. S. Building force fields: An automatic, systematic, and reproducible approach. *J. Phys. Chem. Lett.* **2014**, *5*, 1885−1891.
(39) Holten, V.; Limmer, D. T.; Molinero, V.; Anisimov, M. A. Nature of the anomalies in the supercooled liquid state of the mw model of water. *J. Chem. Phys.* **2013**, *138*, 174501.
(40) Shi, R.; Russo, J.; Tanaka, H. Common microscopic structural origin for water's thermodynamic and dynamic anomalies. *J. Chem. Phys.* **2018**, *149*, 224502.
(41) Wikfeldt, K. T.; Nilsson, A.; Pettersson, L. G. M. Spatially inhomogeneous bimodal inherent structure of simulated liquid water. *Phys. Chem. Chem. Phys.* **2011**, *13*, 19918−19924.
(42) Caupin, F.; Anisimov, M. A. Thermodynamics of supercooled and stretched water: Unifying two-structure description and liquid-vapor spinodal. *J. Chem. Phys.* **2019**, *151*, 034503.
(43) Singh, R. S.; Biddle, J. W.; Debenedetti, P. G.; Anisimov, M. A. Two-state thermodynamics and the possibility of a liquid-liquid phase transition in supercooled TIP4P/2005 water. *J. Chem. Phys.* **2016**, *144*, 144504.
(44) Schlesinger, D.; et al. The temperature dependence of intermediate range oxygen-oxygen correlations in liquid water. *J. Chem. Phys.* **2016**, *145*, 084503.
(45) Stanley, H. E.; Teixeira, J. Interpretation of the unusual behavior of H_2O and D_2O at low-temperatures - tests of a percolation model. *J. Chem. Phys.* **1980**, *73*, 3404−3422.
(46) Geiger, A.; Stanley, H. E. Tests of universality of percolation exponents for a 3-dimensional continuum system of interacting waterlike particles. *Phys. Rev. Lett.* **1982**, *49*, 1895−1898.
(47) Blumberg, R. L.; Stanley, H. E.; Geiger, A.; Mausbach, P. Connectivity of hydrogen-bonds in liquid water. *J. Chem. Phys.* **1984**, *80*, 5230−5241.
(48) Huang, C. C.; et al. Increasing correlation length in bulk supercooled H_2O, D_2O, and NaCl solution determined from small angle x-ray scattering. *J. Chem. Phys.* **2010**, *133*, 134504.
(49) Spah, A.; et al. Apparent power-law behavior of water's isothermal compressibility and correlation length upon supercooling. *Phys. Chem. Chem. Phys.* **2019**, *21*, 26−31.
(50) Xu, X.; Wang, J.; Lv, J.-P.; Deng, Y. Simultaneous analysis of three-dimensional percolation models. *Front. Phys.* **2014**, *9*, 113−119.
(51) Sengers, J. V.; Watson, J. T. R. Improved international formulations for the viscosity and thermal conductivity of water substance. *J. Phys. Chem. Ref. Data* **1986**, *15*, 1291−1314.
(52) *Recommended reference materials for the realization of physicochemical properties*; Blackwell Scientific Publications, 1987.
(53) Ramires, M. L. V.; et al. Standard reference data for the thermal conductivity of water. *J. Phys. Chem. Ref. Data* **1995**, *24*, 1377−1381.
(54) Pil Jang, S.; Choi, S. U. S. Effects of various parameters on nanofluid thermal conductivity. *J. Heat Transfer* **2007**, *129*, 617−623.
(55) Choi, S. U. S.; Zhang, Z. G.; Yu, W.; Lockwood, F. E.; Grulke, E. A. Anomalous thermal conductivity enhancement in nanotube suspensions. *Appl. Phys. Lett.* **2001**, *79*, 2252−2254.
(56) Ben Ishai, P.; Tripathi, S. R.; Kawase, K.; Puzenko, A.; Feldman, Y. What is the primary mover of water dynamics? *Phys. Chem. Chem. Phys.* **2015**, *17*, 15428−15434.
(57) Oleinikova, A.; Brovchenko, I. What determines the thermal stability of the hydrogen-bonded water network enveloping peptides? *J. Phys. Chem. Lett.* **2011**, *2*, 765−769.
(58) Sagar, D. M.; Aoudjane, S.; Gaudet, M.; Aeppli, G.; Dalby, P. A. Optically induced thermal gradients for protein characterization in nanolitre-scale samples in microfluidic devices. *Sci. Rep.* **2013**, *3*, 2130.

https://dx.doi.org/10.1021/acs.jpclett.0c02147
J. Phys. Chem. Lett. 2020, 11, 6704−6711

(59) Adam, G.; Gibbs, J. H. On temperature dependence of cooperative relaxation properties in glass-forming liquids. *J. Chem. Phys.* **1965**, *43*, 139−146.
(60) Wang, F.; et al. Simultaneous phase and size control of upconversion nanocrystals through lanthanide doping. *Nature* **2010**, *463*, 1061−1065.
(61) Jiang, W.; et al. High-performance scalable molecular dynamics simulations of a polarizable force field based on classical drude oscillators in namd. *J. Phys. Chem. Lett.* **2011**, *2*, 87−92.
(62) Eastman, P.; et al. OpenMM 4: A reusable, extensible, hardware independent library for high performance molecular simulation. *J. Chem. Theory Comput.* **2013**, *9*, 461−469.

https://dx.doi.org/10.1021/acs.jpclett.0c02147
J. Phys. Chem. Lett. 2020, 11, 6704−6711

Supporting Information for

Decoding a percolation phase transition of water at ~330K with a nanoparticle ruler

Carlos D. S. Brites[1†], Bilin Zhuang[2,3†], Mengistie L. Debasu[1,4], Ding Ding[5], Xian Qin[6], Fernando E. Maturi[1], Winnie W. Y. Lim[2], De Wen Soh[2], J. Rocha[4], Zhigao Yi[6], Xiaogang Liu[6,7*] and Luís D. Carlos[1*]*

[1]Department of Physics and CICECO – Aveiro Institute of Materials, Universidade de Aveiro, 3810–193 Aveiro, Portugal. [2]Institute of High Performance Computing, Singapore 138632, Singapore. [3]Yale-NUS College, Singapore 138527, Singapore. [4]Department of Chemistry and CICECO – Aveiro Institute of Materials, Universidade de Aveiro, 3810–193 Aveiro, Portugal. [5]Institute of Materials Research and Engineering, Singapore 138634, Singapore. [6]Department of Chemistry, National University of Singapore, 117543, Singapore. [7]Joint School of National University of Singapore and Tianjin University, International Campus of Tianjin University, Fuzhou 350207, P. R. China.

**e-mail: zhuangbl@ihpc.a-star.edu.sg, chmlx@nus.edu.sg, lcarlos@ua.pt*
[†]These authors contributed equally to this work.

This PDF file includes:

Table of contents

S1 Materials and Methods

S1.1 Synthesis and characterization

Synthesis

Materials. Yttrium(III) acetate hydrate (99.9%), ytterbium(III) acetate hydrate (99.9%), erbium(III) acetate hydrate (99.9%), lutetium(III) acetate hydrate (99.9%), sodium hydroxide (> 98%), ammonium fluoride (> 98%), 1-octadecene (90%), and oleic acid (90%) were all purchased from Sigma-Aldrich and used as received unless otherwise noted.

Synthesis of $NaYF_4$:Yb/Er(18/2%)@$NaYF_4$ core-shell nanoparticles (24 nm)

The synthesis procedure was reported previously in Ref. 1.

Synthesis of ligand-free $NaYF_4$:Yb/Er(18/2%)@$NaYF_4$ core-shell nanoparticles. Ligand-free nanoparticles were obtained by a modified literature procedure[1]. Typically, the oleic acid-capped core-shell nanoparticles were dispersed in a solution containing ethanol (1 mL) and hydrochloric acid (1 mL; 1 M) and ultrasonicated to remove the oleic acid. The resulting ligand-free nanoparticles were collected by centrifugation at 16,500 rpm for 20 min, washed with ethanol and redispersed in deionized water (pH = 4.60±0.01).

Synthesis of ligand-free $NaYF_4$:Lu/Yb/Er (50/18/2%) nanoparticles (106 nm)

The fabrication of ligand-free $NaYF_4$:Lu/Yb/Er nanoparticles followed the same procedure adopted for the $NaYF_4$:Yb/Er@$NaYF_4$ core-shell nanoparticles. In a typical procedure, 2 mL aqueous solution of $Ln(CH_3CO_2)_3$ (0.2 M, Ln = Lu, Y, Yb, and Er) was added to a 50 mL flask containing 3 mL of oleic acid and 7 mL of 1-octadecene. The mixture was heated to 150 ºC for 1 h. After cooling down to 50 ºC, a methanol solution (6 mL) containing NH_4F (1.6 mmol) and NaOH (1 mmol) was added under stirring for 30 min. After removal of methanol by evaporation, the solution was heated to 290 ºC under argon for 3 h and then cooled down to room temperature. The resulting nanoparticles were washed with ethanol several times and re-dispersed in 4mL of cyclohexane.

Preparation of luminescent nanofluids. $NaYF_4$:Yb/Er@$NaYF_4$ core-shell nanoparticles (24 nm) were dispersed in water, cyclohexene, and toluene, whereas $NaYF_4$:Lu/Yb/Er nanoparticles (106 nm) were dispersed in water according to a literature procedure[1] (Table S1).

Materials characterization

Electron microscopy. Transmission electron microscopy (TEM, Figure S2a,b) measurements were carried out on a JEOL-JEM 2100F field-emission transmission electron microscope operated at an acceleration voltage of 200 kV.

pH measurements. The pH of the suspensions was measured with a portable pH meter (pH 330i, WTW, Germany) coupled to a combination electrode (Sentek, UK). Two-Point calibration of the pH meter was made using two buffer solutions with pH=4.0 and 7.0 (Sigma Aldrich). Aqueous suspensions of $NaYF_4$:Yb/Er@$NaYF_4$ and $NaYF_4$:Lu/Yb/Er nanoparticles (0.30 mL, 25 mg/mL) were separately dispersed in distilled water (1.70 mL, pH=5.40±0.01) and the pH of the suspensions were measured as 5.10±0.01 and 5.20±0.01, respectively. The pH of the suspension containing $NaYF_4$:Lu/Yb/Er nanoparticles was further changed using HCl (0.5 M) and NaOH (0.5 M) aqueous solutions. First, the pH of distilled water (4 mL) was adjusted to 2.60 using a few drops of the HCl solution. Then, an aqueous suspension of the nanoparticles (0.30 mL, 25 mg/mL) was dispersed in the above solution (1.70 mL) under sonication, and the final pH of the suspension is 2.70±0.01. Nanoparticles' aqueous suspensions with pH = 6.30±0.01 and 8.50±0.01 were prepared by adding drops of the NaOH solution to the distilled water. The mass of the nanoparticles in each suspension was 3.75 mg/mL, and the volume fraction was unchanged. The pH measurements were carried out at 20 °C for all luminescent nanofluids.

Dynamic light scattering and Zeta potential. Dynamic light scattering (DLS) and zeta potential (Figure S2c-f) measurements were carried out at 298 K using a Malvern Zetasizer Nano series instrument, Nano-ZS (Red badge operating with a 632.8 nm laser, Model ZEN3600, UK). A folded capillary cell (Malvern instruments, DTS1070) was used for both the DLS and Zeta potential measurements. For each point, three measurements with ten scans were carried out, and their average values were reported. For each point, three measurements with ten scans were carried out, and their average values were reported. The pH-dependent zeta-potential results shown in Figure **S7** indicate a stable colloidal system in almost all the studied range ($|\zeta| \geq 25$ mV)[2]. Moreover, the pH dependence is similar to that reported before for Er^{3+}/Yb^{3+} codoped $NaYF_4$ nanoparticles (mean particle size of ~25 nm)[3].

S1.2 Experimental setup for temperature measurements

The schematic experimental setup was presented in Figure S1. The scanning position of a CW infrared laser diode (980 nm) was controlled by a moving stage with a minimum step of 0.001 mm. In our study, a ThorLabs quartz cuvette (CV10Q1400) was used as the container and filled with 0.50 mL of a nanofluid. Table S1 summarizes the mass concentration and volume fraction of the different nanofluids used in this work. The temperature is increased at one side of the cuvette by thermal contact with a Kapton thermofoil heater (Minco) mounted in a Cu holder and coupled to a temperature controller (IES-RD31). The temperature controller is equipped with a Barnant thermocouple 100 (model 600-2820, sensitivity 0.1 K). The maximum heat flux from the Kapton thermofoil heater is computed by measuring the variation in the temperature of the Cu holder. Note that the heat capacity of the holder, C_h, is calculated as $C_h = m_h C_c = 8.1\ \mathrm{J \cdot K^{-1}}$, where m_h=21×10^{-3} kg is the mass of the holder and c_c=386 J·kg^{-1}·K^{-1} is the specific heat of Cu. Using the temperature increase rate $\Delta T/\Delta t$ for the temperature increments of 10 and 15 K, 0.16 and 0.24 K·s^{-1}, respectively (measured by the holder-embedded Barnant thermocouple), the corresponding heating power values $P = C_h \Delta T/\Delta t$ are 1.30 and 1.95 W, respectively. Taking the ratio of the heating power to the cuvette's contact area (28 mm^2), the maximum heat flow transferred to the nanofluid suspension Q is 4.63×10^4 and 6.95×10^4 W·m^{-2} for temperature increments of 10 and 15 K, respectively.

The detection system consists of a collimating lens (74-UV, Ocean Optics) and a USB-portable spectrometer (Maya 2000 Pro, Ocean Optics), connected by a QP450-1-XSR optical fiber (Ocean Optics). The spectrometer is controlled by a homemade MatLab® graphical user interface to real-time acquisition and pre-processing of the emission spectra with controllable integration window and boxcar. The baseline of the emission spectra of the luminescent nanofluids was removed, and the integrated areas of the Er^{3+} $^2H_{11/2} \rightarrow {}^4I_{15/2}$ (I_H, 510–535 nm) and $^4S_{3/2} \rightarrow {}^4I_{15/2}$ (I_S, 535–565 nm) transitions were computed. The thermometric parameter Δ is computed for each recorded emission spectrum using the I_H and I_S integrated areas. In all dynamic temperature measurements, the boxcar is maintained constant at one pixel (0.5 nm) and the integration time is set to 0.250 s.

S1.3 Thermometer calibration, relative thermal sensitivity and temperature uncertainty

The reduced temperature $\theta(t)$ is computed by:

$$\theta(t) = \frac{T(t) - T_i}{T_{max} - T_i} \quad \textbf{(S1)}$$

where T(t), T_i and T_{max} are the instantaneous, initial and maximum temperature, respectively. Notice that *T(t)* is determined through Eq. 3 of the manuscript.

The relative thermal sensitivity (S_r) is written as:

$$S_r = \frac{1}{\Delta}\left|\frac{\partial \Delta}{\partial T}\right| \quad \textbf{(S2)}$$

and the temperature uncertainty (δT) as:

$$\delta T = \frac{1}{S_r}\frac{\delta I}{I} \quad \textbf{(S3)}$$

The corresponding maximum relative thermal sensitivity and minimum temperature uncertainty are 1.13±0.02 %·K^{-1} and 0.1 K ($NaYF_4$:Yb/Er@$NaYF_4$) and 1.12±0.02 %·K^{-1} and 0.1 K ($NaYF_4$:Lu/Yb/Er).

S1.4 Signal denoising using the DWT method and critical onset time determination

We adopt a nonlinear noise reduction method, presented by Lang *et al.*[4], that uses the discrete wavelet transforms (DWT) that significantly improve the noise reduction, compared to the original wavelet-based approach[5, 6]. The intensity ratio denoising was implemented using a MatLab® routine that *i*) imports the as-measured intensity ratio, *ii)* converts the intensity ratio into temperature using Eq. S1, *iii)* calculates the reduced temperature using Eq. S2, *iv*) applies the DWT denoising procedure to generate a denoised reduced temperature (threshold parameter: 15, 5 stages) and *v)* computes the noise as the difference between the measured and the denoised reduced temperature. The histogram of the noise values was computed for all the denoised curves, following invariantly a Gaussian profile (r^2>0.980) centered at zero. Figure S8 shows an illustrative example. We conclude that the noise corresponds to an additive white Gaussian signal, thus validating the use of the DWT denoising procedure[5, 6].

The denoised intensity ratio was used to compute the critical onset time (t_{0i}). The routine marks t_{0i} as the time instant in which the denoised signal change is higher than the standard deviation of the noise (extracted from the histograms of the noise values).

S1.5 The crossover temperature

The crossover temperature, T_c, corresponds to the temperature of the intersection of the two straight lines representing the temperature dependence of the instantaneous ballistic Brownian velocity of the 24 and 106 nm upconverting nanoparticles between 300 to 355 K. A MatLab routine was designed to calculate all the possible combinations of two straight lines that fit the bilinear pattern in the mentioned temperature range, and to determine the best fit maximizing the product of the squared correlation coefficients of each line. The uncertainty, ΔT_c, is given by:

$$\Delta T_c = \frac{\sigma_e}{s} \quad \textbf{(S4)}$$

where σ_e and s are the standard error of the estimate and the slope of the linear regime for $T>T_c$, respectively, being the estimate calculated through:

$$\sigma_e^h = \sqrt{\frac{\sum (v - v')^2}{N - 2}} \quad \textbf{(S5)}$$

where v and v' are the measured and the fitted values of the Brownian velocity, respectively, and N is the number of data points for $T>T_c$. A scheme illustrating the determination of $T_c \pm \Delta T_c$ is presented in Figure S9.

S1.6 Temperature dependence of the instantaneous Brownian velocity of the nanocrystals

We repeated the procedure to determine the instantaneous Brownian velocity of the nanocrystals in several heating/cooling cycles generated in different days using distinct heat flows transferred to the nanofluid suspension (Q = 4.63×10^4 and Q = 6.95×10^4 W·m^{-2}), observing systematically the same velocity values. The instantaneous Brownian velocity of the 24 nm nanoparticles in water (pH = 5.10±0.01) measured during three consecutive heating cycles between 303 and 343 K at Q = 6.95×10^4 W·m^{-2} is shown in Figure S10.

S1.7 Modeling the thermal transport

Brites *et al.*[1] demonstrated that the experimentally measured temperature onset does not obey a semi-infinite conduction model. As the experiment involves thermal excitation and measures a macroscopic temperature rise of the nanofluids, it is of interest to further

examine the heat transport physics of the experiment. First, we point out that convection in steady-state thermal measurements of fluids leads to the agreement with Newton's law of cooling[1]. However, the semi-infinite model based purely on conduction agrees well with the equivalent natural convection models[7] at the initial stage of the transport. Thus, we can assume the use of a pure conduction model is valid in determining the onset time in Figure S3 and Figure S4.

Here, we use a double parallel plate conduction model[8] to mimic the heat transport in our nanofluids experiment. As shown in Figure S15, the model assumes two infinitely large parallel plates separated by $L = 1$ cm (same as in the experiment). One plate is held at a temperature $T_{\mathrm{h}} = T_{\mathrm{L}} + \Delta T$ (where ΔT = 9, 21, and 25 K) and the other plate is held at T_{L}. The liquid is assumed to be pure water at the temperature T_{L} for the initial condition at $t = 0$. The solution to the one-dimensional heat conduction with the two-plate boundary condition and constant T_{L} under initial condition is[8]:

$$T(x,t) = T_{\mathrm{L}} + (T_{\mathrm{h}} - T_{\mathrm{L}})\frac{x}{L} + \frac{2}{\pi}\sum_{n=1}^{\infty}\frac{T_{\mathrm{h}}\cos n\pi - T_{\mathrm{L}}}{n}\sin\frac{n\pi x}{L}\, e^{-\frac{\alpha n^2\pi^2 t}{L^2}} + 2\,T_{\mathrm{L}}\sum_{n=1}^{\infty}\sin\frac{n\pi x}{L}\, e^{-\frac{\alpha n^2\pi^2 t}{L^2}}\frac{1-\cos n\pi}{n\pi} \quad \textbf{(S6)}$$

Figure S16a-c, show examples of temperature rise at $x = 0.2$ cm for ΔT=9 K. For a different temperature gradient $T_{\mathrm{h}} - T_{\mathrm{L}}$ across the two plates, ΔT = 21 K (Figure S17a-c) and ΔT = 25 K (Figure S18a-c), $T(x,t)$ reaches a different temperature after 100 seconds. However, the maximum of the second-order derivative of Eq.S6 as a function of time occurs at the same position for all three $T_{\mathrm{h}} - T_{\mathrm{L}}$ values. We have used, thus, the maximum of the second-order derivative as the criterion to determine the onset time t_{0i} for each x_i position Figure S16b. Figure S17b and Figure S18b show the normalized temperature versus time and position using Eq.S6, mimicking Figure S3a-d and Figure S4a,b. The onset position versus time follows a linear trend. There are differences between the figures because Eq. S6 does not necessarily have the same boundary and initial conditions of the experiment. For instance, there is still a finite rise time of the water temperature at x=0, but this is not the case in the model. As already mentioned, this model does not consider the presence of convective effects, but the short time behaviour is almost the same with and without convection. In the Supplementary Information of Brites *et al.*[1], a one-dimensional conduction model is used

and a linear trend of position versus time cannot be obtained. Furthermore, the instantaneous velocity is independent of the temperature gradient $T_h - T_L$ across the entire cuvette. Figure S16a-c shows a temperature rise for three different values of $T_h - T_L$ (inducing a different final equilibrium temperature). However, the second-order derivative maximum is independent of $T_h - T_L$. This maximum recorded for each position x_i follows an approximately linear trend in Figure S16c, Figure S17c, and Figure S18c and a linear fit yields the instantaneous velocity. This velocity describes the motion of the interface between the hot and cold regions, where mixing due to the Brownian motion of the nanoparticles[1] occurs in the nanofluid.

A linear relationship is obtained between the instantaneous velocity of the nanoparticles v versus the thermal diffusivity of pure water α over the temperature range 0-100 °C, as shown in Figure S16d, Figure S17d, and Figure S18d. The data for the thermal diffusivity of pure water is derived from Refs. [9-11]. This linear relationship allows us to write $v = m\,\alpha$, where $m = 1.61$ m^{-1} and, the intercept is zero. There is no difference between the values of m obtained from the linear fit in Figure S16d, Figure S17d, and Figure S18d. With this linear relation, effective thermal diffusivity of the nanoparticle-water mixture can be obtained through linear interpolation, and the data for the enhancement factor compared to pure water (see Figure 2d of the manuscript).

S1.8 Molecular dynamics simulation of SWM4-NDP water model

We carry out molecular dynamics simulations for the polarizable SWM4-NDP water model[12] using an extended Lagrangian dynamics with a dual-Langevin thermostat[13] with the OpenMM package[14]. At each temperature, the size of the cubic simulation box is set such that the density of water molecules in the simulation box matches the density of water at atmospheric pressure (Table S5), with periodic boundary condition applied to the simulation box. For the dual-Langevin thermostat, the friction coefficients for the center-of-mass and for the internal Drude-pair degrees of freedom are 20 ps^{-1} and 1 ps^{-1}, respectively, and the temperature set for the internal Drude-pair is 1 K. The time step for the integration is 1 fs. For each randomly generated initial configuration, the system is first annealed from 373.15 K to the desired temperature in 100 equal-interval temperature steps and 1 ps per step, followed by equilibration at the desired temperature for 1 ns. Then, the configuration state of the water is sampled every 10 ps for 70 ns. The sampling is repeated independently for 8 times for each system size (512 molecules, 768 molecules, and 1024 molecules) and temperature (5 K intervals from 303.15 K to 363.15 K). Thus, for each system size, a total

of 56000 configuration states are sampled. Molecular dynamics simulation results shown in the main text are based on the system with 1024 molecules, and the effects of the finite size of the simulation results are shown in Figure S20 and Figure S21.

S1.9 Computation of orientational order parameters q and q_5

We hereby provide a rigorous mathematical definition for the orientational order parameters *q* and q_5 in Eqs. (1) and (2) in the main text. For a water molecule in consideration, let indices i=1 to 5 denote the first to the fifth nearest neighbor, where the distance between any two water molecules is the distance between the centers of their oxygen atoms. Let us define a function $Q_{i,j,k,l}$ for the water molecule to be:

$$Q_{i,j,k,l} = 1 - \frac{3}{8}\left[\left(\cos\psi_{ij} + \frac{1}{3}\right)^2 + \left(\cos\psi_{ik} + \frac{1}{3}\right)^2 + \left(\cos\psi_{il} + \frac{1}{3}\right)^2 + \left(\cos\psi_{jk} + \frac{1}{3}\right)^2 + \left(\cos\psi_{jl} + \frac{1}{3}\right)^2 + \left(\cos\psi_{kl} + \frac{1}{3}\right)^2\right] \quad \textbf{(S7)}$$

where $\psi_{\alpha\beta}$ denotes the angle extended from the oxygen atom of the molecule considered to the oxygen atoms of α^{th} and β^{th} neighbors. It is easy to see that the definition of the orientational parameter q is simply:

$$q = Q_{1,2,3,4} \quad \textbf{(S8)}$$

Similarly, the orientational parameter q_5 in Eq. (2) in the main text can be equivalently written as:

$$q_5 = \max(Q_{1,2,3,4}, Q_{1,2,3,5}, Q_{1,2,4,5}, Q_{1,3,4,5}, Q_{2,3,4,5}) \quad \textbf{(S9)}$$

S1.10 Peak maxima r_1 and r_2 of O-O pair distribution function

The O-O pair distribution function *g(r)* is calculated with the Python *mdtraj* package[15], with a bin width of 0.005 Å. The pair distribution function at various temperature is plotted in Figure S19a, for the simulation with 1024 water molecules. The peak maxima of r_1 and r_2 are obtained by the least-squares fitting to a Gaussian function $a\ exp\left[-\left(\frac{x-b}{c}\right)^2 + d\right]$, where *a, b, c, and d* are fitting parameters, to the sampled *g(r)* in the ranges 2.75 Å<r_1< 2.78 Å and 4.1 Å<r_2<4.9 Å, respectively. The Gaussian fitted curves are shown in Figure S19b and

Figure S19c. The peak maxima are given by the value of *b* in each fit. The use of Gaussian function in the fitting is the same as the procedure in Skinner *et al.*[16].

The bilinear trend in r_2 revealed by our simulation has not been observed in the simulations of Skinner *et al.*[16]. We note that the use of the nonpolarizable TIP4P/2005 model in their simulations might have overestimated the hydrogen-bond strength at higher temperatures. Here, we employ a polarizable model that captures more realistically the temperature dependence of the hydrogen-bond network[17].

S1.10 Molecular dynamics simulation using TIP4P-FB water model

To show that features observed in our simulation are not specific to the model chosen, we carried out molecular dynamics simulations for the nonpolarizable TIP4P-FB water model [18] using an extended Lagrangian dynamics with a Langevin thermostat with the OpenMM package[14]. At each temperature, the size of the cubic simulation box is set such that the density of water molecules in the simulation box matches the density of water at atmospheric pressure (Table S5). For the Langevin thermostat, the friction coefficients for the center-of-mass is 20 ps^{-1}. The time step for the integration is 1 fs. For each randomly generated initial configuration, the system is first annealed from 373.15 K to the desired temperature in 100 equal-interval temperature steps and 1 ps per step, followed by equilibration at the desired temperature for 1 ns. Then, the configuration state of the water is sampled every 10 ps for 9 ns. The sample size is 1024 molecules at temperatures 303.15 K, 333.15 K, 363.15 K. The simulation results are shown in Figure S21 and Figure S22.

S2 Supplementary Text

S2.1 Estimation of the probability of finding a cooperative region around the nanoparticle

In this section, we estimate the extensiveness of the hydrogen bond network based on the decomposition of molecules into the two local configuration states. For every molecule in each configuration state from the MD simulations, the molecule can be classified into the TH-state of the DT-state by comparing its values of *q* and q_5.

Then, we identify connected clusters of TH-state molecules linked in a hydrogen-bonding network in a low-density-liquid (LDL) motif. Two molecules are connected in the same LDL motif if both are in TH-state, and one is among the four nearest neighbors of the other. For water at ambient conditions, the individual hydrogen bonds may instantaneously break or

form due to thermal fluctuations. Despite this, the long-ranged tetrahedral network may survive at a longer timescale because the hydrogen bonds in a large network do not all break down simultaneously. In addition, through sampling with molecular dynamics simulations, we have also taken into account thermal fluctuations at the individual molecule level within the network.

An LDL motif connecting the left and the right border, the top and the bottom border, and the front and the back border is called a spanning cluster (under periodic boundary condition, as in our simulation, the boundary points need to be neighbors as well to form a spanning cluster). For each configuration state, we determine whether a spanning LDL motif is found. Our definition of a spanning cluster is stricter than the percolated cluster studied in most literature of percolation transition. Usually, a percolated cluster is defined as one that connects the left and the right border, the top and the bottom border, or the front and the back border, i.e., only one of the dimensions needs to be connected. However, in our work, since we are interested in motifs that span in all three dimensions, we require a spanning cluster to be connecting the borders in all three dimensions.

Based on the configuration states sampled from the molecular dynamics simulations at any particular temperature, we can compute $p_{span(simulation\ box)}$, the probability of finding a spanning cluster in the simulation box, being the fraction of instances where the configuration state has a spanning cluster.

To estimate the probability of finding an LDL cluster that spans a bigger volume, let us first consider a $n \times n \times n$ cubic array of simulation boxes. If an LDL cluster is to span the whole volume, then each of the simulation boxes in the cubic array has to be spanned by the cluster. This occurs with probability given by

$$p_{span} \approx \left(p_{span(simulation\ box)}\right)^{n \times n \times n} \quad \textbf{(S10)}$$

For a general cubic region with length $L \gg L_{simulation\ box}$, where $L_{simulation\ box}$ is the side length of the simulation box, the probability of finding a spanning LDL cluster can be obtained from a generalization of Eq. S10 as

$$p_{span}(V) \approx \left(p_{span(simulation\ box)}\right)^{\left(\frac{L}{L_{simulation\ box}}\right)^3} \quad \textbf{(S11)}$$

Applying Eq. S11 to the volume of the nanoparticles $L = d$, where d is the diameter of the nanoparticles, we can estimate the probability p_{span} of finding an LDL cluster spanning the size of the nanoparticles. The result for 24 nm nanoparticles is plotted in Figure 3D of the main text. However, to accurately estimate the p_{span} for a 106 nm nanoparticle, a higher accuracy for $p_{span(simulation\ box)}$ is needed, and that requires at least 10^6 configuration states sampled for simulations with 1024 water molecules. The 106 nm nanoparticle has a volume of 40,000 times of the simulation box with 1024 water molecules. If we are to have 25 independent samples for each of the 40,000 simulation boxes, this tallies to 10^6 configuration states. This is well beyond the computation power available for the current study.

S2.2 The effective mass

In this section, we consider the effective mass of the nanoparticles by analyzing the transport of the liquid in the immediate vicinity of the nanoparticles. In particular, we consider both the fluid that moves with the nanoparticle cooperatively.

First, to understand the hydrodynamic regime of the nanoparticle movement, we compute the Schmidt number $Sc = \nu/D$ of the nanofluid, where ν is the kinematic viscosity of the fluid and D is the diffusion coefficient of the nanoparticle. The diffusion coefficient can be further estimated from the Stokes-Einstein-Sutherland formula $D = k_B T/6\pi\eta a$, where η is the dynamical viscosity of the fluid and a is the radius of the nanoparticle. For the nanofluids studied in this work, $Sc \sim 10^4 - 10^5$ is much greater than unity. Since $Sc \gg 1$, the nanoparticle is in the regime where the momentum transfer is more significant than mass diffusion[19]. In this regime of Brownian transport, a vortex shell of thickness d develops around the particle in Brownian motion[19].

Using a heuristic argument in the spirit to that discussed in Ref. 16, we may relate the effective mass to the nanoparticle mass and the mass of surrounding fluids. We let m_0 be the sum of the mass of the nanoparticle and of the fluid with which it moves cooperatively. At time-scales shorter than the momentum transfer (nanoconvection time scale, approximately 10^{-12} s)[1], the average speed is $v_0 = \sqrt{k_B T/m_0}$, given by the equipartition theorem. This speed is slowed down by hydrodynamic interactions with the fluid. At the time scale τ at which the energy of the Brownian motion propagates, the speed is determined by the conservation of momentum:

$$v = \frac{m_0\, v_0}{(m_0 + m_v)} \qquad \textbf{(S12)}$$

where m_v is the mass of the vortex shell developed during time τ. Combining Eq. S12 and the equipartition theorem, we have:

$$v^2 = \frac{m_0 k_B T}{(m_0 + m_v)^2} = \frac{k_B T}{m^*} \qquad \textbf{(S13)}$$

with the effective mass of the system given by $m^* = (m_0 + m_v)^2/m_0$.

For $T>T_C$, as the nanoparticle is not surrounded by the extended hydrogen network of the LDL motif, we may set m_0 to the mass of the bare nanoparticle. Given the radius of the nanoparticle a, the masses m_0 and m_v are $\frac{4}{3}\pi\rho_N a^3$ and $\frac{4}{3}\pi\rho_w[(a+d)^3-a^3]$, respectively, where ρ_N and ρ_w are respectively the densities of the nanoparticle and the water. From the slope of the v^2 vs. T plot for $T>T_C$, we may estimate the thickness of the vortex shell from Eq. S13. The slopes for the 24 nm nanoparticle at pH=5.10 and for the 106 nm nanoparticle at pH=5.20 in water (Table S4) give a thickness of the vortex shell of about $d = 1\times10^{-7}$ m.

As the kinematic viscosity does not change drastically from $T>T_C$ to $T<T_C$, we may assume that the thicknesses of the vortex shell are the same in the whole temperature range concerned because of $d\sim\sqrt{\nu\tau}$.

At $T<T_C$, and since the nanoparticle is immersed within an extended hydrogen-bond network, there is a non-negligible mass of fluid moving cooperatively with the nanoparticle. In other words, the mass and the size of the nanoparticle are enlarged. Assuming the thickness of the cooperatively-moving fluid b, the mass m_0 should now include this fluid, that is $m_0 = \frac{4}{3}\pi\rho_N a^3 + \frac{4}{3}\pi\rho_w[(a+b)^3-a^3]$. The mass of the vortex shell generated outside the cooperatively-moving fluid is $m_v = \frac{4}{3}\pi\rho_w[(a+b+d)^3-(a+b)^3]$. Based on the slope of the v^2 vs. T plot for $T<T_C$, together with the value of d calculated earlier, we may now compute the thickness of the cooperatively-moving fluid. For the 24 nm nanoparticle at pH=5.10 and for the 106 nm nanoparticle at pH=5.20 in water, the thicknesses of the cooperatively-moving fluid are 1×10^{-6} m and 4×10^{-7} m, respectively. The values are different, but quite close considering that the calculation is heuristic. The calculation corroborates with our simulation observation that the size of the LDL motif grows rapidly at around T_C (Figure 3d of the manuscript). Additionally, we note that the luminescent thermal probes described in this work are hydrophilic ligand-free Ln^{3+}-doped upconverting nanoparticles that are stabilized in aqueous suspensions by electrostatic interactions. There is a double layer structure formed on the nanoparticle surface, which can be quantified by measurements of the zeta potential. Because of the electrostatic interactions, a layer of water “sticks” to the nanoparticle surface. This layer of water should be considered as part of the nanoparticle probe. As a result, what the bulk water see is a nanoparticle with a surface layer of water and the property of the bulk water is not strongly disturbed by the probe. Therefore, it is reasonable that the thickness of the cooperatively-moving fluid is much larger than the size of the bare nanoparticles.

We note that the hydrodynamic effects in this section concern the momentum and mass transport of the fluid surrounding the nanoparticles. The regime of the liquid motion influences the Brownian velocity of the nanoparticles, but should not be confused with the regime of transport of the nanoparticles. The vortex shell that is only formed in the immediate vicinity of the nanoparticles, but not in the entire nanofluid.

S2.3 Instantaneous Brownian velocity and thermal diffusivity

The diffusion of particles with at least one dimension lower than 1000 nm is treated as Brownian motion. There is no principal distinction between diffusion and Brownian motion since both denote the same thermal motion[19]. Specifically, Brownian motion at different time scales is defined relative to the linear momentum relaxation time (τ_M, defined as the time needed for the momentum to relax to 1/e of its initial value). Brownian motion is called ballistic (in the limit $t << \tau_M$) or diffusive (in the limit $t >> \tau_M$). Typical values of τ_M are ~0.1 ns for nanoparticles of 25 nm in diameter.

Different from the methods based on analysis of the Brownian motion of a single microparticle confined by a harmonic optical trap[20], the method described here determines the changes in temperature by mapping luminescence profiles of the nanocrystals suspended in a container.

The velocity obtained in this work corresponds to the instantaneous Brownian velocity of the nanoparticles, as discussed in 2016[1]. Briefly, the increase in temperature increases the instantaneous Brownian velocity of the nanoparticles through nanoconvection at a timescale $\tau_S \sim 10^{-12}$ s (the time required for a sound wave with a velocity v_s to travel a distance equivalent to the radius *a* of the nanoparticle).

During the momentum relaxation time, the nanoparticles are in thermal equilibrium with the solvent molecules, giving rise to changes in each particle's instantaneous Brownian velocity. In other words, as $\tau_S/\tau_M \sim 10^{-2}$, the thermalization occurs in a time period 100 times shorter than the momentum relaxation, the temperature changes occur before the nanoparticles enter the diffusive regime. In this sense, we denote the rate of temperature change in the nanofluid container as the instantaneous Brownian velocity of the nanoparticles.

The linearity obtained between the thermal diffusivity of the nanofluid α and the instantaneous Brownian velocity v of the nanoparticles in the dilute nanofluids (**Figure S16D**, **Figure S17D,** and **Figure S18D**) validates the measurement of Brownian velocity through upconversion thermometry. In fact, as the thermal diffusivity is defined as:

$$\alpha = \frac{\kappa}{\rho c_p} \qquad \textbf{(S14)}$$

where κ is the thermal conductivity, ρ the specific mass and c_p the specific heat of the nanofluid, the linearity between α and v imply that the velocity of the nanoparticles must also be linear to κ. This observation is in agreement with the model postulated by Kumar *et al.*[21]:

$$\kappa = \frac{1}{3} N L c_p \frac{\phi\, r_s}{(1-\phi)a}\; v + k_F \qquad \textbf{(S15)}$$

where N is the mean number of nanoparticles per unit of volume, L is the mean free path of the nanoparticle, v is the average particle velocity (corresponding to the Brownian velocity either in the diffusive or in the ballistic regime), k_F is the thermal conductivity of the base fluid and r_s is the radius of the solvent molecule.

S3 Supplementary Figures

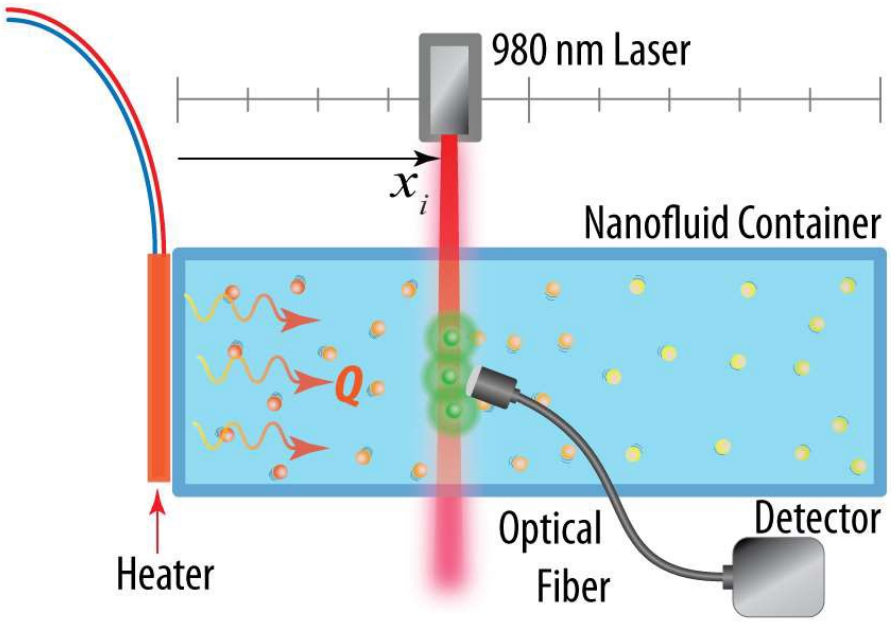

Figure S1. Schematic of the measurement set-up used to record the temperature profiles of the nanofluids. The laser diode is positioned on a precisely controlled moving stage, allowing the nanofluid to be irradiated at different locations along the predesigned path of the heat flux *Q* (*xx* direction). Subsequently, a collimating lens collects the upconversion emission, and the optical signal is guided to a fiber-coupled detector.

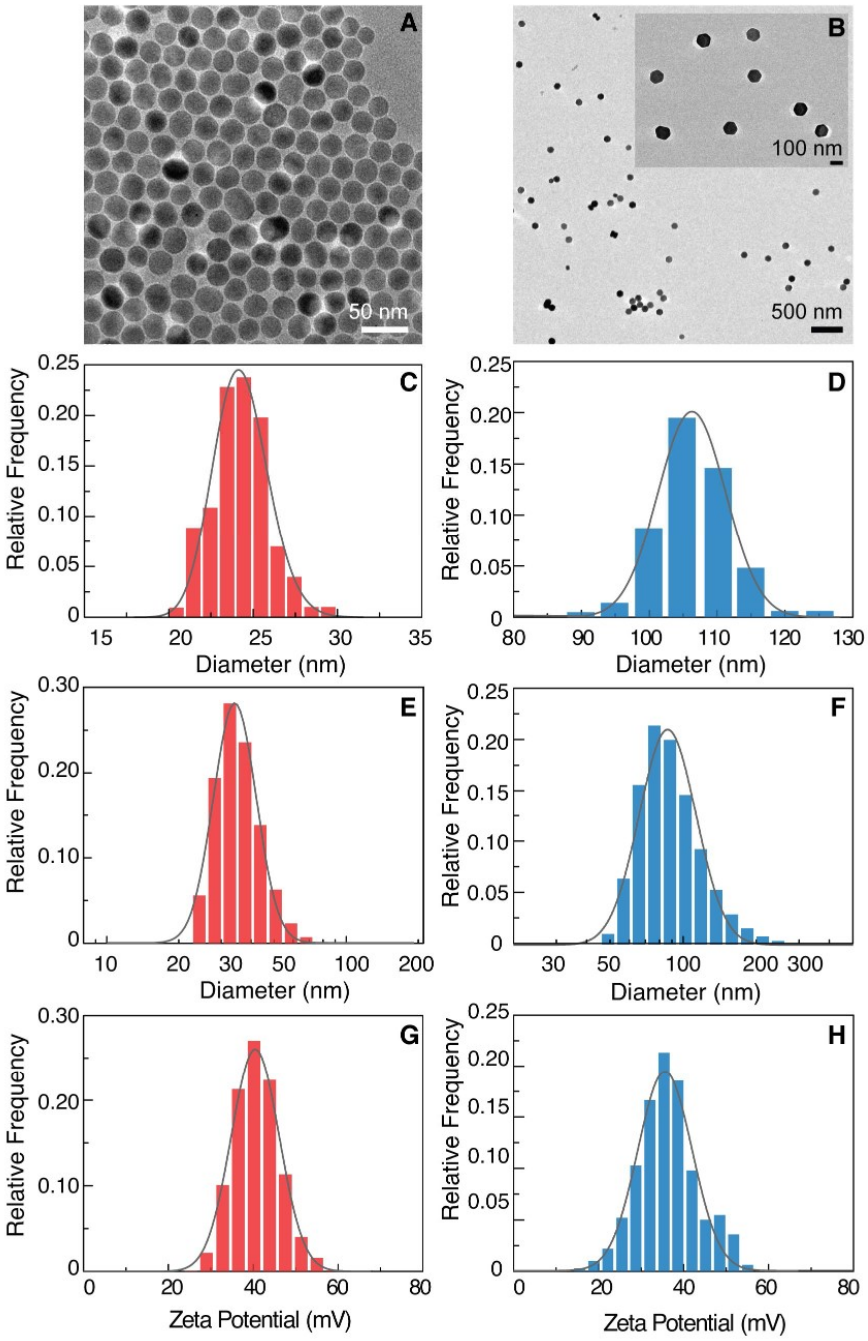

Figure S2. Particle size and zeta potential of the nanocrystals. (**A**) and (**B**) TEM images of $NaYF_4$:Yb/Er@$NaYF_4$ and $NaYF_4$:Lu/Yb/Er, respectively. (**C**) and (**D**) TEM size distribution of $NaYF_4$:Yb/Er@$NaYF_4$ and $NaYF_4$:Lu/Yb/Er, respectively. (**E**) and (**F**) Hydrodynamic size distribution of $NaYF_4$:Yb/Er@$NaYF_4$ and $NaYF_4$:Lu/Yb/Er nanoparticles, in distilled water, pH=5.10±0.01 and pH=5.20±0.01, respectively. (**G**) and (**H**) Zeta potential of $NaYF_4$:Yb/Er@$NaYF_4$ and $NaYF_4$:Lu/Yb/Er in distilled water at the same pH values, respectively. The lines are the best fits for the hydrodynamic and TEM size data (log-normal distribution) and zeta potential (Gaussian distribution). The summary of the fitting results is presented in **Table S2**.

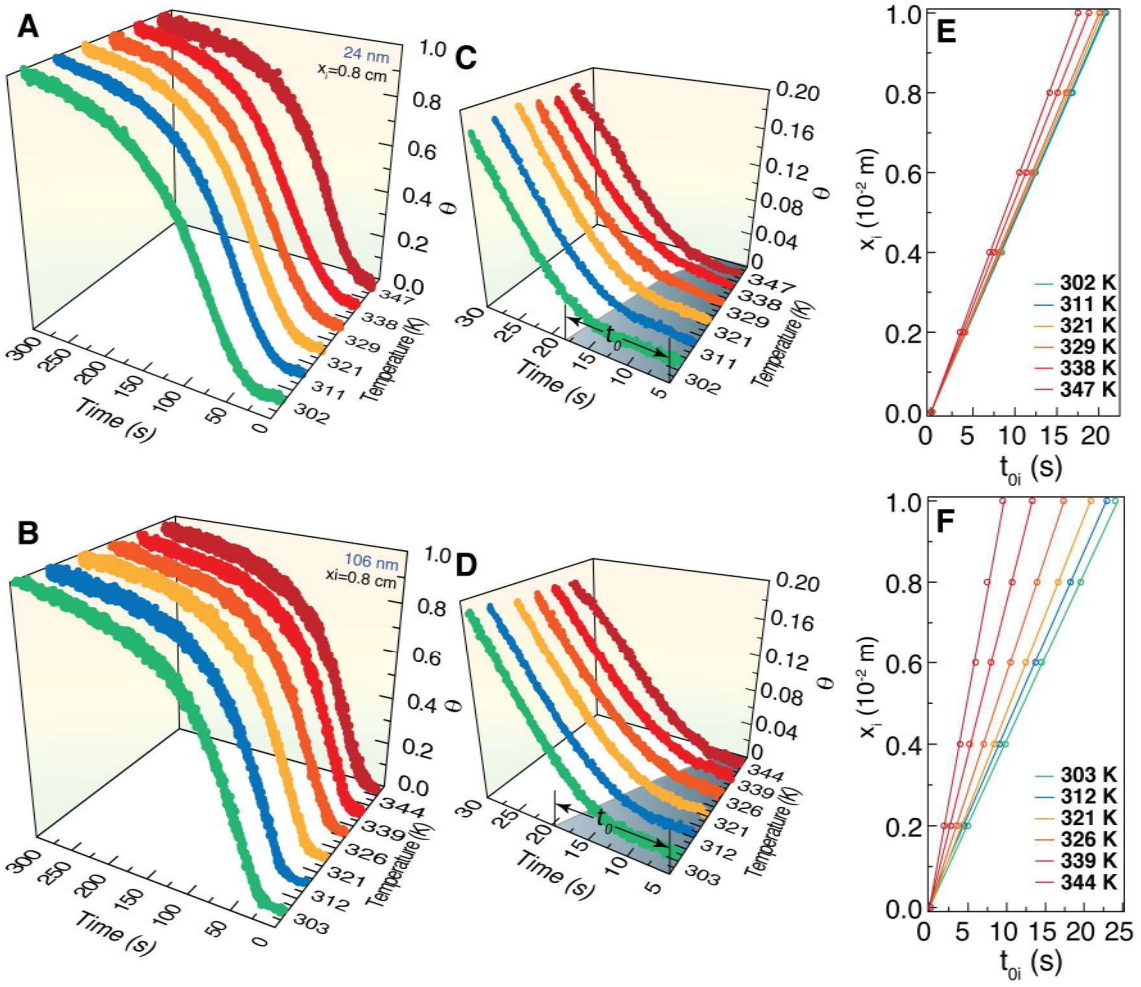

Figure S3. The time-dependent temperature profile of the water-based $NaYF_4$:Yb/Er@$NaYF_4$ and $NaYF_4$:Lu/Yb/Er nanofluids. Keeping the distance to the heating plane fixed at x_i=0.8×10^{-2} m the reduced temperature profiles of the 24 nm (**A**) and 106 nm (**B**) nanoparticles dispersed in water (pH=5.10±0.01 and 5.20±0.01, respectively) are recorded with respect to the elapsed time for distinct initial temperature values of the nanofluids. Similar results are obtained for distinct x_i positions. (**C**) and (**D**) Magnification of the first 30 seconds of the time-dependent profiles of the 24 nm and 106 nm nanoparticles, respectively. The shadowed area marks the critical time t_{0i} when the onset of the change in the intensity ratio is observed due to temperature variation upon turning on the heater. The critical time t_{0i} of the 24 nm and 106 nm nanoparticles depends on the nanofluids' initial temperature. (**E**) and (**F**) The corresponding linear correlation (r^2 >0.994) between x_i and t_{0i} for different nanofluids' temperatures.

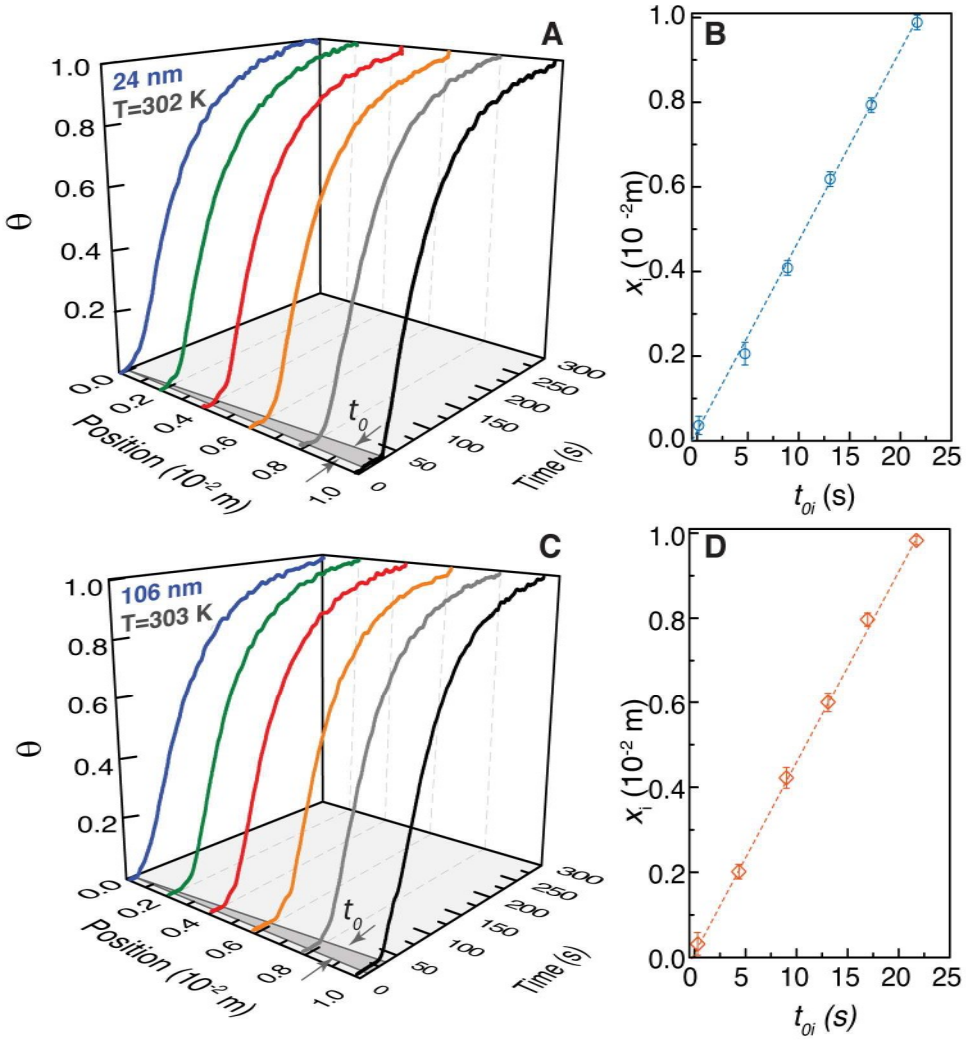

Figure S4. The time-dependent temperature profile of the water-based $NaYF_4$:Yb/Er@$NaYF_4$ and $NaYF_4$:Lu/Yb/Er nanofluids. (**A**) and (**B**) Reduced temperature profile of the 24 nm and 106 nm nanoparticles dispersed in water (ϕ=0.085% and 0.066%, respectively) at an initial temperature of 302 K and pH=5.10±0.01 (smaller particles) and 303 K and 5.20±0.01 (bigger particles), as measured when the laser excitation is positioned at different distances to the heating plane, x_i, along the x*x* direction (Q=4.63×10^4 W·m^{-2}). The shadowed area marks the critical time t_{0i} when the onset of the change in the intensity ratio is observed due to temperature variation upon turning on the heater. (**C**) and (**D**) The corresponding linear correlation (r^2 >0.994) between x_i and t_{0i}.

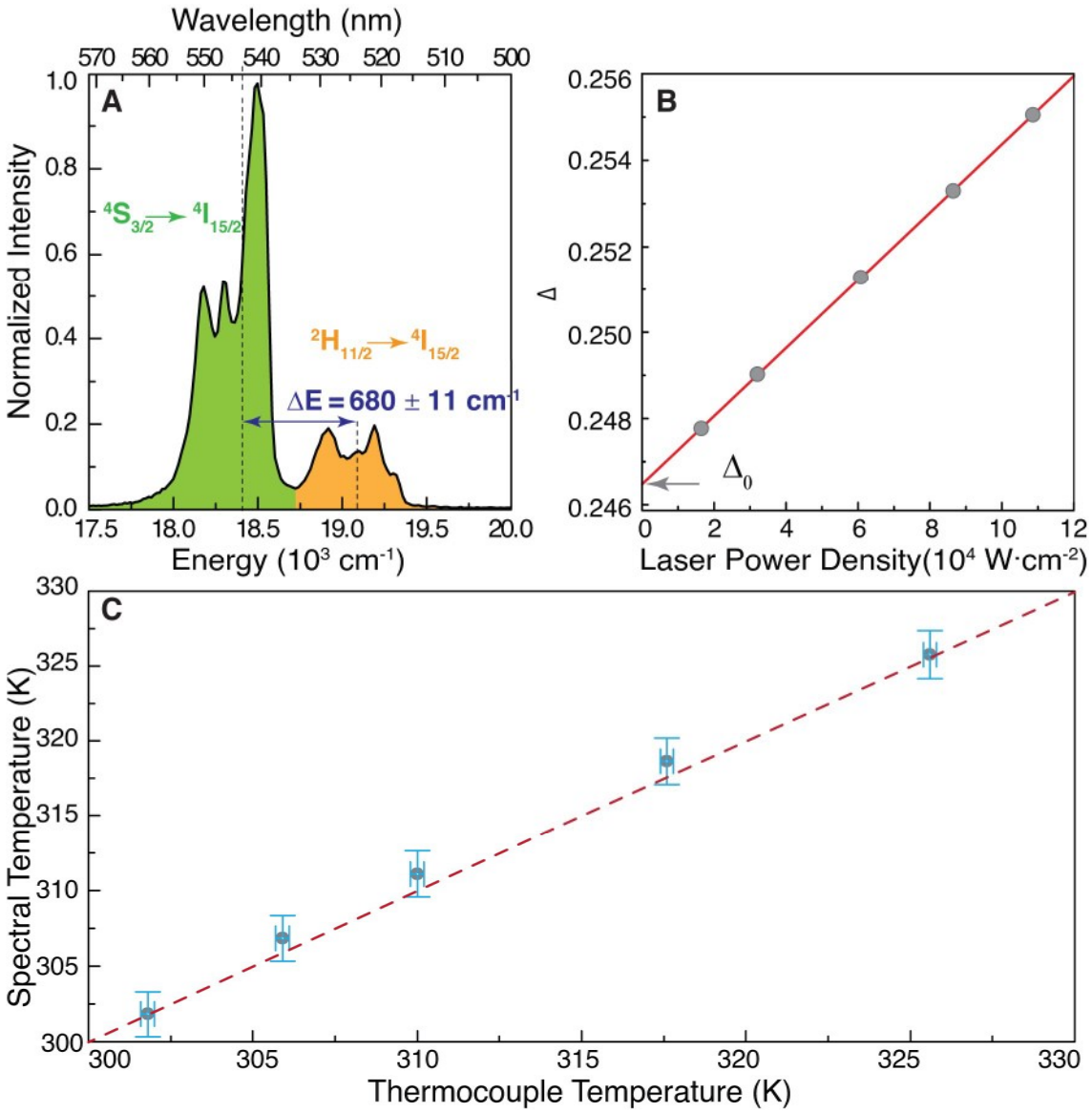

Figure S5. Calibration curve of $NaYF_4$:Yb/Er(18/2%)@$NaYF_4$. (**A**) Barycenters of the $^2H_{11/2} \rightarrow {}^4I_{15/2}$ and $^4S_{3/2} \rightarrow {}^4I_{15/2}$ transitions in the emission spectrum of the water suspension of 24 nm nanoparticles at 300 K. (**B**) Dependence of the parameter Δ on the laser power density. The solid line is the best fit of experimental data to a straight line ($r^2 > 0.999$) and allows for the determination of Δ_0=0.2465 as the intercept corresponding to T_0=300 K. (**C**) Temperature computed from Eq. 3 of the manuscript (spectral temperature, *y*) *versus* temperature reading from the immersed thermocouple (thermocouple temperature, *x*). The straight line is a guide for the eyes and corresponds to *y*=*x*. The agreement between the spectral and thermocouple temperatures is excellent. The horizontal and vertical error bars stand for the experimental temperature uncertainty and the error in the determination of spectral temperature based on the ΔE and Δ_0 values, respectively.

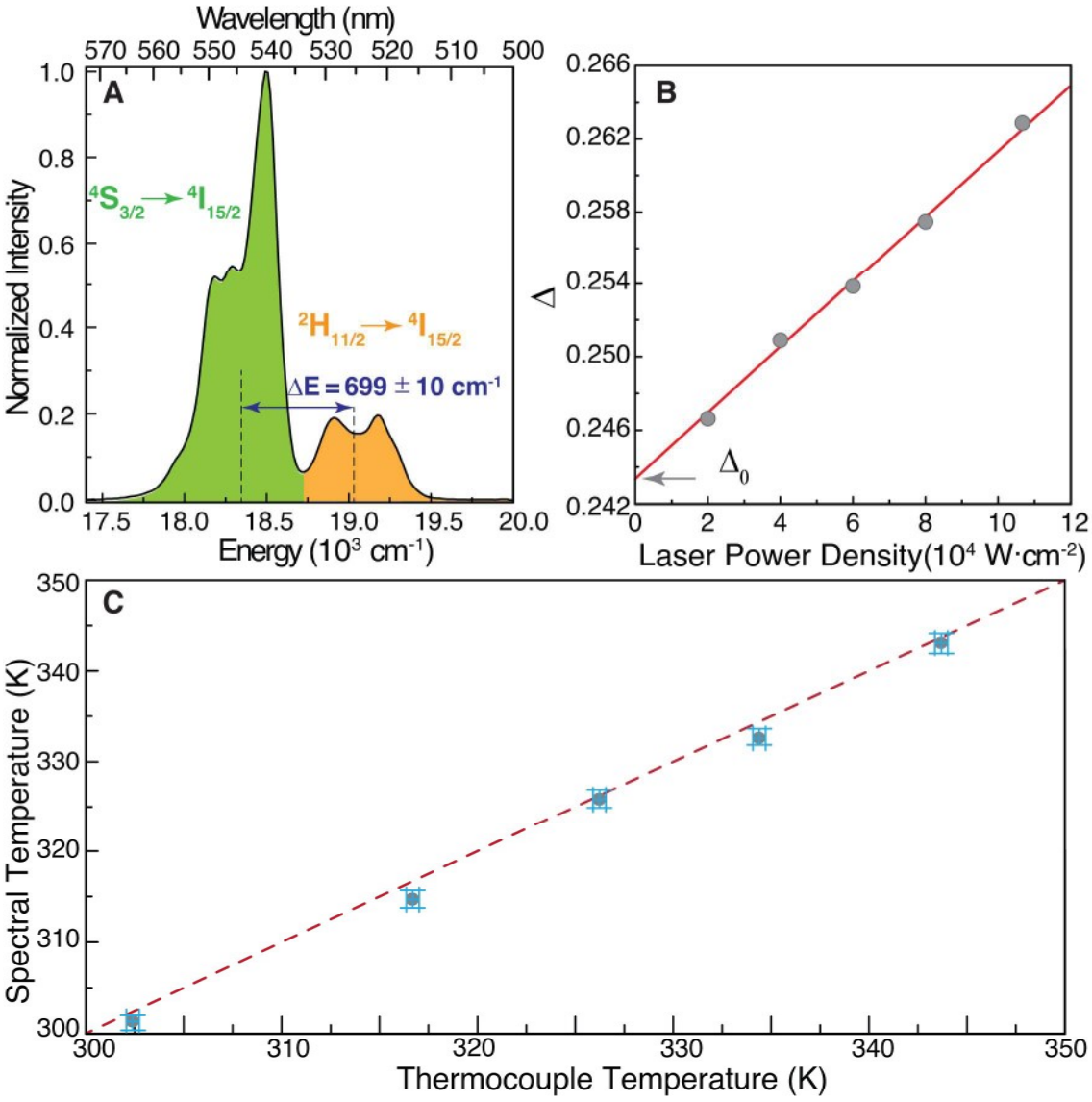

Figure S6. Calibration curve of $NaYF_4$:Lu/Yb/Er (50/18/2%). (**A**) Barycenters of the $^2H_{11/2} \rightarrow {}^4I_{15/2}$ and $^4S_{3/2} \rightarrow {}^4I_{15/2}$ transitions in the emission spectrum of the water suspension of 106 nm nanoparticles at 300 K. (**B**) Dependence of the parameter Δ on the laser power density. The solid line is the best fit of experimental data to a straight line ($r^2 > 0.999$) and allows for the determination of Δ_0=0.2431 as the intercept corresponding to T_0=295 K. (**C**) Temperature computed from Eq. 3 of the manuscript (spectral temperature, *y*) *versus* temperature reading from the immersed thermocouple (thermocouple temperature, *x*). The straight line is a guide for the eyes and corresponds to *y*=*x*. The agreement between the spectral and thermocouple temperatures is excellent. The horizontal and vertical error bars stand for the experimental temperature uncertainty and the error in the determination of spectral temperature based on the ΔE and Δ_0 values, respectively.

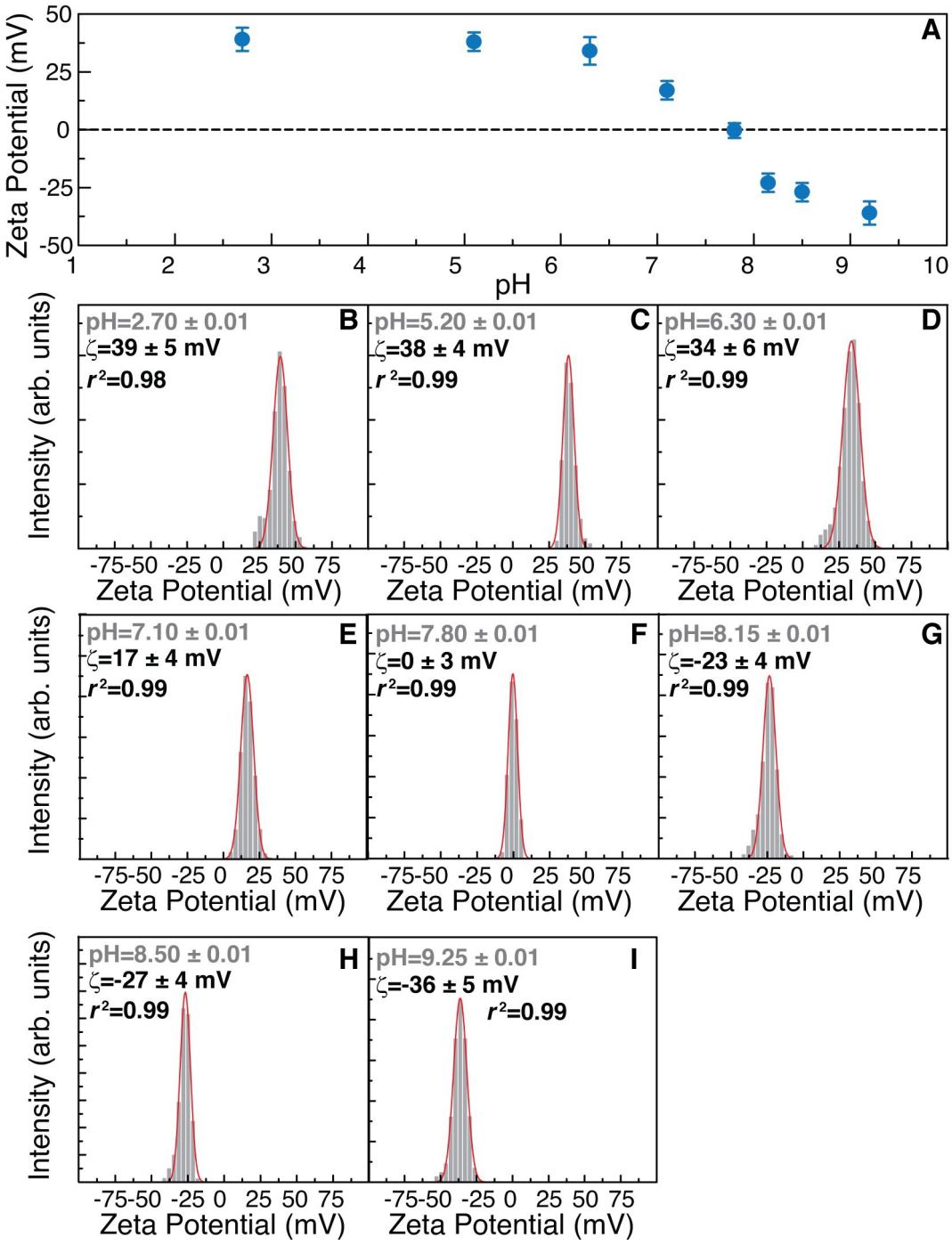

Figure S7. pH dependence of the Zeta potential. (**A**) pH dependence of the Zeta potential of the 106 nm nanoparticles in water. (**B-I**) Corresponding histograms of the Zeta potential for each pH value. The lines are the best fits to the data potential using Gaussian distributions.

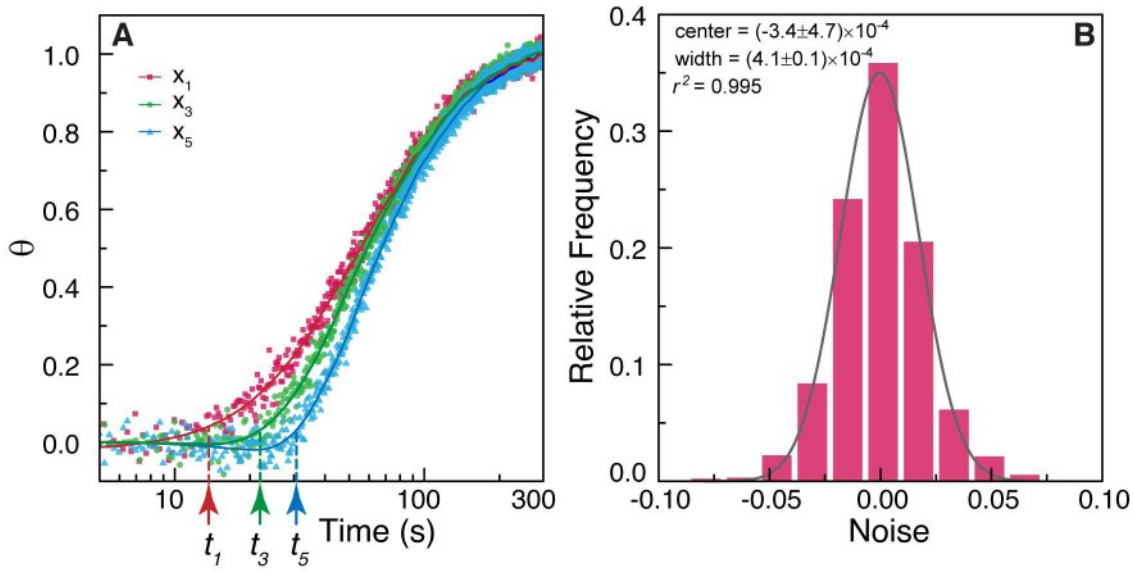

Figure S8. White Gaussian noise. (**A**) Illustrative denoising procedure applied to three reduced temperature curves (symbols) of the 24 nm nanoparticles in water (pH=5.10±0.01, Q=4.63×10^4 W·m^{-2}) acquired at x_1=0.05 cm, x_3=0.40 cm, and x_5=0.80 cm. The solid lines correspond to the denoised data using the DWT method and the corresponding t_{0i} values are indicated. (**B**) Noise histogram (10 classes) calculated for an illustrative experimental curve. The lines are fits to the experimental data using Gaussian functions. Considering the high correlation coefficients, the noise is called white Gaussian noise.

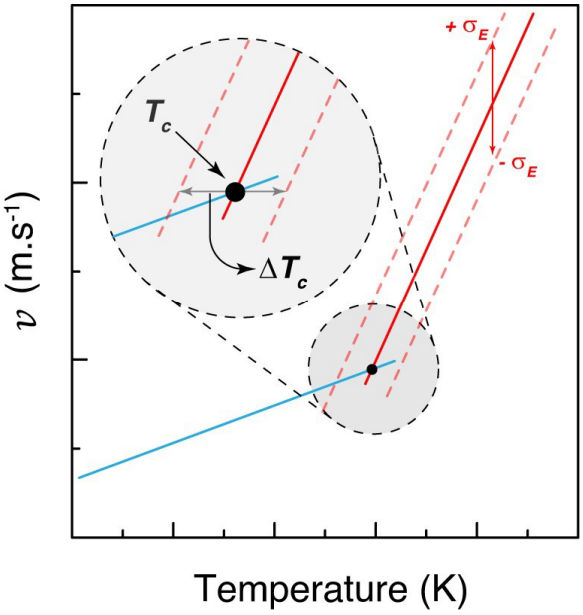

Figure S9. Schematic representation of the calculation of $T_c \pm \Delta T_c$. The solid lines are the best fits to the instantaneous Brownian velocity data below (blue) and above (red) T_c. The dashed lines display the standard error of the estimate for the T>T_c regime.

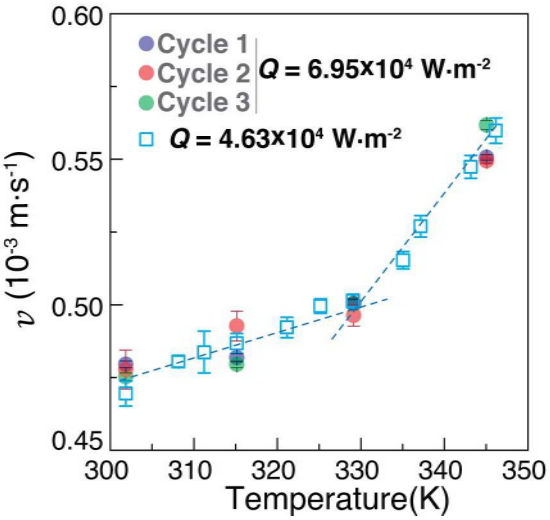

Figure S10. Temperature cycling. Instantaneous Brownian velocity of the 24 nm nanoparticles in water (pH=5.10±0.01) measured during three consecutive heating cycles between 303 and 343 K at Q=6.95×10^4 W·m^{-2}. Values obtained in a different day at Q=4.63×10^4 W·m^{-2} are also depicted. The lines are guides for the eyes.

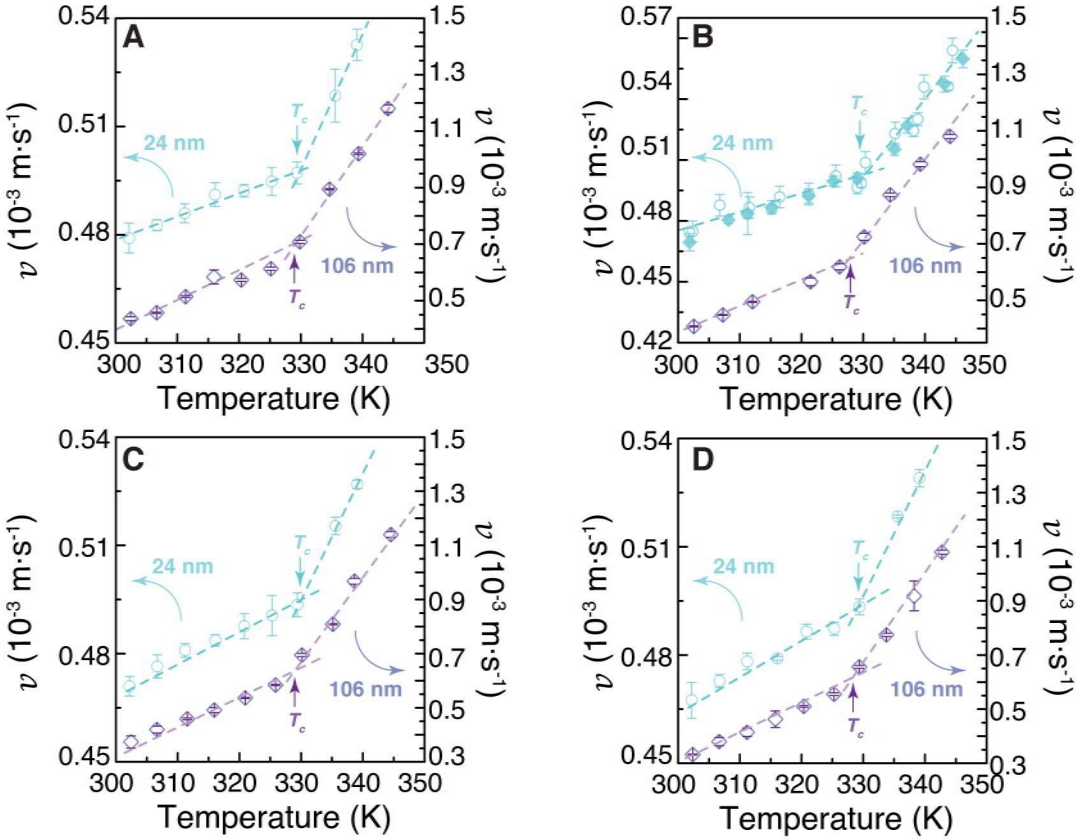

Figure S11. Comparison of the temperature dependence of the instantaneous Brownian velocity for different sized nanocrystals. Temperature-dependent instantaneous Brownian velocities of the 24 nm (circles) and 106 nm (diamonds) nanoparticles suspended in water heated at 4.63×10^4 W m^{-2} at distinct pH values, (**A**) 2.70±0.01, (**B**) 5.10±0.01 (24 nm), and 5.20±0.01 (106 nm), (**C**) 6.40±0.01 and (**D**) 8.50±0.01. The lines are the best fits to straight lines (slopes and correlation coefficients r^2 shown in Table S3).

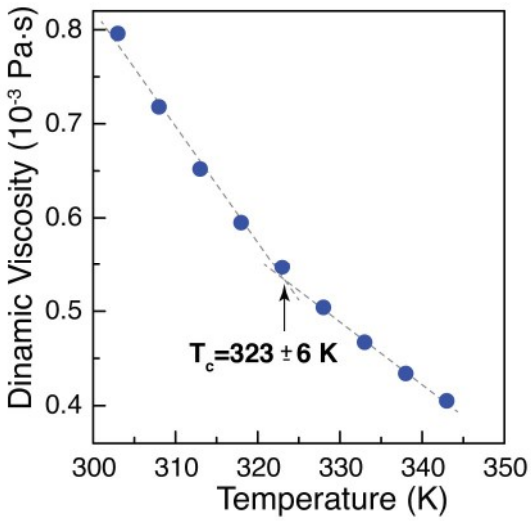

Figure S12. Bi-linear behaviour of the dynamic water viscosity with temperature. The points were extracted from Ref. 19 whereas the dashed lines are the best fits to straight lines with slopes $-(1.24\pm0.06)\times10^{-5}$ Pa·s·K^{-1} and $-(0.66\pm0.02)\times10^{-5}$ Pa·s·K^{-1} (r^2>0.988).

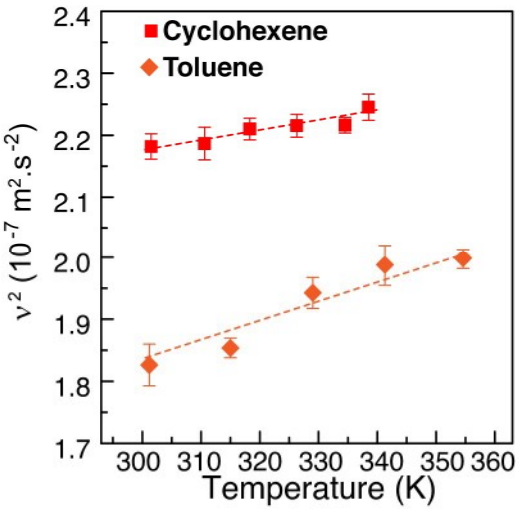

Figure S13. Temperature-dependent v^2 values in toluene and cyclohexene. Temperature-dependent v^2 values of the 24 nm nanoparticles in toluene and cyclohexene (Q=6.95×10^4 W·m^{-2}). The lines are the best fits to straight lines (the slopes and correlation coefficients r^2 are presented in Table S4).

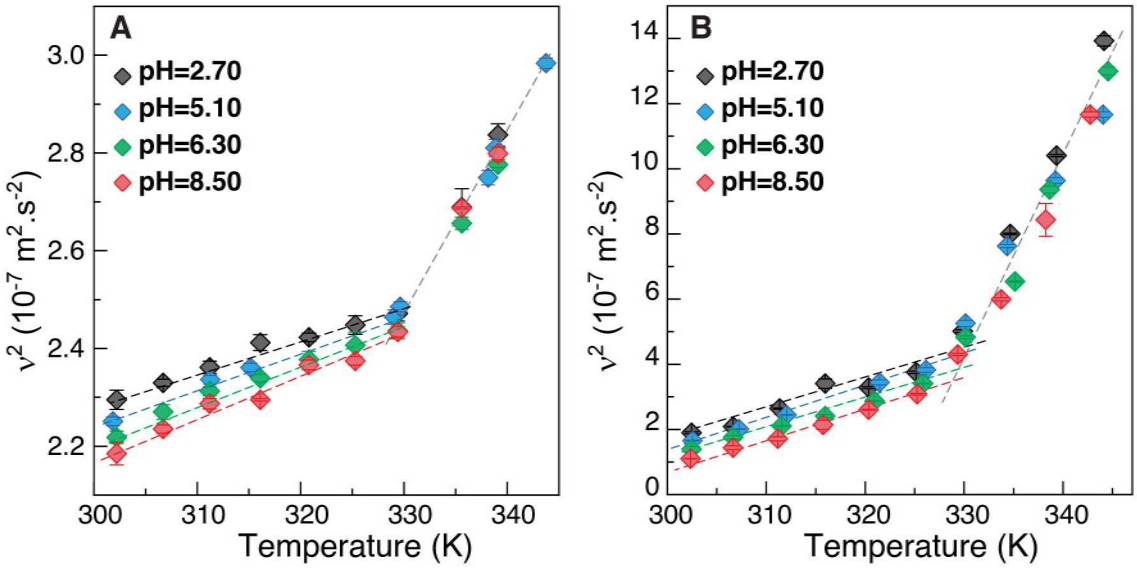

Figure S14. Temperature-dependent v^2 values in water. Temperature-dependent v^2 values of the (**A**) 24 nm and (**B**) 106 nm nanoparticles in the water at distinct pH values (Q=6.95×10^4 W·m^{-2}). The lines are the best fits to straight lines (the slopes and correlation coefficients r^2 are presented in Table S4).

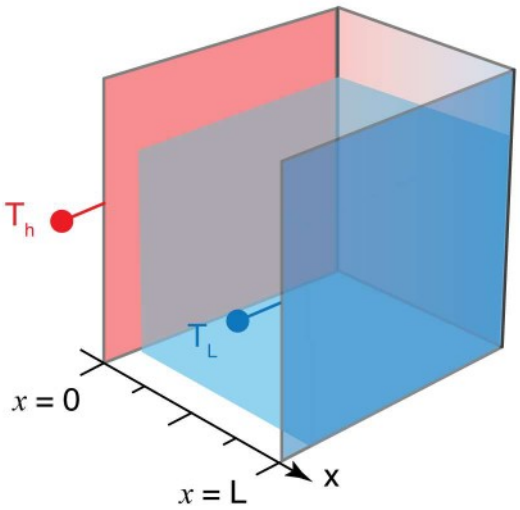

Figure S15. Modeling of heat transport for pure water. The two-plate model used to mimic the thermal transport occurring in the water-based nanofluids. The total transport length is assumed to be 1 cm, as in the experiment.

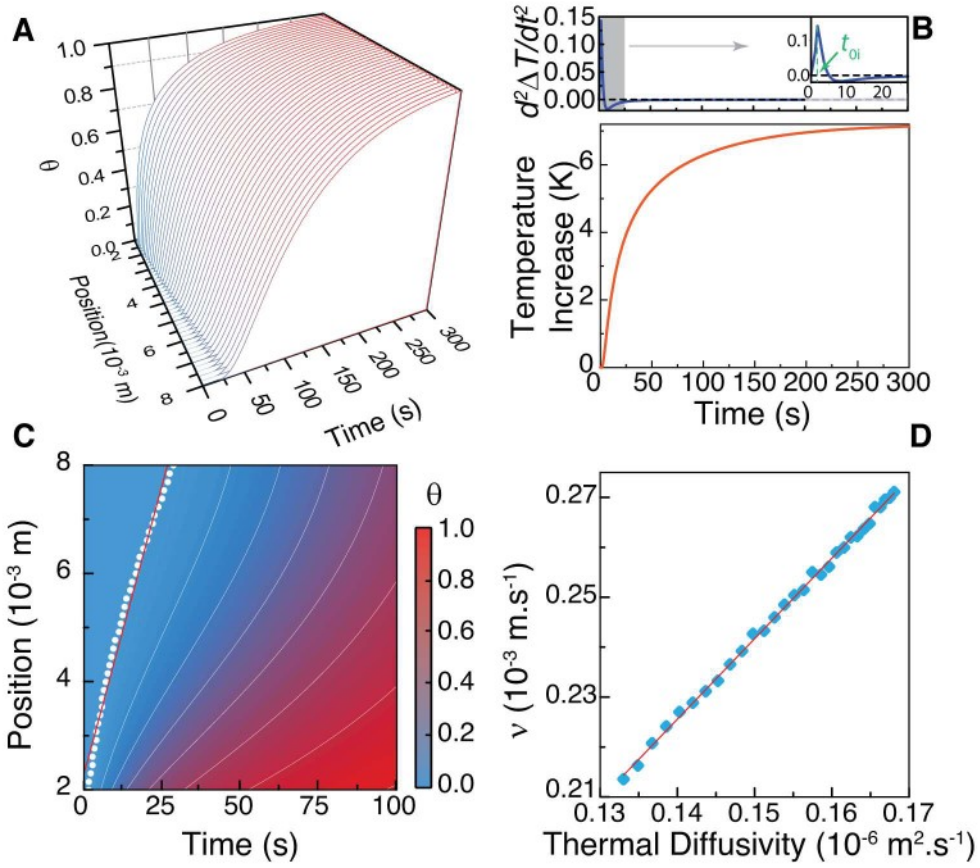

Figure S16. Results from two plate model for T_0-T_L=9 K. (**A**) Three-dimensional plot of normalized temperature as a function of time and position. (**B**) Temperature as a function of time at position x_i=0.2 cm. The time instant corresponding to the maximum of the temperature's second derivative is t_{0i}. (**C**) Zoomed-in contour plot of the first 100 seconds of panel B. The points are the maximum position of the second derivative, and the line is the linear fit, which gives the instantaneous Brownian velocity. (**D**) Instantaneous Brownian velocity versus thermal diffusivity of pure water over the temperature range 273-373 K. The line is the linear fit used to obtain the predicted thermal diffusivity of the nanoparticle-water mixture.

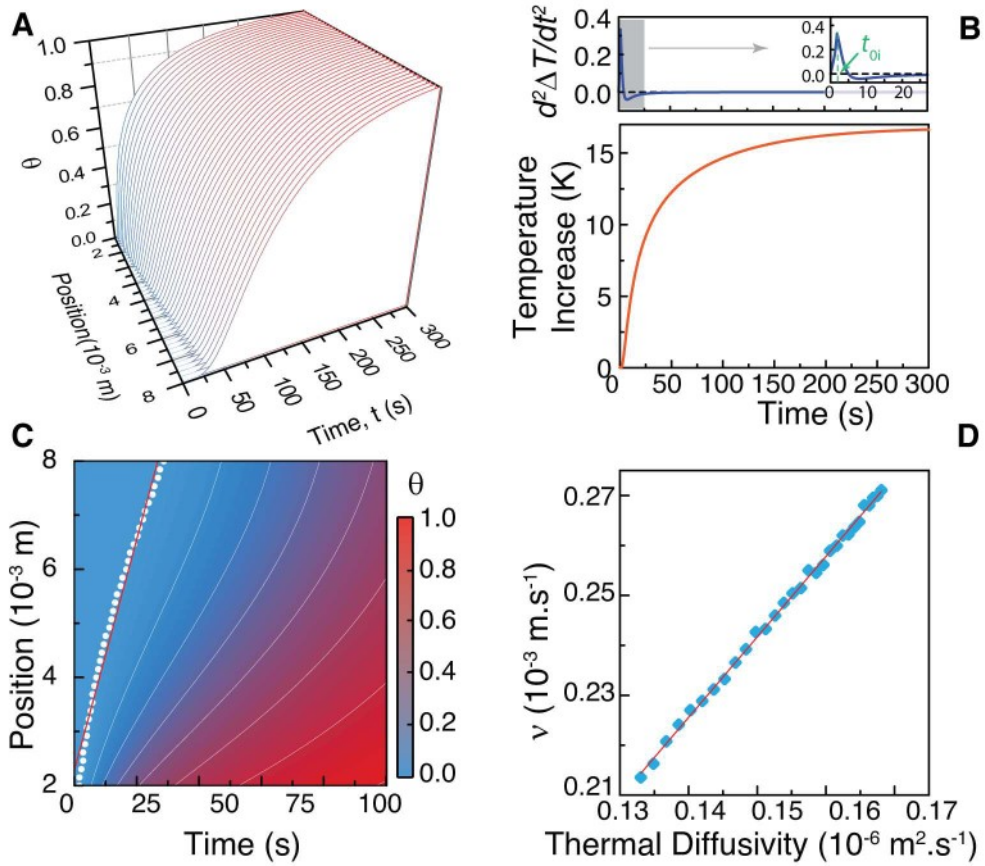

Figure S17. Results from two plate model for T_0-T_L=21 K. (**A**) Three-dimensional plot of normalized temperature as a function of time and position. (**B**) Temperature as a function of time at position x_i=0.2 cm. The time instant corresponding to the maximum of the temperature's second derivative is t_{0i}. (**C**) Zoomed-in contour plot of the first 100 seconds of panel B. The points are the maximum position of the second derivative, and the line is the linear fit, which gives the instantaneous Brownian velocity. (**D**) Instantaneous Brownian velocity versus thermal diffusivity of pure water over the temperature range 273-373 K. The line is the linear fit used to obtain the predicted thermal diffusivity of the nanoparticle-water mixture.

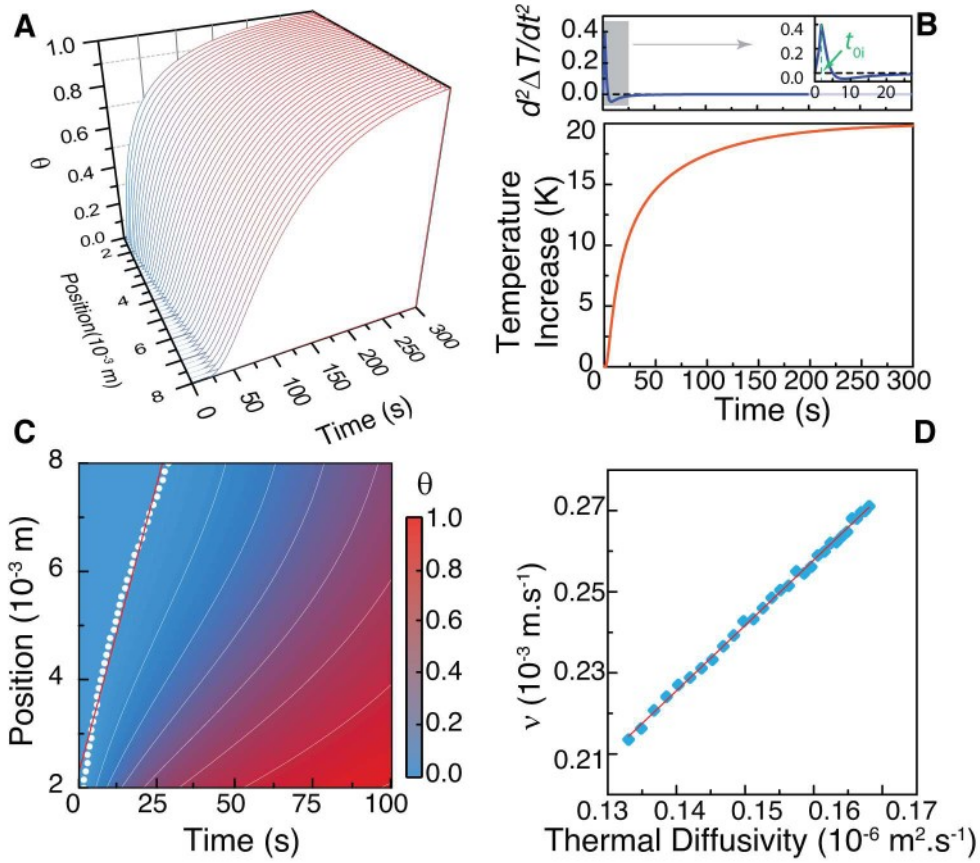

Figure S18. Results from two plate model for T_0-T_L=25 K. (**A**) Three-dimensional plot of normalized temperature as a function of time and position. (**B**) Temperature as a function of time at position x_i=0.2 cm. The time instant corresponding to the maximum of the temperature's second derivative corresponds is t_{0i}. (**C**) Zoomed-in contour plot of the first 100 seconds of panel B. The points are the maximum position of the second derivative, and the line is the linear fit, which gives the instantaneous Brownian velocity. (**D**) Instantaneous Brownian velocity versus thermal diffusivity of pure water over the temperature range 273-373 K. The line is the linear fit used to obtain the predicted thermal diffusivity of the nanoparticle-water mixture.

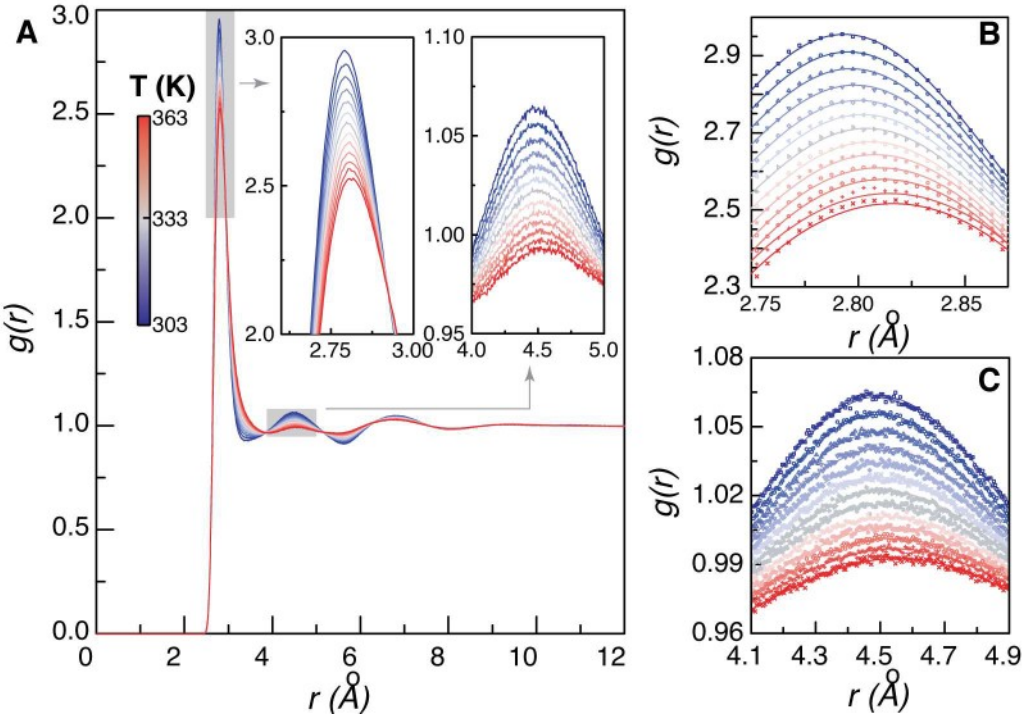

Figure S19. O-O radial pair distribution function and the location of the 1st and the 2nd peak maxima, r_1 and r_2. (**A**) O-O radial distribution function, *g(r)*, computed from a simulation of 1024 water molecules. (**B**) *g(r)* in the vicinity of r_1. Least-square fit by a Gaussian function is shown as black curves. (**C**) *g(r)* in the vicinity of r_2. Least-square fit by Gaussian function is shown as solid curves.

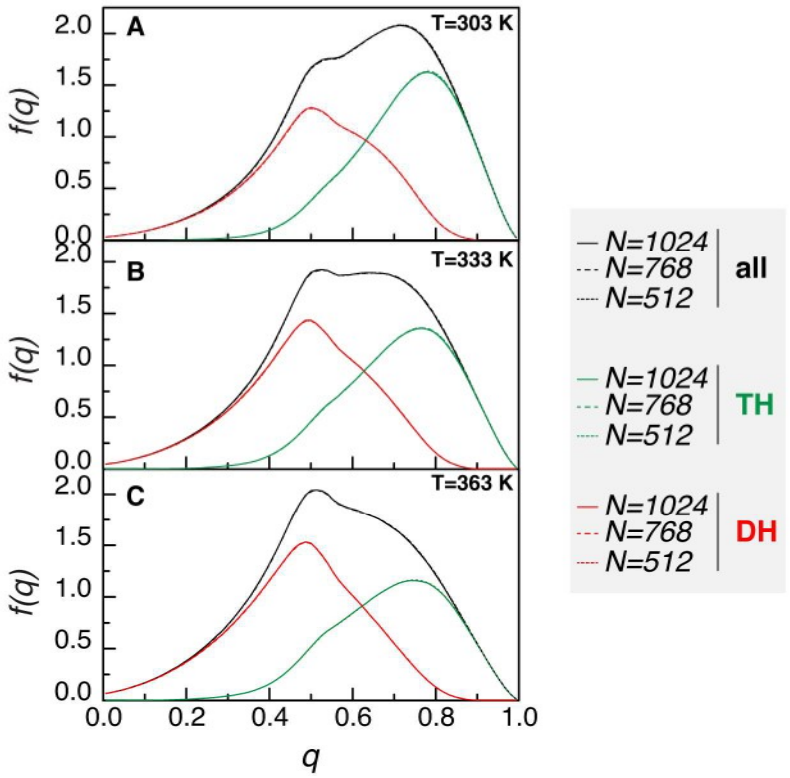

Figure S20. Finite-size effect of the simulation for the probability density function *f*(*q*). The three panels represent the probability density function *f*(*q*) of the orientational order parameter *q* (Eq.1 in the main text) for water at (**A**) 303 K, (**B**) 333 K, and (**C**) 363 K, respectively. In each panel, data is calculated based on the molecular dynamics simulation of a cubic box of N=512, 768, and 1024 water molecules with the polarizable SWM4-NDP water model. The finite-size effect of the simulation is minimal.

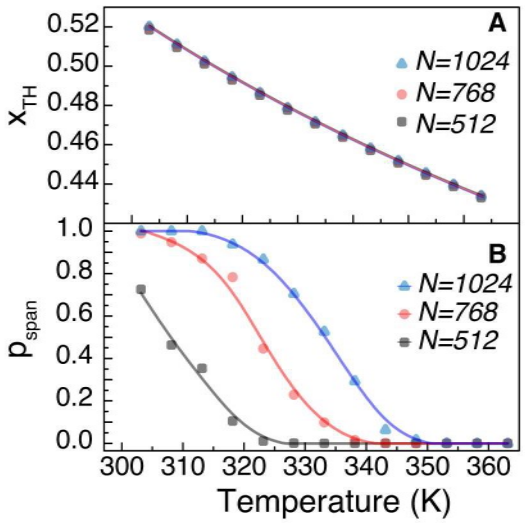

Figure S21. Finite-size effect of the simulation for the statistics of molecular structures. (**A**) The probability x_{TH} for a water molecule to be in the TH-state as a function of temperature from data based on the molecular dynamics simulation of a cubic box of N=512, 768, and 1024 water molecules with the polarizable SWM4-NDP water model. The finite-size effect of the simulation is minimal. (**B**) The probability for the LDL motif to span across a 24 nm nanoparticle based on Eq. S11. Since N=1024 is the largest simulation box considered, it gives the best estimate for the probability p_{span}. All simulations indicate a crossover from 1 to 0 at around T=330 K.

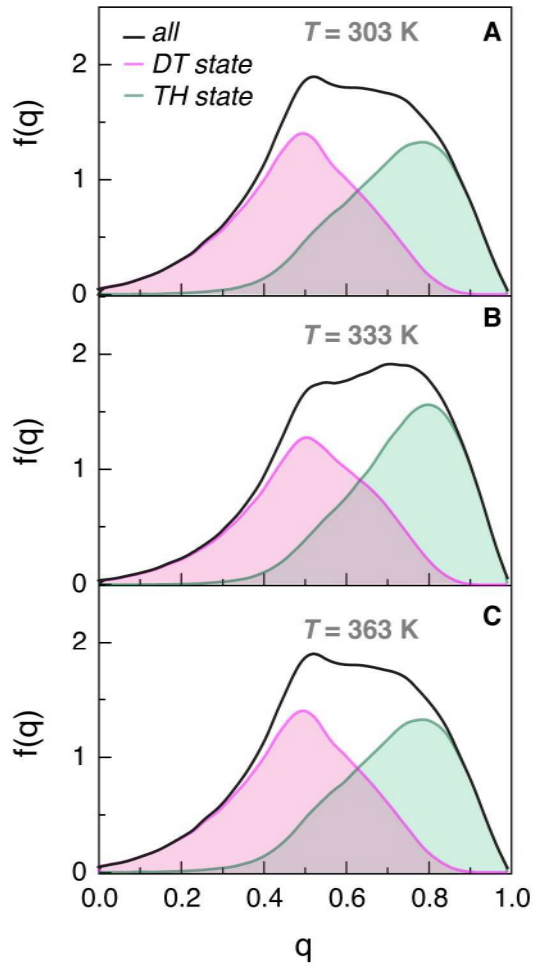

Figure S21. Probability density functions based on simulations using TIP4P-FB model. The probability density function *f(q)* of the orientational order parameter *q* (Eq. 1 in the manuscript) for water at **A** 303 K, **B** 333 K, and **C** 363 K, calculated based on the molecular dynamics simulation of a cubic box of 1024 water molecules with the nonpolarizable TIP4P-FB water model. The contributions towards *f(q)* of the locally tetrahedral (TH) state and the locally disturbed (DT) state are shown as shaded areas.

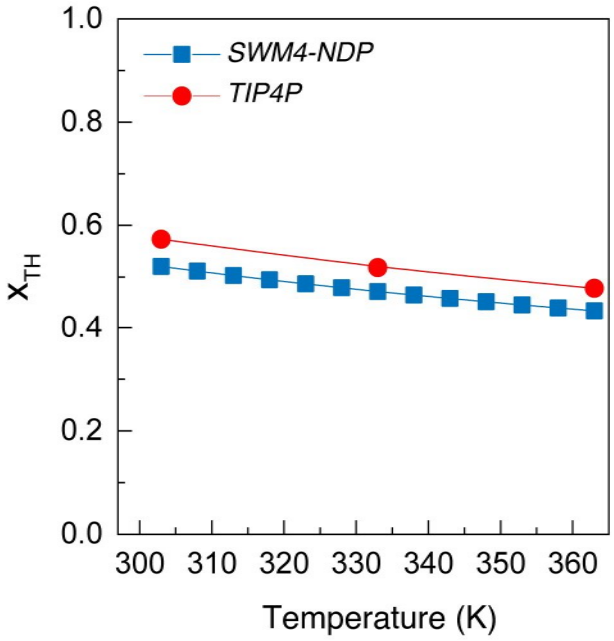

Figure S22. Fraction of molecules in the TH-state computed with simulations using the TIP4P-FB and SWM4-NDP models. The fraction of molecules in the TH-state is denoted as x_{TH}.

S4 Supplementary Tables

Table S1. Mass concentration $\boldsymbol{\rho_F}$ (kg·m^{-3}) and volume fraction $\boldsymbol{\phi}$ (%) of the $NaYF_4$:Yb/Er@$NaYF_4$ and $NaYF_4$:Lu/Yb/Er nanocrystals in water, cyclohexene and toluene.

Solvent	Composition and size	ρ_F	ϕ
Water $\boldsymbol{\phi = \frac{\rho_F}{\rho_N}}$	$NaYF_4$:Yb/Er(18/2%)@$NaYF_4$ (24 nm)	3.75	0.085
	$NaYF_4$:Lu/Yb/Er (50/18/2%) (106 nm)	3.75	0.066
Cyclohexene and toluene $\phi = \frac{\rho_{F(1-x)}}{\rho_N} + \frac{\rho_F \boldsymbol{x}}{\rho_{OA}}$	$NaYF_4$:Yb/Er(18/2%)@$NaYF_4$ (24 nm)	3.75	0.107

ρ_N (24 nm)=4390 kg·m^{-3}; ρ_N (106 nm)=5680 kg·m^{-3} are the densities of the crystals
ρ_{OA}=890 kg·m^{-3} is the density of the oleic acid capping with mass fraction $\boldsymbol{x}$=0.063.

Table S2. TEM and hydrodynamic diameters (nm), Zeta potential (mV) and pH of $NaYF_4$:Yb/Er@$NaYF_4$ and $NaYF_4$:Lu/Yb/Er. The hydrodynamic diameter, Zeta potential and pH are ascribed to water-based suspensions.

Suspension	TEM diameter	Hydrodynamic diameter	Zeta Potential	pH
$NaYF_4$:Yb/Er (18/2%)@$NaYF_4$	24.2±2.1	36±8	40±5	5.10±0.01
$NaYF_4$:Lu/Yb/Er (50/18/2%)	106.3±9.7	93±26	37±6	5.20±0.01

The data of TEM and hydrodynamic size results from the best fits to the distribution data using a log-normal function (r^2>0.998 for TEM fits and r^2>0.980 for the hydrodynamic ones), whereas that of the zeta potential results from the best fits to the distribution data using a Gaussian function (r^2>0.970). The errors correspond to ± fwhm of the corresponding fitting curves.

Table S3. Slopes (s, 10^{-6} $m \cdot s^{-1} \cdot K^{-1}$) and correlation coefficients of $\nu(T)$ in the water-, cyclohexene- and toluene-based nanofluids heated at $Q=4.63\times10^4$ W m^{-2}, and slopes (s, 10^{-7} $m^2 \cdot s^{-1} \cdot K^{-1}$) and correlation coefficients of effective diffusivity for the nanofluid containing 24 nm nanoparticles.

Nanofluid	**Temperature Range**	***pH***	***s***	***r²***
$NaYF_4$:Yb/Er@$NaYF_4$ - *Brownian Velocity*				
Water	$T<T_c$	2.70±0.01	0.69±0.04	0.981
		5.10±0.01	1.08±0.12	0.917
		6.30±0.01	0.84±0.07	0.967
		8.50±0.01	0.81±0.13	0.881
	$T>T_c$	all values	3.37±0.15	0.976
Cyclohexene	302-339	-	0.57±0.03	0.986
Toluene	301-355	-	0.40±0.05	0.928
$NaYF_4$:Lu/Yb/Er - *Brownian Velocity*				
Water	$T<T_c$	2.70±0.01	8.35±0.68	0.968
		5.20±0.01	9.11±0.31	0.997
		6.30±0.01	8.73±0.24	0.996
		8.50±0.01	9.82±0.58	0.999
	$T>T_c$	all values	27.6±2.4	0.896
$NaYF_4$:Yb/Er@$NaYF_4$ - *Effective Diffusivity*				
Water	$T<T_c$	5.10±0.01	6.15±0.81	0.853
	$T>T_c$		28.3±1.2	0.993

Table S4. Slopes (s, 10^{-9} $m^2 \cdot s^{-2} \cdot K^{-1}$) and correlation coefficients r^2 of the temperature dependence of ν^2 values in the water, cyclohexene- and toluene-based nanofluids at $Q=4.63\times10^4$ W m^{-2}.

Nanofluid	Temperature Range	pH	s	r^2
$NaYF_4$:Yb/Er@$NaYF_4$				
Water	$T<T_c$	2.70±0.01	0.67±0.04	0.98
		5.10±0.01	1.01±0.07	0.93
		6.30±0.01	0.81±0.06	0.97
		8.50±0.01	0.77±0.12	0.88
	$T>T_c$	all values	3.49±0.15	0.98
Cyclohexene	302-339	-	0.54±0.02	0.99
Toluene	301-355	-	0.36±0.04	0.93
$NaYF_4$:Lu/Yb/Er				
Water	$T<T_c$	2.70±0.01	8.79±0.67	0.97
		5.20±0.01	8.25±0.40	0.99
		6.30±0.01	8.87±0.40	0.99
		8.50±0.01	8.44±0.12	0.99
	$T>T_c$	all values	45.57±4.3	0.88

Table S5. Temperature (K) dependence of the density of water (ρ_L, 10^3 kg·m^{-3}) that determines the density of water molecules in molecular dynamics simulations.

Temperature	ρ_L
303	0.99565
308	0.99403
313	0.99221
318	0.99022
323	0.98804
328	0.98570
333	0.98321
338	0.98056
343	0.97778
348	0.97486
353	0.97180
358	0.96862
363	0.96531

Table S6. Slopes (s, 10^{-4} Å·K^{-1}) and correlation coefficients of $r_1(T)$ and $r_2(T)$ in water.

Method	g(r) peak	Temperature Range	s	r^2
Simulation of SWM4-NDP	r_1	--	3.80±0.06	0.997
	r_2	$T<T_c$	4.35±0.45	0.960
		$T>T_c$	13.5±0.6	0.988
Experiment by Skinner *et. al.* [16]	r_1	--	3.08±0.19	0.920
	r_2	$T<T_c$	5.42±0.10	0.639
		$T>T_c$	36.3±5.22	0.923

S5 References

1. Brites C. D., *et al.* Instantaneous ballistic velocity of suspended brownian nanocrystals measured by upconversion nanothermometry. *Nat. Nanotechnol.* **11**, 851-856 (2016).
2. Bhattacharjee S. DLS and zeta potential - What they are and what they are not? *J. Control Release* **235**, 337-351 (2016).
3. Bogdan N., Vetrone F., Ozin G. A. & Capobianco J. A. Synthesis of Ligand-Free Colloidally Stable Water Dispersible Brightly Luminescent Lanthanide-Doped Upconverting Nanoparticles. *Nano Lett.* **11**, 835-840 (2011).
4. Lang M., Guo H., Odegard J. E., Burrus C. S. & Wells R. O. Nonlinear processing of a shift-invariant discrete wavelet transform (DWT) for noise reduction. In: Wavelet Applications II; Szu HH, editor. Proc. SPIE 2491; 1995.
5. Donoho D. L. & Johnstone I. M. Ideal spatial adaptation by wavelet shrinkage. *Biometrika* **81**, 425-455 (1994).
6. Donoho D. L. De-noising by soft-thresholding. *IEEE T. Inform. Theory* **41**, 613-627 (1995).
7. Hellums J. D. & Churchill S. W. Transient and steady state, free and natural convection, numerical solutions: Part I. The isothermal, vertical plate. *AIChE J.* **8**, 690-692 (1962).
8. Carslaw H. S. & Jaeger J. C. *Conduction of Heat in Solids*, 2 edn. Oxford University Press: Oxford, U.K., 1986.
9. *Recommended Reference Materials for the Realization of Physicochemical Properties*. Blackwell Scientific Publications: Oxford, U.K., 1987.
10. Ramires M. L. V., *et al.* Standard Reference Data for the Thermal Conductivity of Water. *J. Phys. Chem. Ref. Data* **24**, 1377-1381 (1995).
11. Sengers J. V. & Watson J. T. R. Improved International Formulations for the Viscosity and Thermal Conductivity of Water Substance. *J. Phys. Chem. Ref. Data* **15**, 1291-1314 (1986).
12. Lamoureux G., Harder E., Vorobyov I. V., Roux B. & MacKerell Jr. A. D. A polarizable model of water for molecular dynamics simulations of biomolecules. *Chem. Phys. Lett.* **418**, 245-249 (2006).
13. Jiang W., *et al.* High-Performance Scalable Molecular Dynamics Simulations of a Polarizable Force Field Based on Classical Drude Oscillators in NAMD. *J. Phys. Chem. Lett.* **2**, 87-92 (2011).
14. Eastman P., *et al.* OpenMM 4: A Reusable, Extensible, Hardware Independent Library for High Performance Molecular Simulation. *J. Chem. Theory Comput.* **9**, 461-469 (2013).
15. McGibbon R. T., *et al.* MDTraj: A Modern Open Library for the Analysis of Molecular Dynamics Trajectories. *Biophys. J.* **109**, 1528-1532 (2015).
16. Skinner L. B., Benmore C. J., Neuefeind J. C. & Parise J. B. The structure of water around the compressibility minimum. *J. Chem. Phys.* **141**, 214507 (2014).
17. Chau P.-L. & Hardwick A. J. A new order parameter for tetrahedral configurations. *Mol. Phys.* **93**, 511-518 (1998).
18. Wang L.-P., Martinez T. J. & Pande V. S. Building Force Fields: An Automatic, Systematic, and Reproducible Approach. *J. Phys. Chem. Lett.* **5**, 1885-1891 (2014).
19. Bian X., Kim C. & Karniadakis G. E. 111 years of Brownian motion. *Soft Matter* **12**, 6331-6346 (2016).
20. Huang R. X., *et al.* Direct observation of the full transition from ballistic to diffusive Brownian motion in a liquid. *Nat. Phys.* **7**, 576-580 (2011).
21. Kumar D. H., *et al.* Model for heat conduction in nanofluids. *Phys. Rev. Lett.* **93**, 144301-144304 (2004).

Manuscript 3

Temperature Dependence of Water Absorption in the Biological Windows and Its Impact on the Performance of Ag_2S Luminescent Nanothermometers

T. Muñoz-Ortiz, L. Abiven, R. Marin, J. Hu, D. H. Ortgies, A. Benayas, F. Gazeau, V. Castaing, B. Viana, C. Chanéac, D. Jaque, F. E. Maturi, L. D. Carlos, E. M. Rodríguez, J. G. Solé.

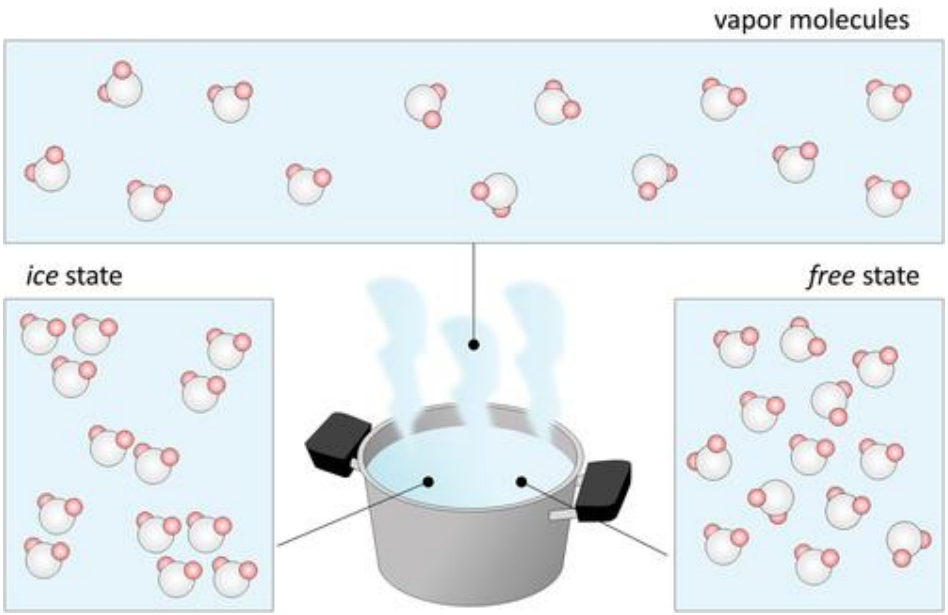

Particle & Particle Systems Characterization, 39 (11), 2200100, 2022.

DOI: https://doi.org/10.1002/ppsc.202200100

RESEARCH ARTICLE

Particle & Particle Systems Characterization
www.particle-journal.com

Temperature Dependence of Water Absorption in the Biological Windows and Its Impact on the Performance of Ag_2S Luminescent Nanothermometers

Tamara Muñoz-Ortiz, Lise Abiven, Riccardo Marin, Jie Hu, Dirk H. Ortgies, Antonio Benayas, Florence Gazeau, Victor Castaing, Bruno Viana, Corinne Chanéac, Daniel Jaque, Fernando E. Maturi, Luís D. Carlos, Emma Martín Rodríguez, and José García Solé*

The application of nanoparticles in the biological context generally requires their dispersion in aqueous media. In this sense, luminescent nanoparticles are an excellent choice for minimally invasive imaging and local temperature sensing (nanothermometry). For these applications, nanoparticles must operate in the physiological temperature range (25–50 °C) but also in the near-infrared spectral range (750–1800 nm), which comprises the three biological windows of maximal tissue transparency to photons. In this range, water displays several absorption bands that can strongly affect the optical properties of the nanoparticles. Therefore, a full understanding of the temperature dependence of water absorption in biological windows is of paramount importance for applications based on these optical properties. Herein, the absorption spectrum of water in the biological windows over the 25–65 °C temperature range is systematically analyzed, and its temperature dependence considering the coexistence of two states of water is interpreted. Additionally, to illustrate the importance of state-of-the-art applications, the effects of the absorption of water on the emission spectrum of Ag_2S nanoparticles, the most sensitive luminescent nanothermometers for in vivo applications to date, are presented. The spectral shape of the nanoparticles' emission is drastically affected by the water absorption, impacting their thermometric performance.

1. Introduction

The first systematic report on the temperature dependence of liquid water absorption in the near-infrared (NIR) was published in 1925.[1] In that work, it was already proposed that the complex spectrum of water results from the coexistence of two kinds of water molecules (or water states) whose relative concentration depends on the temperature. This interpretation was based on the assumption given by Röntgen in 1892 to explain the anomalous properties of liquid water.[2] Röntgen denoted the water molecules belonging to these two states as *water molecules* and *ice molecules*. At that time, it was supposed that they were related to single water molecules (called hydrol) and aggregates of two or three molecules (called dihydrol or trihydrol, respectively). The simultaneous presence of these molecules should contribute to the experimentally observed broadening of the

T. Muñoz-Ortiz
Instituto Investigación Sanitaria Princesa (IIS-IP)
Universidad Autónoma de Madrid
Calle Diego de León, 62, Madrid 28006, Spain
T. Muñoz-Ortiz, R. Marin, D. H. Ortgies, A. Benayas, D. Jaque, E. Martín Rodríguez, J. García Solé
Nanomaterials for bioimaging group (NanoBIG)
Facultad de Ciencias
Universidad Autónoma de Madrid
C/ Francisco Tomás y Valiente 7, Madrid 28049, Spain
E-mail: emma.martin@uam.es

The ORCID identification number(s) for the author(s) of this article can be found under https://doi.org/10.1002/ppsc.202200100.

DOI: 10.1002/ppsc.202200100

L. Abiven, C. Chanéac
Sorbonne Université
CNRS
Collège de France
LCMCP
Place Jussieu 4, Paris 75005, France
L. Abiven, V. Castaing, B. Viana
IRCP
PSL Chimie ParisTech
CNRS
Rue P. & M. Curie 11, Paris 75005, France
L. Abiven, F. Gazeau
Université Paris Diderot
CNRS
MSC
Rue Alice Domon et Léonie Duquet 10, Paris 75013, France
J. Hu
Xiamen Institute of Rare-earth Materials
Haixi Institutes
Chinese Academy of Sciences
Duishanxiheng Road 258, Jimei District Xiamen, Fujian 361024, China

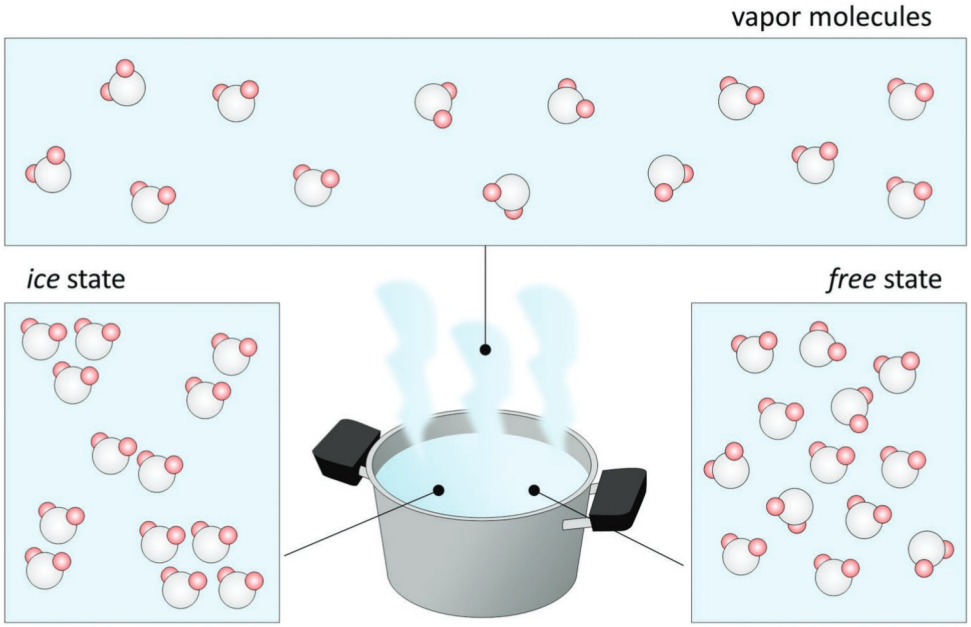

Figure 1. Schematic (artistic) representation of the two kinds of water states coexisting in liquid water. Molecules in the ice state should belong to ordered structures (small clusters), while molecules in the free state should be almost free molecules, close to the ones observed in the vapor state.

absorption bands in the liquid state compared to the vapor state spectrum. As the temperature rises, the relative amount of water molecules should increase at the cost of ice molecules, determining the temperature dependence of the peak position, shape, and intensity of most absorption bands in liquid water. Although several works have dealt with the spectrum of liquid water in different spectral regions,[3] the number of those dealing with the spectral range encompassing the biological windows (NIR-I: 750–950 nm, NIR-II: 1000–1350 nm, NIR-III: 1500–1800 nm[4]), where the luminescence of most of the nanoparticles for deep tissue imaging occurs, is still scarce.[5] In addition, the temperature dependence of the main absorption bands in this spectral range has also been barely analyzed.[1,5c,6] As practically all nanoparticle-based applications use water or water-based solutions as dispersants, it is evident that a careful analysis of the temperature dependence of the main absorption bands of liquid water in the biological windows is of paramount importance. In fact, these bands can dramatically affect the emission spectra of the nanoparticles due to an inner absorption filter effect.

As predicted by Röntgen, nowadays it is widely accepted that the molecules of liquid water display at least two different structural arrangements (water states) in the physiological range of temperature.[7] Despite the nature of these states still being a matter of debate, plenty of information has been obtained concerning the structure and arrangement of water molecules in both states.[7c,8] **Figure 1** illustrates the two water states, which were herein labeled as *ice* state and *free* state, departing slightly from the terms *ice molecules* and *water molecules* adopted by Röntgen just to avoid chemical misinterpretations. Indeed, recently reported experimental results have confirmed that, in the simplest approach, liquid water consists of two water states.[8,9] At temperatures close to 0 °C the water molecules mainly form clusters of few molecules, giving an average dipole moment of 2.8 D for each water molecule. This scenario corresponds to the *ice* state in Figure 1. As the temperature is raised, these clusters are being decoupled to form free molecules (*free* state) with a much lower average dipole moment of 1.8 D.[10]

Within this simple scheme, the molecules in the *ice* state should be dominating at room temperature, while molecules in the *free* state should predominate at temperatures close to the boiling point (100 °C in pure water). As a matter of fact, several physicochemical properties of liquid water show a change in the behavior at temperatures around 40–50 °C.[9–11] The temperature at which these changes occur has been lately labeled crossover temperature. At temperatures below the crossover point, water molecules are mostly arranged in organized clusters (*ice* state) while above the crossover temperature these clusters are decoupled to produce free water molecules (*free* state). This model was successfully applied by Labrador-Paez et al. to explain the anomalous thermal properties in the luminescence of Eu^{3+} aqueous complexes[12] and nanocrystals in water,[13] while Brites et al. moved within this framework to describe the crossover temperature observed in the Brownian velocity of colloidal upconverting nanoparticles in water.[9] In this sense, the

D. H. Ortgies, A. Benayas, D. Jaque, E. Martín Rodríguez, J. García Solé
Nanomaterials for Bioimaging Group (nanoBIG)
Instituto Ramón y Cajal de Investigación
Sanitaria (IRICYS)
Hospital Ramón y Cajal
Ctra. De Colmenar Viejo km 9.100, Madrid 28034, Spain
F. E. Maturi, L. D. Carlos
Phantom-g
CICECO -Aveiro Institute of Materials
Department of Physics
University of Aveiro
Aveiro 3810-193, Portugal

changes in the absorption spectrum of water at different temperatures must be due to the coexistence of both states.

In this paper, we have carried out a systematic analysis of the liquid water absorption spectrum in the biological windows (750–1800 nm) within the 25–65 °C range—a temperature range that encompasses the physiological range (25–50 °C). The main absorption bands have been explained as the convolution of two Gaussian components, each of them corresponding to one of the two above-mentioned states of liquid water. Despite its simplicity, this approach reasonably explains the temperature dependence of the shape of the absorption bands experimentally observed.

From a practical standpoint, the absorption of liquid water can seriously affect the emission spectral shape of nanoparticles in aqueous colloidal dispersions, therefore reducing their reliability for thermal sensing when used as luminescent nanothermometers in biological and/or biomedical applications.[14] Among the proposed nanothermometers, those based on biocompatible Ag_2S nanoparticles (NPs) are the best-performing ones.[15] Their performance is related to their high brightness (the product between absorption cross-section and emission efficiency) in the NIR-II window (1000–1350 nm) and the large sensitivity of different emission features to slight temperature variations within the physiological temperature range. Thus, the second part of this work is dedicated to the evaluation of the effect of water absorption on the emission shape of Ag_2S NPs and how the temperature variation of the absorption bands of water affects the thermometric properties of these nanoparticles.

2. Background: Water Molecule Vibrations and Their Near-Infrared Absorption

Water molecules display three normal vibrational modes that involve symmetric stretching (mode I), symmetric bending (mode II), and asymmetric stretching (mode III) of the covalent bonds. They can be properly described by the three corresponding vibrational quantum numbers ν_1 (mode I), ν_2 (mode II), and ν_3 (mode III). In the ground state, these quantum numbers are all equal to 0, so the ground state can be labeled as (0, 0, 0). The fundamental vibrational transitions of a water molecule correspond to transitions in which only one of the three vibrational quantum numbers changes by one unit. Thus, following the selection rule $\Delta\nu_i = 1$, these transition bands are usually written as[16]

Mode I: (0, 0, 0) → (1, 0, 0);
Mode II: (0, 0, 0) → (0, 1, 0);
Mode III: (0, 0, 0) → (0, 0, 1).

For individual molecules (*free* state), these absorption fundamental transitions lie at 2.73 µm (mode I), 6.27 µm (mode II), and 2.66 µm (mode III), and thus, spectrally far away from the biological windows. Nevertheless, due to anharmonicity, further transitions are allowed from the ground state (0, 0, 0) to higher states with $\Delta\nu_i > 1$ (overtones) and even to excited states with a simultaneous change of more than one vibrational quantum number, i.e., transitions from the (0,0,0) fundamental state to a (ν_1, ν_2, ν_3) excited state, upon absorption of a single photon. In the latter, typically called combination transitions, the excited state is a mixture of the three vibrational modes.

The previously mentioned transitions have been used to describe the absorption spectrum of water in the vapor state,[16] as it is the closest situation to free water molecules. However, compared to the vapor state, the absorption bands of liquid water are noticeably broader, the peaks are usually shifted and they may exhibit several new features. This is partially due to intermolecular vibrations (collective excitation of several molecules) giving rise to a whole new array of vibrational states of the molecule for the same vibrational quantum numbers.[17] Nevertheless, the main features of the liquid water absorption resemble somehow the ones from individual molecules and hence those observed in the vapor phase.[16] Despite the main absorption bands of liquid water have been well labeled in terms of transitions using the quantum numbers of single molecules, the general recognition that liquid water displays two states[7] produces a more complex structure of its absorption spectrum with respect to the one exhibited by water molecules in the vapor state. Thus, in a first approach, this structure could be described via the superposition of the spectra of these two states. As a matter of fact, a two-state outer-neighbor bonding model already provided a good microscopic explanation for the temperature dependence of pure liquid water's absorption in the visible-NIR (550–900 nm) spectral region.[6c]

3. Experimental Results and Discussion

3.1. Absorption of Liquid Water in the Biological Windows

First, since the scattering of water compared to its absorption is very small, we have considered that it can be neglected, and so the term absorption is herein used as a synonym for extinction in water. **Figure 2** shows the room temperature (25 °C) absorption coefficient (α) spectrum of ultrapure water (pH = 7) in the wavelength range 800–1700 nm, i.e., in the spectral range of interest for deep-tissue biomedical applications. The well-known biological windows NIR-I (750–950 nm), NIR-II (1000–1350 nm), and NIR-III (1500–1800 nm) have also been indicated in this figure. The spectrum consists of three main overlapping bands whose intensity increases at longer wavelengths. These bands, roughly centered at 1000, 1200, and 1450 nm, have been labeled as bands I, II, and III, respectively. It can be noted that band I arises in the boundary between NIR-I and NIR-II, band II falls within NIR-II, and band III demarcates the end of NIR-II and the beginning of NIR-III. It is also important to mention that previously reported bands peaking at 836 and 888 nm[5c,6c] are too weak and hence negligible compared to the main bands I, II, and III.

According to previous review works,[16] these bands can be mostly assigned to vibrational combination transitions (see Section 2). The dominant absorption band III should be assigned to the vibrational combination transitions (0, 0, 0) → (a, 0, b), a and b being integer numbers in which; $a + b = 2$. The weaker absorption bands are associated with transitions (0, 0, 0) → (a, 1, b); with $a + b = 2$ (band II), and (0, 0, 0) → (a, 0, b); with $a + b = 3$ (band I). A careful inspection of the shape

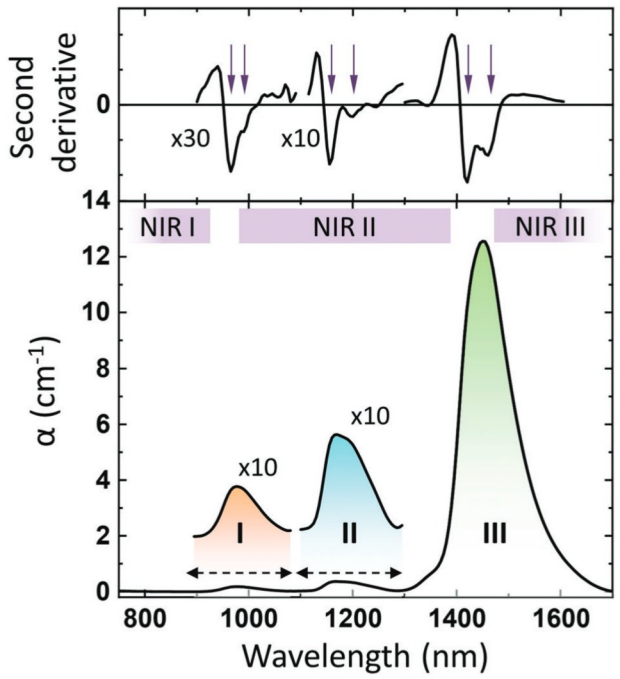

Figure 2. Bottom: Absorption coefficient (α) spectrum of liquid water at room temperature. The three main absorption bands are denoted in different colors and labeled I, II, and III, respectively. NIR-I, NIR-II, and NIR-III biological windows are also displayed. Top: Second derivative of α. The two minima of each peak are indicated by arrows.

of these bands reveals that they are not single absorption bands but consist of more than one component. This observation is supported by the shape of the second derivative of the absorption spectrum (see the top part of Figure 2). Each band is composed of at least two main components (two minima in the corresponding second derivative spectrum) peaking at 965 and 990 nm (band I), 1155 and 1195 nm (band II), and 1415 and 1460 nm (band III). Importantly, the high-energy component of each band is closer to the main peaks reported for water molecules in the vapor state (940 nm (band I), 1130 nm (band II), and 1380 nm (band III)) than the low energy components.[16]

3.2. Temperature Dependence of the Absorption Bands

The absorption spectrum of liquid water (and its second derivative) was systematically recorded as a function of temperature in the range 25–65 °C, with temperature steps of 5 °C (see Figure S1 in the Supporting Information). **Figure 3**a shows the absorption spectra taken at different temperatures for each band separately. This figure reveals that both the shape and the maximum values of the absorption coefficient (α_{max}) of each band are affected by temperature changes. In general, α_{max} of each band is slightly increased (Figure 3b) and blue-shifted (Figure 3c) as the temperature increases, in good agreement with previous results.[5c,6e,6f,6h] More precisely, α_{max} of bands I and II increase by about 11% and 22%, respectively, while α_{max} of band III only increases by about 1.5%, The blue-shifts observed in these bands are about 5 nm (53 cm^{-1}, band I), 5 nm (37 cm^{-1}, band II), and 20 nm (97 cm^{-1}, band III). An important aspect is that signatures of a bilinear behavior appear in the temperature-induced blue-shift trends (peak position vs temperature, Figure 3c) of bands I and III, showing a crossover temperature at around 45 °C. Bilinear behaviors have been previously observed in many physical properties of liquid water.[11] These behaviors have indeed been related to the coexistence of the two different states (*free* and *ice*) of water molecules in the liquid phase, whose relative concentration changes with temperature and produces a crossover temperature between 40 and 50 °C,[9,11,12] depending on the pH of the medium.[12]

To interpret the results given in Figure 3, we assumed the simple two-states approach of liquid water described in the Introduction Section, therefore, each absorption band was fitted by the convolution of two Gaussian components. Within this model, the two components of each band should correspond to the two above-mentioned states of liquid water. **Figure 4**a shows the best fit obtained for the three NIR absorption bands at room temperature (25 °C). All the absorption bands are reasonably fitted (r^2 varying between 0.982 and 0.993) by the convolution of two bands, labeled as *ice* and *free* with the *ice* bands peaking at longer wavelengths than the *free* ones. We could now establish that the dominant bands at lower temperatures should be related to the *ice* state, while the weak bands should be related to the *free* state, i.e., to the small number of free molecules coexisting with the *ice* molecules at 25 °C.

The next step was the evaluation of the evolution of the *ice* and *free* components of the three absorption bands upon heating. For this purpose, the two-band convolution was obtained at each temperature. It is important to point out that the peak positions (λ_{max}) of the *ice* and *free* components were obtained from the corresponding position of the second derivative minima at a given temperature (see Figure S1, Supporting Information) and optimized during the middle step of the fitting procedure, so they are not varying parameters as described in the Experimental Section. Thus, in the last step of the fitting process, the only free parameter is the value of α_{max} of the *ice* and *free* components that should be related to the relative concentration of molecules in the *ice* and *free* state at each temperature.

Figure 4b shows that as temperature rises, the net absorption of *free* bands increases while the one corresponding to the *ice* bands decreases. In other words, a temperature increase produces an increase in the concentration of *free* state molecules and a simultaneous decrease in the concentration of molecules in the *ice* state. As shown in the upper insets of Figure 4b, this approach reasonably explains (within a 4% of uncertainty) the experimental results given in Figure 3b. In addition, this two-Gaussian fit explains (within a 0.3% accuracy) the blue-shift experimentally observed as the temperature is raised. Therefore, by this simple approach, the blue-shift and maximum absorption value variations induced by temperature changes can be reasonably explained by the increase in the concentration of molecules in the *free* state at the cost of a decrease in the concentration of molecules in the *ice* state. Thus, the main temperature-induced shape changes in the absorption bands of liquid water can be convincingly explained because of the

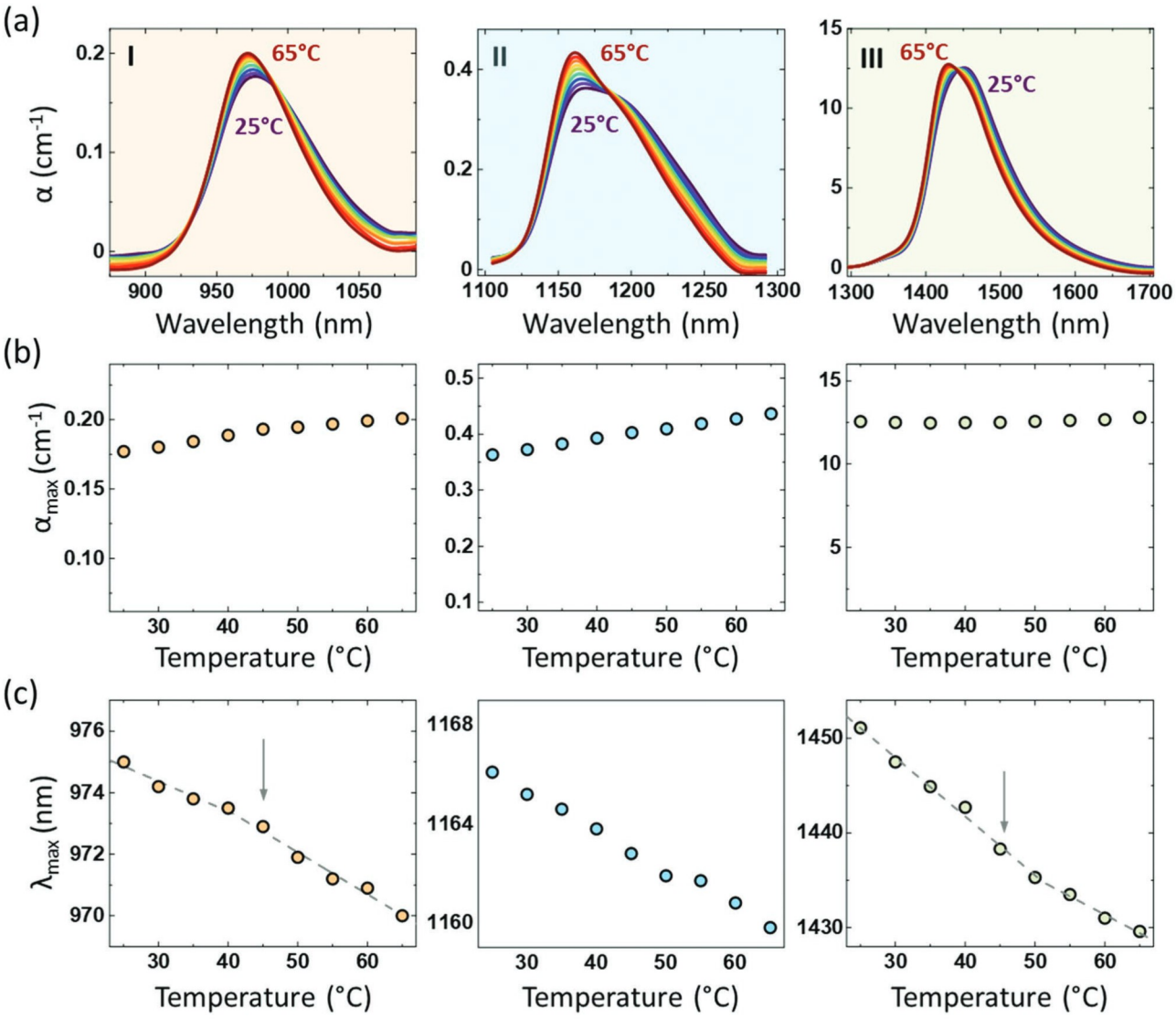

Figure 3. a) Temperature dependence of the I, II, and III absorption bands in the temperature range from 25 to 65 °C. Each band is represented after subtracting the corresponding background. b) Maximum value of the absorption coefficient (α_{max}) of each band as a function of temperature. c) Peak position (λ_{max}) of the bands as a function of temperature. The results for bands I and II have been fitted into a bilinear behavior. Arrows indicate the temperature in which the change of slope takes place.

disaggregation of small water clusters (*ice* state) into free molecules (*free* state) as the temperature increases.

3.3. Effects on Luminescent Nanothermometers

To study the temperature effect of water absorption in an aqueous dispersion of nanoparticles, we have investigated the behavior of Ag_2S nanoparticles (NPs) used as luminescent nanothermometers. Thus, Ag_2S NPs are an excellent case study to examine the effect of water absorption on the spectral shape of NIR-emitting nanoparticles. In that vein, first, the effect of water absorption at room temperature on the emission shape of the Ag_2S NPs was investigated (Section 3.3.1). Second, the study of how these temperature-dependent absorption effects can affect the thermometric properties in the physiological temperature range was performed (Section 3.3.2).

3.3.1. Effect of Water Absorption on the Ag_2S Nanoparticles Emission Spectral Shape

To investigate the effect of water absorption on the emission spectral shape of the Ag_2S nanoparticles, the emission spectrum as a function of the depth in the dispersion was measured, as schematized in **Figure 5**a (for further details of the setup, see the Supporting Information and Figure S2). Briefly, a fixed volume of the Ag_2S NPs/water dispersion (active volume) was excited while recording the room temperature emission spectrum after traveling through different depths *h* in the dispersion

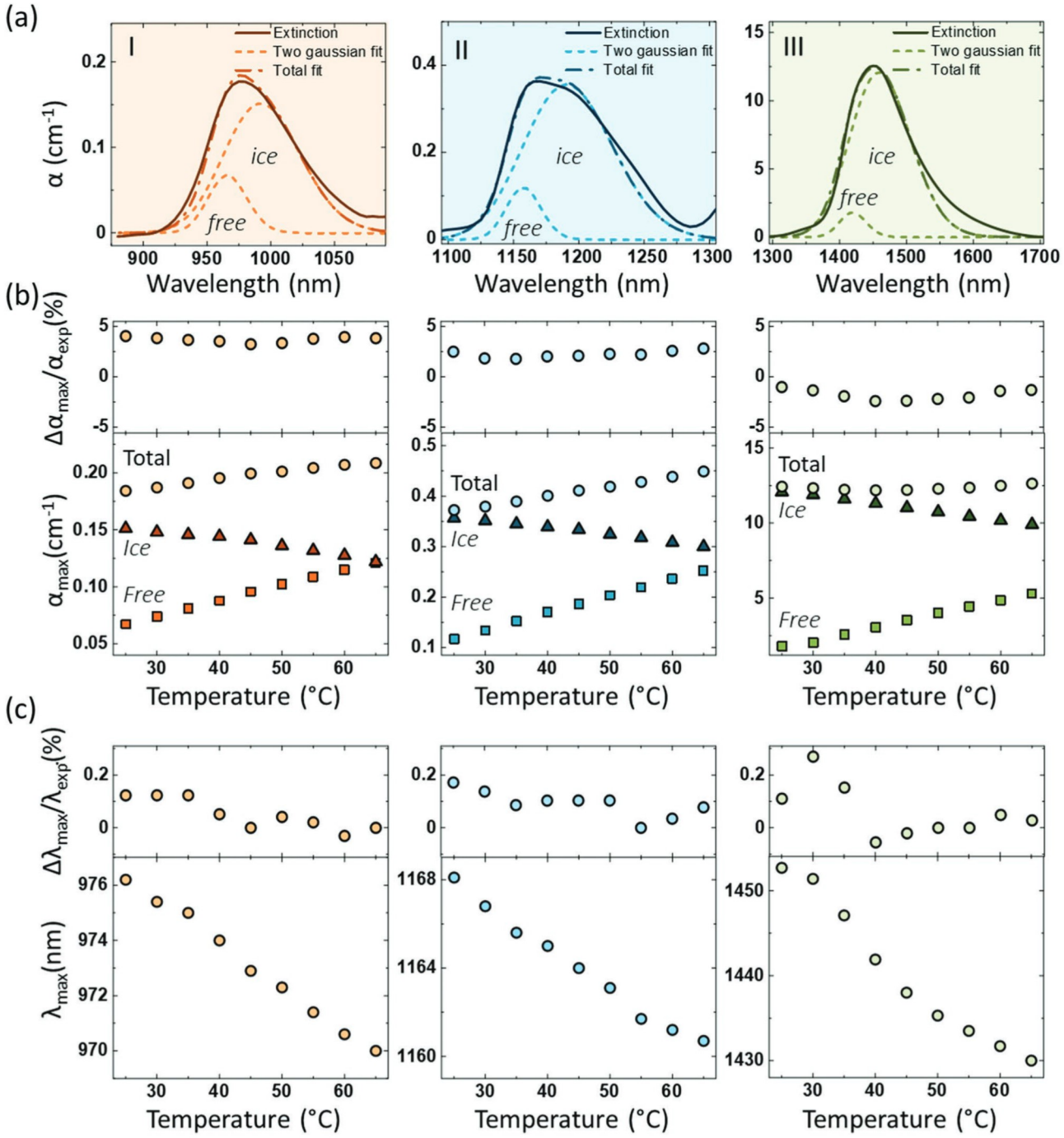

Figure 4. a) Gaussian convolution of the absorption bands at 25 °C. b) Bottom: Temperature evolution of the fitted maximum absorption coefficient (α_{max}) of the two components (*ice* and *free*) and the resulting sum (total). Top: relative error between the fitted α_{max} and the experimental one (α_{exp}). c) Bottom: Peak position (λ_{max}) versus temperature for the I, II, and III bands as obtained by the two Gaussian fits. Top: relative error between the fitted and the experimental peak position (λ_{max}).

(nonactive volume), given by the exceeding volume. The morphological and optical characterization of the Ag_2S NPs used in this work is given in Figure S3 in the Supporting Information.

Figure 5b shows that the emission spectral shape of the nanoparticles is drastically affected as h is increased. In particular, the long-wavelength side of the spectrum (1150–1350 nm) is strongly reduced when h increases and the emitted light pathway in the surrounding medium is increased. To explain this effect, we now consider how the NIR radiation emitted by the Ag_2S nanoparticles is attenuated when traveling along with the surrounding medium. This attenuation is given by the Beer–Lambert law. According to this law, the emission intensity

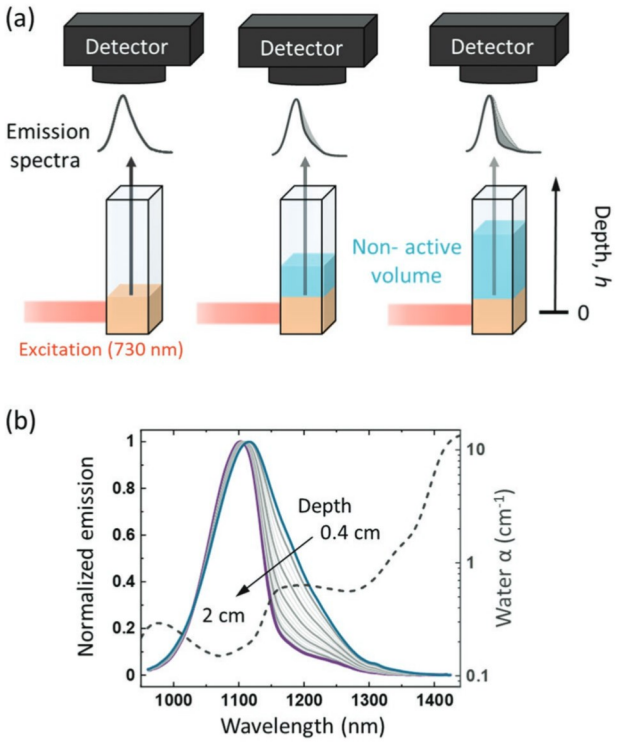

Figure 5. a) Schematic representation of the experiment performed to evaluate the effect of the depth in the dispersion on the emission of the Ag_sS NPs. b) Normalized emission spectrum of the Ag_sS NPs aqueous dispersion at 25 °C as a function of the excitation depth in the cuvette. Absorption coefficient (α) of water in the same spectral region is plotted (see dotted line) to demonstrate that the emission changes are due to water absorption.

reaching the detector, $I(\lambda,h)$, decreases exponentially with the source depth as

$$I(\lambda,h) \sim I_0(\lambda) e^{-h^* \alpha_{ext}(\lambda)} \quad (1)$$

where $I_0(\lambda)$ is the emitted intensity from the active volume, λ is the wavelength of the emitted photons, $\alpha_{ext}(\lambda)$ is the extinction coefficient, and h^* is the average distance traveled by the emitted photons—which depends on h and the number of internal reflections of the emitted photons in the cuvette wall before reaching the detector, h^* being always larger than h. Extinction of emitted light can be due to both absorption and scattering, therefore

$$\alpha(\lambda) = \alpha_{abs}(\lambda) + \alpha_{scat}(\lambda) \quad (2)$$

where $\alpha_{abs}(\lambda)$ and $\alpha_{scat}(\lambda)$ are the absorption and scattering coefficients, respectively. However, in the present study, the scattering effect can be neglected as the scattering centers (nanoparticles) are three orders of magnitude smaller than the analyzed wavelengths. Thus, $\alpha_{ext}(\lambda) \simeq \alpha_{abs}(\lambda)$, and Equation (1) can be written as

$$I(\lambda,h) \sim I_0(\lambda) e^{-h^* \alpha_{abs}(\lambda)} \quad (3)$$

In addition, the absorption of the Ag_2S NPs dispersion at the spectral range of their emission (1000–1300 nm) is very small (see Figures S3 and S7, Supporting Information) even at high concentrations (up to 1 mg mL^{-1}), so we can consider that the absorption coefficient $\alpha_{abs}(\lambda)$ is just that of water.

The absorption spectrum of liquid water (dotted line) in the emission range of the Ag_2S NPs was included in Figure 5b. It is important to point out that the band around 1200 nm (band II in Figure 2) overlaps with the long-wavelength side of the Ag_2S NPs emission spectrum, and so this part of the emission will be more absorbed than the short-wavelength side. Indeed, Figure S4 in the Supporting Information shows that the emitted light at 1200 nm (i.e., the long-wavelength emission side) decreases exponentially with h. This behavior is satisfactorily explained by Equation (3) with $\alpha_{abs}(\lambda) \approx 0.33$ cm^{-1} (the absorption coefficient of liquid water) and an average path of about $h^* = 3h$ (see Section S4 in the Supporting Information), as the emitted light travels an average path larger than the straight path of length h. In fact, this behavior is not observed when the Ag_2S nanoparticles are dispersed in heavy water (D_2O), whose absorption coefficient at this wavelength (0.02 cm^{-1}) is negligible compared to that of water (see Figure S5, Supporting Information). Consequently, the shape modifications in the emission spectrum of the Ag_2S NPs aqueous dispersion as h increases are undoubtedly due to wavelength-dependent water absorption of the photons emitted by the Ag_2S nanoparticles. This result is also supported by the fact that Ag2S NPs do not reabsorb the signal in such spectral range around 1200 nm (see Section S7 in the Supporting Information).

3.3.2. Effect of Water Absorption on Ag_2S Nanothermometric Properties

As previously discussed (Section 3.2), the absorption coefficients of water in the NIR are clearly temperature-dependent. Thus, water absorption effects are expected to have a sizable impact when Ag_2S nanoparticles dispersed in water are used as nanothermometers. Temperature sensing using these NPs is based on the temperature dependence of different emission features. Among those ones, emission intensity, peak position, and the ratio between the intensity at two wavelengths are generally used.[18] Recently, the luminescence lifetime of Ag_2S NPs has been also proposed as a reliable thermometric parameter to overcome the problems related to tissue absorption and scattering.[19] To highlight the importance of the effect of water absorption, we have carried out a comparative study of the temperature-dependent emission of Ag_2S nanoparticles dispersed in H_2O and D_2O.

Figure 6a shows the emission spectra of Ag_2S NPs dispersed in the two solvents at different temperatures. In both dispersions, the emission intensity decreases upon heating. This decrease is mostly due to thermal quenching of the Ag_2S luminescence, because, once the exciton Bohr radius of Ag_2S is 2.2 nm,[20] the luminescence properties of the obtained nanoparticles (3 nm in radius) are not dominated by quantum effects.[20] Regardless of the quenching mechanism, it is important to note that the dispersion in water heavily affects the emission shape of the NPs while it remains almost unaffected when

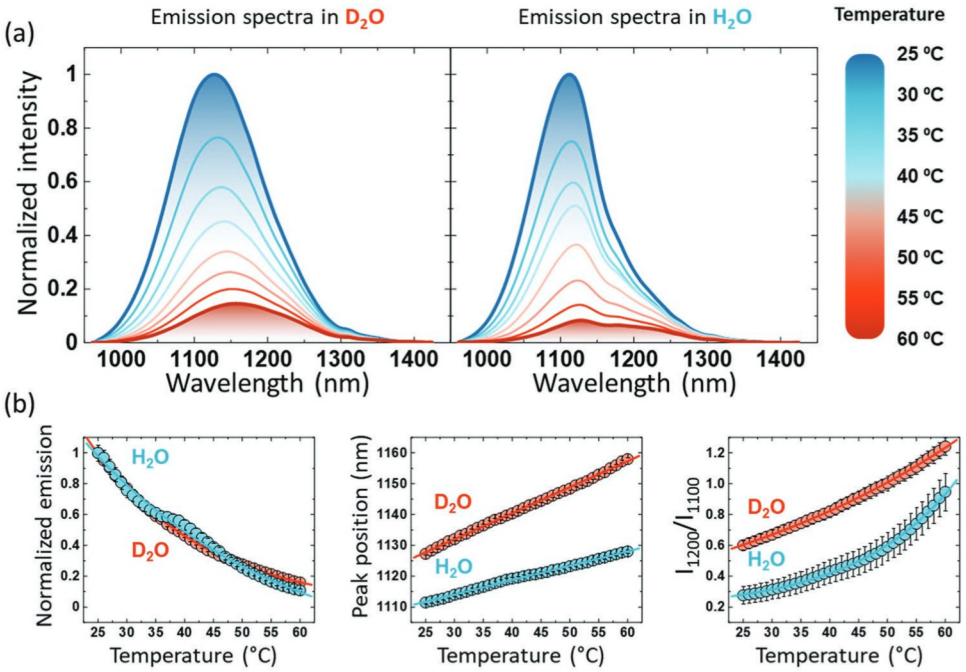

Figure 6. a) Normalized emission spectra of Ag_2S NPs dispersed in heavy water and water at different temperatures. b) Temperature dependence of the different thermometric parameters defined for the Ag_2S NPs dispersed in water (blue) and heavy water (red): normalized total emission intensity (left), peak position (center), and intensity ratio (right). The solid lines are guides for the eyes.

dispersed in heavy water. This occurs because the absorption is significantly smaller in D_2O than in H_2O in the emission range of the Ag_2S NPs (1000–1300 nm, Figure S5, Supporting Information). Additionally, the temperature increase induces a redshift in the emission of the Ag_2S NPs dispersed in heavy water and water, which is related to the temperature dependence of the energy bandgap of Ag_2S.[21]

To investigate how water affects the thermometric parameters of the Ag_2S NPs, Figure 6b reports the temperature dependence of the normalized total emitted intensity (I), peak position, and the intensity ratio between the intensities at 1200 nm (I_{1200}) and 1100 nm (I_{1100}) for the Ag_2S nanoparticles in both dispersion media. While the total intensity in heavy water presents a monotonous decrease with increasing temperature, this decrease is discontinuous for the nanoparticles in water, displaying an anomalous increase around 40–45 °C, just where a water dielectric anomaly takes place.[11a,12] The influence of reabsorption is more dramatic when considering the redshift of the emission peak as the thermometric parameter. As the temperature increases from 25 to 60 °C, the emission redshifts 132 cm^{-1} for the nanoparticles dispersed in H_2O while the redshift is 235 cm^{-1} for the D_2O dispersion. Consequently, a smaller redshift is observed for the Ag_2S nanoparticles dispersed in water because water presents high optical absorption in the same spectral region in which the luminescence of the Ag_2S NPs takes place.

The ratiometric parameter also displays a quite different temperature dependence when comparing the results obtained in D_2O and H_2O, as shown in the corresponding part of Figure 6b. While for the dispersion in heavy water this trend is almost linear, a bilinear trend is observed for the dispersion in water, with a crossover temperature around 45 °C. This is again a signature of the influence of water absorption in the thermometric properties of the aqueous dispersion of Ag_2S nanoparticles.

The impact of the absorption of water on the thermometric parameters of Ag_2S can be further assessed through the evaluation of the thermometric performance of the Ag_2S NPs dispersed in D_2O and H_2O. The performance of a luminescent thermometer is usually evaluated by its relative thermal sensitivity $\left(S_r = \frac{1}{\Delta}\left|\frac{\partial \Delta}{\partial T}\right|\right)$, which is the change in the thermometric parameter (temperature-dependent optical property, usually denoted by Δ) per degree of temperature change, and the uncertainty in temperature $\left(\delta T = \frac{1}{S_r}\frac{\delta \Delta}{\Delta}\right)$, corresponding to the smallest temperature resolvable by the thermometer.[22] The maximum relative thermal sensitivity (S_m) and minimum δT obtained for the different thermometric parameters of the Ag_2S NPs are reported in **Table 1** (see Section S6 of the Supporting Information for a detailed description of the calculation of S_r and δT).

The results in Table 1 demonstrate that the S_m of the total emission intensity (I) and the intensity ratio (I_{1200}/I_{1100}) approaches are higher in H_2O, because the reabsorption by water results in a noticeable change in the emission profile of the Ag_2S NPs, thus producing a wider shift of Δ upon heating. Nevertheless, the relative uncertainty of S_m ($\delta S_m/S_m$) is increased in water, which explains the increase of δT when moving the Ag_2S NPs from heavy water to water. This is a side effect of the reabsorption of water, which reduces the signal-to-noise ratio of the emission spectra, causing the relative

Table 1. Maximum relative thermal sensitivity (S_m), uncertainty in S_m (δS_m), minimum uncertainty in temperature (δT), uncertainty in δT ($\sigma_{\delta T}$), and temperature at which they occur (T_m) for the different thermometric parameters of the Ag_2S nanoparticles dispersed in heavy water and water.

Δ	Heavy water			Water		
	$S_m \pm \delta S_m$ [% °C^{-1}]	$\delta T \pm \sigma_{\delta T}$ [°C]	T_m [°C]	$S_m \pm \delta S_m$ [% °C^{-1}]	$\delta T \pm \sigma_{\delta T}$ [°C]	T_m [°C]
peak position	$(7.48 \pm 0.05) \times 10^{-2}$	0.53 ± 0.01	25	$(4.19 \pm 0.04) \times 10^{-2}$	0.95 ± 0.01	25
I	5.43 ± 0.21	0.44 ± 0.02	60	14.88 ± 1.51	0.42 ± 0.05	60
I_{1200}/I_{1100}	2.09 ± 0.17	2.22 ± 0.21	25	4.65 ± 1.05	3.66 ± 1.03	60

uncertainty of the thermometric parameter ($\delta\Delta/\Delta$) to increase, consequently increasing the uncertainty of the temperature readout in water. These results indicate that despite Ag_2S being the best nanothermometers used for thermal sensing in vivo applications,[23] their thermometric performance is heavily affected by the absorption arising from water, resulting in lower accuracy and reproducibility, which are major drawbacks when performing thermal readouts. Since all the emission features (peak position, redshift, and intensity ratio at two different wavelengths) are affected by the temperature dependence of water absorption, this factor must be carefully considered when using Ag_2S dispersed in water and aqueous media as nanothermometers.

4. Conclusion

In this work, we have systematically analyzed the absorption spectrum of ultrapure water with pH = 7 in the biological spectral windows (750–1800 nm) as a function of temperature in the extended physiological range 25–65 °C. The spectrum consists of three main absorption bands that increase and blue-shift as the temperature is raised. This behavior can be reasonably explained in terms of a two-state model for the water molecules in liquid water. Then we have demonstrated that temperature-induced changes in liquid water absorption have a relevant effect on the performance of Ag_2S luminescent nanothermometers, the most efficient and sensitive nanothermometers reported to date. All the spectral thermometric parameters (emission intensity, peak shift, and intensity ratio) are severely affected due to the water absorption of the Ag_2S nanoparticles emission, demonstrating the need for further standardization in order to achieve improved reproducibility and reliability for nanothermometry applications in aqueous media.

5. Experimental Section

Temperature Dependence of Water Absorption Spectra: The absorption spectra of ultrapure water obtained from a Milli-Q equipment were measured with a double-beam absorption spectrometer (Lambda1050, Perkin Elmer) with a spectral resolution of 5 nm and using a quartz cuvette with 2 mm path length. To investigate the evolution of the water absorption spectrum with temperature, a Peltier temperature controller (Q-pod 2e, Quantum Northwest) was placed inside the spectrometer enabling the selection of the desired temperature. Measurements were taken every 5 °C after 5 min of thermal stabilization in the 25–65 °C range.

Spectral Fitting of Liquid Water Absorption Bands: The NIR absorption spectra were fitted following a three-step approach using a MATLAB (version R2019b) custom code. In the first step, a background signal was defined and used to correct all the spectra. To define the background, the absorption spectrum of water at room temperature was plotted in Origin (version 2017) and the Create Baseline tool with the Second Derivative Method was used. In the second step, the three main absorption bands (see Figure 2) were adjusted to two Gaussian functions. For these fittings, the peak position of each component was set and fixed to the peak wavelengths obtained from the second derivative spectra (see Figure 2 and Figure S1, Supporting Information), while leaving the full-widths at half-maximum and peak heights (maximum value of the absorption coefficients) as free parameters. In the third step, the full-widths at half-maximum were fixed to the mean value for the different temperatures, and both the fixed width and peak position were slightly changed in each iteration until the optimal fitting (the one minimizing the r^2 values) was achieved.

Ag_2S Nanoparticles Dispersions: Silver nitrate ($AgNO_3$), sodium sulfide ($Na_2S{\cdot}9H_2O$), 11-mercaptoundecanoic acid (11-MUA), and ammonia (NH_3) were obtained from Sigma Aldrich and used as received. The Ag_2S nanoparticles were synthesized as follows: 273 mg of 11-MUA were dissolved in 38 mL of water, then 42.5 mg of $AgNO_3$ dissolved in 1.0 mL of water were added. The pH was adjusted to 8 with ammonia. The solution was stirred for 24 h, protected from light. After that time, 30 mg of $Na_2S{\cdot}9H_2O$ dissolved in 11 mL of water was added to the solution. Subsequently, the reaction was transferred to a monomodal microwave cavity and heated up to 100 °C (300 W) for 5 min under magnetic stirring, following the procedures reported elsewhere.[24] After this short microwave heating program, Ag_2S nanoparticles decorated with 11-MUA were washed with absolute ethanol.

Emission Spectra of Ag_2S Nanoparticles Dispersions in Various Media: The emission spectra of Ag_2S NPs dispersions in water and heavy water (both with a concentration of 0.2 mg mL^{-1}) were recorded using the experimental setup described in Figure S2 of the Supporting Information. To evaluate the water-induced changes in the shape of the emission band of the Ag_2S, two different experiments were performed. First, the emission spectra of Ag_2S NPs dispersed in water for different depths (Figure 5) were recorded using an infrared hyperspectral camera (PyLoN-IR, Princeton). The 730 nm excitation beam was collimated with a 5 cm focal collimator to excite the area closest to the dispersion/air interface (see inset of Figure S2, Supporting Information). Then, the dispersion volume was progressively increased from 1.0 to 2.6 mL by adding sequentially 0.1 mL of dispersion.

According to this experimental arrangement, each Ag_2S nanoparticle located inside the illuminated volume behaved as an emitting source of IR light. Due to the nonneglectable spot size, the depth was considered to be starting at the center of the beam, and so, the shortest depth that could be measured was 0.4 cm (when using a volume of 1.0 mL of the sample). For dispersions having a volume higher than 1.0 mL, a certain volume of the sample (denoted as exceeding volume) was located outside the light-emitting diode excitation area. Ag_2S nanoparticles located outside the excitation area were not photoactivated, so they did not emit any photons. Indeed, when the volume of the dispersion of Ag_2S nanoparticles was increased above 1.0 mL, the nonactive volume behaved like a filter placed between the emitting Ag_2S NPs and the detector. Thus, before reaching the detector, the incident emission coming from Ag_2S sources ($i_0(\lambda, T)$) went through the filter-like medium, where photons could be absorbed or scattered. Consequently, the higher

the sample volume, the higher the exceeding volume, and so the larger signal depth in the medium.

The second set of experiments was devoted to the analysis of how the changes in the absorption of water due to temperature differences affect the shape of the emission bands of the Ag_2S NPs. The emission spectra were measured at one fixed depth (h = 1.6 mm) and the temperature was varied in 1.0 °C steps (Figure 6). This experiment was done with the NPs dispersed in water and heavy water to compare the effects of water with those of a nonabsorbing solvent in that spectral range. The processing of the temperature-dependent emission spectra of the Ag_2S NPs dispersed in D_2O and H_2O was performed by using a custom script written in MATLAB (version R2019b) where a polynomial baseline correction was applied to remove the electrical noise from the hyperspectral camera and the obtained spectra were normalized by the maximum intensity of the emission at 25.0 °C for each medium (i.e., heavy water and water) afterward.

Nanothermometry on Ag_2S Nanoparticles: To assess the thermal sensing capability of the obtained nanoparticles in D_2O and H_2O, three distinct thermometric parameters were obtained from the temperature-dependent emission spectra of the Ag_2S NPs. The total emitted intensity was computed as the integrated emission between 960 and 1425 nm (the integrated intensities were normalized by dividing the obtained integrated areas by the integrated area at 25.0 °C for comparison purposes) and its corresponding uncertainty (error bar) was the total integrated intensity multiplied by the inverse signal-to-noise ratio. The peak position was obtained by adjusting a parabola to the emission spectra considering values between 95% and 100% of the maximum intensity from each spectrum and the uncertainty was the spectral resolution (wavelength increment) of the hyperspectral camera. The intensity ratio was the ratio between the intensities at 1200 nm (I_{1200}) and 1100 nm (I_{1100}) for the Ag_2S NPs in both media with the uncertainty corresponding to the propagation of uncertainties from the intensity ratio I_{1200}/I_{1100}.

Supporting Information

Supporting Information is available from the Wiley Online Library or from the author.

Acknowledgements

This work was financed by the Spanish Ministerio de Ciencia e Innovación under project PID2019-106211RB-I00, by the Instituto de Salud Carlos III (PI19/00565), by the Comunidad Autónoma de Madrid (S2017/BMD3867 RENIM-CM) and co-financed by the European structural and investment fund. Additional funding was provided by the European Union Horizon 2020 FETOpen project NanoTBTech (801305), the Fundación para la Investigación Biomédica del Hospital Universitario Ramón y Cajal project IMP21_A4 (2021/0427), and by COST action CA17140. A.B. acknowledges funding support through the TALENTO 2019T1/IND14014 contract (Comunidad Autónoma de Madrid). F.E.M. and L.D.C. acknowledge the financial support received from the project Shape of Water (PTDC/NAN-PRO/3881/2020) through Portuguese funds.

Conflict of Interest

The authors declare no conflict of interest.

Data Availability Statement

The data that support the findings of this study are available from the corresponding author upon reasonable request.

Keywords

nanothermometry, silver sulfide, temperature dependence, water absorption

Received: May 18, 2022
Revised: July 9, 2022
Published online: September 14, 2022

[1] J. R. Collins, *Phys. Rev.* **1925**, *26*, 771.
[2] W. C. Röntgen, *Ann. Phys.* **1892**, *281*, 91.
[3] a) C. K. N. Patel, A. C. Tam, *Nature* **1979**, *280*, 302; b) E. H. Otal, F. A. Iñón, F. J. Andrade, *Appl. Spectrosc.* **2003**, *57*, 661; c) E. D. Jansen, T. G. van Leeuwen, M. Motamedi, C. Borst, A. J. Welch, *Lasers Surg. Med.* **1994**, *14*, 258; d) V. V. Semak, A. Gerakis, M. N. Shneider, *AIP Adv.* **2019**, *9*, 085016; e) D. Theisen-Kunde, V. Danicke, M. Wendt, R. Brinkmann, in *4th European Conf. Int. Federation for Medical and Biological Engineering* (Eds: J. Vander Sloten, P. Verdonck, M. Nyssen, J. Haueisen), Springer, Berlin, Heidelberg **2009**, pp. 2228–2229; f) W. S. Pegau, J. R. V. Zaneveld, *Limnol. Oceanogr.* **1993**, *38*, 188.
[4] a) E. Hemmer, A. Benayas, F. Légaré, F. Vetrone, *Nanoscale Horiz.* **2016**, *1*, 168; b) A. M. Smith, M. C. Mancini, S. Nie, *Nat. Nanotechnol.* **2009**, *4*, 710.
[5] a) L. Sordillo, Y. Pu, S. Pratavieira, Y. Budansky, R. Alfano, *J. Biomed. Opt.* **2014**, *19*, 056004; b) J. A. Curcio, C. C. Petty, *J. Opt. Soc. Am.* **1951**, *41*, 302; c) V. Hollis, T. Binzoni, D. Delpy, *Proc. SPIE* **2001**, *4250*, 434506.
[6] a) S. H. Chung, A. E. Cerussi, S. I. Merritt, J. Ruth, B. J. Tromberg, *Phys. Med. Biol.* **2010**, *55*, 3753; b) J. B. Cumming, *Nucl. Instrum. Methods Phys. Res., Sect. A* **2013**, *713*, 1; c) V. S. Langford, A. J. McKinley, T. I. Quickenden, *J. Phys. Chem. A* **2001**, *105*, 8916; d) L. Kou, D. Labrie, P. Chylek, *Appl. Opt.* **1993**, *32*, 3531; e) N. Kakuta, A. Ozaki, F. Li, H. Arimoto, Y. Yamada, in *29th Annual Int. Conf. IEEE Engineering in Medicine and Biology Society*, IEEE, Piscataway, NJ **2007**, pp. 4564–4567; f) N. Kakuta, F. Li, Y. Yamada, in *Conf. Proc. IEEE Engineering in Medicine and Biology Society*, IEEE, Piscataway, NJ **2005**, pp. 3145–3148; g) N. Kakuta, H. Arimoto, H. Momoki, F. Li, Y. Yamada, *Appl. Opt.* **2008**, *47*, 2227; h) N. Kakuta, K. Kondo, A. Ozaki, H. Arimoto, Y. Yamada, *Int. J. Heat Mass Transfer* **2009**, *52*, 4221.
[7] a) P. Gallo, K. Amann-Winkel, C. A. Angell, M. A. Anisimov, F. Caupin, C. Chakravarty, E. Lascaris, T. Loerting, A. Z. Panagiotopoulos, J. Russo, J. A. Sellberg, H. E. Stanley, H. Tanaka, C. Vega, L. Xu, L. G. M. Pettersson, *Chem. Rev.* **2016**, *116*, 7463; b) J. R. Errington, P. G. Debenedetti, *Nature* **2001**, *409*, 318; c) A. Nilsson, L. G. M. Pettersson, *Nat. Commun.* **2015**, *6*, 8998; d) M. Falk, T. A. Ford, *Can. J. Chem.* **1966**, *44*, 1699; e) J. Russo, H. Tanaka, *Nat. Commun.* **2014**, *5*, 3556.
[8] R. Shi, H. Tanaka, *J. Am. Chem. Soc.* **2020**, *142*, 2868.
[9] C. D. S. Brites, B. Zhuang, M. L. Debasu, D. Ding, X. Qin, F. E. Maturi, W. W. Y. Lim, D. W. Soh, J. Rocha, Z. Yi, X. Liu, L. D. Carlos, *J. Phys. Chem. Lett.* **2020**, *11*, 6704.
[10] J. K. Gregory, D. C. Clary, K. Liu, M. G. Brown, R. J. Saykally, *Science* **1997**, *275*, 814.
[11] a) J. C. del Valle, E. Camarillo, L. Martinez Maestro, J. A. Gonzalo, C. Aragó, M. Marqués, D. Jaque, G. Lifante, J. G. Solé, K. Santacruz-Gómez, R. C. Carrillo-Torres, F. Jaque, *Philos. Mag.* **2015**, *95*, 683; b) L. M. Maestro, M. I. Marqués, E. Camarillo, D. Jaque, J. G. Solé, J. A. Gonzalo, F. Jaque, J. C. D. Valle, F. Mallamace, H. Stanley, *Int. J. Nanotechnol.* **2016**, *13*, 667.
[12] L. Labrador-Páez, E. Montes, M. Pedroni, P. Haro-González, M. Bettinelli, D. Jaque, J. García-Solé, F. Jaque, *J. Phys. Chem. C* **2018**, *122*, 14838.

[13] L. Labrador-Páez, D. J. Jovanović, M. I. Marqués, K. Smits, S. D. Dolić, F. Jaque, H. E. Stanley, M. D. Dramićanin, J. García-Solé, P. Haro-González, D. Jaque, *Small* **2017**, *13*, 1700968.
[14] Y. Shen, J. Lifante, N. Fernández, D. Jaque, E. Ximendes, *ACS Nano* **2020**, *14*, 4122.
[15] a) B. del Rosal, D. Ruiz, I. Chaves-Coira, B. H. Juárez, L. Monge, G. Hong, N. Fernández, D. Jaque, *Adv. Funct. Mater.* **2018**, *28*, 1806088; b) H. D. A. Santos, I. Zabala Gutiérrez, Y. Shen, J. Lifante, E. Ximendes, M. Laurenti, D. Méndez-González, S. Melle, O. G. Calderón, E. López Cabarcos, N. Fernández, I. Chaves-Coira, D. Lucena-Agell, L. Monge, M. D. Mackenzie, J. Marqués-Hueso, C. M. S. Jones, C. Jacinto, B. del Rosal, A. K. Kar, J. Rubio-Retama, D. Jaque, *Nat. Commun.* **2020**, *11*, 2933; c) D. Ruiz, B. del Rosal, M. Acebrón, C. Palencia, C. Sun, J. Cabanillas-González, M. López-Haro, A. B. Hungría, D. Jaque, B. H. Juarez, *Adv. Funct. Mater.* **2017**, *27*, 1604629; d) J. Lifante, Y. Shen, I. Zabala Gutierrez, I. Rubia-Rodríguez, D. Ortega, N. Fernandez, S. Melle, M. Granado, J. Rubio-Retama, D. Jaque, E. Ximendes, *Adv. Sci.* **2021**, *8*, 2003838.
[16] B. Wozniak, J. Dera, in *Light Absorption in Sea Water* (Eds: L. A. Mysak, K. Hamilton), Springer New York, New York, NY **2007**, p. 11.
[17] K. Ramasesha, L. De Marco, A. Mandal, A. Tokmakoff, *Nat. Chem.* **2013**, *5*, 935.
[18] a) D. Jaque, F. Vetrone, *Nanoscale* **2012**, *4*, 4301; b) D. Jaque, B. D. Rosal, E. M. Rodríguez, L. M. Maestro, P. Haro-González, J. G. Solé, *Nanomedicine* **2014**, *9*, 1047.
[19] Y. Shen, J. Lifante, I. Zabala-Gutierrez, M. de la Fuente-Fernández, M. Granado, N. Fernández, J. Rubio-Retama, D. Jaque, R. Marin, E. Ximendes, A. Benayas, *Adv. Mater.* **2022**, *34*, 2107764.
[20] Y. Zhang, Y. Liu, C. Li, X. Chen, Q. Wang, *J. Phys. Chem. C* **2014**, *118*, 4918.
[21] Y. Shen, J. Lifante, E. Ximendes, H. D. A. Santos, D. Ruiz, B. H. Juárez, I. Zabala Gutiérrez, V. Torres Vera, J. Rubio Retama, E. Martín Rodríguez, D. H. Ortgies, D. Jaque, A. Benayas, B. del Rosal, *Nanoscale* **2019**, *11*, 19251.
[22] C. D. S. Brites, S. Balabhadra, L. D. Carlos, *Adv. Opt. Mater.* **2019**, *7*, 1801239.
[23] Y. Shen, H. D. A. Santos, E. C. Ximendes, J. Lifante, A. Sanz-Portilla, L. Monge, N. Fernández, I. Chaves-Coira, C. Jacinto, C. D. S. Brites, L. D. Carlos, A. Benayas, M. C. Iglesias-de la Cruz, D. Jaque, *Adv. Funct. Mater.* **2020**, *30*, 2002730.
[24] a) J.-F. Zhu, Y.-J. Zhu, M.-G. Ma, L.-X. Yang, L. Gao, *J. Phys. Chem. C* **2007**, *111*, 3920; b) W. Yang, L. Zhang, Y. Hu, Y. Zhong, H. B. Wu, X. W. D. Lou, *Angew. Chem.* **2012**, *124*, 11669.

Particle
& Particle Systems Characterization

Supporting Information

for *Part. Part. Syst. Charact.,* DOI: 10.1002/ppsc.202200100

Temperature Dependence of Water Absorption in the Biological Windows and Its Impact on the Performance of Ag_2S Luminescent Nanothermometers

Tamara Muñoz-Ortiz, Lise Abiven, Riccardo Marin, Jie Hu, Dirk H. Ortgies, Antonio Benayas, Florence Gazeau, Victor Castaing, Bruno Viana, Corinne Chanéac, Daniel Jaque, Fernando E. Maturi, Luís D. Carlos, Emma Martín Rodríguez, and José García Solé*

Supporting Information

Temperature dependence of water absorption in the biological windows and its impact on the performance of Ag_2S luminescent nanothermometers

Tamara Muñoz-Ortiz, Lise Abiven, Riccardo Marin, Jie Hu, Dirk H. Ortgies, Antonio Benayas, Florence Gazeau, Victor Castaing, Bruno Viana, Corinne Chanéac, Daniel Jaque, Fernando E. Maturi, Luís D. Carlos, Emma Martín Rodríguez*, and José García Solé

Table of Contents

S1. Water absorption at different temperatures

Figure S1a shows the background-corrected absorption spectra of water measured at different temperatures. Bands I and II have been magnified 10 times to observe their changes with temperature. The second derivative of each band is shown in Figure S1b. For each band, there are two minima in the second derivative, and their position is temperature-independent. For this reason, we took the spectral position of those minima as a first approximation of the position of the two Gaussian functions in the fitting procedure (see Experimental Section of the manuscript).

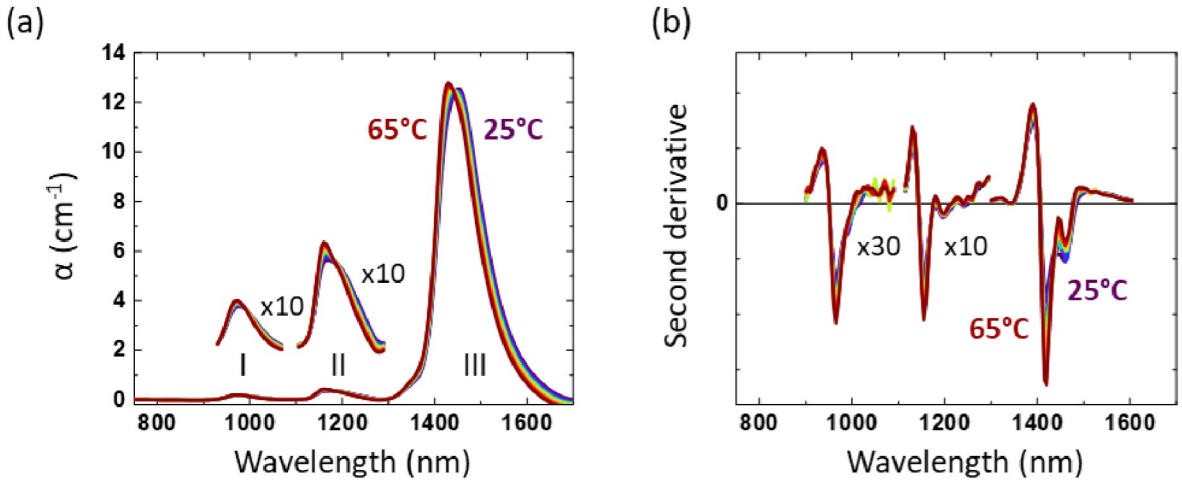

Figure S1. (a) Absorption coefficient (α) of liquid water for different temperatures in the 25-65 ºC range. The three main absorption bands are denoted in different colors and named I, II, and III, respectively. (b) Second derivative of α of water for the different temperatures.

S2. Evaluation of the Ag_2S luminescence: experimental setup

To perform the luminescence experiments varying the depth or the temperature, a quartz cuvette (10 mm path length) containing the dispersion of the Ag_2S nanoparticles was placed inside a Peltier temperature controller (Quantum Northwest, element A in **Figure S2**). All dispersions were excited with a fixed power density of 0.1 W cm^{-2} using a 730 nm LED (Thorlabs, element B in Figure S2) with a 5 cm focal collimator. The diameter of the laser spot was 0.8 cm, giving a total area of illumination of 2 cm^2 (see the inset in Figure S2). The center of the laser beam was considered the zero-depth (h = 0), so the interface between the active (illuminated) volume and the exceeding volume is located at h = 0.4 cm. The emission spectra were acquired using an optical fiber (element C) connected to an infrared hyperspectral camera (PyLoN-IR, Princeton, element D in Figure S2). To minimize thermal noise, the camera was cooled down to –100 °C using liquid nitrogen. In addition, to avoid the

detection of parasitic photons coming from the 730 nm LED and maximize the signal-to-noise ratio, the excitation of the Ag_2S nanoparticles was performed orthogonally to the direction of detection of the emitted photons. A 1000 nm longpass filter was placed in front of the optical fiber to cut off the photons arising from the excitation source.

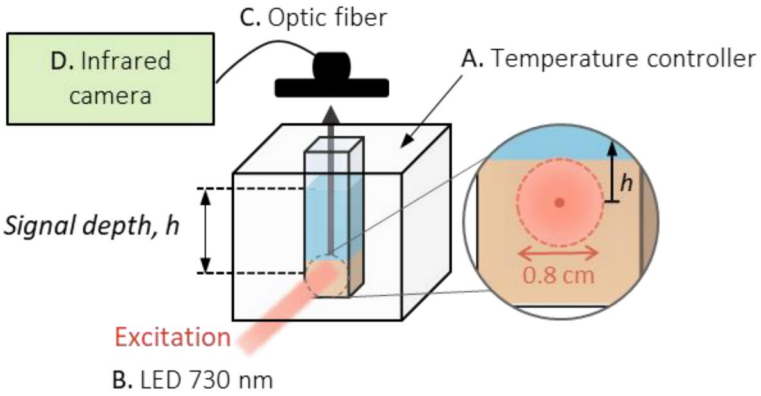

Figure S2. Scheme of the experimental arrangement used to investigate the water reabsorption of the Ag_2S nanoparticles emission**.**

S3. Characterization of the Ag_2S nanoparticles

The characterization of the obtained Ag_2S nanoparticles is presented in **Figure S3**. TEM images (Figure S3a) show that nanoparticles with spherical morphology were obtained with an average diameter of 6 ± 2 nm and rod-like nanoparticles with a lengh of 8 ± 2 nm (Figure S3b). Since the radius of the obtained nanoparticles (~3 nm) is larger than the exciton Bohr radius for Ag_2S (2.2 nm),[20] the synthesized nanoparticles are not in the confinement regime (quantum dots), and behave just as semiconductor nanoparticles displaying properties of bulk Ag_2S crystals. The FTIR spectra included in Figure S3c show that the vibrational bands corresponding to the 11-MUA are found on the surface of the Ag_2S NPs. More specifically, the CH_2 doublet at 2920 cm^{-1} and 2848 cm^{-1}, the broadband at 2549 cm^{-1} related to SH bond, the COO^- band at 1470 cm^{-1}, and the C=O vibrational mode at 1470 cm^{-1}, demonstrating the successful coating of the NPs with 11-MUA. The emission spectrum at room temperature consists of a band peaking around 1150 nm that can be excited at all wavelengths shorter than 900 nm (see Figure S3d).

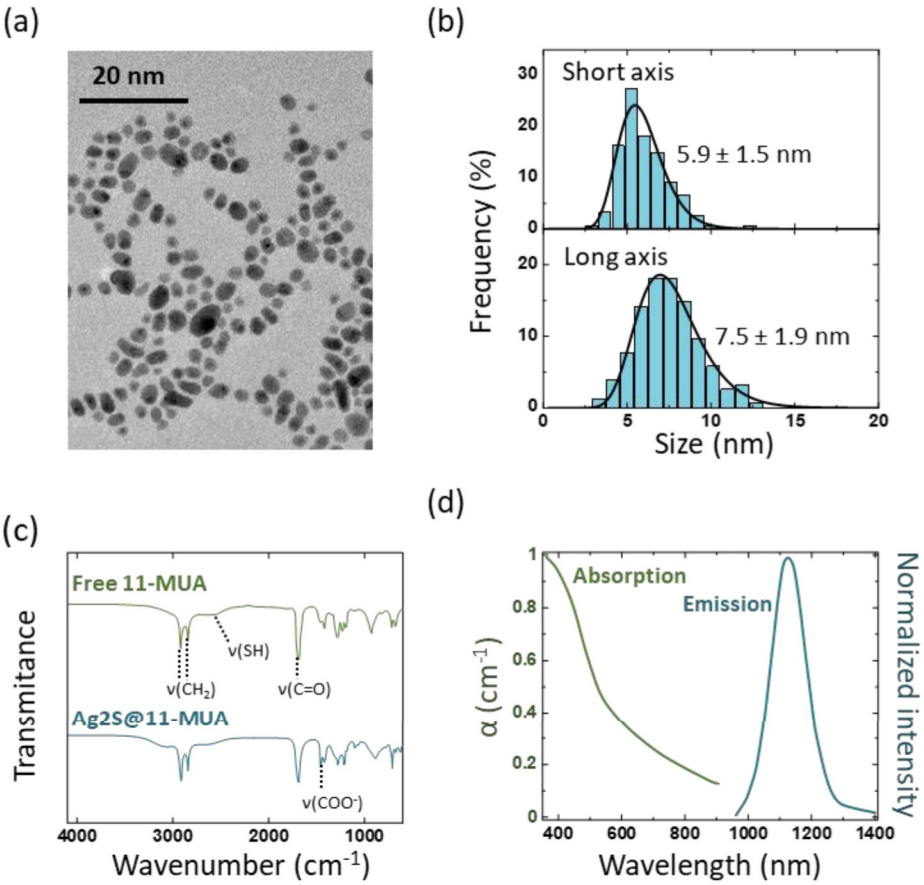

Figure S3. Characterization of Ag_2S nanoparticles. (a) TEM images of the Ag_2S nanoparticles. (b) Size distributions of the nanoparticles extracted from the TEM images. Short axis is the diameter of spherical and rod-like nanoparticles and long axis corresponds to the length of nanorods. (c) FTIR spectra of 11-mercaptoundecanoic acid (Free 11-MUA) and Ag_2S nanoparticles coated with 11-MUA (Ag_2S@11-MUA). (d) Absorption coefficient (α) and emission spectra of the Ag_2S nanoparticles.

S4. Emission intensity evolution with depth. Estimation of the effective depth

The intensity of the emission at 1200 nm (I) for a given depth in the dispersion normalized by the zero-depth intensity (I_0) was calculated, and its natural logarithm was plotted as a function of the different heights (**Figure S4**). If the path traveled by the emitted light were straightforward and no reflection or scattering processes took place, the slope of the linear fitting would match with the absorption coefficient of water at 1200 nm following the Beer-Lambert law (Equation **Error! Reference source not found.** of the manuscript). Since the obtained experimental coefficient is $\alpha_{abs}(\lambda) \approx 0.33$ cm^{-1}, and the value of the slope of the fit (in absolute value) is 0.97 cm^{-1}, it means that the light travels an effective distance h^* that is 3 times larger than h.

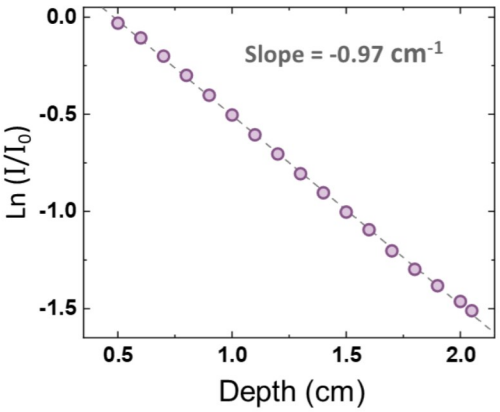

Figure S4. Evolution with the depth of $\ln(I/I_0)$ at 1200 nm. The emission intensities were measured for the nanoparticles dispersed in water. Following the Beer-Lambert law, the slope is related to the absorption coefficient of water.

S5. Room temperature absorption of water and heavy water

The absorption spectra at room temperature of pure water and heavy water were registered with a spectral resolution of 1 nm, as shown in **Figure S5**. Comparing the absorption coefficients of both solvents is reasonable to consider heavy water as a nearly non-absorber dispersant in this region.

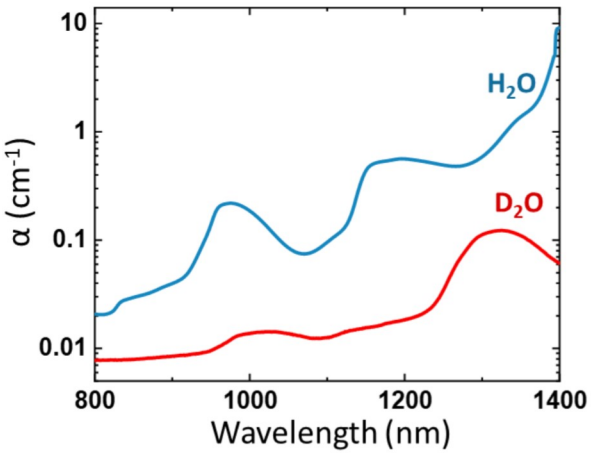

Figure S5. Room temperature absorption coefficient (α) spectra of water and heavy water in the three biological windows spectral range.

S6. Evaluation of the thermometric performance of the Ag_2S nanoparticles

The first figure of merit used to evaluate the thermometric performance of a luminescent thermometer is the relative thermal sensitivity (S_r). The value of S_r shows the percentual change of the thermometric parameter per degree of temperature (in % $^oC^{-1}$) and is given by:

$$S_r = \left|\frac{1}{\Delta}\frac{\partial \Delta}{\partial T}\right| \quad \textbf{(S1)}$$

where Δ is the thermometric parameter and $\partial\Delta/\partial T$ is the derivative of Δ with respect to temperature (T) that represents the rate of changes in Δ as T changes. Therefore, if the thermometric parameter varies linearly according to a linear function ($\Delta = aT + b$, with a and b corresponding to the slope and intercept, respectively), $\partial\Delta/\partial T$ results in the slope of the line and S_r can be described as:

$$S_r = \left|\frac{a}{\Delta}\right| \quad \textbf{(S2)}$$

In this case, the uncertainty in S_r (δS_r) can be estimated by applying the general formula of the propagation of uncertainties:

$$\delta S_r = \sqrt{\left(\frac{\partial S_r}{\partial a}\delta a\right)^2 + \left(\frac{\partial S_r}{\partial \Delta}\delta \Delta\right)^2} = \sqrt{\left(\frac{1}{\Delta}\delta a\right)^2 + \left(-\frac{a}{\Delta^2}\delta \Delta\right)^2} \quad \textbf{(S3)}$$

with δa and $\delta\Delta$ corresponding to the uncertainties in the slope and the thermometric parameter, respectively. This approach can be applied to evaluate the relative thermal sensitivity of the peak position, which increases linearly as the temperature rises. When the total emission intensity and the intensity ratio are used as thermometric parameters, Δ increases or decreases exponentially ($\Delta = A\exp(-T/B) - C$, with A, B, and C corresponding to the amplitude, decay constant, and baseline offset, respectively). For these cases, S_r is calculated as follows:

$$S_r = \left|\frac{1}{\Delta}\frac{\partial \Delta}{\partial T}\right| = \left|-\frac{A\exp(-T/B)}{\Delta B}\right| \quad \textbf{(S4)}$$

Taking into account the uncertainties arising from the amplitude (δA), decay constant (δB), and Δ ($\delta\Delta$), the estimation of δS_r through the formula of the propagation of uncertainties can be written as:

$$\delta S_r = \sqrt{\left(\frac{\partial S_r}{\partial A}\delta A\right)^2 + \left(\frac{\partial S_r}{\partial B}\delta B\right)^2 + \left(\frac{\partial S_r}{\partial \Delta}\delta \Delta\right)^2} \quad \textbf{(S5)}$$

In this sense, the estimation of δS_r for the total emission intensity and the intensity ratio approaches is given by:

$$\delta S_r = \sqrt{\left(\frac{\exp(-T/B)}{\Delta B}\delta A\right)^2 + \left(\frac{(T-B)A\exp\left(-\frac{T}{B}\right)}{\Delta B^3}\delta B\right)^2 + \left(\frac{A\exp(-T/B)}{\Delta^2 B}\delta\Delta\right)^2} \quad \textbf{(S6)}$$

The second figure of merit commonly applied to assess the thermometric performance of a luminescent thermometer is the uncertainty in temperature (δT, in ºC), which describes the smallest temperature that can be resolved by the thermometer, being calculated as:

$$\delta T = \frac{1}{S_r}\frac{\delta\Delta}{\Delta} \quad \textbf{(S7)}$$

where $\delta\Delta/\Delta$ is the relative uncertainty of the thermometric parameter. The uncertainty of S_r can be estimated from Equations S3 or S6 depending on the response of Δ and the uncertainties of Δ are obtained experimentally, as described in the Experimental Section of the manuscript. Therefore, the uncertainty in the estimation of δT ($\sigma_{\delta T}$) can also be obtained by propagating the uncertainties of δT:

$$\sigma_{\delta T} = \sqrt{\left(\frac{\partial\delta T}{\partial S_r}\delta S_r\right)^2 + \left(\frac{\partial\delta T}{\partial\Delta}\delta\Delta\right)^2} = \sqrt{\left(-\frac{1}{{S_r}^2}\frac{\delta\Delta}{\Delta}\delta S_r\right)^2 + \left(-\frac{1}{S_r}\frac{\delta\Delta}{\Delta^2}\delta\Delta\right)^2} \quad \textbf{(S8)}$$

Finally, the uncertainties in S_r and δT can be properly estimated. In this way, **Figure S6** displays the thermal evolution in these two figures of merit calculated for the Ag_2S NPs dispersed in water and heavy water and their respective uncertainties. Additionally, **Table S1** and **Table S2** present the fitting parameters resulting from the temperature-dependent thermometric parameters reported in Figure 6b of the manuscript.

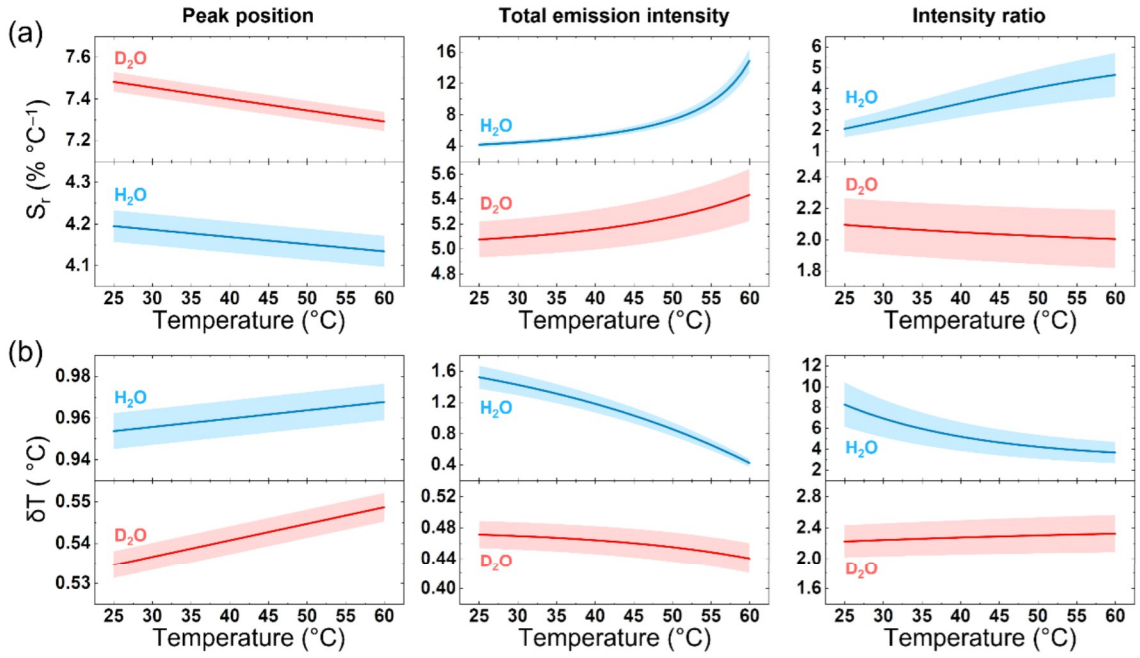

Figure S6. Thermal evolution of the (a) relative thermal sensitivity (S_r) and (b) uncertainty in temperature (δT) of the different thermometric parameters defined for the Ag_2S NPs dispersed in water (blue) and heavy water (red): peak position (left), normalized total emission intensity (center), and intensity ratio (right). The solid lines and the shadowed areas are the calculated values and their respective uncertainties, respectively.

Table S1. Fitting parameters and coefficient of determination (r^2) obtained when using the peak position as the thermometric parameter for thermal sensing with the Ag_2S NPs.

Solvent	Δ	$a \pm \delta a$ [nm °C^{-1}]	$b \pm \delta b$ [nm]	r^2
D_2O	peak position [nm]	0.844 ± 0.005	1106.7 ± 0.2	0.998
H_2O		0.466 ± 0.004	1100.1 ± 0.2	0.997

Table S2. Fitting parameters and coefficient of determination (r^2) obtained when using the normalized total emission intensity and intensity ratio (I_{1200}/I_{1100}) as thermometric parameters for thermal sensing with the Ag_2S NPs.

Solvent	Δ	$A \pm \delta A$	$B \pm \delta B$ [°C^{-1}]	$C \pm \delta C$	r^2
D_2O	Normalized total	3.51 ± 0.05	20.0 ± 0.2	– 0.014 ± 0.005	0.999
H_2O	emission intensity	2.86 ± 0.09	34.2 ± 3.3	– 0.40 ± 0.07	0.993
D_2O	I_{1200}/I_{1100}	0.41 ± 0.02	– 52.2 ± 1.5	– 0.06 ± 0.03	0.999
H_2O		(2.4 ± 0.3)×10^{-2}	– 17.4 ± 0.5	0.180 ± 0.009	0.998

S7. Evolution of the absorption spectra with concentration of Ag_2S NPs in water

Absorption of Ag_2S aqueous dispersion has been recorded for different weight concentrations (0.1 to 1 mg/mL) using a double-beam UV-Vis-NIR CARY 5000 spectrophotometer (Agilent Technologies). The strong absorption band of the nanoparticles' dispersions in the range 1150-1280 nm is attributed to water absorption only because it does not depend on Ag_2S concentration compared to the band at 900-1100 nm whose intensity increases with the concentration of NPs (**Figure S7**a). The spectra of pure water (blue line) has been

superimposed for comparison. To confirm that the absorption of Ag_2S NPs can be neglected for wavelengths longer than 1100 nm, spectra of the different nanoparticles' **dispersions** were measured using pure water as reference, so only the contribution of the NPs absorption is represented. Figure S7b) shows that absorption of Ag_2S above 1100 nm is very low, meaning that the distortion of the emission band between 1100 and 1300 nm reported on Figure 5 cannot be attributed to the reabsorption from Ag_2S NPs.

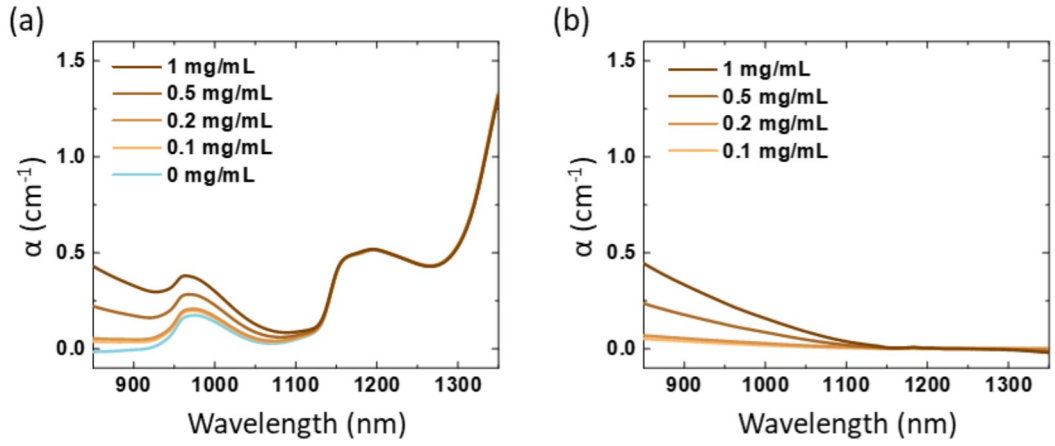

Figure S7. Room temperature absorption coefficient (α) spectra of aqueous dispersions of with different concentrations of Ag_2S NPs from 0.1 to 1 mg/mL and of pure water (a) without and (b) with water contribution correction.

Manuscript 4

Luminescent Pb-free perovskites: low-cytotoxicity materials for primary thermal sensing

L. N. Passini, F. E. Maturi, R. S. Pugina, E. G. Hilário, M. Fontes, H. S. Barud, L. D. Carlos, J. M. A. Caiut, D. Manzani.

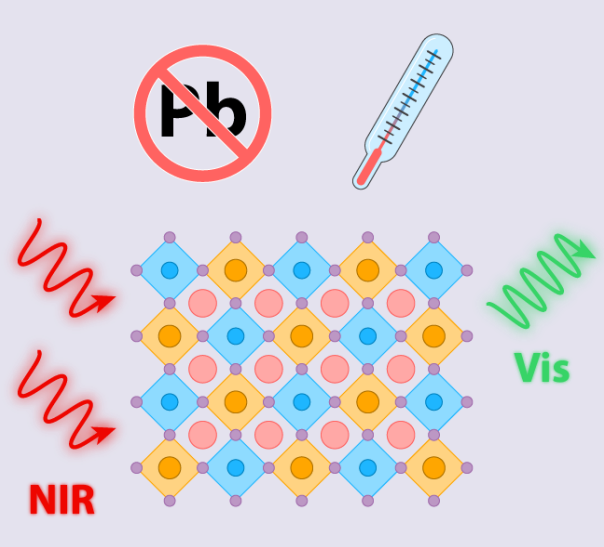

Journal of Materials Chemistry C, 11 (23), 7672-7681, 2023.

DOI: https://doi.org/10.1039/D3TC00768E

Journal of Materials Chemistry C

ROYAL SOCIETY OF CHEMISTRY

PAPER

View Article Online
View Journal | View Issue

Cite this: J. Mater. Chem. C, 2023, 11, 7672

Luminescent Pb-free perovskites: low-cytotoxicity materials for primary thermal sensing†

Luan N. Passini, [a] Fernando E. Maturi, [bc] Roberta S. Pugina, [d] Eloísa G. Hilário, [d] Marina Fontes, [e] Hernane S. Barud, [e] Luís D. Carlos, [b] José Maurício A. Caiut [d] and Danilo Manzani *[a]

Received 3rd March 2023,
Accepted 9th May 2023

DOI: 10.1039/d3tc00768e

rsc.li/materials-c

Selecting a suitable host matrix to perform temperature sensing in biomedical applications requires low cytotoxicity, facile synthesis, and an ability to be doped with light-emitting ions. With this perspective, indium-based halide double perovskites, specifically $Cs_2AgIn_{0.9}Bi_{0.1}Cl_6$, $Cs_2Ag_{0.6}Na_{0.4}InCl_6$, and $Cs_2Ag_{0.6}Na_{0.4}In_{0.9}Bi_{0.1}Cl_6$, were chosen as host materials to develop lanthanide-based primary thermometers due to their low phonon energy and ease of synthesis. The incorporation of Na^+ and Bi^{3+} into the perovskite cubic crystal lattice was confirmed by X-ray diffraction and Raman spectroscopy while the optical properties of both the undoped and Yb^{3+}/Er^{3+} co-doped perovskites were assessed by diffuse reflectance and photoluminescence spectroscopies. The obtained perovskite samples demonstrated excellent thermal stability, with the ability to withstand temperatures as high as 500 °C. A temperature-dependent green emission of Er^{3+} was observed in the co-doped samples upon 980 nm irradiation, yielding a relative thermal sensitivity and uncertainty in temperature values of 1.3% K^{-1} and 0.3 K, respectively. Incorporating the obtained perovskites (0.05 to 0.20 mg mL^{-1}) into L2929 cells as an *in vitro* model resulted in high cell viability, underscoring the benefits of selecting such a low-cytotoxicity material for applications in biological media.

1. Introduction

Lead halide perovskites (LHPs) have attracted significant attention in recent years due to their outstanding optical properties, including high absorption coefficients, low exciton binding energies, high charge-carrier mobilities, and low trap densities.[1–3] These remarkable properties are a result of the conventional ABX_3 structure of the LHPs, which enables the bandgap energy to be fine-tuned by modifying the elements in the A, B, and/or X sites. Typically, the A-site is a monovalent cation, such as Cs^+, $CH_3NH_3^+$, or $CH(NH_2)_2^+$, while the B-site corresponds to a divalent cation (Pb^{2+}), and the X-site is commonly occupied by halides, such as Cl^-, Br^-, or I^-.[1,4] However, the high solubility of lead in water limits the commercial applications of LHPs on a larger scale due to environmental and health concerns.[5–7]

Lead-free double perovskites ($A_2B'B''X_6$) have emerged as a promising alternative to LHPs because they are environmentally friendly and chemically stable while being able to absorb light across the visible spectral range.[8] In particular, indium (In)-based double halide perovskites exhibit a cubic crystal structure with a direct bandgap between the visible (Vis) and ultraviolet (UV) spectral regions, presenting higher photoluminescence quantum efficiencies in comparison with the indirect bandgap double perovskites.[9–11] However, the parity-forbidden transition is a major drawback when dealing with In-based perovskites for luminescent applications. To address this issue, the incorporation of Bi^{3+} and/or Na^+ has been used to break the parity-forbidden transition feature while preserving the direct bandgap transitions.[11–14]

Additionally, In-based perovskite materials present low phonon energy and are excellent candidates for doping with luminescent trivalent lanthanide ions (Ln^{3+}).[15,16] Ln^{3+}-doped luminescent materials are versatile, chemically stable, and show narrow emission bands (<10 nm) covering the UV, Vis, and near-infrared (NIR) spectral ranges, with high Vis emission quantum yields.[17,18] Moreover, their applications for *in vivo* thermal imaging[19] and early tumor detection[20–23] have been

[a] São Carlos Institute of Chemistry, University of São Paulo (USP), São Carlos, SP, 13560-970, Brazil. E-mail: dmanzani@usp.br
[b] Phantom-g, CICECO-Aveiro Institute of Materials, Department of Physics, University of Aveiro, Aveiro, 3810-193, Portugal
[c] Institute of Chemistry, São Paulo State University (UNESP), Araraquara, SP, 14800-060, Brazil
[d] Department of Chemistry, Faculty of Philosophy, Sciences and Letters, University of São Paulo (USP), Ribeirão Preto, SP, 14040-901, Brazil
[e] BioPolMat-Biopolymers and Biomaterials Research Group, University of Araraquara (UNIARA), Araraquara, SP, 14801-040, Brazil

† Electronic supplementary information (ESI) available. See DOI: https://doi.org/10.1039/d3tc00768e

garnering great interest in recent years due to their ability to perform excitation and emission in the biological spectral window where the absorption and scattering of light in biological tissues are reduced.[17,24] Some Ln^{3+} ions also display a strong temperature-dependent luminescence, such as Pr^{3+},[25] Nd^{3+},[26] Eu^{3+},[27] Ho^{3+},[28] Tm^{3+},[29] and Er^{3+},[30–32] making them excellent candidates for thermal sensing, covering intervals from the cryogenic (<100 K) to physiological (298–323 K) temperatures.

Er^{3+}-doped materials are interesting due to their well-established narrow emission bands and long-lived excited states.[33] The $^2H_{11/2}$ and $^4S_{3/2}$ emitting levels of Er^{3+} are particularly attractive because they are so close in energy ($\sim$750 cm^{-1}) that even small temperature variations can change the relative population between them. Although the behavior of these so-called thermally coupled levels can be described by using the Maxwell–Boltzmann statistics,[17] Balabhadra *et al.* reported an ingenious approach to predict the absolute temperature (T) using a thermometric parameter (Δ) based on the luminescence intensity ratio (LIR) between the integrated intensities of the emission bands corresponding to the $^2H_{11/2} \rightarrow {}^4I_{15/2}$ (I_H) and $^4S_{3/2} \rightarrow {}^4I_{15/2}$ (I_S) transitions of Er^{3+} ($\Delta = I_H/I_S$):[32]

$$\frac{1}{T} = \frac{1}{T_0} - \frac{k_B}{\Delta E}\ln\left(\frac{\Delta}{\Delta_0}\right) \quad (1)$$

where T_0 is the room temperature, k_B is the Boltzmann constant, Δ_0 is the value of Δ at T_0 (LIR in the absence of laser-induced heating), and ΔE is the energy gap between the $^2H_{11/2}$ and $^4S_{3/2}$ emitting levels, which is calculated from the difference between the barycenters of the $^2H_{11/2} \rightarrow {}^4I_{15/2}$ and $^4S_{3/2} \rightarrow {}^4I_{15/2}$ emission bands. This method provides a primary thermometric approach for measuring the absolute temperature that relies solely on the emission of the thermally-coupled levels of Er^{3+} regardless of the medium, whereby thermal readouts can be performed based on a well-established equation of state without needing external calibration.[34]

While several primary luminescent thermometers have been reported, such as semiconductor nanoparticles,[35] organic–inorganic hybrids,[36] Ln^{3+} luminescent complexes,[37,38] and Ln^{3+} luminescent nanoparticles,[39,40] Er^{3+}-based LIR primary thermometers are preferred because they require simple instrumentation and are not affected by the local intensity variation (*e.g.*, emitting centers concentration and/or excitation source oscillation),[18] paving the way for developing new reliable thermal sensors without the need for recording time-consuming calibration curves. Furthermore, Suta *et al.* recently suggested that Er^{3+} is the best Ln^{3+} to perform temperature sensing around the room temperature range,[41] with the added benefit of it being able to operate in the biological spectral window when co-doped with Yb^{3+}, where the excitation at 980 nm is safer for tissues in biological applications due to the lower absorption in the NIR.[42]

For this reason, we herein report the structural and optical characterization of novel low-cytotoxicity Er^{3+}/Yb^{3+} co-doped In-based perovskite materials synthesized *via* a simple wet-chemical route, which were then used to predict temperature based on the primary luminescent thermometric ability of Er^{3+} emission in the green spectral range upon Yb^{3+} excitation in the NIR. To the best of our knowledge, this is the first report demonstrating lead-free double halide perovskites working as primary thermometers.

2. Results and discussion

2.1. Structural, optical, thermal, and cytotoxic evaluations

The proposed wet-chemical route used to obtain the In-based perovskites allowed for the synthesis of pure and crystalline samples (see Experimental Section for the detailed compositions and labels), displaying sharp and well-defined diffraction peaks, as shown in Fig. 1. The X-ray diffraction (XRD) results revealed that the In-based perovskites exhibited a cubic crystal system corresponding to the *Fm3m* space group with lattice parameters of 10.48 Å for *a*, *b*, and *c*, and a cell volume of 1151.21 $Å^3$, characteristic of $CsAgInCl_6$ perovskites.[43] However, the addition of bismuth led to an increase in the lattice and cell volume as the larger Bi^{3+} radius of 1.03 Å in comparison to In^{3+} (0.80 Å) affected the assembly of the crystal structure. The diffractograms of the obtained samples presented in Fig. 1 display the characteristic peaks assigned to the (200), (220), (222), (400), (422), (440), (620), and (622) diffraction planes associated with In-based perovskites.[44] The synthesized perovskites showed good agreement with the standard powder XRD pattern taken from the Inorganic Crystal Structure Database (ICSD) number 11524 corresponding to $Cs_2AgInCl_6$, especially the sample $pIn_{0.9}$. Nevertheless, $pAg_{0.6}In$ and $pAg_{0.6}In_{0.9}$ showed more intense (200) and (222) peaks compared to the $pIn_{0.9}$ sample due to the incorporation of Na^+ in the Ag^+ site.[45]

The Yb^{3+}/Er^{3+} co-doped In-based perovskites also gave rise to a crystalline cubic phase with similar diffraction patterns (Fig. 1a–c), although some differences must be highlighted. For instance, the $pAg_{0.6}In$ sample displayed a clear distinction between the intensity of the (222) and (400) planes for each dopant concentration. This intensity change was likely due to the concentration and dopant chemical nature, such as its ionic radius. It is expected that the replacement of In^{3+} (0.80 Å) in the perovskite lattice by Yb^{3+} (0.89 Å) and Er^{3+} (0.87 Å) when doping with Ln^{3+} would lead to an expansion of the crystal lattice. Moreover, in the Ln^{3+} co-doped samples, the diffraction peaks shifted to lower 2θ angles due to the lanthanide incorporation in the lattice. However, there were no significant structural modifications observed when In-based perovskites were doped with Ln^{3+}, probably due to the similarity of the ionic radii of Ln^{3+} and In^{3+}. The morphology of the samples was evaluated by scanning electron microscopy (SEM), which revealed that the samples were obtained with an irregular octahedral shape between 10–20 μm, as shown in Fig. S1 (ESI†).

Fig. 2 presents the Raman spectra of all the synthesized In-based perovskites, revealing up to six vibrational modes below 400 cm^{-1}. The Raman bands centered at 48, 110, 139, 169, 239, and 297 cm^{-1} corresponded to the T_{2g} (L), T_{2g} (Bi^{3+}), T_{2g} (In^{3+}),

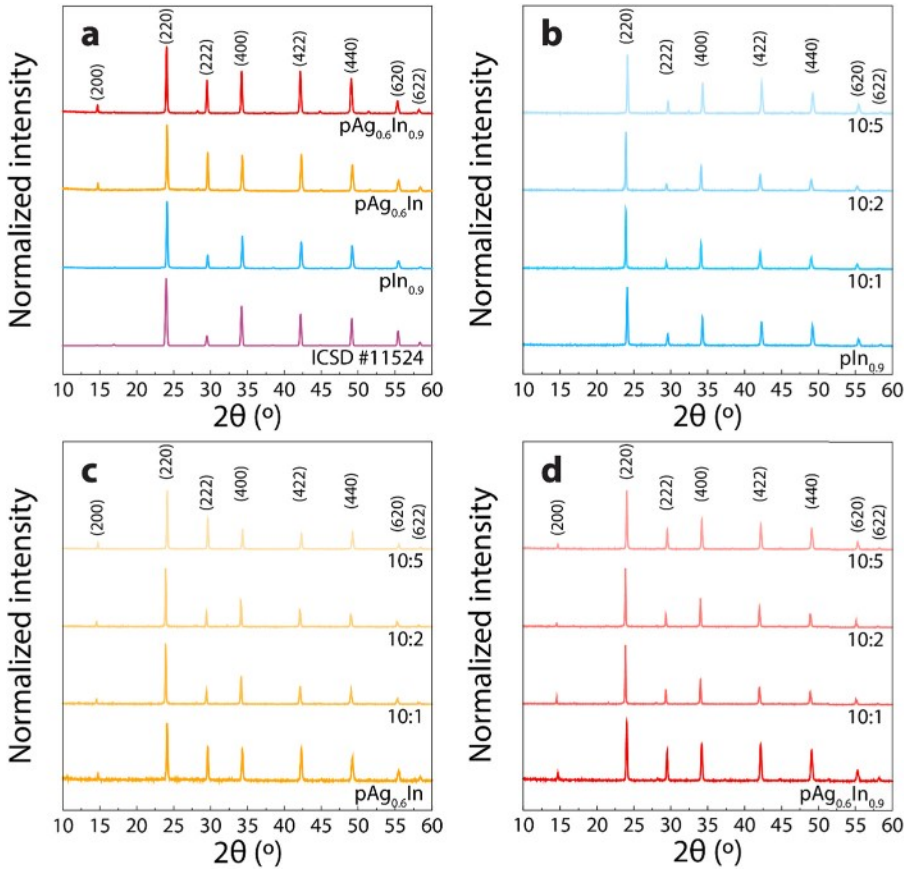

Fig. 1 (a) X-Ray diffractograms of the obtained powders for the $pIn_{0.9}$, $pAg_{0.6}In$, and $pAg_{0.6}In_{0.9}$ undoped perovskite hosts. XRD of the corresponding Yb^{3+}/Er^{3+} co-doped In-based perovskites (b) $pIn_{0.9}$, (c) $pAg_{0.6}In$, and (d) $pAg_{0.6}In_{0.9}$ with $Yb^{3+}:Er^{3+}$ ratios of 10 : 1, 10 : 2, and 10 : 5, respectively.

E_g (In^{3+}), E_g (Bi^{3+}), and A_{1g} vibrational modes in sample $pAg_{0.6}In_{0.9}$, respectively, in excellent agreement with the previously reported values.[43,46] The T_{2g}, E_g, and A_{1g} vibrational modes originated from $AgCl_6$, $InCl_6$, and $BiCl_6$ octahedrons, respectively, in which the T_{2g} (Bi^{3+}) and E_g (Bi^{3+}) vibrational modes from the Bi^{3+}-containing samples were assigned to Bi–Cl stretching. It is noteworthy that the sample $pAg_{0.6}In_{0.9}$ exhibited a greater number of Raman bands compared to the other samples due to the contribution of all the mixed elements, as observed in the XRD results. Moreover, the phonon energy of the In-based perovskites, as indicated by the band peaking around 297 cm^{-1} in all the Raman spectra, was lower than the values reported for host materials commonly used for doping with lanthanide ions (see Table 1 for the reference values). This suggests that the obtained samples are highly suitable for enhancing the optical properties of Er^{3+} and Yb^{3+} in upconverting applications. Furthermore, it is important to highlight that all the Raman spectra of the Yb^{3+}/Er^{3+} co-doped samples presented identical band shapes and positions compared to the host matrices.

Table 1 Phonon energies of different host matrices used for lanthanide-doping

Host	Phonon energy (cm^{-1})	Ref.
$pIn_{0.9}$, $pAg_{0.6}In$, and $pAg_{0.6}In_{0.9}$	297	This work
β-$NaYF_4$	350	47
Y_2O_3	380	48
YOF	400	49

Incorporating Bi^{3+} into an In-based perovskite lattice has been found to change its optical properties, as noted by Siddique *et al.*[43] This is due to the distortion of the octahedron in the perovskite crystal structure caused by Bi-alloying, leading to an increase in the In–Cl bond length and a decrease in the Bi–Cl bond length, resulting in self-trapped excitons (STEs) originating from the structural distortion caused by the Bi^{3+} incorporation. This explains the bright luminescence of Bi^{3+}-doped In-based perovskites.[43] In other words, incorporating a certain amount of Bi^{3+} can maintain the direct bandgap of $Cs_2AgInCl_6$ and break the parity-forbidden transition issue.

The energy bandgap values (E_g) for all the perovskite host matrices were obtained from UV-Vis diffuse reflectance analysis by applying the Tauc plot method.[50] Thus, by manipulating the recorded data utilizing the Kulbelka–Munk function $\alpha = (1 - R)^2/2R$, where α is the optical absorption coefficient and R is the reflectance, it was possible to obtain the values of E_g by extrapolating the linear fit (Tauc plot) to the x-axis. Fig. 3 and Table 2 display the energy graphs and bandgap values obtained for all the In-based perovskites matrices.

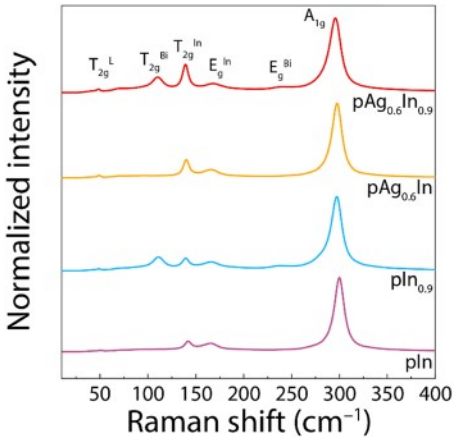

Fig. 2 Raman spectra of the different In-based perovskites.

From the reflectance spectra, two E_g values were extracted from the samples (Fig. 3), which were assigned to the material energy bandgap and to the surface/defect states, which were in excellent agreement with those presented in the literature.[51] These two values of E_g for pIn$_{0.9}$ and pAg$_{0.6}$In$_{0.9}$ perovskites might be related to the energy gap of the material (higher eV), and the surface/defect states (lower eV), as aforementioned in the discussion of the Raman results. The formation of these vacancies/defect states was associated with the addition of Bi^{3+} in the perovskite lattice, since both perovskite samples containing Bi^{3+} showed the same behavior. The incorporation of Er^{3+} and Yb^{3+} into the In-based perovskites' lattice did not significantly change the values of the energy gap. The calculated E_g for the Ln^{3+}-doped samples is presented in Table S1 (ESI†). It is worth pointing out that the incorporation of Bi^{3+} led to lower phonon energies, as seen in Fig. 2. Therefore, the lower E_g of 3.06 and 2.96 eV for pIn$_{0.9}$ and pAg$_{0.6}$In$_{0.9}$, respectively, may be attributed to the formation of STEs.[51–54]

The obtained perovskite samples presented excellent thermal stability, in addition to high crystallinity, low phonon energy, and direct bandgap properties. The thermogravimetric curves in Fig. 4a demonstrate that the samples could withstand temperatures as high as 500 °C. This remarkable thermal stability is a desirable characteristic for perovskite materials and makes them suitable for high-temperature applications.

Table 2 Calculated energy bandgaps of the undoped In-based perovskites

Sample	E_{g1} (± 0.03 eV)	E_{g2} (± 0.03 eV)
pIn$_{0.9}$	3.48	3.06
pAg$_{0.6}$In	3.69	—
pAg$_{0.6}$In$_{0.9}$	3.60	2.96

Additionally, the metabolic viability of the synthesized perovskite samples was assessed using the MTT assay 48 h after exposure to determine their cytotoxicity (Fig. 4b). Here, concentrations of 0.05, 0.10, and 0.20 mg mL^{-1} were deemed safe for all the perovskites, with cell viability exceeding 70%. According to ISO 10993-5, a reduction of cell viability greater than 30% is considered cytotoxic.[46] Thus, perovskite concentrations ranging from 0.05 to 0.20 mg mL^{-1} exhibit high potential for biomedical applications. More detailed biological tests were not performed. The obtained results are encouraging for further works using perovskite NCs aiming for more detailed findings for assessing their application in the medical field.

2.2. Photoluminescent properties of the In-based perovskites

Fig. 5 presents the excitation spectra of the undoped perovskite samples. The In-based perovskite matrices presented a high-intensity excitation band when the emission band peak around 610 nm was monitored. The pIn$_{0.9}$ and pAg$_{0.6}$In samples showed a great difference between the excitation spectra in terms of the shape and band position arising from the incorporation of Bi^{3+} and Na^{+} into the host matrix. The excitation spectrum of the pAg$_{0.6}$In$_{0.9}$ sample showed a shape and band position that resembled a mixture of the previous ones, as a result of the presence of both ions. For the excitation spectra, the most intense regions were centered at 355 nm and 394 nm for pIn$_{0.9}$, 360 nm for pAg$_{0.6}$In, and 360 nm for the pAg$_{0.6}$In$_{0.9}$ sample. Therefore, when excitation occurs at these maximum bands, the sample is excited at the intrinsic bandgap (lower wavelengths) and the surface/defect states (higher wavelengths).[52] The emission spectra shown in Fig. 5d, e and f reveal that all the samples presented a broad emission band from 450 to 800 nm. Samples pIn$_{0.9}$ and pAg$_{0.6}$In$_{0.9}$, in which In^{3+} was mixed with Bi^{3+}, showed an intense and bright

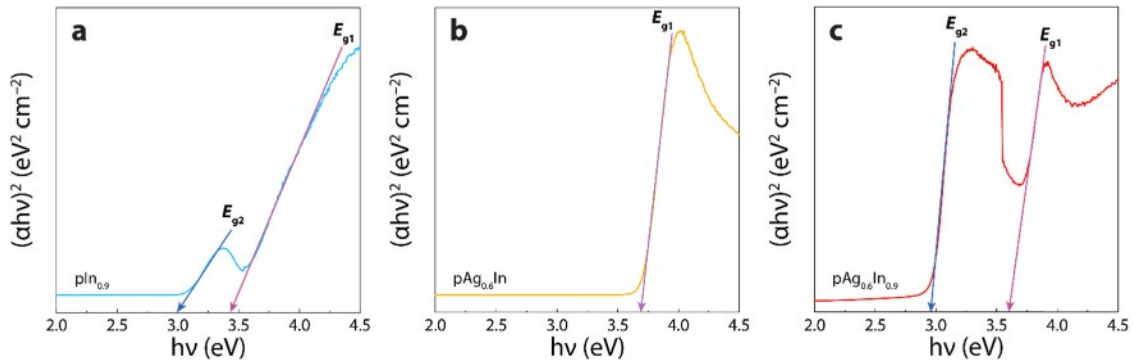

Fig. 3 Tauc plots of the energy bandgap (E_g) determination for the undoped (a) pIn$_{0.9}$, (b) pAg$_{0.6}$, and (c) pAg$_{0.6}$In$_{0.9}$ perovskite samples.

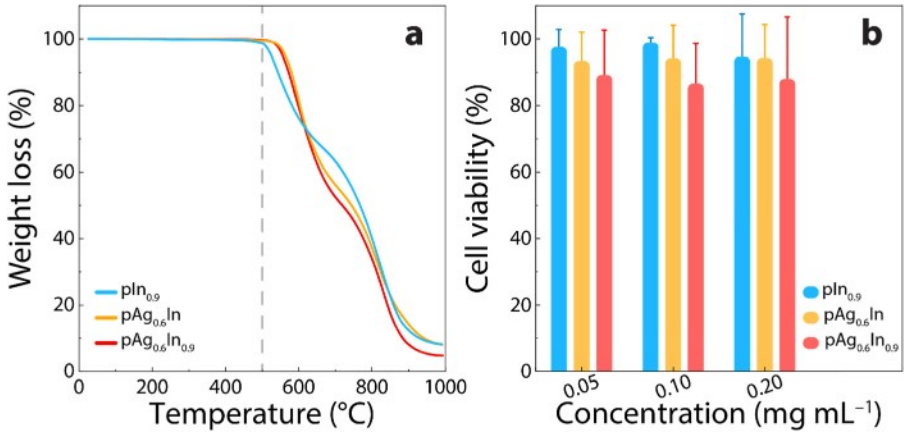

Fig. 4 (a) Thermograms of the undoped perovskite samples highlighting their thermal stability. (b) Cell viability (percentual values) as a function of the undoped perovskites' concentration assessed by the MTT assay. Each value corresponds to the mean ± standard deviation.

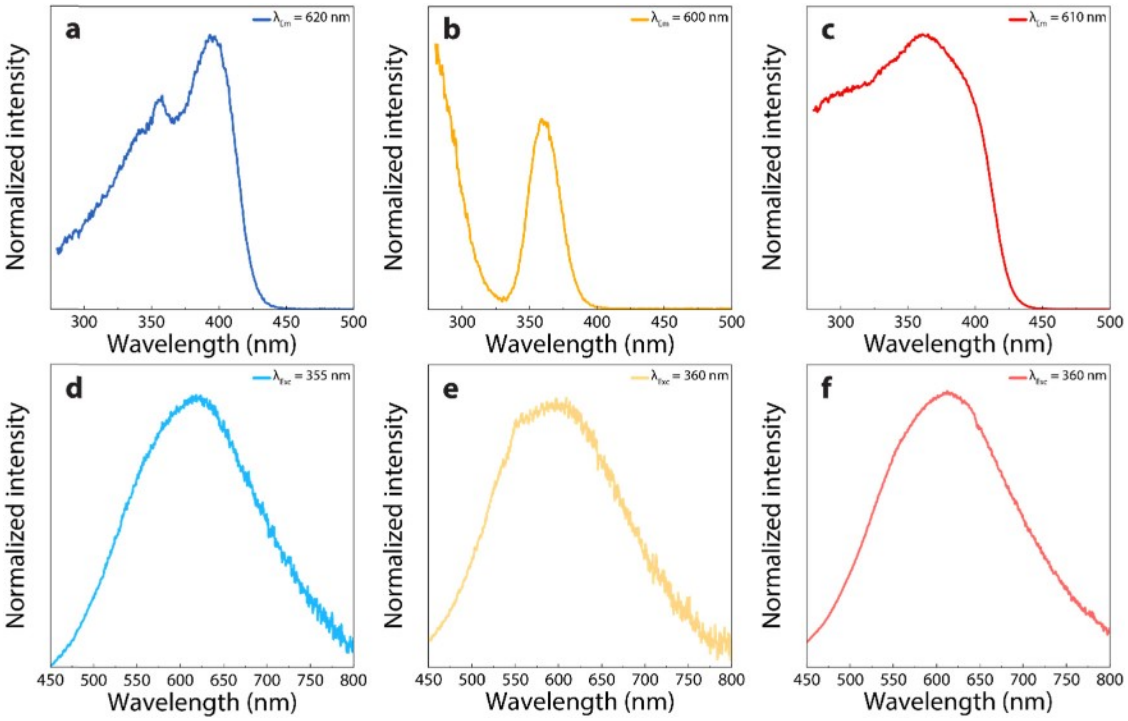

Fig. 5 Excitation spectra of the (a) $pIn_{0.9}$, (b) $pAg_{0.6}In$, and (c) $pAg_{0.6}In_{0.9}$ In-based perovskite matrices when monitoring the emission at 620, 600, and 610 nm, respectively. Emission spectra of the (d) $pIn_{0.9}$, (e) $pAg_{0.6}In$, and (f) $pAg_{0.6}In_{0.9}$ In-based perovskite matrices under excitation at 355, 360, and 360 nm, respectively.

yellowish white luminescence that could be perceived by the naked eye, as shown in Fig. S2 (ESI†).[51]

The co-doped In-based perovskite samples presented a downshifting emission band centered at 1540 nm, attributed to the characteristic $^4I_{13/2} \rightarrow {}^4I_{15/2}$ transition of Er^{3+} in the NIR,[53] which was observed under excitation of the perovskite host matrix (UV) or directly with Er^{3+} (522 nm), indicating an energy transfer from the In-based perovskite matrix to Er^{3+}, where the latter case resulted in a higher emission intensity. Despite the energy transfer from the In-based perovskite to the lanthanide ion, no emission was observed in the visible spectral range, possibly due to the strong broadband emission of the In-based perovskite (Fig. 5). The excitation and emission spectra of the Yb^{3+}/Er^{3+} co-doped samples are presented in Fig. S2 (ESI†). Moreover, the co-doped samples also displayed an upconverting emission of Er^{3+} upon 980 nm continuous-wave (CW) irradiation, as shown in Fig. 6.

The upconverting emission spectra of the $pIn_{0.9}$:Yb^{3+}/Er^{3+} (10 : 5) sample exhibited the characteristic emission bands of Er^{3+} related to the $^2H_{11/2} \rightarrow {}^4I_{15/2}$ (510–541 nm) and $^4S_{3/2} \rightarrow {}^4I_{15/2}$

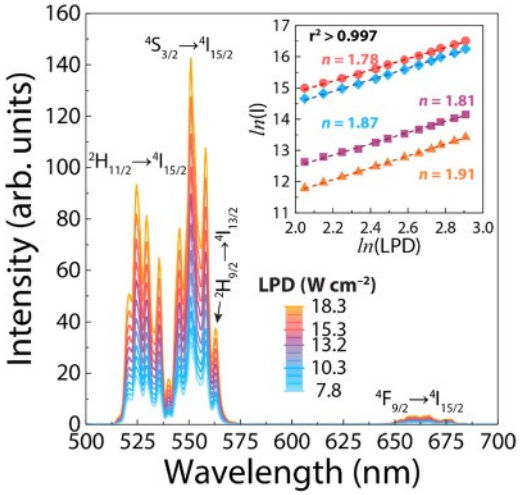

Fig. 6 Upconverting emission spectra under excitation at 980 nm of the $pIn_{0.9}$ sample co-doped with Yb^{3+}/Er^{3+} (10 : 5), when varying the laser power density (LPD) from 7.8 to 18.3 W cm^{-2}. The inset displays the double-logarithmic plot of the integrated emission against the LPD. The data in red, blue, purple, and orange correspond to the estimation of the number of photons (n) involved in the upconversion mechanism of the transitions $^4S_{3/2} \rightarrow {}^4I_{15/2}$, $^2H_{11/2} \rightarrow {}^4I_{15/2}$, $^2H_{9/2} \rightarrow {}^4I_{13/2}$, and $^4F_{9/2} \rightarrow {}^4I_{15/2}$, respectively, with $r^2 > 0.997$ for all the fits.

(541–561 nm) transitions in the green spectral region and the $^4F_{9/2} \rightarrow {}^4I_{15/2}$ (635–690 nm) transition in the red spectral region. Moreover, a shoulder around 562 nm could be observed, corresponding to the $^2H_{9/2} \rightarrow {}^4I_{13/2}$ transition originating from the upper $^2H_{9/2}$ energy level of Er^{3+} due to the low phonon energy of the perovskite host matrix.[18,55,56] The energy transfer upconversion (ETU, 10^{-3}) process is more efficient than excited-state absorption (ESA, 10^{-5}), and was likely responsible for the upconverting emission in the co-doped In-based, although the ESA process could also have contributed.[57,58] Furthermore, it is worth pointing out that the integrated intensity (I) of the emission bands assigned to the above-mentioned transitions of Er^{3+} increased upon increasing the power of the 980 nm excitation source, following the power law $I \propto \mathrm{LPD}^n$, where, n is the number of photons involved in the upconversion mechanism and can be retrieved from the slope of I *versus* LPD in a double-logarithmic plot, as shown in the inset of Fig. 6.[59] The values of n were 1.85, 1.76, 179, and 1.90 for the $^2H_{11/2} \rightarrow {}^4I_{15/2}$, $^4S_{3/2} \rightarrow {}^4I_{15/2}$, $^2H_{9/2} \rightarrow {}^4I_{13/2}$, and $^4F_{9/2} \rightarrow {}^4I_{15/2}$ transitions, respectively, indicating that two photons were involved in the upconversion emission of the perovskite samples. The upconverting emission spectra of Yb^{3+}/Er^{3+} co-doped $pIn_{0.9}$, $pAg_{0.6}In$, and $pAg_{0.6}In_{0.9}$ samples at 10 : 1, 10 : 2, and 10 : 5 ratios under varying LPD, respectively, are displayed in Fig. S3 (ESI†).

2.3. Primary thermometry on the luminescent In-based perovskites

We took advantage of the low-cytotoxicity of the obtained In-based perovskites co-doped with Yb^{3+}/Er^{3+} to assess their thermal sensing ability by applying the primary thermometric approach described by eqn (1) using the temperature-dependent emission spectra of the $pAg_{0.6}In_{0.9}:Yb^{3+}/Er^{3+}$ (10 : 2) sample, as shown in Fig. 7. The results indicated that upon increasing the temperature, I_H and I_S presented a steep and gentle increase, respectively, due to the thermal redistribution between the $^2H_{11/2}$ and $^4S_{3/2}$ emitting levels. Replacing the values of ΔE (753 ± 10 cm^{-1}), T_0 (293.5 ± 0.1 K), Δ_0 (0.4283 ± 0.0007), and the experimental values of Δ obtained from the temperature-dependent emission spectra from sample $pAg_{0.6}In_{0.9}:Yb^{3+}/Er^{3+}$ (10 : 2) in eqn (1) resulted in an excellent agreement between the measured and calculated temperatures, thus validating the primary thermal sensing ability of the obtained sample.

Once the same approach can be applied to the different In-based perovskite samples, it is possible to use the relative thermal sensitivity, $S_r = \frac{1}{\Delta}\left|\frac{\partial \Delta}{\partial T}\right| = \frac{\Delta E}{k_B T^2}$, which gives the relative change of Δ with respect to the temperature, and the uncertainty in temperature, $\delta T = \frac{\delta \Delta / \Delta}{S_r}$, which represents the smallest temperature resolvable by the thermometer.[17] This enables a comparison of the thermometric performance of the obtained samples with different Er^{3+}-based luminescent thermometers, regardless of their particle size or chemical surface functionalization, as presented in Table 3. The thermal evolution of S_r and δT for the temperature range studied in this work are displayed in Fig. S4 (ESI†).

The calculated values of the energy gap were similar for all the obtained samples, therefore, the values of S_m and δT were essentially the same. As S_r is proportional to ΔE, the S_m and δT values are in good agreement with those reported in the literature for Er^{3+}-based primary thermometers (Table 3), which usually lie in the 1.0–1.3% K^{-1} and 0.1–0.9 K ranges, respectively, indicating that the In-based perovskite samples are indeed excellent primary luminescent thermometers for performing thermal readouts regardless of their composition. In this sense, the low cytotoxicity, outstanding optical properties, and reliable thermal sensing ability pave the way for using In-based perovskites for applications in solar energy conversion and *in vitro*/*in vivo* thermometry.

3. Conclusion

In this study, we demonstrated the potential of In-based double halide perovskites as luminescent thermometers for potential use in biomedical applications. The synthesis of highly crystalline perovskites with low cytotoxicity was achieved through a facile wet-chemical route, and the incorporation of Na^+ and Bi^{3+} into the perovskites' crystal lattice was confirmed by XRD and Raman spectroscopy. The optical properties of both the undoped and Ln^{3+}-doped perovskites were characterized, whereby the incorporation of Yb^{3+}/Er^{3+} ions in the perovskites resulted in upconversion luminescence, which was used to develop primary thermometers with a high relative thermal sensitivity of 1.3% K^{-1} and uncertainty in temperature values

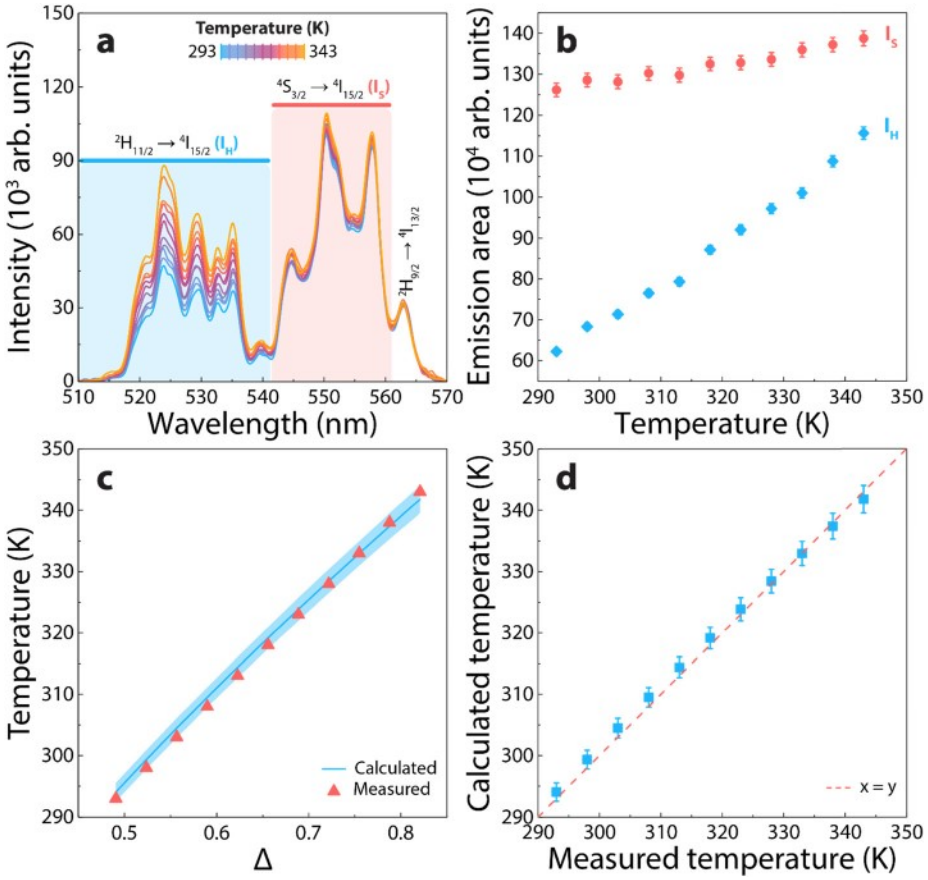

Fig. 7 (a) Temperature-dependent emission spectra of the $pAg_{0.6}In_{0.9}:Yb^{3+}/Er^{3+}$ (10 : 2) sample under laser excitation at 980 nm (LPD = 18.3 W cm^{-2}). (b) Thermal evolution of the integrated emission areas of the $^2H_{11/2} \rightarrow {}^4I_{15/2}$ (I_H) and $^4S_{3/2} \rightarrow {}^4I_{15/2}$ (I_S) transitions. (c) Temperature dependence of the experimental Δ values. The solid blue line presents the values of temperature calculated through eqn (1) and the shadowed area displays their corresponding uncertainties obtained from propagating the uncertainties of eqn (1). The triangles in red display the values of temperature measured with a K-type thermocouple. (d) Correlation between the temperature measured with the thermocouple (x-axis) and the temperature calculated with eqn (1) (y-axis). The dashed red line is a guide for the eyes corresponding to $x = y$.

as low as 0.3 K, which were in good agreement with previously reported values. Furthermore, the excellent thermal stability of the perovskites was demonstrated, with the samples remaining stable at up to 500 °C. The biocompatibility of the perovskites was also evaluated, showing high cell viability in L929 cells, indicating their potential for use in targeted bioimaging and the real-time monitoring of cancer cells. These findings pave the way for using In-based perovskites in biomedical applications, as well as in solar energy conversion.

4. Experimental section

Materials

Hydrochloric acid (HCl, Sigma-Aldrich, 37%), cesium chloride (CsCl, Vetec, P.A.), silver chloride (AgCl, Sigma-Aldrich, 99%), bismuth chloride ($BiCl_3$, Sigma-Aldrich, ≥98%), sodium chloride (NaCl, Synth, P.A. A.C.S.), indium oxide (In_2O_3, Merck, 99%), erbium oxide (Er_2O_3, Sigma-Aldrich, 99.9%), ytterbium oxide (Yb_2O_3, Lumitech, 99.99%), and isopropyl alcohol (Exodo, 99.5%) were purchased and used as received.

Synthesis of the In-based double halide perovskites

In-based double halide perovskites were prepared according to the modified synthesis procedure reported by Kumar Chini *et al.*[64] First, the undoped perovskites with compositions listed in Table 4 and labeled as $pIn_{0.9}$, $pAg_{0.6}In$, and $pAg_{0.6}In_{0.9}$ were prepared following the same procedure. For the $pIn_{0.9}$ sample, a mixture containing the stoichiometric amounts of In_2O_3, $BiCl_3$, and AgCl was added to a flask containing HCl (37%) and heated up to 348 K under vigorous stirring for 15 min. After complete dissolution, 20 mmol L^{-1} of CsCl was added to the first solution, followed by heating to 383 K for 1 h and then allowing to cool to room temperature. The undoped perovskite microcrystals were washed with isopropyl alcohol, centrifuged, and dried overnight at 383 K. The samples $pAg_{0.6}In$ and $pAg_{0.6}In_{0.9}$ were synthesized following the same procedure and using the appropriate raw materials for the desired In-based perovskite compositions as described in Table 4 Yb^{3+}/Er^{3+} co-doped In-based perovskite materials were prepared following the same procedure used for the undoped samples. Each of the three In-based perovskite hosts was obtained with a fixed concentration of Yb^{3+} in 10 mol% with varying the Er^{3+}

Table 3 Energy gap (ΔE), maximum relative thermal sensitivity (S_m), uncertainty in temperature (δT), and the temperature they occur at for different upconverting luminescent thermometers

Sample	ΔE (cm^{-1})	S_m (% K^{-1})	δT (K)	T_m (K)	Ref.
$pAg_{0.6}In_{0.9}:Yb^{3+}/Er^{3+}$ (10 : 1)	752	1.3	0.3	293	This
$pAg_{0.6}In_{0.9}:Yb^{3+}/Er^{3+}$ (10 : 2)	753				work
$pAg_{0.6}In_{0.9}:Yb^{3+}/Er^{3+}$ (10 : 5)	752				
$pAg_{0.6}In:Yb^{3+}/Er^{3+}$ (10 : 1)	752				
$pAg_{0.6}In:Yb^{3+}/Er^{3+}$ (10 : 2)	752				
$pAg_{0.6}In:Yb^{3+}/Er^{3+}$ (10 : 5)	752				
$pIn_{0.9}:Yb^{3+}/Er^{3+}$ (10 : 1)	752				
$pIn_{0.9}:Yb^{3+}/Er^{3+}$ (10 : 2)	753				
$pIn_{0.9}:Yb^{3+}/Er^{3+}$ (10 : 5)	753				
$SrF_2:Yb^{3+}/Er^{3+}$ (20 : 2)	746	1.2	0.3	298	32
$KGd_3F_{10}:Yb^{3+}/Er^{3+}$ (20 : 5)	—	1.2	0.1	298	60
$Y_3NbO_7:Yb^{3+}/Er^{3+}$ (1.5 : 0.5)	823	1.3	0.3	303	61
$Y_3TaO_7:Yb^{3+}/Er^{3+}$ (29 : 0.6)	835	1.3	0.9	303	62
$NaGdF_4:Yb^{3+}/Er^{3+}$ (20 : 2)	686	1.1	0.3	298	63

Table 4 Description of the chemical compositions of the In-based perovskite samples and corresponding labels used in this work

Chemical composition	Sample label
$Cs_2AgIn_{0.9}Bi_{0.1}Cl_6$	$pIn_{0.9}$
$Cs_2Ag_{0.6}Na_{0.4}InCl_6$	$pAg_{0.6}In$
$Cs_2Ag_{0.6}Na_{0.4}In_{0.9}Bi_{0.1}Cl_6$	$pAg_{0.6}In_{0.9}$

amount from 1, 2, and 5 mol% in relation to the content of In, for a total of 9 co-doped samples with $Yb^{3+}:Er^{3+}$ ratios of 10 : 5, 10 : 2, and 10 : 1 for each In-based perovskite matrix.

X-Ray diffractometry

The powder X-ray diffraction (XRD) analysis of the polycrystalline In-based perovskite samples was carried out in a powder X-ray diffractometer equipped with a monochromator for Cu-Kα (λ = 1.5418 Å) radiation (D8 Advance, Bruker). The measurements were performed at room temperature in the 2θ range from 10° to 60° at an angular rate of 0.5 s $step^{-1}$ and a scan step width of 0.02° using a position-sensitive detector (PSD, LynxEye, Bruker).

Raman spectroscopy

Raman scattering spectra were obtained in a Raman spectrometer coupled to a confocal microscope (LabRAM HR Evolution, Horiba) with a He–Ne laser (632.8 nm) excitation source. Data acquisition was performed by using the LabSpec 5 software (Horiba) in the spectral range of 10–400 cm^{-1} with a scan step width of 0.8 cm^{-1} using a 100× objective lens to focus on the samples.

Scanning electron microscopy

SEM micrographs were acquired in a scanning electron microscope (LEO 440, ZEISS) with a detector (7060, OXFORD) operating with an electron beam of 15 kV, 2.82 A current, and 200 pA probe I.

Diffuse reflectance spectroscopy

Diffuse reflectance spectroscopy (DRS) was performed in a UV–Vis–NIR spectrophotometer (UV 3600, Shimadzu) from 250 to 800 nm with a scan step width of 0.5 nm using barium sulfate ($BaSO_4$) as the standard.

Thermogravimetric analysis

Thermogravimetric analysis (TGA) was carried out in a simultaneous differential scanning calorimeter (SDT Q600, TA Instruments) from room temperature to 1000 °C at a heating rate of 10 °C min^{-1} under a nitrogen atmosphere.

Photoluminescence spectroscopy and temperature-dependent measurements

The excitation and emission spectra of the Yb^{3+}/Er^{3+} co-doped In-based perovskites were recorded in a Fluorolog 3 spectrofluorometer (FL3-22, Horiba) equipped with dual excitation and emission monochromators and photomultipliers for the visible (R928, Hamamatsu) and NIR (H10330-75, Hamamatsu) spectral ranges using the front face acquisition mode and a 450 W Xe arc lamp as the excitation source. Upconverting emission spectra were recorded using a 980 nm CW diode laser (DL980, CrystaLaser) as the excitation source. Temperature-dependent upconverting emission spectra of the samples were recorded in the 293–343 K temperature range using increments of 5 K. The samples were placed in a platinum crucible and heated in a temperature-controlled stage (T95-HT, LINKAM Scientific). The emission spectra were corrected by the instrument and obtained with an integration time of 150 ms and an increment of 0.5 nm for both excitation regimes.

Spectral deconvolution and energy gap determination

The emission spectra of the obtained In-based perovskites were analyzed by using a custom routine written in MATLAB 2022a under a license provided to the University of Aveiro. A polynomial baseline correction was applied to remove the electric noise from the spectrofluorometer signal, followed by the conversion of the emission spectrum from wavelength (nm) to energy (cm^{-1}) units using the Jacobian conversion.[65,66] After that, 17 Gaussian functions were adjusted to the energy-converted emission spectra between the 17544–19608 cm^{-1} spectral range. The peak energies were restricted to a ±5 cm^{-1} variation, the bounds of the widths were set between 40–180 cm^{-1}, and the lower bounds of the areas were set to zero to avoid negative values. The fits were considered well-adjusted when $r^2 > 0.99$. The barycenters of the emission bands arising in the green spectral range were computed as the averaged position of the Gaussian components corresponding to the $^2H_{11/2} \rightarrow {}^4I_{15/2}$ (eight Gaussian functions) and $^4S_{3/2} \rightarrow {}^4I_{15/2}$ (eight Gaussian functions) transitions of Er^{3+}. The energy gap (ΔE) between the $^2H_{11/2}$ and $^4S_{3/2}$ emitting levels of Er^{3+} was then calculated from the difference between the barycenter of the $^2H_{11/2} \rightarrow {}^4I_{15/2}$ and $^4S_{3/2} \rightarrow {}^4I_{15/2}$ transitions (Fig. S5a in the ESI†). The Gaussian component peaking in the lower energy side was assigned to the $^2H_{9/2} \rightarrow {}^4I_{13/2}$ transition.

Thermometric analysis

The temperature-dependent upconverting emission spectra of the samples were analyzed by using a different MATLAB 2022a code.

After performing the baseline correction, the integrated emission of the $^2H_{11/2} \rightarrow {}^4I_{15/2}$ (I_H = 510–541 nm) and $^4S_{3/2} \rightarrow {}^4I_{15/2}$ (I_S = 541–561 nm) transitions were calculated by integrating the emission spectra, where the luminescence intensity ratio ($\Delta = I_H/I_S$) was computed for each temperature. The same approach was applied to the power-dependent emission spectra to determine the value of Δ in the no laser-induced heating regime (Δ_0, *i.e.*, the intercept of the Δ *versus* LPD plot, Figure S5b, ESI†).

Cell cultures and viability assay

A murine fibroblast L929 cell line was cultivated in Dulbecco's modified eagle's medium (DMEM, Sigma-Aldrich) with 10% fetal bovine serum (FBS, Sigma-Aldrich) and 1% penicillin–streptomycin at 37 °C in a humidified 5% CO_2 incubator for 24 h and then used to evaluate the cytotoxicity of the obtained perovskites by using the MTT colorimetric assay. First, 1×10^4 of the L929 cells were seeded in a 96 well plate (100 μL per well) and cultured overnight until total adhesion to the plate. Simultaneously, 12.0 mg mL^{-1} of the undoped $pIn_{0.9}$, $pAg_{0.6}In$, and $pAg_{0.6}In_{0.9}$ were prepared at a series of different concentrations (0.05, 0.10, and 0.20 mg mL^{-1}) and then 100 μL was added into each well and incubated for 48 h. Thereafter, 100 μL of 3-[4,5-dimethylthiazol-2-yl]-2,5-diphenyltetrazolium bromide (MTT, 1.00 mg mL^{-1}) reagent was added into each well and the cells were further incubated for 4 h. Finally, the supernatant was removed and 50 μL isopropanol was added into each well. Cell viability was obtained indirectly by measuring the MTT absorbance at 570 nm using a microplate spectrophotometer (SpectraMax ABS, Molecular Devices) and the viability values were calculated based on the absorbance of the control group (cells cultured without the addition of the perovskite samples).

Conflicts of interest

There are no conflicts to declare.

Acknowledgements

The authors acknowledge the financial support provided by the Brazilian research grants from São Paulo Research Foundation – FAPESP (2018/16126-7, 2021/08111-2, and 2019/18828-1), CAPES, and CNPq-Universal (424917/2018-1 and 405048/2021-1). F. E. M. acknowledges the funding received from the European Union's Horizon 2020 research and innovation programme under the Marie Sklodowska-Curie grant agreement no. 823941 (FUNGLASS) and the financial support from the Foundation for Science and Technology (FCT) through the Portuguese research grant UI/BD/151445/2021.

References

1 L. N. Quan, B. P. Rand, R. H. Friend, S. G. Mhaisalkar, T. W. Lee and E. H. Sargent, *Chem. Rev.*, 2019, **119**, 7444–7477.
2 M. Saliba, T. Matsui, J. Y. Seo, K. Domanski, J. P. Correa-Baena, M. K. Nazeeruddin, S. M. Zakeeruddin, W. Tress, A. Abate, A. Hagfeldt and M. Grätzel, *Energy Environ. Sci.*, 2016, **9**, 1989–1997.
3 K. Dave, M. H. Fang, Z. Bao, H. T. Fu and R. S. Liu, *Chem. – Asian J.*, 2020, **15**, 242–252.
4 Q. van Le, K. Hong, H. W. Jang and S. Y. Kim, *Adv. Electron. Mater.*, 2018, **4**, 1–28.
5 A. Babayigit, A. Ethirajan, M. Muller and B. Conings, *Nat. Mater.*, 2016, **15**, 247–251.
6 A. Babayigit, D. Duy Thanh, A. Ethirajan, J. Manca, M. Muller, H.-G. Boyen and B. Conings, *Sci. Rep.*, 2016, **6**, 18721.
7 M. Hauptman, R. Bruccoleri and A. D. Woolf, *Clin. Pediatr. Emerg. Med.*, 2017, **18**, 181–192.
8 M. R. Filip, S. Hillman, A. A. Haghighirad, H. J. Snaith and F. Giustino, *J. Phys. Chem. Lett.*, 2016, **7**, 2579–2585.
9 G. Volonakis, A. A. Haghighirad, R. L. Milot, W. H. Sio, M. R. Filip, B. Wenger, M. B. Johnston, L. M. Herz, H. J. Snaith and F. Giustino, *J. Phys. Chem. Lett.*, 2017, **8**, 772–778.
10 Y. Liu, A. Nag, L. Manna and Z. Xia, *Angew. Chem., Int. Ed.*, 2020, **60**(21), 11592–11603.
11 B. Yang, X. Mao, F. Hong, W. Meng, Y. Tang, X. Xia, S. Yang, W. Deng and K. Han, *J. Am. Chem. Soc.*, 2018, **140**, 17001–17006.
12 R. Chakraborty, P. K. Rajput, G. M. Anilkumar, S. Maqbool, R. Das, A. Rahman, P. Mandal and A. Nag, *J. Am. Chem. Soc.*, 2023, **145**(2), 1378–1388.
13 Y. Pei, D. Tu, C. Li, S. Han, Z. Xie, F. Wen, L. Wang and X. Chen, *Angew. Chem., Int. Ed.*, 2022, **61**(30), e202205276.
14 A. Zhang, Y. Liu, G. Liu and Z. Xia, *Chem. Mater.*, 2022, **34**, 3006–3012.
15 B. Nath, B. Pradhan and S. K. Panda, *New J. Chem.*, 2020, **44**, 18656–18661.
16 Y. Mahor, W. J. Mir and A. Nag, *J. Phys. Chem. C*, 2019, **123**, 15787–15793.
17 C. D. S. Brites, S. Balabhadra and L. D. Carlos, *Adv. Opt. Mater.*, 2019, **7**, 1–30.
18 J. C. Martins, A. R. N. Bastos, R. A. S. Ferreira, X. Wang, G. Chen and L. D. Carlos, *Adv. Photonics Res.*, 2021, **2**, 2000169.
19 T. Miyagawa, T. Fujie, Ferdinandus, T. T. Vo Doan, H. Sato and S. Takeoka, *ACS Appl. Mater. Interfaces*, 2016, **8**, 33377–33385.
20 S. Yu, D. Tu, W. Lian, J. Xu and X. Chen, *Sci. China Mater.*, 2019, **62**, 1071–1086.
21 Y. Shen, J. Lifante, E. Ximendes, H. D. A. Santos, D. Ruiz, B. H. Juárez, I. Zabala Gutiérrez, V. Torres Vera, J. Rubio Retama, E. Martín Rodríguez, D. H. Ortgies, D. Jaque, A. Benayas and B. del Rosal, *Nanoscale*, 2019, **11**, 19251–19264.
22 X. Zhu, W. Feng, J. Chang, Y.-W. Tan, J. Li, M. Chen, Y. Sun and F. Li, *Nat. Commun.*, 2016, **7**, 10437.
23 E. Carrasco, B. del Rosal, F. Sanz-Rodríguez, Á. J. de la Fuente, P. H. Gonzalez, U. Rocha, K. U. Kumar, C. Jacinto, J. G. Solé and D. Jaque, *Adv. Funct. Mater.*, 2015, **25**, 615–626.
24 D. Jaque and F. Vetrone, *Nanoscale*, 2012, **4**, 4301.

25 C. D. S. Brites, K. Fiaczyk, J. F. C. B. Ramalho, M. Sójka, L. D. Carlos and E. Zych, *Adv. Opt. Mater.*, 2018, **6**, 1701318.
26 I. E. Kolesnikov, A. A. Kalinichev, M. A. Kurochkin, E. V. Golyeva, E. Y. Kolesnikov, A. V. Kurochkin, E. Lähderanta and M. D. Mikhailov, *Sci. Rep.*, 2017, **7**, 18002.
27 R. G. Geitenbeek, H. W. de Wijn and A. Meijerink, *Phys. Rev. Appl.*, 2018, **10**, 064006.
28 T. P. Swieten, D. Yu, T. Yu, S. J. W. Vonk, M. Suta, Q. Zhang, A. Meijerink and F. T. Rabouw, *Adv. Opt. Mater.*, 2021, **9**, 2001518.
29 N.-N. Dong, M. Pedroni, F. Piccinelli, G. Conti, A. Sbarbati, J. E. Ramírez-Hernández, L. M. Maestro, M. C. Iglesias-de la Cruz, F. Sanz-Rodriguez, A. Juarranz, F. Chen, F. Vetrone, J. A. Capobianco, J. G. Solé, M. Bettinelli, D. Jaque and A. Speghini, *ACS Nano*, 2011, **5**, 8665–8671.
30 A. D. Pickel, A. Teitelboim, E. M. Chan, N. J. Borys, P. J. Schuck and C. Dames, *Nat. Commun.*, 2018, **9**, 4907.
31 P. Rühl, D. Wang, F. Garwe, R. Müller, M. Haase, K. W. Krämer, W. Paa, R. Heintzmann, S. H. Heinemann and H. Stafast, *J. Lumin.*, 2021, **232**, 117860.
32 S. Balabhadra, M. L. Debasu, C. D. S. Brites, R. A. S. Ferreira and L. D. Carlos, *J. Phys. Chem. C*, 2017, **121**, 13962–13968.
33 M. D. Dramićanin, *Methods Appl. Fluoresc*, 2016, **4**, 042001.
34 T. J. Quinn, *Temperature*, Elsevier, 2nd edn, 1990.
35 A. M. P. Botas, C. D. S. Brites, J. Wu, U. Kortshagen, R. N. Pereira, L. D. Carlos and R. A. S. Ferreira, *Part. Part. Syst. Charact.*, 2016, **33**, 740–748.
36 J. F. C. B. Ramalho, S. F. H. Correia, L. Fu, L. L. F. António, C. D. S. Brites, P. S. André, R. A. S. Ferreira and L. D. Carlos, *Advanced Sci.*, 2019, **6**, 1900950.
37 K. M. N. de Souza, R. N. Silva, J. A. B. Silva, C. D. S. Brites, B. Francis, R. A. S. Ferreira, L. D. Carlos and R. L. Longo, *Adv. Opt. Mater.*, 2022, **10**, 2200770.
38 R. A. S. Ferreira, E. Mamontova, A. M. P. Botas, M. Shestakov, J. Vanacken, V. Moshchalkov, Y. Guari, L. F. Chibotaru, D. Luneau, P. S. André, J. Larionova, J. Long and L. D. Carlos, *Adv. Opt. Mater.*, 2021, **9**, 2101495.
39 N. M. Bhiri, M. Dammak, J. J. Carvajal, M. Aguiló, F. Díaz and M. C. Pujol, *J. Alloys Compd.*, 2022, **921**, 166020.
40 L. F. dos Santos, J. C. Martins, K. O. Lima, L. F. T. Gomes, M. T. de Melo, A. C. Tedesco, L. D. Carlos, R. A. S. Ferreira and R. R. Gonçalves, *Phys. B*, 2022, **624**, 413447.
41 M. Suta and A. Meijerink, *Adv. Theory Simul.*, 2020, **3**, 1–32.
42 E. Hemmer, A. Benayas, F. Légaré and F. Vetrone, *Nanoscale Horiz.*, 2016, **1**, 168–184.
43 H. Siddique, Z. Xu, X. Li, S. Saeed, W. Liang, X. Wang, C. Gao, R. Dai, Z. Wang and Z. Zhang, *J. Phys. Chem. Lett.*, 2020, **11**, 9572–9578.
44 M. B. Gray, J. D. Majher, T. A. Strom and P. M. Woodward, *Inorg. Chem.*, 2019, **58**, 13403–13410.
45 L. R. Morrs and W. R. Robinson, *Acta Crystallogr., Sect. B: Struct. Sci.*, 1972, **28**, 653–654.
46 L. Zhang, Y. Fang, L. Sui, J. Yan, K. Wang, K. Yuan, W. L. Mao and B. Zou, *ACS Energy Lett.*, 2019, **4**, 2975–2982.
47 J. F. Suyver, J. Grimm, M. K. van Veen, D. Biner, K. W. Krämer and H. U. Güdel, *J. Lumin.*, 2006, **117**, 1–12.
48 G. Schaack and J. A. Koningstein, *J. Opt. Soc. Am.*, 1970, **60**, 1110.
49 G. Chai, G. Dong, J. Qiu, Q. Zhang and Z. Yang, *Sci. Rep.*, 2013, **3**, 1598.
50 P. Makuła, M. Pacia and W. Macyk, *J. Phys. Chem. Lett.*, 2018, **9**, 6814–6817.
51 W. Lee, S. Hong and S. Kim, *J. Phys. Chem. C*, 2019, **123**, 2665–2672.
52 D. Manna, T. K. Das and A. Yella, *Chem. Mater.*, 2019, **31**, 10063–10070.
53 W. J. Miniscalco, *J. Light Technol.*, 1991, **9**, 234–250.
54 J. Luo, X. Wang, S. Li, J. Liu, Y. Guo, G. Niu, L. Yao, Y. Fu, L. Gao, Q. Dong, C. Zhao, M. Leng, F. Ma, W. Liang, L. Wang, S. Jin, J. Han, L. Zhang, J. Etheridge, J. Wang, Y. Yan, E. H. Sargent and J. Tang, *Nature*, 2018, **563**, 541–545.
55 K. Zhu, Z. Wang, H. Xu and Z. Fu, *Adv. Opt. Mater.*, 2022, **10**, 2201182.
56 T. P. van Swieten, T. van Omme, D. J. van den Heuvel, S. J. W. Vonk, R. G. Spruit, F. Meirer, H. H. P. Garza, B. M. Weckhuysen, A. Meijerink, F. T. Rabouw and R. G. Geitenbeek, *ACS Appl. Nano Mater.*, 2021, **4**, 4208–4215.
57 F. Auzel, *Chem. Rev.*, 2004, **104**, 139–174.
58 F. Auzel, *J. Lumin.*, 1990, **45**, 341–345.
59 M. Pollnau, D. R. Gamelin, S. R. Lüthi, H. U. Güdel and M. P. Hehlen, *Phys. Rev. B: Condens. Matter Mater. Phys.*, 2000, **61**, 3337–3346.
60 K. de Oliveira Lima, L. F. dos Santos, R. Galvão, A. C. Tedesco, L. de Souza Menezes and R. R. Gonçalves, *Front. Chem.*, 2021, **9**, 712659.
61 F. H. Borges, J. C. Martins, F. J. Caixeta, L. D. Carlos, R. A. S. Ferreira and R. R. Gonçalves, *J. Lumin.*, 2022, **248**, 118986.
62 F. H. Borges, J. C. Martins, F. J. Caixeta, R. R. Pereira, L. D. Carlos, R. A. S. Ferreira and R. R. Gonçalves, *J. Solgel Sci. Technol.*, 2021, **102**, 249–263.
63 J. C. Martins, A. Skripka, C. D. S. Brites, A. Benayas, R. A. S. Ferreira, F. Vetrone and L. D. Carlos, *Front. Photon.*, 2022, **3**, DOI: 10.1007/s10971-021-05673-0.
64 M. Kumar Chini, S. Goverapet Srinivasan, N. K. Tailor, Yukta, D. Salahub and S. Satapathi, *Chem. Phys.*, 2020, **529**, 110547.
65 J. Mooney and P. Kambhampati, *J. Phys. Chem. Lett.*, 2014, **5**, 3497.
66 J. Mooney and P. Kambhampati, *J. Phys. Chem. Lett.*, 2013, **4**, 3316–3318.

Supporting Information

Luminescent Pb-free perovskites: low-cytotoxic materials for primary thermal sensing

*Luan N. Passini[1], Fernando E. Maturi[2,3], Roberta S. Pugina[4], Eloísa G. Hilário[4], Marina Fontes[5], Hernane S. Barud[5], Luís D. Carlos[2], José Maurício A. Caiut[4], and Danilo Manzani[1]**

L. N. P., Prof. D. M.
[1]São Carlos Institute of Chemistry, University of São Paulo (USP), São Carlos, SP, 13560-970, Brazil
*E-mail: dmanzani@usp.br

F. E. M., Prof. L. D. C.
[2]Phantom-g, CICECO – Aveiro Institute of Materials, Department of Physics, University of Aveiro, Aveiro, 3810-193, Portugal

F. E. M.
[3]Institute of Chemistry, São Paulo State University (UNESP), Araraquara, SP, 14800-060, Brazil

Dr. R. S. P., E. G. H., Prof. J. M. A. C.
[4]Department of Chemistry, Faculty of Philosophy, Sciences and Letters, University of São Paulo (USP), Ribeirão Preto, SP, 14040-901, Brazil

M. F., Prof. H. S. B.
[5]BioPolMat – Biopolymers and Biomaterials Research Group, University of Araraquara (UNIARA), Araraquara, SP, 14801-040, Brazil

Keywords: perovskites, lead-free perovskites, upconversion luminescence, thermometry, cytotoxicity

Table of Contents

S1. Scanning electron microscopy

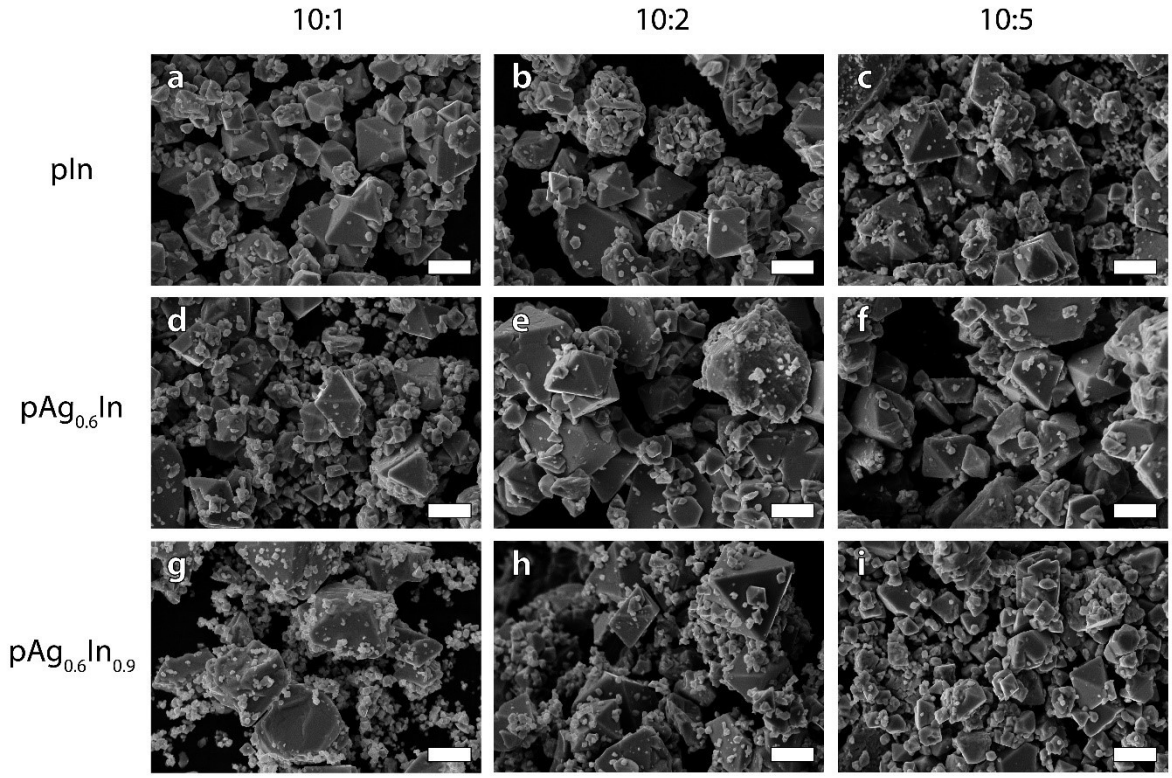

Figure S1. SEM micrographs of the $pIn_{0.9}$ (a, b, and c), $pAg_{0.6}In$ (d, e, and f), and $pAg_{0.6}In_{0.9}$ (g, h, and i) perovskites co-doped with Yb^{3+}/Er^{3+} at 10:1, 10:2, and 10:5 doping ratios. The scale bar is 10 μm for all the panels.

S2. Optical properties of the co-doped In-based perovskites

Table S1. Calculated energy band gap of Ln^{3+}-doped samples.

Yb^{3+}/Er^{3+} ratio	$pIn_{0.9}$		$pAg_{0.6}In$	$pAg_{0.6}In_{0.9}$	
	E_{g1} [± 0.03 eV]	E_{g2} [± 0.03 eV]	E_{g1} [± 0.03 eV]	E_{g1} [± 0.03 eV]	E_{g2} [± 0.03 eV]
10:1	3.36	2.96	3.65	3.44	2.80
10:2	3.40	2.99	3.65	3.38	2.95
10:5	3.42	3.00	3.65	3.30	2.96

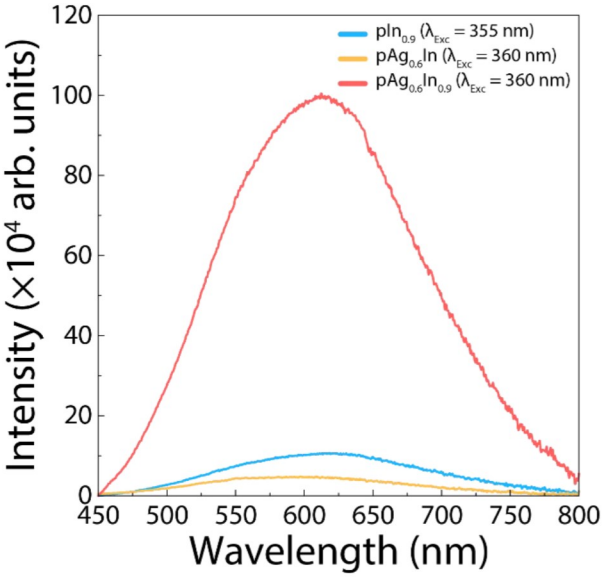

Figure S2. Comparison of the emission spectra of the $pIn_{0.9}$ (blue), $pAg_{0.6}In$ (yellow), and $pAg_{0.6}In_{0.9}$ (red) samples under excitation at 355, 360, and 360 nm, respectively.

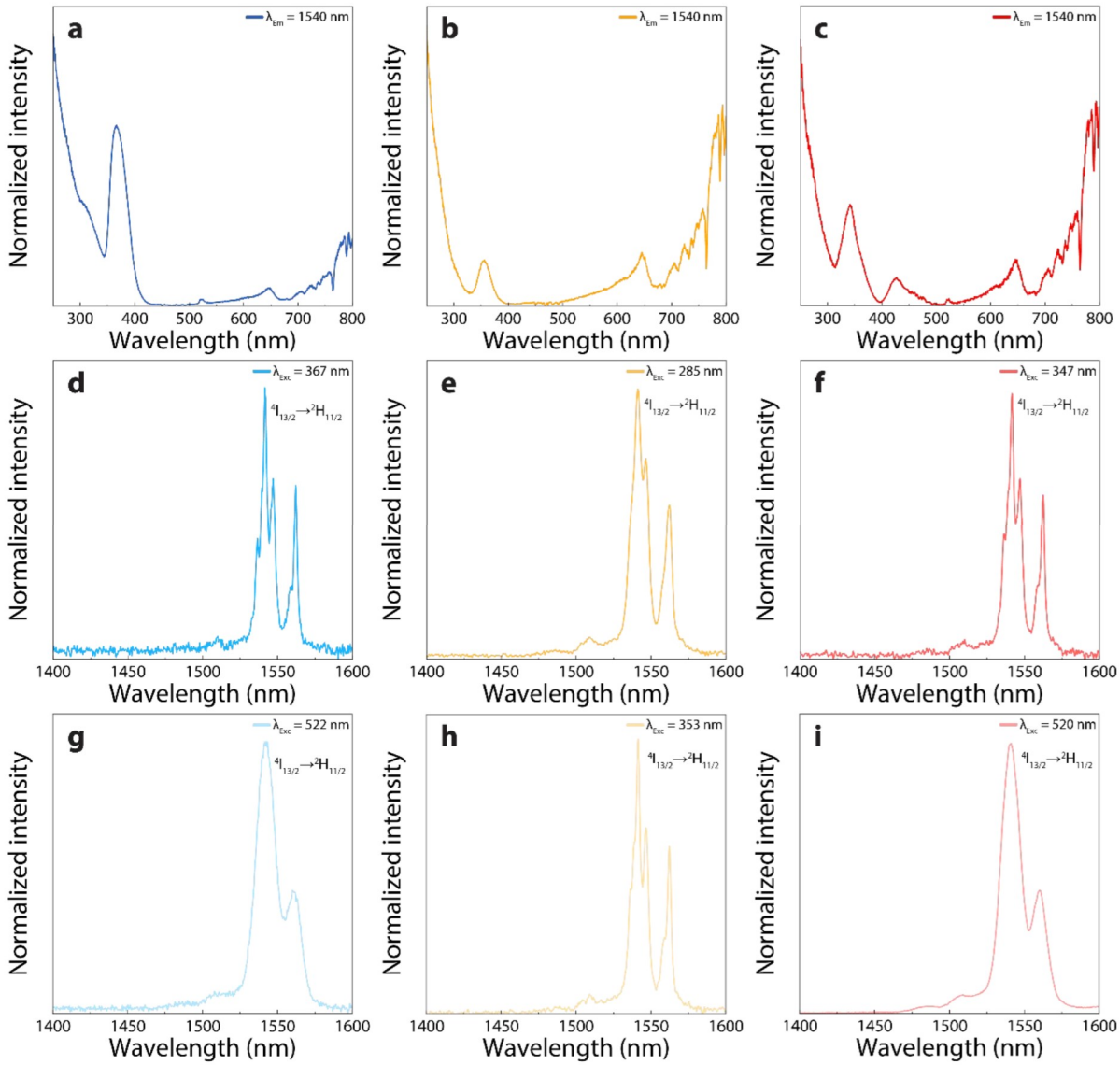

Figure S3. Excitation spectra of the (a) $pIn_{0.9}$, (b) $pAg_{0.6}In$, (c) and $pAg_{0.6}In_{0.9}$ samples doped with Yb^{3+}/Er^{3+} (10:5) monitoring the emission at 1540 nm. Emission spectra of the (d) $pIn_{0.9}$, (e) $pAg_{0.6}In$, (f) and $pAg_{0.6}In_{0.9}$ samples doped with Yb^{3+}/Er^{3+} (10:5) under excitation at 367, 285, and 347 nm, respectively. Emission spectra of the (d) $pIn_{0.9}$, (e) $pAg_{0.6}In$, (f) and $pAg_{0.6}In_{0.9}$ samples doped with Yb^{3+}/Er^{3+} (10:5) under excitation at 522, 353, and 520 nm, respectively.

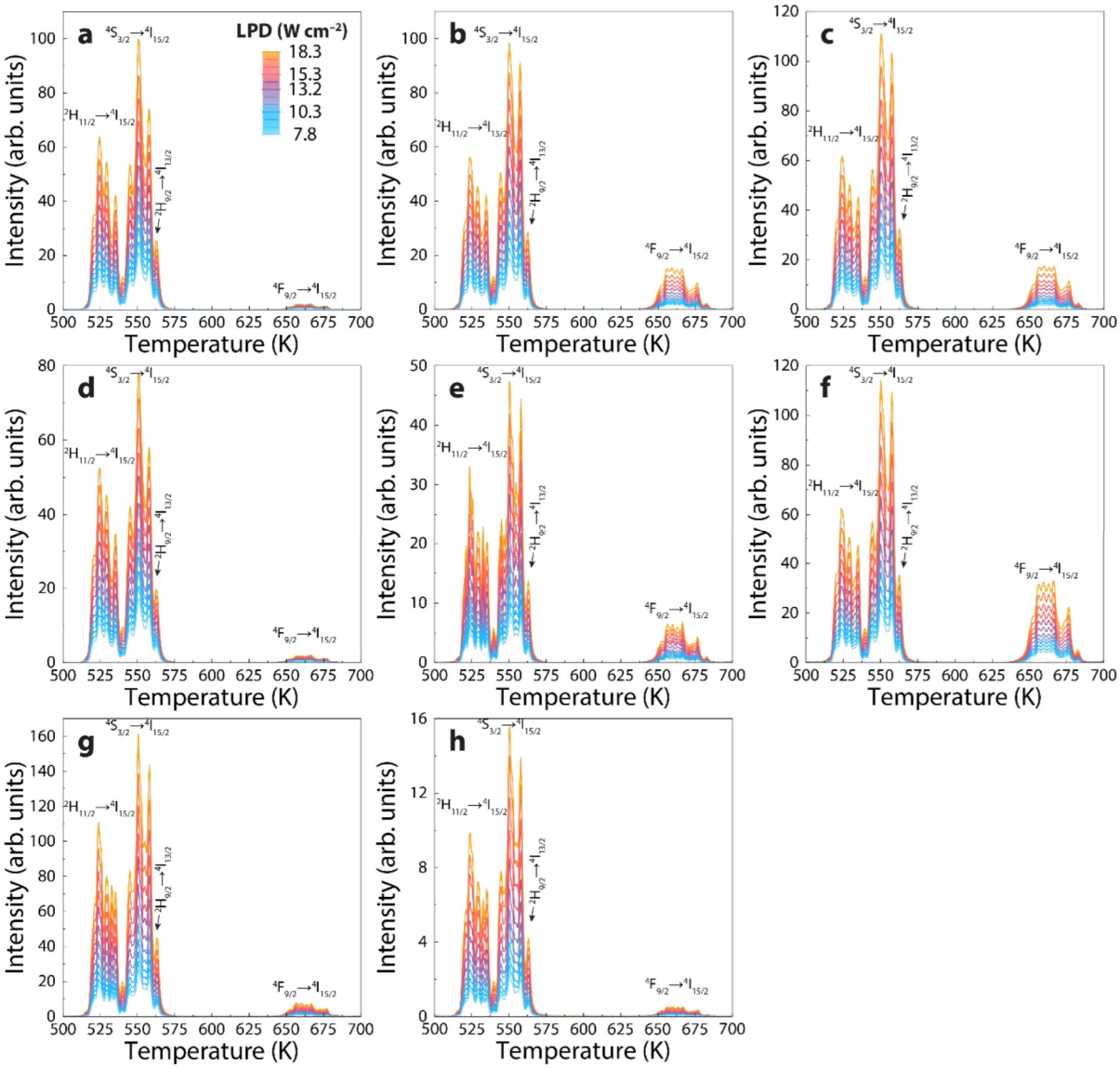

Figure S4. Upconverting emission spectra of In-based perovskite of (a) $pIn_{0.9}$, (b) $pAg_{0.6}In$, and (c) $pAg_{0.6}In_{0.9}$ samples co-doped with Yb^{3+}/Er^{3+} at 10:1; (d) $pIn_{0.9}$, (e) $pAg_{0.6}In$, and (f) $pAg_{0.6}In_{0.9}$ samples co-doped with Yb^{3+}/Er^{3+} at 10:2; and (g) $pAg_{0.6}In$ and (h) $pAg_{0.6}In_{0.9}$ co-doped with Yb^{3+}/Er^{3+} at 10:5. All samples were excited using a 980 nm CW laser varying its laser power density (LPD) from 7.8 to 18.3 W cm^{-2}.

S3. Thermometric performance of the luminescent co-doped In-based perovskites

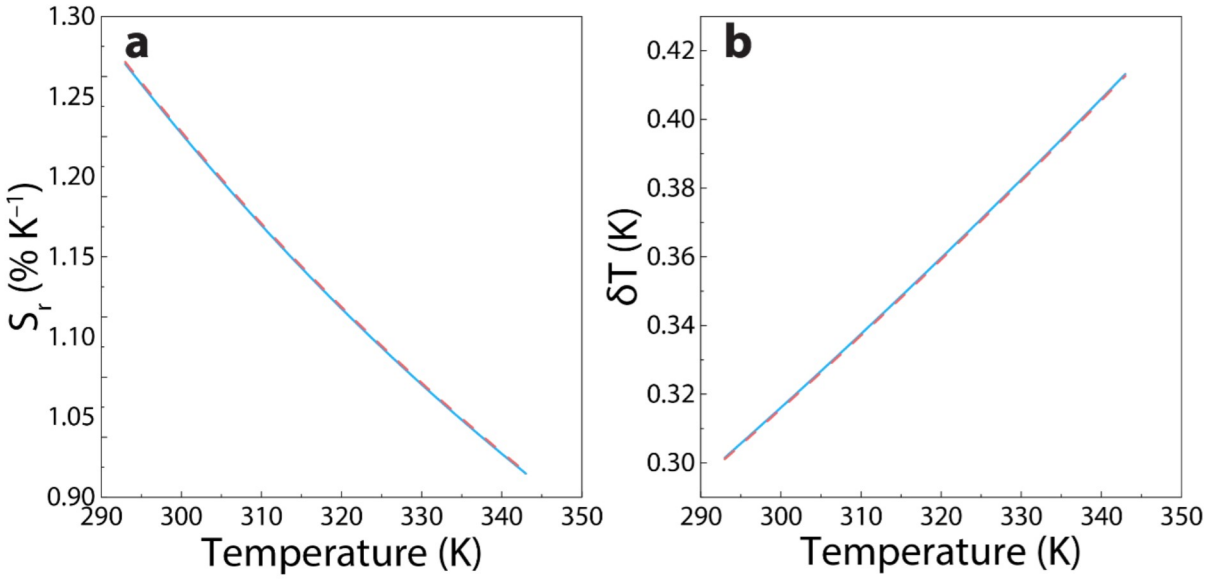

Figure S5. Thermal evolution of the (a) relative thermal sensitivity and (b) uncertainty in temperature for the obtained samples. The blue solid lines represent the results regarding the samples with a $\Delta E = 752 \pm 10$ cm^{-1} ($pAg_{0.6}In_{0.9}$:Yb^{3+}/Er^{3+} (10:1), $pAg_{0.6}In_{0.9}$:Yb^{3+}/Er^{3+} (10:5), $pAg_{0.6}$In:Yb^{3+}/Er^{3+} (10:1), $pAg_{0.6}$In:Yb^{3+}/Er^{3+} (10:2), $pAg_{0.6}$In:Yb^{3+}/Er^{3+} (10:5), and $pIn_{0.9}$:Yb^{3+}/Er^{3+} (10:1)) and the red dashed lines represent the results regarding the samples with a $\Delta E = 753 \pm 10$ cm^{-1} ($pAg_{0.6}In_{0.9}$:Yb^{3+}/Er^{3+} (10:2), $pIn_{0.9}$:Yb^{3+}/Er^{3+} (10:2), and $pIn_{0.9}$:Yb^{3+}/Er^{3+} (10:5)).

S4. Energy gap and power-dependent intensity ratio

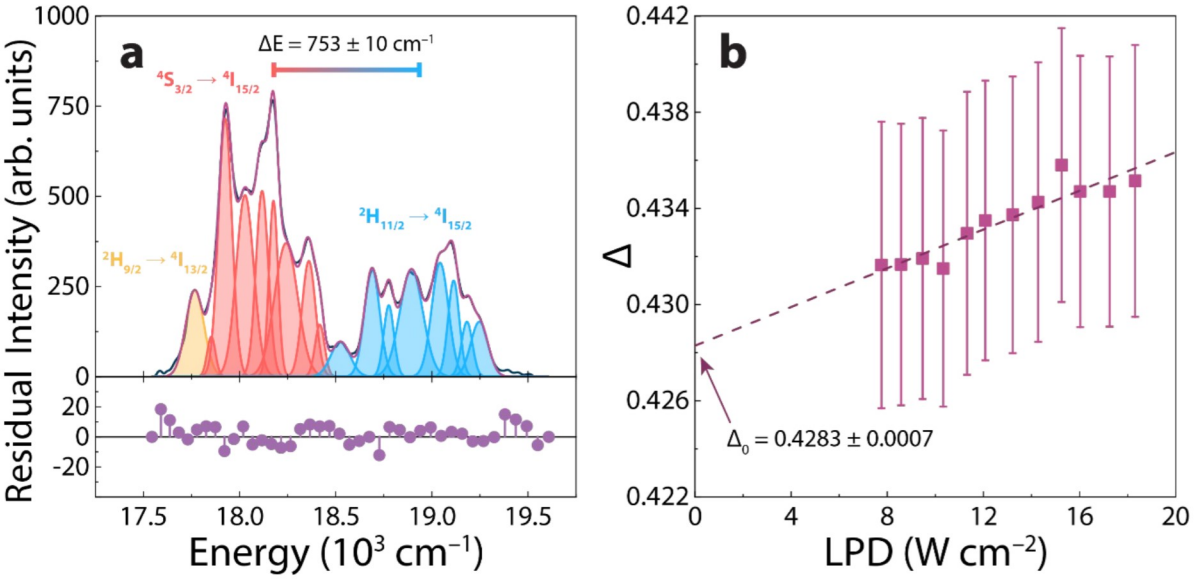

Figure S6. (a) Spectral Gaussian deconvolution illustrated for the emission spectrum of the $pAg_{0.6}In_{0.9}:Yb^{3+}/Er^{3+}$ (10:2) sample measured at 273 K and 18.3 W cm^{-2} under 980 nm excitation. The shadowed areas correspond to the Gaussian fit to the Stark components of the $^4S_{3/2}\rightarrow{}^4I_{15/2}$ (red) and $^2H_{11/2}\rightarrow{}^4I_{15/2}$ (blue) transitions of Er^{3+}, where their respective barycenters were used to calculate ΔE. The $^2H_{9/2}\rightarrow{}^4I_{13/2}$ transition is depicted in yellow. The bottom part demonstrates the residuals of the fitting procedure. (b) Determination of Δ_0 for the $pAg_{0.6}In_{0.9}:Yb^{3+}/Er^{3+}$ (10:2) sample. The power dependence of Δ was analyzed by plotting Δ against the laser power density (LPD) of the excitation laser.

Manuscript 5

Extending the Palette of Luminescent Primary Thermometers: Yb^{3+}/Pr^{3+} Co-Doped Fluoride Phosphate Glasses

F. E. Maturi, A. Gaddam, C. D. S. Brites, J. M. M. Souza, H. Eckert, S. J. L. Ribeiro, L. D. Carlos, D. Manzani.

Chemistry of Materials, 35 (17), 7229-7238, 2023.

DOI: https://doi.org/10.1021/acs.chemmater.3c01508

Featured as Supplementary Cover

CHEMISTRY OF MATERIALS

Open Access

pubs.acs.org/cm

Article

Extending the Palette of Luminescent Primary Thermometers: Yb^{3+}/Pr^{3+} Co-Doped Fluoride Phosphate Glasses

Published as part of the Chemistry of Materials virtual special issue "In Honor of Prof. Clement Sanchez".

Fernando E. Maturi, Anuraag Gaddam, Carlos D. S. Brites, Joacilia M. M. Souza, Hellmut Eckert, Sidney J. L. Ribeiro, Luís D. Carlos,* and Danilo Manzani*

Cite This: *Chem. Mater.* 2023, 35, 7229–7238

Read Online

ACCESS | Metrics & More | Article Recommendations | Supporting Information

ABSTRACT: The unique tunable properties of glasses make them versatile materials for developing numerous state-of-the-art optical technologies. To design new optical glasses with tailored properties, an extensive understanding of the intricate correlation between their chemical composition and physical properties is mandatory. By harnessing this knowledge, the full potential of vitreous matrices can be unlocked, driving advancements in the field of optical sensors. We herein demonstrate the feasibility of using fluoride phosphate glasses co-doped with trivalent praseodymium (Pr^{3+}) and ytterbium (Yb^{3+}) ions for temperature sensing over a broad range of temperatures. These glasses possess high chemical and thermal stability, working as luminescent primary thermometers that rely on the thermally coupled levels of Pr^{3+} that eliminate the need for recurring calibration procedures. The prepared glasses exhibit a relative thermal sensitivity and uncertainty at a temperature of 1.0% K^{-1} and 0.5 K, respectively, making them highly competitive with the existing luminescent thermometers. Our findings highlight that Pr^{3+}-containing materials are promising for developing cost-effective and accurate temperature probes, taking advantage of the unique versatility of these vitreous matrices to design the next generation of photonic technologies.

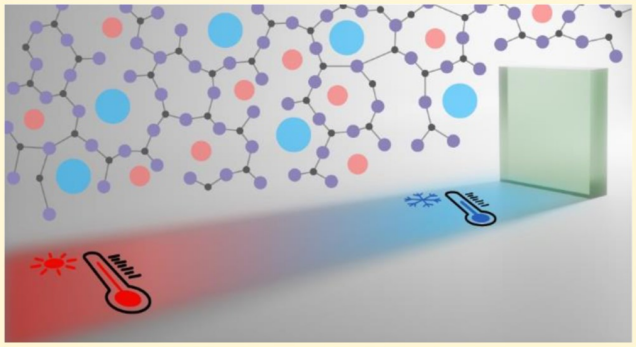

1. INTRODUCTION

Glasses are essential in the development of optical devices and telecommunication technologies due to their tunable chemical composition that can achieve high ion solubility,[1] increased transparency,[2] elevated thermal stability,[3] and low phonon energies.[4] With over 400,000 compositions reported to date, glasses play a crucial role in modern civilization.[5] Among the various types of glasses available, fluoride phosphates have garnered significant interest because they combine the low phonon energies of fluoride glasses with the high chemical, mechanical, and thermal stability of phosphate glasses.[6−9] Moreover, fluoride phosphate glasses present a high solubility of trivalent lanthanide ions (Ln^{3+}), making them suitable for obtaining solid-state lasers,[10,11] magneto-optical fibers,[12] and lighting applications.[13,14] In addition to their unique optical properties, such as narrow absorption and emission bands, long-lived excited states, and high emission quantum yields,[15,16] Ln^{3+} are promising candidates for luminescence thermometry due to their rich energy level structure.[17] The temperature-dependent light emission from various luminescent ions has enabled the development of luminescent thermometers for temperature sensing across a wide range of applications.[18−23]

Luminescence thermometry is a versatile, cost-effective, remote, and minimally invasive technique that relies on the temperature dependence of the luminescence of a phosphor with various response parameters, such as the band shape, peak energy or intensity, and excited state lifetimes and rise times.[24] This technique can afford real-time temperature measurements with high relative thermal sensitivity (S_r > 1% K^{-1}).[25] Most luminescent thermometers require a calibration procedure to establish the relationship between the photophysical features and the temperature, being classified as secondary thermometers. However, the recording of calibration curves is simply not possible in some applications, such as in biological media,[26] living animals,[27] and operating electronic devices.[28]

Received: June 16, 2023
Revised: July 20, 2023
Published: August 2, 2023

The strategy used so far in most of these examples was to assume that a calibration curve recorded in one dispersion medium remains valid in other environments, which is a rough estimation that diminishes the accuracy of the luminescent probe due to artifacts arising from spectral distortion.[29,30]

An alternative to the calibration procedure is to perform an absolute determination of the temperature by relying on well-established equations of state, such as those governing ideal gases and blackbody radiation.[31] These so-called primary thermometers avoid the need for prior temperature calibration, which is a major surplus. Nonetheless, the number of primary luminescent thermometers reported to date remains scarce, with fewer than 20 examples, mainly involving Er^{3+}/Yb^{3+} co-doped materials.[32] Herein, we present, for the first time, a luminescent primary thermometer based on the thermally coupled levels of Pr^{3+}. This novel approach is advantageous because (i) the recording of tedious calibration curves is not necessary and (ii) self-heating induced by the excitation source can be neglected. In this work, we thoroughly investigate the preparation route, structural composition, thermal stability, optical properties, and thermometric performance of Pr^{3+}/Yb^{3+} co-doped fluoride phosphate glasses used as luminescent primary thermometers.

2. EXPERIMENTAL SECTION

2.1. Materials. Lithium carbonate (Li_2CO_3, Sigma-Aldrich, 99.9%), ammonium dihydrogen phosphate ($(NH_4)H_2PO_4$, Alfa Aesar, 98.0%), yttrium fluoride (YF_3, Strem Chemicals, 99.9%), strontium fluoride (SrF_2, Sigma-Aldrich, 99.9%), calcium fluoride (CaF_2, Sigma-Aldrich, 99.9%), praseodymium oxide (Pr_7O_{11}, Lumtec, 99.9%), and ytterbium oxide (Yb_2O_3, Lumtec, 99.9%) were used as received from the companies.

2.2. Synthesis of Lithium Metaphosphate. Lithium metaphosphate ($LiPO_3$) was synthesized through the solid-state reaction between Li_2CO_3 and $(NH_4)H_2PO_4$, where thermal decomposition of the mixture was carried out at 543 K for 12 h in a platinum crucible under an air atmosphere. The temperature was increased, after the decomposition step, at a rate of 10 K min^{-1} up to 1173 K, and the mixture was melted for 30 min before cooling it down to room temperature (298 K). The obtained $LiPO_3$ was stored in a glass desiccator for further use.

2.3. Preparation of the Glasses. Undoped and Pr^{3+}/Yb^{3+} co-doped fluoride phosphate glass samples were obtained by using the conventional melting-quenching method with molar compositions of $50LiPO_3$-$20YF_3$-$20SrF_2$-$10CaF_2$, $98.75[50LiPO_3$-$20YF_3$-$20SrF_2$-$10CaF_2]$:$0.25\ Pr_7O_{11}/1.00Yb_2O_3$, and $97.75[50LiPO_3$-$20YF_3$-$20SrF_2$-$10CaF_2]$:$0.25\ Pr_7O_{11}/2.00Yb_2O_3$, labeled as PY00, PY14, and PY18, respectively. Further details of the preparation procedure and the chemical composition of the samples are presented in Section S1.1 and Table S1 of the Supporting Information.

2.4. Differential Scanning Calorimetry. The differential scanning calorimetry (DSC) curves of the glass samples were registered in a high-temperature calorimeter (DSC 404 F3 Pegasus, Netzsch) to identify the characteristic glass transition temperature (T_g, ± 2 K), the onset temperature of crystallization (T_x, ± 2 K), and thermal stability parameter ($\Delta T = T_x - T_g$, ± 4 K) of the obtained glasses. For this, each glass sample (~15 mg) was placed in an alumina crucible and heated from 298 to 873 K at a heating rate of 10 K min^{-1}, under a nitrogen atmosphere (10 mL min^{-1}). T_g and T_x were assigned to the temperatures at which the first derivative of the heat flow Q (dQ/dT) gives the minimum and maximum values around their corresponding peaks, respectively.

2.5. Solid-State Nuclear Magnetic Resonance Spectroscopy. Solid-state nuclear magnetic resonance (NMR) studies were performed on an NMR spectrometer (DD2, Agilent) with a field strength of 5.7 T using a 3.2 mm probe with a magic angle spinning (MAS) rate of 8.0 kHz for ^7Li, and 24.0 kHz for ^{19}F and ^{31}P MAS-NMR, $^{31}P\{^{19}F\}$ and $^7Li\{^{19}F\}$ rotational-echo double-resonance (REDOR)[33] and constant time REDOR (CT-REDOR),[34] and ^{31}P two-dimensional (2D) J-resolved experiments.[35] All spectra were analyzed using ssNake[36] and/or SIMPSON[37] software. The complete description and experimental conditions of the solid-state NMR experiments are detailed in Section S1.2 of the Supporting Information.

2.6. Absorption Spectroscopy. The absorption spectra of the samples in the visible (Vis) and near-infrared (NIR) spectral regions were measured at room temperature (298 K) in a dual-beam spectrometer (Lambda 950, PerkinElmer) over the 400−2200 nm range with a resolution of 1.0 nm.

2.7. Photoluminescence Spectroscopy and Temperature-Dependent Measurements. The excitation and emission spectra of the Pr^{3+}/Yb^{3+} co-doped glass samples in the visible spectral range were acquired in a Fluorolog3 spectrofluorometer (FL3-2T, Horiba), with a TRIAX 320 emission monochromator (fitted with 1200 grooves mm^{-1} grating blazed at 500 nm with a reciprocal linear density of 2.6 nm mm^{-1}) coupled to a photomultiplier (R928, Hamamatsu) using the front face acquisition mode and a 450 W Xenon arc lamp as the excitation source. The emission spectra were corrected for detection and optical spectral response of the spectrofluorometer while the excitation spectra were corrected for the spectral distribution of the lamp intensity using a photodiode reference detector. The spectral acquisition in the NIR was performed with the same equipment by using a grating with 600 grooves mm^{-1} blazed at 1200 nm and an H10330A-75 photomultiplier (Hamamatsu) without spectral correction. The temperature was controlled by a helium-closed cycle cryostat coupled to a vacuum system (4×10^{-4} Pa) and an autotuning temperature controller (Lakeshore 331, Lakeshore) with a resistance heater. Temperatures were measured with a silicon diode cryogenic sensor (DT-470-SD, Lakeshore) with an accuracy of ± 0.5 K (12−30 K), ± 0.25 K (30−60 K), and ± 0.15 K (60−340 K).

2.8. Emission Quantum Yield. The absolute emission quantum yields (q) were measured at room temperature (298 K) using a Quantaurus quantum yield measurement system (QY Plus C13534, Hamamatsu) with a 150 W Xenon lamp coupled to a monochromator for wavelength discrimination, an integrating sphere as sample chamber, and two multi-channel analyzers for signal detection in the visible spectral range. The values of q for the downshifting emission of Pr^{3+} correspond to the integration over the 450−750 nm spectral range under 443 nm excitation. The reported values present an accuracy of 10%, according to the manufacturer. It was not possible to determine the values of q for the NIR emission of Yb^{3+} once it was too faint to be detected by the equipment.

2.9. Spectral Deconvolution and Energy Separation Determination. The energy separation ΔE between the $^3P_1$ and $^3P_0$ thermally coupled levels of Pr^{3+} was estimated from the difference between the barycenters of the emission bands assigned to the $^3P_1 \rightarrow {}^3H_5$ and $^3P_0 \rightarrow {}^3H_5$ transitions in the deconvoluted emission spectra of the glass samples measured at room temperature. The spectral deconvolution and obtained values of ΔE are presented in Section S1.3 and Figure S1 in the Supporting Information.

2.10. Determination of the Thermometric Parameter. The integrated intensities were obtained by taking the integrated areas in the spectral regions corresponding to the $^3P_1 \rightarrow {}^3H_5$ (I_2, 510−533 nm) and $^3P_0 \rightarrow {}^3H_5$ (I_1, 533−565 nm) transitions of Pr^{3+} from the temperature-dependent emission spectra under excitation at 443 nm. The thermometric parameter Δ was defined as $\Delta = I_2/I_1$. The thermometric performance of Pr^{3+} in the obtained fluoride phosphate glasses was assessed in terms of thermal sensitivity and temperature resolution, as described in Section S1.4 of the Supporting Information.

3. RESULTS AND DISCUSSION

3.1. Thermal Evaluation and Structural NMR Studies. Fluoride phosphate glasses were obtained with densities of 3.48, 3.62, and 3.74 g cm^{-3} for the samples PY00, PY14, and

https://doi.org/10.1021/acs.chemmater.3c01508
Chem. Mater. 2023, 35, 7229−7238

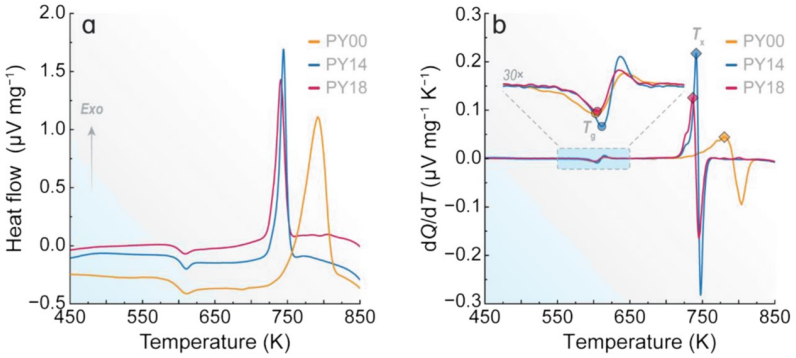

Figure 1. (a) DSC curves and (b) first derivative of the heat flow of the obtained fluoride phosphate samples. The inset in panel b displays the zoomed region of the 550−650 K temperature range. The circles and diamonds indicate the T_g and T_x temperature values obtained from the onset points of the thermal events, respectively.

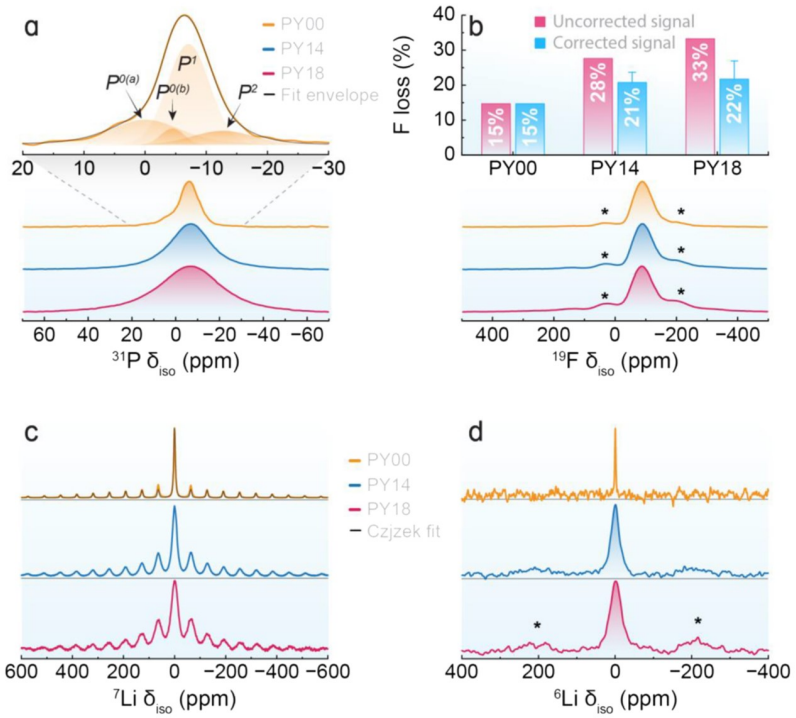

Figure 2. (a) ^{31}P MAS-NMR spectra of the undoped (PY00) and co-doped (PY14 and PY18) fluoride phosphate glasses measured at 5.7 T (bottom). Individual lineshape components extracted from the deconvolution analysis of the undoped PY00 sample based on the R-INADEQUATE data (top). (b) ^{19}F MAS-NMR spectra of the glasses (bottom). Fluorine loss quantified by ^{19}F MAS-NMR (top). The uncorrected signal in pink considers the detection of all F atoms while the corrected signal in blue excludes F atoms coordinated to Yb^{3+}/Pr^{3+}. Results in blue are mean values from three distinct coordination scenarios with the error bars indicating the deviations between them (see Figure S4). (c) ^{7}Li and (d) ^{6}Li MAS-NMR spectra of the PY00, PY14, and PY18 samples. The solid black curve in panel c corresponds to the Czjzek fits of the spinning sideband pattern of the undoped glass. Spinning sidebands are indicated by asterisks in b and d.

PY18, respectively. The increasing density of these glasses follows the increasing Pr^{3+}/Yb^{3+} co-doping content, showcasing the influence of the dopant concentration on the physical properties of the glass matrix. The DSC curves of the obtained samples shown in Figure 1 demonstrate that T_g remains essentially the same regardless of the glasses' composition, indicating that the addition of Pr^{3+} and Yb^{3+} does not cause significant structural changes in the connectivity of the fluoride phosphate glassy network. Nevertheless, the crystallization peak gets narrower and shifts to lower temperatures when increasing the content of ytterbium oxide, indicating that Yb^{3+} may act as a nucleating agent. Although the thermal stability parameter ΔT decreases after co-doping the samples, the obtained values are greater than 100 K, revealing that the obtained glasses present good thermal stability against the devitrification process. The characteristic temperatures of all samples are summarized in Table S2.

Figure 2a displays the ^{31}P MAS-NMR spectra of the obtained glasses. Sample PY00 presents multiple components which were analyzed in terms of contributions from nonbridged orthophosphate (P^0, empirical formula PO_4^{3-}), singly bridged pyrophosphate (P^1, empirical formula $P_2O_7^{4-}$), and doubly bridged metaphosphate (P^2, empirical formula PO_3^-) units,[38] based on additional interaction-selective experiments demonstrated in Section S1.2 of the Supporting Information, where the fitting parameters are listed in Table 1.

https://doi.org/10.1021/acs.chemmater.3c01508
Chem. Mater. 2023, 35, 7229−7238

Table 1. Fitting Parameters of the Obtained ^{31}P NMR Data

		^{31}P R-INADEQUATE				^{31}P MAS-NMR			
sample	units	δ_{max} (ppm)	δ_{iso} (ppm)	FWHM (ppm)	area (%)	δ_{max} (ppm)	δ_{iso} (ppm)	FWHM (ppm)	area (%)
PY00	$P^{0(a)}$	−8.7				−6.8	−0.1	31	28
	$P^{0(b)}$						−4.5	11	5
	P^1		−7.2	22	85		−7.1	19	55
	P^2		−13.6	28	15		−12.7	28	12
PY14						−7.1	−6.6	45	100
PY18						−7.2	−6.5	69	100

Table 2. Fitting Parameters of the Obtained ^{19}F, ^{7}Li, and ^{6}Li NMR Data

	^{19}F MAS-NMR			^{7}Li MAS-NMR			^{6}Li MAS-NMR	
sample	δ_{CG} (ppm)	FWHM (ppm)	δ_{max} (ppm)	δ_{iso} (ppm)	FWHM (ppm)	C_Q (kHz)	δ_{iso} (ppm)	FWHM (ppm)
PY00	−96.1	76.0	−89.2	0.23	6.0	110	−0.65	1.8
PY14	−96.9	79.0	−88.6	−0.10	21.0		−0.87	22.8
PY18	−98.5	84.0	−87.9	−0.01	32.0		−1.12	30.8

The major contribution centered at −7.2 ppm arises from P^1 units (85%), although some contributions from P^0 and P^2 units are also evident. This assignment is supported by the 2D J-resolved spectrum of Figure S2, indicating the doublet structure as expected for P^1 species having P−O−P linkages, with an estimated ^2J coupling constant of 20 Hz. The identity of the P^1 and the P^2 units having P−O−P linkages was further confirmed by the double-quantum filtered signal displayed in Figure S3, showing the NMR signal of only those P species that are involved in P−O−P linkages. We note that the P^1 units identified in the double-quantum filtration experiment show their peak maximum (δ_{max}) at −8.7 ppm, whereas δ_{max} in the single-pulse spectrum appears at −6.8 ppm (Table 1). This ∼2.0 ppm difference suggests that another P^0 contribution may be overlapping the P^1 signal, as also suggested by a more detailed inspection of the contour plot in the J-resolved MAS-NMR spectrum.

Figure 2a also shows the simulation of the ^{31}P MAS-NMR spectrum, constrained by the line shape parameters of the P^1 species via the R-INADEQUATE line shape fit. The possibility for this additional P^0 signal arising from an FPO_3^{2-} unit was tested by analyzing the Fourier transforms of ^{31}P{^{19}F} REDOR difference signals at short dipolar mixing times (Figure S5). As an FPO_3^{2-} unit is expected to show rapid dephasing in such an experiment, a chemical shift difference between the remaining signal and the difference signal would be expected. This, however, was not observed experimentally. The ^{31}P{^{19}F} REDOR curve (Figure S6) also gives no evidence of a fraction of rapidly dephasing phosphate species. Still, we cannot exclude the possibility that the minor feature near −4.5 ppm (labeled $P^{0(b)}$ in Figure 2a) was not detectable by ^{31}P{^{19}F} REDOR owing to sensitivity limitations. Samples PY14 and PY18 show poorly resolved spectra in Figure 2a due to broadening by interactions with paramagnetic Pr^{3+} and Yb^{3+}, precluding a detailed deconvolution analysis.

The ^{19}F MAS-NMR line shape (Figure 2b) of the undoped sample is slightly asymmetric with the center of gravity (δ_{CG}) at −96.1 ppm, whereas δ_{max} is observed near −89.2 ppm, as displayed in Table 2. Considering that the ^{19}F chemical shift values for LiF, CaF_2, SrF_2, and YF_3 are −204, −108, −87, and −62 ppm, respectively, it is possible to attribute the observed signal to fluorine (F) in a mixed-metal environment. These results further indicate that the resonance signals of F species not directly coordinated to Yb^{3+} or Pr^{3+} are little affected by paramagnetic broadening. The observed spectra do not show evidence of P-bonded F species, which would give rise to a peak in the vicinity of −70 ppm. Thus, these samples are better described as fluoride phosphate rather than fluorophosphate glasses.[7]

Fluoride phosphate glasses are known to experience F volatilization during synthesis. Hence, the quantitative nature of NMR was used to estimate the amount of F loss by employing ^{19}F MAS-NMR. By analyzing the detected ^{19}F signal, a significantly higher apparent loss was observed in the paramagnetically co-doped glasses compared to the undoped glass (Figure 2b, top panel), with this loss increasing with the Yb^{3+} content. It is worth noting that once all these glasses were prepared under identical conditions, the fluorine species directly bonded to the paramagnetic dopants cannot be detected due to the excessive paramagnetic broadening of the resonance signal. Although considering 8-fold coordination is a reasonable approximation for estimating the minimum signal loss due to lanthanide ions embedded within a crystalline fluoride structure,[39] previous diffraction studies from Hoppe et al. have shown that the average coordination numbers of Pr^{3+} and Yb^{3+} in metaphosphate glasses are 7.0 and 6.5, respectively.[40] Assuming that these average coordination numbers are similar in fluoride phosphate glasses, the signal loss resulting from paramagnetic interactions can be estimated in the case of dominant Pr−F and Yb−F bonding.

Upon correcting for this additional contribution to the signal loss, the estimated evaporation loss is more consistent with that observed in the undoped sample, yielding 15, 20, and 21% F losses for PY00, PY14, and PY18, respectively (Figure S4). It is important to note that these calculations represent the estimation of the average F loss caused by evaporation, where higher evaporation losses would occur if a significant amount of phosphate ions were present in the first coordination sphere of the lanthanide ions. For instance, assuming half of the ligands to be phosphate and the other half fluoride ions, the maximum corrected evaporation losses would give 24 and 27% for PY14 and PY18, respectively. Therefore, Figure 2b displays the F evaporation loss, which presents the uncorrected values and the corrected mean values from calculations considering the coordination number of Pr^{3+}/Yb^{3+} in crystalline fluoride (8.00/8.00), vitreous fluoride-only (7.00/6.50), and mixed vitreous fluoride phosphate (3.50/3.25) environments. Nevertheless, the enhanced signal loss observed in the co-doped

https://doi.org/10.1021/acs.chemmater.3c01508
Chem. Mater. 2023, 35, 7229−7238

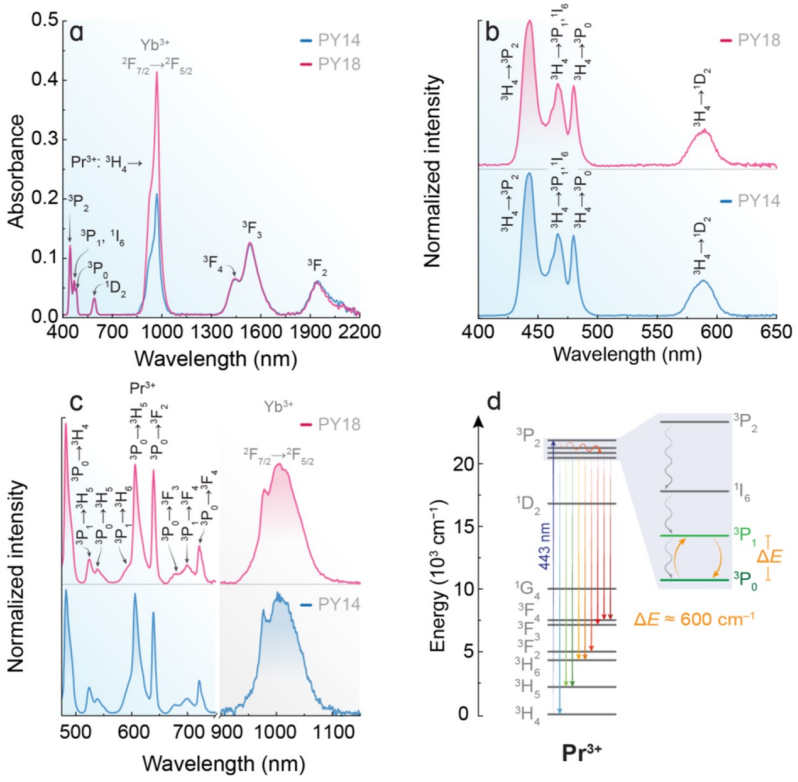

Figure 3. (a) Vis−NIR absorption spectra of the fluoride phosphate glass samples. The absorptions of Pr^{3+} arise from the $^3H_4$ ground state to different excited states while Yb^{3+} exhibits the $^2F_{7/2} \rightarrow {}^2F_{5/2}$ transition. The absorption spectrum of the sample PY00 is not shown because it is optically inactive due to the lack of Yb^{3+} and Pr^{3+} in its composition. (b) Excitation spectra monitoring the emission at 606 nm and (c) emission spectra in the Vis (Pr^{3+}, left) and NIR (Yb^{3+}, right) spectral range under excitation at 443 nm of the samples PY14 and PY18 measured at room temperature. (d) Energy level diagram of Pr^{3+} depicting the downshifting emission in the Vis spectral range, underscoring the thermally coupled levels.

glasses compared to the undoped sample indirectly indicates significant Pr/Yb−F bonding in the co-doped samples.

Figure 2c,d displays the ^{7}Li and ^{6}Li MAS-NMR spectra of the fluoride phosphate glasses, respectively, stressing the paramagnetic broadening effects caused by Pr^{3+} and Yb^{3+} doping. For the undoped PY00 sample, the spinning sideband manifold observed arises from the effect of MAS on the $m = \pm 1/2 \leftrightarrow m = \pm 3/2$ satellite transitions, which are inhomogeneously broadened by the quadrupolar interactions. Furthermore, a comparison of the spinning sideband patterns on the doped and the undoped samples suggests that paramagnetic interactions have an additional effect on the observed spinning sideband intensity distribution. For the undoped sample, the satellite transitions in the ^{7}Li MAS-NMR spectra were fitted with the Czjzek model using the ssNake software (refer to Table 2 for the fitting parameters).[36,41]

As the chemical shift dispersion in $^{6/7}$Li NMR is extremely limited, further spectral editing and characterization were done exploiting the ^{6}Li−^{31}P dipole−dipole interactions using a ^{6}Li{^{31}P} REDOR experiment. In this case, the less abundant isotope ^{6}Li must be chosen as the observed nucleus because the resonance frequencies of ^{7}Li and ^{31}P are too close to enable the necessary double-tuning of the NMR probe. Figure S7 compares the ^{6}Li{^{31}P} REDOR data of PY00 and $LiPO_3$ glass, where the uncorrected second moments extracted from the data by using eq S1 are 0.69 and 0.65 Mrad^2 s^{-2}, respectively, being considered identical within the experimental uncertainty limits of ± 10%. The theoretically calculated $M_{2(\mathrm{Li-P})}$ for crystalline $LiPO_3$ is 2.69 Mrad^2 s^{-2}, based on eq S2. In addition, an analysis of molecular dynamics simulation output for glassy $LiPO_3$ resulted in $M_{2(\mathrm{Li-P})}$ = 1.97 Mrad^2 s^{-2}, and the corresponding parabola predictions are included in Figure S7. The substantial deviation of the experimental REDOR data from the latter simulation suggest a calibration factor f = 0.33. Most likely, this relatively small value arises from the large ^{31}P chemical shift anisotropy interfering with the dipolar recoupling efficiency.

Regardless of this issue, the most surprising result of Figure S7 is the close correspondence of the two experimental values for $LiPO_3$ glass and PY00, despite the considerable dilution of phosphate content in the latter glass. It suggests that the lithium ions exercise a strong preference for being bound to phosphate rather than to fluoride ions in this mixed anion glass. Complementary information is available from ^{31}P spin echo decay data assessing the strength of the homonuclear ^{31}P−^{31}P magnetic dipole−dipole interactions (Figure S8). The $M_{2(\mathrm{P-P})}$ values extracted from these data are much larger than those expected from a random distribution of ^{31}P nuclei in space, as estimated from a Monte Carlo simulation. This is, of course, understandable, as the presence of a considerable fraction of P−O−P linkages brings the P atoms into proximity much more closely than would be expected for a random distribution of P atoms in space. Also, $M_{2(\mathrm{P-P})}$ is significantly larger in $LiPO_3$ glass than in PY00 glass, because it features two P−O−P linkages per P atom whereas the NMR results show that there is less than one P−O−P linkage on average in the latter case.

https://doi.org/10.1021/acs.chemmater.3c01508
Chem. Mater. 2023, 35, 7229−7238

Altogether, these NMR results show that alloying $LiPO_3$ glass with alkaline-earth and yttrium fluorides produces significant network modification. A substantial fraction of P−O−P linkages is broken leading to the depolymerization of a P^2-dominated structure into one that is dominated by P^1 units. The process can be initially visualized as:

$$4O_{2/2} - P(=O)(O^-) + SrF_2 = 2O_{1/2} - P(=O)(O^-)_2 + 2O_{1/2} - P(=O)(O^-) F + Sr^{2+} \quad (1)$$

which may be followed by partial O ↔ F exchange in the melting atmosphere. The latter process is experienced as fluorine loss and may be responsible for our inability to observe specific structural features indicating P−F bonding in the obtained glasses. The $^6Li\{^{31}P\}$ REDOR experiment suggests a clear preference for Li-phosphate over Li-fluoride interaction. The formation of P−F bonds appears to be largely suppressed in these samples.

3.2. Optical Characterization. The absorption spectra of the colorless undoped and greenish Pr^{3+}/Yb^{3+} co-doped fluoride phosphate glass samples are shown in Figure 3a. The Pr^{3+} transitions from the ground state ($^3H_4$) to the $^3P_2$ (443 nm), $^3P_1$ and $^1I_6$ (469 nm), $^3P_0$ (481 nm), and $^1D_2$ (588 nm) upper energy levels are observed in the Vis spectral region. In the NIR spectralrange, the absorption bands peaking at 1440, 1533, and 1941 nm are related to transitions from the $^3H_4$ ground state to the $^3F_4$, $^3F_3$, and $^3F_2$ excited states of Pr^{3+}, respectively. The absorption band observed at 974 nm is assigned to the transition of Yb^{3+} from the ground state $^2F_{7/2}$ to the excited state $^2F_{5/2}$. It is worth pointing out that all the transitions of Pr^{3+} present similar absorbance values because the content of Pr_7O_{11} is the same in both samples while the absorbance of the $^2F_{7/2} \rightarrow {}^2F_{5/2}$ transition of Yb^{3+} at 974 nm is greater for PY18 once it presents twice the content of Yb_2O_3 compared to PY14.

The room-temperature excitation spectra of the Pr^{3+}/Yb^{3+} co-doped glasses were recorded by monitoring the emission of the $^3P_0 \rightarrow {}^3H_6$ transition of Pr^{3+} at 606 nm (Figure 3b), displaying the characteristic absorptions of Pr^{3+} centered at 443 nm ($^3H_4 \rightarrow {}^3P_2$), 469 nm ($^3H_4 \rightarrow {}^3P_1$,$^1I_6$), 481 nm ($^3H_4 \rightarrow {}^3P_0$), and 588 nm ($^3H_4 \rightarrow {}^1D_2$), in good agreement with the absorption spectra of the samples presented in Figure 3a. Under excitation at 443 nm, both co-doped samples present the typical multicolor emission of Pr^{3+} between the blue and red spectral range (Figure 3c). The emission bands within this spectral region arise from the $^3P_0 \rightarrow {}^3H_4$ (482 nm), $^3P_1 \rightarrow {}^3H_5$ (524 nm), $^3P_0 \rightarrow {}^3H_5$ (539 nm), $^3P_1 \rightarrow {}^3H_6$ (589 nm), $^3P_0 \rightarrow {}^3H_6$ (606 nm), $^3P_0 \rightarrow {}^3F_2$ (639 nm), $^3P_1 \rightarrow {}^3F_3$ (677 nm), $^3P_1 \rightarrow {}^3F_4$ (701 nm), and $^3P_0 \rightarrow {}^3F_4$ (721 nm) transitions of Pr^{3+} in a downshifting emission process.[42]

Additionally, the excitation of PY14 and PY18 at 443 nm also gives rise to a broad emission band peaking at 979 and 1006 nm, with the characteristic emission profile of the $^2F_{5/2} \rightarrow {}^2F_{7/2}$ transition of Yb^{3+} in the NIR spectral range (Figure 3c).[43] Under 443 nm excitation, the ^3P_J manifold and $^1I_6$ emitting levels of Pr^{3+} may undergo nonradiative decay to the $^1G_4$ energy level, which is resonant with the $^2F_{5/2}$ level of Yb^{3+}, resulting in the Yb^{3+} NIR emission around 1000 nm, due to a Pr^{3+}-to-Yb^{3+} energy transfer process.[44] By comparing the absorption and excitation spectra of the PY14 and PY18 glasses (Figure S9), it is possible to observe that the relative absorption strengths of the $^3H_4 \rightarrow {}^3P_{2-0}$,$^1I_6$ and $^3H_4 \rightarrow {}^1D_2$ transitions (i.e., the ratio between the integrated intensities from the $^3H_4 \rightarrow {}^3P_{2-0}$,$^1I_6$ and $^3H_4 \rightarrow {}^1D_2$ absorption bands) stay nearly unchanged (Table S3), indicating that the Yb^{3+} NIR emission upon Pr^{3+} excitation is a downshifting mechanism rather than a downconversion emission.[45] This is further supported by the fact that the absolute emission quantum yield in the NIR cannot be measured under 443 nm excitation, as observed in Table S4.

Glasses containing Pr^{3+}/Yb^{3+} are also known for displaying upconversion light emission due to a Yb^{3+}-to-Pr^{3+} energy transfer process, where the emission of Pr^{3+} in the Vis spectral range is induced by NIR excitation of the $^2F_{5/2}$ level of Yb^{3+}.[46,47] Although upconversion was observed for the PY14 and PY18 co-doped glass samples, it required a high laser excitation power density (> 100 W cm^{-2}), with the laser-induced heating resulting in a local temperature increment which was high enough to break the samples. Nevertheless, measurements were performed by using the ground samples prepared for the solid-state MAS-NMR studies, where their upconversion emission spectra under 980 nm laser excitation are presented in Figure S10, displaying the characteristic emission bands of Pr^{3+} in the visible spectral range.

3.3. Primary Pr^{3+}-Based Luminescence Thermometry. When the energy separation between two emitting levels is sufficiently small (200 to 2000 cm^{-1}),[25] they are considered thermally coupled because they exhibit a thermally induced population distribution between them, following the Boltzmann statistics.[48] By taking the ratio between the integrated intensity of the emission bands arising from these levels (I_1 and I_2, namely, the integrated emission intensities of the emission bands arising from the lower and upper energetic emitting levels, respectively), a thermometric parameter Δ can be obtained, translating the temperature-induced changes into a luminescence intensity ratio:

$$\Delta = \frac{I_2}{I_1} = B\exp\left(-\frac{\Delta E}{k_B T}\right) \quad (2)$$

where ΔE is the energy separation between the thermally-coupled levels, k_B is the Boltzmann constant, T is the absolute temperature, and B is a pre-exponential factor given by the ratio of the product of degeneracy and total spontaneous emission of both excited states to the ground state.[48]

Most of the studies on luminescent thermometers based on the Boltzmann statistics are calibrated by performing a fitting procedure that enables the estimation of ΔE and B through eq 2, from the slope and intercept of the ln(Δ) against $1/T$ plot, respectively.[17] However, this introduces artifacts in temperature determination, mainly when emission spectra are measured outside the luminescent thermometer's optimal temperature range[49] or when intruding emission bands (unrelated to the thermally coupled levels) coexist in the same spectral range of I_1 and I_2.[50] Moreover, once this approach determines the values of ΔE and B in a temperature-dependent fitting procedure as in secondary thermometers, it is challenging to perform accurate measurements of the temperature outside the calibration range.

To circumvent these issues, Balabhadra et al. have reported a straightforward procedure that can be used to avoid the recording of calibration curves when dealing with the Boltzmann-based luminescent thermometers discussed here.[51] This methodology consists in determining the

https://doi.org/10.1021/acs.chemmater.3c01508
Chem. Mater. 2023, 35, 7229−7238

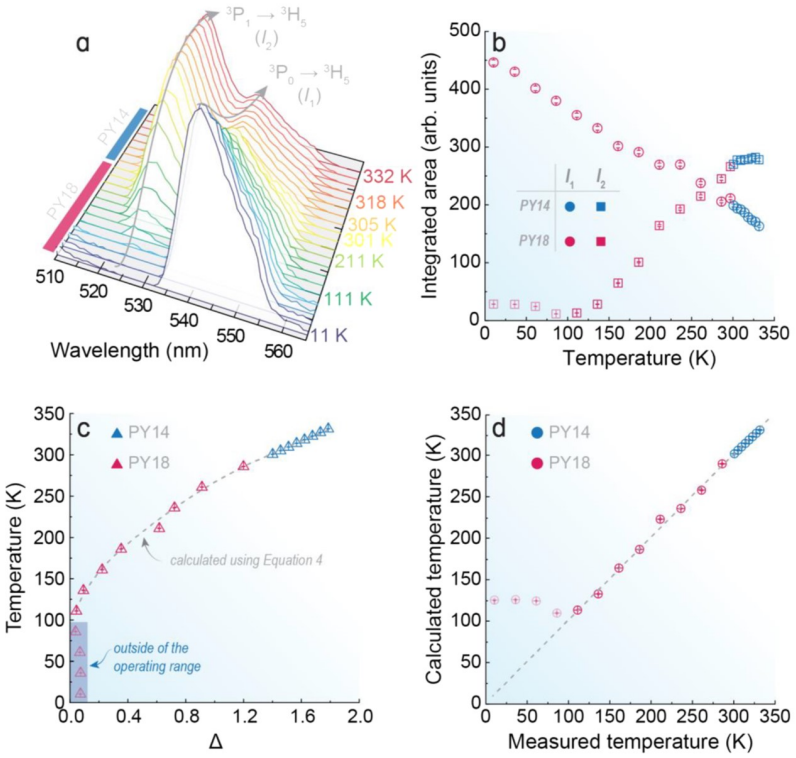

Figure 4. (a) Temperature-dependent emission spectra of the PY14 and PY18 samples under 443 nm excitation, highlighting the emission bands arising from the thermally coupled levels of Pr^{3+}. The emission spectra in the complete spectral range recorded are presented in Figure S11. Temperature dependence of (b) integrated emission intensities I_1 and I_2 and (c) corresponding Δ values. The dashed line in c displays the temperature values calculated through eq 4 and their corresponding uncertainties while symbols are the temperature values measured with the reference silicon diode cryogenic temperature sensor. The shadowed area delimits the temperature range where Boltzmann statistics fail. (d) Correlation between the measured with the reference silicon diode cryogenic temperature sensor (x-axis) and calculated from eq 4 (y-axis) temperature values. The dashed line corresponds to $x = y$.

parameter Δ_0, which is the thermometric parameter Δ (i.e., luminescence intensity ratio from two thermally coupled levels) obtained at room temperature (T_0):

$$\Delta_0 = B\exp\left(-\frac{\Delta E}{k_B T_0}\right) \tag{3}$$

This strategy is ingenious because it paves the way for measuring the absolute temperature T by taking the ratio Δ/Δ_0 from eqs 2 and 3:

$$\frac{1}{T} = \frac{1}{T_0} - \frac{k_B}{\Delta E}\ln\left(\frac{\Delta}{\Delta_0}\right) \tag{4}$$

where T_0 can be easily measured with a temperature sensor, Δ_0 corresponds to the luminescence intensity ratio from the emission spectra recorded at T_0, and the experimental values of Δ are obtained from the emission spectra recorded at different temperatures. Therefore, it is possible to predict T directly from the thermometric parameter Δ by using eq 4. Because Δ_0 and T_0 correspond to experimentally measured values that are obtained apart from any calibration or fitting procedures, they play the role of normalization factors rather than a calibration process. In addition, ΔE is calculated in a nontemperature-dependent way, where this Boltzmann-derived thermometric approach is based on a well-defined equation of state that does not rely on unknown or significantly temperature-dependent values, matching the definition of a primary thermometer.[31]

Even though this methodology precludes the calculation of the pre-exponential factor B and can be virtually applied to any Ln^{3+} displaying thermally coupled levels, it has been predominantly employed for primary temperature sensing using the upconverting emission from Yb^{3+}/Er^{3+} co-doped materials. The major drawback of this preference is the estimation of Δ_0 from the intercept of a straight line fitted to the power dependence of Δ, which may introduce errors in the determination of the temperature. In addition, the temperature readouts are affected by local temperature increases induced by the laser excitation required in upconverting approaches, further compromising the accuracy of the temperature measurements.[51]

The use of Pr^{3+} is advantageous in this context because, besides presenting thermally coupled energy levels ($^3P_1$ and $^3P_0$, $\Delta E \approx 600$ cm^{-1}),[52,53] its downshifting emission can be achieved by using a Xe lamp as the excitation source, where laser-induced heating is absent during the spectral acquisition and Δ_0 can be determined by simply measuring the emission spectrum at room temperature. The only fitting parameter required to perform primary temperature sensing by applying eq 4 to Pr^{3+} is ΔE, which can be easily calculated by deconvoluting the emission spectra measured at room temperature (see Experimental Section). Interestingly, ΔE and Δ can be calculated by using the emission bands of Pr^{3+} arising in the 510−565 nm range ($^3P_1 \rightarrow {}^3H_5$ and $^3P_0 \rightarrow {}^3H_5$) or the 575−632 nm range ($^3P_1 \rightarrow {}^3H_6$ and $^3P_0 \rightarrow {}^3H_6$). Although the latter requires spectral deconvolution to account

https://doi.org/10.1021/acs.chemmater.3c01508
Chem. Mater. 2023, 35, 7229−7238

for the overlapping emission band from the $^3P_0 \rightarrow {}^3F_2$ transition peaking at 639 nm, Pr^{3+} offers two distinct pathways for assessing the temperature-dependent population distribution between the $^3P_1$ and $^3P_0$ emitting levels. This allows using the Pr^{3+}/Yb^{3+} co-doped fluoride phosphate glasses as primary thermometers based on eq 4 without the need for external calibration,[31] showcasing the greater advantage of choosing Pr^{3+} over Er^{3+}-based materials to perform luminescent primary temperature sensing.

Therefore, by replacing the values of ΔE, T_0, Δ_0, and the experimental values of Δ obtained from the temperature-dependent emission spectra of the obtained samples in eq 4, an excellent agreement between the calculated and measured temperatures was achieved, as observed in Figure 4a. This indicates that the proposed methodology is valid for predicting the absolute temperature, without the need for previously recording a calibration curve. The values of ΔE, T_0, and Δ_0 obtained for PY14 and PY18 are listed in Table S6. Although there is a slight difference in the values of ΔE calculated for PY14 and PY18, the integrated intensities of the emission bands related to the thermally coupled levels of Pr^{3+} show the same behavior for the temperature evolution in both samples (Figure 4b). Furthermore, the temperatures predicted by both samples follow the same trend at distinct temperature ranges (Figure 4c,d), indicating that the intrinsic thermal sensing ability of Pr^{3+} is not affected by the chemical environment of the fluoride phosphate glass matrix.

The optimal thermal response of the thermally coupled levels occurs within a specific temperature range that depends on the energy separation ΔE between them $\left(\frac{\Delta E}{(2+\sqrt{2})k_B} \leq T \leq \frac{\Delta E}{2k_B}\right)$, encompassing the optimal operating temperature range where the Boltzmann statistics are still valid.[48] Taking into account that Pr^{3+} presents a ΔE of approximately 600 cm^{-1}, 253−432 K is the best temperature operating range for the obtained fluoride phosphate glasses co-doped with Yb^{3+}/Pr^{3+}. Notably, the intensity of the $^3P_1 \rightarrow {}^3H_5$ transition in sample PY14 is comparable to the noise level for temperatures below 111 K, being I_2 near zero (Figure 4a,b). This is because at these temperatures, the nonradiative rates are comparable to the radiative rates, and there is not enough thermal energy to allow the population distribution between the $^3P_0$ and $^3P_1$ thermally coupled levels of Pr^{3+}. Consequently, only the lower $^3P_0$ emitting level is populated.[48] This means that, from an experimental point of view, the primary thermometric approach can be employed in a broader range of temperatures, working well for Pr^{3+} operating above 111 K. Nevertheless, the thermometric performance was herein evaluated at room temperature T_0 to avoid misinterpretations of the thermal response of the $^3P_1$ and $^3P_0$ levels of Pr^{3+}.

The thermometric performance of Pr^{3+} working as a primary thermometer in the obtained fluoride phosphate glasses was evaluated by using the relative thermal sensitivity (S_r) and uncertainty in temperature (δT), which are crucial figures of merit used to compare the performance of different luminescent thermometers (see Section S1.4 of the Supporting Information for further information).[18] The S_r values obtained for both PY14 and PY18 are ∼1.0% K^{-1} at T_0 (Table S6), consistent with previously reported S_r values for Pr^{3+}.[53−55] The obtained samples present a δT of 0.5 K at T_0, in close correspondence with the primary luminescent thermometers reported for Yb^{3+}/Er^{3+}-containing materials (see Table 2 in ref 32).

It is important to stress that, despite both PY14 and PY18 samples presenting Yb^{3+} and Pr^{3+} in their composition, the energy levels of Yb^{3+} do not participate in the thermalization process between the $^3P_1$ and $^3P_0$ thermally coupled levels of Pr^{3+}, and thus they do not affect the thermometric performance of Pr^{3+}. Hence, once the thermometric response of these Pr^{3+}/Yb^{3+} co-doped fluoride phosphate glasses is solely due to light emission arising from Pr^{3+}, we may conclude that these samples can operate as luminescent primary temperature sensors in different media as far as we guarantee (i) the structural integrity of the vitreous matrix and (ii) no overlapping is occurring between the Pr^{3+} emission and the absorption of an eventual light emitting material placed in the optical path of the samples. These findings indicate that embedding Pr^{3+} into a vitreous matrix is an ingenious strategy for developing highly accurate luminescent thermometers because it does not suffer from temperature deviations from laser-induced heating observed in power-dependent approaches, reducing thermal and spectral artifacts, besides operating in a wide temperature range without requiring time-consuming calibration curves.

4. CONCLUSIONS

We successfully prepared and characterized luminescent fluoride phosphate glasses co-doped with Pr^{3+} and Yb^{3+} performing the structural, thermal, optical, and thermometric evaluation of the glasses. The NMR results showed significant network modification resulting from the addition of alkaline-earth and yttrium fluorides, which led to the depolymerization of phosphate chains through the breaking of P−O−P linkages. A clear preference for Li-phosphate over Li-fluoride interaction was observed and the formation of P−F bonds is largely suppressed in the obtained samples. While the incorporation of Yb^{3+} can induce crystallization, the DSC results suggest that co-doping the samples does not substantially alter the connectivity of the fluoride phosphate glass network. The temperature-dependent emission spectra of the co-doped samples demonstrated the inherent ability of Pr^{3+} to work as a primary thermometer irrespective of the doping content, making these samples suitable for real-world applications due to their elevated thermal stability.

Overall, our work represents a significant contribution to the field of luminescence thermometry by proposing a simpler, faster, and more reliable approach for temperature readouts. The obtained Pr^{3+}/Yb^{3+} co-doped fluoride phosphate glasses constitute a promising platform for the development of cost-effective, accurate, and high-performance temperature sensors, particularly in applications such as biomedical sensors and wearable technology, where a vitreous matrix that can be molded into different shapes is required. These findings demonstrate the potential use of Pr^{3+}-containing materials as luminescent thermometers that do not require thermal calibration.

■ ASSOCIATED CONTENT

Supporting Information

The Supporting Information is available free of charge at https://pubs.acs.org/doi/10.1021/acs.chemmater.3c01508.

Detailed preparation and characterization procedures, advanced NMR studies and molecular dynamics simulations, and additional details of the thermometric performance (PDF)

https://doi.org/10.1021/acs.chemmater.3c01508
Chem. Mater. 2023, 35, 7229−7238

AUTHOR INFORMATION

Corresponding Authors

Luís D. Carlos − *Phantom-g, CICECO - Aveiro Institute of Materials, Department of Physics, University of Aveiro, Aveiro 3810-193, Portugal;* orcid.org/0000-0003-4747-6535; Email: lcarlos@ua.pt

Danilo Manzani − *São Carlos Institute of Chemistry, University of São Paulo, IQSC-USP, São Carlos, São Paulo 13560-970, Brazil;* orcid.org/0000-0001-7280-5404; Email: dmanzani@usp.br

Authors

Fernando E. Maturi − *Phantom-g, CICECO - Aveiro Institute of Materials, Department of Physics, University of Aveiro, Aveiro 3810-193, Portugal; Institute of Chemistry, São Paulo State University (UNESP), Araraquara, São Paulo 14800-060, Brazil;* orcid.org/0000-0002-9305-8185

Anuraag Gaddam − *São Carlos Institute of Physics, University of São Paulo, IFSC-USP, São Carlos, São Paulo 13566-590, Brazil*

Carlos D. S. Brites − *Phantom-g, CICECO - Aveiro Institute of Materials, Department of Physics, University of Aveiro, Aveiro 3810-193, Portugal;* orcid.org/0000-0001-9636-2628

Joacilia M. M. Souza − *São Carlos Institute of Chemistry, University of São Paulo, IQSC-USP, São Carlos, São Paulo 13560-970, Brazil*

Hellmut Eckert − *São Carlos Institute of Physics, University of São Paulo, IFSC-USP, São Carlos, São Paulo 13566-590, Brazil;* orcid.org/0000-0002-6536-0117

Sidney J. L. Ribeiro − *Institute of Chemistry, São Paulo State University (UNESP), Araraquara, São Paulo 14800-060, Brazil;* orcid.org/0000-0002-8162-6747

Complete contact information is available at: https://pubs.acs.org/10.1021/acs.chemmater.3c01508

Notes

The authors declare no competing financial interest.

ACKNOWLEDGMENTS

This work was developed within the scope of the project CICECO-Aveiro Institute of Materials, UIDB/50011/2020, UIDP/50011/2020 & LA/P/0006/2020 and Shape of Water (PTDC/NAN-PRO/3881/2020) financed by Portuguese funds through the FCT/MEC (PIDDAC). F.E.M. acknowledges the funding received from the European Union's Horizon 2020 research and innovation program under the Marie Skłodowska-Curie grant agreement No. 823941 (FUNGLASS) and the financial support from the Foundation for Science and Technology (FCT) through the research grant UI/BD/151445/2021. A.G. is grateful for the post-doctoral support received from São Paulo Research Foundation (FAPESP) under grant 2021/06370-0. The NMR studies were supported by the Center of Research, Technology, and Education of Vitreous Materials (CeRTEV), funded by FAPESP, project number 2013/07793-6. D.M. acknowledges the Brazilian funding agency National Council for Scientific and Technological Development (CNPq, 405048/2021-1). H.E. acknowledges support by CNPq grants 310870/2020-8 and 422159/2018-2.

REFERENCES

(1) Cicconi, M. R.; Pili, E.; Grousset, L.; Florian, P.; Bouillard, J. C.; Vantelon, D.; Neuville, D. R. Iodine Solubility and Speciation in Glasses. *Sci. Rep.* **2019**, *9*, 7758.

(2) Laval, J.-P.; Duclère, J.-R.; Couderc, V.; Allix, M.; Genevois, C.; Sarou-Kanian, V.; Fayon, F.; Coulon, P.-E.; Chenu, S.; Colas, M.; Cornette, J.; Thomas, P.; Delaizir, G. Highly Transparent Fluorotellurite Glass-Ceramics: Structural Investigations and Luminescence Properties. *Inorg. Chem.* **2019**, *58*, 16387−16401.

(3) Yang, M.; Liu, X. J.; Ruan, H. H.; Wu, Y.; Wang, H.; Lu, Z. P. High Thermal Stability and Sluggish Crystallization Kinetics of High-Entropy Bulk Metallic Glasses. *J. Appl. Phys.* **2016**, *119*, 245112.

(4) Abdel-baki, M.; Mostafa, A. M.; Azooz, M. A.; Fayad, A. M. Magnesium Fluoride Borate Glasses for Low Phonon Energy. *J. Electron. Mater.* **2022**, *51*, 5042−5049.

(5) Zanotto, E. D.; Mauro, J. C. The Glassy State of Matter: Its Definition and Ultimate Fate. *J. Non-Cryst. Solids* **2017**, *471*, 490−495.

(6) Dejneka, M. J. Transparent Oxyfluoride Glass Ceramics. *MRS Bull.* **1998**, *23*, 57−62.

(7) Möncke, D.; Eckert, H. Review on the Structural Analysis of Fluoride-Phosphate and Fluoro-Phosphate Glasses. *J. Non-Crystalline Solids X* **2019**, *3*, No. 100026.

(8) Bogdanov, O. A.; Kolobkova, E. V.; Perevislov, S. N. Thermomechanical Properties and Structure of Fluorophosphate Glasses Activated with Nd^{3+} at Different Concentrations of $Ba(PO_3)_2$. *Glass Phys. Chem.* **2021**, *47*, 334−339.

(9) Galleani, G.; Khalil, A. A.; Canioni, L.; Dussauze, M.; Fargin, E.; Cardinal, T.; de Camargo, A. S. S. Fluorine and Sodium Depletion Followed by Refractive Index Modification Imprinted on Fluorophosphate Glass Surface by Thermal Poling. *J. Non-Cryst. Solids* **2023**, *601*, No. 122054.

(10) Rajagukguk, J.; Situmorang, R.; Fitrilawati; Djamal, M.; Rajaramakrishna, R.; Kaewkhao, J.; Minh, P. H. Structural, Spectroscopic and Optical Gain of Nd^{3+} Doped Fluorophosphate Glasses for Solid State Laser Application. *J. Lumin.* **2019**, *216*, No. 116738.

(11) Xiao, Y. B.; Ji, Y.; Liu, J. L.; Wang, W. C. Nd^{3+}-Doped Mixed-Anion Fluoro-Sulfo-Phosphate Glass for 1.06 μm Solid-State Laser. *J. Non-Cryst. Solids* **2019**, *522*, No. 119586.

(12) Bellanger, B.; Ledemi, Y.; Messaddeq, Y. Fluorophosphate Glasses with High Terbium Content for Magneto-Optical Applications. *J. Phys. Chem. C* **2020**, *124*, 5353−5362.

(13) Rao, V. R.; Basavapoornima, C.; Depuru, S. R.; Jayasankar, C. K. Energy Transfer and Red Fluorescence Properties of (Ce^{3+}/Eu^{3+}):Fluorophosphate Glasses for Lighting Applications. *J. Non-Cryst. Solids* **2020**, *549*, No. 120333.

(14) Jayachandra Prasad, T.; Neelima, G.; Ravi, N.; Kiran, N.; Nallabala, N. K. R.; Kummara, V. K.; Gadige, P. Optical and Spectroscopic Properties of Ho^{3+}-Doped Fluorophosphate Glasses for Visible Lighting Applications. *Mater. Res. Bull.* **2020**, *124*, No. 110753.

(15) Binnemans, K. Interpretation of Europium(III) Spectra. *Coord. Chem. Rev.* **2015**, *295*, 1−45.

(16) Bünzli, J.-C. G. Lanthanide Light for Biology and Medical Diagnosis. *J. Lumin.* **2016**, *170*, 866−878.

(17) Dramićanin, M. D. Sensing Temperature via Downshifting Emissions of Lanthanide-Doped Metal Oxides and Salts A Review. *Methods Appl. Fluoresc.* **2016**, *4*, No. 042001.

(18) Brites, C. D. S.; Lima, P. P.; Silva, N. J. O.; Millán, A.; Amaral, V. S.; Palacio, F.; Carlos, L. D. Thermometry at the Nanoscale. *Nanoscale* **2012**, *4*, 4799.

(19) Jaque, D.; Vetrone, F. Luminescence Nanothermometry. *Nanoscale* **2012**, *4*, 4301.

(20) Wang, X.; Wolfbeis, O. S.; Meier, R. J. Luminescent Probes and Sensors for Temperature. *Chem. Soc. Rev.* **2013**, *42*, 7834.

(21) Quintanilla, M.; Liz-Marzán, L. M. Guiding Rules for Selecting a Nanothermometer. *Nano Today* **2018**, *19*, 126−145.

(22) Back, M.; Ueda, J.; Nambu, H.; Fujita, M.; Yamamoto, A.; Yoshida, H.; Tanaka, H.; Brik, M. G.; Tanabe, S. Boltzmann

Thermometry in Cr^{3+}-Doped Ga_2O_3 Polymorphs: The Structure Matters! *Adv. Opt. Mater.* **2021**, *9*, No. 2100033.
(23) Marciniak, L.; Kniec, K.; Elżbieciak-Piecka, K.; Trejgis, K.; Stefanska, J.; Dramićanin, M. Luminescence Thermometry with Transition Metal Ions A Review. *Coord. Chem. Rev.* **2022**, *469*, No. 214671.
(24) Bednarkiewicz, A.; Marciniak, L.; Carlos, L. D.; Jaque, D. Standardizing Luminescence Nanothermometry for Biomedical Applications. *Nanoscale* **2020**, *12*, 14405−14421.
(25) Brites, C. D. S.; Balabhadra, S.; Carlos, L. D. Lanthanide-Based Thermometers: At the Cutting-Edge of Luminescence Thermometry. *Adv. Opt. Mater.* **2019**, *7*, No. 1801239.
(26) Piñol, R.; Zeler, J.; Brites, C. D. S.; Gu, Y.; Téllez, P.; Carneiro Neto, A. N.; da Silva, T. E.; Moreno-Loshuertos, R.; Fernandez-Silva, P.; Gallego, A. I.; Martinez-Lostao, L.; Martínez, A.; Carlos, L. D.; Millán, A. Real-Time Intracellular Temperature Imaging Using Lanthanide-Bearing Polymeric Micelles. *Nano Lett.* **2020**, *20*, 6466−6472.
(27) Shen, Y.; Santos, H. D. A.; Ximendes, E. C.; Lifante, J.; Sanz-Portilla, A.; Monge, L.; Fernández, N.; Chaves-Coira, I.; Jacinto, C.; Brites, C. D. S.; Carlos, L. D.; Benayas, A.; Iglesias-de la Cruz, M. C.; Jaque, D. Ag_2S Nanoheaters with Multiparameter Sensing for Reliable Thermal Feedback during In Vivo Tumor Therapy. *Adv. Funct. Mater.* **2020**, *30*, No. 2002730.
(28) van Swieten, T. P.; van Omme, T.; van den Heuvel, D. J.; Vonk, S. J. W.; Spruit, R. G.; Meirer, F.; Garza, H. H. P.; Weckhuysen, B. M.; Meijerink, A.; Rabouw, F. T.; Geitenbeek, R. G. Mapping Elevated Temperatures with a Micrometer Resolution Using the Luminescence of Chemically Stable Upconversion Nanoparticles. *ACS Appl. Nano Mater.* **2021**, *4*, 4208−4215.
(29) Zhou, J.; del Rosal, B.; Jaque, D.; Uchiyama, S.; Jin, D. Advances and Challenges for Fluorescence Nanothermometry. *Nat. Methods* **2020**, *17*, 967−980.
(30) Shen, Y.; Lifante, J.; Zabala-Gutierrez, I.; Fuente-Fernández, M.; Granado, M.; Fernández, N.; Rubio-Retama, J.; Jaque, D.; Marin, R.; Ximendes, E.; Benayas, A. Reliable and Remote Monitoring of Absolute Temperature during Liver Inflammation via Luminescence-Lifetime-Based Nanothermometry. *Adv. Mater.* **2022**, *34*, No. 2107764.
(31) Fellmuth, B.; Fischer, J.; Machin, G.; Picard, S.; Steur, P. P. M.; Tamura, O.; White, D. R.; Yoon, H. The Kelvin Redefinition and Its Mise En Pratique. *Philos. Trans. R. Soc. A: Math. Phys. Eng. Sci.* **2016**, *374*, No. 20150037.
(32) Martins, J. C.; Brites, C. D. S.; Carneiro Neto, A. N.; Ferreira, R. A. S.; Carlos, L. D. An Overview of Luminescent Primary Thermometers. In *Luminescent Thermometry*; Martí, J. J. C.; Baiges, M. C. P., Eds.; Springer Nature, 2023; pp 1−48.
(33) Gullion, T.; Schaefer, J. Rotational-Echo Double-Resonance NMR. *J. Magn. Reson.* **1989**, *81*, 196−200.
(34) Echelmeyer, T.; van Wüllen, L.; Wegner, S. A New Application for an Old Concept: Constant Time (CT)-REDOR for an Accurate Determination of Second Moments in Multiple Spin Systems with Strong Heteronuclear Dipolar Couplings. *Solid State Nucl. Magn. Reson.* **2008**, *34*, 14−19.
(35) Aue, W. P.; Karhan, J.; Ernst, R. R. Homonuclear Broad Band Decoupling and Two-dimensional J-resolved NMR Spectroscopy. *J. Chem. Phys.* **1976**, *64*, 4226−4227.
(36) van Meerten, S. G. J.; Franssen, W. M. J.; Kentgens, A. P. M. SsNake: A Cross-Platform Open-Source NMR Data Processing and Fitting Application. *J. Magn. Reson.* **2019**, *301*, 56−66.
(37) Bak, M.; Rasmussen, J. T.; Nielsen, N. C. SIMPSON: A General Simulation Program for Solid-State NMR Spectroscopy. *J. Magn. Reson.* **2000**, *147*, 296−330.
(38) Eckert, H.; Meise-Gresch, K.; Anderson, S. E.; Saiki, D. A Solid-State NMR Experiment: Analysis of Local Structural Environments in Phosphate Glasses. *J. Chem. Educ.* **2004**, *81*, 1034−1037.
(39) Karraker, D. G. Coordination of Trivalent Lanthanide Ions. *J. Chem. Educ.* **1970**, *47*, 424.
(40) Hoppe, U.; Brow, R. K.; Ilieva, D.; Jóvári, P.; Hannon, A. C. Structure of Rare-Earth Phosphate Glasses by X-Ray and Neutron Diffraction. *J. Non-Cryst. Solids* **2005**, *351*, 3179−3190.
(41) Czjzek, G.; Fink, J.; Götz, F.; Schmidt, H.; Coey, J. M. D.; Rebouillat, J.-P.; Liénard, A. Atomic Coordination and the Distribution of Electric Field Gradients in Amorphous Solids. *Phys. Rev. B* **1981**, *23*, 2513−2530.
(42) Manzani, D.; Pabœuf, D.; Ribeiro, S. J. L.; Goldner, P.; Bretenaker, F. Orange Emission in Pr^{3+}-Doped Fluoroindate Glasses. *Opt. Mater.* **2013**, *35*, 383−386.
(43) Borrero-González, L. J.; Galleani, G.; Manzani, D.; Nunes, L. A. O.; Ribeiro, S. J. L. Visible to Infrared Energy Conversion in Pr^{3+}−Yb^{3+} Co-Doped Fluoroindate Glasses. *Opt. Mater.* **2013**, *35*, 2085−2089.
(44) Van Wijngaarden, J. T.; Scheidelaar, S.; Vlugt, T. J. H.; Reid, M. F.; Meijerink, A. Energy Transfer Mechanism for Downconversion in the (Pr^{3+}, Yb^{3+}) Couple. *Phys. Rev. B: Condens. Matter Mater. Phys.* **2010**, *81*, No. 155112.
(45) van der Ende, B. M.; Aarts, L.; Meijerink, A. Near-Infrared Quantum Cutting for Photovoltaics. *Adv. Mater.* **2009**, *21*, 3073−3077.
(46) Lozano B, W.; De Araújo, C. B.; Egalon, C.; Gomes, A. S. L.; Costa, B. J.; Messaddeq, Y Upconversion of Infrared-to-Visible Light in Pr^{3+}−Yb^{3+} Codoped Fluoroindate Glass. *Opt. Commun.* **1998**, *153*, 271−274.
(47) Seshadri, M.; Bell, M. J. V.; Anjos, V.; Messaddeq, Y. Spectroscopic Investigations on Yb^{3+} Doped and Pr^{3+}/Yb^{3+} Codoped Tellurite Glasses for Photonic Applications. *J. Rare Earths* **2021**, *39*, 33−42.
(48) Suta, M.; Meijerink, A. A Theoretical Framework for Ratiometric Single Ion Luminescent Thermometers—Thermodynamic and Kinetic Guidelines for Optimized Performance. *Adv. Theory Simul.* **2020**, *3*, No. 2000176.
(49) Suta, M.; Antić, Ž.; Đorđević, V.; Kuzman, S.; Dramićanin, M. D.; Meijerink, A. Making Nd^{3+} a Sensitive Luminescent Thermometer for Physiological Temperatures—An Account of Pitfalls in Boltzmann Thermometry. *Nanomaterials* **2020**, *10*, 543.
(50) Martins, J. C.; Bastos, A. R. N.; Ferreira, R. A. S.; Wang, X.; Chen, G.; Carlos, L. D. Primary Luminescent Nanothermometers for Temperature Measurements Reliability Assessment. *Adv. Photon. Res.* **2021**, *2*, No. 2000169.
(51) Balabhadra, S.; Debasu, M. L.; Brites, C. D. S.; Ferreira, R. A. S.; Carlos, L. D. Upconverting Nanoparticles Working As Primary Thermometers In Different Media. *J. Phys. Chem. C* **2017**, *121*, 13962−13968.
(52) Rai, V. K.; Rai, D. K.; Rai, S. B. Pr^{3+} Doped Lithium Tellurite Glass as a Temperature Sensor. *Sens. Actuators, A* **2006**, *128*, 14−17.
(53) Rai, V. K.; Rai, S. B. A Comparative Study of FIR and FL Based Temperature Sensing Schemes: An Example of Pr^{3+}. *Appl. Phys. B: Lasers Opt.* **2007**, *87*, 323−325.
(54) Pudovkin, M. S.; Morozov, O. A.; Pavlov, V. V.; Korableva, S. L.; Lukinova, E. V.; Osin, Y. N.; Evtugyn, V. G.; Safiullin, R. A.; Semashko, V. V. Physical Background for Luminescence Thermometry Sensors Based on Pr^{3+}:LaF_3 Crystalline Particles. *J. Nanomater.* **2017**, *2017*, No. 3108586.
(55) Pudovkin, M. S.; Kuznetsov, S. V.; Proydakova, V. Y.; Voronov, V. V.; Semashko, V. V. Luminescent Thermometry Based on $Ba_4Y_3F_{17}$:Pr^{3+} and $Ba_4Y_3F_{17}$:Pr^{3+},Yb^{3+} Nanoparticles. *Ceram. Int.* **2020**, *46*, 11658−11666.

NOTE ADDED AFTER ASAP PUBLICATION

This paper was published ASAP on August 2, 2023, with an incorrect equation in equation 2. The corrected version was reposted August 4, 2023.

https://doi.org/10.1021/acs.chemmater.3c01508
Chem. Mater. 2023, 35, 7229−7238

SUPPORTING INFORMATION

Extending the palette of luminescent primary thermometers: Yb^{3+}/Pr^{3+} co-doped fluoride phosphate glasses

Fernando E. Maturi[1,2], Anuraag Gaddam[3], Carlos D. S. Brites[1], Joacilia M. M. Souza[4], Hellmut Eckert[3], Sidney J. L. Ribeiro[2], Luís D. Carlos[1], Danilo Manzani[4*]*

[1]Phantom-g, CICECO - Aveiro Institute of Materials, Department of Physics, University of Aveiro, 3810-193 Aveiro, Portugal
[2]Institute of Chemistry, São Paulo State University (UNESP), 14800-060 Araraquara, SP, Brazil
[3]São Carlos Institute of Physics, University of São Paulo, IFSC-USP, 13566-590 São Carlos, SP, Brazil
[4]São Carlos Institute of Chemistry, University of São Paulo, IQSC-USP, 13560-970 São Carlos, SP, Brazil

*Corresponding authors: lcarlos@ua.pt and dmanzani@usp.br

Table of Contents

S1. Supplementary text

S1.1. Preparation and characterization of the fluoride phosphate glasses

Fluoride phosphate glasses were prepared in batches of 5 g by weighing the raw materials described in **Table S1**, followed by their thorough homogenization in an agate mortar, loading the resulting powder mixture into a platinum crucible, which was covered for melting. The glass samples were obtained by melting the precursors at 1373 K for 30 min to ensure homogenization, cast into a stainless-steel mold pre-heated at 563 K, and annealed at the same temperature for 3 h before cooling it slowly to room temperature. The bulk samples were cut into equal pieces of 1 cm^2 and optically polished with parallel faces and the same thickness (2 mm) for further optical characterizations. The characteristic temperatures, relative absorption strengths, and absolute emission quantum yields of the obtained fluoride phosphate glasses are summarized in **Table S2**, **Table S3**, and **Table S4**, respectively.

S1.2. Solid-state NMR structural studies

The one-dimensional (1D) ^{31}P experiments were recorded using single-pulse acquisition with a $\pi/2$ pulse length of 3.05 μs. Relaxation delays of 900, 10, and 5 s were used for samples PY00, PY14, and PY18, respectively. The ^{31}P chemical shifts were referenced with respect to BPO_4 at −29.3 ppm *versus* 85% H_3PO_4. Two-dimensional ^{31}P J-resolved NMR spectra were measured in a 3.2 mm probe spinning at 10.0 kHz, using π and $\pi/2$ pulses of 3.0 μs and 6.0 μs length, and a relaxation delay of 80 s, following a pre-saturation pulse train. Rotor synchronized echoes were recorded up to an evolution time of 31 ms. Data were acquired using a 32-step phase cycle. ^{31}P refocused (R-) incredible natural abundance double quantum transfer experiment (INADEQUATE) experiments[1] were conducted on a 600 MHz NMR spectrometer (Avance Neo 600, Bruker) operating at 14.1 T, using a 2.5 mm probe with MAS rate of 15.0 kHz. The $\pi/2$ pulse length and recycle delay were 1.825 μs and 60 s, respectively. A single mixing time (2τ) of 8.33 ms, corresponding to a ^{31}P–^{31}P J-coupling constant of 30.0 Hz, was employed. Under the same conditions (pulse length, recycle delay, MAS rate, etc.), a 1D spectrum was recorded for comparison.

The ^{19}F 1D MAS-NMR experiments were recorded using a rotor-synchronized Hahn echo sequence (2 rotor cycles) with a $\pi/2$ pulse length of 3.8 μs. The relaxation delays were 60 s (PY00) and 1 s (PY14 and PY18). The ^{19}F chemical shifts were referenced with respect to NaF at −224

ppm *versus* $CFCl_3$.[2] For $^{31}P\{^{19}F\}$ REDOR, the π/2 and π pulse lengths were 3.05 and 6.10 μs, respectively. The dipolar recoupling π pulse lengths on ^{19}F were 7.90 μs, as optimized on Na_2PO_3F. Before the π/2 excitation pulse on ^{31}P, a saturation pulse train was applied to establish reproducible stationary magnetization conditions, and relaxation delays of 5 s (PY18), 60 s (Na_2PO_3F), and 120 s (PY00) were used. ^{7}Li MAS-NMR spectra were recorded with π/8 pulses of 0.70 μs length as determined using a LiCl solution (1.00 mol L^{-1}). The relaxation delays were 30 s (PY00), 3 s (PY14), and 2 s (PY18). The ^{7}Li chemical shifts were referenced with respect to a LiCl solution (1.00 mol L^{-1}) at 0 ppm.

Since these glasses are prone to F volatilization, the amount of F loss was quantified using a ^{19}F NMR Hahn-Echo sequence. Known quantities of the samples and NaF were ground together and packed in a rotor. To correct potential errors due to different spin-spin relaxation times, the spectra were measured with 2, 4, 6, and 8 rotor cycles. The ratios of the signal intensities were back-extrapolated to 0 rotor cycles. From this ratio, the amount of F in each sample was calculated. The ^{6}Li MAS-NMR spectra were recorded using a Hahn echo sequence with a π/2 and π pulse lengths of 6.2 and 12.4 μs (optimized on a glassy $LiPO_3$ sample), using a 3.2 mm XY probe, operated at a spinning speed of 15.0 kHz. Relaxation delays were 60, 6, and 6 s, for samples PY00, PY14, and PY18, respectively. The ^{6}Li chemical shifts were referenced to the LiCl solution (1.00 mol L^{-1}) at 0 ppm. All spectra were analyzed using ssNake[3] and/or SIMPSON[4] software.

The $^{6}Li\{^{31}P\}$ REDOR measurements on the undoped sample were done on the same probe, using the Schaefer-Gullion sequence.[5] The pulse lengths were optimized using glassy $LiPO_3$. The π/2 and π pulse lengths on ^{6}Li were 6.2 and 12.4 μs, respectively. The dipolar recoupling pulse lengths on ^{31}P were 13.0 μs. Before the π/2 excitation pulse on ^{6}Li, a saturation pulse train was applied, and the REDOR experiments were conducted with relaxation delays of 60 s (PY00). Following previously published procedures, the data were analyzed in terms of the approximate equation:[6]

$$\frac{\Delta S}{S_0} = \frac{S_0 - S}{S_0} = f\frac{4}{3\pi^2}M_{2(Li-P)}(n\tau_r)^2 \qquad \textbf{(S1)}$$

to yield a dipolar second moment $M_{2(\mathrm{Li–P})}$ characterizing the average square of the strength of the magnetic dipole-dipole coupling between the observed nucleus ^{6}Li and the heteronuclear ^{31}P, with $\Delta S/S_0$ corresponding to the normalized signal intensity in the presence (intensity S) and the absence (intensity S_0) of the recoupling pulses. This approximate expression holds in the limit of short

mixing times, where $\Delta S/S_0 \leq 0.2$. Here $n\tau_r$, the number of rotor cycles times the rotor period, defines the dipolar mixing time applied in the experiment and f is a scaling factor obtained by comparing the experimental M_2 value with that of a crystalline reference compound (which can be calculated from the internuclear distances in the crystal structure). It is important that the reference compound presents similar spin dynamics as the glasses and that the data on the glasses and reference compound are measured under identical conditions. As in the present case, no reference compound was available, only the raw data obtained on the two glasses were compared (*i.e.*, we assumed $f = 1$). Static ^{31}P spin echo decay data were measured on an NMR spectrometer system (Avance III Neo, Bruker) operating at a magnetic field strength of 9.4 T, using the Hahn echo sequence $\pi/2$-t_1-π-t_1. The $\pi/2$ and π pulse lengths were 8.3 and 16.6 ms, and a relaxation delay of 300 s was used. The data were analyzed in terms of a Gaussian decay:[7]

$$\frac{I}{I_0} = \exp\left\{-\frac{1}{2}M_{2(P-P)}(2t_1)^2\right\} \quad \textbf{(S2)}$$

yielding the dipolar second moment $M_{2(P–P)}$ as a measure of the average squared strength of the internuclear magnetic dipole-dipole coupling. For a semi-quantitative interpretation of the second moment values $M_{2(Li–P)}$ and $M_{2(P–P)}$, Monte Carlo calculations of random atomic arrangements in space were conducted by randomly generating Li, P, and F atoms in a cubic box, with interatomic cutoff distances based on crystalline materials at concentrations based on density measurements. The periodic boundary conditions were assumed throughout. Then the $M_{2(A–B)}$ values were calculated using:

$$M_{2(A-B)} = \frac{4}{15}\left(\frac{\mu_0}{4\pi}\right)^2 \gamma_A^2\gamma_B^2\hbar^2 S(S+1)\frac{1}{N_A}\sum_{i=1}^{N_A}\sum_{j=1}^{N_B}\frac{1}{r_{ij}^6} \quad \textbf{(S3)}$$

The prefactor of 4/15 was assumed for both homo- and heteronuclear cases, as the spin-exchange (“flip-flop”) term of the homonuclear dipolar Hamiltonian can be considered quenched in glasses where a wide dispersion of resonance frequencies leads to a low probability that nuclei in the proximity of each other have identical resonance frequencies. The parameters γ, $\hbar$, S, r_{ij}, N_A, N_B are gyromagnetic ratios, Dirac constant, nuclear spin quantum number of the nuclei the observed spins are interacting with, internuclear distances, number of observed and unobserved nuclei, respectively. In addition, molecular dynamics (MD) simulations of $LiPO_3$ glass were

carried out, using the LAMMPs code[8] with the potentials developed by Pedone *et al*.[9] The exact details and the parameters used to perform these simulations are presented in the following section.

S1.2.1 Molecular dynamics simulations

Molecular dynamics (MD) simulations were carried out using Pedone Potentials.[9] The potential parameters bond dissociation energy (D_{ij}), the function of the slope of the potential energy well (a_{ij}), and equilibrium bond distance (r_0) for Li–O, P–O, and O–O atomic pair interactions are displayed in **Table S5**. To evaluate long-range Coulomb interactions, we utilized the Ewald sum method with a strength precision of 10–5 and a 12 Å cutoff. Our simulation employed the Verlet velocity algorithm to integrate Newton's equations of motion with a simulation time interval of 1 fs. We controlled the temperature and pressure using a Nosé-Hoover thermostat and a barostat every 100 steps. Additionally, we employed periodic boundary conditions in all three dimensions throughout the simulation, which involved 10,000 atoms initially distributed randomly in a cubic simulation box with dimensions corresponding to the experimental density of the $LiPO_3$ glass (2.34 g cm^{-3}). After minimizing the energy, we heated the glasses from 300 to 5000 K at a rate of 100 K ps^{-1} using the canonical NVT ensemble (Evans thermostat). The sample was held at the melting temperature of 5000 K for 100 ps under the NVT ensemble, then cooled to 300 K at rates of 5 K ps^{-1} under NVT conditions and annealed at 300 K for 100 ps under NVT and 100 ps under NPT. Finally, we analyzed the obtained structures using a laboratory-developed code to calculate the pair distribution functions, the second dipole-dipole moments, and spin echo decay (SED) curves.

S1.3. Energy gap determination of thermally-coupled levels of Pr^{3+}

The areas, peak energies, and widths of the emission bands corresponding to the $^3P_1 \rightarrow {}^3H_5$ and $^3P_0 \rightarrow {}^3H_5$ transitions of Pr^{3+} were calculated from the deconvolution of the emission spectra of the glass samples under 443 nm excitation at room temperature by using a custom script written in MATLAB 2022a under the license provided to the University of Aveiro. In the first step, a polynomial baseline correction was performed to remove the electric noise from the spectrofluorometer signal, followed by the conversion of the emission spectrum from wavelength (nm) to energy (cm^{-1}) units by applying the Jacobian conversion.[10,11] The second step consisted of adjusting 5 Gaussian functions to the energy-converted emission spectra between the 17700–

19600 cm^{-1} spectral range, which is the minimum number of Gaussian functions required to get a good fit ($r^2 > 0.998$ for both samples). In the final step, the barycenters of $^3P_1 \rightarrow {}^3H_5$ and $^3P_0 \rightarrow {}^3H_5$ transitions of Pr^{3+} were computed as their weighted arithmetic means by using the areas and peak energies retrieved from the abovementioned spectral Gaussian deconvolution using the emission spectra of the samples measured at room temperature. The value of ΔE corresponds to the difference between the barycenters of the emission bands assigned to the $^3P_1 \rightarrow {}^3H_5$ (I_2, two Gaussian functions) and $^3P_0 \rightarrow {}^3H_5$ (I_1, three Gaussian functions) transitions of Pr^{3+}, as shown in **Figure S1**. The uncertainty in ΔE ($\delta\Delta E$) was calculated by propagating the uncertainty in ΔE, taking into account the uncertainties of the areas and peak energies of each Gaussian component.

S1.4. Relative thermal sensitivity and uncertainty in temperature

The absolute sensitivity $\left(S_a = \frac{\partial \Delta}{\partial T}\right)$ indicates how much a given thermometric parameter Δ changes by increasing one unit of temperature. Although S_a is a good measure of the temperature dependence of Δ, S_a values of different materials cannot be compared because it is an intrinsic response of the temperature-dependent luminescence of each material. Therefore, the relative thermal sensitivity $\left(S_r = \frac{1}{\Delta}\left|\frac{\partial \Delta}{\partial T}\right| = \frac{|S_a|}{\Delta}\right)$ was introduced as a figure of merit to perform quantitative comparisons between different materials, which is the absolute value of S_a normalized by the magnitude of Δ, usually presented in units of percentage change per unit of temperature change (% K^{-1} or % $°C^{-1}$).

Once the thermometric parameter Δ describing the emission arising from the thermally coupled levels of Pr^{3+} is given by the Boltzmann distribution (Equation 1 of the manuscript), S_r assumes the following form for a Boltzmann-based primary thermometer:

$$S_r = \frac{\left|\frac{d}{dT}\left(B\exp\left(-\frac{\Delta E}{k_B T}\right)\right)\right|}{B\exp\left(-\frac{\Delta E}{k_B T}\right)} = \frac{\left|\frac{\Delta E}{k_B T^2} B\exp\left(-\frac{\Delta E}{k_B T}\right)\right|}{B\exp\left(-\frac{\Delta E}{k_B T}\right)} = \frac{\Delta E}{k_B T^2} \quad \textbf{(S1)}$$

where S_r depends on the energy gap ΔE between the $^3P_1$ and $^3P_0$ emitting levels of Pr^{3+} and the temperature T of the medium. Once ΔE is nearly constant in the temperature range studied in this work, S_r gives higher values for lower temperatures. Nonetheless, we herein report the values of S_r at room temperature (T_0) to make it more suitable for comparisons to the values previously reported in the literature.

The uncertainty in temperature $\left(\delta T = \frac{1}{S_r}\frac{\delta\Delta}{\Delta}\right)$ is another figure of merit used to assess the reliability of the temperature accuracy of luminescent thermometers. Here, δT represents the smallest temperature that can be resolved by the luminescent thermometer while $\delta\Delta/\Delta$ corresponds to the relative uncertainty of the thermometric parameter Δ, which is given by:

$$\frac{\delta\Delta}{\Delta} = \sqrt{\left(\frac{\delta I_2}{I_2}\right)^2 + \left(\frac{\delta I_1}{I_1}\right)^2} \qquad \textbf{(S2)}$$

where δI_2 and δI_1 are the uncertainties in the integrated intensities I_2 and I_1, respectively, estimated by dividing the readout fluctuations of the baseline by the maximum intensity value. Both samples presented a $\delta\Delta/\Delta$ of 0.49%, corresponding to a signal-to-noise ratio (SNR) of 204. **Table S6** displays the parameters used to perform primary thermal sensing based on the downshifting emission of Pr^{3+} and their corresponding values of S_r and δT.

S2. Supplementary figures

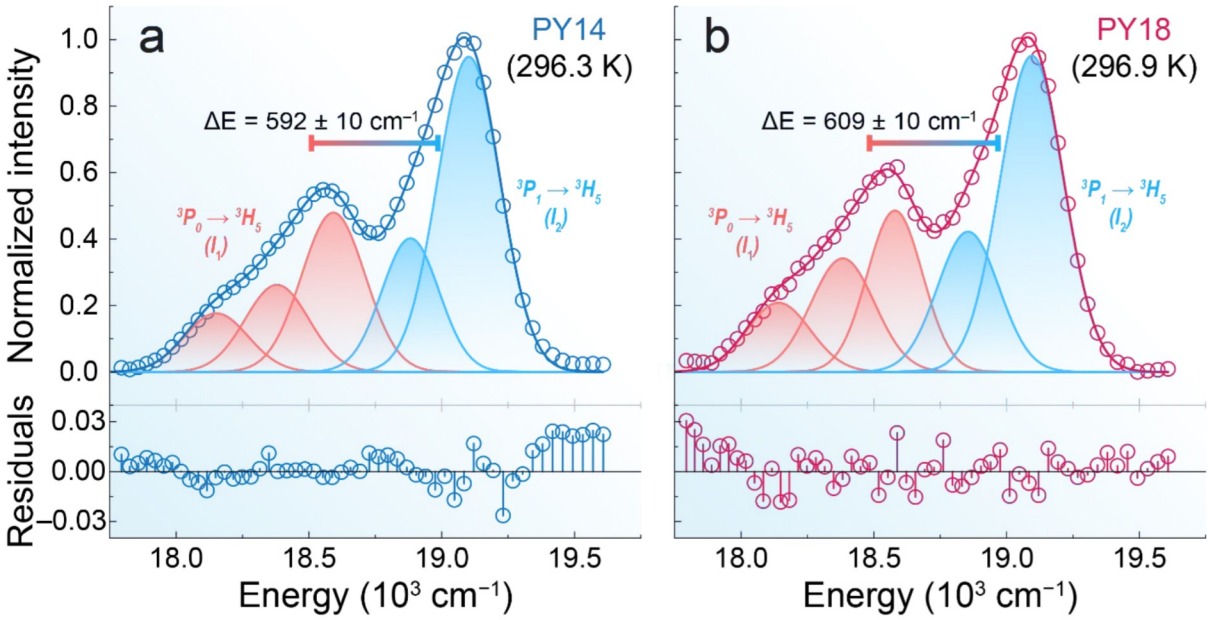

Figure S1. Spectral deconvolution of the emission spectra of samples **(a)** PY14 and **(b)** PY18 measured under excitation at 443 nm. The symbols and the solid darker lines are the emission spectra and the fit envelope, respectively. The Gaussian functions in light red and light blue arise from the $^3P_0 \rightarrow {}^3H_5$ (I_1, three components) and $^3P_1 \rightarrow {}^3H_5$ (I_2, two components) transitions of Pr^{3+}, respectively.

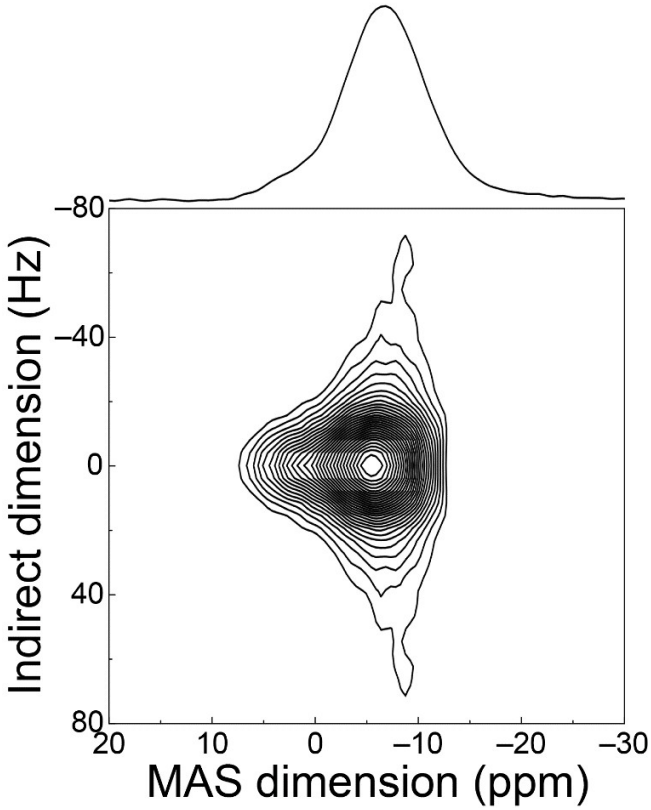

Figure S2. ^{31}P 2D J-resolved MAS-NMR spectrum of the PY00 sample. The spectrum projected on the top part of the figure was taken at an indirect dimension of 0 Hz.

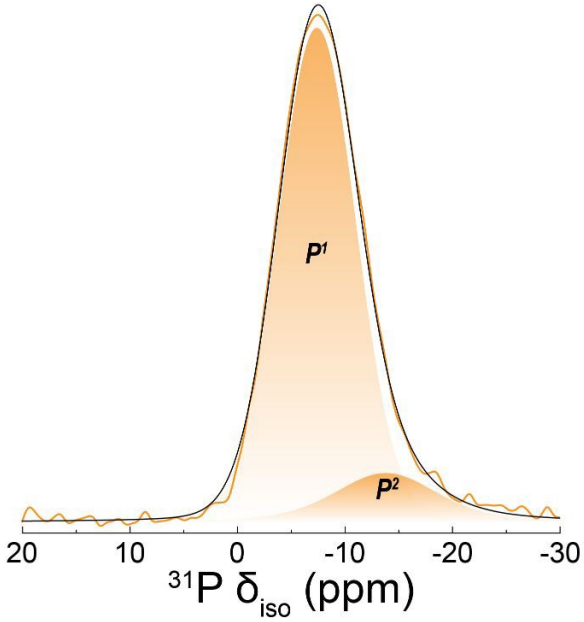

Figure S3. ^{31}P R-INADEQUATE data of the PY00 sample. The solid orange line is the obtained signal, the shadowed areas correspond to the phosphate units, and the dashed black line is the fitted curve.

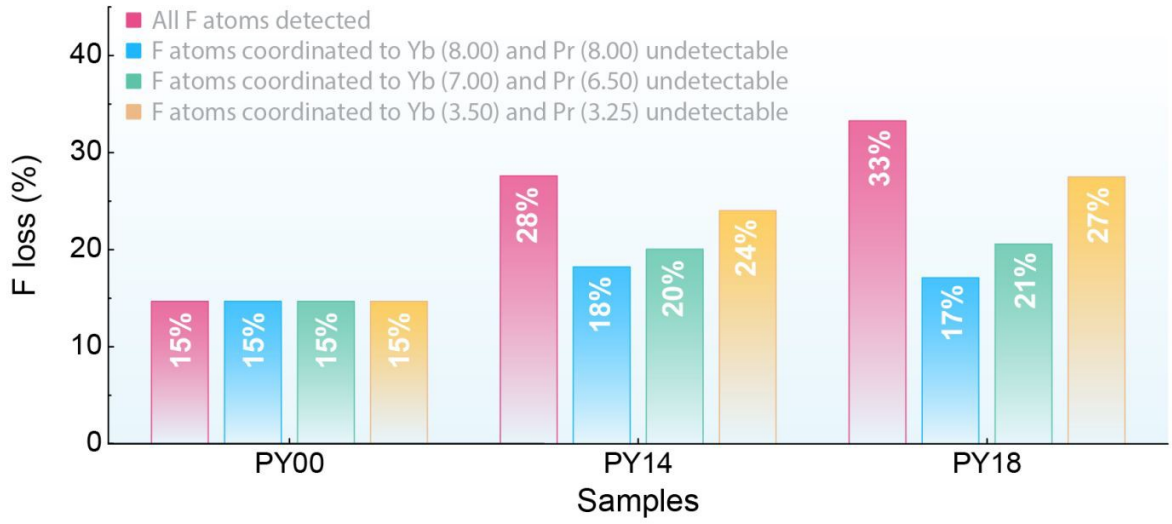

Figure S4. Fluorine (F) loss estimated by ^{19}F MAS-NMR. The results shown in pink are the uncorrected loss values where all F atoms are detected. The results in blue, green, and yellow display the corrected loss values when considering that only a few F atoms are detected due to the coordination to Pr^{3+}/Yb^{3+} with coordination numbers of 8.00/8.00 in crystalline fluoride, 7.00/6.50 in vitreous fluoride-only, and 3.50/3.25 in mixed vitreous fluoride phosphate environments, respectively. The mean corrected F loss values are presented in Figure 2b of the manuscript, taking into account the data from these three distinct coordination scenarios.

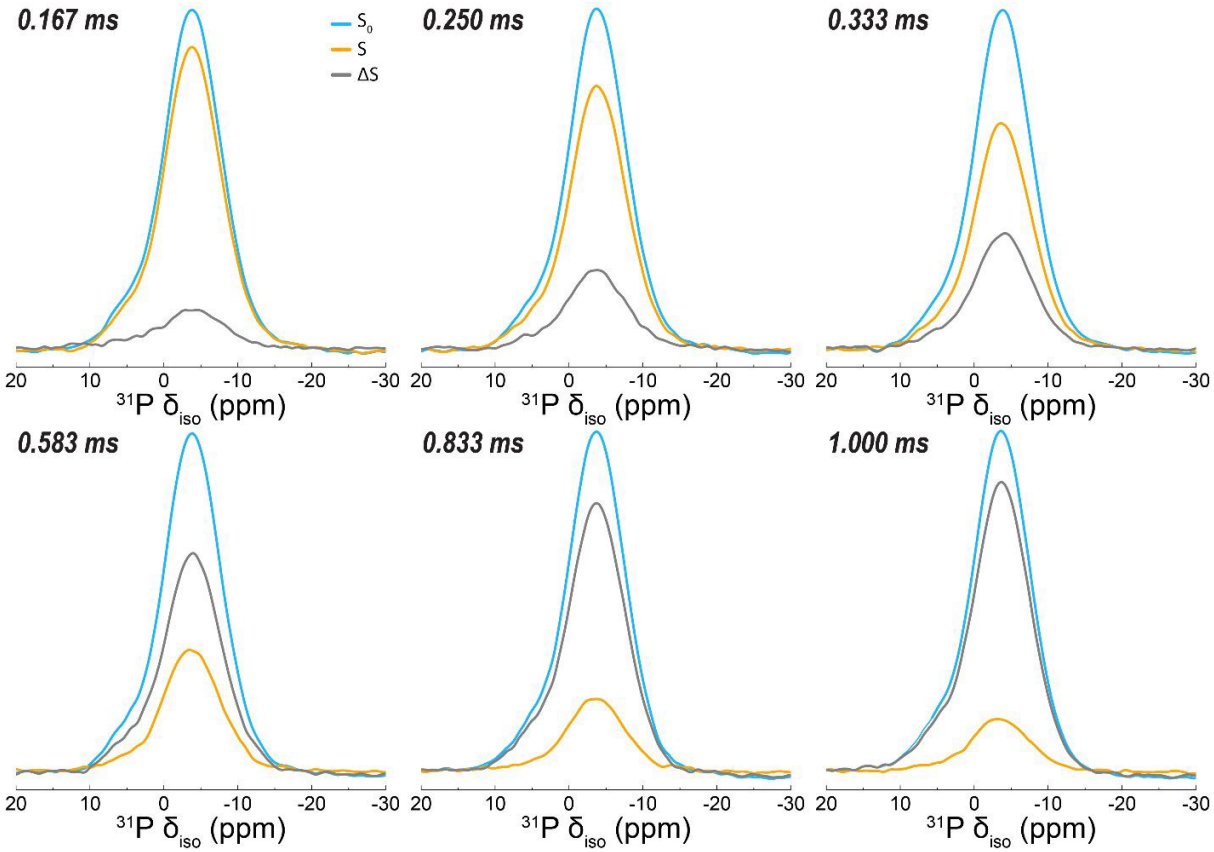

Figure S5. Fourier transforms of the $^{31}P\{^{19}F\}$ REDOR data (yellow curves) and the corresponding REDOR difference signal ($\Delta S = S_0 - S$, gray curves) for a dipolar mixing time between 0.167 and 1.000 ms. The reference signal S_0 is shown in blue. The chemical shifts of both signals are identical within the experimental uncertainty, arguing against a significant contribution from the F-bonded P species.

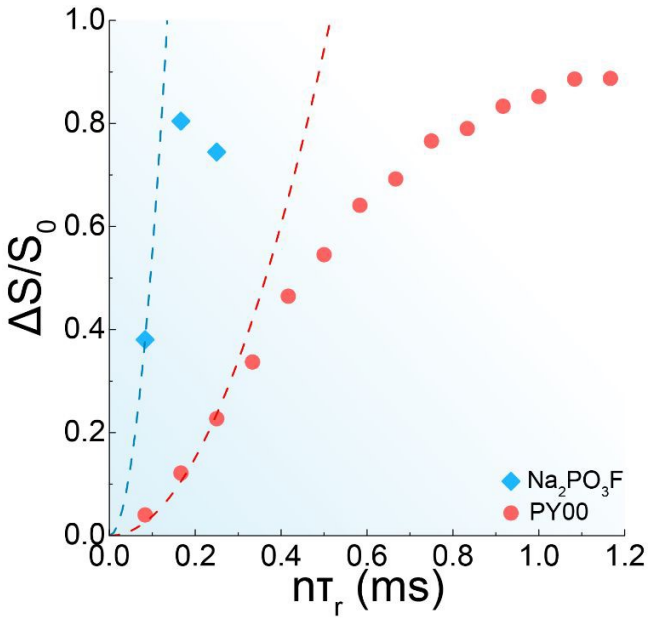

Figure S6. $^{31}P\{^{19}F\}$ REDOR dephasing curves displaying the normalized signal intensity as a function of the dephasing time $n\tau_r$ for the sample PY00 and the model compound Na_2PO_3F. The solid symbols are the experimental results while the dashed lines are the parabolic approximation in the initial regime of the obtained data ($\Delta S/S_0 \leq 0.2$) given by **Equation S1**, resulting in an uncorrected value of $M_{2(P-F)}$ of 28 Mrad^2 s^{-2}. Measurements were carried out at 5.7 T and a spinning frequency of 24.0 kHz.

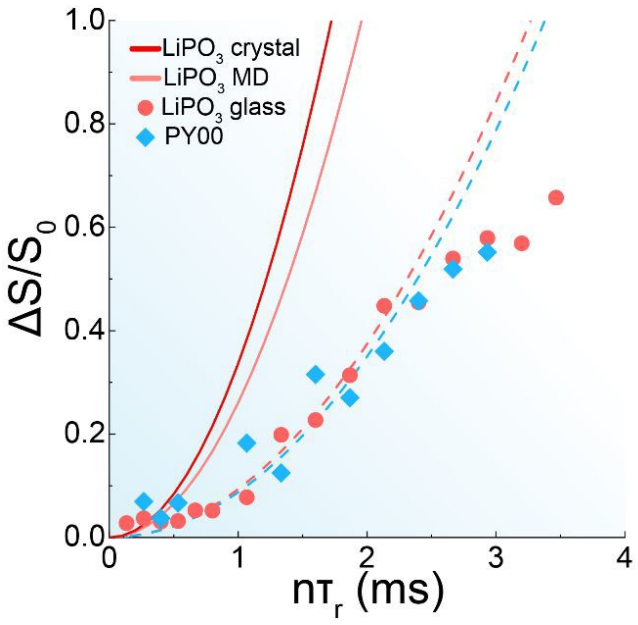

Figure S7. $^{6}Li\{^{31}P\}$ REDOR curves measured for PY00 (diamonds) and $LiPO_3$ glass (circles). Dashed curves indicate fits of the data to Equation S1, while solid curves indicate the expected REDOR behavior for crystalline $LiPO_3$ (dipolar coupling based on the internuclear distances in the crystal structure) and an MD simulation output for $LiPO_3$ glass. The deviation of the experimental data of $LiPO_3$ glass and the parabola calculated from the MD output suggests a calibration factor of 0.33.

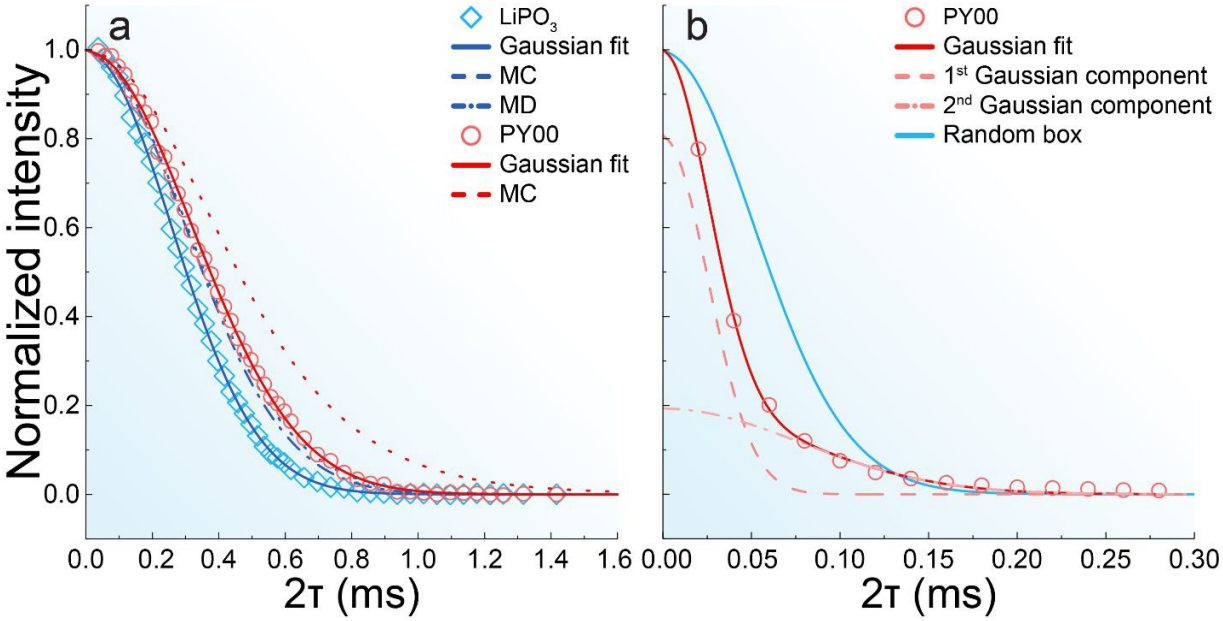

Figure S8. (a) Static ^{31}P SED curves of glasses PY00 (red) and $LiPO_3$ (blue). Solid curves show the fits to **Equation S2**, yielding $M_{2(P-P)}$ values of 9.9 Mrad^2 s^{-2} and 15.2 Mrad^2 s^{-2}, respectively. The dashed and dotted lines are simulated SED curves from MD and Monte Carlo (MC) simulations. **(b)** Static ^{19}F SED curves of the sample PY00.

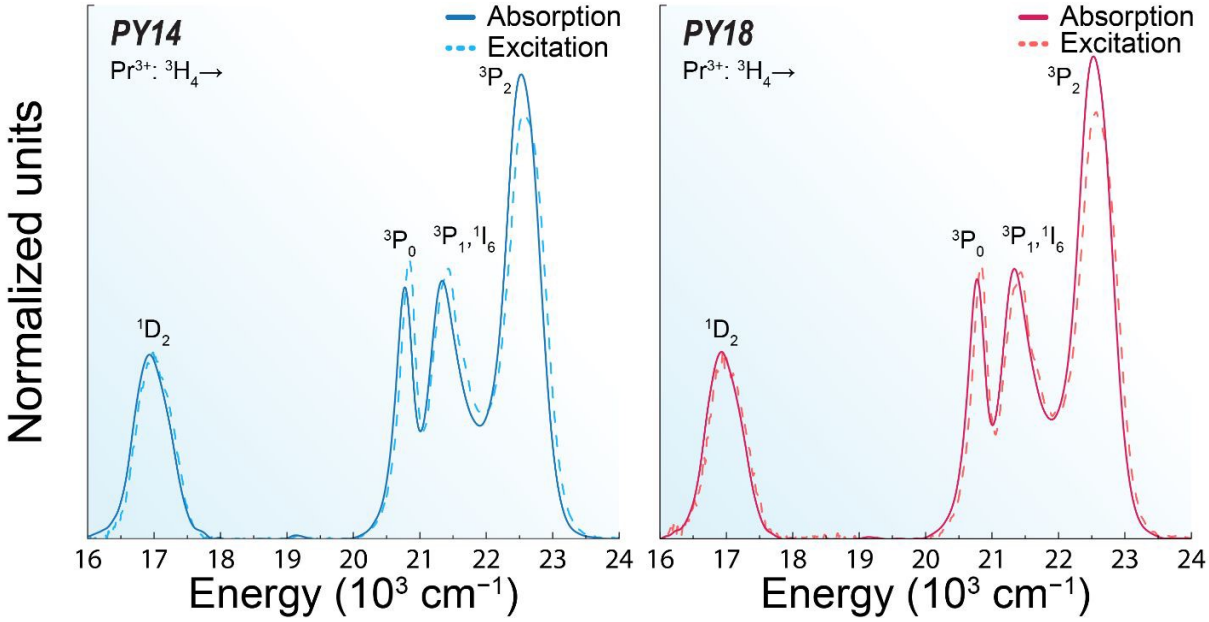

Figure S9. Absorption (solid curves) and excitation (dashed curves) spectra for the PY14 and PY18 samples measured at room temperature. The excitation spectra were recorded by monitoring the emission of Yb^{3+} at 979 nm. All the data were converted from wavelength to energy units by using the Jacobian conversion and then normalized at the $^3H_4 \rightarrow {}^1D_2$ peak for comparison purposes.

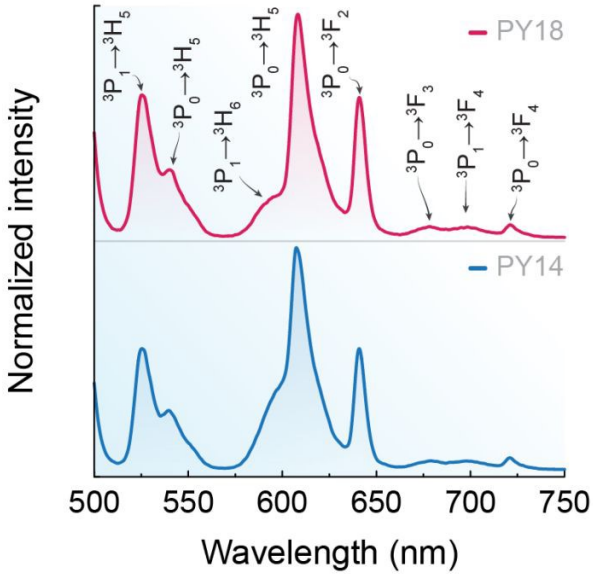

Figure S10. Upconversion emission spectra of the samples PY14 (bottom) and PY18 (top) spectra for the PY14 and PY18 samples measured at room temperature under continuous wave laser excitation at 980 nm (150 W cm^{-2}).

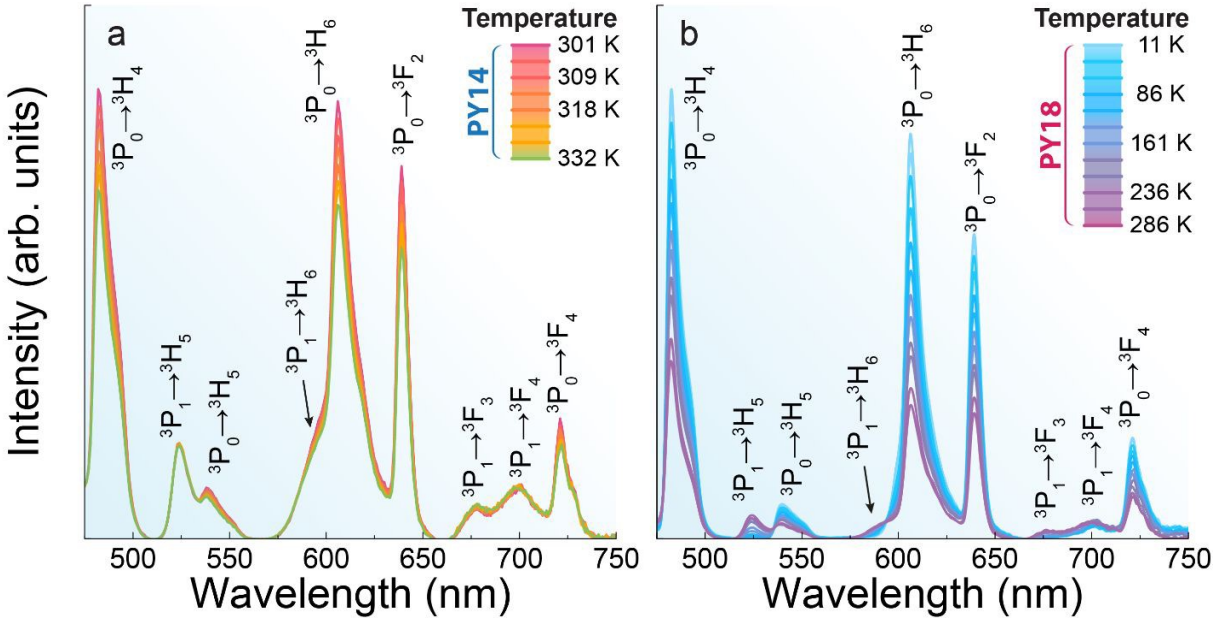

Figure S11. Temperature-dependent emission spectra of the samples **(a)** PY14 and **(b)** PY18 under excitation at 443 nm. The *y*-axis was rescaled for better visualization of all the curves in each panel.

S3. Supplementary tables

Table S1. Chemical compositions and densities of the prepared fluoride phosphate glasses.

Sample	Chemical composition (mol%)						Density
	$LiPO_3$	YF_3	SrF_2	CaF_2	Pr_7O_{11}	Yb_2O_3	(g cm^{-3})
PY00	50.000	20.000	20.000	10.000	-	-	3.48
PY14	49.375	19.750	19.750	9.875	0.250	1.000	3.62
PY18	48.875	19.550	19.550	9.775	0.250	2.000	3.74

Table S2. Characteristic temperatures of the obtained glass samples.

Sample	T_g (± 2 K)	T_x (± 2 K)	ΔT (± 4 K)
PY00	602	781	179
PY14	604	741	137
PY18	602	736	134

Table S3. Integrated areas of the absorption and excitation spectra (in arbitrary units) measured at room temperature of the fluoride phosphate co-doped glass samples. The relative absorption strengths (unitless) are given by the ratio between the $^3H_4 \rightarrow {}^3P_{2-0}, {}^1I_6$ and $^3H_4 \rightarrow {}^1D_2$ emission bands.

Pr^{3+} transition	PY14		PY18	
	Absorption	Excitation	Absorption	Excitation
$^3H_4 \rightarrow {}^1D_2$	710.4	681.2	699.2	703.7
$^3H_4 \rightarrow {}^3P_{2-0}, {}^1I_6$	3186.6	3239.0	3329.6	3205.7
Relative strength	4.5	4.8	4.8	4.6

Table S4. Absolute emission quantum yield (q) of Pr^{3+} in the glass samples in the visible spectral range under excitation at 443 nm, measured at room temperature. The values of q for the near-infrared emission of Yb^{3+} were not determined once the light emission was too faint to be detected by the equipment.

Sample	q
PY14	0.026 ± 0.003
PY18	0.018 ± 0.002

Table S5. Parameters of the potentials used in the MD simulations.[9]

Pair	D_{ij} (eV)	a_{ij} (Å^{-2})	r_0 (Å)	C_{ij} (eV Å^{12})
$Li^{0.6}$–$O^{-1.2}$	0.001114	3.429506	2.681360	1.0
$P^{3.0}$–$O^{-1.2}$	0.831326	2.585833	1.800790	1.0
$O^{-1.2}$–$O^{-1.2}$	0.042395	1.379316	3.618701	22.0

Table S6. Energy gap, room temperature, thermometric parameter at T_0 (Δ_0), relative thermal sensitivity, and uncertainty in temperature of samples PY14 and PY18.

Sample	ΔE (cm^{-1})	T_0 (K)	Δ_0	S_r (% K^{-1})	δT (K)
PY14	592 ± 10	296.3 ± 0.1	1.3277	0.97	0.5
PY18	609 ± 10	296.9 ± 0.1	1.2587	0.99	0.5

S4. References

(1) Cadars, S.; Sein, J.; Duma, L.; Lesage, A.; Pham, T. N.; Baltisberger, J. H.; Brown, S. P.; Emsley, L. The Refocused INADEQUATE MAS NMR Experiment in Multiple Spin-Systems: Interpreting Observed Correlation Peaks and Optimising Lineshapes. *J. Magn. Reson.* **2007**, *188* (1), 24–34.

(2) Miller, J. M. Fluorine-19 Magic-Angle Spinning NMR. *Prog. Nucl. Magn. Reson. Spectrosc.* **1996**, *28* (3–4), 255–281.

(3) van Meerten, S. G. J.; Franssen, W. M. J.; Kentgens, A. P. M. SsNake: A Cross-Platform Open-Source NMR Data Processing and Fitting Application. *J. Magn. Reson.* **2019**, *301*, 56–66.

(4) Bak, M.; Rasmussen, J. T.; Nielsen, N. C. SIMPSON: A General Simulation Program for Solid-State NMR Spectroscopy. *J. Magn. Reson.* **2000**, *147* (2), 296–330.

(5) Gullion, T.; Schaefer, J. Rotational-Echo Double-Resonance NMR. *J. Magn. Reson.* **1989**, *81* (1), 196–200.

(6) Pan, Y.; Gullion, T.; Schaefer, J. Determination of C–N Internuclear Distances by Rotational-Echo Double-Resonance NMR of Solids. *J. Magn. Reson.* **1990**, *90* (2), 330–340.

(7) Eckert, H. Structural Characterization of Noncrystalline Solids and Glasses Using Solid State NMR. *Prog. Nucl. Magn. Reson. Spectrosc.* **1992**, *24* (3), 159–293.

(8) Thompson, A. P.; Aktulga, H. M.; Berger, R.; Bolintineanu, D. S.; Brown, W. M.; Crozier, P. S.; in 't Veld, P. J.; Kohlmeyer, A.; Moore, S. G.; Nguyen, T. D.; Shan, R.; Stevens, M. J.; Tranchida, J.; Trott, C.; Plimpton, S. J. LAMMPS - a Flexible Simulation Tool for Particle-Based Materials Modeling at the Atomic, Meso, and Continuum Scales. *Comput. Phys. Commun.* **2022**, *271*, 108171.

(9) Pedone, A.; Malavasi, G.; Menziani, M. C.; Cormack, A. N.; Segre, U. A New Self-Consistent Empirical Interatomic Potential Model for Oxides, Silicates, and Silica-Based Glasses. *J. Phys. Chem. B* **2006**, *110* (24), 11780–11795.

(10) Mooney, J.; Kambhampati, P. Get the Basics Right: Jacobian Conversion of Wavelength and Energy Scales for Quantitative Analysis of Emission Spectra. *J. Phys. Chem. Lett.* **2013**, *4* (19), 3316–3318.

(11) Mooney, J.; Kambhampati, P. Correction to "Get the Basics Right: Jacobian Conversion of Wavelength and Energy Scales for Quantitative Analysis of Emission Spectra." *J. Phys. Chem. Lett.* **2014**, *5* (20), 3497–3497.

Manuscript 6

Going Above and Beyond: A Tenfold Gain in the Performance of Luminescence Thermometers Joining Multiparametric Sensing and Multiple Regression

F. E. Maturi, C. D. S. Brites, E. C. Ximendes, C. Mills, B. D. Olsen, D. Jaque, S. J. L. Ribeiro, L. D. Carlos.

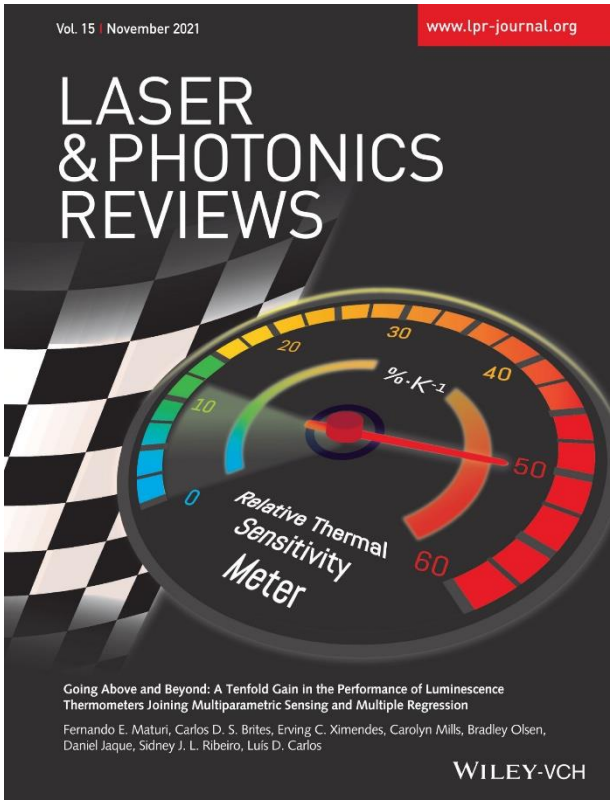

Laser & Photonics Reviews, 15 (11), 2100301, 2021.

DOI: https://doi.org/10.1002/lpor.202100301

Featured as Front Cover

LASER & PHOTONICS REVIEWS

www.lpr-journal.org

Going Above and Beyond: A Tenfold Gain in the Performance of Luminescence Thermometers Joining Multiparametric Sensing and Multiple Regression

*Fernando E. Maturi, Carlos D. S. Brites, Erving C. Ximendes, Carolyn Mills, Bradley Olsen, Daniel Jaque, Sidney J. L. Ribeiro, and Luís D. Carlos**

Luminescence thermometry has substantially progressed in the last decade, rapidly approaching the performance of concurrent technologies. Performance is usually assessed through the relative thermal sensitivity, S_r, and temperature uncertainty, δT. Until now, the state-of-the-art values at ambient conditions do not exceed maximum S_r of 12.5% K^{-1} and minimum δT of 0.1 K. Although these numbers are satisfactory for most applications, they are insufficient for fields that require lower thermal uncertainties, such as biomedicine. This has motivated the development of materials with an improved thermal response, many of them responding to the temperature through distinct photophysical properties. This paper demonstrates how the performance of multiparametric luminescent thermometers can be further improved by simply applying new analysis routes. The synergy between multiparametric readouts and multiple linear regression makes possible a tenfold improvement in S_r and δT, reaching a world record of 50% K^{-1} and 0.05 K, respectively. This is achieved without requiring the development of new materials or upgrading the detection system as illustrated by using the green fluorescent protein and Ag_2S nanoparticles. These results open a new era in biomedicine thanks to the development of new diagnosis tools based on the detection of super-small temperature fluctuations in living specimens.

1. Introduction

Temperature is a physical quantity that measures the thermal energy of a body,[1] and temperature fluctuations play a central role in a myriad of natural and man-made processes.[2–4] Since the time-response of a thermometer is limited by its size, the real-time measurement of temperature at the microscopic scale is hindered by the dimensions of the thermal probe. The size effect motivates the development of novel solutions for temperature determination at the submicrometer scale, in particular, luminescent nanothermometry is based on the emission properties of luminescent nanomaterials and thus allows a remote temperature detection, improving spatial and temporal resolutions in comparison with the macroscopic counterparts.[5–11]

There are plenty of luminescent materials used as nanothermometers, e.g., polymers,[12,13] organic dyes,[14] proteins,[15] quantum dots (QDs),[16,17] and lanthanide-doped particles.[18–21] Different classes of nanothermometers exploit distinct photophysical properties of the emitting center, such as the integrated emission intensity of a single transition,[22] the intensity ratio of two emission bands,[23,24] the energy shift[25] or the bandwidth of an emission line,[26,27] the polarization state of the emission,[28] or the emission lifetime of an excited state.[29] Irrespective of the property analyzed, all these examples are based on a thermometric parameter (usually denoted by Δ) that expresses the relationship between the luminescent property to be analyzed and the temperature.[7]

The different thermometric parameters reported motivated the community to adopt a figure of merit to compare the performance of distinct luminescent nanomaterials regardless of

F. E. Maturi, C. D. S. Brites, L. D. Carlos
Phantom-g
CICECO – Aveiro Institute of Materials
Department of Physics
University of Aveiro
Aveiro 3810-193, Portugal
E-mail: lcarlos@ua.pt

The ORCID identification number(s) for the author(s) of this article can be found under https://doi.org/10.1002/lpor.202100301

DOI: 10.1002/lpor.202100301

F. E. Maturi, S. J. L. Ribeiro
Institute of Chemistry
São Paulo State University (UNESP)
Araraquara, São Paulo 14800-060, Brazil

E. C. Ximendes, D. Jaque
Nanomaterials for Bioimaging Group
Universidade Autónoma de Madrid
Madrid 28049, Spain

C. Mills, B. Olsen
Department of Chemical Engineering
Massachusetts Institute of Technology
Cambridge, MA 02139, USA

the thermometric parameter used.[30,31] This figure of merit is the so-called relative thermal sensitivity, $S_r = \frac{1}{\Delta}|\frac{\partial\Delta}{\partial T}|$,[32] where $\partial\Delta/\partial T$ is the change of Δ with respect to the temperature (also known as absolute sensitivity, S_a), with S_r values commonly presented in units of percentage change per degree of temperature change (% K^{-1}).[5] Currently, the most sensitive luminescent nanothermometer operating at ambient conditions reaches a maximum value of S_r—represented by S_m—of 12.5% K^{-1}.[33]

In the past years, luminescence nanothermometry has been used in both applied and fundamental science. In nanomedicine, for example, the accurate determination of the temperature can yield the development of new thermal diagnosis and therapy methods,[8,11,34] whereas in micro or nanoelectronics tracking the thermal exchanges at submicrometric length scales can afford a detailed understanding of the thermal properties in spatial domains for which the macroscopic transfer laws are not valid anymore.[35] In fact, real-world applications of luminescence thermometry are hindered by the accuracy of the nanothermometers, which is given by the temperature uncertainty, $\delta T = \frac{1}{S_r}\frac{\delta\Delta}{\Delta}$,[7] where $\delta\Delta/\Delta$ is the relative uncertainty in Δ, determined by the detection system used. The best δT value reported by now was achieved by using lanthanide-bearing nanomaterials, with δT ranging between 0.1 and 0.3 K.[4,20]

Nowadays, cutting-edge reports on luminescence nanothermometry are reaching the boundary of the accuracy of the nanothermometers.[11,36] Therefore, the development of new approaches to obtain low-uncertainty luminescent thermal probes is needed to push the field forward, mainly for in vitro and in vivo thermal sensing.[37,38] Two strategies are envisaged to decrease δT. The first one is the design of high sensitivity light detectors and brighter materials to achieve a higher signal-to-noise ratio, consequently decreasing $\delta\Delta/\Delta$. The second one relies on the improvement of S_r, which can be attained either through the fabrication of new materials or the design of new strategies to define the thermometric parameter. In this work, we address the latter approach.

Recently, the reliability of luminescent nanothermometers has been improved using the combination of distinct thermometric parameters.[39–41] This strategy is based on the use of so-called multiparametric nanothermometers in which temperature impacts, simultaneously, different luminescence properties[42–45] or different emitting centers.[46–49] The use of different thermal readouts improves the reliability of temperature measurements by providing self-calibrated nanothermometers, increasing the precision of temperature measurement.[33,40,50] Multiparametric nanothermometers are gaining special attention in biomedicine: Ag_2S nanocrystals have demonstrated their potential for reliable thermal sensing in small animal models,[44,51] whereas the multifaced changes in the band-shape of green fluorescent protein (GFP) can be used for temperature sensing and imaging in cell biology and physiology.[15,28,52–55] Despite it helps to improve the reliability, the so-called multiparameter sensing is still unable to improve significantly the relative thermal sensitivity of the nanothermometers and the reported values are far below the most sensitive luminescent thermometers reported so far.[33,56,57]

Multiple linear regression (MLR) is an ingenious method to fully expand the potential of multiparameter temperature sensing, which may raise luminescence nanothermometry to a whole new level. In its easier form, MLR is a powerful tool that evaluates the impact of multiple independent variables on a single experimental outcome.[58] This technique is widely used in economics to forecast the price of oil[59] or cryptocurrencies,[60] in social sciences to identify fake news[61] and political trends,[62] in medicine to predict blood glucose[63] and cholesterol[64] in overweight patients, and chemistry to quantify metabolites[65] and proteins[66] by mass spectrometry. By analogy, if a luminescent nanothermometer presents different thermometric parameters displaying the same temperature-dependent linear trend, the application of MLR to its multiple thermal reading would lead to a relevant improvement in its performance as a temperature sensor. This possibility has never been proposed neither demonstrated.

Therefore, we herein provide experimental evidence of how the synergy between MLR and multiparametric thermal sensing leads to a tenfold improvement in the performance of multiparametric nanothermometers establishing world-record values for S_r and δT. This is demonstrated by selecting enhanced GFP (EGFP) and Ag_2S nanocrystals as paradigmatic multiparametric thermographic phosphors displaying distinct (and independent) temperature-dependent parameters. In vivo experiments involving Ag_2S nanocrystals were revisited illustrating the impact of this new methodology on the potential application of luminescent nanothermometry in biomedicine.

2. Results and Discussion

2.1. Multiparametric Nanothermometry Using EGFP

Figure 1 shows the temperature-dependent emission spectra of EGFP displaying a significant thermal quenching due to the enhancement of nonradiative decays upon heating.[67,68] The denaturation of EGFP was not observed as the measurement was performed at temperatures below the temperature threshold,[69] as shown by the high repeatability of the emission intensity during different heating and cooling cycles (Figure S1, Supporting Information). The detailed analysis of the band-shape shows that measurable changes are seen after the spectral deconvolution (Section S1.3, Supporting Information), revealing that temperature impacts several parameters such as the intensity ratio of the integrated areas of peaks 1 and 2 ($I_R = A_1/A_2$), peak energy of both peaks (E_1 and E_1), and their respective full width at half maximum (W_1 and W_2). Each of these parameters can be used as independent Δ values for multiparametric thermal reading (Figure 1d–h) and, as their temperature dependencies are described by a single linear fit with a positive correlation, there are five reliable independent pathways for determining the temperature from EGFP in a single experiment. At ambient conditions, I_R, E_1, E_2, W_1, and W_2 present S_m values of 0.17, 1.6×10^{-2}, 2.1×10^{-2}, 0.33, and 0.10% K^{-1}, respectively. These values are within the same thermal sensitivity range that the previously reported nanothermometry data of other EGFP-like proteins (**Table 1**).

We can argue that larger S_r values can be obtained by choosing the energy shift of each peak as thermometric parameters instead of the corresponding peak energies (since S_r depends on $1/\Delta$). However, although the energy shift has already been used in both Raman[70,71] and luminescence[72,73] thermometry, we adopt here the peak energy as a thermometric parameter because it is still

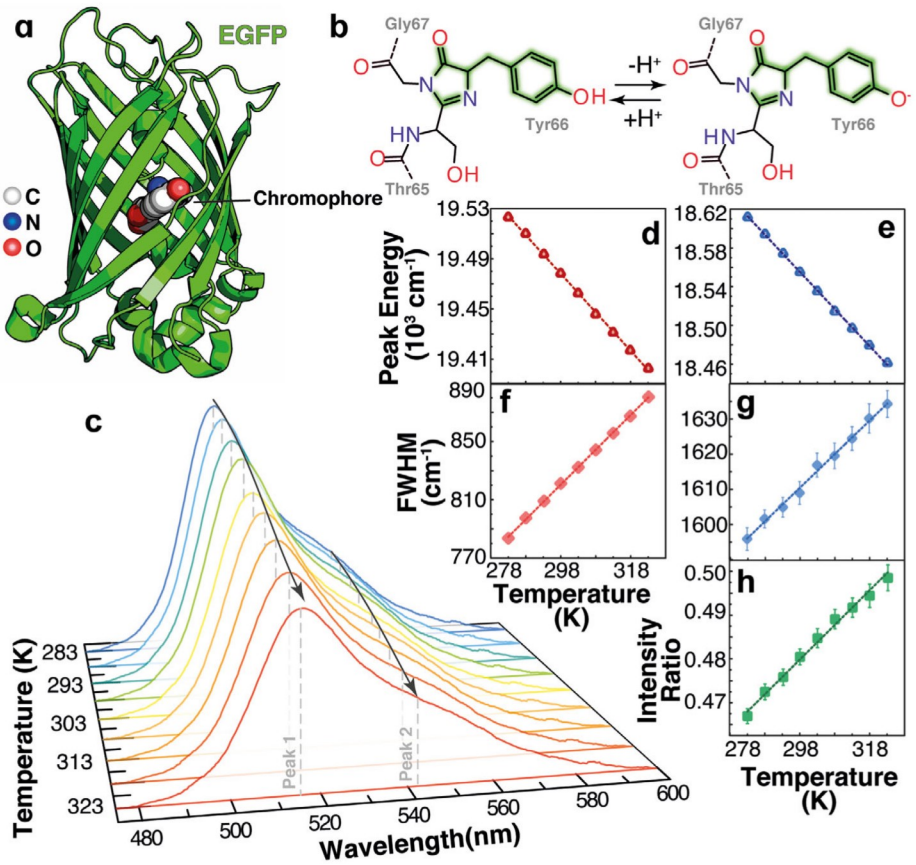

Figure 1. a) 3D view of the EGFP structure (based on Protein Data Bank ID 2y0g). b) Neutral and anionic forms of EGFP chromophore. The amino acid residues are shown close to the anionic form and the optically active part of the chromophore is depicted in a green blur for both forms. c) Emission spectra of EGFP under excitation at 408 nm at different temperatures. Temperature dependence of the distinct thermometric parameters: d) E_1, e) E_2, f) W_1, g) W_2, and h) I_R. The lines are the best linear fits of the data to straight lines ($r^2 > 0.99$ in all cases). The fit parameters are shown in Table S1 (Supporting Information).

Table 1. Temperature calibration range, maximum relative thermal sensitivity (S_m) and the temperature at which it occurs (T_m) for different GFP-based proteins using multi- and single-parametric analysis.

Protein	Temperature range [K]	S_m [% K^{-1}]	T_m [K]	Method	Reference
EGFP	283–323	3.0	283.0	MLR	This work
		0.17	283.0	I_R	
		1.6×10^{-2}	283.0	E	
		2.1×10^{-2}	283.0		
		0.33	283.0	W	
		0.10	283.0		
emGFP-Mito	296–312	2.2	296.0	Peak fraction[e]	[15]
		4.4	312.0	Single intensity[f]	
GFP	293–333	2.1	333.0	Single intensity[g]	[78]
actin-GFP[a]	288–343	0.2	302.0	Lifetime[h]	[53]
tsGFP1[b,c]	307–314	3.0	314.0	I_R	[55]
tsGFP2[b,c]	311–319	3.1	319.0		
gTEMP[d]	278–323	2.6	278.0	I_R	[79]

[a] GFP coupled to actin filaments; [b,c] Fluorophore-forming region of GFP inserted between tandem repeats of the coiled-coil region of TlpA and the full-length TlpA, respectively; [d] Genetically encoded ratiometric fluorescent temperature indicator from Sirius and mT-Sapphire GFP-derived proteins linked by a *Thosea asigna* virus 2A peptide; [e] $(I_1-I_2)/(I_1+I_2)$, where I_1 and I_2 are the integrated emission areas between 495 and 504 nm and 505 and 600 nm, respectively (nonlinear dependence); [f] Fluorescence intensity of the peak maximum at around 510 nm under excitation at 488 nm (nonlinear dependence); [g] Fluorescence intensity of the peak maximum at around 510 nm under excitation at 473 nm; [h] Emission lifetime under excitation at 467 nm monitoring emission at 510 nm.

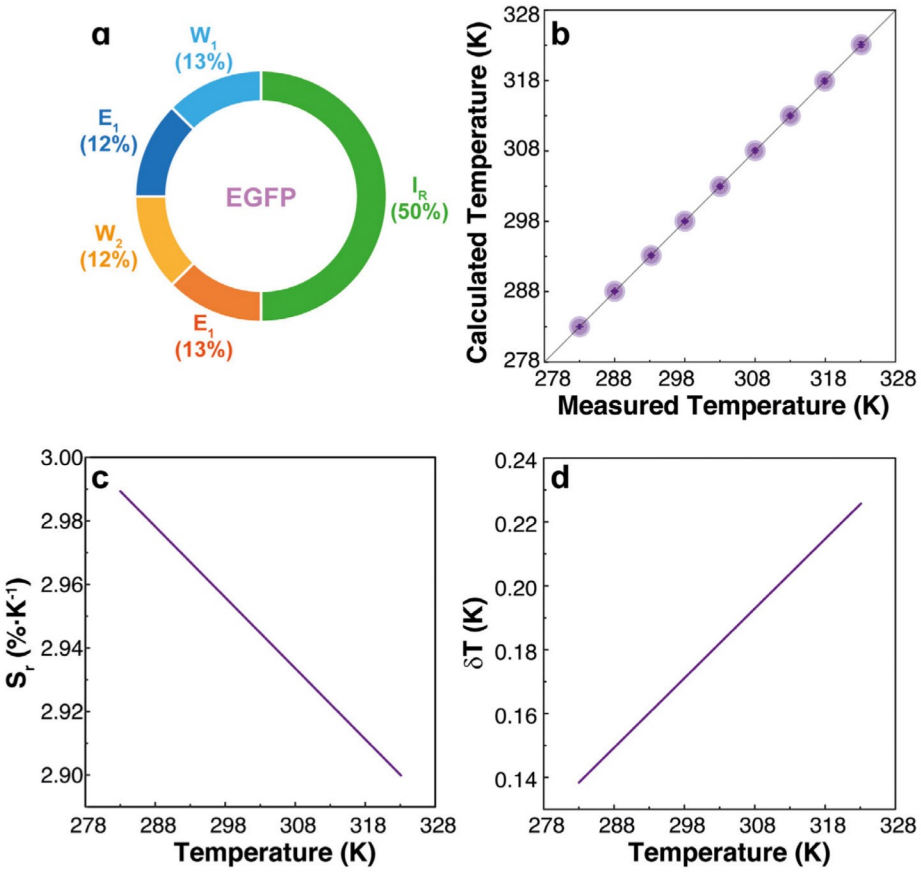

Figure 2. a) Donut chart of the relative weight (values within parenthesis from β weights) of the distinct thermometric parameters considered for MLR applied to EGFP. b) Correlation between the temperature measured with the thermocouple (x-axis) and the temperature calculated from the combination of all the thermometric parameters from EGFP emission spectra through MLR (y-axis). The dashed black lines are guides for the eyes corresponding to $y = x$ (fit parameters are shown in Table S2, Supporting Information). c) Relative thermal sensitivity and d) temperature uncertainty of EGFP using MLR.

the largest reported thermometric parameter. Nevertheless, the pros and cons of using peak energy and energy shift as thermometric parameters are discussed in detail in Section S1.3.3.1 (Supporting Information).

As all the five thermometric parameters defined for EGFP display the same linear temperature dependence, it is possible to further improve S_r and δT by treating the data through the MLR approach. If a nanothermometer displays distinct thermometric parameters that vary linearly with the temperature, i.e., Δ_1, Δ_2, ..., Δ_n, then the temperature can be expressed as a function of each Δ, i.e., $T = f(\Delta_1, \Delta_2, ..., \Delta_n)$

$$T = \beta_0 + \beta_1\Delta_1 + \cdots + \beta_n\Delta_n + \varepsilon = \beta_0 + \sum_{i=1}^{n}\beta_i\Delta_i + \varepsilon \quad (1)$$

where β_0 is the intercept, β_i ($i = 1, ..., n$) is the slope of each thermometric parameter Δ_i (explanatory variable i), and ϵ is the residual.[74] Henceforth, one can rewrite S_r (details in Section S2.2, Supporting Information)

$$S_r = \sqrt{\sum_{i=1}^{n}\left(\frac{1}{\Delta_i}\left|\frac{\partial\Delta_i}{\partial T}\right|\right)^2} = \sqrt{\sum_{i=1}^{n}\left(\Delta_i\left|\frac{\partial T}{\partial\Delta_i}\right|\right)^{-2}} \quad (2)$$

Because the model is linear, the relative thermal sensitivity depends on each thermometric parameter taken into account (Δ_i) and its respective slope (β_i), and thus

$$S_r = \sqrt{\sum_{i=1}^{n}(\Delta_i\beta_i)^{-2}} \quad (3)$$

The MLR was applied to the EGFP data considering the five distinct Δ_i parameters previously defined and the correlation between the temperature measured with a K-type thermocouple and the temperature obtained from MLR is presented in **Figure 2** (see Section S2.4, Supporting Information, for further information). By combining all the parameters, S_m reaches 3.0%K^{-1}, which represents a tenfold increase compared to the highest S_m obtained in single parametric sensing of EGFP (0.33% K^{-1} for W_1). An improved sensitivity obtained through MLR is observed as the model considers the weighted contribution of each temperature-dependent light emission of EGFP (i.e., each Δ_i), therefore reducing the uncertainties provided by measurements of the temperature based on individual Δ. This is well demonstrated by the measurement of consecutive heating and cooling cycles (**Figure 3**), where the thermal transient curves obtained by luminescence thermometry in Figure 3a–e tend to

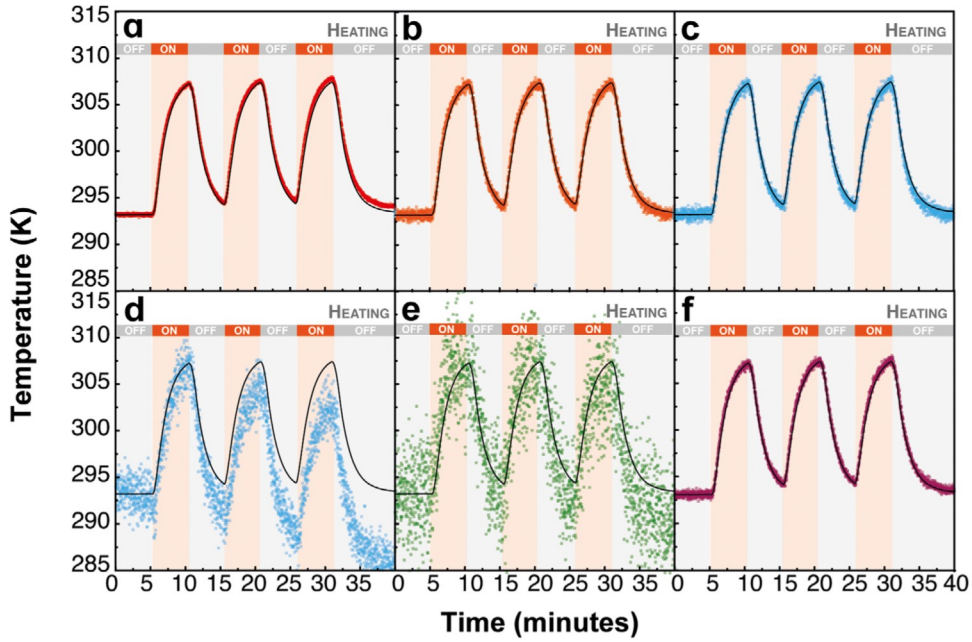

Figure 3. Consecutive heating (red) and cooling (gray) cycles of the EGFP aqueous suspension. The black solid line indicates the measurement of the temperature performed by a reference thermocouple and the symbols the temperature calculated from a) E_1, b) E_2, c) W_1, d) W_2, e) I_R, and f) MLR applied to the EGFP emission spectra. The corresponding histogram of the temperature deviation between the temperature measured with the thermocouple and the temperature calculated using the distinct parameters is presented in Figure S11 (Supporting Information).

deviate from the curve measured by a K-type reference thermocouple (this is much more evident for W_2 and I_R). The histograms of the temperature deviation (ΔT) are presented in Figure S11 (Supporting Information), and the results show that MLR provides a lower temperature deviation in Figure 3f because the uncertainties from each Δ_i were already reduced in the model, validating the improved performance of MLR in multiparametric nanothermometry.

Beyond the giant improvement in the relative thermal sensitivity, this novel approach allows achieving more reliable and accurate thermal readouts without requiring the development of new materials, the upgrade of the detection system, or further time-consuming measurements over long integration times. This last makes, for instance, possible to perform time-resolved measurements in vitro and in vivo.

2.2. Revisiting In Vivo Measurements Using Ag_2S Nanoparticles

Despite the utility of fluorescent proteins, the novelty of MLR is not limited to luminescent organic compounds, but it also can be applied to inorganic nanoparticles with multi-parametric thermal sensing capabilities. We here, indeed, explore the

Table 2. Temperature calibration range, maximum relative thermal sensitivity (S_m), and the temperature at which it occurs (T_m) for different Ag_2S nanoparticles, using distinct methods.

Nanoparticle	Temperature range [K]	S_m [% K^{-1}]	T_m [K]	Method	Reference
Ag_2S-PEG[a)]	295–353	50	295.0	MLR	This work[44]
		9.5×10^{-2}	344.0	E	
Ag_2S-PEG	293–353	5.0	295.0	Single intensity[b)]	[44]
		0.10	295.0	Peak wavelength[c)]	
		2.0	295.0	I_R	
Ag/Ag_2S	288–323	8.5	323.0	Single intensity	[80]
		2.0	323.0	I_R	
Ag_2S-PEG	295–323	3.0	295.0	Lifetime[d)]	[81]
Ag_2S-DDT[e)]		4.0	295.0		
Ag_2S-PEG	299–313	3.0	299.0	Single intensity	[77]
Ag_2S-PEG	293–318	3.0	293.0	Single intensity	[82]

[a)] Nanoparticles functionalized with polyethylene glycol (PEG); [b)] Total integrated emission area (nonlinear dependence); [c)] Wavelength at the maximum intensity of the peak; [d)] Emission lifetime under excitation at 450 nm monitoring emission at the maximum intensity of the peak; [e)] Nanoparticles functionalized with 1-dodecane-thiol (DDT).

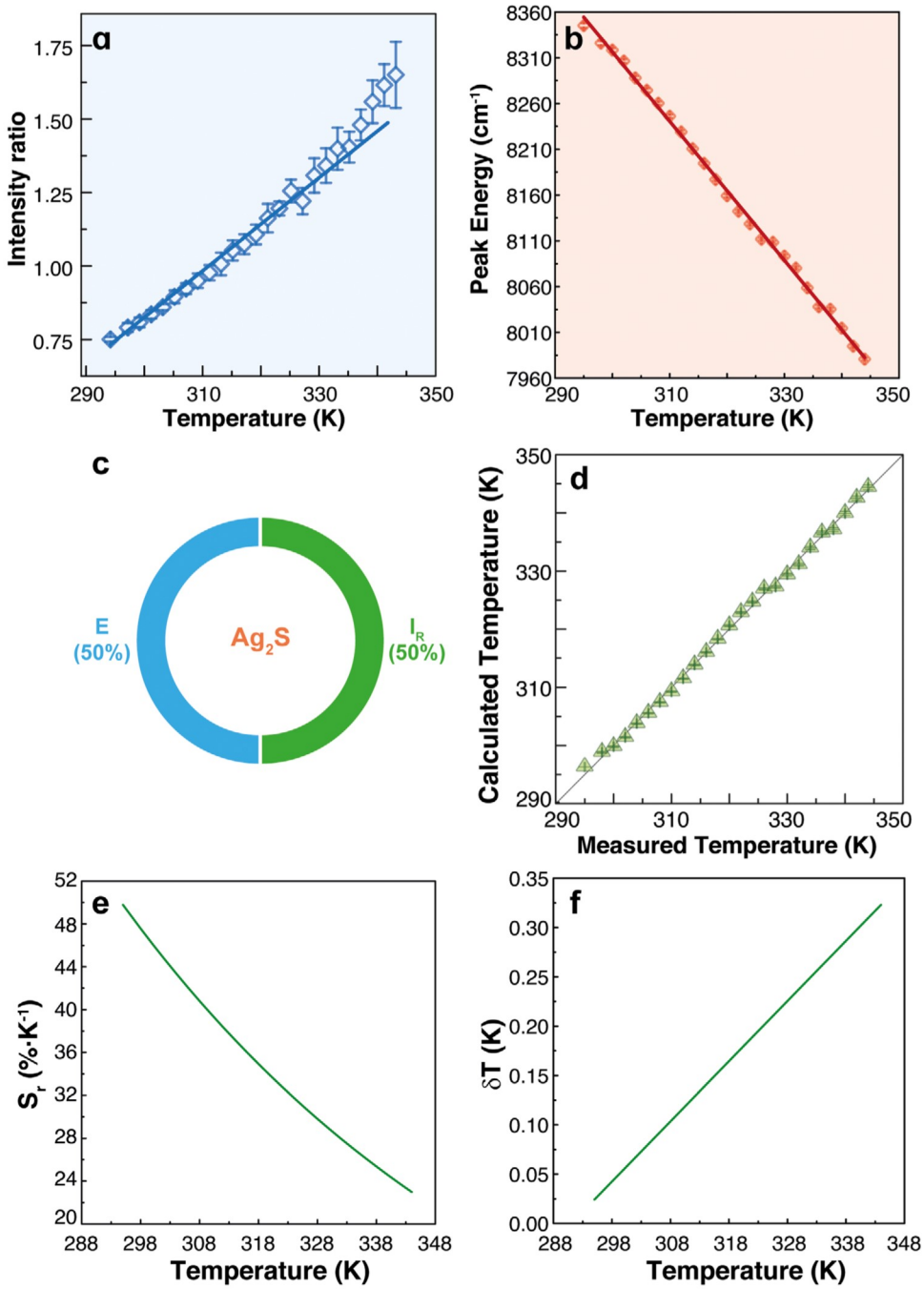

Figure 4. Calibration curves of the Ag_2S NPs using a) the intensity ratio[44] and b) the peak energy. The solid lines are the best fits to straight lines (the correlation coefficients and fitting parameters are presented in Table S3, Supporting Information). c) Donut chart of the relative weight (values within parenthesis from β weights) of the distinct thermometric parameters considered for MLR applied to Ag_2S. d) Correlation between the temperature measured with the thermocouple (x-axis) and the temperature calculated from the combination of all the thermometric parameters from Ag_2S emission spectra through MLR (y-axis). The dashed black lines are guides for the eyes corresponding to $y = x$ (fit parameters are shown in Table S4, Supporting Information). e) Relative thermal sensitivity and f) temperature uncertainty of Ag_2S using MLR.

application of MLR to Ag_2S nanoparticles. Ag_2S nanoparticles possess a unique combination of properties that makes them exceptional for in vivo thermal sensing. They operate in the second biological window (infrared spectral range from 1000 to 1400 nm where tissues become partially transparent[75]) so that they allow for real sub-tissue thermal sensing. Ag_2S nanoparticles show excellent in vivo biocompatibility thanks to their good physical-chemical stability.[44,76,77] The emission band of Ag_2S nanoparticles centered at 1200 nm shows a strong temperature dependence and it has been widely reported how a reduced temperature

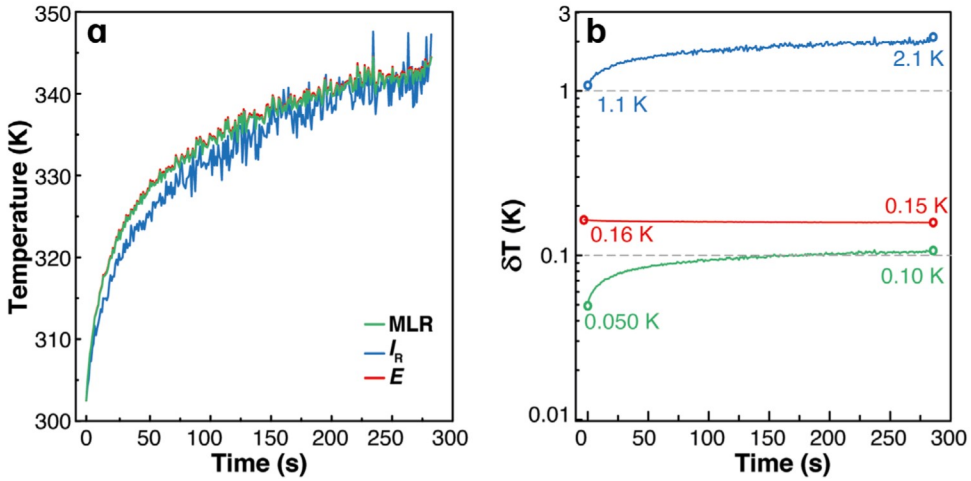

Figure 5. a) Temporal evolution of the 808 nm laser-induced temperature increase of tumor during photothermal treatment, calculated from the intensity ratio (as reported in ref. [44]), peak energy and multiple linear regression (partially overlapped, calculated by us). The transient curves were recalculated from the data published elsewhere.[44] b) The temporal evolution of the corresponding temperature uncertainties.

change around room temperature induces relevant changes in the band shape. These temperature-induced changes have been largely used for thermal reading by analyzing either the peak wavelength or the ratio between the emitted intensities at 1175 and 1260 nm. The use of these two thermometric parameters has made possible reliable thermal reading with modest thermal sensitivities at 310 K ranging from 9.5×10^{-2} to 5.0% K^{-1} (**Table 2**).[44] As a consequence of these "modest" thermal sensitivities, the thermal uncertainty achieved by Ag_2S nanothermometers during in vivo experiments is not better than 0.5°.[44] The temperature dependence of both intensity ratio and peak energy of emission band corresponding to Ag_2S nanoparticles is presented in **Figure 4**, leading to relative thermal sensitivities of 2.0 and 0.10% K^{-1}, respectively. Hereafter, we will focus our attention on these two thermoresponsive parameters as they both display a quasi-linear trend, making them amenable to MLR analysis.

Applying the MLR to the Ag_2S data (giving the relative contributions indicated in Figure 4c), we obtained a calibration curve that depends linearly on the peak energy and intensity ratio parameters with a relative thermal sensitivity up to 50% K^{-1} (Figure 4d). This constitutes a tenfold improvement when compared to that previously reported for Ag_2S nanoparticles and 4 times greater than the greatest S_m value reported so far (12.5% K^{-1} at 293 K, from a lanthanide metal-organic network, using the intensity ratio approach).[33,44] The performance, in terms of S_r and δT, achieved by combining linear regression to the multiparametric reading of Ag_2S nanothermometers is shown in Figure 4e,f. It is evidenced how the use of linear regression procedures makes it possible to drive the thermal uncertainties provided by Ag_2S nanothermometers well below 1.0 K. It is worth pointing out that since the MLR deals with linear models, only the thermometric parameters presenting linear response upon heating and cooling can be considered for multiparametric temperature sensing through MLR, which is the main disadvantage of this newly proposed method. For that reason, the temperature-dependent emission intensity of the Ag_2S nanoparticles was intentionally left out of the calculations when performing the MLR analysis due to its nonlinear trend, as seen in ref. [44].

The MLR-induced thermal sensitivity enhancement of Ag_2S nanothermometers opens the possibility of improving the thermal resolution of in vivo measurements. In recent work, intratumoral thermal transients were measured by analyzing the time evolution of the infrared emission generated by Ag_2S nanoparticles allocated inside a melanoma tumor during laser irradiation. The different intratumoral thermal readings provided by the different thermometric parameters (emission intensity, peak wavelength, and intensity ratio) were used to assess the reliability of measurements but not to improve the accuracy of the final intratumoral readout. The intratumoral emission spectra generated by Ag_2S nanoparticles were re-analyzed by MLR and the new intratumoral thermal transients during photothermal treatment are shown in **Figure 5** (the thermal transients obtained by using the individual calibration curves are also included for comparison). We identify slight differences in the temperature profiles during the transient regime that are explained by the distinct thermal sensitivity provided by each parameter and are within the temperature uncertainty of each thermometric parameter. Moreover, the intratumoral temperature values calculated from MLR are almost identical to those provided by the sole analysis of peak energy which, at first glance does not justify the effort of using MLR.

The improved performance of MLR is, however, reflected in both S_r and δT values calculated from each thermometric parameter (Figure 5b and Table 2). The intensity ratio allows a temperature determination with uncertainty values ranging from 1.1 to 2.1 K (the lower the sensitivity the higher the temperature uncertainty), and the peak energy improves this value roughly by one order of magnitude ($\delta T \approx 0.15$ K). Finally, the MLR approach renders temperature uncertainties between 0.05 and 0.10 K, which represents an improvement of more than 20 times with respect to the obtained with the intensity ratio approach. Note that recent perspective articles pointed out that the real use of luminescence thermometry at the clinical level would require achieving thermal resolutions during in vivo experiments better than 0.1°,[11] which is reached in this work. As a matter of fact, we demonstrate how MLR converts Ag_2S

nanoparticles into ultra-sensitive nanothermometers making them a unique system for in vivo detection, for instance, of brain diseases through precise and remote thermal sensing. Once again, it should be highlighted that such improvement for in vivo thermal uncertainty has been achieved without requiring any change in the experimental setup or sample preparation.

3. Conclusions

Several strategies have been used to improve the reliability and accuracy of luminescent nanothermometers, namely, the combination of different emitting centers or the simultaneous assessment of the temperature via several thermometric parameters. This work demonstrates that any luminescent thermometer presenting a linear correlation of the distinct thermometric parameters with the temperature can be used to achieve higher sensitivity and lower temperature uncertainty through MLR. We demonstrate the potential of the synergy between MLR and luminescent nanothermometry in two of the most promising systems for thermal sensing in biomedicine: GFPs and Ag_2S nanoparticles. The combination of MLR and the multiparametric thermal readout of EGFP leads to a significant increase of its thermal sensitivity, with a tenfold improvement. MLR has been also found to improve the relative thermal sensitivity of intratumoral Ag_2S multiparametric nanothermometers by one order of magnitude, reaching a world record of 50% K^{-1}. Moreover, the re-analysis of in vivo results by using MLR have also demonstrated how is possible to drive the thermal accuracy of in vivo measurements well below 0.1°, starting a new era of luminescent nanothermometry at the preclinical level.

These results support that MLR is a valid and easily implementable strategy, paving the way for reaching a temperature resolution below 0.1° without further upgrade of the detection systems or materials design, an important step forward for the spread of luminescent nanothermometers as a tool for broader diverse scientific proposes.

4. Experimental Section

Photoluminescence Spectroscopy: The emission spectra of EGFP were recorded in the right-angle experimental setup shown in Figure S2 (Supporting Information). The excitation of the sample was carried out at 408 ± 7 nm with a power density of 0.01 W cm^{-2} by using a CW multichannel LED light source (MCLS, Sandhouse Design). The excitation source was collimated twice by attaching an adjustable collimator to the tip of the optical fiber and placing a plano-convex lens (LA1145-AB, Thorlabs) between the optical fiber and the sample. The light emission was registered by a USB-portable spectrometer (Maya 2000 Pro, Ocean Optics) coupled to an optical fiber (QP450-1-XSR, Ocean Optics) using an edge pass filter (FESH0750, Thorlabs) to cut off the excitation signal during the spectral acquisition. A high-precision quartz cuvette (QS, 114F-10-40, Hellma Analytics) was filled with 0.50 mL of the EGFP aqueous suspension to perform the measurements.

Thermal Calibration: The temperature-dependent measurements were performed using the setup described above and a temperature-controlled cuvette holder (Luma 40, Quantum Northwest) coupled to a temperature controller (TC1, Quantum Northwest) using a water circulator (Bath 10, Quantum Northwest) for heating and cooling the sample. The calibration of temperature was performed with a K-type thermocouple with a temperature uncertainty of 0.1 K (KA01-3, TME Thermometers) coupled to a thermocouple data logger (TC-08, Pico Technology).

Cloning of EGFP: The gene of EGFP containing BamHI and HindIII restriction sites at 5′ and 3′ ends of the sequence, respectively, was prepared by polymerase chain reaction (PCR). The pQE9 vector containing the BamHI/HindIII restriction sites and the gene encoding for EGFP was purified through a spin column purification and ligated at 3:1 insert to vector molar ratio.

Protein Expression and Purification: The EGFP plasmid was transformed into *Escherichia coli* strain Tuner (DE3), and the expression of the protein was carried out in Luria broth (LB), where the cells were grown to OD_{600} = 0.8–1.0 at 310 K before induction. The protein expression was induced by the addition of isopropyl-β-D-1-thiogalactopyranoside (IPTG, 0.5 mmol L^{-1}) and a temperature drop to 303 K. The cells were harvested by centrifugation 18–24 h after induction and resuspended in lysis buffer (NaH_2PO_4 = 50 mmol L^{-1}, NaCl = 300 mmol L^{-1}, imidazole = 10 mmol L^{-1} in water, pH = 8.0). The obtained lysates were stored at 193 K. After thawing, lysozyme (1 mg mL^{-1}) was added to resuspended cells, and the cells were incubated at 277 K for 1 h. The resuspended cells were sonicated with a tip probe and clarified by centrifugation (12,400 rpm) at 277 K. The obtained EGFP aqueous suspension was purified by Ni-NTA affinity chromatography (Ni-NTA Agarose, Qiagen) under native conditions and fast protein liquid chromatography (FPLC) at pH = 8.0. FPLC purification was performed using an anion exchange chromatography column (HiTrap Q HP, GE Life Sciences) under 30 column volumes elution with an increasing linear gradient of NaCl concentration from 0 to 2 mol L^{-1}. The suspension of the protein was dialyzed against ultrapure water and the purity of each protein was confirmed by denaturing gel electrophoresis (SDS-PAGE). The resulting EGFP aqueous suspension was diluted in tris buffer at pH = 8.0 and stored at 277 K. The confirmed amino acid sequence of the obtained EGFP is presented in Figure S6 (Supporting Information).

Colloidal Characterization: The hydrodynamic size (diameter, *d*) of EGFP was measured by dynamic light scattering (DLS) in a Malvern Zetasizer Nano series instrument (Nano-ZS Model ZEN3600, Red badge operating with a 632.8 nm laser) at 298 K. The measurement of the zeta potential (ζ) was carried out in the same equipment by using the Smoluchowski model to analyze the colloidal stability of EGFP in aqueous suspension (0.25 mg mL^{-1} in 20 mmol L^{-1} Tris-Cl, pH = 8.00 ± 0.01). The EGFP sample was measured in a folded capillary cell (DTS1070, Malvern Instruments) for both DLS and zeta potential measurements. Three measurements were performed with ten scans each, where the average values are reported in Figure S7 (Supporting Information).

UV–Vis Absorption Spectroscopy: The UV–vis absorption spectrum of the EGFP aqueous solution was recorded in a spectrophotometer (Cary 50, Varian) at 293 K with a spectral resolution of 0.5 nm using a 10 mm pathlength quartz cuvette (Figure S8, Supporting Information).

Supporting Information

Supporting Information is available from the Wiley Online Library or from the author.

Acknowledgements

This work was developed within the scope of the projects CICECO-Aveiro Institute of Materials (UIDB/50011/2020 and UIDP/50011/2020) and Shape of Water (PTDC/NAN-PRO/3881/2020) financed by Portuguese funds through the FCT/MEC and when appropriate co-financed by FEDER under the PT2020 Partnership Agreement. This project has received funding from the European Union's Horizon 2020 research and innovation programme under the Marie Sklodowska-Curie Grant Agreement No. 823941. The support of the European Union's Horizon 2020 FET Open program under Grant Agreement No. 801305 (NanoTBTech) is also acknowledged. F.E.M. acknowledges the financial support from the Brazilian agency FAPESP (Process No. 15/50382-2).

Conflict of Interest

The authors declare no conflict of interest.

Data Availability Statement

Research data are not shared.

Keywords

green fluorescent proteins, luminescence nanothermometry, multiple linear regression, silver sulfide

Received: June 4, 2021
Revised: July 6, 2021
Published online: August 21, 2021

[1] G. Martin, *Nature* **1906**, *73*, 390.
[2] S. E. Gilman, D. S. Wethey, B. Helmuth, *Proc. Natl. Acad. Sci. USA* **2006**, *103*, 9560.
[3] L. Rosso, S. Tabandeh, G. Beltramino, V. Fernicola, *Meas. Sci. Technol.* **2020**, *31*, 034002.
[4] R. Piñol, J. Zeler, C. D. S. Brites, Y. Gu, P. Téllez, A. N. Carneiro Neto, T. E. da Silva, R. Moreno-Loshuertos, P. Fernandez-Silva, A. I. Gallego, L. Martinez-Lostao, A. Martínez, L. D. Carlos, A. Millán, *Nano Lett.* **2020**, *20*, 6466.
[5] C. D. S. Brites, P. P. Lima, N. J. O. Silva, A. Millán, V. S. Amaral, F. Palacio, L. D. Carlos, *Nanoscale* **2012**, *4*, 4799.
[6] D. Jaque, F. Vetrone, *Nanoscale* **2012**, *4*, 4301.
[7] C. D. S. Brites, S. Balabhadra, L. D. Carlos, *Adv. Opt. Mater.* **2019**, *7*, 1801239.
[8] A. Bednarkiewicz, L. Marciniak, L. D. Carlos, D. Jaque, *Nanoscale* **2020**, *12*, 14405.
[9] M. Dramićanin, in *Luminescence Thermometry: Methods, Materials, and Applications* (Ed: M. Dramićanin), Elsevier, Woodhead Publishing **2018**, pp. 63–83.
[10] M. Suta, A. Meijerink, *Adv. Theory Simul.* **2020**, *3*, 2000176.
[11] J. Zhou, B. del Rosal, D. Jaque, S. Uchiyama, D. Jin, *Nat. Methods* **2020**, *17*, 967.
[12] S. Uchiyama, N. Kawai, A. P. De Silva, K. Iwai, *J. Am. Chem. Soc.* **2004**, *126*, 3032.
[13] C. Gota, K. Okabe, T. Funatsu, Y. Harada, S. Uchiyama, *J. Am. Chem. Soc.* **2009**, *131*, 2766.
[14] C. Paviolo, A. H. A. Clayton, S. L. Mcarthur, P. R. Stoddart, *J. Microsc.* **2013**, *250*, 179.
[15] O. A. Savchuk, O. F. Silvestre, R. M. R. Adão, J. B. Nieder, *Sci. Rep.* **2019**, *9*, 7535.
[16] E. J. McLaurin, V. A. Vlaskin, D. R. Gamelin, *J. Am. Chem. Soc.* **2011**, *133*, 14978.
[17] S. Kalytchuk, O. Zhovtiuk, S. V. Kershaw, R. Zbořil, A. L. Rogach, *Small* **2016**, *12*, 466.
[18] C. D. S. Brites, S. V. Kuznetsov, V. A. Konyushkin, A. N. Nakladov, P. P. Fedorov, L. D. Carlos, *Eur. J. Inorg. Chem.* **2020**, *2020*, 1555.
[19] C. Hazra, A. Skripka, S. J. L. Ribeiro, F. Vetrone, *Adv. Opt. Mater.* **2020**, *8*, 2001178.
[20] C. D. S. Brites, X. Xie, M. L. Debasu, X. Qin, R. Chen, W. Huang, J. Rocha, X. Liu, L. D. Carlos, *Nat. Nanotechnol.* **2016**, *11*, 851.
[21] E. C. Ximendes, W. Q. Santos, U. Rocha, U. K. Kagola, F. Sanz-Rodríguez, N. Fernández, A. D. S. Gouveia-Neto, D. Bravo, A. M. Domingo, B. del Rosal, C. D. S. Brites, L. D. Carlos, D. Jaque, C. Jacinto, *Nano Lett.* **2016**, *16*, 1695.
[22] H. Peng, M. I. J. Stich, J. Yu, L. Sun, L. H. Fischer, O. S. Wolfbeis, *Adv. Mater.* **2010**, *22*, 716.
[23] M. Sójka, J. F. C. B. Ramalho, C. D. S. Brites, K. Fiaczyk, L. D. Carlos, E. Zych, *Adv. Opt. Mater.* **2019**, *7*, 1901102.
[24] M. Suta, Ž. Antić, V. Đorđević, S. Kuzman, M. D. Dramićanin, A. Meijerink, *Nanomaterials* **2020**, *10*, 543.
[25] Q. Han, W. Wu, W. Liu, Y. Yang, *RSC Adv.* **2017**, *7*, 35757.
[26] H. Lu, J. Yang, D. Huang, Q. Zou, M. Yang, X. Zhang, Y. Wang, H. Zhu, *J. Lumin.* **2019**, *206*, 613.
[27] A. S. Laia, D. A. Hora, M. V. dos S. Rezende, Y. Xing, J. J. Rodrigues, G. S. Maciel, M. A. R. C. Alencar, *J. Lumin.* **2020**, *227*, 117524.
[28] J. S. Donner, S. A. Thompson, M. P. Kreuzer, G. Baffou, R. Quidant, *Nano Lett.* **2012**, *12*, 2107.
[29] M. Kong, Y. Gu, Y. Chai, J. Ke, Y. Liu, X. Xu, Z. Li, W. Feng, F. Li, *Sci. China: Chem.* **2021**, *64*, 974.
[30] M. Jia, Z. Sun, M. Zhang, H. Xu, Z. Fu, *Nanoscale* **2020**, *12*, 20776.
[31] A. Nexha, J. J. Carvajal, M. C. Pujol, F. Díaz, M. Aguiló, *Nanoscale* **2021**, *13*, 7913.
[32] S. F. Collins, G. W. Baxter, S. A. Wade, T. Sun, K. T. V. Grattan, Z. Y. Zhang, A. W. Palmer, *J. Appl. Phys.* **1998**, *84*, 4649.
[33] D. Zhao, X. Han, S. Wang, J. Liu, Y. Lu, C. Li, *Chem. - Eur. J.* **2020**, *26*, 3145.
[34] D. Jaque, L. Martínez Maestro, B. del Rosal, P. Haro-Gonzalez, A. Benayas, J. L. Plaza, E. Martín Rodríguez, J. García Solé, *Nanoscale* **2014**, *6*, 9494.
[35] J. Cunha, T. Guo, G. Della Valle, A. N. Koya, R. Proietti Zaccaria, A. Alabastri, *Adv. Opt. Mater.* **2020**, *8*, 2001225.
[36] M. Suzuki, T. Plakhotnik, *Biophys. Rev.* **2020**, *12*, 593.
[37] J. Lifante, Y. Shen, I. Zabala Gutierrez, I. Rubia-Rodríguez, D. Ortega, N. Fernandez, S. Melle, M. Granado, J. Rubio-Retama, D. Jaque, E. Ximendes, *Adv. Sci.* **2021**, *8*, 2003838.
[38] A. Bednarkiewicz, J. Drabik, K. Trejgis, D. Jaque, E. Ximendes, L. Marciniak, *Appl. Phys. Rev.* **2021**, *8*, 011317.
[39] Y. Jiang, Y. Tong, S. Chen, W. Zhang, F. Hu, R. Wei, H. Guo, *Chem. Eng. J.* **2021**, *413*, 127470.
[40] J. Liu, X. Yue, Z. Wang, X. Zhang, Y. Xu, *J. Mater. Chem. C* **2020**, *8*, 13328.
[41] L. Marciniak, K. Elzbieciak-Piecka, K. Kniec, A. Bednarkiewicz, *Chem. Eng. J.* **2020**, *388*, 124347.
[42] Z. Cao, X. Wei, L. Zhao, Y. Chen, M. Yin, *ACS Appl. Mater. Interfaces* **2016**, *8*, 34546.
[43] I. E. Kolesnikov, D. V. Mamonova, M. A. Kurochkin, E. Y. Kolesnikov, E. Lähderanta, *J. Lumin.* **2021**, *231*, 117828.
[44] Y. Shen, H. D. A. Santos, E. C. Ximendes, J. Lifante, A. Sanz-Portilla, L. Monge, N. Fernández, I. Chaves-Coira, C. Jacinto, C. D. S. Brites, L. D. Carlos, A. Benayas, M. C. Iglesias-de la Cruz, D. Jaque, *Adv. Funct. Mater.* **2020**, *30*, 2002730.
[45] L. Marciniak, K. Prorok, L. Francés-Soriano, J. Pérez-Prieto, A. Bednarkiewicz, *Nanoscale* **2016**, *8*, 5037.
[46] J. Periša, Z. Ristić, V. Đorđević, M. Sekulić, T. Dramićanin, Ž. Antić, M. D. Dramićanin, *J. Lumin.* **2021**, *238*, 118306.
[47] K. Trejgis, M. D. Dramićanin, L. Marciniak, *J. Alloys Compd.* **2021**, *875*, 159973.
[48] X. Qiu, Q. Zhou, X. Zhu, Z. Wu, W. Feng, F. Li, *Nat. Commun.* **2020**, *11*, 4.
[49] F. Liu, Y. Tian, D. Deng, M. Wu, B. Chen, L. Zhou, S. Xu, *J. Rare Earths* **2020**, 124658.
[50] C. D. S. Brites, E. D. Martínez, R. R. Urbano, C. Rettori, L. D. Carlos, *Front. Chem.* **2019**, *7*, 267.
[51] H. D. A. Santos, I. Zabala Gutiérrez, Y. Shen, J. Lifante, E. Ximendes, M. Laurenti, D. Méndez-González, S. Melle, O. G. Calderón, E. López Cabarcos, N. Fernández, I. Chaves-Coira, D. Lucena-Agell, L. Monge, M. D. Mackenzie, J. Marqués-Hueso, C. M. S. Jones, C. Jacinto, B. del Rosal, A. K. Kar, J. Rubio-Retama, D. Jaque, *Nat. Commun.* **2020**, *11*, 2933.
[52] R. N. Day, M. W. Davidson, *Chem. Soc. Rev.* **2009**, *38*, 2887.
[53] P. L. Silva, O. A. Savchuk, J. Gallo, L. García-Hevia, M. Bañobre-López, J. B. Nieder, *Nanoscale* **2020**, *12*, 21647.

[54] G. G. Lambert, H. Depernet, G. Gotthard, D. T. Schultz, I. Navizet, T. Lambert, S. R. Adams, A. Torreblanca-Zanca, M. Chu, D. S. Bindels, V. Levesque, J. Nero Moffatt, A. Salih, A. Royant, N. C. Shaner, *PLoS Biol.* **2020**, *18*, e3000936.
[55] S. Kiyonaka, T. Kajimoto, R. Sakaguchi, D. Shinmi, M. Omatsu-Kanbe, H. Matsuura, H. Imamura, T. Yoshizaki, I. Hamachi, T. Morii, Y. Mori, *Nat. Methods* **2013**, *10*, 1232.
[56] S. Liang, Y. Wang, X. Wu, M. Chen, L. Mu, G. She, W. Shi, *Chem. Commun.* **2019**, *55*, 3509.
[57] C. Mi, J. Zhou, F. Wang, G. Lin, D. Jin, *Chem. Mater.* **2019**, *31*, 9480.
[58] L. L. Nathans, F. L. Oswald, K. Nimon, *Pract. Assess., Res. Eval.* **2012**, *17*, 9.
[59] M. Elshendy, A. F. Colladon, E. Battistoni, P. A. Gloor, *J. Inf. Sci.* **2018**, *44*, 408.
[60] J. Abraham, D. Higdon, J. Nelson, *SMU Data Sci. Rev.* **2018**, *1*, 22.
[61] C. Buntain, J. Golbeck in *IEEE Int. Conf. Smart Cloud, IEEE*, **2017**, New York, NY, USA, pp. 208–215.
[62] S. C. McGregor, R. R. Mourão, L. Molyneux, *J. Inf. Technol. Polit.* **2017**, *14*, 154.
[63] J. Wang, F. Wang, Y. Liu, J. Xu, H. Lin, B. Jia, W. Zuo, Y. Jiang, L. Hu, F. Lin, *Exp. Clin. Endocrinol. Diabetes* **2016**, *124*, 34.
[64] J. Ma, J. Yu, G. Hao, D. Wang, Y. Sun, J. Lu, H. Cao, F. Lin, *Lipids Health Dis.* **2017**, *16*, 42.
[65] D. J. Creek, A. Jankevics, R. Breitling, D. G. Watson, M. P. Barrett, K. E. V. Burgess, *Anal. Chem.* **2011**, *83*, 8703.
[66] M. Fernández-Fernández, P. Rodríguez-González, M. E. Añón Álvarez, F. Rodríguez, F. V. Á. Menéndez, J. I. G. Alonso, *Anal. Chem.* **2015**, *87*, 3755.
[67] A. M. dos Santos, *J. Fluoresc.* **2012**, *22*, 151.
[68] E. Jacchetti, E. Gabellieri, P. Cioni, R. Bizzarri, R. Nifosì, *Phys. Chem. Chem. Phys.* **2016**, *18*, 12828.
[69] H. F. Arata, F. Gillot, T. Nojima, T. Fujii, H. Fujita, *Lab Chip* **2008**, *8*, 1436.
[70] T. Beechem, A. Christensen, S. Graham, D. Green, *J. Appl. Phys.* **2008**, *103*, 124501.
[71] C. B. Saltonstall, J. Serrano, P. M. Norris, P. E. Hopkins, T. E. Beechem, *Rev. Sci. Instrum.* **2013**, *84*, 064903.
[72] L. M. Maestro, E. M. Rodríguez, F. S. Rodríguez, M. C. I. la Cruz, A. Juarranz, R. Naccache, F. Vetrone, D. Jaque, J. A. Capobianco, J. G. Solé, *Nano Lett.* **2010**, *10*, 5109.
[73] U. Rocha, C. Jacinto da Silva, W. Ferreira Silva, I. Guedes, A. Benayas, L. Martínez Maestro, M. Acosta Elias, E. Bovero, F. C. J. M. van Veggel, J. A. García Solé, D. Jaque, *ACS Nano* **2013**, *7*, 1188.
[74] D. J. Olive, *Linear Regression*, Springer International Publishing, Cham **2017**, pp. 1–494.
[75] E. Hemmer, A. Benayas, F. Légaré, F. Vetrone, *Nanoscale Horiz.* **2016**, *1*, 168.
[76] Y. Zhang, G. Hong, Y. Zhang, G. Chen, F. Li, H. Dai, Q. Wang, *ACS Nano* **2012**, *6*, 3695.
[77] B. del Rosal, D. Ruiz, I. Chaves-Coira, B. H. Juárez, L. Monge, G. Hong, N. Fernández, D. Jaque, *Adv. Funct. Mater.* **2018**, *28*, 1806088.
[78] Y. Kamei, M. Suzuki, K. Watanabe, K. Fujimori, T. Kawasaki, T. Deguchi, Y. Yoneda, T. Todo, S. Takagi, T. Funatsu, S. Yuba, *Nat. Methods* **2009**, *6*, 79.
[79] M. Nakano, Y. Arai, I. Kotera, K. Okabe, Y. Kamei, T. Nagai, *PLoS One* **2017**, *12*, e0172344.
[80] D. Ruiz, B. del Rosal, M. Acebrón, C. Palencia, C. Sun, J. Cabanillas-González, M. López-Haro, A. B. Hungría, D. Jaque, B. H. Juarez, *Adv. Funct. Mater.* **2017**, *27*, 1604629.
[81] H. D. A. Santos, D. Ruiz, G. Lifante, C. Jacinto, B. H. Juarez, D. Jaque, *Nanoscale* **2017**, *9*, 2505.
[82] H. D. A. Santos, E. C. Ximendes, M. del C. Iglesias-de la Cruz, I. Chaves-Coira, B. del Rosal, C. Jacinto, L. Monge, I. Rubia-Rodríguez, D. Ortega, S. Mateos, J. G. Solé, D. Jaque, N. Fernández, *Adv. Funct. Mater.* **2018**, *28*, 1803924.

SUPPORTING INFORMATION

Going above and beyond: A 10-fold gain in the performance of luminescence thermometers joining multiparametric sensing and multiple regression

*Fernando E. Maturi[1,2], Carlos D. S. Brites[1], Erving C. Ximendes[3], Carolyn Mills[4], Bradley Olsen[4], D. Jaque[3], Sidney J. L. Ribeiro[2], and Luís D. Carlos[1]**

Mr. F. E. M., Prof. C. D. S. B., Prof. L. D. C
[1]Phantom-g, CICECO – Aveiro Institute of Materials, Department of Physics, University of Aveiro, Aveiro, 3810-193, Portugal
*E-mail: lcarlos@ua.pt

Mr. F. E. M., Prof. S. J. L. R.
[2]Institute of Chemistry, São Paulo State University (UNESP), Araraquara, São Paulo, 14800-060, Brazil

Dr. E. C. X., Prof. D. J.
[3]Nanomaterials for Bioimaging Group, Universidade Autónoma de Madrid, Madrid, 28049, Spain

Prof. B. O., Dr. C. M.
[4]Department of Chemical Engineering, Massachusetts Institute of Technology, Cambridge, Massachusetts, 02139, United States

Table of Contents

S1. Materials and methods

S1.1. Repeatability

The repeatability of the integrated emission intensity of EGFP is given by:[1]

$$R = 1 - \frac{\max(I_c - I_{mean})}{I_{mean}} \quad \textbf{(S1)}$$

where I_c is the total integrated emission intensity in each cycle and I_{mean} is the mean value at each temperature. The values calculated with the data presented in **Figure S1** are 99.94% and 99.92% at 303.0 K and 313.0 K, respectively.

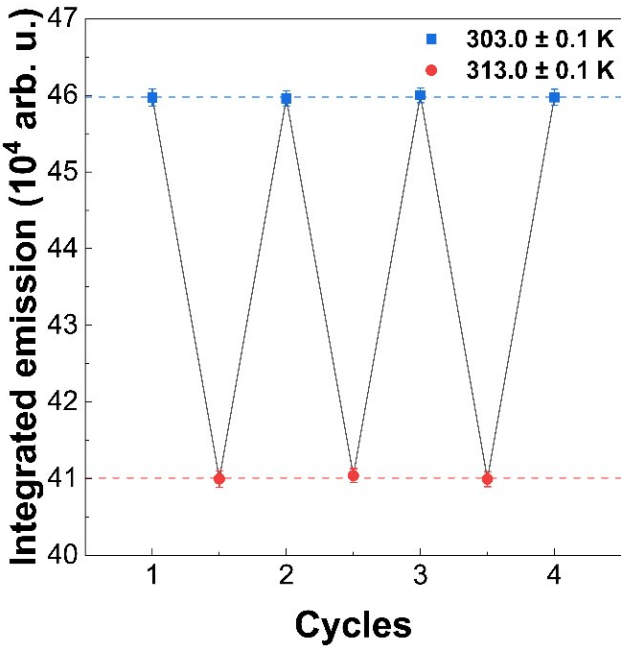

Figure S1. Total integrated emission of EGFP in three consecutive heating/cooling thermal cycles, between 303.0 and 313.0 K.

S1.2. Photoluminescence spectroscopy experimental setup

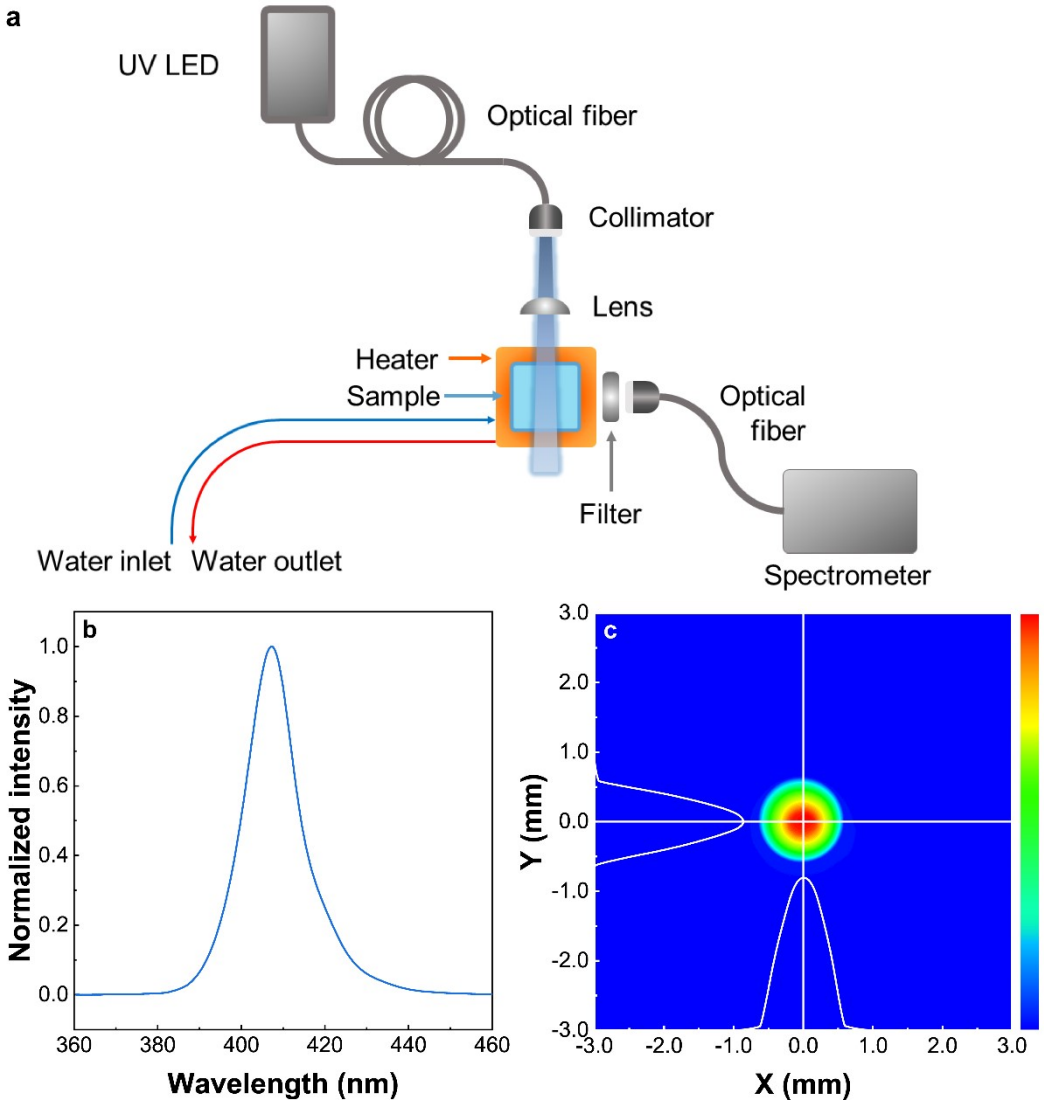

Figure S2. (a) Scheme of the experimental setup used for measuring the temperature of the aqueous suspension of EGFP. The temperature was controlled by using a sample holder coupled to a water circulator. **(b)** UV LED peaking at 408 ± 7 nm used as the excitation source in the photoluminescence experiments. **(c)** The UV beam profile was recorded with a CCD, with beam radius and area of 0.59 mm and 1.09 mm^2, respectively.

S1.3. Spectral correction and thermometric analysis

S1.3.1. Spectral correction

The emission band of EGFP presents a broad spectral width, therefore the emission spectra must be presented as a function of energy instead of wavelength.[2] For that reason, the signal was converted from wavelength to energy:

$$E = \frac{10^7}{\lambda} \quad \textbf{(S2)}$$

where E is the energy (in cm^{-1}) and λ is the corresponding wavelength (in nm). Since the conservation of energy must be taken into account, the intensity signal also needs to be corrected as follows:

$$I_E = I_\lambda \frac{d\lambda}{dE} = I_\lambda \frac{d}{dE}\left(\frac{10^7}{E}\right) = -I_\lambda \frac{10^7}{E^2} \quad \textbf{(S3)}$$

where I_E and I_λ are the intensities as a function of energy and wavelength, respectively. This is known as Jacobian transformation and the minus signal can be ignored because it only shows that integration occurs in opposite directions in wavelength and energy.[3]

S1.3.2. Spectral deconvolution

The corrected emission spectra of EGFP were deconvoluted into two peaks (**Figure S3**) by adjusting a sum of a Gaussian (Peak 1) and a Lorentzian (Peak 2) function:

$$y = y_0 + \left(\frac{A_1}{w_1\sqrt{\pi/2}}\exp\left(-2\frac{\left(x - x_{c_1}\right)^2}{{w_1}^2}\right)\right) + \left(\frac{2A_2}{\pi}\frac{W_2}{4\left(x - x_{c_2}\right)^2 + {W_2}^2}\right) \quad \textbf{(S4)}$$

where y is the corrected emission intensity, x is the energy (in cm^{-1}), y_0 is the baseline, A_1 and A_2 are the areas and x_{c_1} and x_{c_2} are the average energies of Peaks 1 and 2,

respectively. The parameter W_2 indicates the full width at half maximum ($FWHM$) of Peak 2 while w_1 indicates the width of Peak 1.

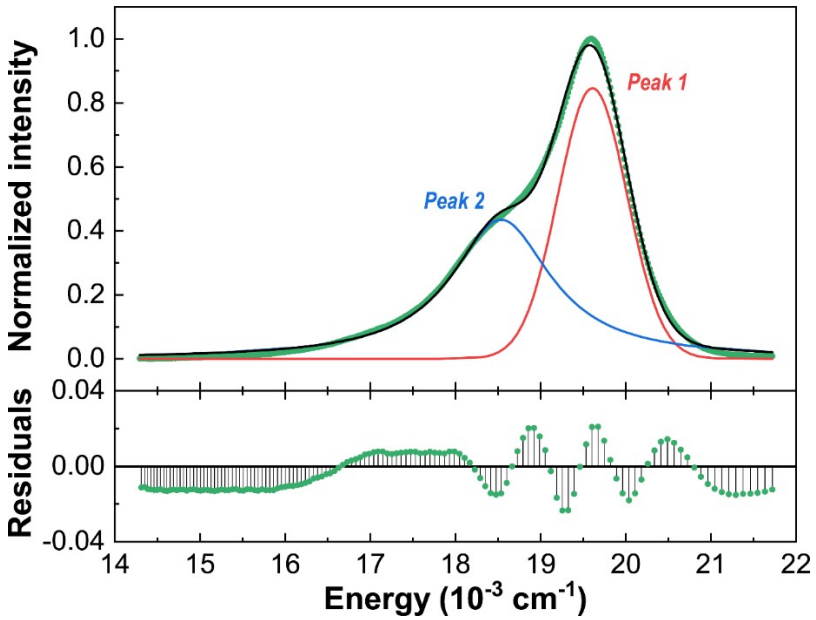

Figure S3. The emission spectrum of EGFP at 283.0 K (green points) under excitation at 408 nm. The spectrum was fitted to a combination of a Gaussian (Peak 1) and a Lorentzian (Peak 2) with r^2>0.99. The black line represents the fit envelope and the corresponding residuals are shown at the bottom part.

S1.3.3. Thermometric analysis

The five distinct thermometric parameters (Δ_i) were defined from the fit parameters as follows: intensity ratio ($I_R = A_1/A_2$), peak energy of Peak 1 ($E_1 = x_{c_1}$), FWHM of peak 1 ($W_1 = w_1\sqrt{2\ln 2}$), peak energy of peak 2 ($E_2 = x_{c_2}$), and FWHM of peak 2 (W_2). The reported Δ_i and the corresponding uncertainty ($\delta\Delta_i$) are the averages and the standard deviation values from 100 measurements per temperature, respectively. The relative thermal sensitivity for single Δ was calculated as $S_r = \frac{1}{\Delta}\left|\frac{\partial\Delta}{\partial T}\right|$ while the values of S_r for multiple Δ were calculated through Equation 3 from the manuscript.

S1.3.3.1. Peak energy and energy shift

Despite both peak energy and energy shift can be used to describe the same temperature-induced band shift of EGFP and Ag_2S, each quantity presents a different physical and mathematical meaning. The peak energy (sometimes referred to as peak wavelength or peak position) describes the average absolute value of the energy distribution resulting from an electronic transition while the energy shift (also known as wavelength shift or peak shift) indicates the relative variation of this energy distribution in a timeframe or temperature range. Since relative values of energy are smaller than the absolute ones, a great improvement of S_r is expected if one uses energy shift instead of the peak energy as a thermometric parameter. However, the energy shift must be only used when its value is higher than the energy step (set by the experimental conditions). Otherwise, the relative change in the energy shift ($\delta E_s/E_s$) tends to zero and, consequently, S_r tends to infinite, which does not present any physical meaning. Note that the energy shift at the reference energy equals zero, therefore this data point must be disregarded, which is the disadvantage of using energy shift as a thermometric parameter.

It is worth pointing out that the standard error of the fit cannot be used as the uncertainty of the peak energy or energy shift when its value is smaller than the energy step defined during the spectral acquisition. This is because the uncertainty cannot be smaller than the minimum energy value measured by the spectrometer. The same rationale applies to the determination of uncertainties in the measurements of emission lifetimes (the uncertainty cannot be smaller than the time step of the measurements).

Figure S4 and **Figure S5** present the thermometric performance of EGFP when considering the values obtained from peak 1 in wavelength and energy units, respectively. As expected, the results show that there is no difference in S_r and δT values when the calculation is performed in wavelength or energy units. However, the use of

energy shift displays an improvement of 3 orders of magnitude in S_r when compared to the same value obtained with peak energy.

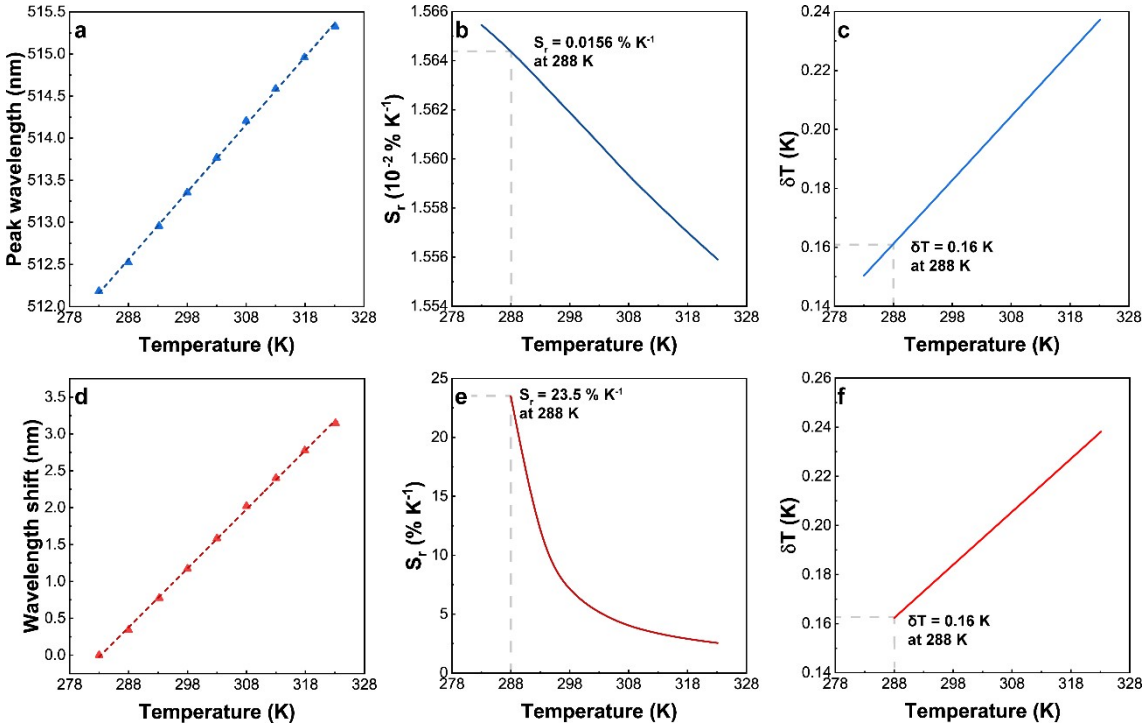

Figure S4. Use of peak wavelength from peak 1 as thermometric parameter (**a**) and its relative thermal sensitivity (**b**) and temperature uncertainty (**c**). Use of wavelength shift from peak 1 as thermometric parameter (**d**) and its relative thermal sensitivity (**e**) and temperature uncertainty (**f**). The values of peak 1 presented in wavelength units were retrieved before the Jacobian transformation of the emission spectra of EGFP.

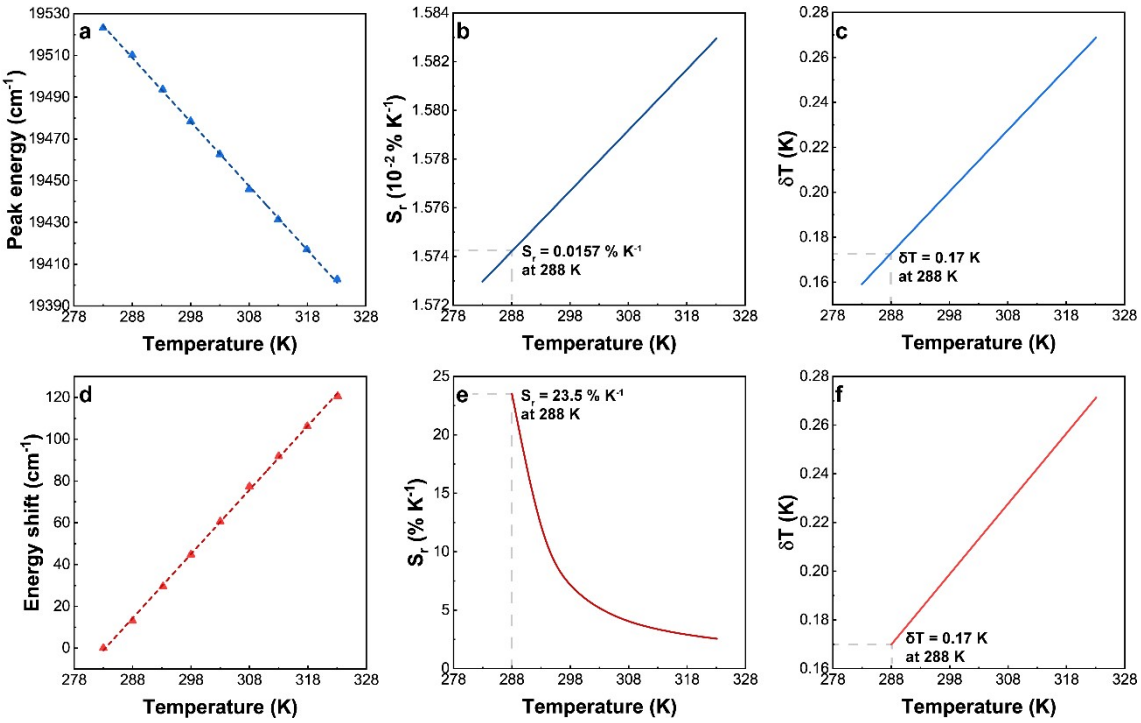

Figure S5. Use of peak energy from peak 1 as thermometric parameter (**a**) and its relative thermal sensitivity (**b**) and temperature uncertainty (**c**). Use of energy shift from peak 1 as thermometric parameter (**d**) and its relative thermal sensitivity (**e**) and temperature uncertainty (**f**). The values of peak 1 presented in energy units were obtained after the Jacobian transformation of the emission spectra of EGFP.

S1.4. Structural and colloidal characterization of EGFP

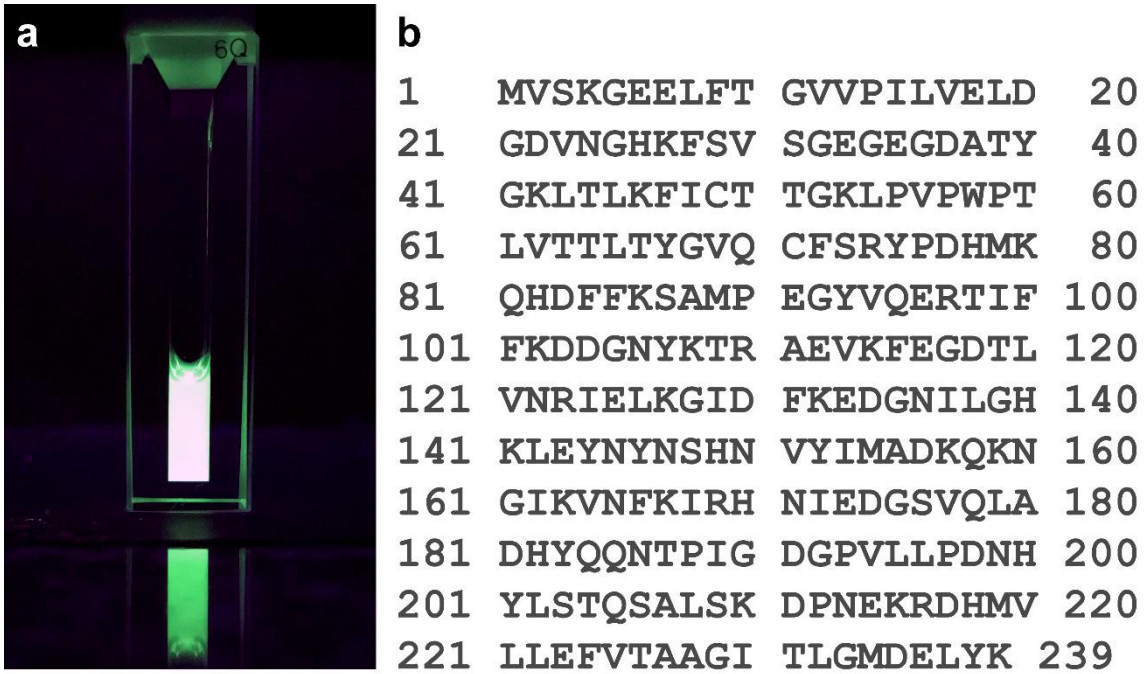

Figure S6. (a) Photograph of EGFP aqueous suspension at room temperature under UV light exposure (365 nm) displaying its characteristic green emission. **(b)** The confirmed amino acid sequence of EGFP.

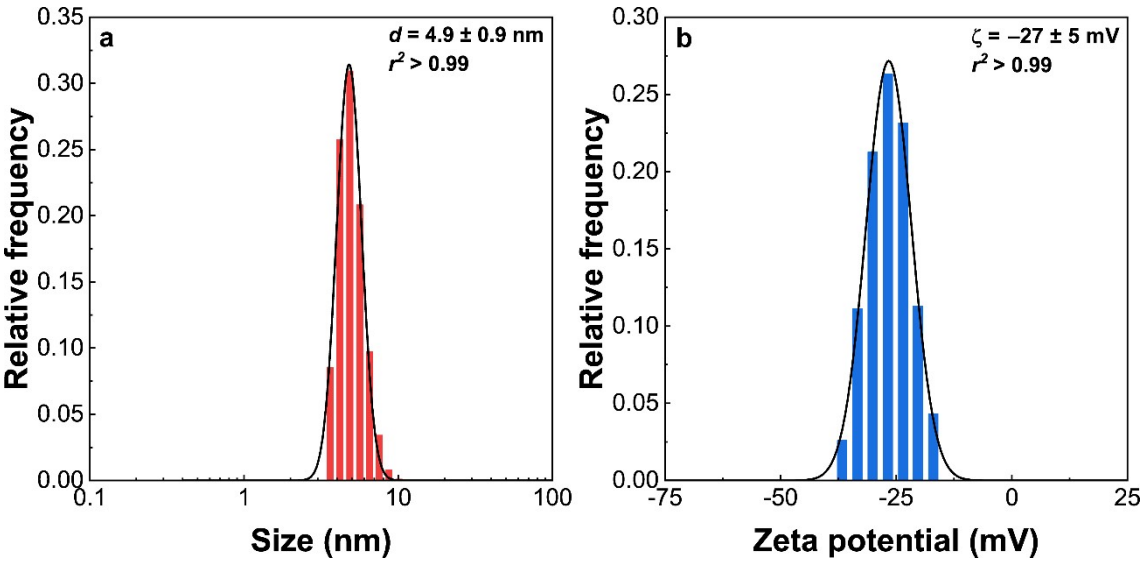

Figure S7. (a) Hydrodynamic size distribution and **(b)** zeta potential of EGFP. The black lines are the best fits for the hydrodynamic size (log-normal distribution) and zeta potential (Gaussian distribution) data. The values of d and ζ obtained for EGFP are in good agreement with expected values.[4,5]

S1.5. UV-Vis absorption spectroscopy

The UV-Vis absorption spectrum of the EGFP (**Figure S8**) presents a band centered at 280 nm, which is related to the characteristic absorption of the aromatic amino acids phenylalanine, tryptophan, and tyrosine.[6] Moreover, the intrinsic absorption of both anionic and neutral forms of EGFP is seen as a broadband with a maximum at 488 nm and a shoulder between 350 and 450 nm, respectively, where the absorption of the neutral form dominates the spectrum due to the higher pH of the aqueous medium.[7]

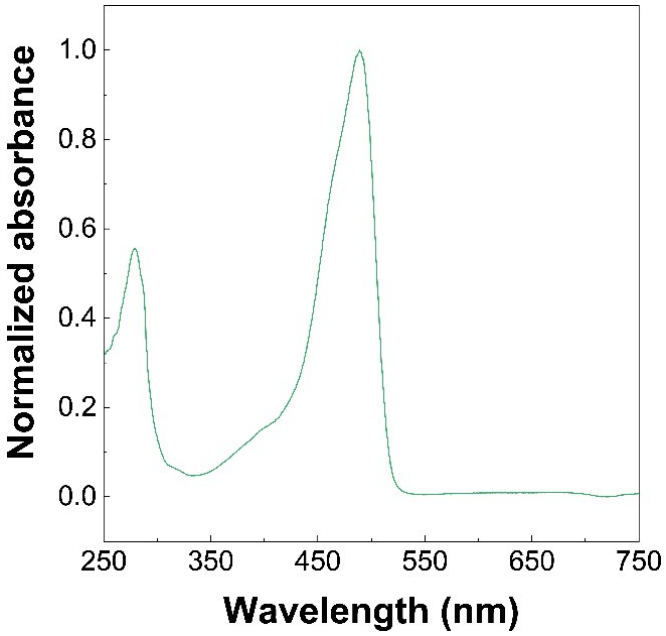

Figure S8. UV-Vis absorbance spectrum of the EGFP aqueous solution.

S2. Multiple linear regression

2.1. Data fitting

When considering single parametric secondary thermometers (the great majority of the examples proposed so far), a calibration curve is necessary to describe the thermometric parameter as a function of the temperature ($\Delta=f(T)$).[8] In this sense, the thermometric parameter is usually fitted to a linear trend through the least-squares method. The same approach can be used when dealing with multiple parameters. However, describing simultaneously multiple thermometric parameters as a function of temperature is not feasible because each parameter presents a different magnitude. For that reason, distinct thermometric parameters (Δ_1, Δ_2, …, Δ_n) are used to predict the reference temperature from a thermocouple, *i.e.*, $T=f(\Delta_1, \Delta_2, \ldots, \Delta_n)$ in the multiple linear regression model (MLR, Equation 1 of the manuscript).

The slopes and coefficient of determination are presented as β and R^2, respectively, in MLR to avoid misinterpretations when comparisons to single linear regression are made. Whereas in this latter case r^2 – the square of the sample correlation coefficient between the observed outcomes and the observed predictor values – should be used, in MLR R^2 – the square of the coefficient of multiple correlation – provides a measure of how well the observed outcomes are replicated by the model. Nevertheless, both single and multiple regression relies on the use of the least-squares method to find the best fit. The contribution of each variable (thermometric parameter) to the predicted value (temperature) in MLR is usually analyzed by taking the weighted values of β, which are the standard scores (z-scores) of β:[9]

$$z = \frac{\beta - \bar{\beta}}{\sigma} \qquad \textbf{(S5)}$$

where z is the z-scored value of each β (β weight), and $\bar{\beta}$ and σ are the mean value and standard deviation of all the β considered, respectively. In this sense, the β weights show how the temperature increases (in standard deviations) when a thermometric parameter is increased by one standard deviation (assuming that the other thermometric parameters are kept constant).

In its easier form, the MLR applied to nanothermometry is a linear combination of multiple thermometric parameters that describes the average value of the temperature. In this work, MLR was performed using a built-in function of MATLAB 2021a under the license provided to the University of Aveiro. The five distinct Δ defined for EGFP in the previous section were used as predictors (n = 5) and the temperature measured with the thermocouple was used as a response variable.

2.2. Relative thermal sensitivity

The relative thermal sensitivity (S_r) of a thermometer is defined as $S_r = \frac{1}{\Delta}\left|\frac{\partial \Delta}{\partial T}\right|$. In order to extend this definition to a multivariate linear analysis, we consider that the rate of change of the temperature for each thermometric parameter ($dT/d\Delta_i$) is the slope of a straight line, *i.e.* β_i. The corresponding S_r for a single thermometric parameter is then:

$$S_r \equiv \frac{1}{\Delta_i}\frac{d\Delta_i}{dT} = \frac{1}{\Delta_i}\frac{1}{\frac{dT}{d\Delta_i}} = \frac{1}{\Delta_i \beta_i} \quad \textbf{(S6)}$$

If the multiparametric linear relation is defined using 2 thermometric parameters, the corresponding calibration is represented in **Figure S9** as the black arrow. The black arrow results from the sum of the blue and red arrows, with a length given by the Pythagorean theorem, which results in a relative thermal sensitivity of:

$$S_r = \sqrt{\sum_{i=1}^{n} \left(\frac{1}{\Delta_i}\left|\frac{\partial \Delta_i}{\partial T}\right|\right)^2} \quad \textbf{(S7)}$$

where n is the total number of Δ_i terms (n = 2 in the example illustrated in Figure S9). Therefore, the S_r for a multiparametric system is given by rewriting the derivatives using the βi values:

$$S_r = \sqrt{\sum_{i=1}^{n} \left(\frac{1}{\Delta_i \beta_i}\right)^2} = \sqrt{\sum_{i=1}^{n} (\Delta_i \beta_i)^{-2}} \quad \textbf{(S8)}$$

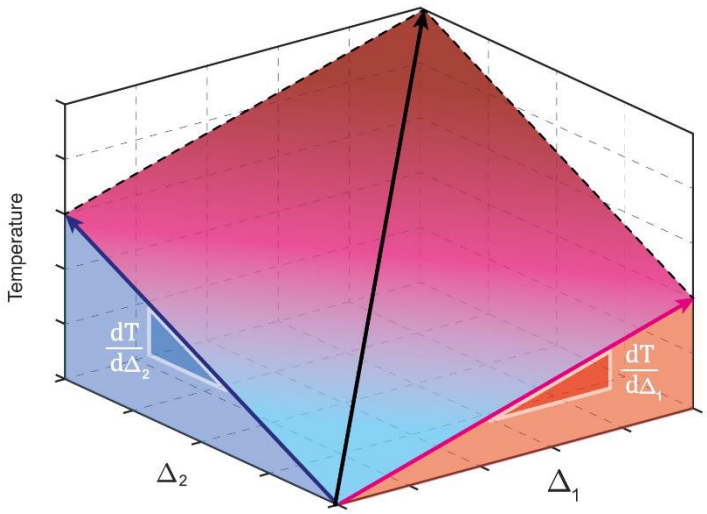

Figure S9. Schematic representation of MLR for the particular case of 2 thermometric parameters. Notice that the black arrow (calibration curve) is given by the vectorial sum of the red and blue arrows.

2.3. Temperature uncertainty

The value of δT in the multiparametric thermal sensing was calculated from MLR as follows, using the same rational followed for defining S_r:

$$\delta T = \frac{1}{S_r}\sqrt{\sum_{i=1}^{n}\left(\frac{\delta\Delta_i}{\Delta_i}\right)^2} \quad \textbf{(S9)}$$

where $\delta\Delta_i/\Delta_i$ is the relative uncertainty in each thermometric parameter.

2.4. Calibration of individual parameters and temperature differences

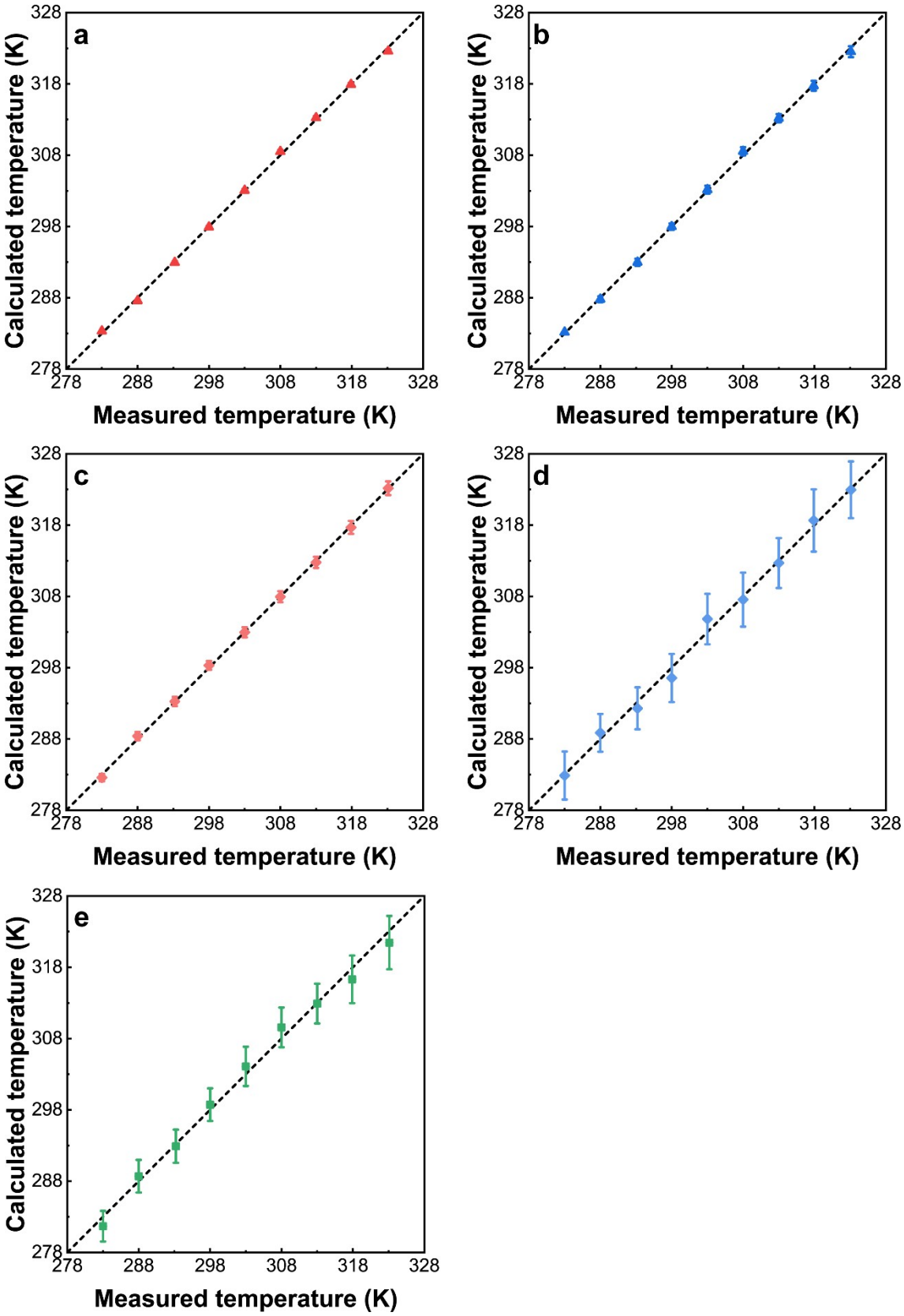

Figure S10. Correlation between the temperature measured with the thermocouple (*x*-axis) and the temperature calculated (*y*-axis) from **(a)** E_1, **(b)** E_2, **(c)** W_1, **(d)** W_2, and **(e)** I_R. The dashed black lines are guides for the eyes corresponding to $y=x$.

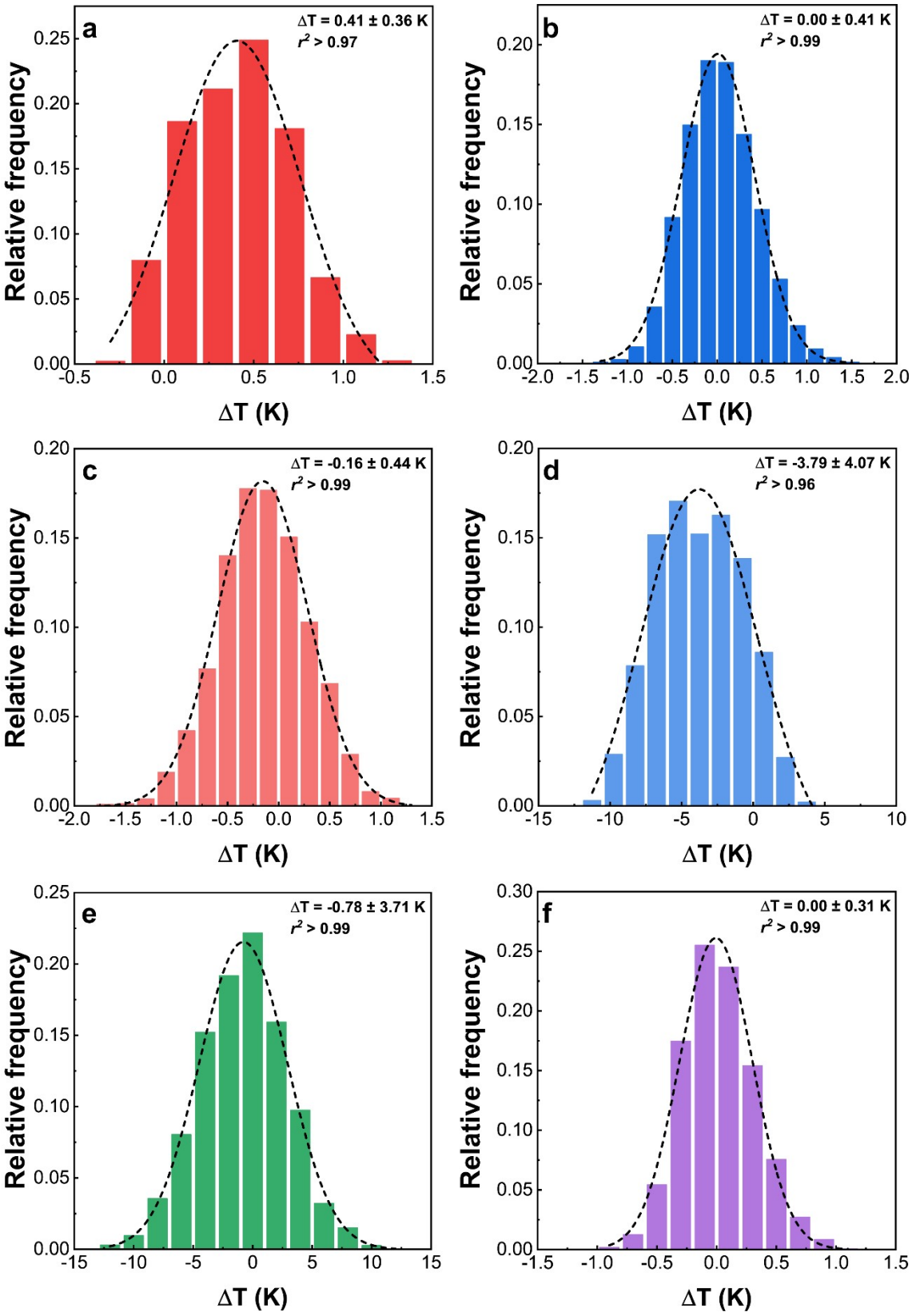

Figure S11. The corresponding histogram of the temperature deviation (ΔT) between the temperature measured with the thermocouple and the temperature calculated through **(a)** E_1, **(b)** E_2, **(c)** W_1, **(d)** W_2, **(e)** I_R, and **(f)** MLR. The resulting histograms were adjusted to a Gaussian distribution, with the best fit displayed by the dashed black lines. The reported ΔT and uncertainty values are the mean and standard deviation values from the fits, respectively.

2.5. Fitting parameters

Table S1. Slopes (***a***), intercepts (***b***), and coefficients of determination (r^2) of the temperature dependence of each thermometric parameter (Δ_i) from EGFP aqueous suspension.

Δ_i	***a***	***b***	r^2
I_R	$(7.9 \pm 0.3)\times10^{-4}$ K^{-1}	0.24 ± 0.01	0.993
E_1 (cm^{-1})	–3.07 ± 0.03 cm^{-1} K^{-1}	20393 ± 9 cm^{-1}	0.999
E_2 (cm^{-1})	–3.83 ± 0.03 cm^{-1} K^{-1}	19697 ± 10 cm^{-1}	0.999
W_1 (cm^{-1})	2.39 ± 0.02 cm^{-1} K^{-1}	108 ± 6 cm^{-1}	0.999
W_2 (cm^{-1})	0.96 ± 0.03 cm^{-1} K^{-1}	1324 ± 8 cm^{-1}	0.994

Table S2. Slopes ($\boldsymbol{\beta_i}$), intercept ($\boldsymbol{\beta_0}$), and coefficient of determination (R^2) of the multiple linear regression performed on EGFP aqueous suspension to predict the temperature by using $\boldsymbol{I_R}$, $\boldsymbol{W_1}$, $\boldsymbol{E_1}$, $\boldsymbol{W_2}$, and $\boldsymbol{E_2}$ as explanatory variables. The weighted value of $\boldsymbol{\beta_i}$ is the *z*-scored value of the slopes, given in standard deviations (unitless).

Fit parameter	***β* value**	***β* weight**	R^2
β_0 (K)	$(2.4 \pm 0.6)\times10^3$	-	0.999
β_{I_R} (K)	$(-2.3 \pm 0.1)\times10^2$	–1.79	
β_{W_1} (K cm^{-1})	0.23 ± 0.04	0.45	
β_{E_1} (K cm^{-1})	0.15 ± 0.04	0.45	
β_{W_2} (K cm^{-1})	0.02 ± 0.01	0.45	
β_{E_2} (K cm^{-1})	–0.28 ± 0.04	0.45	

Table S3. Slopes (***a***), intercepts (***b***), and coefficients of determination (r^2) of the temperature dependence of each thermometric parameter (Δ_i) from Ag_2S nanoparticles.

Δ_i	***a***	***b***	r^2
I_R	$(1.58 \pm 0.04)\times10^{-2}$ K^{-1}	–3.9 ± 0.1	0.984
E (cm^{-1})	–7.4 ± 0.1 K^{-1}	10520 ± 33 K	0.995

Table S4. Slopes ($\boldsymbol{\beta_i}$), intercept ($\boldsymbol{\beta_0}$), and coefficient of determination (R^2) of the multiple linear regression performed on Ag_2S nanoparticles to predict the temperature by using $\boldsymbol{I_R}$ and $\boldsymbol{E}$ as explanatory variables. The weighted value of $\boldsymbol{\beta_i}$ is the *z*-scored value of the slopes, given in standard deviations (unitless).

Fit parameter	***β* value**	***β* weight**	R^2
β_0 (K)	1341 ± 80	-	0.998
β_{I_R} (K)	2.6 ± 0.4	0.71	
β_E (K cm^{-1})	–0.13 ± 0.01	–0.71	

S3. References

[1] L. D. Carlos, F. Palacio, Eds. , *Thermometry at the Nanoscale*, Royal Society Of Chemistry, Cambridge, **2015**.

[2] M. Suta, A. Meijerink, *Adv. Theory Simulations* **2020**, *3*, 2000176.

[3] J. Mooney, P. Kambhampati, *J. Phys. Chem. Lett.* **2013**, *4*, 3316.

[4] R. N. Day, M. W. Davidson, *Chem. Soc. Rev.* **2009**, *38*, 2887.

[5] C. N. Lam, M. Kim, C. S. Thomas, D. Chang, G. E. Sanoja, C. U. Okwara, B. D. Olsen, *Biomacromolecules* **2014**, *15*, 1248.

[6] N. V. dos Santos, C. F. Saponi, T. L. Greaves, J. F. B. Pereira, *RSC Adv.* **2019**, *9*, 22853.

[7] H. E. Seward, C. R. Bagshaw, *Chem. Soc. Rev.* **2009**, *38*, 2842.

[8] S. Balabhadra, M. L. Debasu, C. D. S. Brites, R. A. S. Ferreira, L. D. Carlos, *J. Phys. Chem. C* **2017**, *121*, 13962.

[9] L. L. Nathans, F. L. Oswald, K. Nimon, *Pract. Assessment, Res. Eval.* **2012**, *17*, 1.

Manuscript 7

Sustainable Smart Tags with Two-Step Verification for Anticounterfeiting Triggered by the Photothermal Response of Upconverting Nanoparticles

F. E. Maturi, C. D. S. Brites, R. R. Silva, K. Nigoghossian, D. Wilson, R. A. S. Ferreira, S. J. L. Ribeiro, L. D. Carlos

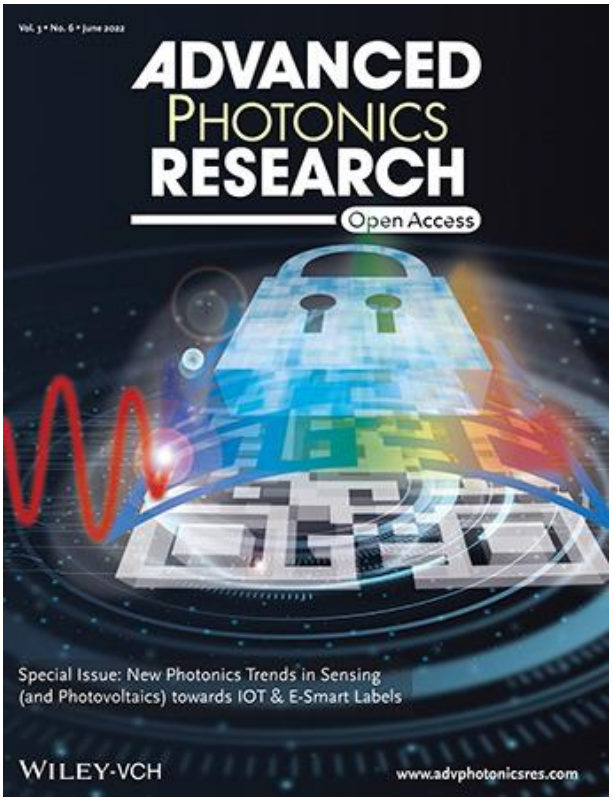

Advanced Photonics Research, 3 (6), 2100227, 2022.

DOI: https://doi.org/10.1002/adpr.202100227

Featured as Front Cover

ADVANCED PHOTONICS RESEARCH
Open Access
www.adpr-journal.com

Sustainable Smart Tags with Two-Step Verification for Anticounterfeiting Triggered by the Photothermal Response of Upconverting Nanoparticles

Fernando E. Maturi, Carlos D. S. Brites, Robson R. Silva, Karina Nigoghossian, Deivy Wilson, Rute A. S. Ferreira, Sidney J. L. Ribeiro, and Luís D. Carlos**

Quick-response (QR) codes are gaining much consideration in recent years due to their simple and fast readability compared with conventional barcodes. QR codes provide increased storage capacity and safer access to information, fostering the development of optical or printed smart tags as preferred tools for the Internet of Things (IoT). Herein, the combination of Yb^{3+}/Er^{3+}-doped $NaGdF_4$ upconverting nanoparticles (UCNPs) with recovered plastic for the fabrication of sustainable screen-printed QR codes is reported. Their photothermal response under distinct power densities of the 980 nm laser irradiation (15–115 W cm^{-2}) induces color-tuning and temperature sensing. This power dependence is exploited to design a double key molecular keylock accessed by a smartphone camera through the red (*R*), green (*G*), and blue (*B*) (*RGB*) additive color model and upconversion thermometry. The latter is based on the integrated areas of the $^2H_{11/2}\rightarrow{}^4I_{15/2}$ and $^4S_{3/2}\rightarrow{}^4I_{15/2}$ Er^{3+} transitions using the interconnectivity and integration into the IoT network of the mobile phone to download the temperature calibration curve of the UCNPs from a remote server. These findings illustrate the potential of QR codes-bearing UCNPs toward the design of smart tags for mobile optical sensing and anticounterfeiting.

1. Introduction

With the ever-growing demand for faster communication methods, higher storage capacity, and improved manufacturing technologies, Industry 4.0 urges to convert passive materials into smart systems to achieve more reliable fabrication routes, easier access to information, unique data identification (ID), and improved anticounterfeiting applications.[1–3] In this sense, the use of smart tags is a good choice because they provide a simple way to perform quick readouts of encrypted information using a smartphone camera in the context of the Internet of Things (IoT).[4–6] Quick-response (QR) codes are a gateway to smart tags because they comprise different information in a 2D barcode matrix composed of black and white square modules, greatly improving the amount of stored information using printed materials.[7]

In the past years, researchers have been striving to develop novel smart tags based on QR codes to improve the level of encryption and further increase the storage capacity. Several methods were reported,[8–11] but the most elegant one is the use of color multiplexing, which relies on the addition of different colors to enhance the storage capacity compared to the common black-white QR codes.[12] This approach paves the road for incorporating additional layers of security by using luminescent materials, as optically active components of inks, to produce the QR codes, where hidden information can be accessed upon exposure to specific light sources.[13,14] Multiplexed QR codes were shown to display twice the storage capacity of a conventional QR code.[4,12] Moreover, luminescent smart QR codes store unique authentication tags that can be securely transmitted to a remote server, enabling trackability and the triggering of security alerts or other additional security features.[15]

Among luminescent materials, lanthanide-doped upconverting nanoparticles (UCNPs) can be highlighted due to their efficient conversion of near-infrared (NIR) low-energy radiation in high-energy light emission in the visible spectral range, by a process known as upconversion.[16–20] Since UCNPs present singular spectroscopic features such as sharp emission bands, long excited-state lifetimes, and photostable response,[21] it is possible to envisage smart tags based on QR codes containing UCNPs that

F. E. Maturi, C. D. S. Brites, R. A. S. Ferreira, L. D. Carlos
Phantom-g, CICECO – Aveiro Institute of Materials
Department of Physics
University of Aveiro
Aveiro 3810-193, Portugal
E-mail: lcarlos@ua.pt

F. E. Maturi, R. R. Silva, K. Nigoghossian, S. J. L. Ribeiro
Institute of Chemistry
São Paulo State University (UNESP)
Araraquara, SP 14 800-060, Brazil
E-mail: sidney.jl.ribeiro@unesp.br

R. R. Silva, D. Wilson
São Carlos Institute of Physics
University of São Paulo
São Carlos, SP 13 566-590, Brazil

The ORCID identification number(s) for the author(s) of this article can be found under https://doi.org/10.1002/adpr.202100227.

DOI: 10.1002/adpr.202100227

present a unique luminescent response provided by NIR excitation sources.[22–27] Although several luminescent materials display light-emitting properties under ultraviolet (UV) excitation,[15,28,29] the use of smart tags containing UCNPs provide a step further in anticounterfeiting applications because NIR excitation is more difficult to replicate. Furthermore, NIR irradiation does not give rise to down-shifting light emission from conventional luminescent materials, avoiding interference from background luminescence during the readout of the QR code.[30] Also, and more exciting, the concomitant controlled heating of the material is an opportunity to explore thermal-dependent features that are not accessible under UV illumination, while transparency is kept.

The use of smart tags containing UCNPs is indeed an ingenious strategy because they can be used in the context of "communicating particles," where a unique color ID and a temperature recorder are integrated into a single platform.[31] A major advantage of using UCNPs in this context is that different emission colors can be achieved using the power-dependent ratio between different emissions (e.g., the Er^{3+} emissions in the red and green spectral regions[32]) while the temperature is registered through, for instance, the intensity ratio of the $^2H_{11/2} \rightarrow {}^4I_{15/2}$ and $^4S_{3/2} \rightarrow {}^4I_{15/2}$ Er^{3+} transitions (Yb^{3+}/Er^{3+} is by far the widely reported pair in Ln^{3+}-luminescent thermometry).[33,34] Therefore, no further nanoparticle doping is required and both temperature and color information can be retrieved with single wavelength excitation. In addition, this approach paves the way for coupling the temperature sensing and color-tuning properties to QR codes to develop optical sensors that can be read by smartphones, which is an exciting approach for mobile optical (mOptical) sensing.[35,36]

Nevertheless, the use of such an advanced strategy for real-world applications only becomes attractive if one may circumvent dispendious fabrication routes of the QR codes, time-consuming data analysis, and complex implementation. In this way, we herein present a novel method to obtain smart tags by serigraph printing using a sustainable strategy to produce optically active inks using polystyrene (PS) recycled from expanded polystyrene (EPS) package wastes through its dissolution into d-limonene, a green solvent extract from orange peel.[37] We demonstrate its applicability to fabricate QR codes embedding $NaGdF_4:Yb^{3+}/Er^{3+}$ UCNPs and presenting color-tuning and temperature sensing simply by changing the power density of a 980 nm laser excitation source. This power-dependent dual-mode encoding is accessed either through a spectrometer or a smartphone. In the latter, photographs of the QR codes are treated by the red (*R*), green (*G*), and blue (*B*) (*RGB*) additive color model to access the first codification level of the system. The interconnectivity and integration into the IoT network of the mobile phone allow the download of the temperature calibration curve of the UCNPs from a remote server ensuring access to the second encoding level.

2. Results and Discussion

2.1. PS Recycling

EPS is usually composed of 98% of air, giving rise to low-density solid wastes with an unattractive small-scale collection, uneconomical bulk volume storage, and noncost effective transportation for commercial purposes, which leads to a recycling rate lower than 1%.[38,39] As the main commercial form of PS is EPS, it is possible to easily recycle PS by dissolving EPS into organic solvents, therefore, providing a low-energy consumption due to room temperature processability, preventing eventual degradation of PS and allowing solvent recovery afterward.[40] The use of d-limonene as solvent is an interesting choice because it can dissolve substantial amounts of EPS (up to 260 g of EPS per liter of d-limonene),[41] besides being a biodegradable and low toxicity compound that presents the lowest contribution to global warming among distinct organic solvents.[37,41,42] Furthermore, it is a solvent from a renewable source, extracted from orange rinds as a byproduct in orange juice production with a world production of over 70 000 tons per year.[43]

To demonstrate the feasibility of using EPS as a reliable source of PS, proton nuclear magnetic resonance (^1H NMR) spectra were registered for a sample of the EPS used in this work and a reference sample of PS with an average molecular weight of 280 000 g mol^{-1} (PS 280 k), presented in **Figure 1**. Both

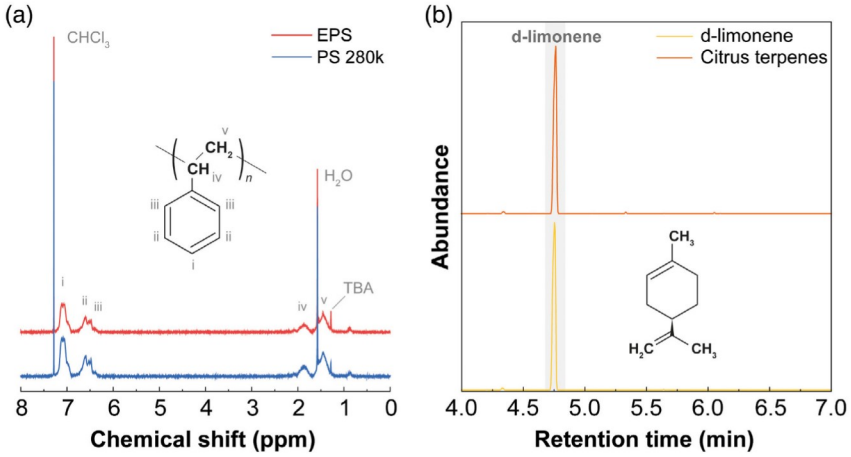

Figure 1. a) ^1H NMR spectra of EPS and PS samples (600 MHz, 298 K, $CDCl_3$). b) GC–MS chromatogram of d-limonene and citrus terpenes samples. The mass spectrum of the d-limonene found in the citrus terpenes sample is presented in Figure S1, Supporting Information.

samples display the typical chemical shifts (δ) of the aromatic protons of benzene rings between 7.25 and 6.30 ppm (i–iii) and the chemical shifts assigned to CH (iv) and CH_2 (v) at 1.86 and 1.45 ppm, respectively.[44,45] Furthermore, residual peaks of *tert*-butyl alcohol (TBA, 1.28 ppm), water (1.60 ppm), and chloroform (7.28 ppm) from impurities in the $CDCl_3$ solvent are seen.[46,47] As there is no structural difference between the samples, EPS can indeed be used as a cheaper and more sustainable source of PS. In addition, reagent grade d-limonene can be replaced by citrus terpenes, which is a high content d-limonene oil obtained through the distillation of the oil extracted from the orange peel. This is supported by the chromatogram of gas chromatography-mass spectrometry (GC-MS) in Figure 1b, where the content of d-limonene (retention time = 4.76 min) is 93% for both citrus terpenes and reagent grade d-limonene. As it is possible to recover PS from EPS wastes by dissolving it in citrus terpenes, these results highlight the feasibility of using renewable solvents to recycle plastics, developing a sustainable approach to fabricate QR codes using low-cost materials and fast printing methods.

2.2. UCNPs Characterization and Thermal Response of the QR Codes

$NaGdF_4:Yb^{3+}/Er^{3+}$ UCNPs were obtained in a hexagonal plate morphology with a hydrodynamic diameter of 183 ± 72 nm, confirmed by the transmission electron microscopy (TEM) micrograph and dynamic light scattering (DLS) size distribution presented in **Figure 2**, respectively. The as-synthesized UCNPs display a good dispersion in nonpolar solvents due to the presence of the hydrophobic oleate capping, making them suitable for incorporation into the d-limonene/PS solution to obtain the UCNPs containing PS ink (PS-UCNPs) used to fabricate the QR codes by serigraphy. The screen-printed QR codes present the characteristic Er^{3+} upconversion upon 980 nm excitation, with the $^2H_{11/2} \rightarrow {}^4I_{15/2}$ (510–534 nm) and $^4S_{3/2} \rightarrow {}^4I_{15/2}$ (534–554 nm) transitions of Er^{3+} observed in the green spectral range, as shown in **Figure 3**. Moreover, the $^2H_{9/2} \rightarrow {}^4I_{13/2}$ originated in the upper energy emitting level of Er^{3+} is observed as a shoulder around 555 nm, consistent with recent reports in the literature.[48,49]

To record the temperature using the photon upconversion of the obtained QR codes, the ratio between the integrated intensities of the $^2H_{11/2} \rightarrow {}^4I_{15/2}$ (I_H) and $^4S_{3/2} \rightarrow {}^4I_{15/2}$ (I_S) transitions in the emission spectra shown in Figure 3a was used to define the thermometric parameter $\Delta = I_H/I_S$ (Experimental Section for details). Further, and as usual in luminescence thermometry,[50] the calibration curve $\Delta(T)$ was acquired (Figure 3b), being T the temperature measured with a K-type thermocouple. The thermal sensing ability of the QR codes was evaluated through their relative thermal sensitivity $\left(S_r = \frac{1}{\Delta}\left|\frac{\partial \Delta}{\partial T}\right|\right)$ and temperature uncertainty $\left(\delta T = \frac{1}{S_r}\frac{\delta \Delta}{\Delta}\right)$, which are the figures of merit used since 2012 to evaluate the performance of luminescent thermometers.[33] The maximum S_r and minimum δT values are

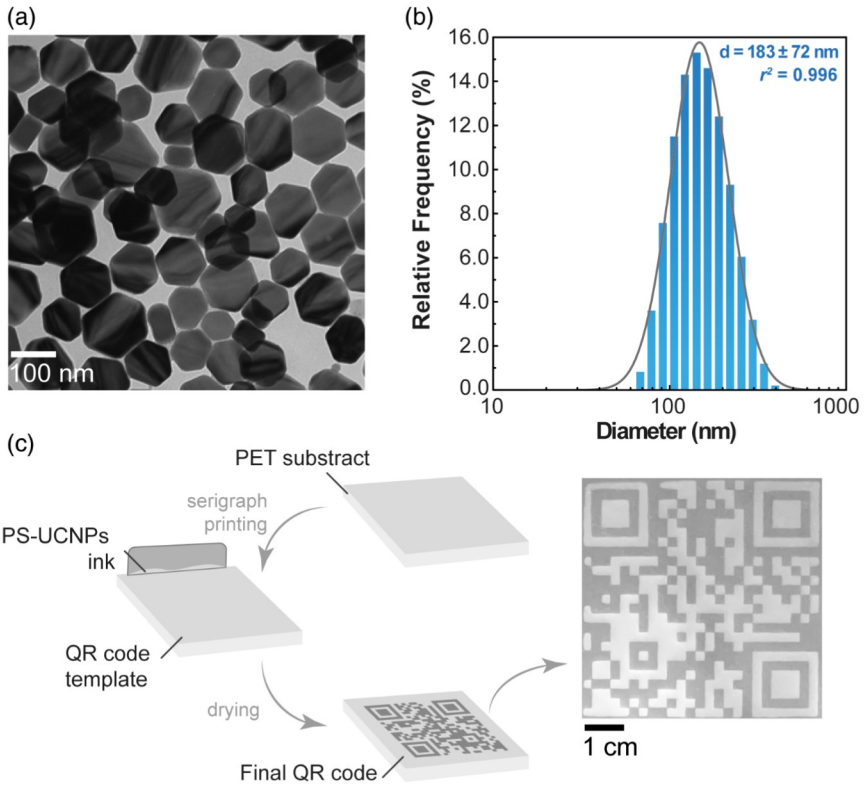

Figure 2. a) TEM images and b) hydrodynamic size distribution of the $NaGdF_4:Yb^{3+}/Er^{3+}$ UCNPs. The gray line is the best fit to the DLS data using a log-normal distribution ($r^2 = 0.996$ and fitting parameters shown in Table S1, Supporting Information). c) Schematic representation of the preparation of the QR codes and the final QR code (encoding the URL http://iq.unesp.br) under white light illumination.

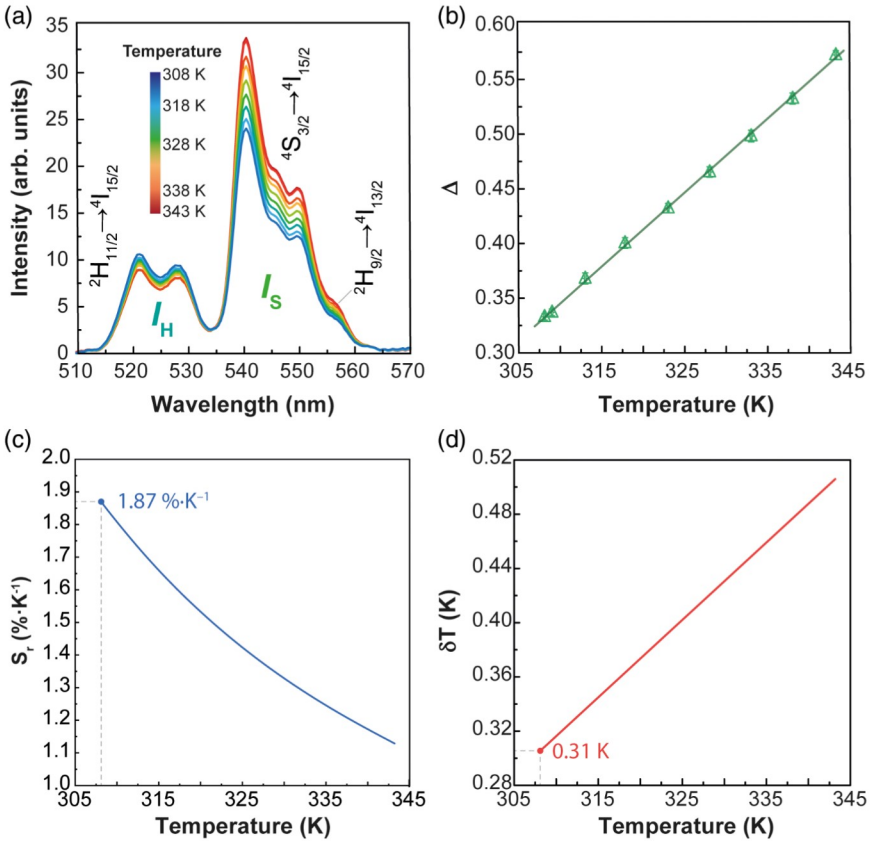

Figure 3. a) Temperature-dependent upconversion emission spectra of the QR codes in the 308–343 K range measured at $P_D = 40\ W\ cm^{-2}$. b) $\Delta(T)$ calibration curve. The solid line is the best fit to the data using a straight line ($r^2 > 0.99$, fitted parameters are shown in Table S2, Supporting Information). c) Relative thermal sensitivity and d) temperature uncertainty of the QR code luminescent thermometer.

1.87 % K^{-1} and 0.3 K at 308.0 K, respectively, in good agreement with expected values for $NaGdF_4:Yb^{3+}/Er^{3+}$ UCNPs.[51] Despite primary luminescent thermometers based on the Boltzmann distribution between the $^2H_{11/2}$ and $^4S_{3/2}$ thermally-coupled Er^{3+} electronic levels was already demonstrated,[33] this approach was not used here because the obtained QR codes absorb light in the spectral region where Boltzmann distribution takes place (Figure S2, Supporting Information). Nevertheless, the thermal calibration indicates that the obtained luminescent QR codes provide accurate temperature readouts from their upconverting emission spectra in the 308–343 K range.

2.3. Power-Dependent Dual-Mode Encoding of the QR Codes

The emission of Er^{3+} in the red and green spectral regions is strongly affected by the power density (P_D) of the excitation source, as already noted in the literature.[32,52,53] Indeed, I_H, I_S, and the integrated areas of the $^2H_{9/2}\rightarrow{}^4I_{13/2}$ and $^4F_{9/2}\rightarrow{}^4I_{15/2}$ (635–685 nm) transitions in the QR codes increase with increasing P_D, following a power law ($I \propto P_D{}^n$, where n describes the number of photons involved in the upconverting process).[34] Therefore, n corresponds to the slope of the integrated intensities (I) versus P_D in a double-logarithmic plot.[54] The values of n for the four Er^{3+} transitions aforementioned are greater than 1.5 (Figure S3, Supporting Information), indicating that the emission in the visible spectral range occurs through a two-photon upconverting process. It is worth pointing out that the contribution of $^4F_{9/2}\rightarrow{}^4I_{15/2}$ transition in the red spectral region is favored at higher P_D because the $^2H_{11/2}$ and $^4S_{3/2}$ upper emitting levels become saturated, favoring the population of the $^4F_{9/2}$ emitting level due to the higher nonradiative relaxations upon the local heating induced by the laser excitation.[32,55] For that reason, the ratio between the integrated intensities of the transitions in the red ($^4F_{9/2}\rightarrow{}^4I_{15/2}$) and green ($^2H_{11/2}\rightarrow{}^4I_{15/2}$, $^4S_{3/2}\rightarrow{}^4I_{15/2}$, and $^2H_{9/2}\rightarrow{}^4I_{13/2}$) spectral regions, defined as θ, increases upon increasing P_D, resulting in the shift of the emission color from the green to the yellow regions (**Figure 4**), together with a temperature increase induced by the absorbed photons in the PS substrate and $NaGdF_4:Yb^{3+}/Er^{3+}$ UCNPs that are further partially converted into heat. This power-dependent color change gives rise to a simple approach for tuning the emission response of the QR codes without further doping of the obtained UCNPs, allowing easy anticounterfeiting measures based on color matching criteria for the validation of the QR code readout through NIR laser irradiation.

Indeed, it is possible to use the power-dependent upconverting emission spectra of the QR codes upon 980 nm irradiation as input for playing the role of a double key in a molecular keylock.

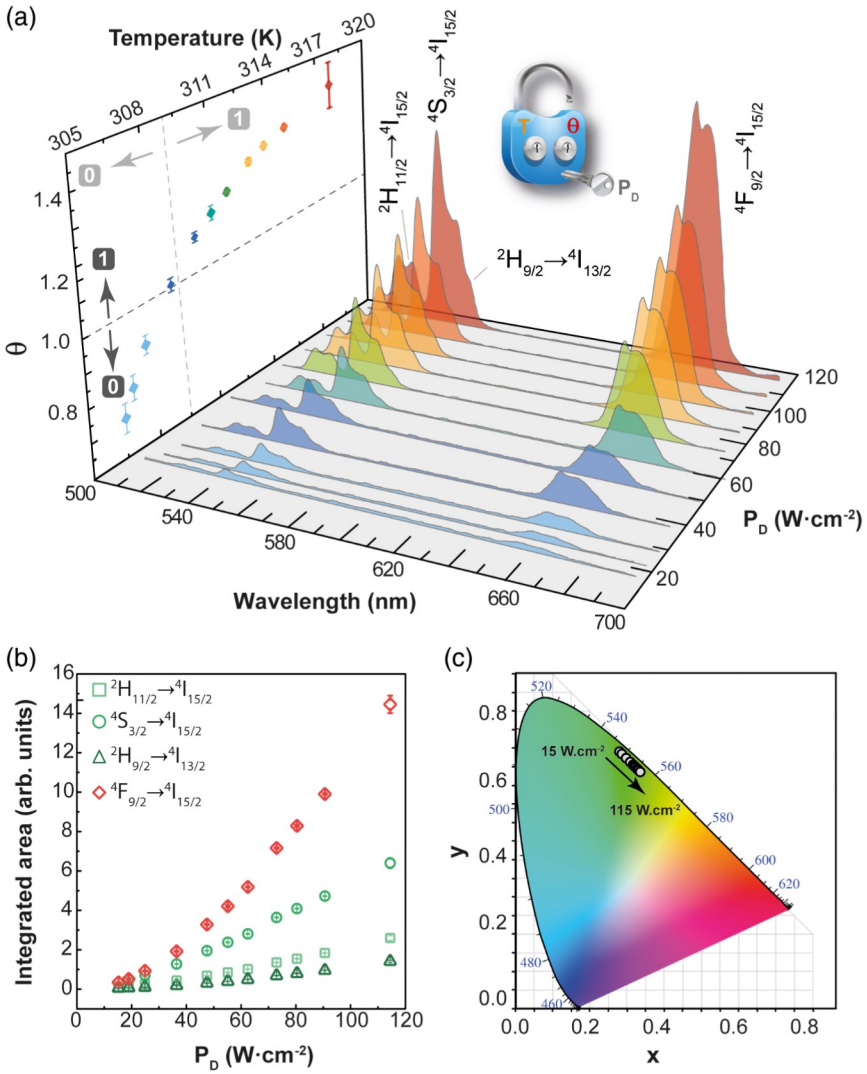

Figure 4. a) Upconverting emission spectra of $NaGdF_4:Yb^{3+}/Er^{3+}$ UCNPs under excitation at 980 nm varying P_D. The intensity ratio θ between the integrated intensities of the transitions in the red ($^4F_{9/2}\rightarrow{}^4I_{15/2}$) and green ($^2H_{11/2}\rightarrow{}^4I_{15/2}$, $^4S_{3/2}\rightarrow{}^4I_{15/2}$, and $^2H_{9/2}\rightarrow{}^4I_{13/2}$) spectral regions is presented in the inset. The keylock represents the dual encoding of the QR code emission (unlocked by P_D values) enabling a two-step verification using temperature (T) and θ. b) Integrated emission intensities of the $^2H_{11/2}\rightarrow{}^4I_{15/2}$, $^4S_{3/2}\rightarrow{}^4I_{15/2}$, $^2H_{9/2}\rightarrow{}^4I_{13/2}$, and $^4F_{9/2}\rightarrow{}^4I_{15/2}$ transitions. c) CIE 1931 chromaticity diagram coordinates of the QR code at different P_D values.

The P_D physical input triggers simultaneously color and temperature changes. Therefore, by setting a threshold for $\theta = 1.0$ (same intensities in the red and green spectral regions, corresponding to a $P_D = 40\ W\ cm^{-2}$), we can design the first encoding level of the system. Whenever this first θ-key opens the system, we can go further to the second level of encoding determining the absolute temperature for $P_D > 40\ W\ cm^{-2}$ with the calibration curve described in Section 2.2. The threshold to open the system with this temperature key (T-key) is $T = 309$ K, the temperature corresponding to $\theta = 1$ (Figure 4a). It is important to point out that despite the calibration curve was only recorded at $P_D = 40\ W\ cm^{-2}$, it is still possible to extrapolate its use to different P_D because there is a good agreement between the temperature calculated with the calibration curve and the temperature measured with a thermocouple.

2.4. Molecular Keylock Through RGB Color Space Readout

Figure 5 shows the color variation of the photographs of the luminescent QR codes under different P_D taken with a smartphone camera. Each image is composed of an *RGB* additive color model, creating the color through the mix of red (*R*), green (*G*), and blue (*B*) primary colors (Figure S4, Supporting Information). The changes in the emission color of the QR codes observed in Figure 5b are assessed by the ratio of intensities of the *R* and *G* color channels (*R*/*G*), similarly to what we describe for the θ parameter shown in Figure 4a. As expected, the intensity of all color channels increases when increasing P_D, with the *R* and *G* channels playing a major role in the composition of the color emission of the QR codes (Figure 5c). The intensity of the *B* channel is detected during the decomposition of the photographs

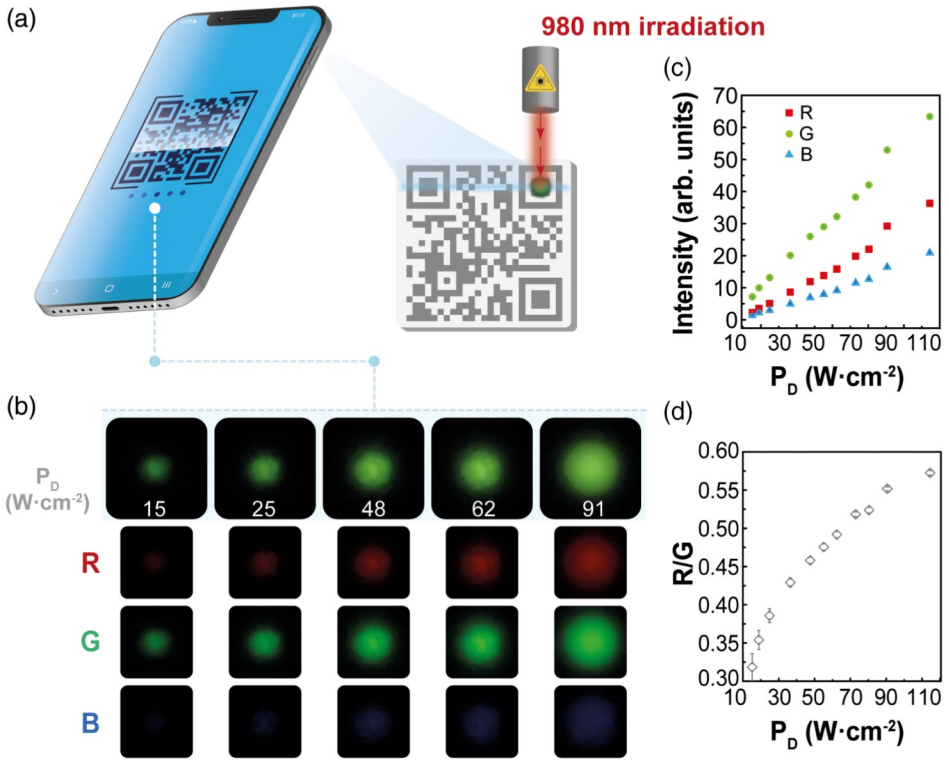

Figure 5. a) Scheme of the simultaneous QR code readout and image acquisition. b) Power-dependent photographs of the QR codes upon 980 nm irradiation and the corresponding color channels. c) Integrated intensities of the red, green, and blue color channels. d) Evolution of the red-to-green ratio upon power density increasing.

due to the $^2H_{9/2}\rightarrow{}^4I_{15/2}$ emission in the blue spectral region (Figure S4, Supporting Information), despite being too faint to be perceived by naked eyes.

Nevertheless, as the *R* and *G* channels cover almost the spectral regions of the $^4F_{9/2}\rightarrow{}^4I_{15/2}$ and $^2H_{11/2}\rightarrow{}^4I_{15/2}/{}^4S_{3/2}\rightarrow{}^4I_{15/2}/{}^2H_{9/2}\rightarrow{}^4I_{13/2}$ transitions, respectively, the ratiometric response of the *R* and *G* channels obtained from the images of the QR codes at distinct P_D (Figure 5d) presents the same power-dependent profile observed for the ratiometric θ curve shown in Figure 4a. In addition to the same profile, both cases show the same twofold improvement in the ratiometric evolution when increasing P_D from 15 to 115 W cm^{-2} (Figure S5, Supporting Information). Therefore, the first codification level of the system can be accessed by the smartphone readout of the photographs of the luminescent QR codes setting $R/G = 0.43$ as the threshold, equivalent to $\theta = 1.0$. Direct access to the second encoding level is not possible based only on the photographs because the *RGB* additive color model does not permit the determination of the temperature. This apparent limitation is, however, overcome by the integration of the smartphone into the IoT network allowing the download of the calibration curve of these UCNPs from a remote server, since the temperature dependence of θ can be extrapolated to the temperature dependence of *R*/*G* (Figure S5, Supporting Information). This permits a faster and user-friendly *T*-key decryption route, without jeopardizing the θ-key access. Moreover, the direct decoding of the *T*-key only by spectral measurements results in different access privileges to distinct readout methodologies, a feature that is an added benefit of the reported methodology.

3. Conclusions

The preparation through a facile sustainable route of screen-printed luminescent QR codes acting as two-step encoding smart tags was demonstrated. Luminescent inks were obtained by recycling PS from EPS wastes, using d-limonene as a green solvent, and incorporating $NaGdF_4:Yb^{3+}/Er^{3+}$ UCNPs in the obtained PS/d-limonene solution. QR codes were fabricated through a low-cost printing method (serigraph printing in this case, however, inked or spaying could be also used). Taking advantage of the radiation-to-heat conversion of the UCNPs-bearing QR codes under 980 nm irradiation, we exploited their power-dependent emission, and the corresponding temperature increase, to create a double key molecular keylock accessible either through spectral features or the *RGB* additive color model. Setting the irradiation power density to 40 W cm^{-2}, and adopting threshold values $\theta = 1.0$ or $R/G = 0.43$, we designed the color encoding level of the system (first level) that is accessed both by a spectrometer or a smartphone. Then, the temperature encoding level (second level) is implemented based on the integrated areas of the $^2H_{11/2}\rightarrow{}^4I_{15/2}$ and $^4S_{3/2}\rightarrow{}^4I_{15/2}$ transitions in the green spectral range that enable the absolute temperature determination. Direct access to this second encoding level is not possible based on the photographs of the QR codes. This apparent limitation is, however,

overcome using one of the main advantages of smartphones: their interconnectivity and integration into the IoT network that allows the real-time download of the calibration curve of the $NaGdF_4$:Yb^{3+}/Er^{3+} UCNPs from a remote server. The impossibility to directly decode one level of a system by a specific technology results in different access privileges to distinct readouts. This approach can be easily generalized to other UCNPs and is a step toward the design of smart-tags for anti-counterfeiting.

4. Experimental Section

Materials: Gadolinium oxide (Gd_2O_3), ytterbium oxide (Yb_2O_3), erbium oxide (Er_2O_3), trifluoroacetic acid (CF_3CO_2H), sodium trifluoroacetate (CF_3CO_2Na), oleic acid, 1-octadecene, silicon dioxide (SiO_2) nanopowder (10–20 nm particle size), (*R*)-(+)-limonene (d-limonene), and PS with average molecular weight of 280 000 g mol^{-1} (PS 280 k) were purchased from Sigma-Aldrich. Citrus terpenes were supplied by Citrosuco S/A (Matão, Brazil). EPS were obtained from packaging materials and used as a source of PS.

Synthesis of Yb^{3+}/Er^{3+} Codoped $NaGdF_4$ Upconverting Nanoparticles: The UCNPs were prepared through the thermal decomposition of sodium and lanthanide trifluoroacetates into $NaGdF_4$:Yb^{3+}/Er^{3+} following a previously reported method with minor modifications.[56] First, the lanthanide trifluoroacetate precursor was prepared by reacting Gd_2O_3 (353.4 mg, 0.975 mmol), Yb_2O_3 (98.5 mg, 0.250 mmol), and Er_2O_3 (9.6 mg, 0.025 mmol) with CF_3CO_2H in a mixture with water (1:1, 10 mL) in a 50 mL three-neck round bottom flask (molar ratio of Gd:Yb:Er = 78:20:2). The mixture was refluxed at 353 K for 12 h. After obtaining a clear solution, the temperature was lowered to 333 K, and the flask was opened to evaporate the solvents and get the precursor powder. The second step consists of adding 340 mg of CF_3CO_2Na and 7.5 mL each of oleic acid and 1-octadecene to the flask. In a second three-neck round bottom flask (100 mL), 12.5 mL each of oleic acid and 1-octadecene were added. The flasks were connected to a Schlenk line to remove moisture and oxygen for 30 min at 398 K under vacuum and magnetic stirring. Subsequently, the flask containing oleic acid and 1-octadecene was heated to 593 K under argon flow at a heating rate of 10 K min^{-1}. The precursor solution kept at 398 K was then collected with a glass syringe and injected into the second flask (injection rate of 1.5 mL min^{-1} controlled by a pump system). The temperature was kept at 583 K for 90 min under stirring and argon flow. After cooling down to room temperature, the nanoparticles were precipitated by addition of ethanol and collected by centrifugation at 5350 RCF for 10 min. The nanoparticles were redispersed in hexane and washed twice with ethanol (1:5 v/v). The oleate capped $NaGdF_4$:Yb^{3+}/Er^{3+} nanoparticles were finally redispersed in hexane for further use.

Preparation of Luminescent Ink: A clear and viscous solution was obtained by dissolving EPS (2.0 g) in citrus terpenes (5.0 mL), followed by its centrifugation at 7500 rpm to remove particulate material from the packaging used as the source of EPS. The UCNPs containing PS inks (PS-UCNPs) were prepared through the addition of 30 wt% SiO_2 nanopowder as a thickening agent and 0.1 wt% of UCNPs into the previously prepared solution and then mixing them in a SpeedMixer (DAC150.1 FVZ-K, FlackTek) by 2 min at 2000 rpm.

Fabrication of Luminescent QR Codes by Serigraph Printing: A QR code template (6 × 6 cm^2) linking to the website of the Institute of Chemistry, UNESP (http://iq.unesp.br/) was fabricated in a 150-mesh polyester screen to print the luminescent QR codes using an automatic press (IMAH, Paraná, Brazil) through a press-printing method (serigraph printing). The previously prepared luminescent ink was cast onto the polyester screen containing the QR code template and then pressed against the screen to print the luminescent QR codes onto polyethylene terephthalate (PET) substrates. This method allowed for printing ten individual codes per minute using 10 mL of luminescent ink. Three different (and illustrative) QR codes obtained through this methodology are shown in Figure S6, Supporting Information.

Transmission Electron Microscopy: The morphological structure and size of the UCNPs were analyzed from TEM images acquired in an electron microscope (Tecnai G2 Spirit BioTwin, FEI) operating at 120 kV.

Dynamic Light Scattering: The hydrodynamic size (diameter, *d*) of the UCNPs was measured by DLS in a Zetasizer Nano ZS instrument (ZEN3600, Malvern) operating with a 632.8 nm He–Ne laser at 298 K. The UCNPs samples dispersed in hexane were measured with a dip cell kit (ZEN1002, Malvern) coupled to a square glass cell (PCS1115, Malvern) by performing three measurements with ten scans each, where the average value is reported in Figure 2b.

Proton Nuclear Magnetic Resonance: The ^{1}H NMR spectra of EPS and PS were acquired in a 600 MHz Bruker Avance III spectrometer (HD 600, Bruker) operating at 14.1 T. Samples were dissolved in deuterated chloroform ($CDCl_3$, 8 mg mL^{-1}) and the spectra were registered at 298 K in the manual mode. Automated tuning, locking, shimming, and calibration of 90° pulses were performed using standard Bruker routines.

Gas Chromatography–Mass Spectrometry: The GC–MS analysis was used to determine the content of d-limonene in standard and citrus terpenes samples. The analysis was carried out in a gas chromatography equipment (7890B, Agilent) coupled to a mass spectrometer (5977 A, Agilent) using a capillary column with a stationary phase of (5%-phenyl)-methylpolysiloxane (30 m length × 0.25 mm inner diameter, HP5-MS Agilent) with electron impact ionization at 70 eV, helium as the carrier gas (flow rate = 1 mL min^{-1}) and a split ratio of 100:1. The GC–MS temperature program was as follows: 353 K for 3 min, then ramp to 553 K at 30 K min^{-1}, then hold 10 min. The samples were prepared by diluting d-limonene and citrus terpene in ethyl acetate (HPLC grade, 1 mg mL^{-1}).

Photoluminescence Spectroscopy: The emission spectra of the luminescent QR codes were recorded in the experimental setup shown in Figure S7, Supporting Information. The excitation of the sample was carried out at 980 ± 10 nm with a collimated fiber-coupled continuous-wave (CW) laser system (MDL-980-FC-10 W, CNI). The emission spectra were registered by a USB-portable spectrometer (Maya 2000 Pro, Ocean Optics) coupled to an optical fiber (QP450-1-XSR, Ocean Optics) using an edge pass filter (FESH0750, Thorlabs) to cut off the excitation signal during the spectral acquisition (100 spectra were recorded for each temperature and P_D using an integration time of 250 ms).

Thermal Calibration: The temperature-dependent measurements were performed attaching a homemade Peltier temperature controller (0.1 K resolution) to the abovementioned experimental setup. The calibration of temperature was performed by placing a K-type thermocouple with a temperature uncertainty of 0.1 K (KA01-3, TME Thermometers) coupled to a thermocouple data logger (TC-08, Pico Technology) onto the surface of the QR code, 0.5 cm away from the laser spot to avoid heating the thermocouple with the beam spot.

Calculation of the Integrated Areas: The areas corresponding to the Er^{3+} $^2H_{11/2}\rightarrow{}^4I_{15/2}$, $^4S_{3/2}\rightarrow{}^4I_{15/2}$, $^2H_{9/2}\rightarrow{}^4I_{13/2}$, and $^4F_{9/2}\rightarrow{}^4I_{15/2}$ transitions were obtained through the deconvolution of the emission spectra of the QR codes using a custom code written in MATLAB 2021a under the license provided to the University of Aveiro. First, each emission spectrum was converted from wavelength to energy units using the Jacobian conversion.[57] Good fits ($r^2 > 0.99$) were obtained by adjusting 11 Gaussian functions to the experimental data, as presented in Figure S8, Supporting Information. The reported areas and errors are the average and standard deviation values from 100 spectra measured per temperature or P_D. The integrated emission of $^2H_{11/2}\rightarrow{}^4I_{15/2}$ and $^4S_{3/2}\rightarrow{}^4I_{15/2}$ transitions correspond to the sum of the areas of their respective Gaussian functions. The integrated emission of the red spectral region is the sum of the areas corresponding to the $^4F_{9/2}\rightarrow{}^4I_{15/2}$ transition while the integrated emission of the green spectral region is the sum of the areas of the Gaussian functions corresponding to the $^2H_{11/2}\rightarrow{}^4I_{15/2}$, $^4S_{3/2}\rightarrow{}^4I_{15/2}$, and $^2H_{9/2}\rightarrow{}^4I_{13/2}$ transitions.

Power Density Determination: The CW laser power and the corresponding beam profile were measured with a power meter (FieldMaxII – TOPOP – 2 Vis, Coherent) and a charge-coupled device (CCD) camera (BC106N – VIS/M, Thorlabs) coupled to a neutral density

filter (NE50B-B, Thorlabs), respectively. The resulting beam profile intensity was obtained for each laser power by averaging the intensity of ten sequential scans. The beam profile intensity values were calibrated to power density considering that the integrated area of the beam profile is the laser power (in W) measured with the power meter. Therefore, the average laser power density was calculated considering the values above 13.5% ($1/e^2$, the cut-off value for Gaussian beams). The beam cross-section at $1/e^2$ is displayed in Figure S9, Supporting Information.

Image Acquisition: Photographs of the luminescent QR codes under 980 nm irradiation were taken with a smartphone camera (iPhone 12, Apple) with a resolution of 3024×4032 pixel^2, aperture of $f/1.6$, and a sensor dimension of 1/3.6″. Images were acquired using the commercially available Camera+ 2 app to ensure the same lighting conditions during the experiment, setting the shutter speed to 1/45 s and locked ISO 1000 to avoid pixel saturation from the bright light emission from the QR codes under 980 nm exposure.

Image Processing: The *RGB* color model was used to evaluate the changes in the emission color of the QR codes upon increasing laser power density. A custom MATLAB 2021a code was designed to analyze the ratio between the intensity of the red and green channels (*R*/*G*). The code imports the power-dependent pictures of the QR codes cropping them in a 251×251 pixel^2 region centered in the laser spot. Each cropped image was split into three-color channels: red (*R*), green (*G*), and blue (*B*). The intensity profiles reported to each channel along the orthogonal directions correspond to the line and column integration of the intensities. The reported integrated intensities values correspond to the total integrated intensities of each channel. The corresponding uncertainties were obtained by multiplying the integrated intensity by the inverse signal-to-noise ratio retrieved from the intensity profiles in the two orthogonal directions. The red-to-green ratio (*R*/*G*) is finally calculated as the ratio between the integrated intensities of the *R* and *G* channels. Detailed information on the image processing procedure is given in Section S1.4, Supporting Information.

Supporting Information

Supporting Information is available from the Wiley Online Library or from the author.

Acknowledgements

This work was developed within the scope of the projects CICECO-Aveiro Institute of Materials (UIDB/50011/2020 and UIDP/50011/2020) and Shape of Water (PTDC/NAN-PRO/3881/2020) financed by Portuguese funds through the FCT/MEC and when appropriate cofinanced by FEDER under the PT2020 Partnership Agreement. F.E.M. acknowledges the funding received from the European Union's Horizon 2020 research and innovation programme under the Marie Sklodowska-Curie grant agreement no. 823941. The support of the European Union's Horizon 2020 FET Open program under grant agreement no. 801305 (NanoTBTech) is also acknowledged. R.R.S. acknowledges the financial support from the Brazilian agency FAPESP (process no. 16/06612-6).

Conflict of Interest

The authors declare no conflict of interest.

Data Availability Statement

Research data are not shared.

Keywords

anticounterfeiting, luminescence thermometry, quick-response codes, two-step verification, upconverting nanoparticles

Received: July 30, 2021
Revised: October 5, 2021
Published online: December 21, 2021

[1] B. Tjahjono, C. Esplugues, E. Ares, G. Pelaez, *Procedia Manuf.* **2017**, *13*, 1175.
[2] E. Sisinni, A. Saifullah, S. Han, U. Jennehag, M. Gidlund, *IEEE Trans. Ind. Informatics* **2018**, *14*, 4724.
[3] R. A. Khalil, N. Saeed, M. Masood, Y. M. Fard, M.-S. Alouini, T. Y. Al-Naffouri, *IEEE Internet Things J.* **2021**, *8*, 11016.
[4] J. F. C. B. Ramalho, S. F. H. Correia, L. Fu, L. L. F. António, C. D. S. Brites, P. S. André, R. A. S. Ferreira, L. D. Carlos, *Adv. Sci.* **2019**, *6*, 1900950.
[5] H. Elazhary, *J. Netw. Comput. Appl.* **2019**, *128*, 105.
[6] G. Aceto, V. Persico, A. Pescapé, *J. Ind. Inf. Integr.* **2020**, *18*, 100129.
[7] J. F. C. B. Ramalho, L. C. F. António, S. F. H. Correia, L. S. Fu, A. S. Pinho, C. D. S. Brites, L. D. Carlos, P. S. André, R. A. S. Ferreira, *Opt. Laser Technol.* **2018**, *101*, 304.
[8] N. Victor, *Int. J. Comput. Appl.* **2012**, *60*, 17.
[9] M. M. Umaria, G. B. Jethava, in *Int. Conf. Comput. Intell. Commun. Networks,* IEEE, Piscataway, NJ **2015**, pp. 1094–1096.
[10] A. Abas, Y. Yusof, R. Din, F. Azali, B. Osman, *Bull. Electr. Eng. Informatics* **2020**, *9*, 2555.
[11] J. Chiang, C. Hsia, H. Li, *Electron. Lett.* **2013**, *49*, 1381.
[12] P. S. André, R. A. S. Ferreira, *Electron. Lett.* **2014**, *50*, 1828.
[13] L. Yang, Z. Wang, S. Fan, J. Feng, Y. Zhong, T. Zhao, Y. Hu, Y. Liu, *Nanosci. Nanotechnol. Lett.* **2019**, *11*, 451.
[14] F. Miller, S. Wintzheimer, J. Prieschl, V. Strauss, K. Mandel, *Adv. Opt. Mater.* **2021**, *9*, 2001972.
[15] J. F. C. B. Ramalho, S. F. H. Correia, L. Fu, L. M. S. Dias, P. Adão, P. Mateus, R. A. S. Ferreira, P. S. André, *NPJ Flex. Electron.* **2020**, *4*, 11.
[16] F. Auzel, *Chem. Rev.* **2004**, *104*, 139.
[17] F. Wang, Y. Han, C. S. Lim, Y. Lu, J. Wang, J. Xu, H. Chen, C. Zhang, M. Hong, X. Liu, *Nature* **2010**, *463*, 1061.
[18] M. Haase, H. Schäfer, *Angew. Chem. Int. Ed.* **2011**, *50*, 5808.
[19] J. Zhou, Q. Liu, W. Feng, Y. Sun, F. Li, *Chem. Rev.* **2015**, *115*, 395.
[20] M. Bettinelli, L. Carlos, X. Liu, *Phys. Today* **2015**, *68*, 38.
[21] J.-C. Boyer, F. Vetrone, L. A. Cuccia, J. A. Capobianco, *J. Am. Chem. Soc.* **2006**, *128*, 7444.
[22] N. M. Sangeetha, P. Moutet, D. Lagarde, G. Sallen, B. Urbaszek, X. Marie, G. Viau, L. Ressier, *Nanoscale* **2013**, *5*, 9587.
[23] M. You, J. Zhong, Y. Hong, Z. Duan, M. Lin, F. Xu, *Nanoscale* **2015**, *7*, 4423.
[24] M. You, M. Lin, S. Wang, X. Wang, G. Zhang, Y. Hong, Y. Dong, G. Jin, F. Xu, *Nanoscale* **2016**, *8*, 10096.
[25] W. Yao, Q. Tian, J. Liu, Q. Xue, M. Li, L. Liu, Q. Lu, W. Wu, *Nanoscale* **2017**, *9*, 15982.
[26] G. Gong, Y. Song, H. Tan, S. Xie, C. Zhang, L. Xu, J. Xu, J. Zheng, *Compos. Part B Eng.* **2019**, *179*, 107504.
[27] F. Kaboli, N. Ghazyani, M. Riahi, H. Zare-Behtash, M. H. Majles Ara, E. Heydari, *ACS Appl. Nano Mater.* **2019**, *2*, 3590.
[28] Y. Ma, Y. Dong, S. Liu, P. She, J. Lu, S. Liu, W. Huang, Q. Zhao, *Adv. Opt. Mater.* **2020**, *8*, 1901687.
[29] N. Katumo, L. A. Ruiz-Preciado, V. Kumar, G. Hernandez-Sosa, B. S. Richards, I. A. Howard, *Adv. Mater. Technol.* **2021**, *6*, 2100047.
[30] J. M. Meruga, W. M. Cross, P. Stanley May, Q. Luu, G. A. Crawford, J. J. Kellar, *Nanotechnology* **2012**, *23*, 395201.

[31] J. Reichstein, F. Miller, S. Wintzheimer, K. Mandel, *Adv. Funct. Mater.* **2021**, *2104189*, 2104189.
[32] M. Kraft, C. Würth, V. Muhr, T. Hirsch, U. Resch-Genger, *Nano Res.* **2018**, *11*, 6360.
[33] C. D. S. Brites, S. Balabhadra, L. D. Carlos, *Adv. Opt. Mater.* **2019**, *7*, 1801239.
[34] C. D. S. Brites, S. V. Kuznetsov, V. A. Konyushkin, A. N. Nakladov, P. P. Fedorov, L. D. Carlos, *Eur. J. Inorg. Chem.* **2020**, *2020*, 1555.
[35] N. Katumo, G. Gao, F. Laufer, B. S. Richards, I. A. Howard, *Adv. Opt. Mater.* **2020**, *8*, 2000507.
[36] J. F. C. B. Ramalho, L. D. Carlos, P. S. André, R. A. S. Ferreira, *Adv. Photonics Res.* **2021**, *2*, 2000211.
[37] R. Ciriminna, M. Lomeli-Rodriguez, P. D. Carà, J. A. Lopez-Sanchez, M. Pagliaro, P. Demma Carà, J. A. Lopez-Sanchez, M. Pagliaro, *Chem. Commun.* **2014**, *50*, 15288.
[38] M. D. Samper, D. Garcia-Sanoguera, F. Parres, J. López, *Prog. Rubber Plast. Recycl. Technol.* **2010**, *26*, 83.
[39] EPA, Plastics, **2015** https://archive.epa.gov/epawaste/conserve/tools/warm/pdfs/Plastics.pdf (accessed: March 2015).
[40] Y.-B. Zhao, X.-D. Lv, H.-G. Ni, *Chemosphere* **2018**, *209*, 707.
[41] M. T. García, I. Gracia, G. Duque, A. de Lucas, J. F. Rodríguez, *Waste Manag.* **2009**, *29*, 1814.
[42] G. Paggiola, S. Van Stempvoort, J. Bustamante, J. M. V. Barbero, A. J. Hunt, J. H. Clark, *Biofuels Bioprod. Biorefining* **2016**, *10*, 686.
[43] M. Firdaus, L. M. de Espinosa, M. A. R. Meier, *Macromolecules* **2011**, *44*, 7253.
[44] J. Zhang, H. Huang, Y. Guan, D.-F. Wei, F.-Z. Hu, A.-N. Zheng, H.-N. Xiao, *J. Appl. Polym. Sci.* **2010**, *117*, 2566.
[45] J. W. Wackerly, J. F. Dunne, *J. Chem. Educ.* **2017**, *94*, 1790.
[46] H. E. Gottlieb, V. Kotlyar, A. Nudelman, *J. Org. Chem.* **1997**, *62*, 7512.
[47] G. R. Fulmer, A. J. M. Miller, N. H. Sherden, H. E. Gottlieb, A. Nudelman, B. M. Stoltz, J. E. Bercaw, K. I. Goldberg, *Organometallics* **2010**, *29*, 2176.
[48] J. C. Martins, A. R. N. Bastos, R. A. S. Ferreira, X. Wang, G. Chen, L. D. Carlos, *Adv. Photonics Res.* **2021**, *2*, 2000169.
[49] T. P. Van Swieten, T. Van Omme, D. J. van den Heuvel, S. J. W. Vonk, R. G. Spruit, F. Meirer, H. H. P. Garza, B. M. Weckhuysen, A. Meijerink, F. T. Rabouw, R. G. Geitenbeek, *ACS Appl. Nano Mater.* **2021**, *4*, 4208.
[50] C. D. S. Brites, A. Millán, L. D. Carlos, in *Handb. Phys. Chem. Rare Earths*, (Eds: B. Jean-Claude, P. Vitalij K.), Elsevier, Amsterdam, **2016**, 339–427.
[51] K. Nigoghossian, Y. Messaddeq, D. Boudreau, S. J. L. Ribeiro, *ACS Omega* **2017**, *2*, 2065.
[52] X. Zhang, Z. Zhang, Z. Liu, C. Zhang, B. Zhang, X. Mi, H. Zheng, *J. Lumin.* **2019**, *205*, 374.
[53] H. Bae, E. Lee, K. T. Lee, *Phys. Chem. Chem. Phys.* **2021**, *23*, 14587.
[54] M. Pollnau, D. R. Gamelin, S. R. Lüthi, H. U. Güdel, M. P. Hehlen, *Phys. Rev. B* **2000**, *61*, 3337.
[55] J. F. Suyver, A. Aebischer, S. García-Revilla, P. Gerner, H. U. Güdel, *Phys. Rev. B* **2005**, *71*, 125123.
[56] E. Hemmer, M. Quintanilla, F. Légaré, F. Vetrone, *Chem. Mater.* **2015**, *27*, 235.
[57] J. Mooney, P. Kambhampati, *J. Phys. Chem. Lett.* **2013**, *4*, 3316.

SUPPORTING INFORMATION

Sustainable of smart-tags with 2-step verification for anti-counterfeiting triggered by the photothermal response of upconverting nanoparticles

Fernando E. Maturi[1,2], Carlos D. S. Brites[1], Robson R. Silva[2,3], Karina Nigoghossian [2], Deivy Wilson[3], Rute A. S. Ferreira[1], Sidney J. L. Ribeiro [2], and Luís D. Carlos[1]**

Mr. F. E. M., Prof. C. D. S. B., Prof. R. A. S. F., Prof. L. D. C.
[1]Phantom-g, CICECO – Aveiro Institute of Materials, Department of Physics, University of Aveiro, Aveiro, 3810-193, Portugal
*E-mail: lcarlos@ua.pt

Mr. F. E. M., Dr. R. R. S., Dr. K. N., Prof. S. J. L. R.
[2]Institute of Chemistry, São Paulo State University (UNESP), Araraquara, SP, 14800-060, Brazil
*E-mail: sidney.jl.ribeiro@unesp.br

Dr. R. R. S., Dr. D. W.
[3]São Carlos Institute of Physics, University of São Paulo, São Carlos, SP, 13566-590, Brazil

Table of Contents

S1. Materials and methods

S1.1. Mass spectrometry

The mass spectrum of the d-limonene found in the citrus terpenes sample is presented in **Figure S1**. The characteristic ionized fragments of d-limonene were identified in the mass spectrum through their mass-to-charge ratio (*m*/*z*): $C_4H_5^+$ (*m*/*z* = 53), $C_5H_8^+$ (68), $C_6H_7^+$ (79), $C_7H_9^+$ (93), $C_8H_{11}^+$ (107), $C_9H_{13}^+$ (121), and $C_{10}H_{16}^+$ (136),[1] therefore confirming that d-limonene is the main compound in citrus terpenes samples.

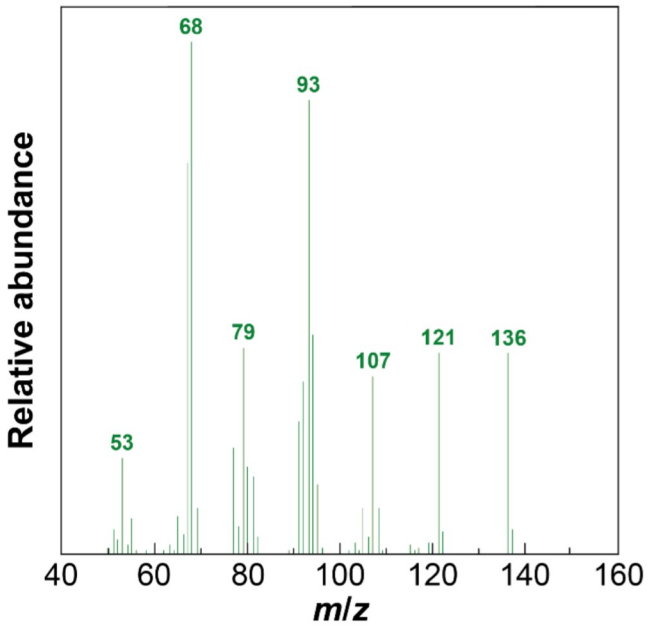

Figure S1. Mass spectrum of the d-limonene found in the citrus terpenes sample. The abundance was normalized to *m*/*z* = 68.

S1.2. UV-Vis absorption spectroscopy

The UV-Vis-NIR absorption spectra of the QR codes were recorded in a spectrophotometer (Lambda 950, Perkin-Elmer) at 298 K with a spectral resolution of 1 nm. **Figure S2** shows that the obtained QR codes absorb light in the spectral region of the $^2H_{11/2}\rightarrow{}^4I_{15/2}$ (I_H) and $^4S_{3/2}\rightarrow{}^4I_{15/2}$ (I_S) transitions of Er^{3+}. Since the light absorption is not equal in the whole green spectral region, the determination of temperature through the Boltzmann distribution in the I_H and I_S spectral regions $\left(\Delta = \frac{I_H}{I_S} = B\exp\left(-\frac{\Delta E}{k_B T}\right)\right)$ is not feasible.

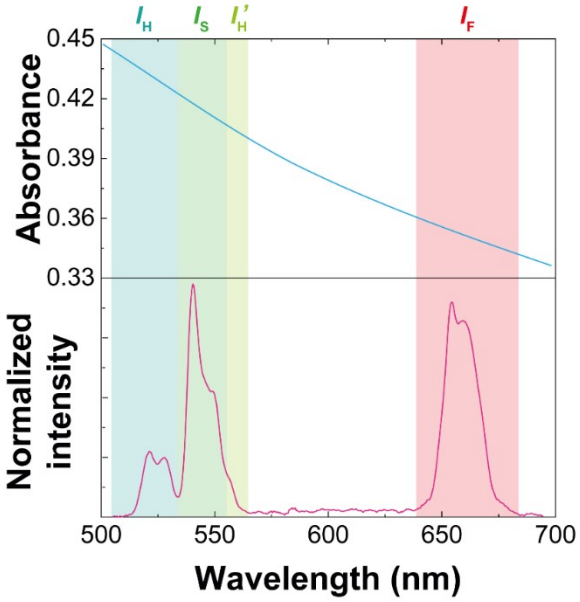

Figure S2. UV-Vis absorption spectrum (blue) and emission spectrum under 980 nm excitation at a laser power density of 40 W·cm^{-2} (pink) of the obtained QR codes at 298 K. The $\boldsymbol{I_H}$, $\boldsymbol{I_S}$, $\boldsymbol{I'_H}$, and $\boldsymbol{I_F}$ shadowed areas are the spectral regions corresponding to the $^2H_{11/2}\rightarrow{}^4I_{15/2}$, $^4S_{3/2}\rightarrow{}^4I_{15/2}$, $^2H_{9/2}\rightarrow{}^4I_{13/2}$, and $^4F_{9/2}\rightarrow{}^4I_{15/2}$ Er^{3+} transitions, respectively.

S1.3. Upconversion laser power density dependence

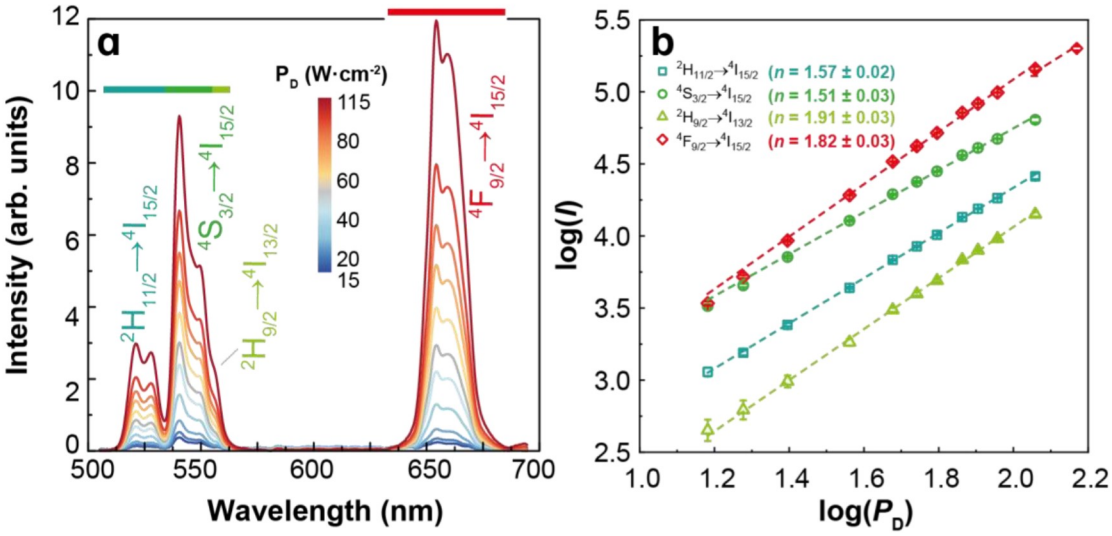

Figure S3. (a) Upconverting emission spectra of the QR codes under 980 nm excitation at distinct power densities. **(b)** Double-logarithmic plot of the integrated areas of Er^{3+} transitions *versus* the laser power density. The dashed lines are the best linear fit (r^2 > 0.99) with the *n* values corresponding to their slopes and uncertainties.

S1.4. Color identification

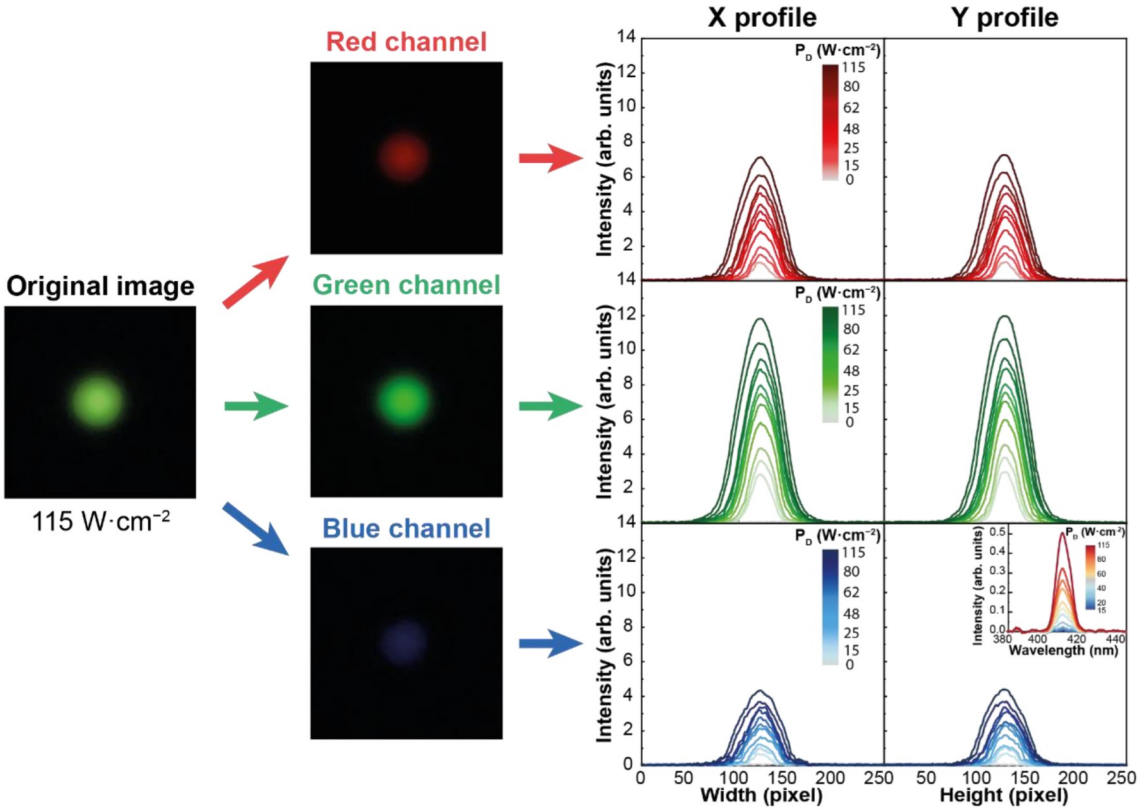

Figure S4. Schematics of the image processing used to obtain the intensities of the *RGB* color channels from the photographs of the QR codes irradiated at different power densities. The images on the left side correspond to the picture taken at 115 W·cm^{-2} while the graphs on the right side show the evolution of the X and Y intensity profiles of each channel upon increasing power density. The inset in the blue Y profile shows the power dependence of the $^2H_{9/2} \rightarrow {}^4I_{15/2}$ transition in the blue spectral region.

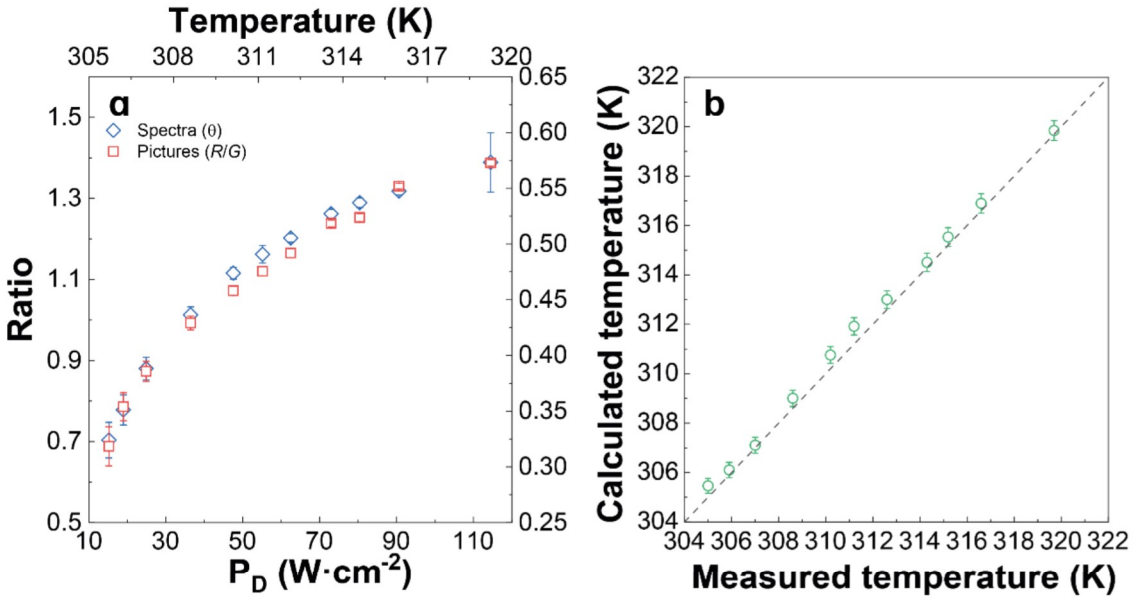

Figure S5. (a) Comparison of the θ and R/G ratios in the tested power density range. **(b)** Correlation between the temperature measured (x axis) with the K-type thermocouple (see experimental section) and the temperature calculated with the calibration curve using the power-dependent emission spectra of the QR codes (y axis). The dashed line is a guide for the eyes corresponding to $x = y$.

S1.5. Reproducibility of the printing method

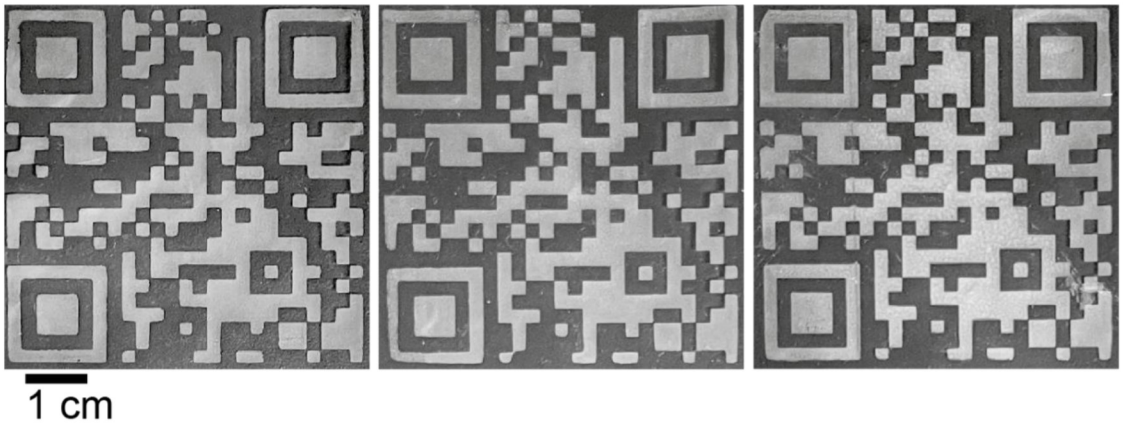

Figure S6. Three different QR codes obtained using the serigraph printing method and an automatic press.

S1.6. Photoluminescence spectroscopy experimental setup

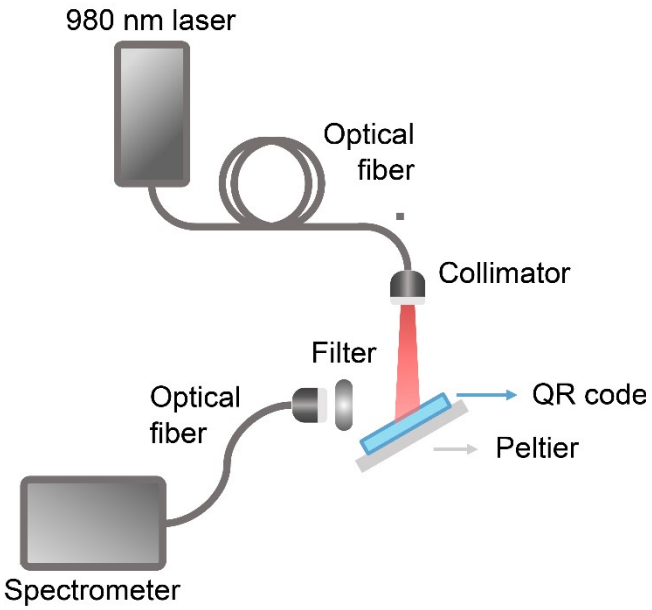

Figure S7. Scheme of the experimental setup used for measuring the power-dependent emission spectra of the QR codes, and the corresponding temperature.

S1.7. Spectral analysis

S1.7.1. Spectral correction

The raw emission spectra of the QR codes were converted from wavelength to energy units:

$$E = \frac{10^7}{\lambda} \quad \textbf{(S1)}$$

where E is the energy (cm^{-1}) and λ is the corresponding wavelength (nm). Since energy and wavelength are inversely proportional, the wavelength step ($d\lambda$) is not uniformly spaced in the energy spectrum. For that reason, the intensity recorded in wavelength units (I_λ) must be corrected to keep the conservation of energy valid after the conversion of λ to E. Therefore, the energy-dependent intensity (I_E) can be obtained as follows:

$$I_E = I_\lambda \frac{d\lambda}{dE} = I_\lambda \frac{d}{dE}\left(\frac{10^7}{E}\right) = -I_\lambda \frac{10^7}{E^2} \quad \textbf{(S2)}$$

This is known as the Jacobian conversion and the minus signal does not play a role in the calculation because it only indicates that integrations in wavelength and energy are performed in opposite ways.[2]

S1.7.2. Spectral deconvolution

The emission spectra of the obtained QR codes were deconvoluted into eleven peaks (**Figure S8**) by adjusting a combination of Gaussian functions to their corrected emission spectra:

$$y = \sum_{i=1}^{n} \left(\frac{A_i}{w_i \sqrt{\pi/2}} \exp\left(-2 \frac{\left(x - x_{c_i}\right)^2}{{w_i}^2} \right) \right) \quad \textbf{(S3)}$$

where y is the corrected emission intensity, x is the energy (cm^{-1}), A_i are the integrated areas (arbitrary units), x_{c_i} are the average energies (cm^{-1}), and w_i are the widths of the peaks, with n = 11. Two, four, one, and four Gaussian functions were assigned to the $^2H_{11/2} \rightarrow {}^4I_{15/2}$, $^4S_{3/2} \rightarrow {}^4I_{15/2}$, $^2H_{9/2} \rightarrow {}^4I_{13/2}$, and $^4F_{9/2} \rightarrow {}^4I_{15/2}$ transitions of Er^{3+}, respectively.

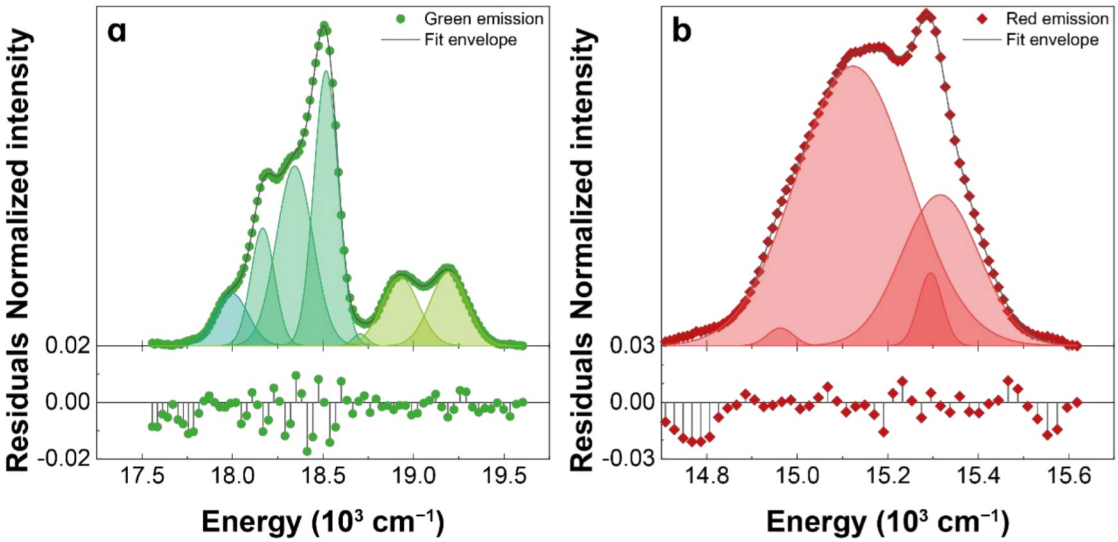

Figure S8. Deconvolution of the **(a)** green and **(b)** red spectral regions of the emission spectrum of the QR codes at 308.1 K under excitation at 980 nm (40 $W \cdot cm^{-2}$).

S1.8. Calculation of the laser power density

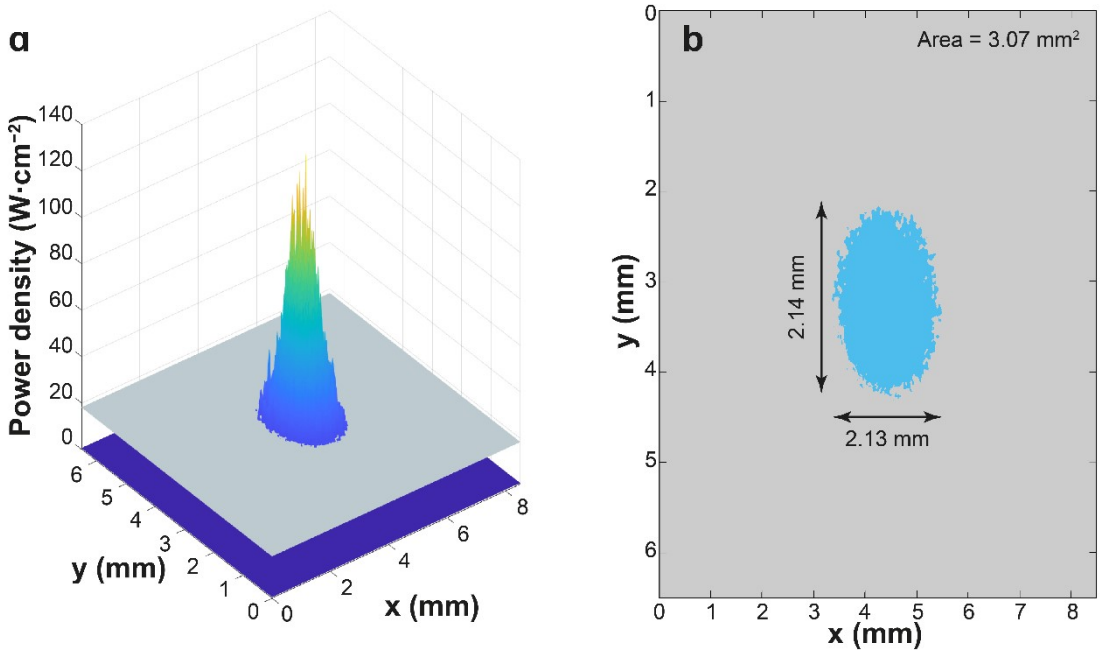

Figure S9. (a) Beam profile of the 980 nm CW laser used as excitation source at a power density of 40 W·cm^{-2} and **(b)** the corresponding beam cross-section at 1/e^2.

S1.9. Fitting parameters

S1.9.1. Size distribution

The hydrodynamic size distribution of the obtained $NaGdF_4$:Yb^{3+}/Er^{3+} upconverting nanoparticles was determined by adjusting the dynamic light scattering data to a log-normal distribution:

$$y = \frac{A}{\sqrt{2\pi}wx}\exp\left(\frac{-\left(\ln\frac{x}{x_c}\right)^2}{2w^2}\right) \qquad \textbf{(S4)}$$

where y is the relative frequency, x is the diameter, x_c is the center, A is the area, and w is the natural logarithm standard deviation. The fitting parameters are presented in Table S1.

Table S1. Center (x_c), log standard deviation (w), area (A), and coefficient of determination (r^2) of the hydrodynamic size distribution of the $NaGdF_4$:Yb^{3+}/Er^{3+} upconverting nanoparticles.

x_c	w	A	r^2
170 ± 1 nm	(3.79 ± 0.04)×10^{-1} nm	23.7 ± 0.2 arbitrary units	0.996

The hydrodynamic diameter and uncertainty values reported in Figure 2b of the manuscript correspond to the mean diameter $(\mu = \exp(\ln(x_c) + 0.5w^2))$ and the standard deviation $\left(\sigma = (\exp(\ln(x_c) + 0.5w^2))\sqrt{\exp(w^2) - 1}\right)$ values, respectively.

S1.9.2. Thermal calibration

The thermal calibration was performed by fitting a straight line to the data of the thermometric parameter (Δ) recorded as a function of the temperature measured with a K-type thermocouple. The parameters of the fit are shown in **Table S2**.

Table S2. Slope (***a***), intercept (***b***), and coefficient of determination (r^2) of the temperature dependence of the thermometric parameter (**Δ**) defined for the obtained QR codes.

Δ	***a***	***b***	r^2
I_H/I_S	$(6.06 \pm 0.09)\times10^{-3}$ K^{-1}	-1.54 ± 0.03	0.998

S2. References

[1] R. B. de Castilho, C. V. Nunez, L. H. Coutinho, A. F. Lago, R. B. Bernini, G. G. B. de Souza, *J. Electron Spectros. Relat. Phenomena* **2007**, *155*, 77.

[2] J. Mooney, P. Kambhampati, *J. Phys. Chem. Lett.* **2013**, *4*, 3316.

Universidade de Aveiro
Universidade Estadual Paulista "Júlio de Mesquita Filho"
2024

Fernando Eduardo Maturi

Estudo da anomalia estrutural da água líquida usando termometria por conversão ascendente de energia de nanopartículas Brownianas

Study of the structural anomaly of liquid water using upconverting thermometry of Brownian nanoparticles

Relatório Complementar

Relatório escrito elaborado nos termos dos artigos 63.º e 64.º-1 do Regulamento de Estudos da Universidade de Aveiro

Supplementary Report

Written report in compliance with Articles 63 and 64-1 of the University of Aveiro Studies Regulations

1 Motivation and state-of-the-art

1.1 Introduction

Undoubtedly, water stands as the quintessential liquid, holding fundamental significance in countless biological, chemical, physical, geological, industrial, and environmental processes [1-6]. Indeed, the vital role of water extends to the point where it defines the parameters for investigating the potential existence of life beyond Earth [7]. Despite its ubiquity, understanding water remains a formidable challenge due to its complex nature under varying temperatures and pressures, setting its behavior apart from other common liquids, and yielding a myriad of anomalous properties that continue to intrigue and elude full comprehension.

Many of the anomalies associated with water become apparent when its temperature is lowered below its freezing point (273 K), a phenomenon known as supercooling. Within this temperature regime, water remains in the liquid state at low temperatures (down to 230 K at 1 atm) [8]. Nevertheless, water anomalies are also observed at higher temperatures, including minimum specific heat capacity (c) at 308 K, negative values of thermal expansion coefficient (α) for temperatures below 277 K, and minimum isothermal compressibility (κ_T) at 319 K [9-12], as summarized in **Table 1**.

Table 1. Anomalous properties of liquid water taking place at ambient conditions.

Anomalous property	Temperature of occurrence	Definition	Quantities involved
Specific heat capacity	308 K	$c = T\left(\frac{\partial S}{\partial T}\right)_P$	S = entropy T = temperature P = pressure V = volume
Thermal expansion coefficient	< 277 K	$\alpha = \frac{1}{V}\left(\frac{\partial V}{\partial T}\right)_P$	
Isothermal compressibility	319 K	$k_T = -\frac{1}{V}\left(\frac{\partial V}{\partial P}\right)_T$	

The simple existence of these anomalies is of paramount importance for the maintenance of life on Earth. For instance, the density maximum at 277 K along with the fact that ice is less dense than liquid water, have significant ecological implications. This unique property allows wintry lakes to freeze from the top down, establishing a crucial support system for aquatic life in cold regions. Additionally, the remarkable specific heat capacity of liquid water (c = 4.2 J·g^{-1}·K^{-1} [13])

plays a pivotal role in shaping the dynamics of Earth's climate, facilitating the efficient transport of heat from the tropics to the northern and southern latitudes, profoundly influencing the habitability of regions across the globe.

These peculiar characteristics of liquid water are directly linked to its exceptional ability to form hydrogen bonds (H-bonds), a strong and directional intermolecular interaction. These bonds are arranged in a dynamic configuration, with water molecules predominantly adopting a tetrahedral arrangement, which is widely believed to be the underlying reason for water's unusual properties. The constant breaking and reformation of H-bonds on a picosecond timescale [11, 14] introduce fluctuations in the local structure of liquid water, where water motifs with different densities emerge [12]. While both experimental and computational studies have provided substantial evidence for the existence of tetrahedral motifs with varying densities in water, interpreting these results has given rise to divergent explanations for the same experimental data [15-17]. Nowadays, two prominent schools of thought are dedicated to elucidating the anomalous properties of water in terms of its structural fluctuations. The first proposes that density fluctuations follow an unimodal distribution, as anticipated by continuous distribution models of water [15, 18, 19]. In contrast, the second argues that these anomalies arise from the coexistence of two distinct configurations of water molecules possessing distinct physical properties: a more organized tetrahedral motif and a more distorted structure [3, 11, 20]. These opposing viewpoints have been at the center of a vigorous debate over the past few decades, although the latter two-state idea has garnered far more attention because it defies the prevalent notion of water as a homogeneous liquid [21].

1.2 Two-state model of water

Although the concept may appear contemporary, the notion that liquid water comprises two different molecular organizations traces its origins back to the 19th century. In 1892, well before the recognition of the existence of the H-bonds, the German physicist Wilhelm Röntgen suggested that water consists of a mixture of two distinct coexisting phases [22]. Accordingly, cold water could be microscopically described as small icebergs floating in a fluid sea [2], whose relative ratio between them within the mixture depends on the pressure and temperature, which can trigger their interconversion. Fast forward to 1992, exactly a century later, Stanley and collaborators from Boston University reignited the discussions regarding this two-state paradigm in their seminal

work on the liquid-liquid phase transition (LLPT) hypothesis [23], highlighting the metastable behavior of liquid water. Nowadays, this two-state scenario appears very likely given that the coexistence of two structural motifs of water has been observed by both *in silico* [24-27] and experimental works [28-35], especially upon supercooling.

In general, phase transitions occur when a substance transforms from one state to another while preserving its chemical composition. Hence, an LLPT implies the existence of different liquid states of water with distinct properties [36]. Phase transitions are classified as either continuous or discontinuous, depending on their thermodynamic behavior. A discontinuous phase transition involves the absorption or release of energy during a constant-temperature process, resulting in a discontinuity in entropy (S), known as latent heat $L = T\Delta S$, where T is the temperature. When it comes to water, discontinuous phase transitions are evident during processes such as melting (solid-liquid phase transition) and boiling (liquid-gas phase transition) [37]. According to Paul Ehrenfest [38], discontinuous phase transitions can also be referred to as first-order transitions because they have discontinuities in the first derivatives of the Gibbs free energy (G). Otherwise, continuous phase transitions occur when L is not involved in the process and S changes continuously. A classic example of a continuous phase transition is the magnetization of ferromagnetic materials, which gradually decreases as temperature rises [39]. Following Ehrenfest's classification (**Table 2**), continuous phase transitions are called second-order transitions because they have discontinuities in the second derivatives of G.

Table 2. Comparison between discontinuous and continuous phase transitions, displaying their corresponding order transitions according to Ehrenfest's classification. The quantities c, α, and κ_T were previously described in Table 1.

Phase transition	Ehrenfest's classification	Discontinuities
Discontinuous	First-order	$\left(\frac{\partial G}{\partial T}\right)_P = -S$ $\left(\frac{\partial G}{\partial P}\right)_T = V$
Continuous	Second-order	$\left(\frac{\partial^2 G}{\partial T^2}\right)_P = -\frac{c}{T}$ $\left(\frac{\partial^2 G}{\partial P \partial T}\right) = \alpha V$ $\left(\frac{\partial^2 G}{\partial P^2}\right)_T = -k_T V$

In this sense, according to the LLPT hypothesis, water exhibits a second critical point within the supercooled regime, marking a discontinuous, or first-order, phase transition between a low-density phase (low-density liquid, LDL) and a high-density one (high-density liquid, HDL) [3, 11]. At the molecular level, the formation of the voluminous LDL occurs when water molecules in the first hydration shell arrange into an organized tetrahedral H-bonding network [40]. Conversely, the more tightly connected HDL appears when an additional molecule of water from the second hydration shell infiltrates the first shell, disrupting the LDL organization and creating a smaller and distorted H-bonding motif [40]. In this context, LDL motifs contribute to the formation of a more spacious H-bonding network, whereas the HDL motifs lead to a denser and more compact network, as illustrated in **Figure 1**. Direct observations of the LLPT pose considerable challenges due to the rapid crystallization of supercooled liquid water, which only exists in one state below 215 K [41, 42]. Nevertheless, recent studies of isothermal volume changes in diluted polyol and trehalose aqueous solutions under varying pressure have provided empirical support for the existence of two states of water experiencing an LLPT [43, 44]. This corroborating evidence suggests that pure water also undergoes an LLPT between the metastable LDL and HDL states.

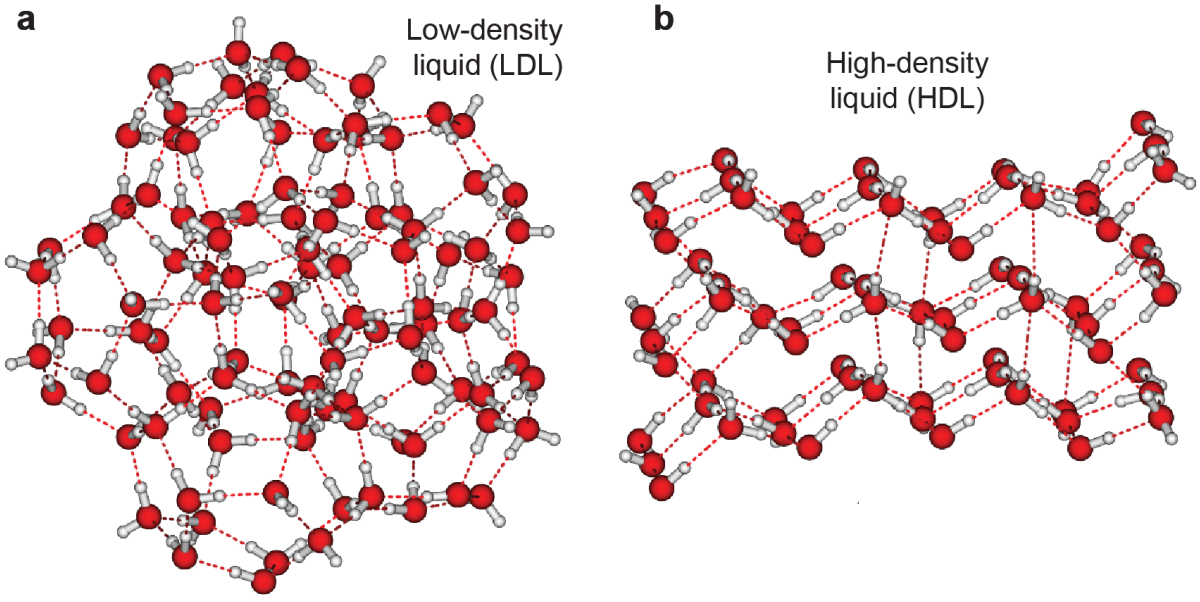

Figure 1. Schematics of the three-dimensional arrangement of H-bonding networks of the **(a)** LDL and the **(b)** HDL states. The hydrogen and oxygen atoms of water molecules are depicted as white and red spheres, respectively. The dashed lines illustrate the H-bonds. Adapted from Reference [45].

The LLPT hypothesis offers a fresh perspective for understanding the singular behavior of liquid water, particularly in the context of LDL and HDL motifs under varying pressure and temperature conditions, as depicted in the hypothetical phase diagram illustrated in **Figure 2**. Initially introduced by Poole, Sciortino, Essmann, and Stanley through molecular dynamics simulations [23, 46], this schematic representation has since been refined with theoretical and experimental findings [3, 11, 20, 47, 48]. This phase diagram portrays the liquid-liquid coexistence line, marking the crossover between LDL and HDL phases within regions of simple liquid behavior. In the supercooled regime, the Widom line (W) represents the extension of the coexistence line, effectively dividing the liquid phase into two distinct regions [48]. One region, situated at high temperatures and pressures, mimics the characteristics of the HDL state, while the other, found at low temperatures and low pressures, exhibits similarities to the LDL state. According to the LLPT hypothesis, the structural motifs of LDL and HDL persist in a mixed state near W. This means that one state can emerge within the regime primarily dominated by the other, owing to the significant rate of change between them [49].

Additionally, the phase diagram also includes the liquid-liquid critical point, where the presence of fluctuations on various length scales may give rise to locally spatially separated regions in the anomalous range. Notably, the amorphous solid states of LDL and HDL can exist at extremely low temperatures as low-density (LDA, low pressure) and high-density (HDA, high pressure) amorphous ice, respectively, primarily distinguished by their 20% density difference [45]. Remarkably, recent findings have unveiled the potential for the formation of medium-density amorphous ice under specific conditions of pressure and temperature [50]. This discovery indicates that the proposed phase diagram still has room for optimization and potential for further improvements.

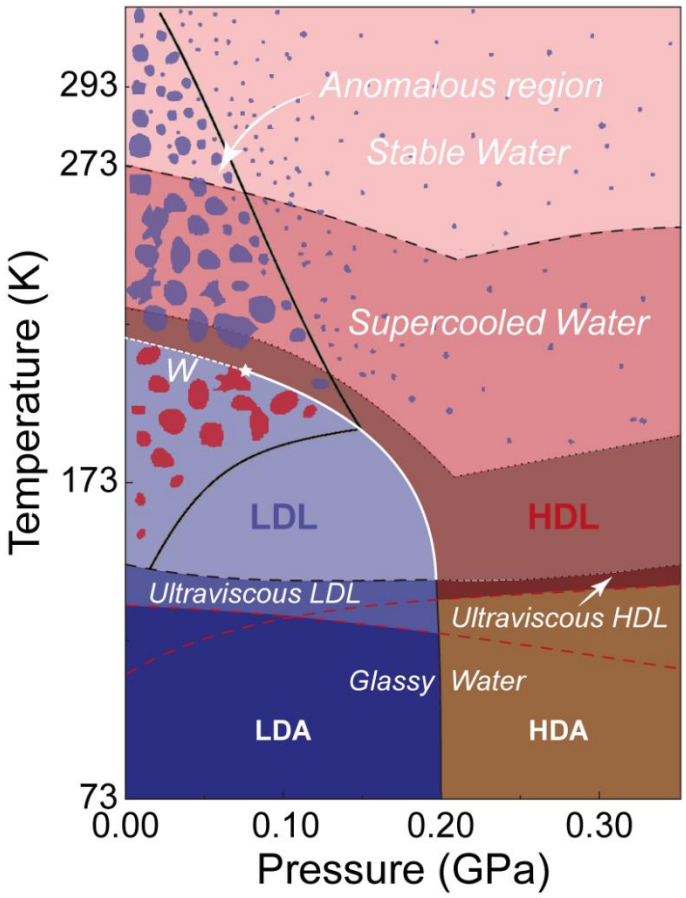

Figure 2. Hypothetical phase diagram of liquid water showing the coexistence of LDL (blue) and HDL (red) domains near the W line. Below W, LDL dominates with fluctuations in HDL domains, whereas above W HDL dominates with LDL fluctuations. The white star represents the liquid-liquid critical point. The farther away from the critical point one moves, the smaller the fluctuations become, as indicated by the size of the blobs. The black line delimits the so-called "funnel of life" at which water exhibits its unusual properties that are crucial to the maintenance of life. Adapted and modified from Reference [20].

Additional experimental evidence supporting the existence of inhomogeneous structures in liquid water and the fluctuations between HDL and LDL patches have emerged from various experiments, such as the isosbestic point observed in the temperature-dependent OH stretch Raman signal [51, 52], temperature-dependent infrared spectra of liquid water [53], optical Kerr effect measurements [54], and X-ray absorption and emission spectroscopy [14, 28-30, 55], although the coexistence of these fluctuations at ambient conditions and their implications remain elusive and controversial. The most popular methods employed to deliver experimental evidence regarding density fluctuations in liquid water rely on high-energy radiation, such as small-angle X-ray and

neutron scattering [14]. Unfortunately, these techniques are typically restricted to a length scale of approximately 1 nm, as depicted in **Figure 3**. Once these techniques only provide an average picture of the local structure of liquid water, unraveling the contributions of different water domains to the behavior of supramolecular structures dwelling in aqueous solutions of electrolytes and suspensions of biomolecules and inorganic materials becomes exceedingly challenging. These insights are fundamental to our understanding of biochemistry, as the conditions that support life as we know might be intricately linked to the coexistence of two distinct H-bond organizations within liquid water [1, 7, 56]. In this context, there is a strong demand for experimental techniques that can provide a microscopic elucidation of H-bond structures in liquid water and reveal their influence on the surrounding macroscopic world.

In recent years, numerous research groups have risen to the challenge of investigating the temperature-dependent properties of aqueous solutions and suspensions, encompassing those containing metallic nanoparticles [57], semiconductors nanoparticles [58], trivalent lanthanide-based materials [59-61], and organic molecules [62-64]. This endeavor has opened a new chapter in the quest to unveil the anomalous behavior of liquid water due to the striking resemblance of these results to those obtained for pure water, suggesting that these materials can serve as probes of the organization of the H-bonding networks of water molecules in their vicinity. What makes this approach particularly intriguing is that all the temperature-dependent properties examined exhibit a bilinear behavior marked by a crossover temperature (T_c). The values of T_c typically fall within the range of 320–330 K [56], aligning closely with the minimum value of k_T observed for water. This correlation is attributed to the structural geometric transition from a more to a less organized tetrahedral arrangement, induced by density increases upon heating [31]. Thus, it stands to reason that T_c emerges due to the change in the volume between LDL and HDL motifs while increasing temperature.

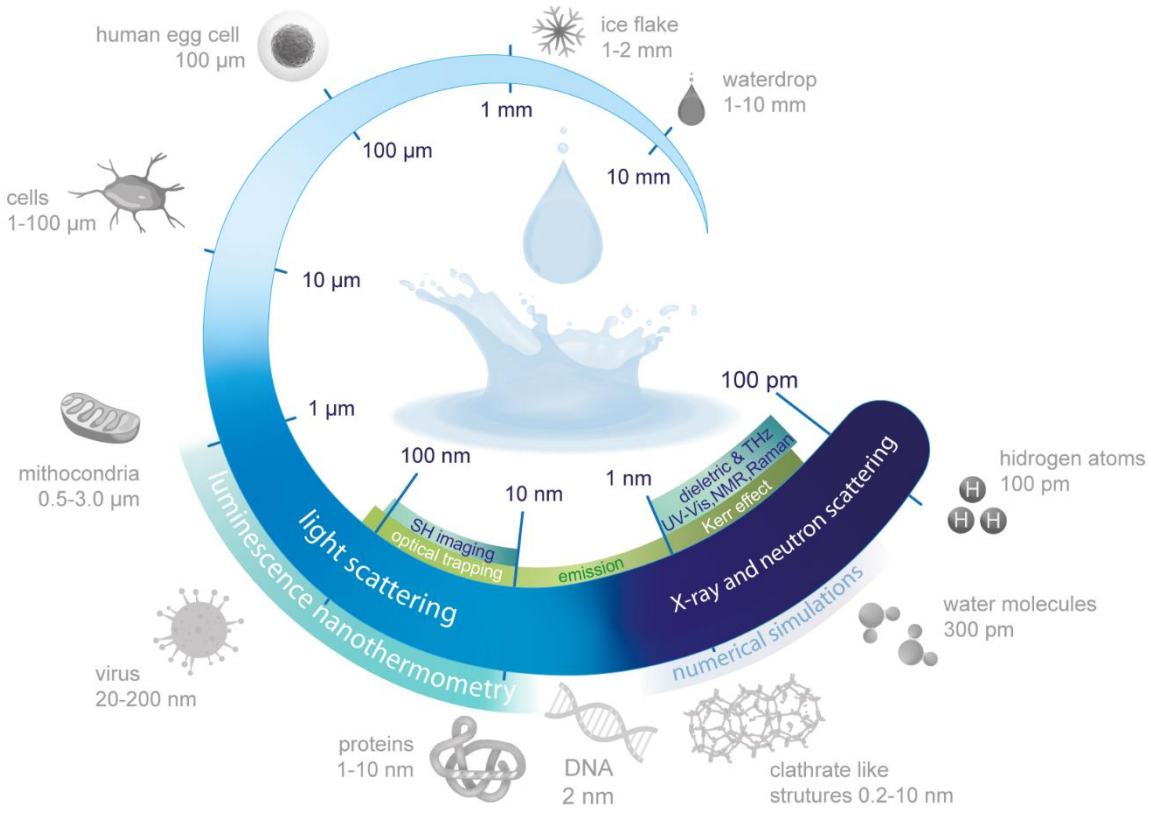

Figure 3. Schematic representation of the length scales covered by different techniques used to investigate the anomalies of liquid water. The temperature dependence of the H-bond networks has been explored at different length scales. While X-ray and neutron scattering, numerical simulations, Kerr effect, dielectric, THz, UV-Vis, NMR, and Raman spectroscopies operate at the length scale of hydrogen atoms and water molecules, second harmonic (SH) imaging works at longer scales. Light scattering and luminescence thermometry, as shown in this thesis, could also be used up to a submicrometric length scale.

While numerous reports have managed to distinguish between two states of H-bonding in liquid water, up until the beginning of this Ph.D. project, none of the previous research had successfully established a conclusive link between the emergence of T_c and the existence of the LDL and HDL domains. For instance, the first correlation between T_c and fluctuations between high-density and low-density liquid states was elucidated in

Manuscript 2 [65] through upconversion luminescence thermometry. This manuscript served as the cornerstone for the direction of this thesis, aiming at bridging the gap between the absence of experimental evidence regarding LDL and HDL motifs coexisting at ambient conditions and the need for more straightforward experimental methods to investigate them. Therefore, upconversion luminescence thermometry was herein chosen as a primary tool to evaluate low-to-high density fluctuations in liquid water.

1.3 Luminescence thermometry

Using luminescence for performing thermal sensing is a clever approach because temperature changes strongly impact the light-emitting properties of luminescent materials [66-68]. As the temperature rises, the additional thermal energy causes the nonradiative processes (phonons) to compete with the light emission from radiative ones (photons). This is translated as changes in the luminescent response, which, in turn, depends on the specific nature of the material employed.

The most common effect of increasing the temperature of luminescent materials is a reduction in emission intensity. In this case, nonradiative processes become more pronounced, resulting in luminescence thermal quenching, as typically observed in organic dyes [69]. However, employing the temperature dependence from emission-based measurements comes with notable disadvantages, mainly arising from issues regarding samples' photobleaching and drift of the optical excitation [70]. Consequently, as nonradiative decays are enhanced as temperature rises, a reduction in the emission lifetime is also observed [71]. Although emission lifetime remains independent of the concentration of the luminescent material within a certain range of concentrations where no chemical or physical interactions are observed between the light-emitting centers [72], assessing temperature dependence through lifetime-based methods relies on expensive optoelectronics to perform time-resolved measurements.

To overcome these issues, ratiometric approaches are often employed because they rely on intensity ratios between two emission bands, which remain unaffected by local intensity fluctuations, concentration variations of the light-emitting centers, or fluctuations in the intensity of the excitation source, all while requiring less complex instrumentation [73]. In addition, temperature-induced spectral shifts typically occur due to the narrowing of the bandgap, resulting in a redshift of the peak energy [74]. Furthermore, as the temperature rises, the bandwidth of the

emission band may broaden due to increased thermal energy, which enhances vibrations within the material's crystal lattice [75, 76]. Although spectral shift and bandwidth approaches are useful for evaluating the temperature dependence of several luminescent materials, they are not commonly employed due to the smaller sensitivity to temperature variations in comparison to single intensity, intensity ratio, and lifetime-based approaches.

Developing a new luminescent thermometer is a relatively straightforward process, where the measurement of the temperature through luminescence starts by defining a thermometric parameter (Δ) that establishes a correlation between temperature and changes in the emission spectra, which can encompass any of the aforementioned temperature-dependent luminescent properties. To facilitate the comparison of various luminescent materials regardless of the specific thermometric parameter employed, researchers rely on a figure of merit known as relative thermal sensitivity (S_r) [77]:

$$S_r = \frac{1}{\Delta}\left|\frac{\partial \Delta}{\partial T}\right| \quad (\mathbf{1})$$

where $\partial\Delta/\partial T$ indicates the change of Δ concerning the temperature T (also referred to as absolute sensitivity, S_a). The value of S_r is the absolute value of S_a normalized by the magnitude of Δ, allowing for quantitative comparisons between different materials, which is expressed in units of percentage change per unit of temperature change (%·°C^{-1} or %·K^{-1}).

Another essential figure of merit employed to evaluate the temperature accuracy in luminescence thermometry is the uncertainty in temperature δT [78]:

$$\delta T = \frac{1}{S_r}\frac{\delta \Delta}{\Delta} \quad (\mathbf{2})$$

here, δT is the smallest temperature that can be reliably measured by the luminescent thermometer. It mostly depends on δΔ, which corresponds to the uncertainty in the determination of Δ, where $\delta\Delta/\Delta$ indicates the relative uncertainty of Δ. In the pursuit of an optimal luminescent thermometer, researchers aim to maximize S_r and reduce δT. Several approaches can be used to accomplish this, including the design of brighter materials or the development of higher-sensitivity detectors to reduce $\delta\Delta/\Delta$, thus diminishing δT. Additionally, engineering luminescent materials or adopting alternative methods for describing Δ can lead to improvements in S_r. Recently, significant efforts have been made to employ materials exhibiting multiple temperature-dependent luminescent

properties [79-82], an alternative approach that can be further improved to describe Δ through multiparametric equations, reaching a remarkably tenfold improvement in both S_r and δT, as firstly explored in **Manuscript 6** [83].

Luminescent thermometers are usually sorted into different categories to help in selecting the best thermometer for a specific application. The most important categorization evaluates the relationship between Δ and the thermal calibration method, where luminescent thermometers are classified either as primary or secondary [84]. Primary thermometers rely on well-established thermodynamic laws and quantities, providing reliable temperature readouts without requiring additional calibration against a temperature reference. However, their S_r values are typically as low as 1.0 %·K^{-1}. In contrast, S_r values of secondary thermometers are usually higher than 3.0 %·K^{-1} [85], although they require calibration with a reference thermal probe, mainly when changing from one operating medium to another. Hence, the classification as primary or secondary does not mean that the latter is less reliable than the first one, where the choice between them depends entirely on the specific requirements of the desired application.

Although there are plenty of luminescent materials that can be used for designing primary or secondary luminescent thermometers, such as fluorescent polymers [86, 87], organic dyes [88], fluorescent proteins [89], quantum dots [90], and metal-organic frameworks [91], lanthanide-based materials offer greater advantages [92]. This is attributed to their singular electron configuration, which gives rise to exceptional optical properties that make them suitable for performing temperature readouts across a wide range of temperatures, spanning from cryogenic temperatures (< 100 K) up to physiological conditions (298–323 K). This becomes evident when examining the temperature-dependent luminescent properties of various lanthanide-based materials, including Pr^{3+} [93], Nd^{3+} [76], Sm^{3+} [94], Eu^{3+} [95], Tb^{3+} [96], Ho^{3+} [97], Er^{3+} [84], and Tm^{3+} [98] ions embedded into different host matrices. As a result, lanthanide-based materials have found widespread applications in the development of luminescent thermometers, from medical to industrial processes [99]. Hence, it is imperative to gain a thorough understanding of the properties that make lanthanides such a great deal for luminescence thermometry.

1.3.1 Lanthanide ions for luminescence thermometry

The group of elements known as lanthanides (Ln) consists of a set of 15 chemically similar elements belonging to the f-block of the periodic table, with their atomic numbers spanning from

57 (lanthanum, La) to 71 (lutetium, Lu). Lanthanides have a generic electron configuration of $[Xe]4f^n5d^16s^2$, with the gradual filling of the 4f orbitals, where *n* varies from 0 to 14 (La–Lu). The trivalent Ln ions (Ln^{3+}) present the electron configuration $[Xe]4f^n$, which is the most stable oxidation state in aqueous solutions. The electron configuration of Ln^{3+} ions is responsible for unique optical properties, as the filled $5s^2$ and $5p^6$ orbitals shield the 4f electrons from interactions with the surroundings [100], as observed in **Figure 4**. As a result, 4f orbitals do not directly participate in chemical bonding, where the spectral profile of Ln^{3+} is weakly affected by the crystal field, giving rise to fingerprint emission bands characterized by a high color purity [101, 102]. Another consequence is that intraconfigurational 4f-4f transitions occur due to the partially filled 4f-shell, resulting in narrow absorption and emission bands (< 10 nm), high luminescence quantum yields, long emission lifetimes (up to 1 ms), and luminescence ranging from ultraviolet (UV) and visible (Vis) to near-infrared (NIR) spectral regions [100]. Due to these outstanding optical properties, Ln^{3+} ions have been widely used in various areas of interest, where cancer diagnosis and therapy [103], light generation and amplification in lasers [104], waveguides and optical fibers [105, 106], biosensors [107], and bioimaging [108] are just a few of the possible applications.

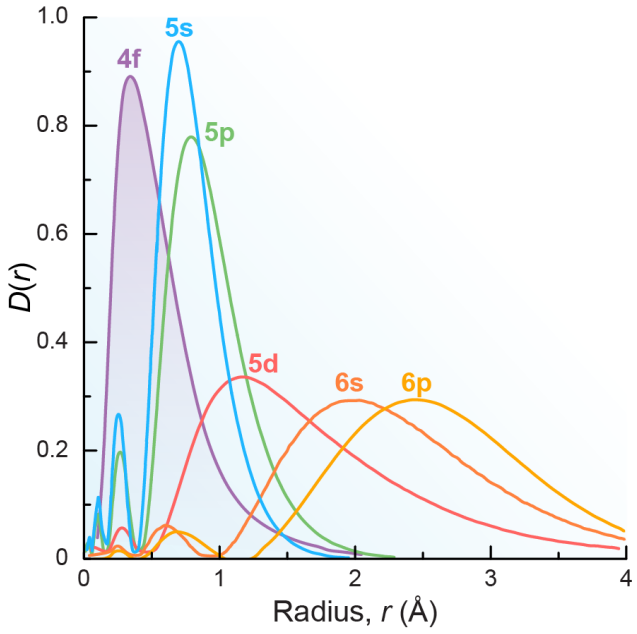

Figure 4. Radial distribution probability densities ($D(r) = r^2R(r)^2$, where $R(r)$ is the radial wave function) as a function of the radius (r) for the 4f, 5s, 5p, 5d, 6s, and 6p electrons of neodymium

atoms (Nd, Z = 60, $[Kr]4d^{10}5s^25p^66s^24f^45d^06p^0$). The shadowed area highlights the shielded 4f electrons. Adapted from Reference [109].

Intraconfigurational transitions are typically forbidden according to Laporte's selection rule, as they do not involve a change in the parity of electrons. However, 4f-4f transitions are partially allowed for Ln^{3+} embedded in a host matrix due to the influence of the crystal field effect, which induces the mixing of 4f levels with higher energy levels. As a consequence, these transitions are observed in absorption and excitation spectra as bands with low molar absorptivity coefficients ε ($1<\varepsilon<10$ $L \cdot mol^{-1} \cdot cm^{-1}$ [110]), making the direct excitation of Ln^{3+} inefficient, resulting in low-intensity emissions. To overcome this limitation, doping low-symmetry and low-phonon-energy crystalline host matrices with Ln^{3+} may enhance the likelihood of 4f-4f transitions [111].

Lanthanide halides exhibit low phonon energies, with values of 175 and 260 cm^{-1} for $LaBr_3$ and $LaCl_3$ [112, 113], respectively, nonetheless, they are highly hygroscopic and water-soluble [113], hindering their efficiency as host matrices for Ln^{3+}. Conversely, lanthanide oxides and phosphates offer high chemical stability, although their phonon energies are relatively high, as observed for Y_2O_3 (600 cm^{-1}), Gd_2O_3 (700 cm^{-1}), and $LaPO_4$ (1050 cm^{-1}) [114-116]. In this case, the sensitization of the luminescence is not efficient because nonradiative decays are facilitated by phonons, resulting in the relaxation of the Ln^{3+} excited states. For these reasons, lanthanide fluorides are frequently the preferred choice as a host matrix for Ln^{3+} doping due to the combination of low phonon energy (*ca.* 350 cm^{-1} [117]) and excellent chemical stability. Additionally, cations such as Na^+ and Y^{3+} have similar radii to Ln^{3+} dopants, reducing the occurrence of crystal defects and lattice stress during the synthesis [118]. For these reasons, sodium yttrium fluoride ($NaYF_4$) stands out as the most used host matrix in the synthesis of Ln^{3+}-doped nanoparticles [119]. While these nanoparticles typically exhibit a size distribution due to nanocrystal growth variations during synthesis, which may vary from batch to batch, the inorganic nature of Ln^{3+}-doped nanoparticles enhances their thermal and photostability, making them suitable for long-term light exposure [116].

1.3.1 Upconversion luminescence thermometry

Beyond their particular optical properties, a select few Ln^{3+} ions offer the unique ability to observe unusual light-emitting processes, such as upconversion. Upconversion is a nonlinear

optical phenomenon that enables the conversion of low-energy excitation (longer wavelengths, *e.g.*, NIR) into high-energy emission (shorter wavelengths, *e.g.*, UV-Vis [120]). This remarkable capability arises from the ladder-like energy level structure of Ln^{3+} and their long-lasting emission lifetimes, allowing the sequential absorption of multiple low-energy photons [121]. The multiple absorption occurs from the ground state to an excited state through intermediate ones, resulting in higher-energy upconverting anti-Stokes emission during the relaxation [122]. The upconversion mechanism can manifest within individual ions or through energy transfer between ion pairs, involving a sensitizer and an activator.

To produce Ln^{3+}-doped upconverting nanoparticles (UCNPs), it is essential that the host matrix display transparency to both the excitation and emission wavelengths, besides exhibiting low phonon energy to minimize nonradiative relaxations. This is because, the narrower the energy gap between two emitting levels (or the greater the energy of phonons), the higher the likelihood that multiphonon emission can bridge this gap, thus increasing the probability of non-radiatively transitioning excited electrons to a lower energy state [123]. This is particularly pertinent when dealing with scenarios requiring the conversion of three or more photons. Considering these requirements, $NaYF_4$ once again emerges as an optimal host matrix for the synthesis of Ln^{3+}-doped UCNPs [113].

Commonly, Nd^{3+} and Yb^{3+} are employed as sensitizers because they present absorption bands in the NIR peaking around 808 and 980 nm, respectively. These absorption bands match the electronic energy gap of activator ions, facilitating the multiphoton absorption. Additionally, Nd^{3+} and Yb^{3+} display large absorption cross-section values of $\sim 10^{-19}$ cm^2 (808 nm) and $\sim 10^{-20}$ cm^2 (980 nm), respectively, enhancing the efficiency of the NIR absorption [122]. Other Ln^{3+} such as Pr^{3+}, Ho^{3+}, Er^{3+}, and Tm^{3+} are usually employed as activators because they display different emission spectra, which can be used for fine-tuning the luminescent response in the UV-Vis spectral range upon NIR excitation [122]. The Yb^{3+}/Er^{3+} pair is typically used for synthesizing UCNPs because the excitation can be performed through the $^2F_{7/2} \rightarrow {}^2F_{5/2}$ transition of Yb^{3+} (sensitizer) by using a 980 nm laser diode. Moreover, energy transfer from Yb^{3+} to Er^{3+} (activator) can occur, eventually reaching the $^4F_{7/2}$ and $^2H_{11/2}$ excited levels by two-photon absorption, giving rise to the emission in the Vis spectral range [118].

Once the energetic separation ΔE between the $^2H_{11/2}$ and $^4S_{3/2}$ emitting levels of Er^{3+} is relatively small, it allows a thermal-induced population redistribution according to the Boltzmann statistics:

$$\Delta = \frac{I_{20}}{I_{10}} = \frac{A_{20}g_2}{A_{10}g_1}\exp\left(\frac{-\Delta E}{k_B T}\right) = B\exp\left(\frac{-\Delta E}{k_B T}\right) \quad (3)$$

where Δ is the beforementioned thermometric parameter, I_{20} and I_{10} are the emission intensities from the $^2H_{11/2}\rightarrow{}^4I_{15/2}$ ($|2\rangle\rightarrow|0\rangle$) and $^4S_{3/2}\rightarrow{}^4I_{15/2}$ ($|1\rangle\rightarrow|0\rangle$) transitions of Er^{3+}, respectively, A is Einstein's coefficient for spontaneous emission from the excited states to the ground state ($|2\rangle$ and $|1\rangle$ to $|0\rangle$), g is the degeneracy of each state, k_B is the Boltzmann constant, T is the absolute temperature, and $\Delta E \approx 750$ cm^{-1} [78, 124]. It is important to recall that, despite usually misreported in the literature, the intensities I_{20} and I_{10} do not depend on the emission energies $\omega\hbar_{20}$ and $\omega\hbar_{10}$, respectively, because nowadays, commonly employed spectrofluorometers use single photon counting detectors [124, 125], where the intensity is measured as the average number of photon counts per second (s^{-1}). For this reason, the pre-exponential factor B is described as the ratio $B = \frac{A_{20}g_2}{A_{10}g_1}$. Noteworthy, if the depopulation of the levels $|2\rangle$ and $|1\rangle$ involves other energy levels than $|0\rangle$, Equation 3 must be corrected by the ratio β_{20}/β_{10}, where β is the branching ratio (*i.e.*, the fraction of the total emission from $|2\rangle$ and $|1\rangle$ to $|0\rangle$ [78]).

Typically, the Boltzmann distribution is a good description of the emission intensity ratio when two emitting energy levels present ΔE between 200 and 2000 cm^{-1}. Within this ΔE range, these levels are close enough to undergo thermalization, reaching a thermodynamical quasi-equilibrium state, which is the reason why they are considered thermally coupled [78]. Virtually, any Ln^{3+} featuring thermally coupled levels meets the requirements for performing luminescence thermometry based on the Boltzmann statistics (**Figure 5**). Nevertheless, the criteria for fulfilling this relationship include the thermodynamic considerations stated above and also the kinetic ones due to the order of magnitude of the thermalization rates for the relevant emitting levels, as elegantly discussed in the work of Suta and Meijerink [124].

It is noteworthy that in the specific context of Boltzmann-based luminescent thermometers, Equation 1 transforms into $S_r = \Delta E/k_b T^2$, where the relative thermal sensitivity depends on both the energetic separation between the thermally coupled levels and the temperature. When the temperature range is limited, ΔE remains nearly constant and S_r is primarily determined by T.

However, it is crucial to emphasize that at lower temperatures, there is not sufficient thermal energy to populate the upper-emitting energy level. Moreover, with a larger ΔE, higher temperatures become necessary to overcome the energy separation between the emitting levels. For these reasons, appreciable thermal response can be achieved in various temperature ranges by selecting Ln^{3+} exhibiting thermally coupled levels with distinct ΔE, as illustrated in Figure 5 and given by [124]:

$$\frac{\Delta E}{(2+\sqrt{2})k_B} \leq T \leq \frac{\Delta E}{2k_B} \quad (4)$$

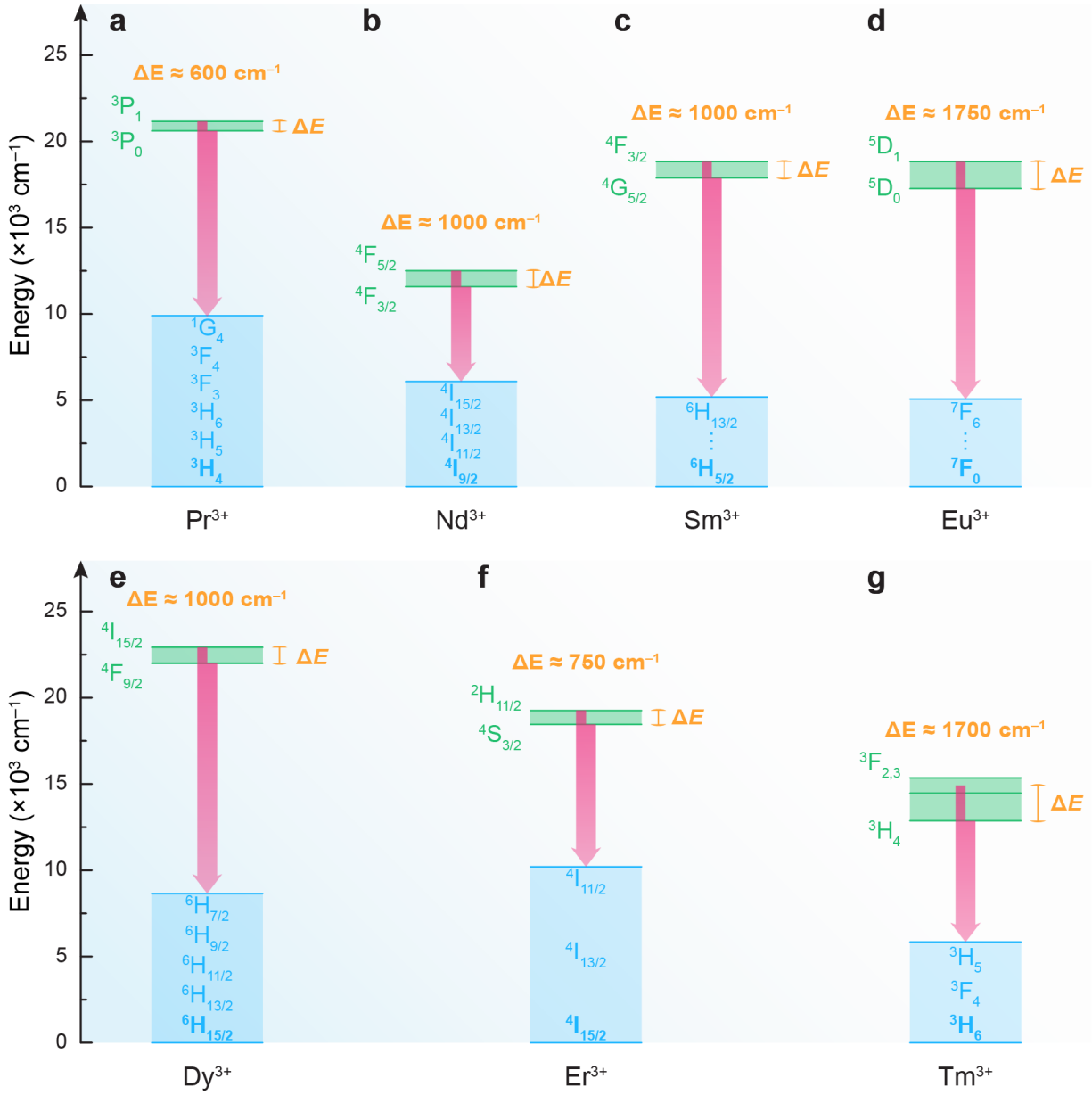

Figure 5. Thermally coupled levels of **(a)** Pr^{3+}, **(b)** Nd^{3+}, **(c)** Sm^{3+}, **(d)** Eu^{3+}, **(e)** Dy^{3+}, **(f)** Er^{3+}, and **(g)** Tm^{3+}. Here, Boltzmann statistics were explored for Er^{3+} and Pr^{3+}. Adapted from Reference [92].

In the specific scenario involving Er^{3+}, the thermally coupled $^2H_{11/2}$ and $^4S_{3/2}$ emitting levels enables to apply Equation 3 for determining the temperature of the medium in which the UCNPs are dispersed, as $\Delta = I_{20}/I_{10}$, k_B, and ΔE are known values. Interestingly, the parameter Δ can be written as Δ_0 in the absence of laser-induced heating [84]:

$$\Delta_0 = B \exp\left(\frac{-\Delta E}{k_B T_0}\right) \quad (5)$$

where T_0 corresponds to the room temperature. This is possible because, without the heating induced by the laser excitation, the temperature of the material used as a thermometer is the temperature of the environment in which it is placed, according to the Zeroth law of thermodynamics. Despite the value of the constant B can be calculated by the Judd-Ofelt theory [126, 127], it is not necessary here because it is possible to combine Equations 3 and 5, and thus the absolute temperature can be determined directly from the ratio Δ/Δ_0:

$$\frac{1}{T} = \frac{1}{T_0} - \frac{k_B}{\Delta E} \ln\left(\frac{\Delta}{\Delta_0}\right) \quad (6)$$

By using Equation 6, the prediction of the temperature is performed by using a well-defined equation of state without unknown or significantly temperature-dependent values [128]. In this Boltzmann-derived approach, no prior knowledge of B is required and ΔE is calculated in a non-temperature-dependent way. Because Δ_0 and T_0 correspond to experimentally measured values that are obtained apart from any calibration or fitting procedures, they work as scaling/normalization factors rather than a calibration process, where this thermometric approach matches the concept of primary thermometers. In this context, UCNPs containing Yb^{3+}/Er^{3+} present themselves as luminescent primary thermometers due to the intrinsic thermal-sensing ability of Er^{3+} upon 980 nm excitation. For these reasons, the most successful cases of using thermally coupled levels to perform upconversion luminescence thermometry are based on the Yb^{3+}/Er^{3+} ion pair, whose partial energy levels diagram is schemed in **Figure 6**.

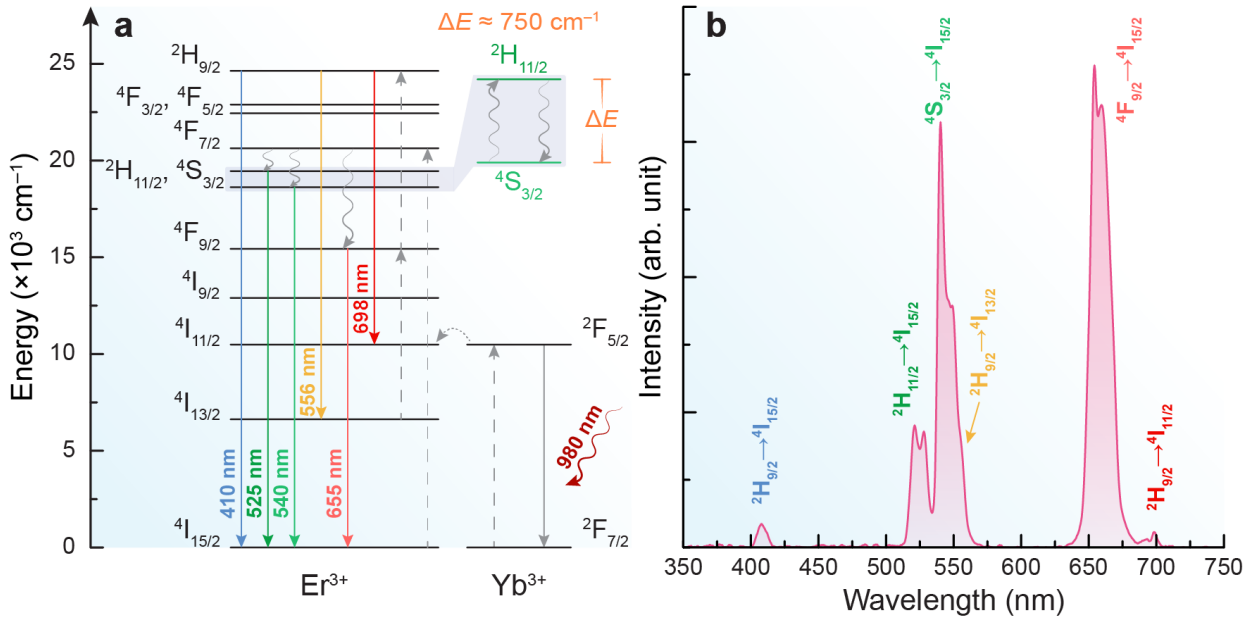

Figure 6. (a) Partial energy level diagram of Yb^{3+} and Er^{3+} ions showing the absorption of Yb^{3+} under 980 nm excitation, depicting the energy transfer from Yb^{3+} to Er^{3}. The zoomed region depicts the thermally coupled levels of Er^{3+}. Solid lines indicate radiative transitions, dashed lines are cross-relaxation processes, curly arrows display nonradiative decays, and the dotted line represents nonradiative energy transfer. **(b)** Upconverting emission spectrum of $NaYF_4$:Yb^{3+}/Er^{3+} (18%/2%) UCNPs with 52 nm in diameter upon continuous-wave laser excitation at 980 nm (power density = 62 W·cm^{-2}). The radiative transitions of Er^{3+} are assigned to their corresponding emission bands, matching the solid lines shown in panel **a**.

On top of the aforementioned advantages of using UCNPs for luminescent primary thermal sensing, the choice of this kind of material offers the benefit of mapping the local temperature in the vicinity of the nanoparticles. This particular feature enables the access of thermal events taking place even at nano- and submicrometric scales [129], a spatial resolution that cannot be achieved by using conventional thermometers. For these reasons, this thesis primarily concentrates the efforts on employing aqueous suspensions of $NaYF_4$ UCNPs co-doped with Yb^{3+} and Er^{3+} ($NaYF_4$:Yb^{3+}/Er^{3+}) as a reliable tool for investigating low-to-high density fluctuations in liquid water. Through temperature measurements, valuable insights can be gained concerning the coexistence of HDL and LDL at standard conditions of pressure and temperature.

1.4 Brownian motion

Although working with particles or nanoparticles suspended in a liquid seems a tedious trivial task, lots of actions are happening because particles suspended in a liquid are never

stationary. This exciting microscopical adventure was first described in 1827 by the Scottish botanist Robert Brown, who observed that small particles suspended in a fluid display erratic, seemingly stochastic movements [130]. The understanding of this curious behavior remained elusive for nearly eight decades until the early 20th century, when Albert Einstein [131], William Sutherland [132], and Marian Smoluchowski [133] laid the theoretical foundation to explain this behavior. Today, we refer to this random movement as Brownian motion, a phenomenon mainly driven by the interactions between solvent molecules themselves and with the suspended particles. These interactions keep the particles suspended and cause them to move spontaneously without any apparent external force.

While both diffusion and Brownian motion involve thermal motion, diffusion can be described as the net movement of fluid due to thermal gradients (thermal diffusion or the Soret effect) whereas the Brownian motion describes the diffusion of particles presenting at least one dimension smaller than 1000 nm [134]. Although Einstein contended in 1907 that the time scale for measuring the instantaneous Brownian velocity was too short [135], recent technological advancements have paved the road to measuring the velocity of Brownian particles with remarkable temporal and spatial resolution.

The upsides of using luminescent nanoparticles in this case lie in the capacity to leverage the temperature-dependent luminescence properties to gain insights into their thermal motion, thus converging luminescence thermometry with Brownian motion. This was nicely demonstrated by a couple of recent works published by Brites *et al.* [136] and Lu *et al.* [137], which highlight the possibility of using $NaYF_4$:Yb^{3+}/Er^{3+} UCNPs to measure the Brownian velocity through upconversion luminescence thermometry and optical tweezers, respectively. The feasibility of using the light-emitting properties of UCNPs to assess their thermal motion presents exciting opportunities for investigating the temperature dependence of the H-bond network. This is because, after understanding that the Brownian motion of a particle is intricately linked to the properties of its surrounding liquid, such as viscosity and temperature [138], the measurement of the Brownian velocity of UCNPs suspended in water would allow delving deeper into the structural aspects of water and its associated anomalous properties. Moreover, the temperature-dependent Brownian velocity of UCNPs may also be sensitive to the identification of T_c in water suspensions, making it possible to study low-to-high-density liquid fluctuations.

1.5 Contributions of this thesis to the state-of-the-art

To evaluate the anomalous behavior of liquid water at ambient conditions, this thesis focuses its attention on examining structural fluctuations between HDL and LDL water motifs by using luminescence thermometry as a reliable tool. In **Manuscript 1**, the Brownian velocity of UCNPs dispersed in water and other solvents containing H-bonds was investigated, revealing that is possible to replicate the influence of temperature and pressure on the HDL and LDL H-bond networks by precisely controlling both the nanoparticle size and the pH of the aqueous medium. These findings provide experimental evidence supporting the predictions in the hypothesized phase diagram of liquid water presented in Figure 2. Within nanofluids, the local environment around nanoparticles exerts a significant influence on their physical-chemical properties, being different from bulk due to interaction with the particle surface. **Manuscript 1** underscores the substantial impact of these interactions, serving as compelling evidence of this effect for the specific example of luminescent nanoparticles. It demonstrates that the versatility of UCNPs, with their customizable dimensions and surface properties, renders them indispensable instruments for experimentally quantifying the HDL/LDL proportion in the hydration water surrounding particle surfaces. Moreover,

Manuscript 2 [65] shows that the unusual bilinear trend observed in the temperature-dependent Brownian velocity of UCNPs is attributed to two motion regimes of the UCNPs, wherein UCNPs move slower for $T<T_c$ due to the higher proportion of voluminous LDL motifs, while they move faster for $T>T_c$ because all LDL motifs were already converted into HDL ones. This interpretation is corroborated by molecular dynamic simulations, which shed light on the distortion of the tetrahedral arrangement of water molecules as temperature increases.

The peculiar behavior of liquid water can significantly impact the thermometric capabilities of other luminescent nanoparticles, as demonstrated in

Manuscript 3 [58]. Given water's strong NIR absorption, the luminescence of silver sulfide, a highly sensitive secondary luminescent thermometer employed for *in vivo* applications, experiences drastic distortions. This compromises its thermometric performance when performing temperature readouts in biological aqueous media. Additionally,

Manuscript 3 highlights the less anomalous behavior of heavy water in contrast to regular water, which was also observed and discussed in **Manuscript 1**.

Although $NaYF_4$ provides a chemically stable host matrix for developing upconverting nanoparticles, the Yb^{3+}/Er^{3+} pair can also be embedded into different classes of materials to design primary luminescent thermometers, as explored in **Manuscript 4** [139]. Indium-based halide perovskites co-doped with Yb^{3+}/Er^{3+} demonstrate not only low cytotoxicity in L929 murine fibroblast cells but also exceptional thermal stability up to 500 °C, paving the road for using them in biomedical contexts. In addition, **Manuscript 5** [140] introduces the possibility of extending the scope of primary luminescent thermometers to include other trivalent lanthanide ions besides Er^{3+}, underscoring the inherent thermal sensing capability of Pr^{3+}. Choosing Pr^{3+} over Er^{3+} for luminescent primary temperature sensing offers a significant advantage, allowing the use of a low-intensity Xe lamp as the excitation source and minimizing temperature deviations associated with laser-induced heating observed in upconverting approaches.

Irrespective of whether a luminescent thermometer is classified as primary or secondary, the primary objective of designing new luminescent thermometers remains the same: enhancing the relative thermal sensitivity while minimizing temperature uncertainty. Among the various strategies aiming to achieve this, **Manuscript 6** pinpoints the advantage of integrating multiparametric luminescence thermal sensing with multiple regression analysis [83]. This combination enhances the reliability and precision of thermal measurements for *in vivo* applications, resulting in a remarkable tenfold improvement in both S_r and δT. Beyond providing contactless measurements of temperature, luminescence thermometry opens up new avenues for incorporating additional layers of information into everyday devices. This potential is elegantly illustrated in

Manuscript 7 [141], where the incorporation of UCNPs within a QR code platform leads to the development of a luminescent smart label. This smart label is capable of providing distinct color and temperature outputs upon NIR excitation. Additionally, this manuscript introduces an innovative approach to addressing plastic waste concerns, demonstrating the feasibility of using a solvent derived from renewable sources to print luminescent QR codes.

2 Objective and organization of the thesis

2.1 Objectives

The primary goal of this thesis was to assess high-to-low-density liquid water fluctuations by using luminescence thermometry. To achieve this, comprehensive structural, optical, and thermometric characterization of various luminescent materials was performed. To fulfill the main objective of this thesis, the following secondary goals were established:

i) Evaluate the reliability of the Brownian velocity of upconverting nanoparticles in probing density fluctuations between two liquid states of water.

ii) Identifying how the singular behavior of liquid water impacts the performance of luminescent thermometers.

iii) Enhance the performance of luminescent thermometers either through the development of new materials or the proposal of novel analysis methodologies.

2.2 Organization

This thesis consists of seven original research manuscripts along with their corresponding supporting information. The first manuscript has been submitted and is still under the referees' evaluation while the other six manuscripts have already been peer-reviewed and published in scientific journals with worldwide recognition. The documents within this thesis are presented in a thematic organization rather than following a strict chronological order.

A supplementary report was written following Articles 63 and 64-1 in compliance with the University of Aveiro Studies Regulations. The overall organization of the supplementary report is divided into five chapters. In Chapter 1, the state-of-the-art is presented, overviewing the anomalous behavior of liquid water that motivated the development of this work. Chapter 2 outlines the goals and the overall organization of this thesis. In Chapter 3, the contributions of the author to each research manuscript are summarized and identified. At least, Chapter 4 summarizes the main conclusions drawn from the research carried out, while Chapter 5 provides perspectives about this work.

3 Relevance and original contributions

3.1 Manuscript 1

Title: Deciphering density fluctuations in the hydration water of Brownian nanoparticles via upconversion thermometry

Summary: We investigate the intricate relationship between temperature, pH, and the Brownian velocity in a spectrum of differently sized upconversion nanoparticles (UCNPs) dispersed in water. These UCNPs, acting as nano-rulers, offer insights into assessing the relative proportion of high-density and low-density liquid in the surrounding hydration water. The study reveals a size-dependent reduction in the onset temperature of liquid-water fluctuations, indicating an augmented presence of high-density liquid domains at nanoparticle surfaces. The observed upper-temperature threshold is consistent with a hypothetical phase diagram of water, validating the two-state model. Moreover, an increase in pH disrupts water molecule organization, similar to external pressure effects, allowing simulation of the effects of temperature and pressure on hydrogen bonding networks. The study highlights the versatility of UCNPs as tools to quantify high-to-low-density liquid ratios and sheds light on the intricate interplay between water and diverse interfaces. The findings underscore the significance of the surface-to-volume ratio in suspended nanoparticles or biomolecules for understanding liquid fluctuations and water behavior at charged interfaces.

Novelty:

- The Brownian velocity of 15-nm size nanoparticles dispersed in water, heavy water, and ethanol (so-called nanofluids) was measured, elucidating why the Brownian velocity of the nanoparticles decreases as the solvent density increases.
- The bilinear dependence of the Brownian velocity of the nanoparticles in water was explained. This is attributed to the presence of two distinct motion regimes, regardless of the size of the particles. For temperatures lower than a crossover temperature ($T_c < 330$ K), interpreted for the first time explicitly as the onset temperature of high-to-low density liquid water fluctuations, there are HDL fluctuations into more voluminous LDL regions within the HDL dominant phase. Consequently, this gives rise to a greater effective mass

of the nanoparticles, resulting in lower Brownian velocity values. Conversely, when T_c > 330 K, the density fluctuations cease because all LDL motifs were already converted into HDL ones.

- A pronounced reduction in the T_c values of the nanofluids was observed as the diameter d of the nanoparticles increased. As this value progressively decreases, T_c asymptotically converges towards a limiting value of 331.2 ± 0.2 K. This temperature is interpreted as the onset temperature of the fluctuations between high- and low-density liquid states in pure water (d = 0). Remarkably, this upper-temperature threshold for fluctuations in the region dominated by HDL domains at ambient conditions agrees with previously published data from the hypothetical phase diagram of water under ambient conditions, 325.0 ± 1.0 K. The experimental observation can, thus, support the previous estimation of the upper limit of the "funnel of life" (the region in the abovementioned phase diagram at which water exhibits its unusual properties that are crucial to the maintenance of life).
- The reduction in the T_c values of the aqueous nanofluids, as compared to pure water, was attributed to a decrease in high-to-low-density liquid water fluctuations. This decrease results from the prevalence of a higher concentration of HDL patches relative to LDL regions within the nanofluid volume, which move cooperatively with the nanoparticles. Notably, this result corroborates previous molecular dynamics findings about the HDL/LDL proportion in the hydration water of the lysozyme protein (defined as the water molecules encompassing the protein within a 0.6 nm shell). This is the first experimental evidence pointing out changes in the HDL/LDL proportion in aqueous solutions of electrolytes and suspensions of biomolecules and inorganic materials, compared to pure water.
- Increasing the pH of the aqueous nanofluids disrupted the tetrahedral organization of the LDL regions, akin to the impact of external pressure on pure water. Therefore, raising the pH of the aqueous nanofluids is an ingenious strategy for evaluating the microscopic changes in its H-bond networks by effectively simulating a pressure-like effect.
- Through precise control of both the nanoparticle size and pH levels of the medium, it was possible to simulate the effects of temperature and pressure on the HDL and LDL H-bond networks, mirroring the predictions in the abovementioned hypothesized phase diagram.

- A decrease in the Brownian velocity of the nanoparticles was observed upon rising pH, resulting in the concomitant decrease in the T_c values. This indicates that low-to-high-density liquid fluctuations at the surface of the UCNPs cease at lower temperatures in basic media, compared to an acidic one. This dependence was explained by considering the influence of pH on the surface charge of the nanoparticles.
- While previous experiments have successfully demonstrated how surface charge can influence the structure of water near an interface and how pH adjustments can be employed to investigate this effect, the findings of this work represent the first experimental result revealing a direct correlation: the higher the surface charge, the greater the thermal energy required to initiate HDL-to-LDL fluctuations at the particle interface. Consequently, this results in a greater prevalence of LDL domains within hydration water. These observations indicate that the rate of LDL domain reduction with increasing temperature is more gradual at the interface of a biomolecule.

Contributions: This manuscript showcases most of the research work that I have carried out throughout my doctoral studies. My contributions encompass the colloidal characterization of different-sized upconverting nanoparticles dispersed in water, heavy water, and ethanol, as well as their photoluminescence, assessing their thermometric performance as primary luminescent thermometers capable of measuring the instantaneous ballistic Brownian velocity. In addition to the data treatment and the image editing, I have worked on the writing of the manuscript, actively contributing from its initial draft through to the final submitted version. I have also engaged in a thorough discussion of the results obtained with the co-authors.

3.2 Manuscript 2

Title: Decoding a Percolation Phase Transition of Water at ~330 K with a Nanoparticle Ruler

Summary: Liquid water, despite its simple molecular structure, remains one of the most fascinating and complex substances. Most notably, many questions continue to exist regarding the phase transitions and anomalous properties of water, which are subtle to observe experimentally. Here, we report a sharp transition in water at 330 K unveiled through experimental measurements

of the instantaneous Brownian velocity of $NaYF_4$:Yb/Er upconversion nanoparticles in water. Our experimental investigations, corroborated by molecular dynamics simulations, elucidate a geometrical phase transition where low-density liquid (LDL) clusters become percolated below 330 K. Around this critical temperature, we find the sizes of the LDL clusters to be similar to those of the nanoparticles, confirming the role of the upconversion nanoparticle as a powerful ruler for measuring the extensiveness of the LDL hydrogen-bond network and nanometer-scale spatial changes (20–100 nm) in liquids. Additionally, a new order parameter that unequivocally classifies water molecules into two local geometric states is introduced, providing a new tool for understanding and modeling water's many anomalous properties and phase transitions.

Novelty:

- In this work, anomalous behavior of liquid water at elevated temperatures was observed through the monitoring of upconversion photoluminescence of lanthanide-doped nanoparticles during thermal fluctuation. An abrupt crossover temperature (~330 K) in the instantaneous Brownian velocity of the nanoparticles in water was unambiguously identified. This bilinear alteration in the nanoparticle's velocity, indicative of two distinct Brownian motion regimes at elevated temperatures, was attributed to the nano convection-dominated cooperative movement of the nanoparticles with their neighboring water molecules, suggesting the presence of different effective masses.
- The experimental findings, corroborated by molecular dynamics simulations, unveiled two distinct forms of the hydrogen-bond network in water at elevated temperatures. These observations indicate a geometrical percolation phase transition of water occurring at approximately 330 K, a critical temperature at which the size of the low-density-liquid motif becomes comparable to that of the nanoparticles.
- Two distinct forms of the hydrogen-bond network in water have been identified through molecular dynamics simulations. Specifically, the tetrahedral state and the disturbed state were discerned, as supported by the presence of two distinct peaks in the temperature-dependent probability density function of the tetrahedral orientational order parameter. This is the first computational observation of two well-separated peaks in this widely used probability density function at an elevated temperature regime.

- It has been experimentally demonstrated that the sharp transition in the instantaneous Brownian velocity of the nanoparticle can be reliably detected when the diameter of the nanoparticle is in the range of 24 to 106 nm. Remarkably, despite the considerable size variation of 82 nm, the impact of the nanoparticle-based ruler on the intrinsic behavior of water is negligible. In comparison to experimental techniques involving X-ray irradiation, this upconversion nanoparticle-based ruler emerges as a powerful tool well-suited for investigating the anomalous properties of water, such as thermal conductivity, proton spin-lattice relaxation time, refractive index, and surface tension.

Contributions: In this work, my contributions encompassed several key aspects. Firstly, I have contributed to the colloidal characterization of $NaYF_4$:Yb/Er upconverting nanoparticles, focusing on assessing their stability in aqueous media for measuring the instantaneous ballistic Brownian velocity. Furthermore, I significantly contributed to the development of the algorithm written to estimate the crossover temperature, a critical parameter showing the temperature at which the temperature-dependent Brownian velocity undergoes a substantial change from its linear trend. Additionally, I have participated in several stages of the development of the manuscript, including writing, revising, and proofreading the document from the initial draft to the final round of revision.

3.3 Manuscript 3

Title: Temperature Dependence of Water Absorption in the Biological Windows and Its Impact on the Performance of Ag_2S Luminescent Nanothermometers

Summary: The application of nanoparticles in the biological context generally requires their dispersion in aqueous media. In this sense, luminescent nanoparticles are an excellent choice for minimally invasive imaging and local temperature sensing (nanothermometry). For these applications, nanoparticles must operate in the physiological temperature range (25–50 °C) but also in the near-infrared spectral range (750–1800 nm), which comprises the three biological windows of maximal tissue transparency to photons. In this range, water displays several absorption bands that can strongly affect the optical properties of the nanoparticles. Therefore, a

full understanding of the temperature dependence of water absorption in biological windows is of paramount importance for applications based on these optical properties. Herein, the absorption spectrum of water in the biological windows over the 25–65 °C temperature range is systematically analyzed, and its temperature dependence considering the coexistence of two states of water is interpreted. Additionally, to illustrate the importance of state-of-the-art applications, the effects of the absorption of water on the emission spectrum of Ag_2S nanoparticles, the most sensitive luminescent nanothermometers for in vivo applications to date, are presented. The spectral shape of the nanoparticles' emission is drastically affected by the water absorption, impacting their thermometric performance.

Novelty:

- This manuscript demonstrates the temperature dependence of the water absorption spectrum in the near-infrared, which can be deconvoluted into two components, with each of them explained by the existence of a distinct state of liquid water.
- The strong water absorption in the NIR spectral region imposes challenges in using luminescent nanothermometers operating within the same spectral range, critically impacting the line shape of the emission bands of silver sulfide.
- Despite its status as the best-performing luminescent thermometer for *in vivo* applications, silver sulfide undergoes a reduction in its thermometric reliability when working in aqueous media due to water reabsorption
- A comparison between the thermometric performance of silver sulfide in water and heavy water underscores the necessity for standardization to improve the reproducibility of thermal readouts in biomedical and biological applications.

Contributions: Throughout this work, I have contributed to the assessment of the thermometric performance of various luminescent properties of silver sulfide nanoparticles dispersed in both water and heavy water, in terms of temperature-dependent luminescence, relative thermal sensitivity, and uncertainty in temperature. These evaluations underscored the profound influence of the peculiar behavior of liquid water on the performance of silver sulfide as a reliable thermometer in the near-infrared spectral range. Furthermore, I actively engaged in collaborative

efforts involving manuscript writing, image editing, and meticulous revision of both the main manuscript and its supporting information.

3.4 Manuscript 4

Title: Luminescent Pb-free perovskites: low-cytotoxicity materials for primary thermal sensing

Summary: Selecting a suitable host matrix to perform temperature sensing in biomedical applications requires low cytotoxicity, facile synthesis, and an ability to be doped with light-emitting ions. With this perspective, indium-based halide double perovskites, specifically $Cs_2AgIn_{0.9}Bi_{0.1}Cl_6$, $Cs_2Ag_{0.6}Na_{0.4}InCl_6$, and $Cs_2Ag_{0.6}Na_{0.4}In_{0.9}Bi_{0.1}Cl_6$, were chosen as host materials to develop lanthanide-based primary thermometers due to their low phonon energy and ease of synthesis. The incorporation of Na^+ and Bi^{3+} into the perovskite cubic crystal lattice was confirmed by X-ray diffraction and Raman spectroscopy while the optical properties of both the undoped and Yb^{3+}/Er^{3+} co-doped perovskites were assessed by diffuse reflectance and photoluminescence spectroscopies. The obtained perovskite samples demonstrated excellent thermal stability, with the ability to withstand temperatures as high as 500 °C. A temperature-dependent green emission of Er^{3+} was observed in the co-doped samples upon 980 nm irradiation, yielding a relative thermal sensitivity and uncertainty in temperature values of 1.3% K^{-1} and 0.3 K, respectively. Incorporating the obtained perovskites (0.05 to 0.20 mg mL^{-1}) into L2929 cells as an *in vitro* model resulted in high cell viability, underscoring the benefits of selecting such a low-cytotoxicity material for applications in biological media.

Novelty:

- This is the first work introducing Er^{3+}-based primary thermometers embedded within a lead-free In-based double perovskite host. This approach substantially broadens the potential applications and creates fresh opportunities for these materials.
- The primary Boltzmann thermometer, developed within this research, exhibits a maximum relative thermal sensitivity of 1.3 % K^{-1} and uncertainty in temperature of 0.3 K. Remarkably, these findings align closely with the most recent research in the literature, affirming the reliability and precision of the developed thermometer.

- Through the assessment of perovskites' non-toxicity, evaluated via L929 cell viability through MTT assay, the obtained materials reveal promising potential. These results highlight the possibility of employing perovskite materials in targeted bioimaging and the real-time monitoring of cancer cells.

Contributions: In this work, I conceived the framework for the utilization of Yb^{3+}/Er^{3+} co-doped perovskites as primary luminescent thermometers. Subsequently, I performed the analysis of the temperature-dependent upconverting emission spectra of the synthesized materials. This allowed the investigation of the optical properties and a rigorous assessment of their thermometric performance. In addition to these contributions, I was also actively involved in the conceptualization of the figures, as well as the writing and subsequent revisions of the manuscript.

3.5 Manuscript 5

Title: Extending the Palette of Luminescent Primary Thermometers: Yb^{3+}/Pr^{3+} Co-Doped Fluoride Phosphate Glasses

Summary: The unique tunable properties of glasses make them versatile materials for developing numerous state-of-the-art optical technologies. To design new optical glasses with tailored properties, an extensive understanding of the intricate correlation between their chemical composition and physical properties is mandatory. By harnessing this knowledge, the full potential of vitreous matrices can be unlocked, driving advancements in the field of optical sensors. We herein demonstrate the feasibility of using fluoride phosphate glasses co-doped with trivalent praseodymium (Pr^{3+}) and ytterbium (Yb^{3+}) ions for temperature sensing over a broad range of temperatures. These glasses possess high chemical and thermal stability, working as luminescent primary thermometers that rely on the thermally coupled levels of Pr^{3+} that eliminate the need for recurring calibration procedures. The prepared glasses exhibit a relative thermal sensitivity and uncertainty at a temperature of 1.0% K^{-1} and 0.5 K, respectively, making them highly competitive with the existing luminescent thermometers. Our findings highlight that Pr^{3+}-containing materials are promising for developing cost-effective and accurate temperature probes, taking advantage of

the unique versatility of these vitreous matrices to design the next generation of photonic technologies.

Novelty:

- This work demonstrates that embedding trivalent lanthanide ions, such as Yb^{3+} and Pr^{3+}, into a vitreous network enables the preparation of luminescent glasses operating as luminescent thermometers, with exceptional thermal and chemical stability, which can be molded into various shapes. This finding presents a crucial advantage over conventional thermometers, as the glass materials can be customized to fit a wide range of experimental setups.
- The manuscript presents a novel approach to luminescence thermometry, as it is the first example of a new type of primary luminescent thermometer based on Pr^{3+} ions with the corresponding reduction of self-heating during temperature readouts. Up to now, all the Ln^{3+}-based luminescent primary thermometers are based on the Yb^{3+}/Er^{3+} upconverting emission. The work extends the working principle of luminescent primary thermometers to other lanthanide ions than Er^{3+}, with the added benefit of avoiding temperature deviations arising from laser-induced heating. This outcome broadens the range of available materials for primary luminescent thermometers, enabling researchers to measure temperature in a more diverse set of experimental conditions.

Contributions: My contributions to this research paper encompassed several significant aspects. Firstly, I carried out a thorough analysis of both the thermal and optical properties presented within the manuscript. Furthermore, I have conceived the main idea of using the temperature-dependent luminescence of Pr^{3+} as a primary thermal sensing, eliminating the necessity for laser excitation. I have worked on the writing of the text, image editing, extensive result discussions, and meticulous revision. My contribution extended from the preparation of the initial draft to the final stages of manuscript revision. Due to its significant novelty in the field, this manuscript reached the Supplementary Cover of the Journal.

3.6 Manuscript 6

Title: Going Above and Beyond: A Tenfold Gain in the Performance of Luminescence Thermometers Joining Multiparametric Sensing and Multiple Regression

Summary: Luminescence thermometry has substantially progressed in the last decade, rapidly approaching the performance of concurrent technologies. Performance is usually assessed through the relative thermal sensitivity, S_r, and temperature uncertainty, δT. Until now, the state-of-the-art values at ambient conditions do not exceed maximum S_r of 12.5% K^{-1} and minimum δT of 0.1 K. Although these numbers are satisfactory for most applications, they are insufficient for fields that require lower thermal uncertainties, such as biomedicine. This has motivated the development of materials with an improved thermal response, many of them responding to the temperature through distinct photophysical properties. This paper demonstrates how the performance of multiparametric luminescent thermometers can be further improved by simply applying new analysis routes. The synergy between multiparametric readouts and multiple linear regression makes possible a tenfold improvement in S_r and δT, reaching a world record of 50% K^{-1} and 0.05 K, respectively. This is achieved without requiring the development of new materials or upgrading the detection system as illustrated by using the green fluorescent protein and Ag_2S nanoparticles. These results open a new era in biomedicine thanks to the development of new diagnosis tools based on the detection of super-small temperature fluctuations in living specimens.

Novelty:

- This is the first research work exploring the feasibility of combining several temperature-dependent light-emitting properties to develop multiparametric luminescent thermometers with improved S_r and reduced δT.
- This work pioneers the exploration of combining diverse temperature-dependent light-emitting properties to create multiparametric luminescent thermometers, exhibiting enhanced relative thermal sensitivity while greatly reducing temperature uncertainty.
- By employing a multiple linear regression approach to model the temperature-dependent luminescence of different materials, a remarkable tenfold improvement in both relative

thermal sensitivity and the accuracy of temperature measurements was achieved. This novel methodology promises to revolutionize the reliability of luminescent thermometry.

- This manuscript sets a new world record in luminescence thermometry, achieving impressive values of 50% K^{-1} and 0.05 K for S_r and δT, underscoring the potential of this new approach to redefining the standards in luminescent temperature sensing.

Contributions: For my contribution to this work, I synthesized the enhanced green fluorescent protein and carried out its structural and optical characterization. Additionally, I took the initiative to develop the multiple linear regression approach to take advantage of the protein's multiparametric sensing capabilities. In addition to my experimental and analytical work, I made significant contributions to the manuscript by participating actively in its writing and subsequent revisions. Furthermore, I contributed to extending this innovative approach beyond its initial application, showcasing other classes of materials previously documented in the literature, exemplified by the silver sulfide case. This manuscript was highlighted in the Front Cover of the corresponding issue of the Journal.

3.7 Manuscript 7

Title: Sustainable Smart Tags with Two-Step Verification for Anticounterfeiting Triggered by the Photothermal Response of Upconverting Nanoparticles

Summary: Quick-response (QR) codes are gaining much consideration in recent years due to their simple and fast readability compared with conventional barcodes. QR codes provide increased storage capacity and safer access to information, fostering the development of optical or printed smart tags as preferred tools for the Internet of Things (IoT). Herein, the combination of Yb^{3+}/Er^{3+}-doped $NaGdF_4$ upconverting nanoparticles (UCNPs) with recovered plastic for the fabrication of sustainable screen-printed QR codes is reported. Their photothermal response under distinct power densities of the 980 nm laser irradiation (15–115 W cm^{-2}) induces color-tuning and temperature sensing. This power dependence is exploited to design a double-key molecular keylock accessed by a smartphone camera through the red (*R*), green (*G*), and blue (*B*) (*RGB*) additive color model and upconversion thermometry. The latter is based on the integrated areas of the $^2H_{11/2} \rightarrow {}^4I_{15/2}$ and

$^4S_{3/2} \rightarrow {}^4I_{15/2}$ Er^{3+} transitions using the interconnectivity and integration into the IoT network of the mobile phone to download the temperature calibration curve of the UCNPs from a remote server. These findings illustrate the potential of QR code-bearing UCNPs toward the design of smart tags for mobile optical sensing and anticounterfeiting.

Novelty:

- This is the first manuscript to explore the well-known dependence of the Er^{3+} upconversion under 980 nm irradiation on the laser power density to develop a double-encoded security tag.
- Setting an irradiation power density of 40 $W \cdot cm^{-2}$ and adopting a threshold for R/G = 1, we design the first encoding level of the system. Then, the second encoding level is based on the $^2H_{11/2} \rightarrow {}^4I_{15/2}$ and $^4S_{3/2} \rightarrow {}^4I_{15/2}$ transitions in the green spectral range that enable the absolute temperature determination. The double-keylock system is validated exclusively when $R/G>1$ and $T> 313$ K, concurrently.
- These findings support the working principle of two orthogonal spectral readouts based on the ratiometric spectral encoding of upconverting nanoparticles embedded in luminescent QR codes, corroborating the concept of communicating nanoparticles.

Contributions: In this manuscript, I was in charge of designing and printing the luminescent QR codes, which served as a crucial foundation for the development of the double-key molecular keylock. Additionally, I have prepared the upconverting luminescent inks and conducted the characterizations of the upconverting nanoparticles. Furthermore, I also performed the color analysis methodology using a smartphone, which was a dealbreaker to our experimental approach. Beyond the experimental aspects, I made substantial contributions to the writing of the manuscript and dedicated substantial effort to its thorough revision. It is worth pointing out that this manuscript was featured in the Front Cover of the Journal.

4 Conclusions

Although it is the most used liquid, we know very little about water due to its anomalous behavior at varying temperatures and pressures. The great challenge in deciphering the peculiar properties of water resides in the lack of experimental techniques that can link its microscopical structure to macroscopical observations, making life possible on Earth.

In this sense, this thesis compiles a coherent and relevant set of recent research works reporting on the assessment of structural fluctuations of liquid water at ambient conditions, demonstrating the robustness of upconversion luminescence thermometry as a powerful tool for giving new insights regarding the structure of H-bonding networks in the vicinity of luminescent nanoparticles. The main results from this thesis can be summarized as follows:

- The singular properties of water are explained under the light of a two-state model comprising low-density and high-density liquid motifs. The study of temperature-dependent Brownian velocity of UCNPs revealed the coexistence of LDL and HDL domains in liquid water at ambient conditions, where the LDL ones are virtually nonexistent above a threshold temperature marked by an abrupt change in the linear trend of the UCNPs' Brownian velocity.
- Changing the size of the UCNPs and the pH of the aqueous media play a significant role in the HDL and LDL H-bond networks, reproducing the effects of temperature and pressure on water domains, as predicted by the hypothesized phase diagram of two-state liquid water.
- Luminescent nanomaterials are sensitive to the anomalous behavior of liquid water, either by observing structural fluctuations or changing the thermometric performance.
- Luminescence thermometry stands out as a powerful technique to perform temperature readouts in numerous contexts, regardless of the light-emitting center or the host matrix, which can be further improved by using multiparametric sensing and proposing cutting-edge applications.

The research work carried out within this thesis marks an important advancement in understanding the properties of liquid water at ambient conditions as it introduces luminescence thermometry as a reliable tool, circumventing the use of dispendious and time-consuming experiments, besides avoiding complex data analysis. In addition, this thesis emphasizes the need for developing systematic processes to study the properties of liquid water that make life possible.

5 Perspectives

Despite recent breakthroughs providing significant experimental evidence regarding the existence of two distinct states of H-bonding organization in liquid water, this subject still demands further exploration to untangle the intricacies associated with these two states and their pivotal role in sustaining life on Earth. This is because merely observing the coexistence of LDL and HDL motifs at ambient conditions is insufficient to fully comprehend the anomalous behavior of water, which plays a crucial role in various industrial processes and everyday life. Furthermore, it is imperative to expand the scope of this research to include the study of aqueous media relevant to biological systems, where the complex interactions between water, biomolecules, and electrolytes are of paramount importance. Therefore, given the extensive use of upconversion luminescence thermometry in this thesis to investigate density fluctuations in liquid water, it is essential to address several challenges related to its application. Opportunities for improvement exist both in the field of luminescence thermometry and in the study of aqueous media, and these should be explored to advance our understanding of the behavior of water in different contexts.

While the popularization of luminescence thermometry has grown exponentially in the past decade, it remains common to find research works that misapply this technique. This misapplication often arises from the misconception that performing luminescence thermometry solely involves measuring emission spectra as a function of temperature, with insufficient attention to the fundamental requirements necessary for ensuring the reliability of a luminescent thermometer in delivering accurate temperature readouts. Consequently, significant focus is placed on S_r as a key figure of merit for selecting an appropriate luminescent thermometer, while the associated uncertainties arising from the spectral acquisition and their impact on the determination of temperature uncertainty δT are frequently overlooked [142]. In this context, it is crucial to expedite the dissemination of standardized guidelines for this technique, to promote a more comprehensive and accurate application of luminescence thermometry [67].

Additionally, it is imperative to devote efforts to prevent artifacts in luminescence thermometry, particularly in the case of upconversion. The reason for this concern lies in the fact that under varying experimental conditions, such as Yb^{3+}/Er^{3+} doping concentration and the power density of the 980 nm laser excitation, emission bands that are unrelated to the thermally coupled levels of Er^{3+} may appear. These unexpected emissions can interfere with the accuracy of thermal readings, making it essential to provide analytical tools that can mitigate the overlap between

emission bands in the green spectral range [73, 143]. Furthermore, it is important to note that most studies involving upconversion luminescence thermometry employ the Boltzmann statistics to depict the temperature dependence of luminescence in Yb^{3+}/Er^{3+}-containing materials. This is accomplished through a fitting procedure, enabling the estimation of ΔE and B through Equation 3, from the slope and intercept of the $\ln(\Delta)$ against $1/T$ plot, respectively [92, 144]. However, it is crucial to recognize that this approach, which determines the values of ΔE and B in a temperature-dependent fitting procedure, as in secondary thermometers, should not be used to perform temperature readouts beyond the calibration range. To expand the range of applications for luminescent thermometers, the opportunity to explore alternative Ln^{3+} for the development of novel primary luminescent thermometers should be seized. This strategic choice allows for optimal thermal response to be achieved at distinct temperature ranges, driven by the selection of ions with different values of ΔE [124].

Nevertheless, the reliability and accuracy offered by luminescent thermometry for assessing the local temperature dependence of nanomaterials dispersed in aqueous media present new opportunities for investigating the actual influence of LDL and HDL motifs on the organization of biomolecules, including lipid membranes and proteins. This can be achieved through the functionalization of the surface of the UCNPs with biologically relevant ligands (see, for instance, Reference [145]). Another ingenious strategy could be the use of recombinant proteins that can be modified or conjugated with other biomolecules, such as the well-known green fluorescent protein, which displays a remarkable temperature-dependent luminescent response in the temperature range relevant to physiological applications [146, 147].

Likewise, the consequences of fluctuations between HDL and LDL domains on the transport of electrolytes can be examined by investigating how ionic strength impacts the surface charge of UCNPs and subsequently influences their Brownian velocity. This endeavor will push upconversion primary luminescence thermometry to its limits since the increase in ionic strength of the aqueous media is known to affect the colloidal stability of suspended nanoparticles [148], potentially playing a significant role in their thermometric response.

Bearing all of this in mind, I firmly believe that luminescence thermometry holds a bright future for shedding light (pun intended) on our comprehension of temperature-dependent properties in water, aqueous solutions, and suspensions, and how these factors play a crucial role in shaping life on Earth.

References

[1] M. Chaplin, Opinion - Do we underestimate the importance of water in cell biology? *Nature Reviews Molecular Cell Biology,* vol. 7, no. 11, pp. 861-866, 2006.

[2] P. Ball, Water — an enduring mystery. *Nature,* vol. 452, no. 7185, pp. 291-292, 2008.

[3] P. Gallo *et al.*, Water: A Tale of Two Liquids. *Chemical Reviews,* vol. 116, no. 13, pp. 7463-7500, 2016.

[4] M. C. Bellissent-Funel *et al.*, Water Determines the Structure and Dynamics of Proteins. *Chemical Reviews,* vol. 116, no. 13, pp. 7673-7697, 2016.

[5] E. Brini, C. J. Fennell, M. Fernandez-Serra, B. Hribar-Lee, M. Luksic, and K. A. Dill, How Water's Properties Are Encoded in Its Molecular Structure and Energies. *Chemical Reviews,* vol. 117, no. 19, pp. 12385-12414, 2017.

[6] P. Ball, Water is an active matrix of life for cell and molecular biology. *Proceedings of the National Academy of Sciences,* vol. 114, no. 51, pp. 13327-13335, 2017.

[7] A. Pohorille and L. R. Pratt, Is Water the Universal Solvent for Life? *Origins of Life and Evolution of Biospheres,* vol. 42, no. 5, pp. 405-409, 2012.

[8] C. Goy *et al.*, Shrinking of Rapidly Evaporating Water Microdroplets Reveals their Extreme Supercooling. *Physical Review Letters,* vol. 120, no. 1, p. 015501, 2018.

[9] J. R. Errington and P. G. Debenedetti, Relationship between structural order and the anomalies of liquid water. *Nature,* vol. 409, no. 6818, pp. 318-321, 2001.

[10] M. Chaplin. "Water Structure and Science." https://water.lsbu.ac.uk/water/water_structure_science.html (2017).

[11] A. Nilsson and L. G. M. Pettersson, The structural origin of anomalous properties of liquid water. *Nature Communications,* vol. 6, p. 8998, 2015.

[12] J. Russo, K. Akahane, and H. Tanaka, Water-like anomalies as a function of tetrahedrality. *Proceedings of the National Academy of Sciences,* vol. 115, no. 15, pp. E3333-E3341, 2018.

[13] V. Artemov, *The Electrodynamics of Water and Ice* (Springer Series in Chemical Physics). Cham: Springer International Publishing, 2021.

[14] K. Amann-Winkel *et al.*, X-ray and Neutron Scattering of Water. *Chemical Reviews,* vol. 116, pp. 7570-7589, 2016.

[15] J. Niskanen *et al.*, Compatibility of quantitative X-ray spectroscopy with continuous distribution models of water at ambient conditions. *Proceedings of the National Academy of Sciences,* vol. 116, no. 10, pp. 4058-4063, 2019.

[16] L. G. M. Pettersson, Y. Harada, and A. Nilsson, Do X-ray spectroscopies provide evidence for continuous distribution models of water at ambient conditions? *Proceedings of the National Academy of Sciences,* vol. 116, no. 35, pp. 17156-17157, 2019.

[17] J. Niskanen *et al.*, Reply to Pettersson et al.: Why X-ray spectral features are compatible to continuous distribution models in ambient water. *Proceedings of the National Academy of Sciences,* vol. 116, no. 35, pp. 17158-17159, 2019.

[18] A. K. Soper, Is water one liquid or two? *The Journal of Chemical Physics,* vol. 150, no. 23, p. 234503, 2019.

[19] A. Pietzsch *et al.*, Cuts through the manifold of molecular H_2O potential energy surfaces in liquid water at ambient conditions. *Proceedings of the National Academy of Sciences,* vol. 119, no. 28, p. e2118101119, 2022.

[20] L. G. M. Pettersson, A Two-State Picture of Water and the Funnel of Life. *Springer Proceedings in Physics,* vol. 223, pp. 3-39, 2019.
[21] C. Huang *et al.*, The inhomogeneous structure of water at ambient conditions. *Proceedings of the National Academy of Sciences,* vol. 106, no. 36, pp. 15214-8, 2009.
[22] W. C. Röntgen, Ueber die Constitution des flüssigen Wassers. *Annalen der Physik und Chemie,* vol. 281, pp. 91-97, 1892.
[23] P. H. Poole, F. Sciortino, U. Essmann, and H. E. Stanley, Phase-Behavior of Metastable Water. *Nature,* vol. 360, no. 6402, pp. 324-328, 1992.
[24] J. Russo and H. Tanaka, Understanding water's anomalies with locally favoured structures. *Nature Communications,* vol. 5, p. 3556, 2014.
[25] F. Martelli, Unravelling the contribution of local structures to the anomalies of water: The synergistic action of several factors. *The Journal of Chemical Physics,* vol. 150, no. 9, p. 094506, 2019.
[26] Y. T. Gao, H. W. Fang, K. Ni, and Y. X. Feng, Water clusters and density fluctuations in liquid water based on extended hierarchical clustering methods. *Scientific Reports,* vol. 12, no. 1, p. 8036, 2022.
[27] P. M. C. de Oliveira, J. I. R. de Souza, J. A. B. da Silva, and R. L. Longo, Temperature Dependence of Hydrogen Bond Networks of Liquid Water: Thermodynamic Properties and Structural Heterogeneity from Topological Descriptors. *Journal of Physical Chemistry B,* vol. 127, no. 10, pp. 2250-2257, 2023.
[28] P. Wernet *et al.*, The Structure of the First Coordination Shell in Liquid Water. *Science,* vol. 304, pp. 995-999, 2004.
[29] T. Tokushima *et al.*, High resolution X-ray emission spectroscopy of liquid water: The observation of two structural motifs. *Chemical Physics Letters,* vol. 460, no. 4-6, pp. 387-400, 2008.
[30] Y. Harada *et al.*, Selective Probing of the OH or OD Stretch Vibration in Liquid Water Using Resonant Inelastic Soft-X-Ray Scattering. *Physical Review Letters,* vol. 111, p. 193001, 2013.
[31] L. B. Skinner, C. J. Benmore, J. C. Neuefeind, and J. B. Parise, The structure of water around the compressibility minimum. *The Journal of Chemical Physics,* vol. 141, no. 21, p. 214507, 2014.
[32] J. A. Sellberg *et al.*, Ultrafast X-ray probing of water structure below the homogeneous ice nucleation temperature. *Nature,* vol. 510, no. 7505, pp. 381-4, 2014.
[33] L. M. Maestro *et al.*, On the existence of two states in liquid water: impact on biological and nanoscopic systems. *International Journal of Nanotechnology,* vol. 13, no. 8-9, pp. 667-677, 2016.
[34] J. N. Stern, M. Seidl-Nigsch, and T. Loerting, Evidence for high-density liquid water between 0.1 and 0.3 GPa near 150 K. *Proceedings of the National Academy of Sciences,* vol. 116, no. 19, pp. 9191-9196, 2019.
[35] R. Shi and H. Tanaka, Direct Evidence in the Scattering Function for the Coexistence of Two Types of Local Structures in Liquid Water. *Journal of the American Chemical Society,* vol. 142, pp. 2868-2875, 2020.
[36] P. Papon, J. Leblond, and P. H. E. Meijer, "The Physics of Phase Transitions," P. Papon, J. Leblond, and P. H. E. Meijer, Eds., 2nd ed. Berlin, Heidelberg: Springer Berlin Heidelberg, 2006, pp. 1-409.

[37] P. Atkins and J. de Paula, "Atkins' Physical Chemistry," 9th ed. Oxford: Oxford University Press, 2010, p. 1060.
[38] G. Jaeger, The Ehrenfest Classification of Phase Transitions: Introduction and Evolution. *Archive for History of Exact Sciences,* vol. 53, no. 1, pp. 51-81, 1998.
[39] O. Sarig, "Continuous Phase Transitions for Dynamical Systems," in *Communications in Mathematical Physics* vol. 267, ed, 2006, pp. 631-667.
[40] S. Fanetti *et al.*, Structure and Dynamics of Low-Density and High-Density Liquid Water at High Pressure. *The Journal of Physical Chemistry Letters,* vol. 5, pp. 235-240, 2014.
[41] K. Oka *et al.*, Two States of Water Converge to One State below 215 K. *The Journal of Physical Chemistry Letters,* vol. 12, no. 24, pp. 5802-5806, 2021.
[42] L. Kringle, W. A. Thornley, B. D. Kay, and G. A. Kimmel, Reversible structural transformations in supercooled liquid water from 135 to 245 K. *Science,* vol. 369, no. 6510, pp. 1490-1492, 2020.
[43] Y. Suzuki, Experimental estimation of the location of liquid-liquid critical point for polyol aqueous solutions. *The Journal of Chemical Physics,* vol. 149, no. 20, p. 204501, 2018.
[44] Y. Suzuki, Direct observation of reversible liquid-liquid transition in a trehalose aqueous solution. *Proceedings of the National Academy of Sciences,* vol. 119, no. 5, 2022.
[45] G. Camisasca, D. Schlesinger, I. Zhovtobriukh, G. Pitsevich, and L. G. M. Pettersson, A proposal for the structure of high- and low-density fluctuations in liquid water. *The Journal of Chemical Physics,* vol. 151, no. 3, p. 034508, 2019.
[46] O. Mishima and H. E. Stanley, The relationship between liquid, supercooled and glassy water. *Nature,* vol. 396, no. 6709, pp. 329-335, 1998.
[47] H. E. Stanley, "Mysteries of Water," in *Hydration Processes in Biology: Theoretical and Experimental Approaches, Proceedings of the NATO Advanced Study Institute*, vol. 305, M.-C. Bellissent-Funel Ed., no. NATO Science Series: Life Sciences). Amsterdam: IOS Press, 1999.
[48] K. H. Kim *et al.*, Maxima in the thermodynamic response and correlation functions of deeply supercooled water. *Science,* vol. 358, no. 6370, pp. 1589-1593, 2017.
[49] L. Xu *et al.*, Relation between the Widom line and the dynamic crossover in systems with a liquid-liquid phase transition. *Proceedings of the National Academy of Sciences,* vol. 102, pp. 16558-16562, 2005.
[50] A. Rosu-Finsen *et al.*, Medium-density amorphous ice. *Science,* vol. 379, no. 6631, pp. 474-478, 2023.
[51] Q. Sun, Local statistical interpretation for water structure. *Chemical Physics Letters,* vol. 568-569, pp. 90-94, 2013.
[52] T. Morawietz, O. Marsalek, S. R. Pattenaude, L. M. Streacker, D. Ben-Amotz, and T. E. Markland, The Interplay of Structure and Dynamics in the Raman Spectrum of Liquid Water over the Full Frequency and Temperature Range. *The Journal of Physical Chemistry Letters,* vol. 9, no. 4, pp. 851-857, 2018.
[53] Y. Maréchal, The molecular structure of liquid water delivered by absorption spectroscopy in the whole IR region completed with thermodynamics data. *Journal of Molecular Structure,* vol. 1004, no. 1-3, pp. 146-155, 2011.
[54] A. Taschin, P. Bartolini, R. Eramo, R. Righini, and R. Torre, Evidence of two distinct local structures of water from ambient to supercooled conditions. *Nature Communications,* vol. 4, p. 2401, 2013.

[55] I. Zhovtobriukh, N. A. Besley, T. Fransson, A. Nilsson, and L. G. M. Pettersson, Relationship between X-ray emission and absorption spectroscopy and the local H-bond environment in water. *The Journal of Chemical Physics,* vol. 148, no. 14, p. 144507, 2018.
[56] P. Wiggins, Life depends upon two kinds of water. *PLoS One,* vol. 3, no. 1, p. e1406, 2008.
[57] J. C. del Valle *et al.*, Dielectric anomalous response of water at 60 °C. *Philosophical Magazine,* vol. 95, pp. 683-690, 2015.
[58] T. Muñoz-Ortiz *et al.*, Temperature Dependence of Water Absorption in the Biological Windows and Its Impact on the Performance of Ag_2S Luminescent Nanothermometers. *Particle & Particle Systems Characterization,* vol. 39, no. 11, p. 2200100, 2022.
[59] L. Labrador-Páez *et al.*, Effect of H_2O and D_2O Thermal Anomalies on the Luminescence of Eu^{3+} Aqueous Complexes. *The Journal of Physical Chemistry C,* vol. 122, no. 26, pp. 14838-14845, 2018.
[60] L. Labrador-Páez *et al.*, pH dependence of water anomaly temperature investigated by Eu(III) cryptate luminescence. *Analytical and Bioanalytical Chemistry,* vol. 412, pp. 73-80, 2020.
[61] L. Labrador-Páez, U. Kostiv, J. Widengren, and H. C. Liu, Water: An Influential Agent for Lanthanide-Doped Luminescent Nanoparticles in Nanomedicine. *Advanced Optical Materials,* vol. 11, no. 11, p. 2200513, 2022.
[62] J. Catalan and J. A. Gonzalo, Liquid water changes its structure at 43 °C. *Chemical Physics Letters,* vol. 679, pp. 86-89, 2017.
[63] J. Catalan and J. C. Del Valle, Molecule 1-Methyl-5-nitroindoline Probes the Structural Change of Liquid Water with Temperature. *ACS Omega,* vol. 3, no. 12, pp. 18930-18934, 2018.
[64] Y.-H. Cheng, H.-C. Yang, and P.-T. Chou, Could Chemical Reaction at the Molecular Level Show Distinction between Two Liquid-Water States? Study of the Excited-State Water-Catalyzed Proton Transfer Reaction Provides a Clue. *The Journal of Physical Chemistry Letters,* vol. 11, no. 21, pp. 9468-9475, 2020.
[65] C. D. S. Brites *et al.*, Decoding a Percolation Phase Transition of Water at ∼330 K with a Nanoparticle Ruler. *The Journal of Physical Chemistry Letters,* vol. 11, no. 16, pp. 6704-6711, 2020.
[66] D. Jaque and F. Vetrone, Luminescence nanothermometry. *Nanoscale,* vol. 4, no. 15, pp. 4301-26, 2012.
[67] A. Bednarkiewicz, L. Marciniak, L. D. Carlos, and D. Jaque, Standardizing luminescence nanothermometry for biomedical applications. *Nanoscale,* vol. 12, no. 27, pp. 14405-14421, 2020.
[68] C. D. S. Brites *et al.*, Spotlight on Luminescence Thermometry: Basics, Challenges, and Cutting-Edge Applications. *Advanced Materials,* vol. 35, no. 36, p. e2302749, 2023.
[69] C. Paviolo, A. H. Clayton, S. L. McArthur, and P. R. Stoddart, Temperature measurement in the microscopic regime: a comparison between fluorescence lifetime- and intensity-based methods. *Journal of Microscopy,* vol. 250, no. 3, pp. 179-88, 2013.
[70] L. D. Carlos and F. Palacio, Eds. *Thermometry at the Nanoscale: Techniques and Selected Applications* (Nanoscience & Nanotechnology Series). The Royal Society of Chemistry, 2015.
[71] Y. Shen *et al.*, Reliable and Remote Monitoring of Absolute Temperature during Liver Inflammation via Luminescence-Lifetime-Based Nanothermometry. *Advanced Materials,* vol. 34, no. 7, p. e2107764, 2022.

[72] M. Y. Berezin and S. Achilefu, Fluorescence lifetime measurements and biological imaging. *Chemical Reviews,* vol. 110, no. 5, pp. 2641-84, 2010.
[73] J. C. Martins, A. R. N. Bastos, R. A. S. Ferreira, X. Wang, G. Y. Chen, and L. D. Carlos, Primary Luminescent Nanothermometers for Temperature Measurements Reliability Assessment. *Advanced Photonics Research,* vol. 2, no. 5, p. 2000169, 2021.
[74] Q. Han, W. Wu, W. Liu, and Y. Yang, The peak shift and evolution of upconversion luminescence from $CsPbBr_3$ nanocrystals under femtosecond laser excitation. *RSC Advances,* vol. 7, no. 57, pp. 35757-35764, 2017.
[75] H. Lu *et al.*, Ultranarrow NIR bandwidth and temperature sensing of YOF:Yb^{3+}/Tm^{3+} phosphor in low temperature range. *Journal of Luminescence,* vol. 206, pp. 613-617, 2019.
[76] A. S. Laia *et al.*, Comparing the performance of Nd^{3+}-doped LiBaPO4 phosphors as optical temperature sensors within the first biological window exploiting luminescence intensity ratio and bandwidth methods. *Journal of Luminescence,* vol. 227, p. 117524, 2020.
[77] C. D. Brites *et al.*, Thermometry at the nanoscale. *Nanoscale,* vol. 4, no. 16, pp. 4799-829, 2012.
[78] C. D. S. Brites, S. Balabhadra, and L. D. Carlos, Lanthanide-Based Thermometers: At the Cutting-Edge of Luminescence Thermometry. *Advanced Optical Materials,* vol. 7, no. 5, p. 1801239, 2019.
[79] Y. Shen *et al.*, Ag_2S Nanoheaters with Multiparameter Sensing for Reliable Thermal Feedback during In Vivo Tumor Therapy. *Advanced Functional Materials,* vol. 30, no. 49, p. 2002730, 2020.
[80] J. Periša *et al.*, Multiparametric luminescence thermometry from Dy^{3+}, Cr^{3+} double activated YAG. *Journal of Luminescence,* vol. 238, p. 118306, 2021.
[81] J. Perisa, Z. Ristic, W. Piotrowski, Z. Antic, L. Marciniak, and M. D. Dramicanin, All near-infrared multiparametric luminescence thermometry using Er^{3+}, Yb^{3+}-doped YAG nanoparticles. *RSC Adv,* vol. 11, no. 26, pp. 15933-15942, 2021.
[82] K. Trejgis, M. D. Dramićanin, and L. Marciniak, Highly sensitive multiparametric luminescent thermometer for biologically-relevant temperatures based on Mn^{4+}, Ln^{3+} co-doped $SrTiO_3$ nanocrystals. *Journal of Alloys and Compounds,* vol. 875, p. 159973, 2021.
[83] F. E. Maturi *et al.*, Going Above and Beyond: A Tenfold Gain in the Performance of Luminescence Thermometers Joining Multiparametric Sensing and Multiple Regression. *Laser & Photonics Reviews,* vol. 15, no. 11, p. 2100301, 2021.
[84] S. Balabhadra, M. L. Debasu, C. D. S. Brites, R. A. S. Ferreira, and L. D. Carlos, Upconverting Nanoparticles Working As Primary Thermometers In Different Media. *The Journal of Physical Chemistry C,* vol. 121, no. 25, pp. 13962-13968, 2017.
[85] C. D. S. Brites, E. D. Martinez, R. R. Urbano, C. Rettori, and L. D. Carlos, Self-Calibrated Double Luminescent Thermometers Through Upconverting Nanoparticles. *Frontiers in Chemistry,* vol. 7, p. 267, 2019.
[86] S. Uchiyama, N. Kawai, A. P. de Silva, and K. Iwai, Fluorescent polymeric AND logic gate with temperature and pH as inputs. *Journal of the American Chemical Society,* vol. 126, no. 10, pp. 3032-3, 2004.
[87] C. Gota, K. Okabe, T. Funatsu, Y. Harada, and S. Uchiyama, Hydrophilic fluorescent nanogel thermometer for intracellular thermometry. *Journal of the American Chemical Society,* vol. 131, no. 8, pp. 2766-7, 2009.
[88] Y. Wu, J. Liu, J. Ma, Y. Liu, Y. Wang, and D. Wu, Ratiometric Nanothermometer Based on Rhodamine Dye-Incorporated F127-Melamine-Formaldehyde Polymer Nanoparticle:

Preparation, Characterization, Wide-Range Temperature Sensing, and Precise Intracellular Thermometry. *ACS Applied Materials & Interfaces,* vol. 8, no. 23, pp. 14396-405, 2016.
[89] O. A. Savchuk, O. F. Silvestre, R. M. R. Adao, and J. B. Nieder, GFP fluorescence peak fraction analysis based nanothermometer for the assessment of exothermal mitochondria activity in live cells. *Scientific Reports,* vol. 9, no. 1, p. 7535, 2019.
[90] S. Kalytchuk, O. Zhovtiuk, S. V. Kershaw, R. Zboril, and A. L. Rogach, Temperature-Dependent Exciton and Trap-Related Photoluminescence of CdTe Quantum Dots Embedded in a NaCl Matrix: Implication in Thermometry. *Small,* vol. 12, no. 4, pp. 466-76, 2016.
[91] T. Amiaud, V. Jubera, and H. Serier-Brault, A new highly sensitive cryogenic luminescent MOF thermometer built with pyromellitic acid. *Journal of Materials Chemistry C,* vol. 11, no. 32, pp. 10951-10956, 2023.
[92] M. D. Dramicanin, Sensing temperature via downshifting emissions of lanthanide-doped metal oxides and salts. A review. *Methods and Applications in Fluorescence,* vol. 4, no. 4, p. 042001, 2016.
[93] P. Bolek, J. Zeler, C. D. S. Brites, J. Trojan-Piegza, L. D. Carlos, and E. Zych, Ga-modified YAG:Pr^{3+} dual-mode tunable luminescence thermometers. *Chemical Engineering Journal,* vol. 421, p. 129764, 2021.
[94] R. Pinol *et al.*, Real-Time Intracellular Temperature Imaging Using Lanthanide-Bearing Polymeric Micelles. *Nano Letters,* vol. 20, no. 9, pp. 6466-6472, 2020.
[95] K. M. N. de Souza *et al.*, Novel and High-Sensitive Primary and Self-Referencing Thermometers Based on the Excitation Spectra of Lanthanide Ions. *Advanced Optical Materials,* vol. 10, no. 19, 2022.
[96] J. Drabik and L. Marciniak, $KLaP_4O_{12}$:Tb^{3+} Nanocrystals for Luminescent Thermometry in a Single-Band-Ratiometric Approach. *ACS Applied Nano Materials,* vol. 3, no. 4, pp. 3798-3806, 2020.
[97] T. P. van Swieten *et al.*, A Ho^{3+}-Based Luminescent Thermometer for Sensitive Sensing over a Wide Temperature Range. *Advanced Optical Materials,* vol. 9, no. 1, 2020.
[98] K. Saidi, M. Dammak, K. Soler-Carracedo, and I. R. Martin, A novel optical thermometry strategy based on emission of Tm^{3+}/Yb^{3+} codoped $Na_3GdV_2O_8$ phosphors. *Dalton Transactions,* vol. 51, no. 13, pp. 5108-5117, 2022.
[99] C. D. S. Brites, A. Millán, and L. D. Carlos, "Chapter 281 - Lanthanides in Luminescent Thermometry," in *Handbook on the Physics and Chemistry of Rare Earths*, vol. 49, B. Jean-Claude and P. Vitalij K Eds.: Elsevier, 2016, pp. 339-427.
[100] J. C. Bunzli, Benefiting from the unique properties of lanthanide ions. *Accounts of Chemical Research,* vol. 39, no. 1, pp. 53-61, 2006.
[101] K. Binnemans and C. Görller-Walrand, On the color of the trivalent lanthanide ions. *Chemical Physics Letters,* vol. 235, no. 3-4, pp. 163-174, 1995.
[102] K. Binnemans, Lanthanide-based luminescent hybrid materials. *Chemical Reviews,* vol. 109, no. 9, pp. 4283-374, 2009.
[103] J. Yan, B. Li, P. Yang, J. Lin, and Y. Dai, Progress in Light-Responsive Lanthanide Nanoparticles toward Deep Tumor Theranostics. *Advanced Functional Materials,* vol. 31, no. 42, 2021.
[104] G. Tessitore, G. A. Mandl, S. L. Maurizio, M. Kaur, and J. A. Capobianco, The role of lanthanide luminescence in advancing technology. *RSC Advances,* vol. 13, no. 26, pp. 17787-17811, 2023.

[105] X. Chen, T. Sun, and F. Wang, Lanthanide-Based Luminescent Materials for Waveguide and Lasing. *Chemistry An Asian Journal,* vol. 15, no. 1, pp. 21-33, 2020.
[106] D. Manzani, J. F. Petruci, K. Nigoghossian, A. A. Cardoso, and S. J. Ribeiro, A portable luminescent thermometer based on green up-conversion emission of Er^{3+}/Yb^{3+} co-doped tellurite glass. *Scientific Reports,* vol. 7, p. 41596, 2017.
[107] X. Qiu, J. Xu, M. Cardoso Dos Santos, and N. Hildebrandt, Multiplexed Biosensing and Bioimaging Using Lanthanide-Based Time-Gated Forster Resonance Energy Transfer. *Accounts of Chemical Research,* vol. 55, no. 4, pp. 551-564, 2022.
[108] H. Dong *et al.*, Lanthanide Nanoparticles: From Design toward Bioimaging and Therapy. *Chemical Reviews,* vol. 115, no. 19, pp. 10725-815, 2015.
[109] J. B. Lu, X. L. Jiang, H. S. Hu, and J. Li, Norm-Conserving 4f-in-Core Pseudopotentials and Basis Sets Optimized for Trivalent Lanthanides (Ln = Ce-Lu). *Journal of Chemical Theory and Computation,* vol. 19, no. 1, pp. 82-96, 2023.
[110] L. D. Carlos, R. A. Ferreira, Z. Bermudez Vde, and S. J. Ribeiro, Lanthanide-containing light-emitting organic-inorganic hybrids: a bet on the future. *Advanced Materials,* vol. 21, no. 5, pp. 509-34, 2009.
[111] P. Agbo and R. J. Abergel, Ligand-Sensitized Lanthanide Nanocrystals: Merging Solid-State Photophysics and Molecular Solution Chemistry. *Inorganic Chemistry,* vol. 55, no. 20, pp. 9973-9980, 2016.
[112] P. Egger, P. Rogin, T. Riedener, H. U. Güdel, M. S. Wickleder, and J. Hulliger, Ba_2ErCl_7—a new near IR to near UV upconversion material. *Advanced Materials,* vol. 8, no. 8, pp. 668-672, 2004.
[113] J. Zhou, Q. Liu, W. Feng, Y. Sun, and F. Li, Upconversion luminescent materials: advances and applications. *Chemical Reviews,* vol. 115, no. 1, pp. 395-465, 2015.
[114] Y. Lei *et al.*, Upconversion luminescence, intensity saturation effect, and thermal effect in $Gd_2O_3:Er^{3+},Yb^{3+}$ nanowires. *The Journal of Chemical Physics,* vol. 123, no. 17, p. 174710, 2005.
[115] J. Shan, W. Kong, R. Wei, N. Yao, and Y. Ju, An investigation of the thermal sensitivity and stability of the β-$NaYF_4$:Yb,Er upconversion nanophosphors. *Journal of Applied Physics,* vol. 107, no. 5, 2010.
[116] M. V. DaCosta, S. Doughan, Y. Han, and U. J. Krull, Lanthanide upconversion nanoparticles and applications in bioassays and bioimaging: a review. *Analytica Chimica Acta,* vol. 832, pp. 1-33, 2014.
[117] J. F. Suyver, J. Grimm, M. K. van Veen, D. Biner, K. W. Krämer, and H. U. Güdel, Upconversion spectroscopy and properties of NaYF4 doped with Er^{3+},Tm^{3+} and/or Yb^{3+}. *Journal of Luminescence,* vol. 117, no. 1, pp. 1-12, 2006.
[118] M. Haase and H. Schafer, Upconverting nanoparticles. *Angewandte Chemie International Edition,* vol. 50, no. 26, pp. 5808-29, 2011.
[119] J. Chen and J. X. Zhao, Upconversion nanomaterials: synthesis, mechanism, and applications in sensing. *Sensors,* vol. 12, no. 3, pp. 2414-35, 2012.
[120] M. Bettinelli, L. D. Carlos, and X. G. Liu, Lanthanide-doped upconversion nanoparticles. *Physics Today,* vol. 68, no. 9, pp. 38-44, 2015.
[121] G. Chen, H. Qiu, P. N. Prasad, and X. Chen, Upconversion nanoparticles: design, nanochemistry, and applications in theranostics. *Chemical Reviews,* vol. 114, no. 10, pp. 5161-214, 2014.

[122] K. Malhotra *et al.*, Lanthanide-Doped Upconversion Nanoparticles: Exploring A Treasure Trove of NIR-Mediated Emerging Applications. *ACS Applied Materials & Interfaces,* vol. 15, no. 2, pp. 2499-2528, 2023.
[123] R. Shi and A.-V. Mudring, Phonon-Mediated Nonradiative Relaxation in Ln^{3+}-Doped Luminescent Nanocrystals. *ACS Materials Letters,* vol. 4, no. 10, pp. 1882-1903, 2022.
[124] M. Suta and A. Meijerink, A Theoretical Framework for Ratiometric Single Ion Luminescent Thermometers—Thermodynamic and Kinetic Guidelines for Optimized Performance. *Advanced Theory and Simulations,* vol. 3, no. 12, p. 2000176, 2020.
[125] L. Blois *et al.*, On the Experimental Determination of 4f–4f Intensity Parameters from the Emission Spectra of Europium (III) Compounds. *Optics and Spectroscopy,* vol. 130, no. 1, pp. 10-17, 2022.
[126] B. R. Judd, Optical Absorption Intensities of Rare-Earth Ions. *Physical Review,* vol. 127, no. 3, pp. 750-761, 1962.
[127] G. S. Ofelt, Intensities of Crystal Spectra of Rare-Earth Ions. *The Journal of Chemical Physics,* vol. 37, no. 3, pp. 511-520, 1962.
[128] J. Fischer, Low uncertainty Boltzmann constant determinations and the kelvin redefinition. *Philosophical Transactions of the Royal Society A: Mathematical, Physical and Engineering Sciences,* vol. 374, no. 2064, p. 20150038, 2016.
[129] C. D. S. Brites, S. V. Kuznetsov, V. A. Konyushkin, A. N. Nakladov, P. P. Fedorov, and L. D. Carlos, Simultaneous Measurement of the Emission Quantum Yield and Local Temperature: The Illustrative Example of SrF_2:Yb^{3+}/Er^{3+} Single Crystals. *European Journal of Inorganic Chemistry,* vol. 2020, no. 17, pp. 1555-1561, 2020.
[130] R. Brown, XXVII. A brief account of microscopical observations made in the months of June, July and August 1827, on the particles contained in the pollen of plants; and on the general existence of active molecules in organic and inorganic bodies. *The Philosophical Magazine,* vol. 4, no. 21, pp. 161-173, 2009.
[131] A. Einstein, Über die von der molekularkinetischen Theorie der Wärme geforderte Bewegung von in ruhenden Flüssigkeiten suspendierten Teilchen. *Annalen der Physik,* vol. 322, no. 8, pp. 549-560, 1905.
[132] P. Adumeau, C. Gaillard, D. Boyer, J. L. Canet, A. Gautier, and R. Mahiou, Two-Photon Absorption Properties of Eu^{3+}-DPA-Triazolyl Complexes and the Derived Silica Nanoparticles Embedding These Complexes. *European Journal of Inorganic Chemistry,* vol. 2015, no. 7, pp. 1233-1242, 2014.
[133] M. von Smoluchowski, Zur kinetischen Theorie der Brownschen Molekularbewegung und der Suspensionen. *Annalen der Physik,* vol. 326, no. 14, pp. 756-780, 1906.
[134] X. Bian, C. Kim, and G. E. Karniadakis, 111 years of Brownian motion. *Soft Matter,* vol. 12, no. 30, pp. 6331-46, 2016.
[135] A. Einstein, Theoretische Bemerkungen Über die Brownsche Bewegung. *Zeitschrift für Elektrotechnik und Elektrochemie,* vol. 13, no. 6, pp. 41-42, 1907.
[136] C. D. Brites *et al.*, Instantaneous ballistic velocity of suspended Brownian nanocrystals measured by upconversion nanothermometry. *Nature Nanotechnology,* vol. 11, no. 10, pp. 851-856, 2016.
[137] D. S. Lu *et al.*, Exploring Single-Nanoparticle Dynamics at High Temperature by Optical Tweezers. *Nano Letters,* vol. 20, no. 11, pp. 8024-8031, 2020.
[138] K. Kroy, Levitating nanoparticles: Non-equilibrium nano-thermometry. *Nature Nanotechnology,* vol. 9, no. 6, pp. 415-7, 2014.

[139] L. N. Passini *et al.*, Luminescent Pb-free perovskites: low-cytotoxicity materials for primary thermal sensing. *Journal of Materials Chemistry C,* vol. 11, no. 23, pp. 7672-7681, 2023.
[140] F. E. Maturi *et al.*, Extending the Palette of Luminescent Primary Thermometers: Yb^{3+}/Pr^{3+} Co-Doped Fluoride Phosphate Glasses. *Chemistry of Materials,* vol. 35, no. 17, pp. 7229-7238, 2023.
[141] D. Aiello *et al.*, Blue-emitting mesoporous films prepared via incorporation of luminescent Schiff base zinc(II) complex. *Journal of Sol-Gel Science and Technology,* vol. 47, no. 3, pp. 283-289, 2008.
[142] T. P. van Swieten, A. Meijerink, and F. T. Rabouw, Impact of Noise and Background on Measurement Uncertainties in Luminescence Thermometry. *ACS Photonics,* vol. 9, no. 4, pp. 1366-1374, 2022.
[143] J. A. O. Galindo, A. R. Pessoa, Y. E. Serge-Correales, S. J. L. Ribeiro, L. D. Menezes, and A. M. Amaral, Method for separating spectrally overlapping multiphoton upconverted emission bands through spectral power dependence analysis. *Journal of Luminescence,* vol. 257, 2023.
[144] R. S. Pugina, D. L. da Silva, A. Riul, M. L. da Silva-Neto, A. S. L. Gomes, and J. M. A. Caiut, Silk fibroin-Yb/Er:YAG composite films and their thermometric applications based on up-conversion luminescence. *Polymer,* vol. 241, 2022.
[145] A. R. N. Bastos *et al.*, Thermal properties of lipid bilayers derived from the transient heating regime of upconverting nanoparticles. *Nanoscale,* vol. 12, no. 47, pp. 24169-24176, 2020.
[146] S. Kiyonaka *et al.*, Genetically encoded fluorescent thermosensors visualize subcellular thermoregulation in living cells. *Nature Methods,* vol. 10, no. 12, pp. 1232-8, 2013.
[147] C. Di Rienzo, V. Piazza, E. Gratton, F. Beltram, and F. Cardarelli, Probing short-range protein Brownian motion in the cytoplasm of living cells. *Nature Communications,* vol. 5, p. 5891, 2014.
[148] S. Bhattacharjee, DLS and zeta potential - What they are and what they are not? *Journal of Controlled Release,* vol. 235, pp. 337-351, 2016.